

**Synthesis and Characterisation of Stable Fluorescent Silicon
Nanoclusters Produced Using Liquid Jet Method**

Thesis submitted for the degree of
Doctor of Philosophy
at the University of Leicester

by

Hanieh Yazdanfar MSc Physics
Condensed Matter Physics Group
Department of Physics and Astronomy
University of Leicester

August 2015

Synthesis and Characterisation of Stable Fluorescent Silicon Nanoclusters Produced Using Liquid Jet Method

Hanieh Yazdanfar

Abstract

Fluorescent silicon nanoclusters were produced via a novel liquid jet method (using water or alcohols). The jet initially passes through a plume of atomized silicon in vacuum. The silicon atoms are captured in the jet, which then agglomerate to nanoclusters, and are ultimately deposited on a cold trap. In this method, several millilitres of sample can be produced in only a few minutes.

AFM measurements show the nanoclusters produced have a size of ~1 nm. Samples can be produced in different solvents such as water, ethanol, and isopropanol. Fluorescence emission spectra showed two different fluorescence peaks at 310 nm and 365 - 440 nm; the former is constant, but the latter's wavelength is highly dependent on the solvent used. This strong solvent sensitivity showed that fluorescence originated from an electronic state localized on the cluster surface.

Measurements over long time periods prove these fluorescent particles are chemically and optically stable in solution over several years without further [chemical] stabilization. Samples of silicon deposited in water jets showed a fluorescence quantum yield of 8 - 10% three years after production.

Solvent exchange shows the wavelength of fluorescent peaks not only depends on the chemical reactions of silicon particles on/in the liquid jet during nanocluster growth, but also in the solvents in which the nanoclusters were solvated. Solvent transfer experiments show fluorescence peaks shift depending on solvent in a reversible manner. A sample transferred to a specific solvent is equivalent to a sample directly deposited in that solvent.

Nanocluster fluorescence lifetime measurements show decay times of a few nanoseconds (between 3.7 to 5.6 ns) that depend on the solvent; Si-water samples have shorter lifetimes with respect to alcoholic samples.

Film samples produced by evaporating the solvent show the first and second fluorescence peaks at ~300 - 310 nm and at 420 - 440 nm, respectively. Film samples present longer fluorescence lifetimes and higher fluorescence intensities than liquid samples. Changing the temperature shows the particles have a shorter fluorescence lifetime at higher temperatures and fluorescence intensity decreases with increasing temperature.

Chemical analysis of nanoparticles using XPS and ATR revealed that practically all the silicon was oxidized, and clusters produced in water are in the highest oxidation states. Also, the number of silicon particles which interact with the solvent is greater in water than in alcohols. Infrared absorption bands were attributed to SiOH, SiH, SiO, SiO₂ and SiO_x ($x > 2$) species. The solvent exchange experiments suggest that several stable forms of silicon nanoclusters in different oxidation states exist in solution. These can be interchanged by reversible reduction and oxidation depending on the solvent. Our observations suggest that an intrinsically stable form of silicon nanocluster in water exists, and that the deep-blue fluorescence we observed emerges from oxygen-rich states.

Acknowledgement

Firstly, I would like to thank my supervisor Dr. Klaus von Haeften, for welcoming me into his group at the university of Leicester, and express my acknowledgement and respect to him for his great supervision, advice, helping me in understanding the subject, and he granted his time kindly even for answering some of my basic questions, and spent a lot of time to read my thesis.

I am very grateful to Dr. Mark Watkins for a lot of hours he patiently spent reading the drafts of my thesis, and for his considered guidance and instructive scientific discussion as well as discussion on the English language of my thesis.

I extremely acknowledge Mr. Stuart Thornton for his great technical help and immense technical expertise in the lab, and also for his kind miscellaneous assistance during my study.

I appreciate Dr. Steve Baker for his kindly advice and assistance. I would also like to thank all members of CMP group for helping me in my project and their friendly behaviour and nice co-operation.

Words cannot express my sincere emotion and gratitude to my beloved parents and sister. I would especially like to thank my family for encouraging me throughout my studies, providing financial support during my PhD, and supporting emotionally in the years being away from home and helping to cope with difficulty arisen during this period and made this journey possible for me. Completion this thesis could not be possible without their varied and extensive support; I will forever be thankful. I appreciate my father, Mr. Daryoush Yazdanfar, who helped me become confident in many ways during the course of my PhD. I am especially grateful to my mother, Mrs. Mehrnoush Moghaddam, who was by my side whole my life as my best friend and spent countless time for proof reading of all my reports during my PhD and especially for my thesis. I would like to thank my sister, Mrs. Hana Yazdanfar, who bore being far away and took responsibility of everything on my behalf. I love them from the depths of my heart and am forever indebted to them.

I acknowledge my friends, Mumin Koc, Luis Mendoza, Gediminas Galinis, Michael McNally, and Atea Akraiam for their assistance during my study and also their friendship.

*This thesis is dedicated to the most precious
gift that life has offered me.*

*Daryoush, Mehrnoush and Hana
who made my dream come true!*

Contents

Chapter 1 Introduction	1
1.1 Application of fluorescent silicon nanoparticles	1
1.2 A brief history of silicon nanoparticles research.....	2
1.3 Silicon nanoparticles	2
1.4 Development of production methods	5
1.5 Previous method to produce silicon nanoclusters	7
1.6 Novel method to produce fluorescent nanoclusters	9
1.7 Silicon nanoclusters properties produced by liquid jet method	10
1.8 Advantages of fluorescent silicon nanoparticles.....	11
1.9 Organization of the thesis.....	12
Chapter 2 Producing silicon nanoparticles	13
2.1 Overview	13
2.2 Experimental setup.....	14
2.2.1 Vacuum.....	16
2.2.2 Liquid jet.....	17
2.2.3 Sputtering.....	20
2.2.4 Cold target	21
2.2.5 Heating.....	23
2.2.6 Clustering.....	24
Chapter 3 Characterisation methods	25
3.1 Optical characterisation methods	25
3.1.1 Fluorescence spectroscopy: general remarks	25

3.1.1.1 Stokes shift.....	30
3.1.1.2 Light diffusion: Rayleigh and Raman scattering	31
3.1.2 Employed fluorescence spectrometer	32
3.1.2.1 Light source.....	32
3.1.2.2 Monochromators	33
3.1.2.3 Sample chamber	34
3.1.2.4 Detectors	34
3.1.3 Sample preparation for fluorescence measurement.....	35
3.1.3.1 Liquid sample.....	35
3.1.3.2 Film sample.....	36
3.1.4 Recording Fluorescence spectra	37
3.1.5 UV/Vis spectrophotometry.....	38
3.1.6 Employed UV/Vis spectrometer.....	40
3.1.6.1 Light source.....	40
3.1.6.2 Monochromator.....	40
3.1.6.3 Detector	41
3.1.6.4 Sample compartment.....	41
3.1.7 Sample preparation for UV/Vis measurement.....	41
3.1.8 Recording UV/Vis spectra.....	41
3.1.9 Fluorescence quantum yield	42
3.1.10 Fluorescence lifetime.....	43
3.1.11 Fluorescence quenching	45
3.1.12 Temperature effect.....	46
3.1.13 Reversible interaction of solvents.....	47
3.1.14 Concentration effect	48
3.2 Chemical characterisation methods.....	48
3.2.1 X-ray photoelectron spectroscopy (XPS).....	48

3.2.2 XPS spectrometer Employed for analysis	51
3.2.2.1 X-ray source	52
3.2.2.2 XPS analyser and detector	53
3.2.2.3 Detector	54
3.2.3 Sample preparation for XPS spectroscopy	54
3.2.4 Recording XPS spectra	55
3.2.5 XPS measurements	56
3.2.5.1 Effect of substrate	57
3.2.5.2 Effect of thickness of sample	58
3.2.5.3 Solvent effect	58
3.2.5.4 Solvent exchange	62
3.2.6 Peak analysis with CasaXPS	62
3.2.7 Attenuated Total Reflection (ATR) and Fourier Transform Infrared Spectroscopy (FTIR)	63
3.2.7.1 Principle of ATR spectroscopy	64
3.2.8 Devices employed for ATR/FTIR experiments	66
3.2.8.1 ATR accessories	67
3.2.8.2 FTIR accessory	67
3.2.9 Sample preparation for ATR spectroscopy	68
3.2.10 Sample preparation for FTIR spectroscopy	69
3.2.11 Recording ATR spectra	70
3.2.12 Recording FTIR spectra	71
3.2.13 Interpretation of ATR/FTIR spectra	72
Chapter 4 Optical characterisation of silicon nanoparticles	76
4.1 Overview	76
4.2 Characterisation of silicon nanoclusters by using Fluorescence spectroscopy: Reproducibility of the samples, and quality of the product	76
4.2.1 Florescence of silicon particles directly deposited on isopropanol	78

4.2.2	Florescence of silicon particles directly deposited on ethanol	82
4.2.3	Florescence of silicon particles directly deposited on water	85
4.2.4	Florescence of silicon particles directly deposited on hexane.....	92
4.2.5	Florescence of silicon particles directly deposited on formic acid.....	93
4.3	Characterisation of silicon nanoclusters using UV/Vis spectroscopy: absorbance spectra, and electronic structure of the samples.....	94
4.3.1	Absorbance of silicon particles directly deposited on isopropanol	95
4.3.2	Absorbance of silicon particles directly deposited on ethanol	96
4.3.3	Absorbance of silicon particles directly deposited on water	96
4.3.4	Absorbance of silicon particles directly deposited on hexane.....	98
4.4	Effect of solvent on absorbance and fluorescence wavelength and intensity	99
4.4.1	Jablonski diagram of silicon nanoparticles produced in different solvents	106
4.4.2	Band gap measurements	108
4.5	Fluorescence stability	109
4.6	Concentration of sample	110
4.7	Solvent exchange	114
4.8	Quantum yield	120
4.9	Oxidation investigation	121
4.10	Time-correlated fluorescence spectroscopy	122
4.10.1	Si-ethanol liquid sample	123
4.10.2	Si-ethanol film sample.....	125
4.10.3	Si-IPA liquid sample	127
4.10.4	Si-IPA film sample	129
4.10.5	Si-water liquid sample	131
4.10.6	Si-water film sample.....	133
4.11	Dependence of fluorescence on temperature	135
4.12	Life time measurements	137

4.12.1	Dependence of fluorescence lifetime on solvent.....	137
4.12.2	Dependence of fluorescence lifetime on emission and excitation wavelength	140
4.12.3	Comparison of fluorescence lifetimes of liquid and film samples.....	141
4.12.4	Effect of temperature on fluorescence lifetime	142
4.13	Effect of production parameters on the fluorescence spectrum.....	143
4.13.1	Effect of different distances and angles between cold trap and liquid jet	144
4.14	Conclusion.....	146
Chapter 5	Chemical characterisation of silicon nanoparticles.....	150
5.1	XPS characterisation	150
5.1.1	Effect of substrate.....	151
5.1.2	Effect of sample thickness.....	153
5.1.3	Solvent effect.....	155
5.1.4	Solvent exchange.....	158
5.1.5	Peak analysis with CASA XPS	160
5.2	ATR/FTIR characterisation.....	161
5.2.1	ATR characterisation.....	162
5.2.1.1	Absorbance spectra of Si-IPA sample by using ATR spectroscopy	162
5.2.1.2	Absorbance spectra of Si-ethanol samples using ATR spectroscopy...	170
5.2.1.3	Absorbance spectra of Si-water sample using ATR spectroscopy .	176
5.2.2	Solvent effect on ATR spectrum	188
5.2.3	Solvent exchange.....	190
5.2.4	FTIR characterisation	193
5.2.4.1	Solvent dependence transmittance	194
5.2.5	Comparison of ATR and FTIR spectroscopy	195
5.3	Conclusions	197

Chapter 6	Conclusions, discussion, and further work	198
6.1	Discussion and Conclusions.....	198
6.2	Further work.....	203
Appendix 1	Equipment operation to produce silicon nanoclusters	204
Appendix 2	XPS operation	206
Appendix 3	Complementary information about ATR and FTIR experiments	210
3.1	Quality of the beam and PV test	210
3.2	ATR and FTIR accessories	210
3.3	ATR spectra correction	212
Appendix 4	Complementary spectra to chapter 4.....	213
4.1	Absorbance spectra	213
4.2	Effect of filter on fluorescence.....	215
4.3	Time-correlated fluorescence spectroscopy.....	217
4.3.1	Silicon-ethanol liquid	217
4.3.2	Silicon-ethanol-film.....	220
4.3.3	Si-IPA-film	224
4.3.4	Si-water-film.....	226
4.3.5	Si-water-liquid.....	228
4.4	Dependence of fluorescence on temperature	230
4.5	Lifetime measurements	234
4.5.1	Dependence of fluorescence lifetime on emission and excitation wavelength	234
4.5.2	Fluorescence lifetime measurement at low temperature	236
4.5.3	Effect of temperature on fluorescence lifetime	239
4.6	Effect of argon pressure, sputter head power and Deposition time	240
Appendix 5	Complementary spectra to chapter 5.....	243
5.1	XPS survey spectra	243

5.2 Silicon wafer XPS spectra.....	246
5.3 ATR spectra of film samples.....	246
5.3.1 ATR spectra of film samples using HOPG substrate	249
5.3.2 ATR spectra of film samples using one layer HOPG substrate	252
5.3.3 FTIR spectra of film samples	254
Appendix 6 Atomic Force Microscopy (AFM)	256
6.1 AFM image and size distribution.....	256
List of publications and presentations	260
Bibliography	262

List of Figures

Figure 1-1. The conversion of an indirect band gap of silicon to a quasi-direct band gap by reducing cluster size.....	4
Figure 1-2. Schematic of the experimental set up to produce silicon nanoclusters [16]. .	8
Figure 2-1. This schematic shows different parts of our novel device. A liquid jet passes through the atomic silicon vapour, captures the vapourised atoms and, deposits the nanoparticles thus formed on the inner surface of cold target.	15
Figure 2-2. The BOC Edwards thin film coater which was modified to produce fluorescent silicon nanoparticles. The positions of the liquid tank, sputter head and cold target in the setup are shown. This figure (left-front view) shows the device whilst working, with a vacuum within the glass jar placed on top of the plate. The figure on the right shows the top view of the setup.	16
Figure 2-3. The picture on the left shows the cold trap, the liquid jet, the capillary heater and the sputter target (clockwise) giving an idea of distance between capillary and cold target. The dotted rectangle marks the region of the liquid jet and shown as zoomed picture on the right. The red arrow points onto the liquid jet which is collimated for atleast 2 cm.....	20
Figure 2-4. The picture in the left (a)) shows the sputter head working in vacuum and its position in the chamber. Picture b) is a top view, showing the position of the cold target in the chamber and the frozen cone-shaped deposit of silicon and water on the inner wall of the cold target. The picture on the right (c)) shows the frozen deposit of silicon and ethanol on the cold target from the side. In all figures the frozen deposit is indicated with a red arrow. Co-deposition of silicon with alcoholic solvents did not form an ice on the cold target wall, and it was similar to boiling liquid deposition, although when the alcoholic solutions hit the wall they froze. However, these solutions then started melting immediately.	22
Figure 2-5. Schematic showing the difference between direct and indirect deposition.	22

Figure 2-6. Heating wire wrapped around the nozzle (left). A schematic of the filament and its shield as heater (right).	23
Figure 3-1. Jablonski diagram [108]. This diagram shows electronic transitions for absorption and fluorescence processes. S_0 refers to the electronic ground state, S_1 and S_2 to electronically excited singlet states and T_1 refers to the excited triplet state.	27
Figure 3-2. This schematic shows the position of the main parts in a fluorescence spectrometer. Some particular parts, such as the beam splitter or the reference detector, are not shown because they are not used in the main light path.	29
Figure 3-3. Emission spectrum of Xenon lamp which is used in our experiment [114].	33
Figure 3-4. A diffraction grating splitting an incident beam into its component wavelengths. The saw-tooth profile (called the ‘blaze’) aims to enhance the intensity of certain wavelength regions.	34
Figure 3-5. The schematic shows how TCSPC method measure the fluorescence and fluorescence photon can be detected in different time window.	37
Figure 3-6. The schematic shows how a double beam UV/Vis spectrophotometer works.	40
Figure 3-7. Schematic explaining the broadening of fluorescence spectra by increasing the temperature. Increasing the temperature redistributes the ground state population across more states.	46
Figure 3-8. This figure shows the process of solvent exchange experiment. In each experiment, sample residue was transferred between two solvents in four steps, with fluorescence spectra recorded for each step.	47
Figure 3-9. A schematic showing the photoemission process.	50
Figure 3-10. The XPS spectrometer and its components [129].	51
Figure 3-11. Cross-section through x-ray source components [130].	52
Figure 3-12. This figure shows the hemispherical analyser and its components (right) [131]; it also shows the trajectory of the photoelectrons (left), where R_0 is the electron trajectory radius [132].	53
Figure 3-13. Molecular vibrations. Molecules vibrate in symmetric or asymmetric mode, and hence (in this case) IR active and IR inactive, respectively [222].	63
Figure 3-14. This figure shows the principle of ATR spectroscopy. The number of reflections depends on the length of the sample and the angle of the incident radiation [223].	66

Figure 3-15. Figure showing the liquid cell (left) and a schematic showing the cell assembly (right) [228, 229].....	68
Figure 4-1. Figure showing blue fluorescence from our liquid sample in air.	78
Figure 4-2. Figure showing emission spectra of Si-IPA samples excited at 270 nm as recorded by a fluorescence spectrometer. The first peak at 270 nm is first-order Rayleigh scattering, the second sharp peak at 295 nm is the first-order Raman peak of IPA, the second-order scatter being seen at 540 nm and 590 nm. The fluorescence peaks of Si-IPA samples can be seen at ~310 nm (first fluorescence peak) and ~357 nm (second fluorescence peak).	79
Figure 4-3. Excitation energy dependence of the fluorescence. Sample A2 Si-IPA has been excited at 250 nm, 270 nm and 308 nm (top figure). The emission wavelength is unaffected by changing the excitation energy. The figure on the bottom shows excitation spectra emitted at 310 nm and 365 nm. Their peaks are at 275 nm and 293 nm.....	81
Figure 4-4. Figure showing fluorescence spectra of Si-ethanol samples excited at 250 nm (top) and 270 nm (bottom). They have fluorescence peaks at ~310 nm and ~364 nm. The two peaks at ~310 nm and ~364 nm appear to merge when excited at 270 nm.	83
Figure 4-5. Figure depicting the fluorescence spectra of the Si-ethanol sample A4 excited at 250 nm, 270 nm, and 308 nm (top), and excitation spectra of sample A4 emitted at 303 nm and 370 nm (bottom).	84
Figure 4-6. Figure showing Si-water samples excited at 270 nm. The plot on the bottom shows the sample with lower fluorescence intensities, which have two fluorescence peaks around 307 - 314 nm and ~430 nm, while higher intensity spectra (top) have peaks around 300 - 330 nm and 420 - 440 nm.....	86
Figure 4-7. Figure showing Si-water samples excited at 308 nm. All samples have a peak at 420 nm.	87
Figure 4-8. Figure depicting the fluorescence spectra of Si-water sample C2 excited at 250 nm, 270 nm, and 308 nm (top) and excitation spectra, fluorescence recorded at 340 nm and 420 nm (bottom).	90
Figure 4-9. Figure showing fluorescence spectra of Si-water sample C9 excited at 250 nm, 270 nm, and 308 nm (top) and excitation spectra emitted at 315 nm, 335 nm, 420 nm and 440 nm (bottom).....	91
Figure 4-10. Figure showing fluorescence spectra of Si-hexane sample excited at 250 nm, 270 nm, and 308 nm (top) and excitation spectra emitted at 320 nm, and 410 nm (bottom).	93

Figure 4-11. Figure showing fluorescence spectra of Si-formic acid sample excited at 270 nm, and 308 nm.	94
Figure 4-12. Absorbance spectra of Si-IPA samples.	95
Figure 4-13. Absorbance spectra of Si-ethanol samples.	96
Figure 4-14. Absorbance spectra of Si-water samples.	97
Figure 4-15. Comparison of absorbance and fluorescence excitation spectra of sample C2 and C9.	98
Figure 4-16. Figure showing the absorbance of Si-hexane.	99
Figure 4-17. Figure showing fluorescence spectra of silicon clusters in isopropanol, ethanol and water. Their first fluorescence peaks are at 310 nm for all samples, with the second fluorescence peaks at 365 nm for Si-IPA, 370 nm for Si-ethanol, and ~440 nm for Si-water. Fluorescence shows sensitivity to solvents. The fluorescence wavelength depends on the solvent; alcohols show a blue shift in their fluorescence peaks relative to water.	100
Figure 4-18. The relationship between dipole moment of the solvent and fluorescence shift. The figure shows the energy of the fluorescence bands and that, therefore, the fluorescence energy shift for alcoholic solvent and water depends on the dipole moments of the solvents; the larger the dipole moment, the greater the shift to longer wavelengths.	103
Figure 4-19. Excitation spectra for the first and second fluorescence peaks. Top: samples were investigated for the first fluorescence peaks; positions of the excitation spectra show that silicon particles in three different solvents have the same excited state. Bottom: excitation spectra of the second fluorescence peaks, which show sensitivity to the solvent used in each case.	105
Figure 4-20. Absorbance of silicon clusters produced in three different solvents.	106
Figure 4-21. Jablonski diagram of the emission spectra. The diagram shows the transitions for the first and the second fluorescence peaks for Si-IPA, Si-ethanol and Si-water samples.	107
Figure 4-22. Jablonski diagram of the excitation spectra. The diagram shows the transitions for the first and the second fluorescence peaks for Si-IPA, Si-ethanol and Si-water samples.	107
Figure 4-23. Taus plot of Si-IPA, Si-ethanol, and Si-water. The band gap can be calculated from this plot, as shown by the arrows.	108

Figure 4-24. Figure showing emission spectra of a Si-water sample which was measured when produced (June 2012) and a approximately a year later (April 2013). The results show the samples are chemically stable. 109

Figure 4-25. Si-ethanol sample, diluted in ten steps (by a factor of two at each stage). Fluorescence intensity is decreased by dilution. The insets show scattered light and the last seven steps of first fluorescence peak. The sample was excited at 270 nm. 111

Figure 4-26. Figure showing the Stern-Volmer plot for Si-ethanol. As can be seen, the intensity of the Rayleigh peak and the Raman peak decrease with increasing the concentration whilst the intensities of the two fluorescence peaks increase. 111

Figure 4-27. Figures show the changing absorbance of the sample with concentration. The absorbance was measured usign a UV/Vis spectrometer. The relationship between absorbance and concentration is linear. 112

Figure 4-28. Dependence of fluorescence intensity on concentration. A Stern-Volmer plot shows fluorescence intensity decreases with decreasing concentration, and that this relationship is linear. There is a clear deviation from a linear relationship for the original sample, which is shown with red line. 113

Figure 4-29. Figures showing the repeated transfer of the sample between ethanol and isopropanol over four steps. The original sample was produced in ethanol. In the top figure, samples were excited at 250 nm and show that the first peak did not change with solvent, but that second peak, which showed solvent dependence in the previous trials, did. In the bottom figure, samples were excited at 308 nm. Here, it is clear that the second peak changed with [each] solvent exchange. 115

Figure 4-30. Figure showing the result of repeatedly transferring clusters between ethanol and water over four steps. 116

Figure 4-31. Figure showing replacment of IPA with water, and water with IPA, over four steps. Silicon clusters were produced in isopropanol. All spectra show a peak at 310 nm, which we attribute to intrinsic fluorecence of the bulk species in the nanoparticles. A second peak appears at ~370 nm and at ~420 nm, depending on the solvent. By swapping the solvents, the position of the second peak changes. Two spectra which belong to water have a peak at ~420 nm, and three spectra which belong to isopropanol have peak around 370 nm. The results also show that this process in reversible. 117

Figure 4-32. Figure showing fluorecence excitation spectra of directly deposited Si-ethanol and silicon particles transferred to IPA and water. The top figure shows fluorecence spectra which belong to the first fluorecence peak ($\lambda_{em}=310$ nm). Similar

to directly deposited samples, it shows the fluorescence of the first peak is not solvent dependent. The bottom figure shows excitation spectra for the second fluorescence peaks ($\lambda_{em(alcohol)}=360$ nm, $\lambda_{em(water)}=420$ nm) are solvent dependent, similar to the directly deposited sample..... 118

Figure 4-33. Figure showing absorbance of the original sample (Si-ethanol) and the absorbance when nanoparticles were transferred to IPA and water. The results are similar to those for direct deposition samples..... 119

Figure 4-34. Figure showing the changing fluorescence profile of an Si-IPA sample when a drop of pure water was added. As can be seen, by adding only one drop of water, the peak at 440 nm appears and the peak at 360 nm almost vanishes. The sample is excited at 270 nm. The figure in the bottom shows the whole spectrum, while the figure on the top shows an expanded view of the spectrum..... 122

Figure 4-35. Figure showing emission (top) and excitation (bottom) spectra with int, fast and slow components for Si-ethanol in the liquid phase. The fluorescence peak is at 308 nm. The excitation spectra were cut off at 190 nm due to suprasil's cut-off wavelength. 124

Figure 4-36. Figure showing emission (top) and excitation (bottom) spectra with int, fast and slow components for Si-ethanol in the liquid phase. 125

Figure 4-37. Figure showing emission (top) and excitation (bottom) spectra with int, fast and slow components for a Si-ethanol film sample. Fluorescence peaks are at 294 nm and 415 nm. The excitation spectrum shows peaks at 203 nm, 228 nm and 295 nm..... 127

Figure 4-38. Figure showing emission (top) and excitation (bottom) spectra with int, fast and slow components for Si-IPA in the liquid phase. The fluorescence peak is at 306 nm. The excitation spectrum shows a peak at 206 nm. 128

Figure 4-39. Figure showing emission (top) and excitation (bottom) spectra with int, fast and slow components for Si-IPA film. The fluorescence emission spectrum has three peaks at 300 nm, 412 nm and 585 nm. The excitation spectrum shows several peaks peak at 100 nm, 115 nm, 145 nm, 200 nm and 294 nm. 130

Figure 4-40. Figure showing emission (top) and excitation (bottom) spectra with int, fast and slow components for Si-water in liquid phase. Fluorescence emission peaks are observed at 320 nm and 422 nm. The excitation spectra shows peaks at 195 nm, 207 nm, 224 nm, 284 nm, and 303 nm. 132

Figure 4-41. Figure showing emission (top) and excitation (bottom) spectra with int, fast and slow components for Si-water film sample. Fluorescence peaks are observed at 308

nm, 440 nm and 570 nm. The excitation spectrum shows peaks at 190 nm and around 300 nm.	133
Figure 4-42. Figure showing the effect of changing temperature on fluorescence intensity. By cooling the sample, fluorescence intensity is increased.	136
Figure 4-43. Figure showing the dependence of intensity on temperature for three different components of int, fast, and slow measurements.	136
Figure 4-44. Figure showing the results of lifetime measurements for Si-water, Si-ethanol and Si-IPA. Measurements were done in the liquid phase. The figure has been plotted on a logarithmic scale.	138
Figure 4-45. Comparison of first and second fluorescence peaks lifetime of Si-water..	138
Figure 4-46. Figure showing the results of fluorescence lifetime measurements for the first (top) and second (bottom) fluorescence peaks for Si-water, Si-ethanol and Si-IPA film samples.	139
Figure 4-47. Figure showing lifetime dependence on excitation wavelengths. A Si-ethanol film sample was measured at three different excitation wavelengths (203 nm, 228 nm and 290 nm) for each fluorescence peak wavelength; lifetime measurements were performed for two emission wavelengths (300 nm and 410 nm).	141
Figure 4-48. Comparison between fluorescence lifetime of Si-ethanol film and liquid samples.	142
Figure 4-49. Figure showing lifetime dependence on temperature; lifetime decreases with increasing temperature [276].	143
Figure 4-50. Figure showing spectra of Si-IPA samples which are produced at different distances and angles between the cold target and liquid jet.	145
Figure 4-51. Figure showing spectra of Si-IPA samples which were produced at different distances and angles between the cold target and liquid jet.	146
Figure 5-1. Figure comparing carbon (1s) (a), oxygen (1s) (b) and silicon peaks (2s, 2p) (c, d) for one drop (5 μ l) of Si-ethanol sample on three different substrates (copper, molybdenum and HOPG).	151
Figure 5-2. Figure showing the peaks belonging to the substrate before and after putting sample was applied.	153
Figure 5-3. The effect of the sample thickness on the substrate. There are some silicon impurities in pure water, but this does not interfere with the peaks due to our samples, which show oxidised silicon.	154

Figure 5-4. Figure showing XPS peaks of O (1s), C (1s), Si (2s), Si (2p) for silicon clusters in IPA, ethanol, and water on HOPG. High oxidation happens for the Si-water sample, and a lower level of oxidation for alcoholic samples.	157
Figure 5-5. Figure comparing the XPS peaks of Si-ethanol sample on HOPG with the ones produced from subsequent solvent exchange with IPA and water on HOPG.....	159
Figure 5-6. Oxygen peak (left) and carbon peak (right) of Si-water sample, as analysed with CASA XPS.	160
Figure 5-7. Figure showing the analysis the Si (2s) peak (left) and Si (2p) peak (right) of Si-water sample by using CASA XPS.....	161
Figure 5-8. Absorbance spectrum of Si-IPA film. The sample shows silicon-oxygen, silicon-hydrogen and silicon-carbon bands in this spectrum.....	164
Figure 5-9. Increasing the film thickness of Si-IPA sample A3.....	165
Figure 5-10. ATR spectrum of Si-IPA film, sample A1. This sample has all the peaks which were seen in sample A3, and in addition it has a peak characteristic of the Si-CH ₃ bending vibration at 1260 cm ⁻¹	166
Figure 5-11. The ATR spectra of sample A1, sample A3, and pure IPA are compared. The peaks related to silicon species are clear when these data are plotted on same scale with pure isopropanol.	167
Figure 5-12. In this figure, film and liquid phase samples are compared; shown are sample A3 (bottom) and sample A1 (top).....	169
Figure 5-13. ATR spectrum of Si-ethanol film sample. The spectrum shows SiO, SiOH, and SiH bands which are due to silicon bonding with ethanol molecules (cluster-solvent interaction).	171
Figure 5-14. Affect on absorbance of increasing the film thickness of Si-ethanol sample A6.....	172
Figure 5-15. Absorbance of Si-ethanol with ten layers film, sample D5, (top) and increasing the thickness of the film from one layer to ten layers (bottom).	173
Figure 5-16. Comparison between Si-ethanol films samples A6 and D5, and pure ethanol film. As can be seen, the intensity of the sample A6 ATR spectrum is much higher than D5, but the SiO band, as indicated by the green arrow, is clear in the ATR spectrum of sample D5.	174
Figure 5-17. Film and liquid Si-ethanol samples A6 (top) and D5 (bottom) are compared.	175

Figure 5-18. Si-water film ATR spectrum of sample D2 (first measurement). Increasing the thickness shows not only the absorbance increased by increasing the thickness, but also the peak around 1100 cm^{-1} became broader and a shoulder at 1177 cm^{-1} arose, which belongs to an SiO_2 (or SiO_{2+x}) vibration..... 178

Figure 5-19. ATR spectrum of Si-water film from sample D2 with less noise (top). Effect of the thickness of the film on the ATR spectrum is depicted in this figure (bottom). 179

Figure 5-20. Third measurement for sample D2. The intensity is very high and the position of the peaks identical to those in previous measurements; however, peaks are broader in this measurement, and the peaks at 1014 cm^{-1} - 1130 cm^{-1} have overlapped. Some features detected for thin sample layers could not be observed for thicker sample layers..... 181

Figure 5-21. Effect of thickness for Si-water film for sample D2 (in third measurement) is shown. By increasing the thickness, the intensity of the bands is increased, which shows an emerging band at 1130 cm^{-1} ; however, broadening the bands leads to deconvolution difficulties and the actual disappearance of some smaller features. 182

Figure 5-22. ATR spectrum of Si-water film, sample C9. The blue spectrum shows sample measurement after putting on the tenth layer. The intensity of the peak is high enough for silicon compounds bands, but for Si-water samples, even though the intensity is high for such a thick sample, broadening prevents us distinguishing the peaks. For this reason, the sample with seven layers of thickness is shown (green spectrum); although the intensity is lower in this spectrum, it is obvious that there are four silicon-water related peaks, which are SiH_2 scissors at 918 cm^{-1} , Si-O-Si stretch at 1015 cm^{-1} , SiO_2 stretch at 1117 cm^{-1} , and the SiO_{2+x} (or SiO_2) stretch at 1176 cm^{-1} 183

Figure 5-23. Different thicknesses of Si-water, sample C9. By increasing the thickness, the OH stretching band could be observed. Note the conversion of four bands to two bands in fingerprint region. 185

Figure 5-24. Comparison between the ATR spectra of pure water film and those of silicon deposited in water samples. The peaks related to silicon-water species are clear and intense. Pure water has negative signal for the triplet bands around 2900 cm^{-1} because this band may exist in the background (air), thus subtracting makes it negative in the pure water film. 186

Figure 5-25. Figure showing the comparison of spectra of samples C9 and C2 in film and liquid phases. Bands belong to silicon bonding with water molecules are very clear in the film samples..... 187

Figure 5-26. ATR spectra of silicon deposited in three different solvents are compared in this figure. The Si-IPA sample has the lowest absorbance and Si-water sample has the highest. As ATR spectra shows the bands and therefore the silicon oxygen species exist in samples as well as their intensity depend on the solvent..... 189

Figure 5-27. Comparison of ATR spectra of silicon deposited in IPA, ethanol and water. 190

Figure 5-28. Figure showing the ATR spectra of recorded during the solvent exchange experiment. The reference sample was silicon deposited in ethanol (sample A5, as a film). In the inset, the highlighted square shows which sample step was actually being recorded. 192

Figure 5-29. A comparison between transmittance spectra of silicon deposited in different solvents. It shows that transmittance of silicon clusters depend on the solvent used... 194

Figure 5-30. Figure showing absorbance and transmission spectra for Si-water sample C9. The top figure shows the use of the same amount of sample for all measurements (10 μ l). In the bottom figure, the amount of sample used for the absorbance experiment was five times higher. 196

Figure A.2-1. Left: Top view of the XPS spectrometer. Right: Ion gauge controllers showing the pressures of the different chambers..... 207

Figure A.2-2. X-ray controller software. In this interface we can choose the anode, and also define filament current, emission current and anode voltage..... 208

Figure A.2-3. An example survey spectrum. The parameters which were chosen for experiment can be seen in the table at the bottom of the software interface (these are generally just used as file metadata when the experimental data is saved, and mostly do not actually affect the experiment itself). By choosing appropriate elements in the software library, the probable identity of each atomic peak is defined. 209

Figure A.2-4. EA125 software control interface. By changing the position of the sample, the intensity will change and one can optimize the peak intensity and signal/noise ratio of the experiment..... 209

Figure A.3-1. The iD5 accessory for ATR measurements. Picture on the right shows iD5 device, and it has been installed in iS5 spectrometer in picture on the left. 211

Figure A.3-2. The iD1 transmission accessory. Left, the device has been installed in an iS5 spectrometer, to measure transmission spectra. The position of the liquid cell in the transmission accessory is shown in the picture on the right. 211

Figure A.4-1. Absorbance spectra of Si-IPA samples. The absorption peak wavelength is different for different spectra.	213
Figure A.4-2. Absorbance spectra of Si-ethanol samples.....	214
Figure A.4-3. Absorbance spectra of Si-water samples.....	214
Figure A.4-4. Figure comparing emission spectra of samples before and after filtration. The samples were excited at 250 nm, 270 nm, and 308 nm. The plots on the right belong to Si-IPA sample D4, and the left to Si-IPA sample B2.....	216
Figure A.4-5. Difference between fluorescence intensity before and after filtration of Si-ethanol sample.	217
Figure A.4-6. Emission spectra of different components of Si-ethanol liquid sample.	218
Figure A.4-7. Excitation spectra of different components of Si-ethanol liquid sample. The normalised int component at 300 nm is shown as a comparison with the same spectrum before normalization.	219
Figure A.4-8. Emission spectra of different components of Si-ethanol B5 film sample.	220
Figure A.4-9. Excitation spectra of different components of sample B5 Si-ethanol B5 film.....	221
Figure A.4-10. Emission spectra of different components of Si-ethanol film, sample B6.	222
Figure A.4-11. Excitation spectra of different components of Si-ethanol film, sample B6.	223
Figure A.4-12. Emission spectra of different components of Si-IPA C4 film sample.	224
Figure A.4-13. Excitation spectra of different components of Si-IPA C4 film sample.	225
Figure A.4-14. Emission spectra of different components of Si-water D8 film sample.	226
Figure A.4-15. Excitation spectra of different components of Si-water D8 film sample.	227
Figure A.4-16. Emission spectra of different components of Si-water liquid sample C2.	228
Figure A.4-17. Excitation spectra of different components of Si-water liquid sample C2.	229
Figure A.4-18. Temperature dependence study of emission spectra excited at 203 nm.	231

Figure A.4-19. Temperature dependence study of emission spectra excited at 228 nm.	232
Figure A.4-20. Temperature dependence study of emission spectra excited at 290 nm.	233
Figure A.4-21. Fluorescence lifetime dependence excitation wavelength for Si-ethanol film sample B5.....	234
Figure A.4-22. Fluorescence lifetime dependence on emission and excitation wavelength for Si-IPA film sample C4.	235
Figure A.4-23. Fluorescence lifetime dependence on emission wavelength for Si-water liquid sample C2.	236
Figure A.4-24. Decay time measurements of Si-ethanol film sample B6 at 8 K.	237
Figure A.4-25. Decay time measurements of Si-ethanol film sample A6 at 10 K.	238
Figure A.4-26. Figure showing lifetime dependence on temperature; lifetime decreases with increasing temperature.....	239
Figure A.4-27. Figure showing the effect of changing the stagnation pressure on fluorescence spectrum.....	240
Figure A.4-28. Figure showing the effect of changing the magnetron power on fluorescence spectrum.....	241
Figure A.4-29. Figure showing the effect of deposition time on the fluorescence spectrum.	242
Figure A.5-1. XPS survey spectrum of nanoparticle film produced by deposition of silicon onto an ethanol liquid jet. The colloidal nanoparticles were drop cast in air onto an unspecified copper substrate.....	243
Figure A.5-2. XPS survey spectrum of Si-ethanol sample on Molybdenum substrate.	244
Figure A.5-3. XPS survey spectrum of Si-ethanol sample on HOPG substrate.	244
Figure A.5-4. XPS survey spectrum of Si-IPA sample on HOPG substrate.	245
Figure A.5-5. XPS survey spectrum of Si-water sample on HOPG substrate.....	245
Figure A.5-6. XPS spectra of silicon wafer are recorded as a reference.	246
Figure A.5-7. Si-IPA sample absorbance spectra.	247
Figure A.5-8. Si-ethanol sample absorbance spectra.....	248
Figure A.5-9. Si-water sample absorbance spectra. These samples show four bands around 950- 1300 cm^{-1}	248

Figure A.5-10. Si-water sample absorbance spectra. The two broad bands in the fingerprint region are a superposition of four narrow peaks in lower absorbance samples.	249
Figure A.5-11. ATR spectra of Si-IPA sample A2 using HOPG substrate applied in four steps.	250
Figure A.5-12. ATR spectra of Si-water sample C9 using HOPG substrate applied in two steps.	250
Figure A.5-13. A comparison between ATR measurements with and without HOPG are illustrated. Although for the blue line (without HOPG) the amount of sample is ten times more than for red line (with HOPG), the absorbance of the sample on HOPG is five times higher.	251
Figure A.5-14. Figure showing ATR spectra of silicon deposited on three different solvents by using a layer of HOPG as substrate.	253
Figure A.5-15. A comparison of ATR spectra of Si-water sample on HOPG substrate and a layer of HOPG on sellotape. Using a layer of HOPG on sellotape gives peaks with higher intensities that are also sharper and distinguishable.....	253
Figure A.5-16. All water solvent sample transmittance spectra and a pure water spectrum as a reference are shown in this figure.....	254
Figure A.5-17. Transmittance spectra of Si-IPA (top) and Si-ethanol (bottom). As it can be seen, some silicon oxide peaks exist in these spectra but, similar to ATR measurements, the intensities of vibrational frequencies due to silicon species deposited in alcohol is very low.....	255
Figure A.6-1. AFM image and size distribution of Si-IPA sample. Distance between two peaks show the height of layer.....	256
Figure A.6-2. AFM imagea, size distribution and height profiles of Si-ethanol sample.	257
Figure A.6-3. AFM image and size distribution of Si-water sample.....	258
Figure A.6-4. AFM image and size distribution of silicon clusters transferred to IPA.	258
Figure A.6-5. AFM image and size distribution of silicon clusters transferred to water.	259

List of Tables

Table 1-1. Blue-fluorescent silicon species produced via different experimental methods.	6
Table 2-1. Laminar volume flow rate for water.....	19
Table 3-1. Silicon components and their binding energies.....	59
Table 3-2. Silicon components of different amount of oxygen, carbon and hydrogen and their binding energies. Different stoichiometries of each compound are shown by the numbers.....	60
Table 3-3. Carbon components and their binding energies.	61
Table 3-4. Oxygen components and their binding energies.	61
Table 3-5. Silicon (2s) components and their binding energy.....	62
Table 3-6. Some molecular vibrations with corresponding wave numbers.....	73
Table 4-1. Fluorescence peak position of Si-IPA samples (silicon deposited onto isopropanol liquid jet in vacuum). Excitation energy is 270 nm.	79
Table 4-2. Si-ethanol samples excited at 250 nm.	85
Table 4-3 Si-water excited at 250 nm and 308 nm.....	88
Table 4-4. Fluorescence characteristics of silicon deposited in IPA, ethanol, and water.	147

Chapter 1

Introduction

1.1 Application of fluorescent silicon nanoparticles

Our aim in this project is the production and investigation of fluorescent nanostructures composed of silicon. Fluorescent silicon nanoclusters are of considerable scientific interest, both as means of studying the fundamental properties of silicon, one of the most important technological materials of our age, and for their possible applications. Luminescent nanoclusters of silicon, oxidised silicon and silicon dioxide are interesting topics in fundamental and in applied research, and have applications in optoelectronic devices [1] and lasers [2]; silicon is the de-facto standard in electronics, fluorescent silicon and silicon dioxide have the potential to be integrated in high-performance integrated circuits with existing material standards in microelectronics [3]. Performance of [integrated] electronic chips would be enhanced in the future by technologies such as use of optical signal transmission, as with standard technology the longer interconnections cause considerable losses in speed. Applied research on nanoparticles in the field of microelectronics has developed considerably, but still is not a reality. Variability of the nanoparticles' size and size-dependent properties have a wide range of applications in medical diagnostics and therapy [4]. Silicon nanoparticles have also been suggested for biolabelling [5, 6] and sensors (biosensing) [7-10], because of their expected suitable (that is, high) biotolerance [11]; their - presumably - non-toxicity gives an considerable advantage over other light emitting materials, which tend to have potentially serious implications for health were they deployed *in vivo*. Nanoparticles in solution are particularly interesting due to their potential applications in medical and biological imaging and diagnostic labelling [12], since a requirement for applications in biomedicine is stability in an aqueous environment. Recently, blue light emission has

been reported for silicon nanoparticles in water, produced by various methods [13-18], some of which show exceptional long-term fluorescence stability [19, 20].

In all examples of applications, the production method is very important and can be reflected in the final fluorescence properties of the product. This is due to minor variation during production, which can have a bearing on the molecular properties - and, therefore, usage - of the product. All these methods are good and useful but still it is challenging to achieve a stability fit for, say, medical purposes. Therefore, any new research into the fabrication method is interesting in itself.

1.2 A brief history of silicon nanoparticles research

The history of nanoparticle research dates back to the late 1960's and early 1970's. Special attention is given to the years between 1970 and the early 1980's because this period represents the initial growth of nanoparticle development. Further progresses focused on especially interesting improvements, such as nanoparticles for drugs delivery across the blood-brain barrier (BBB) and PEGylated nanoparticles with a prolonged blood circulation time. Using silicon as a fluorescent source was not the first choice, because bulk silicon does not fluoresce efficiently. Since finding light emission from porous silicon at room temperature two decades ago, creation of devices such as silicon-based fluorescence emitting diodes [21] and lasers [22] had shown a great deal of successful development, and many scientific groups reported a large variety of types of photoluminescent silicon, including nanowires, nanotubes [23-29] Si/SiO layers, Si/SiOH sandwiches, and core-shell systems [30-32]. There are also many reports in the literature on silicon clusters produced by laser photolysis [33, 34], or by implantation of silicon ions in silica glass [35, 36]. Also, fluorescent silicon quantum dots in liquid phase have been studied [13, 14, 37].

1.3 Silicon nanoparticles

Nanoparticles often have size-related properties that are different from those observed in bulk materials. Bulk materials have 'constant' properties which are not size-

dependent; however, the properties of materials will change when their size approaches the nanoscale, and the number of atoms at the surface of such materials becomes important to any such consideration.

Nanoparticles are very interesting to science because they are a bridge between bulk materials and atomic or molecular structures. At the beginning of the 1990s, Canham [38] discovered a relatively intense visible light emission in porous, nanosize silicon. Bulk silicon is an indirect band gap semiconductor; a band structure in which it is not possible for the electron to be transferred from the conduction band to the valance band without a change in momentum, so it is a forbidden transition. Therefore, recombination of electron and hole occurs when energy is converted into a phonon, which is only accompanied by low intensity emission. When microscopic silicon's bulk size is reduced, at a size of a few nanometers a point is reached where the nanosized silicon is a semiconductor with a direct band gap. So, recombination of electron and hole does not have any effect on momentum, and recombination results in an allowed fluorescence transition (Figure 1-1). Photon emission in bulk silicon is inefficient because of its indirect band gap, but silicon nanoclusters between 1-3 nm in diameter show intense luminescence at visible wavelengths and at room temperature [39]. The quantum size effects and therefore the enlargement of the band gap of small clusters can lead to this novel luminescent property.

Bulk crystalline silicon is eminent in microelectronics for its low fluorescence efficiency because of its indirect band gap. To overcome this limitation, many and various methods have been used to produce different forms of silicon structures, such as porous silicon [38, 40, 41], silicon nanoparticles [35, 42], lanthanide-doped silicon [3, 43, 44] and silicon nanowires [23]. The procedure, which leads to light emission from materials with an indirect band gap in the bulk, is very interesting both from a fundamental science point of view, and also in applications [45, 46]. A prerequisite for applications of nanoparticles is a thorough understanding of both pure nanoparticles, and of nanoparticles in contact with, or *in situ* in, an environment.

Bulk materials are usually characterized by properties such as structure or chemical composition, but nanoscale materials are characterized by an extra dimension, their size, so the properties of materials will change when their size approaches the nanoscale. One reason for this is the increasing number of atoms at the surface, relative to the bulk atoms, when the size of nanoparticles decreases. Another reason for the distinct properties of nanoparticles is their reduced dimensionality. Atomic clusters are a fascinating state of

matter with unique properties and many potential applications [47-50]. With decreasing size, clusters exhibit an increasing volume fraction of atoms on the surface, giving rise to specific thermodynamic [51], photochemical [52] and catalytic [53] properties and, indeed, surface site-specific effects have been identified for electronic excitations [54-57]. The novel properties of nanoclusters originate from the high surface-to-volume ratio of the clusters and the quantum confinement effects [58] due to their small size. As a large fraction of nanoclusters component atoms reside on the surface, they should be sensitive to their environment. For example, a silicon cluster with 1000 atoms has approximately 25% of its atoms at its surface (whilst this is the equivalent of 0.0001% for 1 mm³ bulk silicon), so surface properties are very important on the nanoscale. The high density of ‘dangling’ [59, 60] bonds at silicon nanocluster surface increases the reactivity of clusters compared with bulk silicon. Highly reactive silicon clusters are easily oxidised when exposed to the atmosphere, or can recombine with impurities. Clearly, this will change the optical and chemical properties, and may cause, for instant, non-radiative recombination in the end product, rather than allowing observation of fluorescence [61]. So, to produce a stable fluorescent silicon nanocluster, [surface] passivation is necessary.

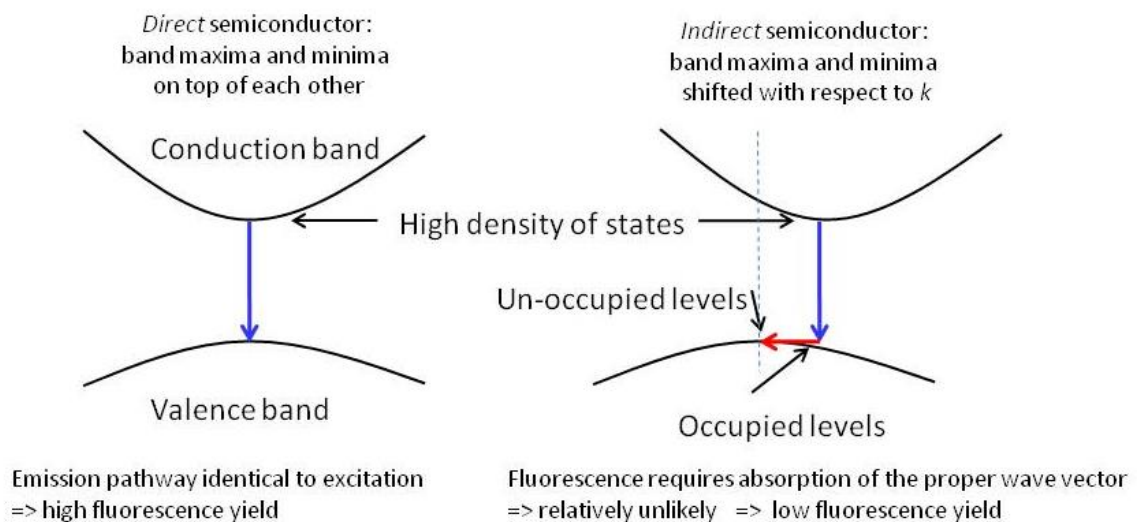


Figure 1-1. The conversion of an indirect band gap of silicon to a quasi-direct band gap by reducing cluster size.

1.4 Development of production methods

Although bulk silicon emits inefficient, fluorescence from silicon nanoclusters is achievable by a variety of different production methods [41, 62, 63]. The ability to produce chemically stable nanoscale particles with specific size, shape, composition and optical and chemical properties is a challenge in nanotechnology research. Molecular beam machines produce silicon clusters which show direct band gaps. The molecular beam technique used for producing luminescent silicon particles has many advantages. Molecular beams can produce nanoparticles in a wide range of tuneable size distributions [64-67], allow for *in situ* investigation of particles in the beam itself [68, 69], or the cluster can be co-doped in vacuum by a pick-up process [70] or by co-deposition with another gas onto a cold substrate [71, 72]. They can produce free silicon clusters in the range of a few atoms [33, 66, 69, 73-75], but a major requirement to achieve fluorescence from silicon clusters is an appropriate passivation of the cluster surface [76], as pure free silicon clusters have dangling bonds which efficiently quench fluorescence through their chemical reactivity [17]. In various methods, cluster sources were used, but which also show passivation problems [77, 78]. There are also many chemical methods like etching but, again, all of these show a similarly poor passivation. Recently, the production of stable, deep blue-emitting silicon nanoparticles has been reported, which uses a chemical route to stabilize the particles [79]. Table 1-1 shows a few examples of blue-fluorescent silicon particle production from the literature.

Table 1-1. Blue-fluorescent silicon species produced via different experimental methods.

Wavelength (nm)	Species	Fluorescence assignment	Method	Reference
330	Porous silica	Si-OH	sol-gel	[80]
370	Si oxide	SiO ₃	high temperature reaction and anodization (alkali-treated Si and anodized Si in a NaOH solution)	[81]
430-480, 650-800	oxidized porous silicon	SiO ₂	anodic etching of silicon wafer in ethanol:HF mixture	[82]
~460	Silicon nanocrystal	oxidized silicon nanocrystals	electrochemical etching of a monocrystalline Si wafer in a solution comprising hydrofluoric acid, ethanol and H ₂ O ₂	[83]
460	SiNPs	Silicon nanoparticles	growth under microwave irradiation, by using hydrophilic molecules trimethoxysilane, (C ₆ H ₁₇ NO ₃ Si), as silicon source.	[79]
270–295, 330–350, 410, 450	porous silicon porous glass	silicon/silicon oxide (oxidized porous silicon)	PSi and OPSi layers were prepared from silicon wafers, by electrochemical etching -growing oxide shell around the nanocrystals using highpressure water vapor annealing.	[84]
320-400	Si nanocrystals	Si nanocrystals	laser ablation in liquids	[85]
470	Silicon nanocrystals	Silicon nanocrystals	pulsed laser ablation	[86]
415, 435	Silicon nanocrystals	Silicon nanocrystals	laser ablation	[87]
398, 423	nanocrystalline silicon	nanocrystalline silicon in silicon oxide matrix	mechanical milling followed by chemical oxidation	[88]

1.5 Previous method to produce silicon nanoclusters

The dangling bonds of silicon nanoparticles, which are a prevalent feature of any production method, should be passivated to fluoresce, otherwise silicon nanoparticles can decay non-radiatively, even though they have direct band gap. In previous work in our lab this passivation was achieved using a novel, two step method. Silicon nanoparticles were produced in a cluster beam using a magnetron sputtering and a conventional gas aggregation technique [89] under ultrahigh vacuum (UHV) conditions similar to the method described by the von Issendorf, Palmer, and Milani [66, 67, 69, 90]. Passivation of the clusters surface dangling bonds was performed by passing the clusters through a localised high pressure region of a passivation gas. Clusters were co-deposited with a vaporised molecular water beam onto a liquid nitrogen cooled trap.

Figure 1-2 shows a schematic of the experimental setup that the CMP group previously used for producing samples [91]. In the aggregation chamber of device, there was a sputtering magnetron source to produce atomic silicon particles. Further, aggregation of sputtered atoms in the gas phase occurred in this part of device via a cold and inert aggregation gas in our case, we used argon gas for gas aggregation. Our silicon nanoclusters were formed in this part by three-body collisions. In the next part, the clusters were deposited on TEM grids in the gas phase and their structure and size distributions were subsequently investigated. The chamber was also equipped with a Crystal Thickness Monitor (XTM or crystal microbalance) to measure the beam intensity. Clusters were transferred to the deposition chamber in a stream of inert aggregation gas. In the deposition chamber, we had a second gas jet for co-deposition using solvents such as water, and a liquid nitrogen-cooled cold trap. Silicon nanoparticles were co-deposited with the solvent molecules on the wall of cold trap forming a solid phase, usually water ice. After deposition, the solid was melted, and collected. The liquid constituted our sample in suspension [17, 91]. This part of our method was a novel technique designed by our group, and which facilitated the study the clusters in solution. All chambers were held under UHV conditions (base pressure $\sim 10^{-9}$ mbar).

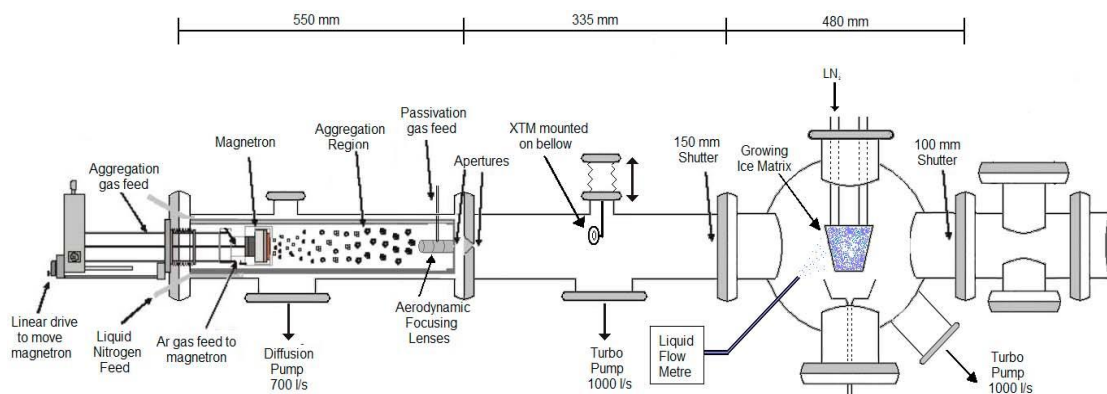


Figure 1-2. Schematic of the experimental set up to produce silicon nanoclusters [16].

The TEM images of silicon nanoclusters deposited on carbon TEM grids, as described above, showed spherical clusters, flake-like and nanotube-like structures with size ranges of 30 nm to 100 nm [91]. Other TEM measurements were performed by using liquid samples; a drop of sample was placed onto a TEM grid and allowed to dry (in air). These results were completely different to the gas phase experiments, marked particularly by the disappearance of the large clusters. AFM studies of films produced by drop-casting solutions of clusters in water on freshly cleaved highly oriented pyrolytic graphite (HOPG) showed the existence of single and laterally agglomerated nanoclusters of about 1 nm in height, irrespective of the production conditions [19, 92, 93]. This indicated that the solution contained predominantly very small clusters.

The sample produced via this method, and collected after co-deposition, showed a number of extraordinary properties; melting of the frozen cluster-ice mixture yielded an aqueous suspension that strongly fluoresced in deep blue wavelengths when exposed to UV light ($\sim 240 - 300$ nm), and remarkably, over time (several months), the overall fluorescence intensity did not degrade [17]. The silicon clusters produced with this same method, but directly deposited on a substrate without interaction with the water beam, did not show any fluorescence; thus, we concluded that the interaction of water and clusters was critical for fluorescence. This interaction most likely caused a chemical reaction, and produced fluorescent sites at the silicon cluster surface [18]. We believed that water provided a strongly oxidising environment and led to formation of fluorescent clusters; however, it could not be the only reason for luminance because non-luminescent, directly deposited samples were also oxidised by their exposure to air. The fact that mixing of water and silicon was critical for fluorescence ultimately led us to our liquid jet method of producing fluorescent silicon nanoclusters. A key idea was that this mixing would be

much more effective if the gas jet was replaced by a liquid jet. Absence of 50 nm clusters and existence of 1 nm clusters in the liquid sample indicates that only silicon atoms in the beam reacted with the liquid and formed fluorescent silicon clusters.

1.6 Novel method to produce fluorescent nanoclusters

In our method, silicon clusters were not provided as initial material. The nanoparticles were rather grown once the silicon atoms attached at the liquid surface and became dispersed. It should therefore be possible to produce fluorescent silicon clusters by direct interaction of single silicon atoms and liquid in order to disperse silicon particles and to provide sufficiently high nanoparticle densities. This required generation of atomic silicon vapour, which was only possible in vacuum, and a liquid, which was difficult since solvents cannot normally exist in their liquid phase in vacuum. To investigate the possibility of forming nano-sized luminescent clusters of oxidised silicon by direct mixing of atomic silicon vapours with liquid oxidants, we employed a liquid jet and directed it through silicon vapour generated by magnetron sputtering. Liquid jets provided particle densities that were sufficiently high for agglomeration of the silicon atoms that became trapped after hitting the liquid surface. Liquid jets of suitable agents represented efficient oxidants; we chose beams of water and alcohols. On the surface of the liquid, and within the liquid, the particles had very high mobility compared to the solid phase, so chemical equilibrium should be reached quickly. A liquid jet was generated following the pioneering work of Faubel, Schlemmer and Toennies [94].

Comparison of the present results with our previous work using co-deposition of silicon clusters shows that reactive self-assembly of clusters on liquid surfaces is a very efficient process. Our results are important for the general understanding of interactions of atoms with liquid surfaces, in particular the entirely unexplored field of reactions of metals and semiconductors with liquid surfaces, the formation of fluorescent silicon, and the site-specific optical properties of atomic clusters.

Possible applications of site-specific fluorescence of clusters are in biomedicine, because silicon and silica are generally regarded as bio-tolerable [11]. Non-toxic, chemically stable clusters in the nanosize range would have significant potential as

chemical sensors that could reach regions in cells that are inaccessible for common, much larger nanoparticles.

1.7 Silicon nanoclusters properties produced by liquid jet method

Our group have developed a revolutionary synthesis method by which several millilitres of blue-fluorescent silicon cluster solution can be produced within a few minutes. All nanoparticles produced so far have been fluorescent, with constant yields over up to three years, and suggested that an intrinsically stable form of silicon nanoclusters in solution existed, showing exceptional stability without further treatment for stabilization. This intense fluorescence wavelength ranged from 310 – 420 nm, depended on the specific solvent used for the liquid jet, and that deep-blue fluorescence emerged from oxygen rich states [81]. When water was used as solvent, the results showed great similarity to [79] (although the authors of this work found they needed to stabilize the sample). The results of our new method were very similar to our previous results for producing stable silicon nanoclusters [16, 17, 19]. The silicon clusters fluoresced a deep blue colour, with the wavelength of the fluorescence similar to our previous work [18] and other groups that used different fabrication methods [80]. We believe that silicon-oxygen and SiOH groups are formed at the cluster surface. In our method, silicon particles could be produced in any solvent to generate silicon clusters with different levels of oxidation. The particles could be transferred to any solvent depending on the required application. Results showed transferring to another solvent was equivalent to producing the cluster in that solvent. Oxidation by addition of one drop of water showed clusters were heavily oxidized in the presence of water. Lifetime measurements showed clusters had a fluorescence lifetime of about a few nanoseconds depending on film and liquid samples and also depending on the solvent which were used as liquid jet. Our Si-water samples had a quantum yield of 10%. Concentration effect, with respect to fluorescence, showed the Si-water sample did not quench, conversely, silicon deposited in alcohol did show quenching, although we could not measure the concentration in this latter case directly, quenching could be concluded from a Stern-Volmer plot. And, also, the results show chemical stability of the samples.

AFM of film samples prepared by drop-casting nanoparticles on HOPG showed exceptionally monodisperse heights of 1 nm, a value that we interpreted as the cluster diameter in solution. We attributed this small cluster size to intense chemical interaction with the solvent during growth and unfavourable physisorption after growth had completed. While the samples were produced in the liquid phase and were stable in solution, they could be dried on the surface of a substrate to form a film with a height of a few nanometers. When the sample was dried, its structure and fluorescence properties changed. The differences suggested that we may have two kinds of cluster in our solvated samples; bulk and surface clusters. Transferring the particles to another solvent reinforced this assumption. The clusters which belonged to the bulk did not change during the drying or solvent exchange, but structure of the surface cluster changed by changing the phase (between the liquid and film ‘phases’) and environment. However, the lifetime measurements made our assignment about bulk clusters doubtful, as they showed different lifetimes for these clusters depending on the solvent. XPS and FTIR/ATR analysis confirmed that the silicon was present in a high oxidation state and that the clusters were extremely oxygen rich. Oxidation states (chemical reactivity) of the samples depended on the solvent. So, we attributed the origin of observed blue fluorescence to oxidised silicon nanoclusters.

1.8 Advantages of fluorescent silicon nanoparticles

As was briefly mentioned in section 1.1, nanoparticles can give us information about biological processes in the cells by emitting fluorescent light, for which silicon nanoparticles are a good choice as they show non-toxic effect on both humans and the environment [95]. Semiconductor quantum dots have high fluorescence and quantum yields [96] but their application in the human body is not straightforward as they contain toxic elements [97]. Therefore, silicon-based fluorescent biomarkers would represent a presumably non-toxic alternative to state-of-the-art quantum dots like CdTe, CdSe, CdSO₄, etc. Nanoparticles that have fluorescence sites at their surface and are chemically stable would provide a promising means to reach efficient and useful bio-sensors, which is our goal in this project. Silicon nanoparticles produced by our novel technique show a number of extraordinary properties. Clusters smaller than 1 nm in diameter form a stable phase in water and do not agglomerate. Samples show strong and exceptionally stable

fluorescence when excited with UV light. As nondegrading photoluminescence is usually difficult to achieve [98], long-term stability in water is a remarkable advantage, as our sample have these properties they can be considered as suitable candidates for applications *in vivo*. Also the solvents which we used for synthesis are not biologically harmful. Our findings suggest a simple, fast and cost-effective method to produce fluorescent silicon clusters.

1.9 Organization of the thesis

This thesis explains how we produced fluorescent silicon nanoclusters and which outstanding physical, optical and chemical properties they have. In the second chapter, the production of silicon clusters by the liquid jet method is described. In chapter three, the methods of characterisation, and the devices we used for characterisation, are described. The methods involved fluorescence spectroscopy and UV/Vis spectroscopy, which were used for optical investigation, whilst ATR/FTIR spectroscopy and XPS spectroscopy were used to examine chemical properties. In chapter four, the results of studies of optical properties are explained and parameters such as fluorescence intensity and wavelength, absorbance, quantum yield, and lifetime are measured. Interesting topics such as fluorescence stability, solvent exchange, effect of temperature, sample concentration, chemical stability, oxidation, and effects of varying physical parameters on fluorescence (like gas pressure, magnetron power, distance and angle of cold target) are investigated. In chapter five, the results of chemical property studies are shown. The samples were produced with water and alcoholic solvents. During the interaction of single silicon atoms with aqueous or alcoholic liquids, the silicon atoms could react and formed compounds containing oxygen, carbon and hydrogen. To investigate the chemical composition and structure of the samples, and to clarify what reaction took place, we used X-ray Photoelectron Spectroscopy (XPS), and Attenuated Total Reflectance (ATR). Chapter six concludes the results, discusses our achievements and suggests some future works.

Chapter 2

Producing silicon nanoparticles

2.1 Overview

Unlike bulk silicon, nano-structured silicon is able to emit light. Fluorescent silicon nanoparticles have a quasi-direct band gap because of their small size, but whilst they are potentially able to emit light, the surface of the silicon nanoparticles needs to be passivated in order to achieve this. Free silicon clusters produced in molecular beam machines have some advantages [16, 33, 66, 99]. Owing to their small size, they have a quasi-direct band gap. They can also be produced in different sizes, but they often have ‘dangling’ bonds where electronic excitations can decay non-radiatively. To produce fluorescent silicon nanoparticles, the dangling bonds need to be passivated by changing the surface structure via chemical reaction(s).

Prior to this thesis, our group investigated the possibility of producing fluorescent silicon clusters of variable size by using the gas aggregation method [100] combined with co-deposition via a beam of vaporised water onto a cold target. It was anticipated that the surface of the clusters would become passivated after contact with the water [16]. Melting the frozen cluster-water mixture indeed yielded a suspension that fluoresced a blue colour when excited with UV light (~240 – 300 nm). TEM experiments (a TEM grid was mounted inside the chamber) confirmed that the clusters produced by gas aggregation were around 50 nm in size. TEM images of cluster films produced by drop-casting of the fluorescent solution onto thin carbon showed that 50 nm sized clusters were absent. AFM analysis [19] has confirmed that the clusters were 1 nm in size. It was concluded that atoms mixed with water must have formed the small clusters.

Consequently, it was decided that gas aggregation and co-deposition was not necessary to produce small fluorescent clusters. This gave rise to the development of a novel method to produce fluorescent nanoclusters: by the use of a liquid jet. A liquid jet

provides more experimental degrees of freedom as different solvents can be added. In this method, sputtering could be used to evaporate silicon, liquid water could be provided in vacuum, and this method incurs only a low gas loaded compare to cluster beam methods. It was anticipated that the fluorescent properties of silicon nanoparticles would change with solutions of variable concentrations and different compounds.

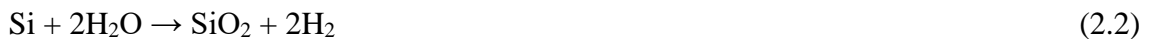
In this chapter, the setup of a liquid microjet and the production of fluorescent silicon clusters is described. Different production parameters, such as liquid jet capillary diameter, liquid jet operation, flow rate and volume of liquid jet, magnetron sputter head, and volume of atomic vapour used are discussed.

2.2 Experimental setup

We set up an experiment to generate fluorescent silicon nanoclusters by deposition of silicon vapours onto a liquid jet. Towards this aim, we employed a professional Auto 306 BOC Edwards thin film coater [101] that was modified to allow for the set up of the liquid jet. The new microjet nanoparticle fabrication technique employs a liquid jet that is passed through a plume of atomised metals or semi-metals in vacuum. Atomic silicon vapour was generated by zero grade (99.99%) Ar ion sputtering of a p-doped silicon target (Kurt J. Lesker Co. Ltd. 3.00" diameter \times 0.250" thickness, 0.005-0.020 ohm-cm). The silicon atoms collided with the surface of the liquid jet, became trapped and aggregated into clusters. The aggregated silicon clusters remained suspended within the liquid solvent, and were ultimately co-deposited with the solvent onto a liquid nitrogen-cooled trap. The water (and other solvents) provides an oxidizing environment for silicon [102] which is needed to passivate the cluster surfaces and to create fluorescent defects. After deposition, the frozen cluster solution was melted and bottled.

The mean free path of silicon atoms produced by the sputter head is around 1 cm, because of the chamber pressure of $\sim 10^{-2}$ mbar (depends on the Ar pressure and liquid pressure). The distance between sputter head and liquid jet is 4 cm. So 3-4 two-body collisions (between silicon particles or silicon and argon molecules) happen before silicon particles reach the liquid beam. As the number of collisions is very low, three-body collisions can be practically excluded.

When the particles reach the liquid jet surface, the atoms can be repelled, pass through the liquid medium, be trapped by the liquid molecules, diffused, and react/interact with other atoms or liquid molecules. The type of nanoparticles that grow depends on the interaction. In the case of using water as a liquid jet, different interactions are possible, such as:



Collective effects are important. In Equation (2.1), the product proton can only be stabilised in bulk water. For example, in helium droplets, the reaction between single Si and $2\text{H}_2\text{O}$ ($\text{Si} + \text{H}_2\text{O} \rightarrow \text{SiOH}^{\text{aq}} + \text{H}^{\text{aq}}$) was not observed [103].

A schematic of the device is shown in Figure 2-1, whilst Figure 2-2 shows the modified device for producing the fluorescent silicon nanoclusters. The operation of each part of the setup is described in detail below.

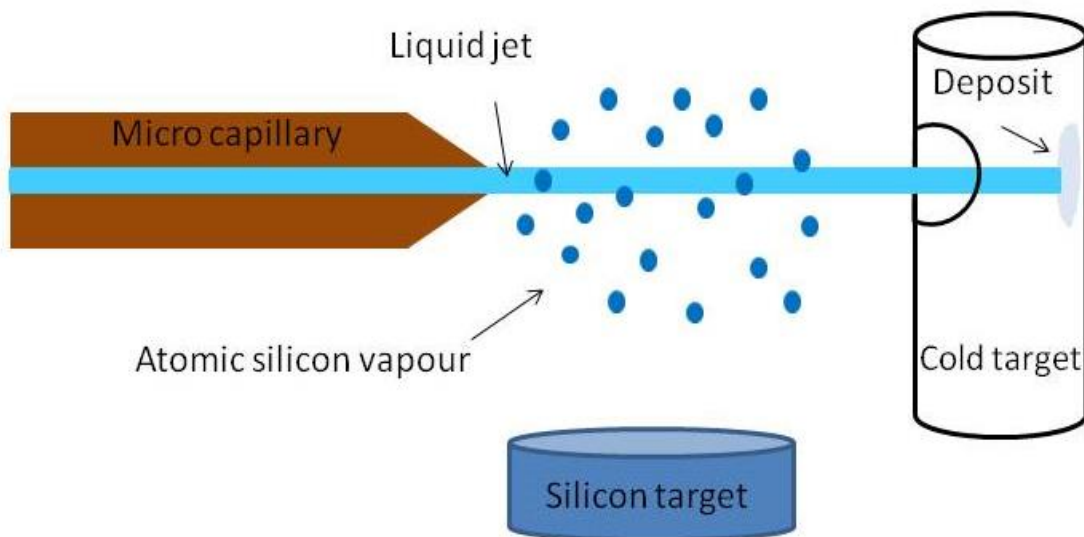


Figure 2-1. This schematic shows different parts of our novel device. A liquid jet passes through the atomic silicon vapour, captures the vapourised atoms and, deposits the nanoparticles thus formed on the inner surface of cold target.

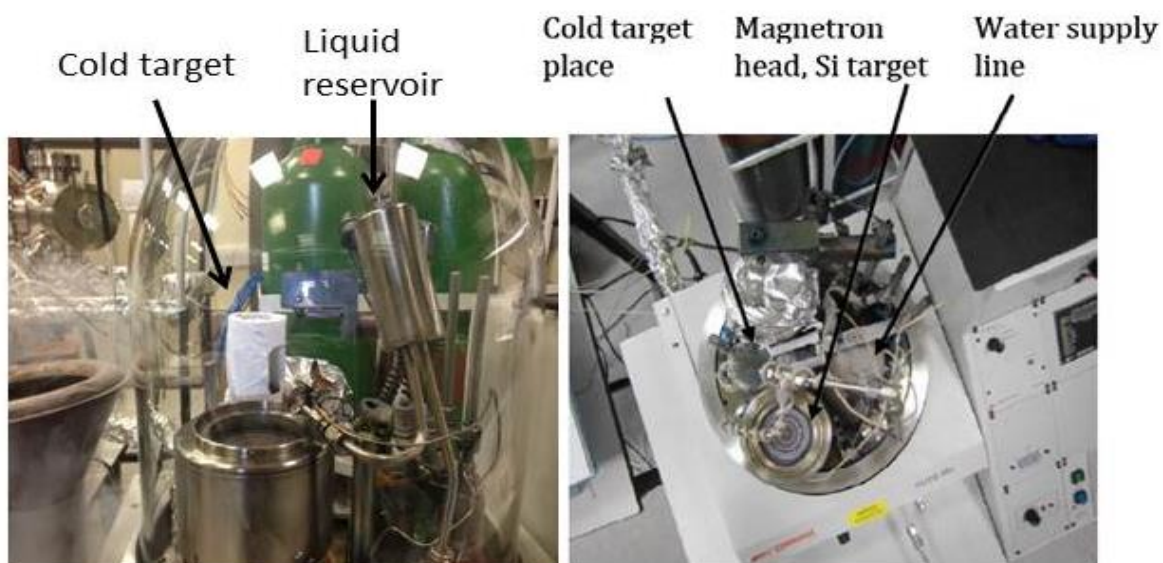


Figure 2-2. The BOC Edwards thin film coater which was modified to produce fluorescent silicon nanoparticles. The positions of the liquid tank, sputter head and cold target in the setup are shown. This figure (left-front view) shows the device whilst working, with a vacuum within the glass jar placed on top of the plate. The figure on the right shows the top view of the setup.

2.2.1 Vacuum

The chamber which contains the different parts of the setup is not particularly big. As can be seen in Figure 2-2, all such parts were contained within a bell jar on a plate with a 40 cm diameter. A glass bell shaped jar, 50 cm high, is placed on top of this plate to form the vacuum vessel. For evacuating the chamber, a pressure in the order of 6×10^{-6} mbar can be reached within less than 10 minutes using a rotary pump and a turbopump. Sputtering requires argon at the pressure of 10^{-2} mbar to be introduced into the vacuum system. After samples had been produced and the sputtering and liquid jet had been stopped, the device could be vented (to ~ 1 bar in argon).

In previous method described in section 1.5, deposition using water vapour (or, indeed, other solvents) was complicated because of the associated high vapour flux, with the concomitant load on the vacuum pumps preventing the apparatus achieving the required internal pressures ($\sim 10^{-6}$ mbar, as above), so it was replaced with water jet.

2.2.2 Liquid jet

The liquid jet source comprised an off-the-shelf fused silica chromatography capillary. In our experiment, a stainless steel cylindrical reservoir with 2 mm wall thickness was used as a solvent/ liquid reservoir to which the capillary was connected. It had two joint pipes connected to the Ar gas supply and the capillary. The capacity of liquid tank was 150 ml, and was of dimensions 15 cm high by 3.5 cm in diameter. By applying a high stagnation pressure of gas in the column behind the liquid, the device was able to reach the desired hydrostatic pressure of liquid to produce a liquid beam in vacuum. The high pressure generation via inert gas was a simple and cost-efficient solution. Our setup worked in a similar manner to a piston, effectively driving the liquid through the capillary. The high pressure tank was safety tested up to 70 bar, but in our experiments the pressure was not allowed to exceed 50 bar. Before evacuation of the chamber, we tested the capillary in air and made sure we were able to obtain a jet in atmosphere. Figure 2-2 shows the position of the liquid tank with respect to other experimental components, and Figure 2-3 shows a liquid filament being produced in vacuum.

When the chamber was evacuated, at a higher chamber pressure liquid droplets emerged at first from the end of the capillary; at lower chamber pressures they subsequently froze; by then applying high pressure Ar gas into the reservoir, liquid was ejected into vacuum. By increasing the stagnation pressure further, a point was reached (~40 bar in water, and 30 bar in alcohol) when a liquid jet was formed. When the stagnation pressure was then reduced, the liquid inside the capillary itself was found to freeze. Therefore, only heating helped to re-engage the liquid jet. Freezing was frequently observed when using water as a solvent because of its freezing temperature. The capillary needed to be heated up to melt the ice. Conversely, for alcoholic solvents, no heating was required and re-applying the pressure by itself could reform the jet.

In our experiment two different diameters of capillary, 50 μm and 25 μm , each with a length of 6 cm, were used. At first we used the 50 μm capillary because the larger diameter was expected to reduce the freezing of the liquid jet because of the thicker gas sheath surrounding wider liquid filament. However, it was found to be very difficult to reach high vacuum and stay within the required pressure regime due to the higher flux from this capillary when the liquid jet was in operation. So, we left the capillary to freeze when the coater was evacuated. We then heated the nozzle (in the case of a water solvent)

and applied a high stagnation pressure. The blocked capillary eventually opened and allowed a liquid filament to establish.

We faced two problems in forming the jet; the liquid capillary changed its direction while operating, within an angle of about 15 degrees. Additionally, when water was used to form the liquid jet, when the jet touched the cold target it froze, and ice grew quickly back along the direction of the jet towards the nozzle and blocked the entire jet and the capillary; this could happen on a timescale of less than a minute. To counter the latter problem, we simply increased the distance between cold target and the capillary and changed the angle between them (different distances and angles are shown in section 2.2.4, and the effects of changing these parameters on fluorescence are shown in chapter 4). This helped, though not much, so to further reduce this back-freezing problem, we decided to use a 25 μm capillary, also using the smaller capillary would obviously reduce the gas load on the vacuum pumps.

Whilst the 25 μm capillary was operating [in vacuum], we observed a different height profile of the deposited water; in contrast to the 50 μm capillary, it seemed to provide much better control of the location of the frozen deposit, also gave a very narrow angular distribution (estimated of $\sim 5 - 10^\circ$ from the long axis of the capillary). As the flux of liquid was less with the 25 μm capillary, the rate of back-freezing decreased considerably and thus took more time to block the capillary; during this time we could produce more sample, despite the reduced diameter of the liquid jet. Although using the smaller capillary helped, the back-freezing problem still existed, so a heater used to melt the ice, as described in section 2.2.5.

By increasing the hydrostatic pressure slowly, the capillary started jetting around 20 bar for alcoholic solvents and 30 bar for water. At these pressures, although the jet started, it was more like a 'spray' of liquid and did not form a distinct, neat filament, so initially the liquid divergence with clearly over much wider angles than when the compact liquid filament was properly formed. As we used polar solvents, the direction of jet sometimes changed during the jetting (when water was used as solvent, this happened more than when alcohol solvents were used), direction change was also more frequent when we used lower Ar stagnation pressures, with the jet behaving like spray. When the stagnation pressure was increased by 10 bar, the liquid jet emerged faster and more like a liquid filament; it was more homogenous and the divergence angle was smaller. We could not increase the pressure too much, because the reservoir was safety limited to a

maximum stagnation pressure of 50 bar. Additionally, at these kinds of stagnation pressure the amount of liquid and the speed of liquid was high, so the rate of deposition – and thus back-freezing – increased, severely limiting the control we had over the experimental conditions. So, we concluded that Ar pressures higher than 40 bar were not suitable for a water solvent. The best Ar pressures were found empirically to be ~40 bar for water, and ~35 - 40 bar for alcohols.

Depending on the capillary length, diameter and viscosity, the pressure was chosen so that Reynolds Numbers greater than 2000 were obtained. Under these conditions, turbulent flow was established, preventing the liquid from freezing in vacuum. We were able to sustain a collimated liquid jet in vacuum over several centimetres.

Laminar volume flow through an ideal capillary is described by the Hagen-Poiseuille law (Equation 2.3). The flow of jet depends on diameter and length of capillary.

$$q_v = \pi r^4 / 8\eta l \Delta p \quad (2.3)$$

Here, q_v is the laminar volume flow rate in m^3s^{-1} , r is the radius of the capillary (in m), η is the kinematic viscosity of liquid in m^2s^{-1} , l is the length of the capillary (in m), Δp is the pressure gradient from one end of the capillary to the other (in Pa). Table 2-1 shows the effect of some parameters we used on laminar volume flow for water. The kinematic viscosity of water was assumed at 20 °C, because we increased the temperature of the filament to around this temperature to avoid freezing.

We produced a variety of samples using water [104], ethanol (<0.2%) [105] and isopropanol [106] as solvents to study environment effects on sample properties. In all cases we could see photofluorescence, but they had different fluorescence properties.

Table 2-1. Laminar volume flow rate for water

r (m)	Δp (pa)	q_v (m^3s^{-1})
25×10^{-6}	30×10^5	2.18×10^{-10}
25×10^{-6}	40×10^5	1.63×10^{-10}
25×10^{-6}	50×10^5	1.30×10^{-10}
50×10^{-6}	30×10^5	4.36×10^{-10}
50×10^{-6}	40×10^5	3.27×10^{-10}
50×10^{-6}	50×10^5	2.61×10^{-10}

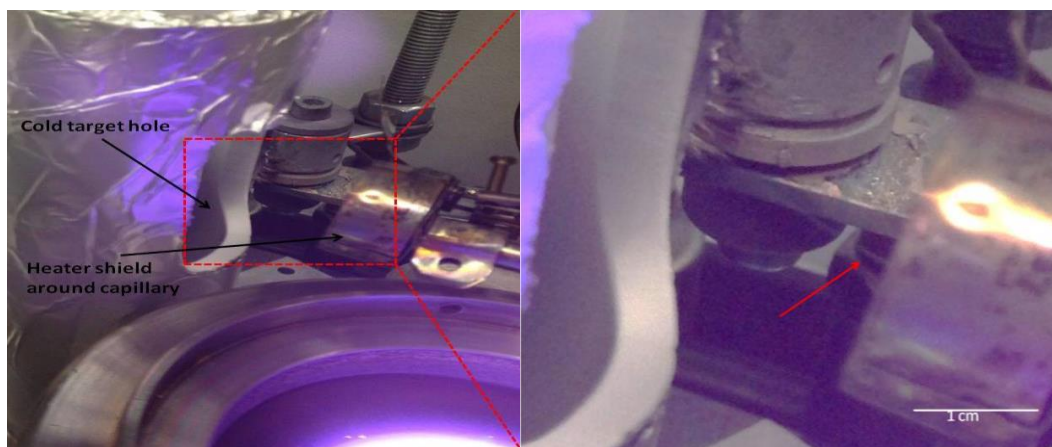


Figure 2-3. The picture on the left shows the cold trap, the liquid jet, the capillary heater and the sputter target (clockwise) giving an idea of distance between capillary and cold target. The dotted rectangle marks the region of the liquid jet and shown as zoomed picture on the right. The red arrow points onto the liquid jet which is collimated for at least 2 cm.

2.2.3 Sputtering

We generated silicon vapour by argon sputtering at partial pressures of $2 - 3 \times 10^{-2}$ mbar. Sputtering is a standard procedure to achieve metallic or semiconductor vapours in vacuum. We required a sputtering gas, usually argon, and a sputtering target. To produce atomic silicon vapour, a p-doped silicon target was bombarded with Ar gas. We used argon because it was easily ionized, chemically inert, relatively cheap, and did not lead to target poisoning. The Ar gas plasma was ignited by applying a high voltage between the magnetron cover (anode) and the sputter target (cathode), the two being located a small distance apart. Initial electrons from the target surface cause cascade ionization in the gas, forming an electrically neutral plasma which is magnetically confined above the target by a strong magnet. By flowing the Ar gas, the pressure of the chamber reaches $\sim 2 \times 10^{-2}$ mbar, and the rest of the process occurs at this pressure. A chamber pressure of 2×10^{-2} mbar was sufficient to ignite sputtering, which meant that the argon atoms were spontaneously ionized and accelerated towards the silicon target. The target's negative potential accelerates the ions from the plasma towards the target material, where they impact with sufficient kinetic energy to eject neutral target atoms by energy transfer. Because argon and silicon atoms have a similar mass, the exchange of kinetic energy with silicon atoms was fairly efficient. The atomic silicon gas was created in the vacuum, through which a liquid jet of solvent was passed. The atoms that hit the surface of the

liquid jet decelerated, and then diffused and aggregated to nanoparticles within the body of the solvent, and were subsequently deposited on the inner wall of the cold target (together with the solvent).

The power used for sputtering varied between 35 W and 100 W. The best samples were produced at ~50 W (see chapter 4). When a power of 100 W was used, the samples had yellow colour and sometimes precipitates formed on the storage vials, and it was found that using these kinds of power levels did not allow for the formation of homogeneous samples.

A picture of p-doped silicon target used as a sputter head can be seen in Figure 2-4 (to the left). To produce a clean sample, we started sputtering a few minutes before starting the liquid jet.

2.2.4 Cold target

We used a cold target to trap nanoparticles, liquids and metal vapour. The trap was formed from a 4 mm stainless steel cylinder with a hole on it to allow the liquid jet and nanoparticles to enter the inside of the cold target. The cold target was 15 cm high and 4 cm in diameter, and the hole was located 2 cm from the top with a diameter of 2 cm. This hole was used to help increase the purity of the sample; due to the nature of sputtering, a few silicon atoms flew through the hole with the liquid jet and froze on the inner walls, but the vast majority of the silicon landed on the outside of the cylinder, thus helping to prevent contamination of the sample by atomic silicon. As the direction of the jet changed during the experiment and hit the edge of the hole (and caused back-freezing in shorter distance), we increased the diameter of the hole to 3 cm to capture all the liquid. Before we evacuated the chamber, we wrapped the cold target with aluminium foil; we then used liquid nitrogen to cool it by immersing into liquid nitrogen and waited until boiling stopped, indicating that thermal equilibrium was reached, and finally placing the cold target onto a petri dish in the chamber before its subsequent evacuation. This temperature was sufficiently low to allow the experiment to be performed for up to 30 minutes without noticeable melting. After deposition, we vented the chamber with nitrogen or argon and the target was left outside the chamber to defrost.

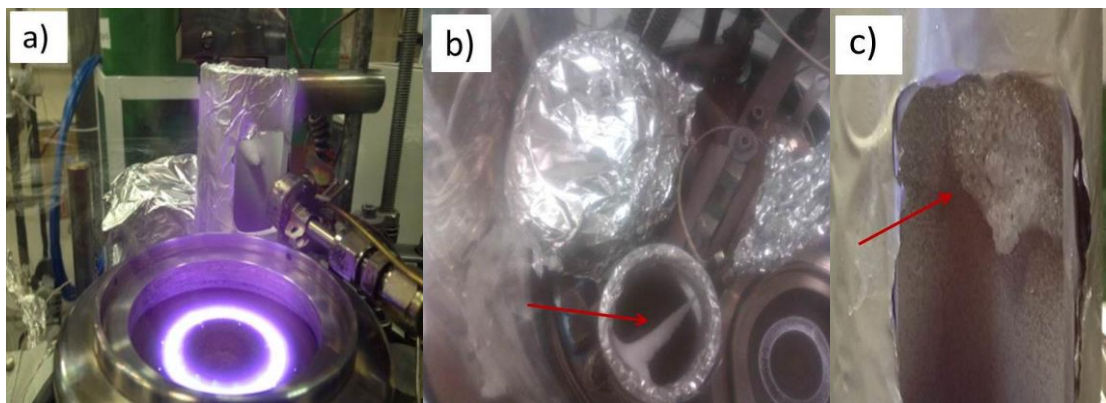


Figure 2-4. The picture in the left (a)) shows the sputter head working in vacuum and its position in the chamber. Picture b) is a top view, showing the position of the cold target in the chamber and the frozen cone-shaped deposit of silicon and water on the inner wall of the cold target. The picture on the right (c)) shows the frozen deposit of silicon and ethanol on the cold target from the side. In all figures the frozen deposit is indicated with a red arrow. Co-deposition of silicon with alcoholic solvents did not form an ice on the cold target wall, and it was similar to boiling liquid deposition, although when the alcoholic solutions hit the wall they froze. However, these solutions then started melting immediately.

Two different distances and angles were used between capillary and sputter head and cold target. Different angles are shown in Figure 2-5; in the case of different distances, the distance between the end of the capillary and the cold target was varied. By tilting the cold target, we prevent the silicon atoms landing directly on the cold target's inside wall. The results of these experiments are shown in chapter 4.

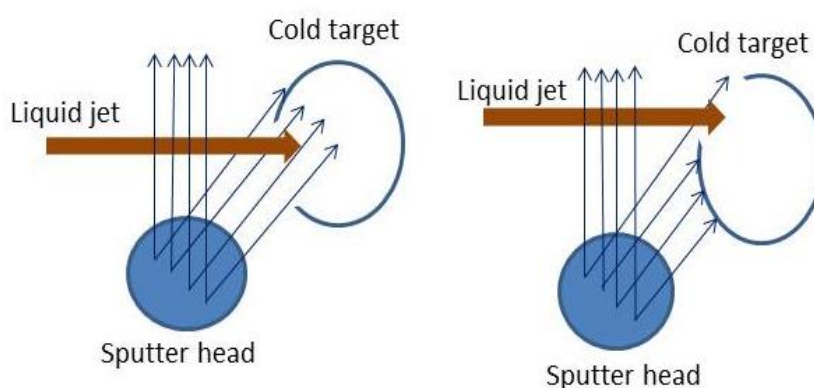


Figure 2-5. Schematic showing the difference between direct and indirect deposition.

2.2.5 Heating

When we evacuated the chamber, the capillary froze due to the lowering pressure during the pumping, so we used a heater to melt the frozen capillary and to reform the jet as necessary; we invariably needed a heater in the case of water as the solvent. As water froze on the cold target during the co-deposition, the ice back-froze along the path of the liquid jet towards the capillary and, ultimately, blocked it, the capillary could be warmed to melt the ice and reform the jet.

The first method we tried for heating, as can be seen in Figure 2-6 (left), we used heating wire wrapped around the nozzle to defrost the ice. It could be left turned on during the experiment, and we could change the temperature depending on the amount of ice forming. We always used 20 – 30 °C to defrost the ice. However, because of the excess of water vapour in the environment, the heater wires became wet and could short-circuit during the experiment, so we decided to use another setup for the heater. In our second method, we used a tungsten filament with a shield to prevent heat loss, and placed the filament very close to the capillary. In this case, we turned on the filament for melting the ice before starting the jet at the beginning of the experiment, and further when water back-froze to block the capillary. However, once the ice melted and the jet reformed, we turned the heating off to prevent the deposition of the heating filament materials in the liquid jet, resulting in sample contamination. For the heating, we applied 2 V and 3 A which caused the filament to glow red hot; we did not exceed this value because we did not want to evaporate filament materials excessively and cause contaminants to enter the cold target. Figure 2-6 (right) shows a schematic of the shielded filament that was mounted on the pipe surrounding the capillary (the pipe is not shown in the figure).

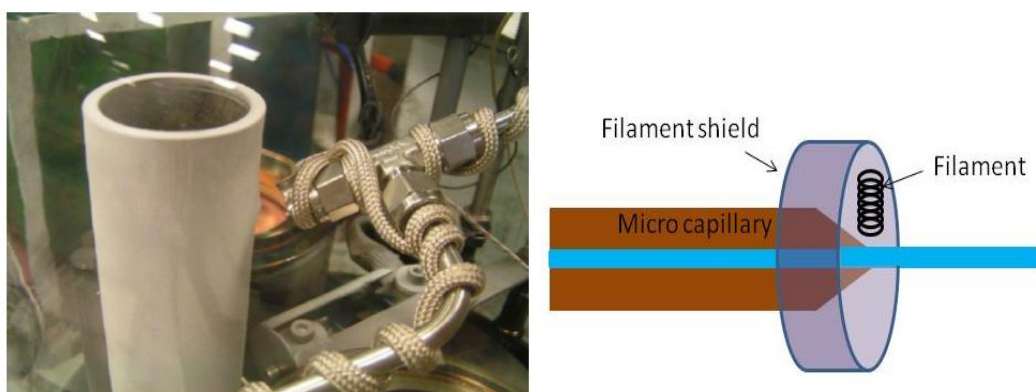


Figure 2-6. Heating wire wrapped around the nozzle (left). A schematic of the filament and its shield as heater (right).

2.2.6 Clustering

In our experiment, there were two possible mechanisms for cluster formation; clusters may have been formed during the interaction of the silicon atoms with the liquid within the liquid filament, or they may have been formed when the cold target was defrosted and the silicon atoms dispersed within the melting ice.

In each run of the experiment, 15 ml of sample could be produced in 20 minutes. When deposition on the cold target was completed, the apparatus was vented by Ar gas, the cold target allowed to defrost and the melted sample was collected by using a clean pipe from a Petri dish underneath the cold target. The sample was then bottled as a liquid sample.

Chapter 3

Characterisation methods

To characterize optical and chemical properties of silicon nanoclusters produced with our method, and their interaction with their (solvent) environment, several methods were used. Fluorescence and UV/Vis spectroscopy were used to investigate optical properties and define some important characteristics of samples such as fluorescence intensity, absorbance, quantum yield, lifetime, the effect of the solvent (solvent exchange), temperature, filtering, oxidation, concentration (quenching) and production parameters (such as distance and angle between liquid jet and cold target, magnetron power, liquid jet pressure and duration of deposition) of sample characteristics was studied. To investigate the chemical and physical composition of the samples, their structure and their chemical bonding, and also to characterize their interaction with their environment, XPS and ATR/FTIR spectroscopies were used.

3.1 Optical characterisation methods

3.1.1 Fluorescence spectroscopy: general remarks

Simply, fluorescence spectroscopy is a method used to measure the intensity of photons which are emitted from a sample - after absorbing photons (of a lower wavelength) from an illuminating source - as a function of wavelength. It has many applications in analytical science because of its high sensitivity and selectivity.

A material which is capable of fluorescence is called fluorophore. In atoms, energy can only be released via emission of electrons or via fluorescence (or, generally less efficiently, phosphorescence). A fluorescence line therefore gives us direct information of the energy difference between the initial and final electronic states involved in the

transition. For molecules, nanoparticles and bulk matter, the situation is more complicated because of the additional degrees of freedom added by vibrations (and rotations).

Generally, fluorescence is accompanied by vibrational relaxation and often vibrational relaxation competes with fluorescence. A typical scenario is illustrated by the following: Absorption of a photon by a molecule excites electrons from the singlet ground state to a singlet excited state. Vibrational states in the excited electronic state are also populated as the (excess) energy of the illuminating photon is partitioned into the available degrees of freedom of the absorbing molecule(s). It can return to the ground state in a two-step process: in the first step, the molecule returns to the lowest level of the excited state by transferring a part of its electronic and vibrational energy to the environment, for example via collisions with other molecules (e.g., radiationless decay via internal conversion). In the second step, the molecule then decays back to the ground state by emission of a photon. This process is called fluorescence, as opposed losing energy to the environment in a nonradiative manner. Often there is a triplet excited state lower in energy than the singlet excited states and the molecule changes from singlet to triplet and dissipates part of its energy which is called intersystem crossing. The similar relaxing processes occur for the molecules which are excited to the triplet excited state, in this case emission of photon is called phosphorescence. The phosphorescent energy in most cases is lower in energy than that of fluorescence energy. So for the fluorescence processes, molecules emit a photon and drop to one of the vibrational levels of ground electronic state; because molecules can decay to many vibrational levels in ground state, the emitted photons will generally show a broad spectrum of energies rather than a single discrete line. By analysing these different wavelengths and their intensities - and depending on the method used (see latter) - the energetic positions of different vibrational levels and the potential energy curve of the ground state, or excited state, can be determined [107].

These processes are shown in the Jablonski Diagram or electronic transitions diagram, in Figure 3-1 [108].

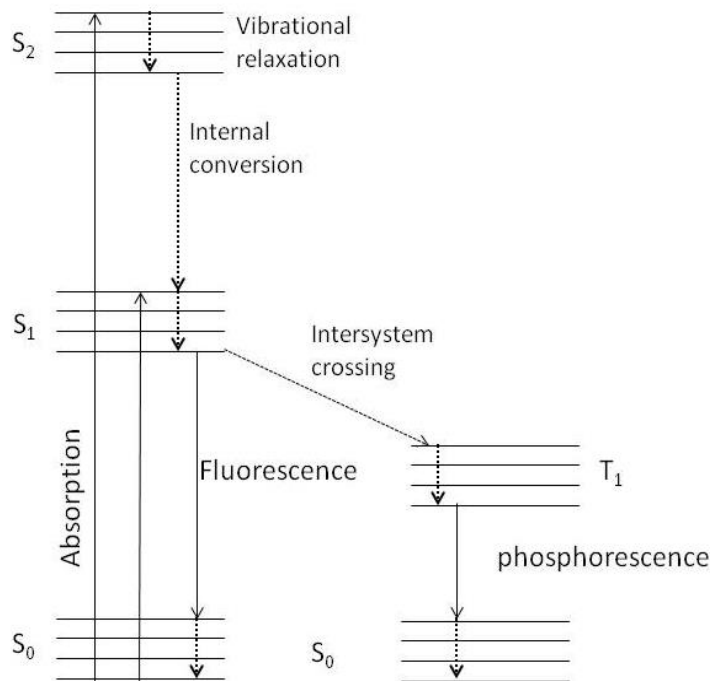


Figure 3-1. Jablonski diagram [108]. This diagram shows electronic transitions for absorption and fluorescence processes. S_0 refers to the electronic ground state, S_1 and S_2 to electronically excited singlet states and T_1 refers to the excited triplet state.

The energy of emitted photons (emission energy) is always lower than the energy of the absorbed photons (absorption energy), because there are many more de-excitation processes than fluorescence emission to return the molecule to the ground state. In most cases, fluorescence happens from the lowest vibrational level of the excited electronic state and the molecule decays to an excited vibrational state of the electronic [ground] state, depending on the various Franck-Condon factors. Thus, fluorescence peaks are detected at longer wavelengths than the absorbance or excitation peaks. The wavelength (thus energy) and the intensity of the fluorescence peaks give information about structure and environment of the sample.

For large molecules and nanoparticles, emission from excited state occurs often independently of the excitation wavelength; in other words, the emission energy (wavelength) is unchanged and independent of the excitation wavelength. This is the case when vibrational energy distribution within the electronically excited states is efficient and populates always the same initial state before fluorescence.

As the absorption occurs from the ground electronic state, so the absorption, or excitation, spectrum characterizes the population distribution in the ground state.

Fluorescence and phosphorescence happen from excited states, so the emission spectrum describes the population distribution across the excited states. Emission and excitation spectra also characterize the electronic state distribution in a molecule.

The intensity of the peaks, the emission wavelength and decay lifetime are some of the observable phenomena which can characterize the sample. Each molecule and sample has its own unique fluorescence spectrum and observable parameters. These properties are intrinsic, but can be modified by the environment.

A fluorometer is used for the acquisition of spectra, and consists of: an excitation source, which can be a lamp or laser, an excitation monochromator (if a lamp is used as excitation source), a cuvette and a cuvette holder, an emission monochromator, photon detector, and a recorder. These parts are described in following sections in details.

A continuous spectrum emitted by a Xenon lamp shines onto an excitation monochromator (first monochromator). It selects a small subset of wavelengths for excitation. This monochromatic excitation light is directed into the sample. When the sample absorbs this light, it fluoresces. The fluorescence light is directed into the emission monochromator (second monochromator). The second monochromator selects a band of wavelengths as emission wavelengths and directs them onto a photomultiplier. The signal from detector is sent to system controller and computer to process with software.

The fluorescence beam is emitted in all directions, so just a portion of this light enters the second monochromator and then detector. The detector usually is placed at 90 degrees to the light from the excitation source to minimise the incident light reaching the detector. Figure 3-2 shows a schematic of the fluorescence setup.

A fluorescence emission spectrum is recorded by keeping the excitation wavelength constant (first monochromator) and the scanning the emitted light as a function of wavelength (emission monochromator sweeps the whole spectral range). An excitation spectrum is recorded by keeping the emission light at constant wavelength (second monochromator) and the excitation light is scanned as a function of wavelength (excitation monochromator is run for all required wavelengths). In fluorescence emission spectra, photon counting is measured, whilst in fluorescence excitation spectra photon current is measured.

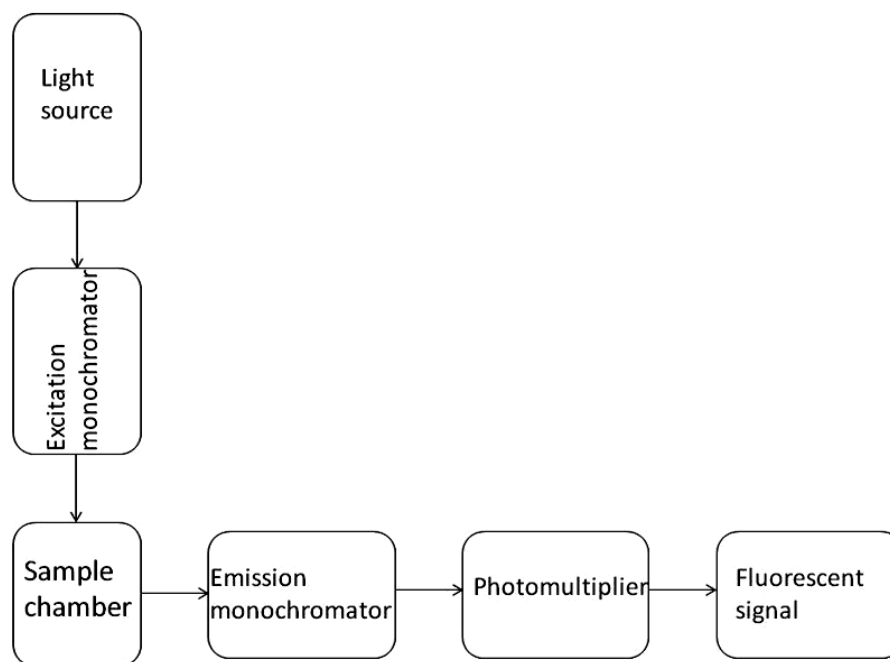


Figure 3-2. This schematic shows the position of the main parts in a fluorescence spectrometer. Some particular parts, such as the beam splitter or the reference detector, are not shown because they are not used in the main light path.

Fluorescence is defined by intensity, quantum yield and lifetime. Fluorescence intensity, I_F , at a specific wavelength is the number of fluorescence photons, n , multiplied by the photon energy, E , (Equation (3.1)).

$$I_F = nE \quad (3.1)$$

The fluorescence quantum yield Φ_F is the number of fluorescence photons, n , divided by the number of absorbed photons, n_{abs} . So, I_F and Φ_F are proportional. The fluorescence lifetime, τ_0 , is the time the molecules spend, on average, in their excited state before decaying. Quantum yield and the fluorescence emission maximum are sensitive to the surrounding environment. Fluorescence lifetime and quantum yield are described in the following sections.

Excitation and fluorescence spectra can quantify (by comparison to known references) the concentration (at low concentration, fluorescence intensity is proportional to concentration) and identify a fluorescent compound, as the excitation and emission properties of a specific molecular species are fixed for the same environmental condition. The wavelength of the emitted photon is characteristic of the molecular structure.

Although the intensity of fluorescence peak, F , depends on the intrinsic properties of a given molecular species and its environment, experimental parameters such as intensity of absorbed light, concentration of sample, length of the cell can also have an effect. The relation of these parameters with fluorescence is described by Equation (3.2):

$$F = \phi I_0(1 - e^{-\epsilon bc}) \quad (3.2)$$

Where ϕ is quantum efficiency, I_0 is intensity of the incident light, ϵ is the molar absorptivity, b is the path length of cell, and c is the molar concentration of sample [109]. Low intensity of fluorescence shows a low concentration of the fluorophore.

3.1.1.1 Stokes shift

As some of the energy of molecule is lost via heat or vibration, the emitted energy is usually less than the excitation energy, and the emission wavelength occurs in longer wavelength than the excitation wavelength. This difference between excitation and emission wavelengths is called the Stokes shift.

The energy absorbed by a molecule is generally different from the emitted energy. The absorption and emission energies are described by Equations (3.3) and (3.4) [107]:

$$E_a = hc/\lambda_a \quad (3.3)$$

$$E_{em} = hc/\lambda_{em} \quad (3.4)$$

And

$$E_{em} < E_a \quad (3.5)$$

So:

$$\lambda_{em} > \lambda_a \quad (3.6)$$

Where λ_a and λ_{em} are absorption and emission spectra maxima. It shows emission spectrum maximum shifts to longer wavelength respect to absorption spectrum maximum.

So, the Stokes shift, δE , is described by Equation (3.7):

$$\delta E = E_{em} - E_{ex} \quad (3.7)$$

Where E_{em} and E_{ex} are emission and excitation energies. Stokes shift depends on the structure of the molecule (sample) and its medium (solvent).

3.1.1.2 Light diffusion: Rayleigh and Raman scattering

There are two sources of diffused light that contribute to an emission spectrum: Rayleigh scattering and Raman scattering. When diffused photons and excited photons have the same energy, this is called Rayleigh scattering; the excitation peak occurs at the same wavelength. Raman diffusion occurs at a wavelength longer (Stokes) or shorter (anti-Stokes) than the excitation wavelength. Raman scattering is the result of excitation of a virtual electronic state by the excitation light and relaxation to a vibrational excited level other than the vibrational ground state [110]. In other words, this is a two photon process.

Raman peak energies change when the excitation wavelength is changed, but this change is always proportional to the excitation wavelength (and Rayleigh peak) for the same sample. For example, for water, the Raman peak appears 3367 cm^{-1} lower than the excitation light frequency. Different solvents and samples have different Raman peaks. In typical emission spectra, the intensity of the Raman peak is much lower than that of the Rayleigh (scattering) peak.

In an aqueous environment, the symmetric H-O-H vibration is responsible for the Raman peak. Alcoholic media create two Raman peaks. As the position of the Raman peak is excitation wavelength-dependent, the position of the Raman Peak in an aqueous environment can be calculated using Equation (3.8) [107]:

$$1/\lambda_{ram} = 1/\lambda_{ex} - 0.0003367/nm \quad (3.8)$$

The wavelengths here are in nanometers.

To distinguish between Raman and fluorescence peaks, we can change the excitation wavelength. As fluorescence often does not depend on the excitation wavelength, but the Raman process does in a very specific way, Raman peaks can thus be identified by changing the excitation wavelength. Because the Raman peak(s) of some solvents can be complex, it is better to run an emission spectrum of the pure solvent before the analysis of any solvated particles.

In general, the higher the fluorescence peak intensity, the lower the Raman peak intensity, because these are competing processes, and fluorescence is the much more efficient than Raman scattering.

3.1.2 Employed fluorescence spectrometer

A fluorometer is an analytical device used to record fluorescence excitation and fluorescence emission spectra of a sample, so the excitation wavelength, or emission wavelength, can be scanned while the other is kept constant.

We used a fluoroMax-P (Jobin-Yvon Horiba) to measure the fluorescence spectra of the samples [111]. The device was controlled by the DataMax spectroscopy software [112]. The detail of each part of the spectrometer is described in the following sections.

3.1.2.1 Light source

The sample can be excited by using different light source such as: lasers, photodiodes, lamps, xenon arcs, and mercury vapour.

A 150 W continuous wave (CW) Ozone-free Xenon arc-lamp was used as the illuminating source [113]. Light from the lamp was collected by a mirror, and then focussed on the entrance slit of the excitation monochromator. The lamp was separated from the excitation monochromator by a quartz window to prevent heat entrance into the instrument. The spectrum of Xenon lamp used for our experiment is shown in Figure 3-3.

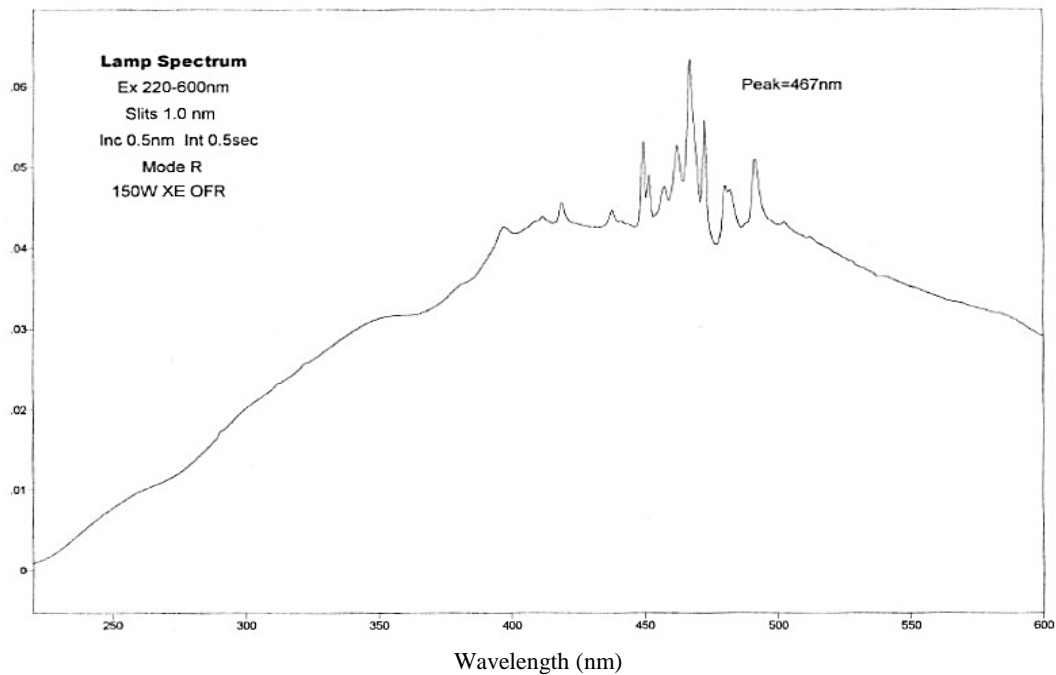


Figure 3-3. Emission spectrum of Xenon lamp which is used in our experiment [114].

3.1.2.2 Monochromators

A monochromator selects for wavelength by using a diffraction grating. Collimated light enters a grating and leaves at a different, wavelength-dependent, angle. Therefore, the monochromator can be adjusted (angle selected) to select which wavelengths to transmit.

The device was equipped with two Czerny-Turner monochromators, as excitation and emission monochromators. The Czerny-turner design allowed high resolution (up to 0.3 nm) across the entire spectral range, whilst minimizing spherical aberrations and diffraction [113]. The most important part of the monochromator is the grating, which disperses light by virtue of its vertical grooves. A spectrum was achieved by rotating the gratings, and recording the intensity values at each wavelength/ angle.

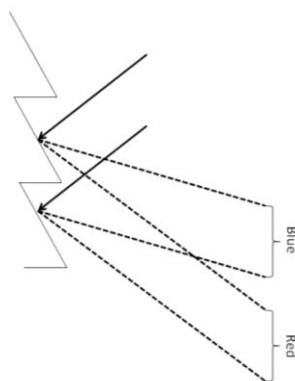


Figure 3-4. A diffraction grating splitting an incident beam into its component wavelengths. The saw-tooth profile (called the ‘blaze’) aims to enhance the intensity of certain wavelength regions.

In the instrument used for our measurements, the wavelengths selected were optimum for excitation in the UV and visible range (from 250 nm to 700 nm), and for emission in the high-UV to near-IR (from 200 nm to 800 nm) [113].

The entrance and exit slits of each monochromator could be controlled by the DataMax software. For the excitation monochromator, the width of the slits controlled the bandwidth of light incident on the sample. For the emission monochromator, the slit width controlled the intensity of fluorescence light incident on the grating. When the width of slits was increased, the more light reached the sample and detector, so the intensity of the spectrum increased, but at the cost of spectral resolution.

3.1.2.3 Sample chamber

The beam from the excitation monochromator was focused onto the sample. Fluorescent light emitted at 90 degrees from the sample, with respect to the incident beam, was collected. Fluorescence from the sample was directed onto the emission monochromator. About 8% of the beam from the excitation monochromator was split by a beam splitter before reaching to the sample, and used to illuminate a reference photodiode [113].

3.1.2.4 Detectors

The detector can be operated as a single channel (PMT, photodiode, etc) or multiple channels (CCD, MCP, etc). A single channel detector can only detect only a single

wavelength from a sample at any one time, but a multiple channel detector can detect intensities of multiple wavelengths at the same time.

The instrument we used contained two detectors, a signal detector and a reference detector, to assess the quality of the excitation light source. The signal detector was a photon-counting detector. It had an R928P photomultiplier tube, which sent the signal to a photon counter. It could detect in the range from 180 - 850 nm, with dark counts <1000 cps. The photon counter had a linear range of 1cps to 4×10^6 cps, but the working range was up to about 1 cps to 2×10^6 cps; above 4×10^6 cps it became saturated, and the detector response was no longer linear. The reference detector detected the xenon lamp to correct it for wavelength dependent and time dependent output of the lamp. It operated in the range of 190 - 980 nm and was located just before sample chamber [113].

3.1.3 Sample preparation for fluorescence measurement

3.1.3.1 Liquid sample

The fluorescent samples that we used were in solution, and so could be analysed in a standard sample cuvette. The cuvette had to be non-fluorescing, to prevent contamination of the sample's fluorescence spectrum, and also had to have little absorption in the wavelength range of interest. A quartz (fused silica) cuvette is ideal in these regards as they allow high-efficiency transmission from 200 nm – 2500 nm; some forms of quartz can transmit up to 3500 nm.

We used a suprasil 115-QS Hellma cuvette with light path of 10 mm. Its dimensions were 40mm height, 12.5mm length, and 12.5mm width, but the liquid was in a sub-compartment of the cuvette volume (of dimensions 10 mm \times 1 mm \times 40 mm). The volume that could contain the sample was 400 μ l. It had a Teflon cap to contain the liquid. This cuvette fitted in a cell holder inside the sample chamber. Before measurement, the cuvette was cleaned with acetone and then again using the same pure solvent as sample solvent. We always kept the samples in ultraclean vials. For fluorescence measurements, 400 μ l of sample was transferred from the vial to the cuvette by a glass pipette.

3.1.3.2 Film sample

In addition to liquid samples we made film samples to investigate the properties of the samples outside the solvent environment and exposed to the atmosphere, provided that the nanoparticles did not chemically react with the solvents. We expected that by evaporating the solvent, all samples would show the same results as their spectra were no longer had any solvent dependency. A suprasil substrate was used for film sample preparation; a film of sample was made by putting 50 drops of sample on the substrate, each drop being added when previous one had dried completely. The sequence was repeated 50 times to make a film with a thickness of approximately 50 nm, as AFM measurements showed our clusters have a height of ~ 1 nm. Film samples were used for measuring excitation and emission spectra and also for measuring the lifetime at the Superlumi end station at beam I, Hasy lab, Desy, Hamburg. In these measurements, pulsed synchrotron radiation was used as an excitation source, allowing to discriminate scattered light from fluorescence light. This was important for the characterisation of the films, because they inevitably produce strong scattered light by diffuse reflection.

To measure the samples, we used pulsed synchrotron radiation and time-correlated single photon counting (TCSPC) method. In this method a pulsed light source (monochromatic synchrotron radiation) excites the sample. When a detector detected a photon, the time with respect to the source pulsed timer was measured. All photon events had to be detected between two consecutive pulses of light from the source with so-called single-channel analyser time windows, which can be set as required. We used time windows for scattered light detection [0- 5 ns], fast fluorescence [5- 10 ns] and slow fluorescence [50- 150 ns]. A photon arriving within one of these time windows was counted in separate counters. In addition, all photons were counted in a counter for integral measurement. The schematic in Figure 3-5 shows how the fluorescence photon is detected in this method. The optical parameters of the Superlumi end station are reported in publications by Zimmerer such as a photon flux $\leq 7 \times 10^{12}$ photon/(nm.sec), base pressure $\sim 10^{-10}$ and pressure during experiment $\sim 10^{-9}$ [115]. Deviating from these parameters we used a resolution of 0.3 nm for the primary monochromator. A turbo pump and an ion getter pump were used for evacuating the chamber [116].

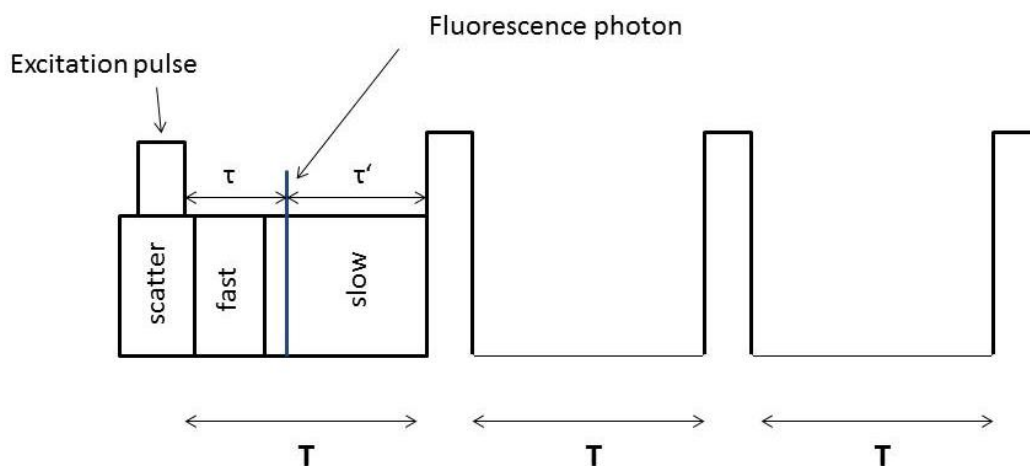


Figure 3-5. The schematic shows how TCSPC method measure the fluorescence and fluorescence photon can be detected in different time window.

3.1.4 Recording Fluorescence spectra

For recording Fluorescence emission spectra, in software, we chose emission acquisition as our experiment type in the data acquisition software. For our measurements, scans were started 10 nm on the higher energy side to the excitation wavelength, because we wanted to measure the Rayleigh and Raman peaks as well as the fluorescence peaks, because they are useful as wavelength and intensity benchmarks. The end points were chosen at 800 nm, with integration time and increment set to 0.5 s and 1 nm respectively. Both entrance and exit slits of emission monochromator were set to a width corresponding to 2 nm resolution.

For recording fluorescence excitation spectra, we chose excitation acquisition for as our experiment type in the data acquisition software. The parameters we used for our experiments were: scan start point 200 nm, scan end point 500 nm, integration time 1 s, increment 0.5 nm, and entrance and exit slits widths corresponding to 1 nm resolution in the excitation monochromator.

We also measured the fluorescence spectra of our samples as a film and in the liquid phase at the Superlumi end station at beam I, Hasylab, Desy, in Hamburg. Here, the detector could detect the different components of fluorescent light: scatter, fast and slow components, and could integrate all of these components.

3.1.5 UV/Vis spectrophotometry

UV/Vis spectroscopy designates absorption spectroscopy in the ultraviolet (UV) and visible (Vis) spectral ranges. This method investigates electronic transitions, and is complementary to fluorescence spectroscopy. [Dispersed] fluorescence spectroscopy gives information about transitions from the excited state to the ground state, while UV/Vis spectroscopy measures the absorbance and gives information about transitions from the ground state to the excited state [117].

UV/Vis spectrometry is used for identification of unknown components (qualitative analysis) and the measurement of concentration of individual compounds present (quantitative analysis) of organic and inorganic compounds in wide range of applications.

Molecules in their ground level absorb light and go to an excited state from where different processes, including fluorescence, de-excite the molecules. If a sample is illuminated with a light beam with an intensity I_0 , the absorption, I_{abs} , and transmitted, I_{trans} , light intensities depend on the concentration of the absorber, which is the molar concentration (particle density), c , the path length (length of the absorber), b , and the molar absorptivity (cross section for light absorption), ϵ . The Beer-Lambert law shows how intensities depend on these parameters [118]:

$$I_{trans} = I_0 e^{-\epsilon cb} \quad (3.9)$$

$$I_{abs} = I_0 (1 - e^{-\epsilon cb}) \quad (3.10)$$

$$I_{trans} = I_0 - I_{abs} \quad (3.11)$$

And absorbance is defined as:

$$A = \log \frac{I_0}{I_{trans}} = \epsilon cb \quad (3.12)$$

The Beer-Lambert law defines absorbance of a sample by Equation (3.12), where A is absorbance. As c is a function of wavelength, the Beer-Lambert law is valid only for a single wavelength.

And transmittance defined as:

$$T = \frac{I_{trans}}{I_0} \quad (3.13)$$

A UV/Vis spectrometer consists of a UV and visible source, a monochromator for wavelength selection, sample and reference containers, detectors, and a signal processor. In addition, depending on the design of the instrument, they may have mirrors and a beam splitter, etc.

A UV/Vis spectrometer can be a single beam or double beam. In a single beam spectrometer, a beam from a light source hits the monochromator, becomes monochromatic light, which is then passed through the sample and ultimately illuminates the detector. The single beam spectrometers are microprocessor-based and have facility to store the reference spectrum (baseline). In this case I_0 should be measured without the sample cell present as a reference or background, the reference spectrum is measured first and stored. When a sample is measured, the software determines the transmittance, T .

In a double beam spectrometer, light leaving the monochromator is split into two beams before it reaches the sample. One beam is used as a reference beam whilst the other is passed through the sample. The simple schematic in Figure 3-6 shows how a double beam spectrometer works; A UV/Vis source produces a light beam in the ultraviolet and visible range (some devices use two sources to cover the entire range). The light beam illuminates a monochromator and is separated into its component wavelengths using a diffraction grating (or using a prism). The monochromatic beam leaves the monochromator and is split into two equal intensity beams by a beam splitter or a half-mirrored device. One beam, the sample beam, passes through the sample which is located in the sample chamber, whilst the other one is used for the reference beam, which should suffer no light absorption. The intensity of the reference beam is the same as the initial beam (I_0) and the intensity of the sample beam is I . The monochromator scans the selected wavelength range automatically. The output result is a graph of absorbance versus wavelength. The software determines the transmittance, T , by dividing the sample signal, I , (which is the signal transmitted by the sample) with the background, I_0 , (which is proportional to the signal before it reaches to the sample). By definition, the absorbance, A , is the logarithm of the inverse of the transmittance, T [119]. The user can choose to display the absorbance or transmittance in a spectrum.

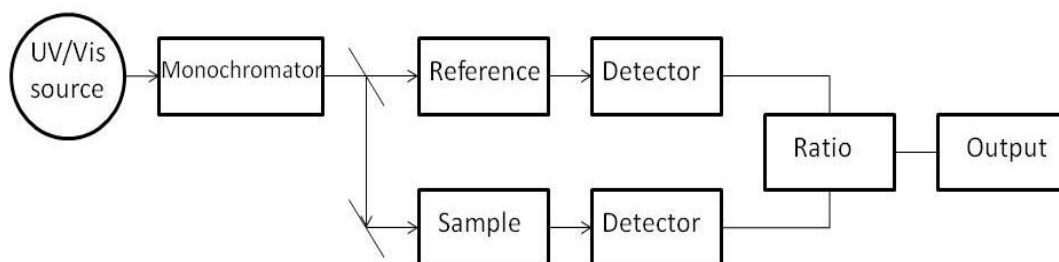


Figure 3-6. The schematic shows how a double beam UV/Vis spectrophotometer works.

3.1.6 Employed UV/Vis spectrometer

We used an Evolution 220 UV-visible spectrophotometer (Thermo Fisher Scientific, Inc.) to measure the absorbance spectra of our samples [120]. The Evolution 220 is a double beam spectrophotometer, so it corrects automatically for any change in source light intensity. Before each measurement, a reference scan was performed. The ratio of the sample to the reference beam at each data point (wavelength), eliminates errors that could arise from detector sensitivity drift. This spectrometer works in the range 190 - 1100nm.

3.1.6.1 Light source

UV/Vis spectrometer can be adapted to light sources that cover the whole range of ultraviolet and visible wavelengths, for instance the xenon arc lamp, or have two different light sources to cover this range, like a tungsten filament and a deuterium arc lamp.

Our spectrometer used a xenon flash lamp that covered the UV and visible range with high intensity [120]. It did not need any warm up before measurement. It sent intense flashes of light only when measurements were being taken.

3.1.6.2 Monochromator

Similar to a fluorometer, our UV/Vis spectrometer employed a Czerny-Turner grating monochromator [120]. The source beam entered the monochromator via the entrance slit. It was collimated by a collimator and then directed onto the reflection grating at an angle, splitting the beam into its component wavelengths. By changing the angle of grating, light of only a specific wavelength left the monochromator via the exit slit (Figure 3-4).

3.1.6.3 Detector

Generally, detectors can be photomultipliers, photodiodes, or charge-coupled devices (CCD). The Evolution 220 UV/Vis spectrophotometer used in our measurements employed dual silicon photodiodes as detectors [120]. Photodiode detectors were used with scanning monochromators, and only a single wavelength reached the detector at one time. By changing the angle of the diffraction grating for each wavelength, the detector could measure the intensity of the beam as a function of wavelength. Because the device had two detectors, the sample and reference beams were measured at the same time to eliminate errors caused by drift of the light source or changes in the sample over time.

3.1.6.4 Sample compartment

The device was equipped with AFBG (Application Focused Beam Geometry) which optimized the optical configuration of the instrument [120]. The holder cell which embraced the cuvette was allowed for a highly reproducible sample location with respect to the beam. The holder cell position could be fine-tuned by two vertical and horizontal screws. The micro-AFBG tightly focused the beam and allowed light to pass through the 2×2 mm aperture.

3.1.7 Sample preparation for UV/Vis measurement

As glass and plastic cuvettes absorb light in the UV region, only quartz/ fused silica glass cuvettes are recommended because they are transparent to light with high transmittance across the entire UV, visible and near infrared regions.

The cuvette we used for this experiment was the same as the one used for fluorescence spectroscopy. The cuvette volume was 400 μl , hence only 400 μl of sample was required for each experiment. Light was passed only through a 2 mm \times 2 mm window in the cell holder.

3.1.8 Recording UV/Vis spectra

To record spectra, data collection and analysis, the INSIGHT software [121] was used. The software had four different sample analysis modes: Fixed, Scan, Quant, Rate.

In this work only the scan mode was used, which measured the light passing through the sample over a wide range of wavelengths. For starting the experiment, one had to select the appropriate scan option in the software. Then, in the setting window, the user needed to select the appropriate parameters for the experiment. We chose “Absorbance” as data mode and the values which were used for our measurements were: start wavelength 1000 nm, end wavelength 200 nm, bandwidth 2 nm, integration time 0.1 s, and data interval 0.5 nm. Backgrounds (“blanks”) and calibrations were automatically measured prior to the experiment itself.

For higher accuracy we needed to measure the blank before beginning of each experiment. Both sample and reference spectra were normalised using the “blank” spectrum in each measurement automatically. The sample spectrum was corrected by the reference spectrum (background) in each measurement automatically. For the blank measurement the sample chamber was left empty. The cuvette used for sample measurements was the same cuvette that was used for fluorescence measurement. Preparing the sample and cleaning the cuvette was the same as for the fluorescence measurement. After measuring the background, the sample spectrum was recorded.

3.1.9 Fluorescence quantum yield

Fluorescence quantum yield is defined by Equation (3.14):

$$\phi_F = \frac{\text{emitted photons}}{\text{absorbed photons}} \quad (3.14)$$

The quantum yield of a molecule is calculated by comparing the fluorescence intensity of the molecule with the fluorescence intensity of a reference molecule of known quantum yield, as described in Equation (3.15) [107]:

$$\phi_{\text{sample}} = \frac{OD_{\text{reference}} \times \sum F_{\text{sample}}}{OD_{\text{sample}} \times \sum F_{\text{reference}}} \phi_{\text{reference}} \quad (3.15)$$

Where ϕ_{sample} and $\phi_{\text{reference}}$ are the quantum yields of sample and reference, F_{sample} and $F_{\text{reference}}$ are the fluorescence intensities of the sample and reference, OD_{sample} and $OD_{\text{reference}}$ are the optical density of sample and reference (absorbance).

As a reference, stilbene 3 was used. Stilbene 3 has a fluorescence peak at 422 nm when excited at 308 nm, and has therefore very similar properties as silicon nanoclusters produced by deposition of silicon atomic vapour on water (see chapter 4). So, to calculate the quantum yield of the sample, we measured the optical densities of sample and reference at the excitation wavelength, which was 308 nm for our experiment. To measure the optical density, absorbance spectra were measured by the UV/Vis spectrometer. We could replace the sum of the fluorescence intensities by the maximum fluorescence intensity as the sample and reference had the same fluorescence maximum wavelength, which was 422 nm. So Equation (3.15) could be written as (3.16):

$$\Phi_{sample} = \frac{OD_{reference} \times I_{sample}}{OD_{sample} \times I_{reference}} \Phi_{reference} \quad (3.16)$$

If the sample and reference have different refractive indices, Equation (3.16) is changed to Equation (3.17) [122-124]:

$$\Phi_{sample} = \frac{OD_{reference} \times I_{sample}}{OD_{sample} \times I_{reference}} \left(\frac{n_{sample}}{n_{reference}} \right)^2 \Phi_{reference} \quad (3.17)$$

Where n_{sample} and $n_{reference}$ are the refractive indices of the sample and the reference. As we dissolved stilbene 3 in ethanol and we used Si-water samples to calculate quantum yield, we used Equation (3.17) for our calculations.

3.1.10 Fluorescence lifetime

When a molecule is excited, it remains in the excited state for only a short time, depending on the decay processes in operation, before returning to the ground level. In the visible spectral range fluorescence lifetimes are roughly in the range of nanoseconds. The fluorescence lifetime is described by Equation (3.18) [107]:

$$\tau_f = 1/k = 1/(k_r + k') \quad (3.18)$$

Where k_r and k' are radiative and nonradiative rate constants. De-excitation of the molecule includes all radiative and nonradiative processes to define the fluorescence lifetime. The radiative lifetime ($\tau_r = 1/k_r$) is the real emission lifetime, but it cannot be measured independently of the other de-excitation processes, because they occur in parallel. Therefore, the time of all de-excitation processes is measured and this time is called the fluorescence lifetime and it is lower than the radiative lifetime.

The fluorescence intensity is reduced exponentially with time. If the molecule's excited state population is $N(t)$ at time t , the rate of decreasing the population is [107]:

$$-\frac{dN(t)}{dt} = (k_r + k')N(t) \quad (3.19)$$

A solution for $N(t)$ in Equation (3.19) is Equation (3.20).

$$N = N_0 e^{-t/\tau} \quad (3.20)$$

Where N_0 is the initial excited state population. When $t = \tau$:

$$N = N_0 e^{-1} = \frac{N_0}{e} \quad (3.21)$$

Therefore, fluorescence lifetime is the average time required for the population in the excited state to reduce to $1/e$ of the initial population on excitation.

Fluorescence lifetime often depends on the structure of the fluorophore itself [125], but its interaction with environment can affect on it [107].

To measure the lifetime, we used pulsed synchrotron radiation and the time-correlated single photon counting (TCSPC) method (as described in section 3.1.3.2), at the Superlumi end station at beam I, Hasylab, Desy, in Hamburg. Fluorescence decay curves were also measured using a fixed excitation wavelength. The distance between two excitation pulses is divided by the 500 'channels' within the trigger timebase and the time between arrival of the photon and excitation pulse is measured for every photon with respect to this channel. The photons are counted separately for every channel. As can be

seen in Figure 3-5, lifetime, τ , is related to the measured time, τ' , when T is the period (the trigger timebase); $\tau = T - \tau'$.

The environment and its interaction with the molecule can affect lifetime, particularly when the sample is in polar environments.

The results of lifetime measurements are shown in section 4.12.

3.1.11 Fluorescence quenching

Interaction with the environment may quench the fluorescence and therefore reduce the fluorescence intensity and quantum yield. In dense gases or liquids, quenchers reduce the fluorescence when they collide with fluorescent molecules or when they form a non-fluorescent species with fluorescent molecules. When quencher and fluorescent molecules collide, the molecules share energy, after which they separate again. Quenching of fluorescence because of collisions is called dynamic quenching, whilst formation of non-fluorescent species is called static quenching. According to Equation (3.1), in the case of static quenching the number of emitted photons reduces, whilst in the case of dynamic quenching the energy of fluorescent molecule reduces; therefore, the fluorescence intensity and quantum yield will decrease in both cases. Although static quenching reduces the fluorescence intensity and quantum yield (because the number of fluorescent molecules is reduced due to binding to quencher), it does not change the fluorescent lifetime because all the fluorescent molecules in the sample have the same fluorescent lifetime. In presence of dynamic quenching, the fluorescent molecules lose energy, so the fluorescence lifetime of these molecules is lower than those that do not undergo collisions. Therefore, the mean fluorescent lifetime in the case of dynamic quenching is lower than the mean lifetime in the absence of quenchers. So, in dynamic quenching, fluorescence intensity, quantum yield and lifetime decrease[107].

Increasing the temperature can increase dynamic quenching in the sample, because the colliding particles have more kinetic energy and therefore mean free path before collision is reduced.

At high concentrations or short path lengths, particles interact with each other and lose their energy through means other than fluorescence emission, which can induce dynamic quenching.

3.1.12 Temperature effect

As temperature can change the population of the ground state, excitation of phonons and molecular [kinetic] energy, it can and therefore affect fluorescence. Therefore, we investigated the effect of changing temperature on fluorescence wavelength and intensity of film samples at the Superlumi end station at beam I, Hasylab, Desy. In this experiment, the fluorescence of Si-ethanol film samples was measured at four different temperatures (8 K, 28 K, 60 K and 300 K). For bulk silicon, increasing the temperature increases the fluorescence intensity; however, in silicon nanoparticles, cooling the sample results in an increase of fluorescence intensity. As increasing the temperature redistributes ground state population across more states, it causes broadening of the fluorescence peak [126], as illustrated in Figure 3-7.

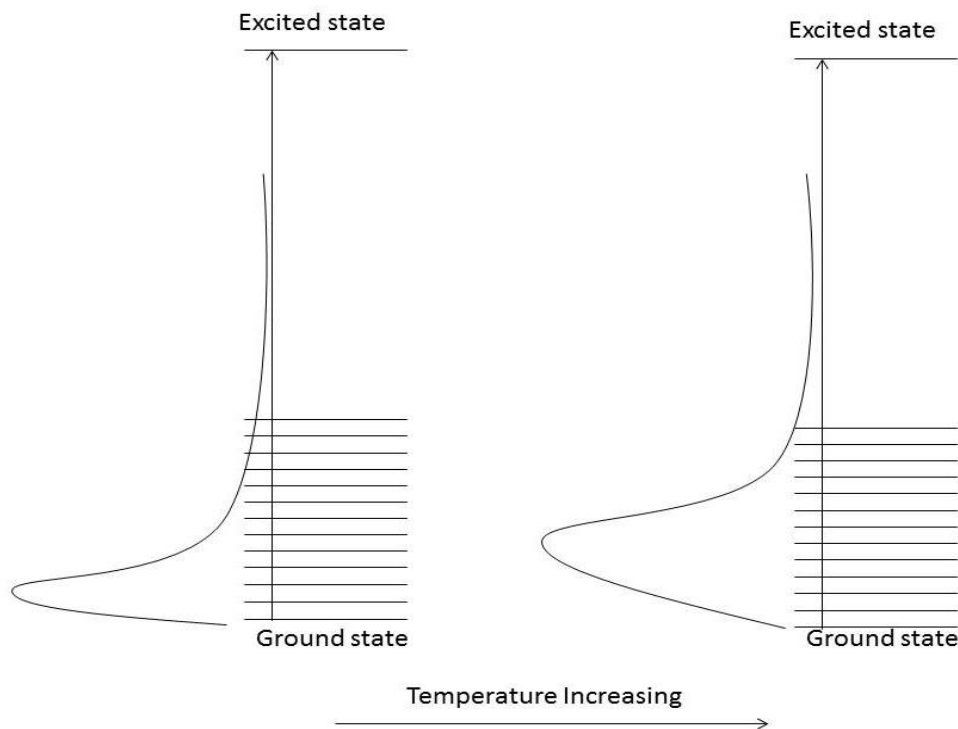


Figure 3-7. Schematic explaining the broadening of fluorescence spectra by increasing the temperature. Increasing the temperature redistributes the ground state population across more states.

3.1.13 Reversible interaction of solvents

To find whether the optical and chemical properties of the samples depended on the solvent used for the liquid jet - or as the environment in which the sample was suspended - and to assess whether this solvent dependence, should it exist, could be due to chemical reactions during nanoparticle growth on the surface of the liquid jet, a solvent exchange experiment was performed. This was done to compare a sample of directly deposited silicon particles in solvent with one where the silicon clusters were transferred from one solvent to another.

In this experiment, as shown in Figure 3-8, we started with a Si-ethanol sample, for which we recorded fluorescence spectra. Then ethanol was then completely evaporated such that the silicon particles remained in the sample vial as residue. The vial was then topped up with water and fluorescence spectra were again recorded. In a third step, the water was evaporated and the residue transferred back to ethanol (the origin solvent), and fluorescence spectra were once again recorded. Finally, the ethanol was once again replaced by water in the same manner as above, and a final set of fluorescence spectra recorded. The same experiment was performed using the Si-ethanol samples and isopropyl alcohol (IPA, propan-2-ol). In all evaporation steps, a hot plate was used but the temperature was held below the boiling point of the solvents in question. The results of this experiment are shown in section 4.7.

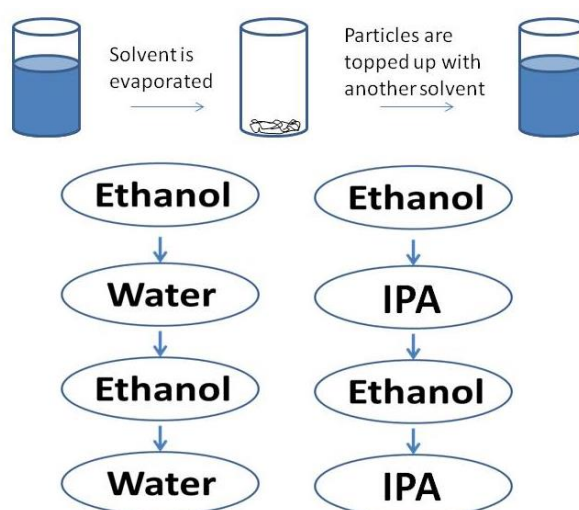


Figure 3-8. This figure shows the process of solvent exchange experiment. In each experiment, sample residue was transferred between two solvents in four steps, with fluorescence spectra recorded for each step.

3.1.14 Concentration effect

We study the concentration and interaction of the nanoparticles to verify fluorescence quenching and chemical stability (using UV/Vis spectroscopy) of the samples. In this experiment, a Si-ethanol stock sample was diluted in 10 steps, and by 50% in each step. This dilution experiment was performed to see the effect of concentration of sample on fluorescence intensity and absorbance. A Stern-Volmer graph was plotted to show this dependence (see section 4.6).

3.2 Chemical characterisation methods

By deposition of silicon into the different solvents, we expect different chemical reactions and different chemical properties. These chemical reactions should be investigated. To achieve this, FTIR and XPS were used.

3.2.1 X-ray photoelectron spectroscopy (XPS)

All materials interact with their environment via their surface, and the type of interaction defines the physical and chemical composition and structure of the materials and their surface. Analysis of the surface is very important; however, surfaces of bulk materials have a small proportion of atoms, and this proportion depends on the shape and roughness of the surface and also the composition and structure of the materials.

X-ray photoelectron spectroscopy (XPS) is a sensitive technique which can analyse a surface, and answer questions such as which elements, how much of them and in what electronic and oxidation states these elements exist. Furthermore, chemical composition, chemical bonding and interaction with environment, electronic state of the samples and the composition of the material at the surface can often be determined.

In XPS, electrons are released from a sample as a result of a photoemission process. The spectrometer consists of a soft X-ray source for primary radiation (often $AlK\alpha$ or $MgK\alpha$), and an electron analyser. X-ray spectroscopy is performed under ultrahigh vacuum conditions. In XPS, an electron ejects from a core level due to impact with an x-ray photon. An electron spectrometer analyses the energy of the emitted photoelectrons, via the intensity of emitted electrons versus the electron energy. The spectrometer

measures the kinetic energy (E_K) of the emitted electron, which depends on both the energy of the primary X-ray photon ($h\nu$) and the material. The binding energy of the electron (E_B) defines the element from which the electron originates and via its unique atomic energy levels. Equation (3.22) shows the relationship between these parameters [127].

$$E_B = h\nu - E_K - W \quad (3.22)$$

Where W is work function and $h\nu$ is primary photon energy.

Identification of the elements that exist in the sample is the first aim of XPS analysis. So, recording a survey spectrum that includes all elements peaks from 0 to around 1200 eV is necessary. Sometimes there is an unwanted feature in the XPS spectrum which are called satellite peaks, which arise if non-monochromatic radiation is used, and the sample is excited by weaker emission lines of the X-ray source, the so-called satellite emissions (for example $AlK_{\alpha 3,4}$, $AlK_{\alpha 5,6}$, and AlK_{β}). To distinguish elemental peaks from satellite peaks, Auger transitions in an XPS spectrum are considered because they are independent of the excitation energy and, therefore, do not show satellite features. The next step after recording the survey is the acquisition of high(er) resolution spectra in a small region around the peaks of interest.

Some parameters should be considered during the analysis, such as the number of components, the degree of symmetry of the peaks, the width and the FWHM of the components, the shape of the peaks, and the shape of the background. Most of elemental peak show chemical shift in the XPS spectrum from one to several electron-volts. These shifts can be classified in two groups, as being due to initial state or final state effects. In the case of initial state effects, the atom before photoemission is partially charged due to bonding to another element, causing a shift in binding energy. The bonds with higher electronegative atoms show the greater chemical shift toward higher binding energy. The final state effect happens after photoemission, and can have several causes, such as core hole screening, relaxation of electron orbitals and the polarization of surrounding ions. As it can be seen in Figure 3-9, after ejecting of an electron, its corresponding atom becomes ionised, and unstable. The atom tends to return to stable state by redistribution of its atoms (relaxation). An important relaxation channel is the so-called Auger decay.

When the core hole generated by the photoelectron is filled by decay of a higher lying electron the excess energy is released by emission of an electron from a higher lying shell which has lower binding energy.

Furthermore, there is a high probability for inelastic scattering of photoelectrons which is causing the electrons to lose energy, generate further, secondary electrons and affect the background. The secondary electrons produce a background with positive slope instead of a horizontal background. This background is superimposed with the peaks of the primary photoelectrons. Energy conservation permits the emission of many secondary electrons as a consequence of the primary process of photoelectron generation.

To assign XPS peaks, the National Institute of Standard and Technology (NIST) has provided a source of standard data for the elements and their components [128].

Given the intensity of the components, the stoichiometry of the sample can be determined. For quantitative analysis of XPS spectra, peak intensities can be converted to atomic concentrations in software.

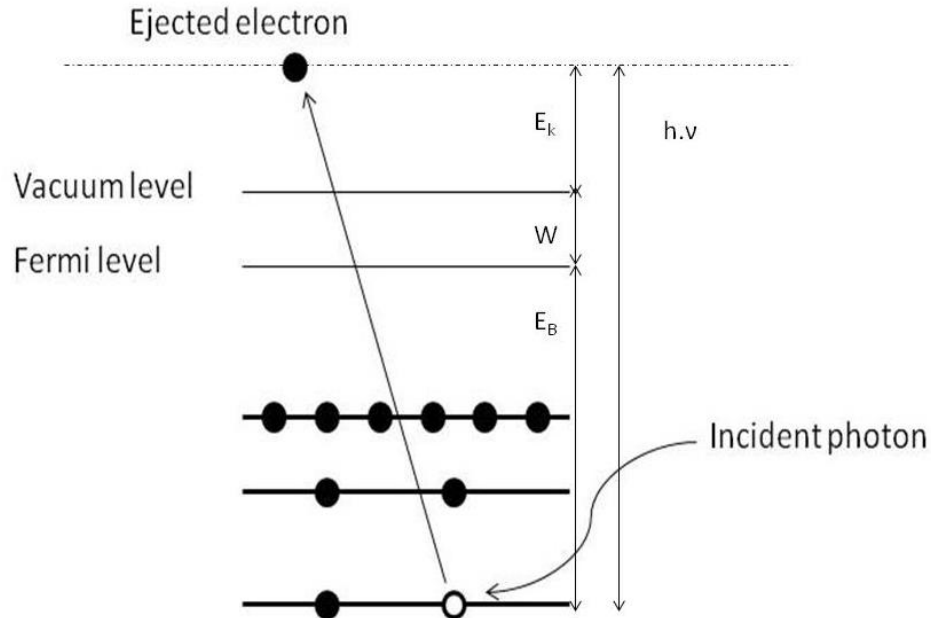


Figure 3-9. A schematic showing the photoemission process.

3.2.2 XPS spectrometer Employed for analysis

All XPS setups have several features which are necessary for analysis, including a primary beam source (X-ray), an electron energy analyser and a detector. All are situated in a vacuum chamber held under ultrahigh vacuum (10^{-8} to 10^{-11} mbar). A data recording system is also required.

We used an OMICRON ultrahigh vacuum system for X-ray spectroscopy. The system was a Multiprobe; it has a two chamber setup referred to as the preparation and analysis chambers, in addition a fast load lock chamber. The most important attached components were a dual anode X-ray source for photoelectron spectroscopy (DAR 400) and an electrostatic analyser for measuring the kinetic energy of electrons and ions (EA 125 U). All the vacuum chambers had their own vacuum pumps and pumping stages. Manual and elecropneumatic gate valves were used to allow separation of the different regions of the apparatus, allowing them to be independently pumped (and, if necessary, accessed). The system had two magnetically-coupled probe transporters which were used to carry the sample from the load lock chamber to the sample transfer head in the preparation chamber, and from the sample transfer head to the manipulators in the analysis chamber, respectively. The device also had a system controller that monitored the pressure of the chambers, the status of the pumps, the electrically operated valves and controlled the bakeout procedure to allow for reliable and safe operation. Figure 3-10 shows a schematic of the XPS device.

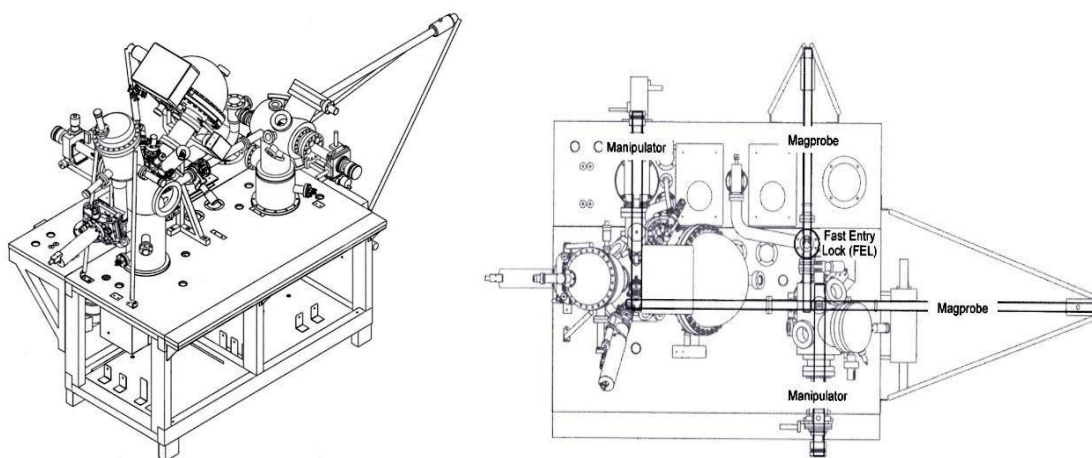


Figure 3-10. The XPS spectrometer and its components [129].

3.2.2.1 X-ray source

In an XPS gun, X-ray photons are produced by bombardment of an anode with high energy electrons. A thermal source, which is usually a tungsten filament, emits electrons, which are accelerated towards the anode using voltages in the kV range and then bombard the selected surface of an anode. The energy of the electrons defines the X-ray photon energy, and the photon flux depends on the electron current that bombards the anode. The anode is held at a high positive potential. The electron trajectories toward the anode are defined by the shape of the nose cone and the focus ring. Each face of the anode has its own filament for excitation. The material chosen as anode should generate photons with a high enough energy to excite an intense photoelectron from all elements. Usually, the anode materials are aluminium and magnesium, which produce AlK_{α} and MgK_{α} photons at 1486.6 eV and 1253.6 eV, respectively [127]. They form a twin anode in a single X-ray gun. The X-rays are generated on the anode surface and pass through an aluminium window and hit the sample. The aluminium window between the source and the sample forms a partial vacuum barrier and allows the source to be differentially pumped.

A schematic of an X-ray gun is shown in Figure 3-11. The X-ray gun is always water-cooled to remove the heat that is generated at the anode. It is used to cool the anode to prevent the evaporation of aluminium and magnesium from the anode surfaces.

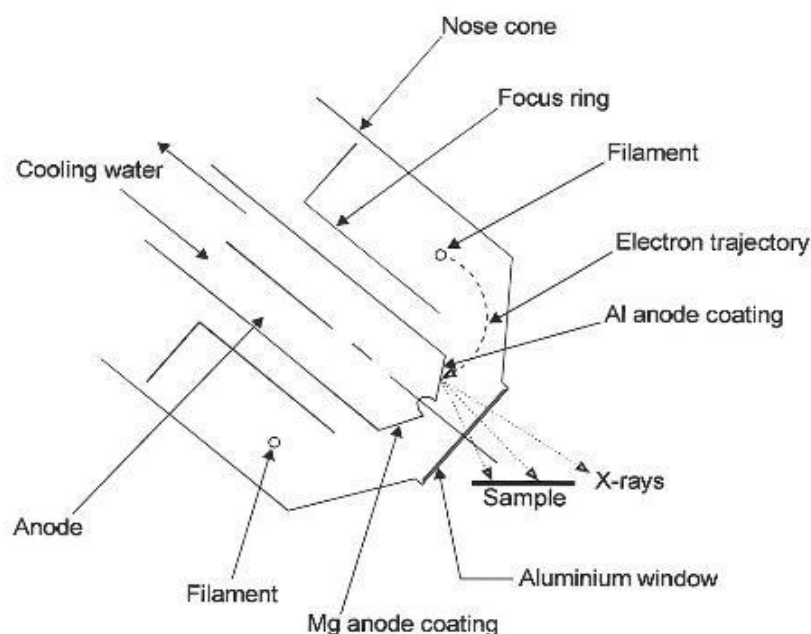


Figure 3-11. Cross-section through x-ray source components [130].

In our experiment the DAR 400 unit designed specifically for XPS was used as the source. It has a twin anode with easy selection of either $\text{MgK}\alpha$ (1253.6 eV) or $\text{AlK}\alpha$ (1486.6 eV) radiation. We used the Mg anode for our experiments.

3.2.2.2 XPS analyser and detector

XPS devices have a hemispherical sector analyser which contains a pair of concentric hemispherical electrodes; the outer electrode is held at a more negative potential than the inner. There is a gap between the two to allow the passage of the photoelectrons, which are dispersed by the analyser according to their energy across the exit plane that is located between two hemispheres. Analysers focus electrons in angular dimensions, from the entrance to the exit plane, as in Figure 3-12.

There is an input lens that collects electrons and focuses them onto the entrance slit of the analyser, and adjusts their kinetic energy to match with the ‘passing energy’ of the analyser.

Our sample analyser was the EA 125 which was an energy radius (centre of the flight path) of 125 mm in the electrostatic hemispherical deflection analyser.

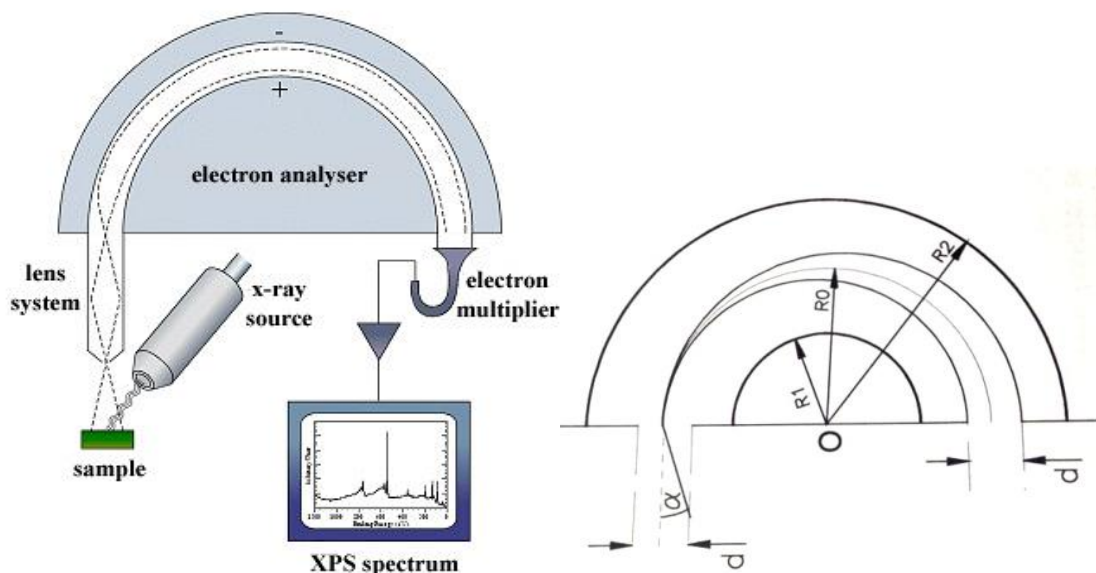


Figure 3-12. This figure shows the hemispherical analyser and its components (right) [131]; it also shows the trajectory of the photoelectrons (left), where R_0 is the electron trajectory radius [132].

3.2.2.3 Detector

Two kinds of electron multiplier can be used as the detector in XPS to count electrons: channel electron multipliers known as channeltrons, and channel plates.

In our device, a channeltron (seven channel electron multipliers) was located across the exit plate of the analyser, as a detector. The current of due to the electrons was amplified by channeltron by a factor of about 10^8 . This current pulse at the output of the channeltron was passed through a vacuum feedthrough into a preamplifier, and then a pulse counter for processing and generating an electron energy spectrum.

3.2.3 Sample preparation for XPS spectroscopy

As our samples were liquid, we needed to make a film using drop casting for XPS experiments. In the first experiment, to choose a good substrate (is described in section (3.2.5.1)) we tested molybdenum, copper, and HOPG as substrates. In the case of copper and molybdenum, the substrates were first cleaned with acetone and isopropanol, and then by the pure sample solvent. By using a clean pipe, a drop of 5 μl of sample was put on the substrate; when the solvent had evaporated completely, the sample was ready to insert to the load lock chamber. In the case of HOPG, we cleaved the surface of HOPG by sellotape several times to be sure of having a fresh and clean surface, which was done under a laminar flow of clean air. Similar to the other substrates, a 5 μl drops of sample were dropped on the substrate.

In some experiments we used several drops to ensure a thicker sample layer and higher concentration of clusters; the results of our investigation into different sample thicknesses is discussed in chapter 5. In this case, each drop of sample solution was added to substrate after the previous one had completely dried. HOPG, for reasons that will be made clear later on, was chosen as substrate.

When we used silicon deposited in alcohol sample, by putting a drop of sample on the substrate, we found that the sample immediately spread over the surface of and covered the entire substrate, while in Si-water samples this did not happen. In the latter case, we had to ensure the whole substrate was covered with the sample, rather than dropping the sample onto it. The difference between an XPS peak of a Si-water sample

for complete covered and incomplete coverage of the HOPG substrate is shown in chapter 5.

To start X-ray photoelectron spectroscopy, the pressure of the chambers should be verified. The appropriate pressure for the preparation chamber was $\sim 10^{-10}$ mbar and for analysis chamber was $\sim 10^{-11}$ mbar. When the sample was ready (as described) it should be inserted into the load lock chamber, which is then evacuated. When a suitable pressure is reached, the sample is transferred to the preparation chamber and then subsequently analysis chamber. It can take several hours to reach the appropriate pressures to allow for transfer between chambers.

3.2.4 Recording XPS spectra

The XPS data acquisition software was EIS/EIS sphera, running in XPS experiment mode. Before investigation of a specific peak, we needed to have a survey of the sample. To do a survey scan, the parameters required [to be entered at the bottom of software window] were: start point 0, end point 1200, 0.5 eV step, sweep 1 (number of scans; if greater than one, software automatically averages), Dwell 0.2 s (dwell time was time to record each data point, effectively an ‘exposure time’), CAE mode (Constant Analyser Energy mode –see below), CAE/CRR ratio 50 (this ratio is related to a pass energy of 50 eV), high magnification, 6 mm diameter entrance slit and 3 mm \times 10 mm exit slit. Increasing the dwell time increased the data precision (signal- to- noise ratio).

The hemispherical analyzer can be operated in two modes, Constant Analyzer Energy (CAE), or Constant Retard Ratio (CRR). In CAE mode, the pass energy of the analyzer is kept at a constant value and the transfer lens system is scanned to retard the kinetic energy of incident electrons to a range that can be accepted by the analyzer. The CRR mode scans the lens system but also adjusts the analyzer pass energy to allow a constant value of initial incident electron energy. For recording XPS spectra, CAE mode is needed, whilst CRR is used for recording Auger spectra. Decreasing the CAE/CRR ratio increased peak resolution. We always used high magnification mode and set the entrance slits to their widest settings, as silicon produced in alcohol had very weak intensity peaks.

The survey spectrum usually took a few minutes. By using the library feature of the software, we could generally tentatively determine which peak belonged to which

element. Figure A.2-3 in appendix 2 shows a sample survey, and the use of the library to identify peaks. After getting the survey, the signal should be optimized (see appendix 2). When the signal was optimized, a higher resolution scan across a shorter energetic region could be performed for observed peaks. The narrow scans were used to define the chemical state of the elements that presented in the sample, and additionally for quantitative analysis. For higher resolution and to gain sharper peaks we used a CAE/CRR ratio of 10, at the cost of signal intensity. For compensating the lower signal we decreased the step width of the scan to 0.05 eV and increased the number of sweeps and the dwell time.

3.2.5 XPS measurements

To investigate the chemical composition and electronic bonding of the samples we used X-ray photoelectron spectroscopy (XPS), and concentrated on the peaks belonging to silicon, oxygen, and carbon. We wanted to know how silicon atoms reacted with the solvents and which chemical species might have formed. For example, would silicon atoms break the hydroxyl bonds and react with carbon or would silicon react with [the oxygen in] the water, or would we have pure silicon in the samples?

The binding energy for these elements and their components were found in the literature and on the NIST website. According to the literature, compounds showed shift in binding energy respect to bulk elements, we compared the measured peaks of our samples with their values in references and found what material our samples had.

Our experiments consisted of:

1. Investigation of effect of thickness
 - Si-water on HOPG (1drop)
 - Si-water on HOPG (10 drops)
 - Si-water on HOPG (10 drops – central on substrate). For this sample, we made a film with ten layers of sample droplets but only in the centre of the HOPG; we did not cover the whole of the substrate. For the other samples, we covered the whole of the substrate with sample solution.
2. Investigation of effect of substrate

- HOPG substrate. To find out whether our samples interacted with the HOPG, or otherwise, and to record a background and reference for HOPG, and the samples.
 - Pure water on HOPG. We made a film with five drops of pure water, to use it as a reference and background spectrum.
 - Si-ethanol on HOPG substrate
 - Si-ethanol on Mo plate
 - Si-ethanol on Cu plate
3. Investigation of solvent effect
- Si-ethanol on HOPG
 - Si-IPA on HOPG
 - Si-water on HOPG
4. Investigation of solvent exchange effects on sample
- Si-ethanol sample transferred to IPA
 - Si-ethanol sample transferred to water

[As a calibration of XPS experiments we used a silicon wafer as a reference for pure silicon.]

3.2.5.1 Effect of substrate

AFM measurements showed the height of the nanoparticles to be in the region of 1 nm. For such small nanoparticle sizes, strong substrate effects were expected because a large fraction of the atoms in the nanoclusters was in direct contact with the substrate.

Four peaks, which were silicon (2p), silicon (2s), carbon (1s) and oxygen (1s), were measured to investigate substrate effects using three different substrates (HOPG, Cu and Mo).

Carbon peaks existed in all XPS measurements because, during preparation, the sample was exposed to air [133].

All experiments in this part were performed by one drop of sample solution, with a volume of 5 μl .

3.2.5.2 Effect of thickness of sample

An experiment was performed for different thicknesses of sample because we wanted to determine if, by using a single drop and forming only one layer of film, to what degree this layer might interact with the substrate; conversely, if we made a thick film with several layers, whether the top layer would be able to interact with the substrate, and thus we might detect variations in the XPS spectra of the two different environments. As the AFM measurements showed a 1 nm height for our samples, we nominally assumed that thickness of the sample was increased by around 1 nm with each additional layer added. So, to investigate the effect of thickness, Si-water samples drop cast with different numbers of drops were investigated.

For the first sample, one drop of sample was used for making a thin layer on HOPG; for the second, 10 drops of sample were used to make a thicker sample. A film of 5 drops of pure water was made on the HOPG to allow a reference to be recorded. A comparison of XPS spectra of these samples and the reference is shown in chapter 5. In all cases, the surface of HOPG was covered by the samples.

In another experiment, 10 drops of Si-water sample were put only at the centre of the HOPG to determine if there was any difference between the XPS spectrum of sample on covered and uncovered HOPG. We expected to detect two different carbon peaks in the spectrum of the uncovered sample, from HOPG itself, and from the sample itself or the sample and its interaction with HOPG.

3.2.5.3 Solvent effect

To investigate the solvent effect on the chemical structure of the clusters, we recorded XPS spectra for samples of silicon deposited onto a jet of water, ethanol and isopropanol, respectively. 1 drop of 5 μl was used to make a film on an HOPG substrate for all measurements in this experiment.

Si ($2p$) was the first peak which was investigated. The software library showed the binding energies for bulk Si ($^2P_{1/2}$), Si ($^2P_{3/2}$) were 99.2 eV and 99.8 eV respectively. In some references, the value for binding energy of Si ($^2P_{3/2}$) was defined as being between 98.80 eV [134] and 99.85 eV [135], but the most references found it at 99.83 eV [136-139]. For Si ($2p$) generally (disregarding the spin state), the literature mentioned binding energies from 98.40 eV [140] to 99.80 eV [141], with the majority of the literatures

reported a value of 99.6 eV [142-148]. Our samples showed shifts with respect to the bulk silicon (which are explained in detail in chapter 5) which may have been caused by interaction of silicon with other elements in the solvents or substrate, but from the variation of the substrates outlined in section 3.2.5.1 (substrate effect experiment) and their results (see chapter 5), we learned that the clusters did not interact with HOPG, so the observed shifts could only be due to silicon-solvent interacts or their size; (again, see chapter 5).

To have guide for the interpretation we used the literature as reference to find similarities between our peaks and those in the literature. Table 3-1 and Table 3-2 show the binding energies of silicon compounds with carbon, hydrogen, and oxygen. By comparing our XPS peak to these data, we could determine sample structure with a high degree of confidence. These values, all belongs to SiO_x , SiH_x , and SiC_x compound but they are different in x value, so they show different shift respect to silicon.

Table 3-1. Silicon components and their binding energies.

Compound	Spin state/ Origin orbital	Binding energy (eV)	Reference
SiO	2p	102	[149]
SiO ₂	2p	103, 103.10, 103.20 103.3, 103.40 103.50, 103.60, 103.70, 103.80 103.9, 104, 104.10	[150, 151], [152], [153, 154] [155], [156, 157] [158], [151, 159, 160] [150, 161, 162], [163] [147], [148, 164], [165]
SiC	2p	99.85, 100.1, 100.2, 100.3, 100.4, 100.6, 100.7, 100.8	[166], [167], [167, 168] [169], [167, 170, 171], [172, 173], [167], [162, 167]
SiH	2p	98.90	[174]

Table 3-2. Silicon components of different amount of oxygen, carbon and hydrogen and their binding energies. Different stoichiometries of each compound are shown by the numbers.

Compound	Spin state/ Origin orbital	Binding energy (eV)	Reference	Compound	Spin state/ Origin orbital	Binding energy (eV)	Reference
SiO 0.4	2p	99.80, 103.8	[175]	SiC 1.3	2p	100.1	[171]
SiO 0.93	2p	101.90	[141]	SiC 1.5	2p	100	[171]
SiO 1.02	2p	102.20	[176]	SiC 1.7	2p	100.30	[171]
SiO 1.05	2p	102.20	[141]	SiC 1.9	2p	100.20	[171]
SiO 1.19	2p	102.40	[176]	SiC 2.3	2p	100.20	[171]
SiO 1.24	2p	102.40	[141]	SiH 0.01	$^2P_{3/2}$	98.90, 99	[177]
SiO 1.35	2p	102.70	[141]	SiH 0.02	$^2P_{3/2}$	98.90, 98.80	[177]
SiO 1.4	2p	99.80, 103.8	[175]	SiH 0.1	2p	99.60	[143]
SiO 1.49	2p	102.80	[141]	SiH 0.2	2p	99.65	[143]
SiO 1.52	2p	102.80	[176]	SiH 0.25	$^2P_{3/2}$	99.20	[177]
SiO 1.78	2p	103.10	[141]	SiH 0.26	$^2P_{3/2}$	99.10	[177]
SiO 1.8	$^2P_{3/2}$	103.20	[178]	SiH 0.33	$^2P_{3/2}$	99.30, 99.40	[177]
SiO 1.8	2p	103.80	[175]	SiH 0.35	$^2P_{3/2}$	99.50	[177]
SiO 1.9	2p	103.40	[157]	SiH 0.40	$^2P_{3/2}$	99	[177]
SiO 1.91	2p	103.20	[141]	SiH 0.46	$^2P_{3/2}$	99	[177]
SiO 2.05	2p	103.70	[176]	SiH 0.47	$^2P_{3/2}$	99	[177]
SiO 2.08	2p	103.70	[141]	SiH 0.55	$^2P_{3/2}$	99	[177]

The second important peak was the carbon peak. The binding energy for carbon was given as 284.70 eV in the software library, whilst in the literature it was reported as being in the range from 284.30 eV [179, 180] to 284.65 eV [181]; some references reported a binding energies as low as 283.80 eV [182], and 284.18 eV [183] and as high as 285.70 eV [182]. There were some shifts in our samples' XPS carbon peaks because of the binding of silicon and carbon (silicon carbide), and carbon and oxygen (carbon monoxide or carbon dioxide). Reference components with these shifted values from the bulk carbon are shown in Table 3-3 and simple comparison suggested we had these components in our samples.

Table 3-3. Carbon components and their binding energies.

Compound	Spin state/ Origin orbital	Binding energy (eV)	Reference
C/Si	1s	284.40, 285	[184],[185]
SiC	1s	281.26, 281.30 281.45, 282.50 282.60, 282.90, 283.40, 283.80	[186], [187] [188], [189] [173], [162] [170-172, 189, 190], [191]
SiC 1.3	1s	283.30	[171]
SiC 1.5	1s	283.20	[171]
SiC 1.7	1s	283.30	[171]
SiC 1.9	1s	283.30	[171]
SiC 2.3	1s	283	[171]
C-O-H	1s	286.4, 286.5	[192], [193]
C-O-C	1s	286.5	[193]
C=O	1s	288, 288.4	[193], [192]
CO ₂	1s	291.90	[194]

The third peak investigated was oxygen, the binding energy for oxygen according to software library was O (¹S_{1/2}): 531 eV, and again there were some bonds between oxygen and other elements in our samples such as carbon and silicon whose shifts can be seen in our measurements (chapter 5). These shifts belonged to silicon oxide, carbon oxide, and carbon dioxide. Table 3-4 shows several components and their binding energy shifts with respect to elemental oxygen, as reported in the literature.

The fourth peak investigated was Si (2s). The value for the bulk silicon was given as 150.5 eV according to software library. Our samples showed shifts to higher binding energies, implying our silicon clusters were reacted with oxygen. Table 3-5 shows some binding energies related to silicon (2s) and its compounds.

Table 3-4. Oxygen components and their binding energies.

Compound	Spin state/ Origin orbital	Binding energy (eV)	Reference
SiO	1s	532.50	[195]
SiO 1.8	1s	532.20	[178]
SiO 1.9	1s	532.60	[157]
SiO ₂	1s	532, 532.10, 532.30, 532.40, 532.50, 532.60, 532.70, 532.80, 532.90, 533, 533.10, 533.20, 533.30, 533.40, 533.70, 534.30, 533.80	[150], [196], [197], [198], [197, 199], [197, 200], [156, 157], [201-203], [197, 203- 207], [197, 208], [197, 209], [155, 210], [211], [195], [212], [197], [147]

Table 3-5. Silicon (2s) components and their binding energy.

Compound	Spin state/ Origin orbital	Binding energy (eV)	Reference
Si	2s	150.50, 150.70	[213, 214], [142, 215]
SiC	2s	151.70	[191]
SiO _x /Si (different level of oxidation)	2s	150.20, 153.90	[216],[216]
Si/SiO ₂	2s	151	[217]
SiO ₂	2s	154.20, 154.30, 154.40, 154.50, 154.60, 154.70, 154.80, 154.90, 155.30	[218], [156], [200, 219], [220], [160, 219], [219], [211, 219], [219], [212]

3.2.5.4 Solvent exchange

Again XPS was used to compare the chemical properties and structure of the clusters resulting from our solvent exchange experiments. As Figure 3-8 shows, the sample was produced in ethanol; after recording its XPS spectrum it was split in two vials, after evaporation of the ethanol, into one vial topped up with IPA and the other with water, and the XPS spectra of these samples recorded.

3.2.6 Peak analysis with CasaXPS

For a more detailed analysis of the peaks, peak fitting/ analysis software (CasaXPS) [221] was used to study the shape of the peaks. Each peak in an XPS spectrum is a superposition of several ‘component’ peaks; sometimes the asymmetry of the peak shows this; whilst this does not preclude a symmetric peak from having several components, this latter case is clearly more difficult to justify. We used this software to break down peaks to their components. By matching the binding energy of the components with NIST data, we could identify the elements observed and, possibly, determine something of their structural and chemical environment in the sample. Figure 5-6 and Figure 5-7 in chapter 5 shows the analysis performed with CasaXPS for all Si-water peaks.

With CasaXPS, we chose the peak area and then tried to fit several curves until the superposition of these curves was equal to the origin peak, so the main peak divided to several sub peaks. We tried to fit 50%-50% of Gaussian-Lorentzian distribution to our peak with Shirley background and tried to minimize the number of the peaks.

3.2.7 Attenuated Total Reflection (ATR) and Fourier Transform Infrared Spectroscopy (FTIR)

Infrared spectroscopy is used to identify the molecular composition of samples, and it can be used for all kind of organic and inorganic compounds, but the molecules under study must be IR active. FTIR can give some information about the compound and chemical structure of the samples by comparing the spectrum of an unknown compound with the literature.

FTIR-ATR spectroscopy measures absorption in the mid-infrared region. All atoms in molecules are vibrating at any temperature above absolute zero; when the frequency of this vibration is equal to frequency of the IR beam which is used to irradiate the molecule, the molecule absorbs the radiation. A molecule in the sample absorbs a photon of infrared radiation and is excited to a higher vibrational state. The energy of the photon should be the same as the separation of the vibrational states in the sample. On the other hand, a change in dipole moment should occur for a vibration to absorb infrared energy (strictly speaking, the dipole moment must oscillate with respect to the field of the incident radiation to be spectrally active). Frequencies of molecular vibrations are determined by the masses in motion and the binding force between them (strength of the bonds), which is directly related to molecular composition and structure (vibrational frequencies are unique to any given molecular structure and electronic state). Figure 3-13 shows the type of molecules vibrations.

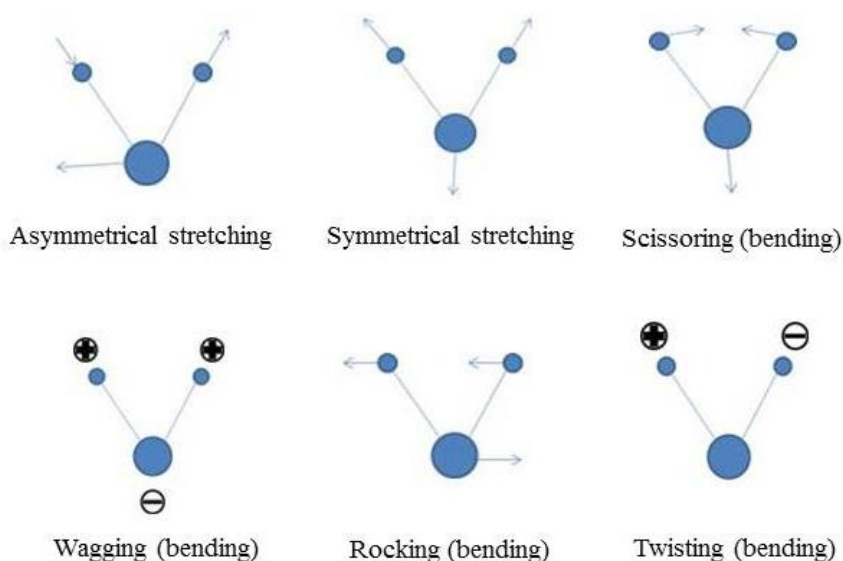


Figure 3-13. Molecular vibrations. Molecules vibrate in symmetric or asymmetric mode, and hence (in this case) IR active and IR inactive, respectively [222].

This method can be used for gases, liquids and solids. The spectral range of IR spectroscopy is from roughly 13000 to 10 cm^{-1} , and is bounded by the visible region at high frequencies and the microwave region at low frequencies. For mid-infrared measurements the region is from 4000 to 400 cm^{-1} .

If quantitative analysis is required, the Beer-Lambert law can be used. This law can be used for calculating the concentration of the sample. For a single compound in a homogeneous medium, the absorbance at any frequency is expressed as:

$$A_{\lambda} = \varepsilon_{\lambda}bc \quad (3.23)$$

Where A_{λ} is absorbance of the sample, ε_{λ} is the molecular absorptivity (which is as function of wavelength), b is the length of the sample through which the beam passes, and c is the concentration of the sample. The Beer-Lambert law shows the intensity of absorption bands is linearly proportional to the concentration of the sample. This law usually valid; however, at low concentrations, the measurement error can be large due to low signal intensities and thus low signal to noise ratios.

Absorbance can be described by Equation (3.24):

$$A = -\log_{10} \left(\frac{I}{I_0} \right) \quad (3.24)$$

Where I_0 is the intensity of incident beam and I is intensity measured after passing the sample, and it ranges from infinity to zero.

3.2.7.1 Principle of ATR spectroscopy

When light transits between two materials with different optical densities, refraction occurs. If the transition is from a higher refractive index medium to a one of a lower refractive index, the incident angle is smaller than the transmitted angle. When the incident angle reaches a particular angle, the transmitted angle can align to 90 degrees and the transmitted light travels parallel to the surfaces – i.e., along the interface – of the two materials. This is called the critical angle.

In ATR spectroscopy, an infrared beam enters the crystal at an angle greater than the critical angle of the crystal, so the beam is totally internally reflected at the interface of the crystal and the sample. Since the refractive index of the crystal is much higher than the sample, the beam, in a classical sense, does not enter the sample.

In an ATR experiment, the beam propagates inside of an internal reflecting material which is infrared transparent. As the beam is reflected off the inside surface of the crystal, a small amount of this radiation, known as an evanescent wave, interacts with the sample, by penetrating past the interface (this, it should be noted, is a quantum effect). Thus the intensity of the beam is attenuated when the sample absorbs light in the IR region. Depending on the refractive index of the crystal, the penetration depth can vary. Penetration depth is the depth of the interaction of the evanescent wave with the sample, and is equivalent to the pathlength (sample thickness) in a transmission measurement. The depth of penetration is about a few microns only. In a multi-reflection ATR crystal, the incident beam is reflected several times onto the interface and penetrates a [very short distance] into the sample with each reflection. In a multi-reflection ATR crystal, the pathlength is calculated by the penetration depth multiplied by the total number of internal reflections in the crystal. The penetration depth at each reflection point depends on several factors, such as the crystal and sample refractive indices, and is wavelength-dependent. Waves with longer wavelengths penetrate deeper than those of a shorter wavelength. Figure 3-14 shows a schematic of the process for ATR measurement.

The crystal is a high refractive index material such as diamond, germanium or zinc selenide (ZnSe), and the sample always has a lower refractive index regards to crystal. The crystal must also, of course, be infrared transparent. Diamond is the hardest crystal and it has a very high refractive index. Sometimes it is used with a focusing element like ZnSe to reduce cost and improve the optical energy throughput. Germanium is a fairly hard crystal; it is resistant against scratching and has a high refractive index, so it can be used for measuring samples which are heavily absorbing. For materials with weak absorbance, a diamond ATR crystal is better because the penetration depth is higher and gives stronger absorption bands. The refractive indices of diamond and germanium are 2.4 and 4.0, respectively, and yield an average penetration depth for diamond for a single reflection of 2.01 microns, and 0.66 microns for germanium.

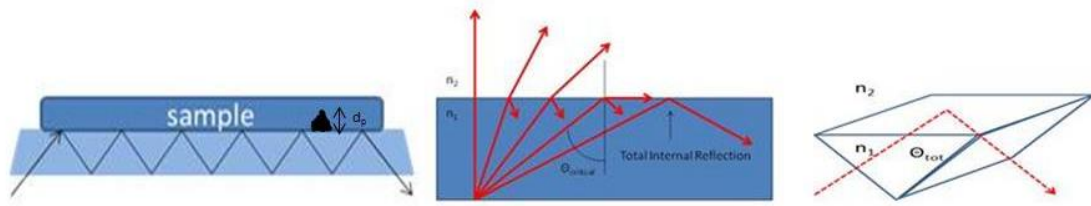


Figure 3-14. This figure shows the principle of ATR spectroscopy. The number of reflections depends on the length of the sample and the angle of the incident radiation [223].

ATR measures the intensity of the reflected beam between the interface of the crystal and the sample. ATR and FTIR spectra of a specific sample show identical peak positions but differing intensities.

The condition for total internal reflection is:

$$\theta_{tot} > \theta = \arcsin\left(\frac{n_2}{n_1}\right) \quad (3.25)$$

Penetration depth, d_p , in sample is described as below:

$$d_p = \lambda / \left(2\pi n_1 [\sin^2 \theta - n_{21}^2]^{1/2}\right) \quad (3.26)$$

Where λ is the wavelength of incident beam, θ is incident light angle, and n is refractive index.

3.2.8 Devices employed for ATR/FTIR experiments

The spectrometer model was a Nicolet iS5 spectrometer (Thermo Fisher Scientific, Inc.) [224]. It could be used as an ATR or FTIR spectrometer by using the appropriate ATR and FTIR accessories. The light source was an IR diode laser. It was equipped with a DTGS detector and a KBr beam splitter [225]. The ATR and FTIR accessories are described in detail in the following sections.

3.2.8.1 ATR accessories

ATR measurements used an iD5 attenuated total reflectance device installed in our Nicolet iS5 spectrometer [226]. ATR crystals of differing materials were used, as appropriate to the wavenumber ranges required for analysis of any particular sample, and for different penetrations depths of beam. For the results shown in chapter 5, diamond and germanium crystals, which were iD5 diamond and iD5 Ge (iDR-Diamond and iDR-Ge), were used. Diamond crystal was the strongest optical material which was available as an ATR crystal with range of 650 - 4200 cm^{-1} a 2.01 micrometer penetration depth at 1000 cm^{-1} , a refractive index of 2.4 and useful a pH range of 1-14; diamond is also, of course, chemically inert [223, 226]. The germanium crystal is a hard material with a high refractive index which is useful for dark and strongly absorbing samples. It has a range of 400 - 4000 cm^{-1} , a 0.66 micron penetration depth at 1000 cm^{-1} , a refractive index of 4.0, and a useful pH range of 1-14. Both crystals covered the mid-IR region, though with some variation at the end of the low wavenumber region [223, 226]. The spectral range was also affected by spectrometer configuration, the thickness of the crystal, the quantity of the infrared light inside the crystal and the number of internal reflections inside the crystal.

When a spectrometer accessory was installed, the spectrometer tested the intensity automatically and showed the intensity of the light (as an interferogram) in the data acquisition software. When the iD5 ATR accessory showed a smaller beam peak intensity [in the test window of the software] than the beam peak intensity for the iD1 transmission accessory because the ATR crystals themselves absorb energy. The ATR spectrometer works in atmosphere, and can be used for liquid, film or solid samples. It had a pressure tower (anvil) that should have been pushed down to press the solid sample onto the crystal, though this accessory was not required for film or liquid samples. A diagram of the iD5 ATR accessory installed in the Nicolet iS5 spectrometer and pressure tower are shown in appendix 3.

3.2.8.2 FTIR accessory

An iD1 transmission accessory installed in the spectrometer was used for FTIR measurements [227]. It can be used for solid, film, liquid and gas samples by use of appropriate transmission substrates and cells. The transmission accessory used for

transmission measurements is shown in appendix 3. An image of the liquid cell and a schematic of its components is shown in Figure 3-15.

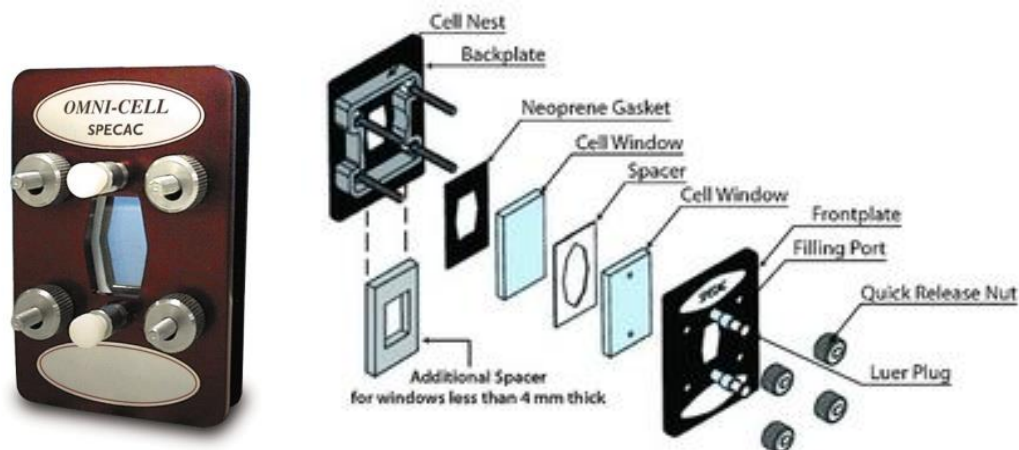


Figure 3-15. Figure showing the liquid cell (left) and a schematic showing the cell assembly (right) [228, 229].

3.2.9 Sample preparation for ATR spectroscopy

A 5 μl drop of solvent was put on the crystal, which had previously been cleaned with acetone and pure sample solvent to cover the crystal. The drop was allowed to dry completely before taking the background spectrum. To record a sample spectrum, a 5 μl drop of sample was put on the ATR crystal. When the solvent had evaporated completely, a very thin film of nanoparticles was left as a residue on the crystal. Then spectrum of the film was recorded. ATR measurements can be performed in the liquid phase, but in our case, because water and alcohol were being used as solvents their high absorbance prevented us from being able to distinguish the silicon particles bands from solvent bands. Hence, a thin film of nanopartilces had to be prepared by letting the solvent evaporate.

In some experiments, to increase the intensity of the peaks, several drops of sample were used, with each drop being added only after the previous drop had dried completely. At every step, a sample spectrum was taken. To measure the background spectrum for these xperiments, a 5 μl drop of pure solvent was put on the ATR crystal and, after evaporating, a background spectrum was measured. The background was taken once for these experiments before starting sample measurements.

In another method that was used for ATR measurements, a drop of sample was put on cleaved HOPG, and the side of the HOPG on which the sample resided was placed on the ATR crystal interface; by pushing down the pressure tower, the HOPG was pressed to the ATR crystal. In this case, the background was taken with a clean solvent on cleaved HOPG. In this method, several drops could be used to increase intensity. When this method was used, we again needed to wait until each drop had completely dried before the next was added. We used this method because when we put a drop of sample directly on the ATR crystal, it could sometimes spread beyond the crystal edges. We believed that our clusters were often being washed away past the crystal boundary by this method, and so were not being detected by the ATR measurement. This particularly seemed to be the case for the IPA solvent because it spread more easily than the other solvents, (conversely, the most easily controlled solvent was water, where we could put small droplet of the water sample on the ATR crystal without significant spreading).

In some experiments, we cleaved HOPG and used a fresh and clean layer which was stuck on sellotape, and made a film with 5 μl of sample on the clean HOPG surface. We used this method to ensure the use of just one thin layer of HOPG substrate in order to eliminate any spectral features which might have belonged to underlying layers of HOPG. A background spectrum for this method was recorded after putting 5 μl of sample solvent on a single layer of HOPG and allowing it to evaporate.

3.2.10 Sample preparation for FTIR spectroscopy

To measure the FTIR spectra for liquid samples, a liquid cell with ZnSe windows was used. There were different spacers to change the separation between the two windows. To record the sample spectra, the liquid cell was filled with sample by using a syringe. Caution was taken to ensure the cell was completely filled, and particularly that there were no remain air bubbles or pockets as these would adversely affect the spectrum. We left the light path empty to record background spectra before any sample measurement.

To measure the transmission spectra of film, a 5 μl drop of sample was put on the ZnSe substrate and the solvent allowed to evaporate, so just a sample particle residue remained. Similar to ATR, if the intensity of the bands was very low, after drying the solvent another drop of sample was added; this procedure was repeated until the intensity

in the spectrum became acceptable. To record the background, 5 μl of pure sample solvent was placed on the substrate and allowed to evaporate.

Before measurement, the cell and substrate were cleaned with acetone, IPA and finally pure sample solvent.

3.2.11 Recording ATR spectra

To start the ATR experiment, the iD5 accessory with the relevant ATR crystal was installed. The ATR spectrometer is a single-beam instrument, so to measure the absorbance of the sample the background absorption spectrum had to be taken initially to remove any effects of the atmosphere and ambient gas in the beam path. The sample absorption spectrum could then be recorded, and the data acquisition software subtracted the background automatically.

To record a background spectrum, the crystal was cleaned and left in atmosphere, and set as the background spectrum in the data acquisition software during subsequent recording. This showed the response of the system when no sample was present. We used the same solvent which was used for the sample.

To collect data, using Thermo Fisher's Omnic software [230] for data acquisition, we chose the experimental parameters as follow: in the collect tab; Number of scans: 16, Resolution: 4, Final format Absorbance for ATR measurements (Transmittance for FTIR measurements), correction for water and CO_2 ; in the bench tab; Detector: DTGS, Beamsplitter: KBr, Source: IR, Accessory: iD5 ATR, Max range limit: 4000 cm^{-1} , and Min Range limit: 400 cm^{-1} .

Absorbance bands in ATR measurements are shifted to lower wavenumbers compared to transmittance bands. By comparing these data (which can be automated in software), these shifts can be corrected. Also, Advanced ATR Correction Result could have been set in the data acquisition software to correct the spectrum for the common shift that always appears in ATR measurements (see appendix 3). All spectra shown in this thesis are presented without this correction.

The measurements were performed for silicon samples which are produced in water, ethanol, and isopropanol, in the liquid phase and as films.

3.2.12 Recording FTIR spectra

To record FTIR spectra of our samples, we installed the iD1 transmission accessory. As described, we used transmission measurements for liquid and film samples.

The liquid cell used for liquid sample measurements had different spacers to change the gap between the two windows (see Figure 3-15). Different spacers allowed for different absorption and transmission properties of the sample. By using larger spacers, all the incident beam was completely absorbed by the water in Si-water samples; absorption was also very high for alcoholic samples, so the smallest spacer (~20 microns) was used. Even then, absorbance was still too high. Since absorption was also very high for the pure solvents, we could not use solvents as background spectra to subtract from. Consequently, the empty cell was instead used to measure the background spectrum. Unfortunately, this presented severe difficulties in being able to distinguish silicon compound bands from solvent bands, so we decided to measure the transmittance of the samples as a film instead. The results of this study are shown in section 5.2.4 and appendix 5.

Transmission measurements of film samples proceeded in the same as ATR measurements in terms of background and sample spectra, with the data acquisition software automatically subtracting the background spectrum from the sample spectrum, leaving just the pure sample spectrum. To record the background, a cleaned ZnSe substrate was used and the absorption due to the substrate eliminated from the result. In some experiments, the background spectrum was taken without the substrate; the spectrum of cleaned ZnSe substrate was additionally recorded and subtracted manually from subsequent sample spectra (in addition to the automatic subtraction of the background).

The parameters used for transmission measurements were the same as ATR measurements, but accessory iD1 transmission was chosen in the final format section of the software

Similar to ATR measurements, transmission measurements were performed for silicon samples which are produced in water, ethanol, and isopropanol. The results of the film sample measurements are shown in chapter 5.

3.2.13 Interpretation of ATR/FTIR spectra

Absorbance spectra show a distribution of absorbance intensities for a beam passing through a sample over a range of wavelengths. The positions of the peaks are determined by the functional groups causing the observed molecular vibrations produced by the incident IR beam when absorbed by the molecule. Molecular vibrations are not exactly harmonic; nevertheless, absorption happens for stronger vibration at near multiples of the fundamental frequency.

The shape of the absorbance spectrum depends on each IR wavelength's absorbance by the sample, thus giving detail about the sample's molecular structure.

An alternative definition to Equation (3.24) is Equation (3.27), which shows how the absorbance spectrum is calculated. The value of sample spectrum in each wavelength is divided by the value of background spectrum at the same wavelength, and the negative logarithm of the result is value of absorbance in each wavelength.

$$A = -\log_{10}(\text{sample}/\text{background}) \quad (3.27)$$

In the spectral region 4000 to 2500 cm^{-1} , there are some strong absorption bands which belong to stretching vibrations between hydrogen and some other atoms with mass of 19 or less. O-H and N-H [stretching] vibrational frequencies are in the range 3700 to 2500 cm^{-1} , and in the range 3300 to 2700 cm^{-1} for C-H (depending on the environment of the C-H bond). So bonds to hydrogen have higher stretching frequencies than those to heavier atoms.

For a given type of vibration (e.g., a stretch) absorption bands for triple-bonds molecules happen at higher frequency (2700 to 1850 cm^{-1}) than for double bonds (1950 to 1450 cm^{-1}), and both are higher than single bond molecules (except for bonds to hydrogen).

As it is easier for a molecular bond to bend than to stretch, stretching frequencies are generally higher for a given type of bond than its corresponding bending frequency.

The 1300 to 910 cm^{-1} region in IR spectroscopy is known as the Fingerprint Region, and is formed from a number of lower frequency vibrations that generally can't be individually distinguished but, taken as a whole, form another unique molecular

signature; each compound, for all intents and purposes, has a unique ‘fingerprint’ in this spectral region.

Table 3-6 shows some possible silicon compounds vibration and their wave number and also some of the most important and famous bonds which are often exist in ATR/FTIR spectrum.

Table 3-6. Some molecular vibrations with corresponding wave numbers.

Wave number (cm ⁻¹)	Compound vibration	Reference
458	Rocking SiO	[231-233]
460	Bending Si-O-Si	[234, 235]
460, 467	Wagging vibration SiO ₂	[236], [80, 237]
465	Rocking SiO ₂	[232]
520	Si-Si in Si planes	[235]
600-700	C-H deformation bending	[238]
600-850	Bending /Wagging Si-H	[239]
610	Si-Si bond vibrations in the bulk	[240-242]
611	Si-Si bond	[243, 244]
620	Si-Si bonds vibrations on the surface and near the surface regions of porous silicon	[240]
630, 640, 670, 680	Bending SiH	[245, 246], [234, 235], [240], [240]
650-770	O-H bending (out-of-plane)	[238]
660-690	Si-Si bonds	[231, 247, 248]
675-730*	RCH=CHR bending	[238]
690-900	C-H bending	[238]
706	Bending SiO ₂	[235]
720-725	CH ₂ rocking bending	[238]
798, 849	Stretching Si-C and rocking CH ₃	[249, 250], [249]
800, 806	Bending SiO ₂	[232], [80, 237]
812	Si-O bending	[231-233]
812	Si-O-Si bending in SiO ₂	[231]
835	Wagging SiH ₂	[234, 235]
870	Scissors SiH ₂	[234, 235]
880-995	=C-H, =CH ₂ bending	[238]
882-885	Si ₂ O ₃	[231, 251, 252]
900	Si-O-H bending	[240, 253]
900, 910	Scissors SiH	[239], [239]
905, 910	Scissors SiH ₂	[243, 254], [243, 254]
935	stretching Si-O-Si	[235]
937, 948	Bending OH	[255], [256]
940	Stretching vibration of oxygen doped in amorphous silicon	[232]

950	Si-OH	[257, 258]
960	Si-OH	[259]
1000-1250	C-N stretching	[238]
1020, 1090	Si-O-Si stretching vibration	[260]
1025	Stretching SiO _{1.3}	[232]
1040-1160	Stretching Si-O-Si	[234]
1050-1150	Stretching Si-O-Si	[261]
1055, 970-1250, 1000-1300	Stretching C-O	[262, 263], [238], [238]
1062	Stretching SiO _{1.9}	[232, 264]
1065	Stretching modes of Si-O-Si bridges in SiO _x	[243, 265]
1075	Stretching vibration non-crystalline SiO ₂	[232]
1082	Stretching on phase Si-O	[231-233]
1084	Si-O-Si stretching in SiO ₂	[231]
1090	Stretching SiO ₂	[80, 237]
1100	Stretching Si-O-Si	[234, 235, 240]
1100	Stretching SiO (SiO ₂ vibrations)	[239]
~1100	Si-O-H stretching	[240]
1100	C-C-C bending	[238]
1102	Stretching C-O	[262]
1105	Stretching Si-O-Si	[240]
1105	Asymmetrical stretching of Si-O-Si bridges in stoichiometric SiO ₂	[243, 266]
1150	Asymmetrical stretching of Si-O-Si	[243, 266]
1150	Stretching SiO ₂	[232]
1177	Si-O Stretching out of phase	[231-233]
1210-1320	O-C stretching	[238]
1250	SiO ₃	[81]
1250±10	Si-CH ₃	[238], [253]
1261	CH ₃ symmetric deformation of Si-CH ₃	[267]
1270	Si-CH ₃	[268]
1296	Stretching C-O	[256]
1330-1430	O-H bending (in-plane)	[238]
1350-1470	CH ₂ , CH ₃ deformation bending	[238]
1395-1440	C-O-H bending	[238]
1412	CH ₃ Asymmetric deformation of Si-CH ₃	[269]
1419	Bending OH	[256]
1500	C=C stretching	[238]
1500-1560, 1590-1650	N-H bending	[238], [238]
1550-1650	NH ₂ scissoring, NH ₂ and N-H wagging	[238]
1620	Bending OH	[235]
1630-1680	C=C stretching	[238]

1636	Bending vibration of water molecule	[80, 237]
1721, 1710-1740, 1705-1720 (H-bonded), 1755-1820 (2-bands), 1735-1750, 1630-1695	Stretching C=O	[238], [238], [238], [238], [238]
1900-2000	C=C asymmetric stretch	[238]
2000-2300	Contains Si-H (SiH, SiH ₂ , SiH ₃) and H-Si-O stretching	[234, 240, 270]
2050-2150, 2087, 2100	Stretching SiH	[239], [243, 265, 271], [234, 235]
2100-2360	Si-H silane	[238]
2100-2250	C≡C stretching	[238]
2100-2270	-N=C=O, -N=C=S, -N=C=N-, -N ₃ , C=C=O stretching	[238]
2106	Stretching SiH ₂	[243, 265, 271]
2150	Stretching Si-H in Si ₂ O	[272]
2200	Stretching Si-H in SiO ₂	[272]
2250	Stretching Si-H in SiO ₃	[235, 272]
2200, 2250	Stretching O-Si-H	[235], [234]
2240-2260	C≡N stretching	[238]
~2250	Si-H stretching modes which are characteristic for Si-H vibrations where O is back-bonded to the Si (105)	[235, 239]
2250	Stretching H-SiO ₃	[273]
2330-2360	Stretching SiH _x	[243]
2850-3000	SP ³ C-H stretching	[238]
2860	Symmetric stretching CH ₂	[243, 274]
2921	Asymmetric stretching CH ₂	[243, 274]
2960, 2905	Asymmetric stretching CH ₃	[243, 274]
>3000, 3030 (may be several bands)	SP ² C-H stretching	[238], [238]
3020-3100	=C-H, =CH ₂ (usually sharp)	[238]
3200-3550 (H-bonded) usually broad	O-H stretching	[238]
~3300	O-H stretching	[239]
3300	SP C-H stretching	[238]
3300-3400	N-H stretching	[238]
3400-3580, 3580-3650 (free) usually sharp	Stretching OH	[234, 235], [238]
3440	OH stretching vibration coming from the silanol groups on the surface which are hydrogen bonded to atmospheric molecular water	[80, 237]
3747	Vibration of surface isolated silanol groups	[80, 237]

Chapter 4

Optical characterisation of silicon nanoparticles

4.1 Overview

Our goal in this project was the production of fluorescent silicon nanoclusters. As explained in chapter 2, clusters are produced using a novel deposition method developed within our group. In this chapter we have investigated the optical properties of silicon clusters to explain how our product can be useful in application. To this end, we characterised our sample(s) using fluorescence spectroscopy and UV/Vis spectroscopy to define important physical characteristics such as fluorescence and absorbance intensity and wavelength, fluorescence stability, chemical stability, quantum yield, and fluorescence lifetime. We have also studied the dependence of these characteristics on the solvent in which the particles were produced, the concentration of these solutions, phase of the sample (liquid or film), exchange solvent, and temperature. In addition, the effect of production parameters such as stagnation pressure, power of sputter head, length and angle between target and liquid jet, and the duration of the deposition on the optical properties of the samples have also investigated.

4.2 Characterisation of silicon nanoclusters by using Fluorescence spectroscopy: Reproducibility of the samples, and quality of the product

Each fluorophore has its own intrinsic fluorescence properties, though these can be modified to some greater or lesser degree by their environment. We used fluorescence spectroscopy to characterise the optical properties of the samples. The intensity, position of the emission wavelength, quantum yield and fluorescence lifetime are the most

important characteristics required to describe a fluorophore. A fluorescence spectrum is a plot of the fluorescence intensity as a function of wavelength. To obtain the fluorescence spectrum of a sample, the sample is excited at a given wavelength and the emitted intensity at different wavelengths is recorded; to record a fluorescence excitation spectrum, the intensity of emitted light is recorded while the excitation light is scanned. We measured the emission and excitation fluorescence of samples at different wavelengths; for dispersed fluorescence, we empirically found the appropriate wavelength to excite the samples was 270 nm.

To understand the production, we used different solvents as liquid jet, in the following sections, the results of fluorescence measurements for silicon directly deposited on ethanol, isopropanol and water are discussed in detail. The fluorescence measurement was also performed for silicon clusters produced in hexane and formic acid (described briefly below). We tried to use the solvent with high purity but, as we will explain later, hexane and formic acid may contain some water impurities and, also as we will discuss in next chapter, water has some carbon and other impurities like fluoride, chloride and etc. All samples were produced using our experimental methods were fluorescent. The samples produced with the liquid jet and deposition method all have strong, stable fluorescence. Figure 4-1 shows a sample excited at 266 nm with a UV light which is fluorescing blue.

All the samples' spectra were recorded in the air and in liquid phase, unless those measured with TSPC method at the synchrotron light source. There, the liquid samples were investigated within a sealed, UV-transparent cuvette inside a vacuum chamber. The films were investigated directly inside the vacuum chamber (as described in chapter 3). Whether liquid and film samples were investigated is indicated in the figures labels and captions. All the samples produced in the same conditions, different names only show they were produced in different run of experiment.



Figure 4-1. Figure showing blue fluorescence from our liquid sample in air.

4.2.1 Fluorescence of silicon particles directly deposited on isopropanol

Fluorescence spectra of all Si-IPA samples are shown in Figure 4-2 to show reproducibility of the method. Samples were excited at 270 nm. The spectra show the sharp Rayleigh peak of the scattered excitation light at 270 nm (which is at the same wavelength as the excitation wavelength), the second sharp peak is a Raman peak, and first and second broad peaks are the first and second fluorescence peaks, respectively, with their second order peaks to higher wavelength. Isopropanol has two Raman peaks, the first of which cannot be recognized as its intensity is very low (it can be seen if sample is excited at longer wavelength because the fluorescence intensity is lower), whilst the second can be seen at 295 nm. All samples show the first fluorescence peak around 310 nm and second fluorescence peak around 357 nm, except for sample A3, which has the second peak at 400 nm, where there is a possibility of contamination with water. Table 4-1 shows the fluorescence wavelength of the first and second peaks for all Si-IPA samples. The average wavelengths of the first and second peaks are 310.63 nm, and 357.90 nm, respectively; we excluded the sample A3 in the average for the second fluorescence band.

Table 4-1. Fluorescence peak position of Si-IPA samples (silicon deposited onto isopropanol liquid jet in vacuum). Excitation energy is 270 nm.

Sample	First fluorescence band (nm)	Second fluorescence band (nm)
A1	310 ± 1	365 ± 1
A2	310 ± 1	365 ± 1
A3	308 ± 1	400 ± 1
B2	310 ± 1	358 ± 1
B4	313 ± 1	342 ± 1
C2	309 ± 1	374 ± 1
C3	311 ± 1	353 ± 1
C4	314 ± 1	352 ± 1
D2	308 ± 1	368 ± 1
D3	311 ± 1	356 ± 1
D4	313 ± 1	346 ± 1

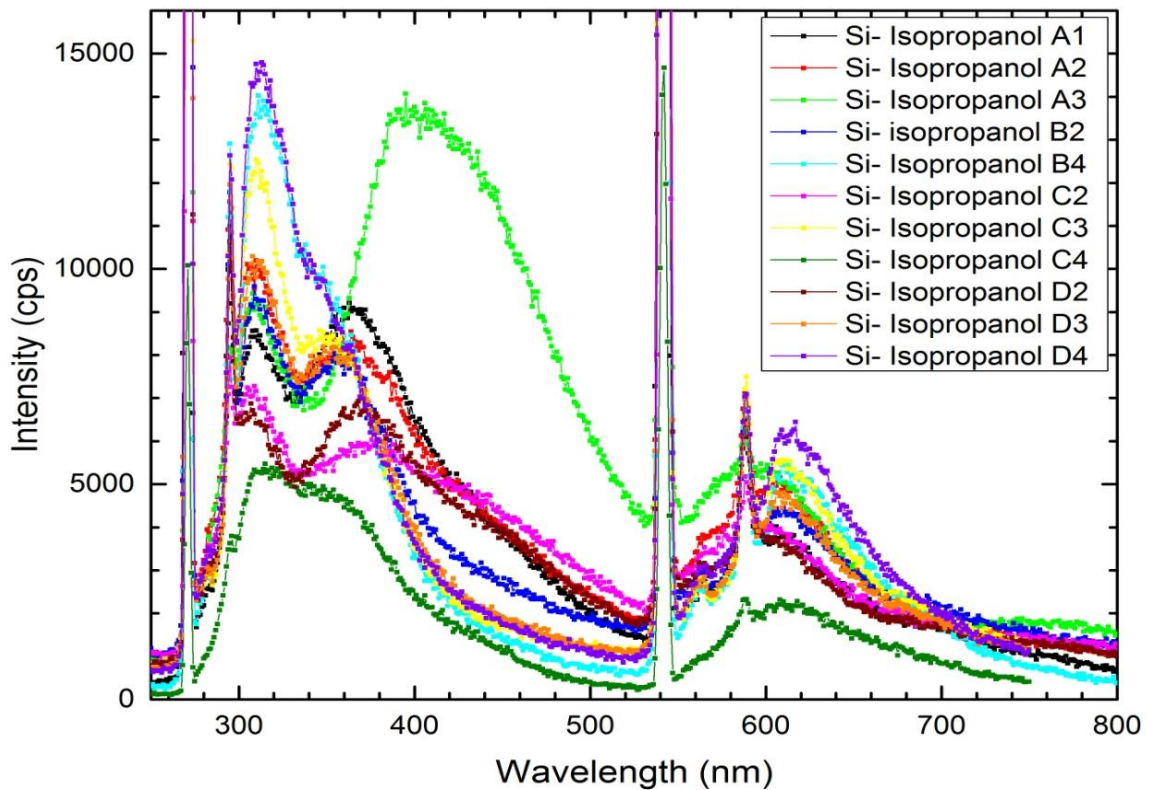


Figure 4-2. Figure showing emission spectra of Si-IPA samples excited at 270 nm as recorded by a fluorescence spectrometer. The first peak at 270 nm is first-order Rayleigh scattering, the second sharp peak at 295 nm is the first-order Raman peak of IPA, the second-order scatter being seen at 540 nm and 590 nm. The fluorescence peaks of Si-IPA samples can be seen at ~310 nm (first fluorescence peak) and ~357 nm (second fluorescence peak).

All samples were excited at different wavelengths ranging from 250 nm to 350 nm to investigate the effect of excitation wavelength on fluorescence intensity and position. In Figure 4-3, sample A2 is shown when excited at three different wavelengths. Fluorescence emission occurs from the excited state independent of the excitation wavelength. Therefore, as expected, Figure 4-3 shows the emission wavelength is independent of the excitation wavelength and the wavelengths of fluorescence peaks are constant. It means energy is transferred to localised fluorescent states, and fluorescence originates from a localised transition. However, variation of the excitation wavelengths changes fluorescence intensity (but not, of course, spectral position). This behaviour is characteristic for defect luminescence [19]. Note the intensity of the second fluorescence peak is increased with increasing excitation wavelength.

As the sample has fluorescence maxima at 310 nm and 365 nm, the excitation spectra were recorded by emitting at these wavelengths (Figure 4-3). Excitation spectra show different peak wavelengths, hence the first and second fluorescence peaks actually originate from different excited states. It seems that by exciting at 270 nm, we excite the first fluorescence band, and by exciting at 308 nm we have excited the second fluorescence band. The first peak is more prominent at excitation wavelengths below 300 nm and the second fluorescence peak is more prominent at excitation wavelengths longer than 300 nm.

As we explain in following section, we attribute the second fluorescence peak (365-440 nm depending on the solvent) to cluster surface sites (see section 4.4). According to our results, presented in the next chapter, and also from the literature, the second band can be attributed to surface silicon in various oxidation states [84]. XRD experiments of silicon nanoclusters show the blue fluorescence originates from oxidized amorphous particles, which is similar to the blue luminescence reported in references [29, 79, 80]. The assumption of the fluorescence origin as for the second peak is the same for silicon nanoclusters produced in any solvent. Conversely, the first peak was initially attributed to bulk cluster, though this hypothesis later come into doubt (see section 4.4).

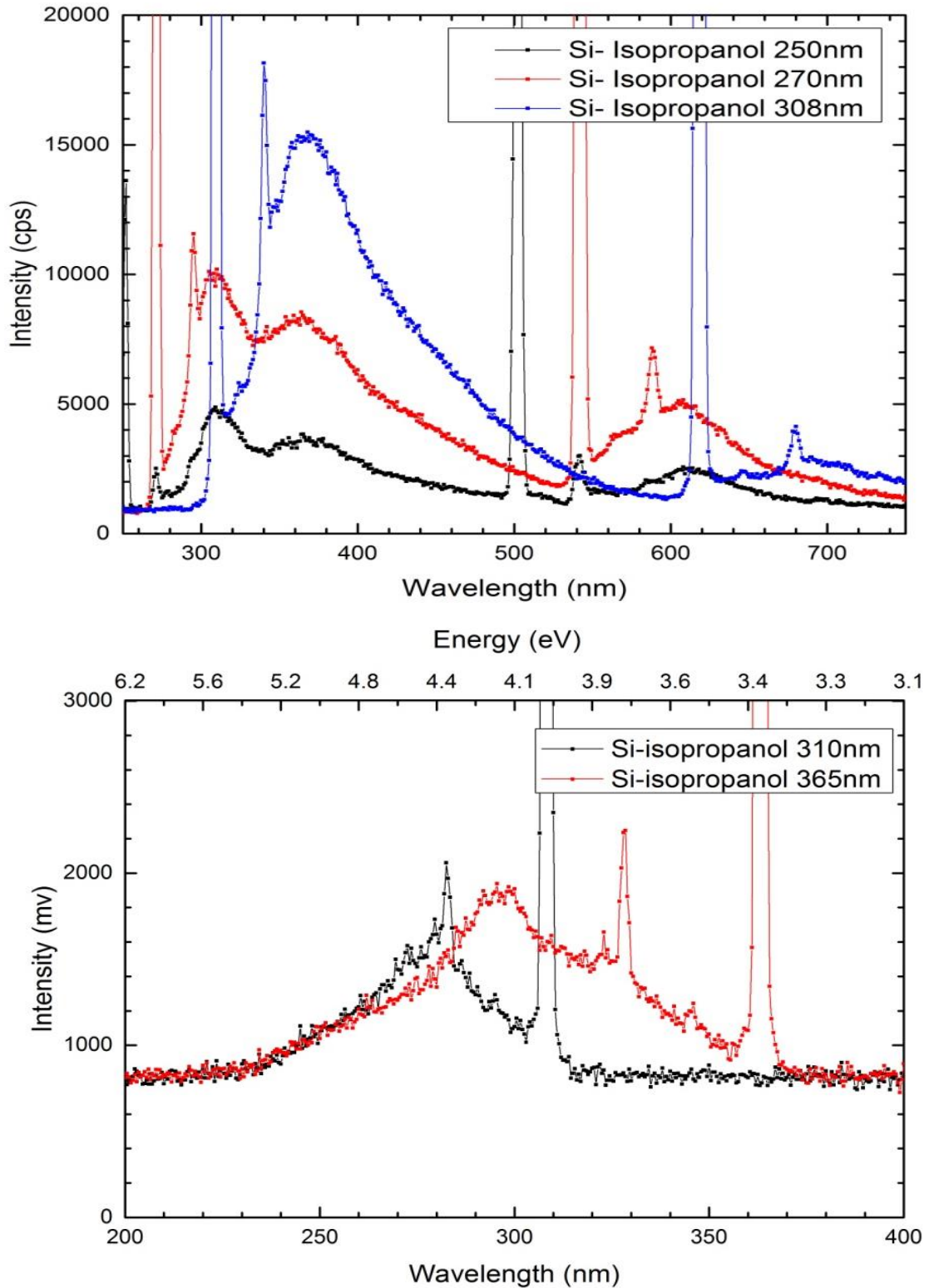


Figure 4-3. Excitation energy dependence of the fluorescence. Sample A2 Si-IPA has been excited at 250 nm, 270 nm and 308 nm (top figure). The emission wavelength is unaffected by changing the excitation energy. The figure on the bottom shows excitation spectra emitted at 310 nm and 365 nm. Their peaks are at 275 nm and 293 nm.

4.2.2 Florescence of silicon particles directly deposited on ethanol

We produced two kinds of Si-ethanol samples; yellow samples and clear samples. Yellow samples were produced with sputter head power higher than 50 W and clear samples produced with power of 40-50 W. Here we only show the fluorescence spectra of clear samples as the yellow samples had very week fluorescence intensities (lower than 1500 cps).

All Si-ethanol samples were excited at 270 nm, the results of which are shown in Figure 4-4. All Si-ethanol samples have two peaks around 310 nm and 364 nm; when the intensity of first peak is very high, as it is in some of our spectra, then the second peak can appear merely as a shoulder to the first. Although 270 nm is the best wavelength to excite the samples (since they show high fluorescence intensities when excited at 270 nm), it makes distinguishing between these two peaks difficult, so samples were ultimately measured after excitation at 250 nm; although fluorescence intensity is lower, the two peaks are clearer. The results of emission fluorescence of all Si-ethanol samples are shown in Figure 4-4. The first Raman peak is obvious in the spectrum excited at 308 nm, and is located at 324 nm. The second Raman peak can be seen in all three spectra. The second Raman peak is at 340 nm, 295 nm and 271 nm when sample is excited at 308 nm, 270 nm and 250 nm, respectively.

Table 4-2 shows the fluorescence wavelength of first and second fluorescence peaks for all Si-ethanol samples. The average wavelengths of the first and second peaks are 310.71 nm, and 364.14 nm, respectively.

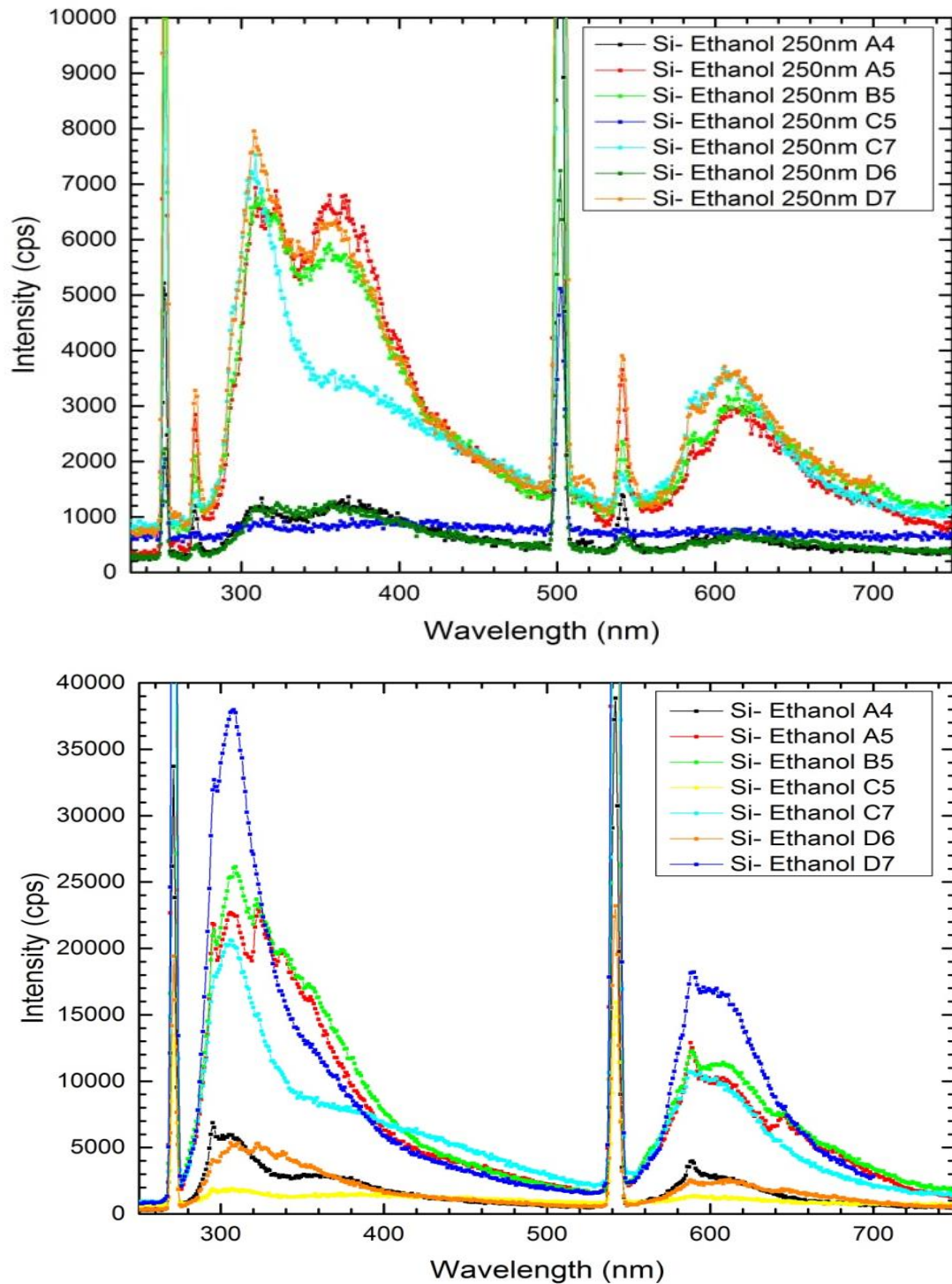


Figure 4-4. Figure showing fluorescence spectra of Si-ethanol samples excited at 250 nm (top) and 270 nm (bottom). They have fluorescence peaks at ~ 310 nm and ~ 364 nm. The two peaks at ~ 310 nm and ~ 364 nm appear to merge when excited at 270 nm.

Emission and excitation spectra of Sample A4 are plotted in Figure 4-5, which shows the Si-ethanol A4 sample excited at 250 nm, 270 nm, and 308 nm. Emission spectra at three different excitation wavelengths confirm the peaks at 310 nm and 370 nm to

originate from fluorescence. The excitation spectrum of sample A4 emitted at 303 nm and 370 nm. The spectrum for the sample emitted at 303 nm has two peaks at 238 nm and 370 nm in the excitation spectra, whilst spectrum for the sample emitted at 370 nm shows two broad bands centred at 278 nm and 300 nm.

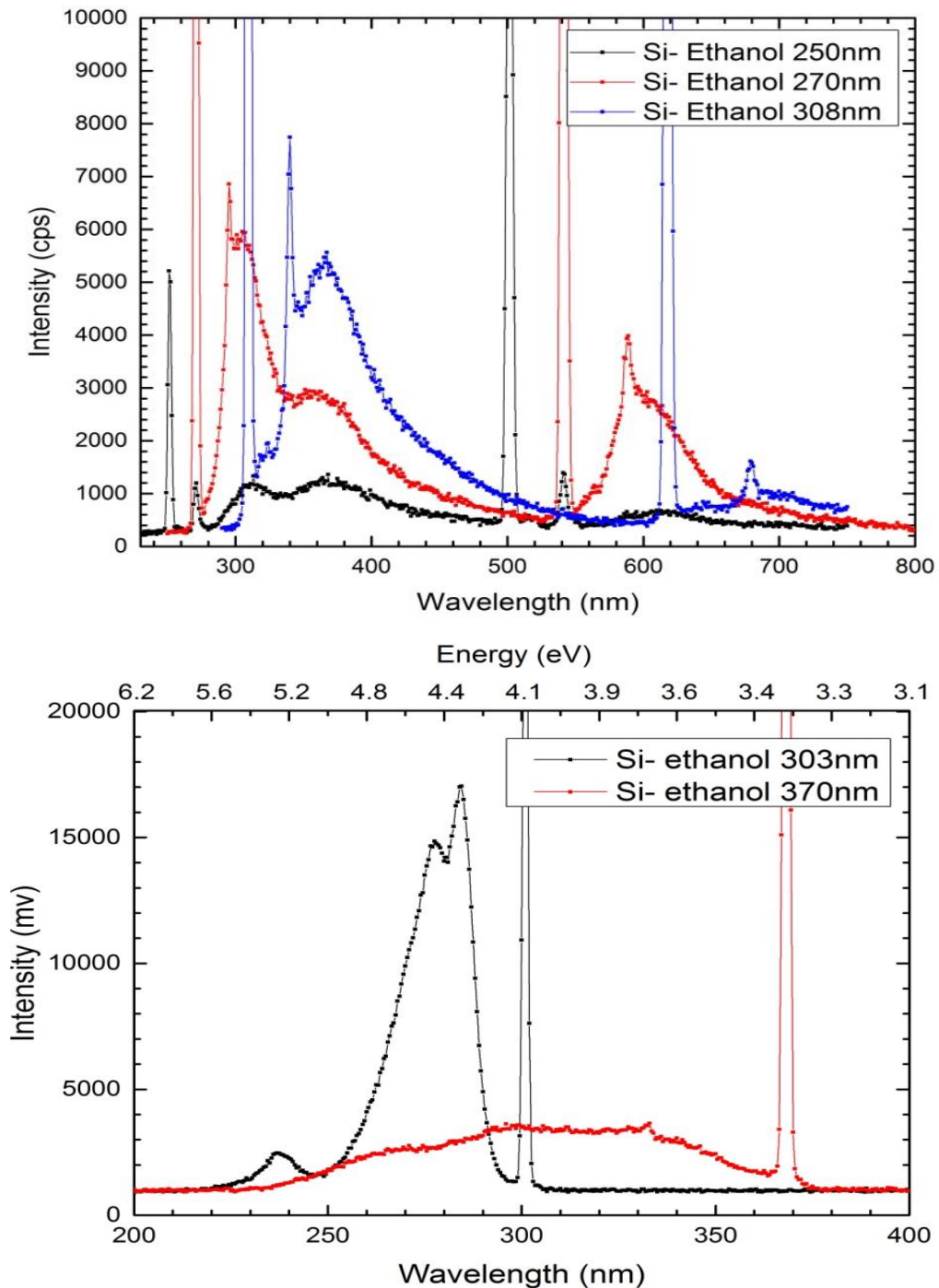


Figure 4-5. Figure depicting the fluorescence spectra of the Si-ethanol sample A4 excited at 250 nm, 270 nm, and 308 nm (top), and excitation spectra of sample A4 emitted at 303 nm and 370 nm (bottom).

Table 4-2. Si-ethanol samples excited at 250 nm.

Sample	First fluorescence band (nm)	second fluorescence band (nm)
A4	310 ± 1	370 ± 1
A5	310 ± 1	370 ± 1
B5	313 ± 1	360 ± 1
C5	311 ± 1	366 ± 1
C7	308 ± 1	362 ± 1
D6	315 ± 1	361 ± 1
D7	308 ± 1	360 ± 1

4.2.3 Florescence of silicon particles directly deposited on water

Similar to alcoholic samples, water samples were measured at different excitation wavelengths; the results for excitation at 270 nm and 308 nm are shown in Figure 4-6 and Figure 4-7. Amongst Si-water samples, most show the same shape and similar intensity distributions whilst some have very high intensity peaks; the samples recorded are plotted in two separate graphs because of this.

By exciting the Si-water sample at 308 nm, the peak at 420 - 440 nm is excited and has highest intensity, so its position can be defined accurately. In measurement at an excitation wavelength of 270 nm, samples show fluorescence around 420 - 440 nm (with average of ~429 nm), but when they are excited at 308 nm all Si-water samples show a peak around 420 nm (with average of ~421 nm).

Table 4-3 shows the fluorescence wavelength of the first and second peaks for all Si-water samples. The average wavelengths of the first and second peaks are 309.50 nm, and 429.35 nm (when excited at 250 nm) and 421.64 nm (when excited at 308 nm), respectively. The second peak is slightly red-shifted when excited at 308 nm with respect to the peak excited at 250 nm, because when the sample is excited at 250 nm, the first peak will be excited so the position of the second band is not precise, but when the sample excited at 308 nm the second peak will be excited so the position of this band can be determined accurately.

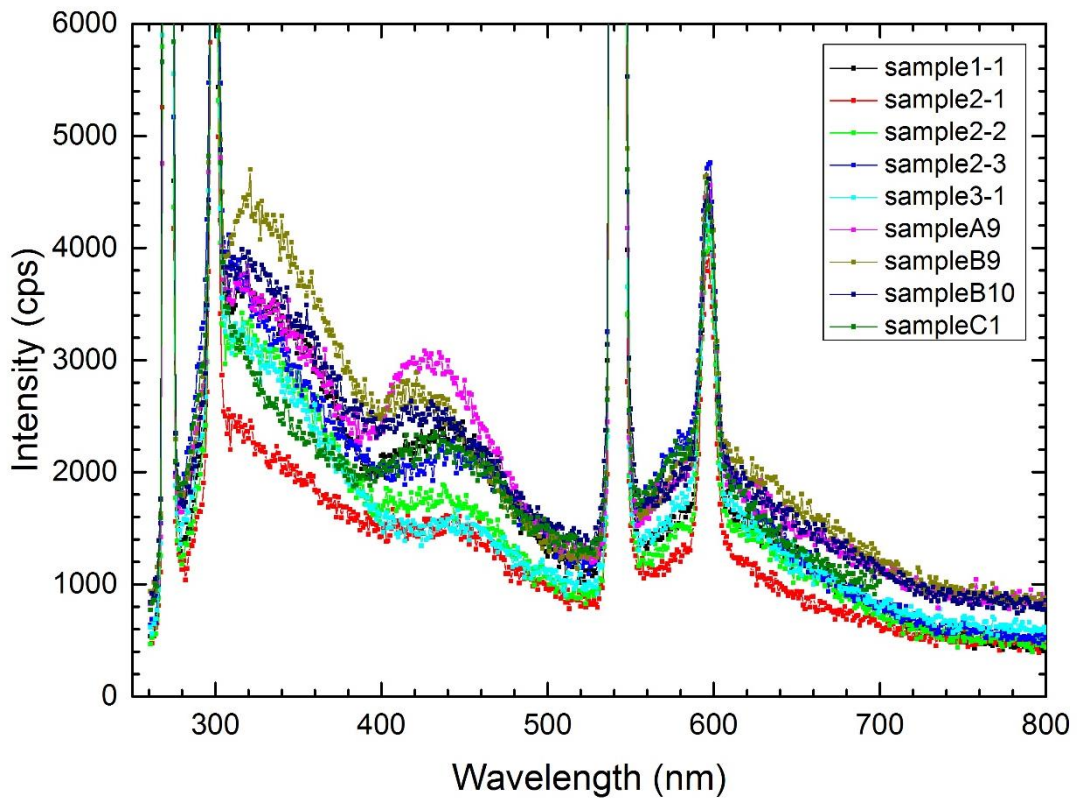
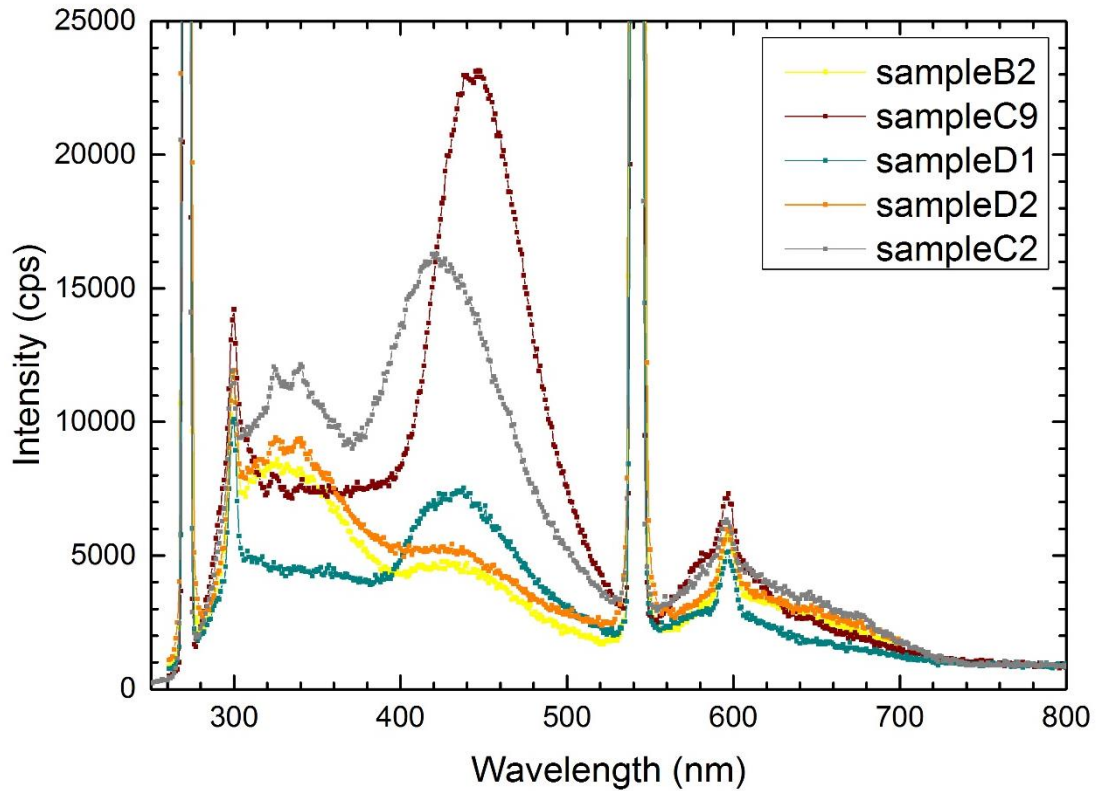


Figure 4-6. Figure showing Si-water samples excited at 270 nm. The plot on the bottom shows the sample with lower fluorescence intensities, which have two fluorescence peaks around 307 - 314 nm and ~430 nm, while higher intensity spectra (top) have peaks around 300 - 330 nm and 420 - 440 nm.

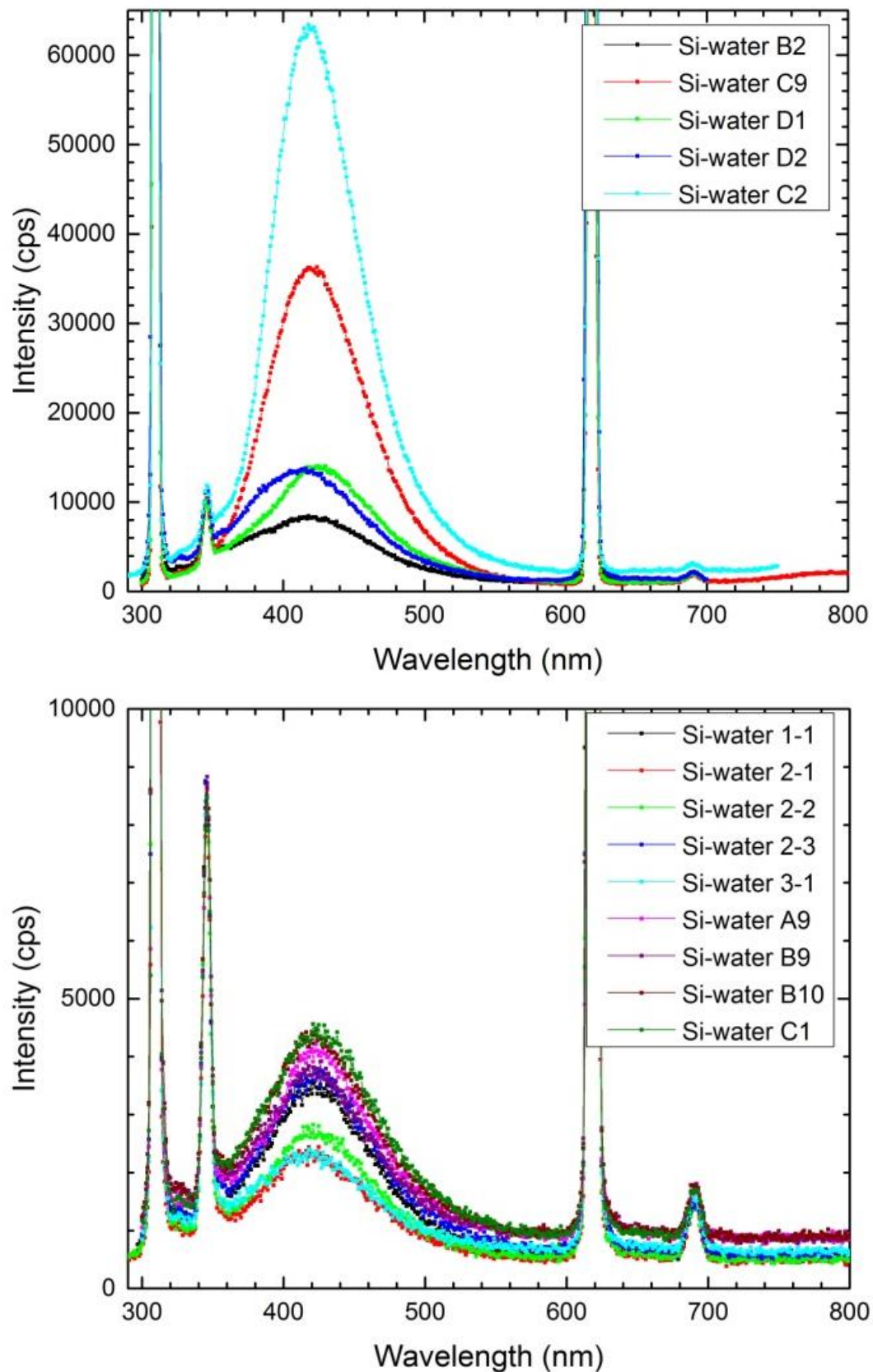


Figure 4-7. Figure showing Si-water samples excited at 308 nm. All samples have a peak at 420 nm.

Table 4-3 Si-water excited at 250 nm and 308 nm

Sample	First fluorescence band (nm)	Second fluorescence band (nm), excited at 250 (nm)	Second fluorescence band (nm), excited at 308 (nm)
1-1	312 ± 1	437 ± 1	424 ± 1
2-1	312 ± 1	428 ± 1	420 ± 1
2-2	313 ± 1	428 ± 1	420 ± 1
2-3	307 ± 1	432 ± 1	424 ± 1
3-1	311 ± 1	422 ± 1	420 ± 1
A9	312 ± 1	430 ± 1	424 ± 1
B2	307 ± 1	428 ± 1	418 ± 1
B9	308 ± 1	424 ± 1	424 ± 1
B10	308 ± 1	424 ± 1	424 ± 1
C1	307 ± 1	433 ± 1	424 ± 1
C2	310 ± 1	423 ± 1	418 ± 1
C9	310 ± 1	442 ± 1	422 ± 1
D1	308 ± 1	434 ± 1	426 ± 1
D2	308 ± 1	426 ± 1	415 ± 1

Distinguishing the first peak is difficult in Si-water due to it having the same wavelength as the associated pure water Raman peak and the fluorescence peak of the clusters. However, if samples are excited at lower wavelengths, such as at 250 nm, the first peak can be seen at ~310 nm similar to alcoholic samples (although its intensity is very low when excited at 250 nm). This peak can be seen in Figure 4-8 and Figure 4-9 when samples C2 and C9 are excited at 250 nm.

Samples C2 and C9 show three different fluorescence peaks, the intensity of which depends on the excitation wavelength. When these samples are excited at 250 nm, all three bands are clear and distinct although their absolute intensities are very low. Each peak becomes prominent when the sample is excited at an appropriate wavelength. As Raman peak wavelength changes with excitation wavelength, at some excitation wavelengths the Raman peak of water superposes with the fluorescence peak and makes it difficult to distinguish the either the peak or, consequently, its position. All Si-water samples may have these three peaks, but their intensity is very low and they are not distinguishable.

In Figure 4-8 and Figure 4-9, sample C9 and sample C2 are excited at 250 nm, 270 nm, and 308 nm. The emission spectrum of sample C9 excited at 250 nm shows three peaks, although their intensity is very low. The first peak can be seen at 310 nm when they are excited at 250 nm. The second peak is observable when sample C9 is excited at

250 nm, and it is also clear when sample C2 is excited at 270 nm. The third peak exists in all spectra as its intensity is high enough to be observed directly. All excitation spectra show three different excitation levels. Excitation spectra of sample C2 shows peaks at 230 nm, 284 nm, and 309 nm, which confirms from the fluorescence peaks of this water sample that it has three different excited states. Excitation spectra of sample C9 emitted at 420 nm and 440 nm, which also shows these peaks originate from different states. The peaks are red-shifted with respect to those in sample C2. The excitation spectrum of sample C9 shows fluorescence peaks at 275 nm when emitted at 315 nm, and at 270 nm, 311 nm, and 380 nm when emitted at 440 nm.

As the intensity of the second peak is very low, is a very broad band, and also was seen in only these highly fluorescent samples (samples C2 and C9) we call the band at ~310 nm the first peak, and the band at 420 - 440 nm the second peak, in the following discussion.

As explained in more detail in the next chapter, analysis confirms Si-water particles are highly oxidized, and in all samples, oxygen bonds are responsible for the luminescence of the sample. The intensity of the fluorescence of Si-water samples is higher than alcoholic samples, and the literature suggests siloxene derivatives are the origin of the strong room temperature luminescence in oxidized silicon [235], although this is not the only possible candidate and, as we discussed in the introduction, the blue luminescence can originate from different species; as we will discuss later (see chapter 5), we attribute the fluorescence of our nanoparticles to various silicon oxide species.

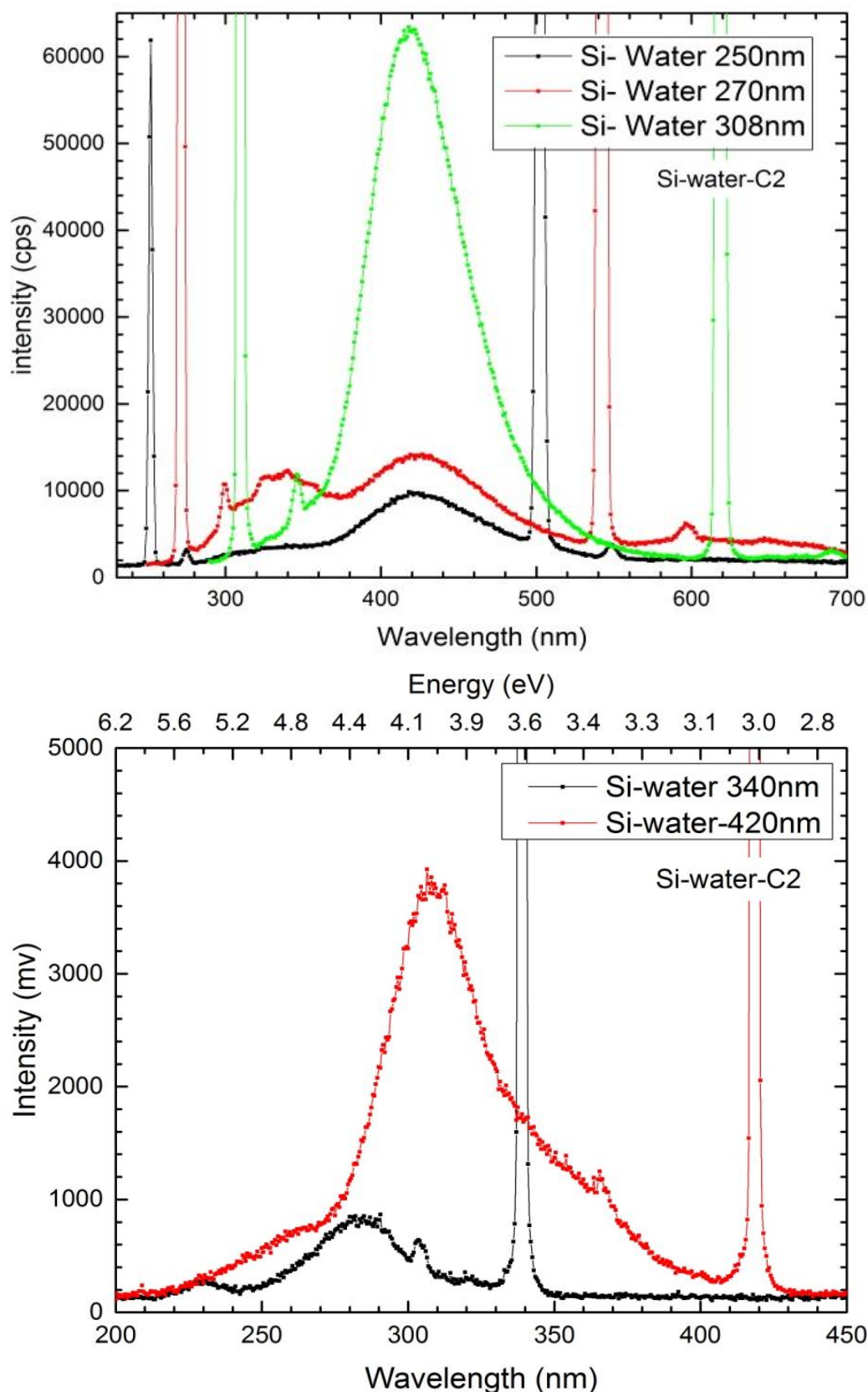


Figure 4-8. Figure depicting the fluorescence spectra of Si-water sample C2 excited at 250 nm, 270 nm, and 308 nm (top) and excitation spectra, fluorescence recorded at 340 nm and 420 nm (bottom).

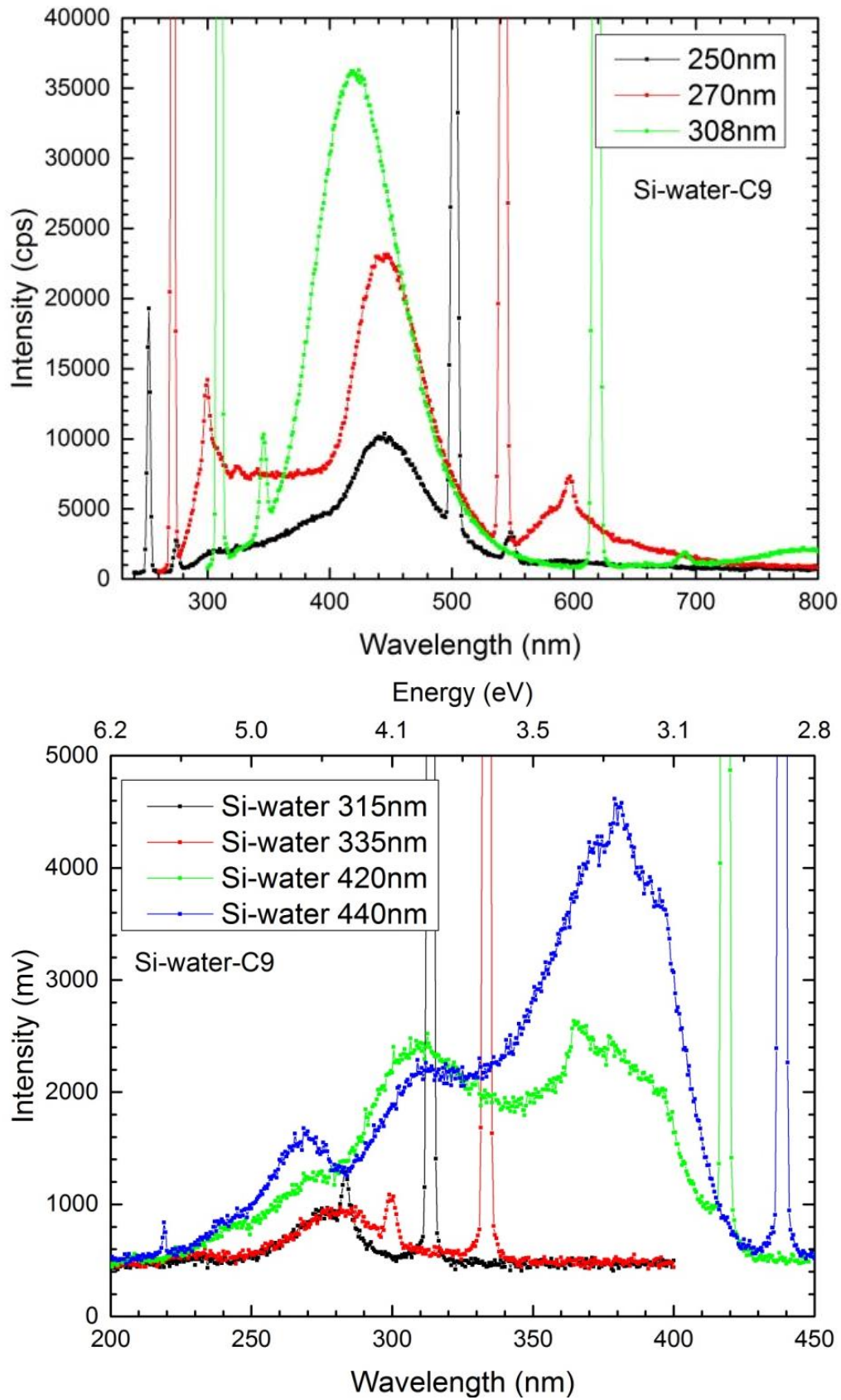


Figure 4-9. Figure showing fluorescence spectra of Si-water sample C9 excited at 250 nm, 270 nm, and 308 nm (top) and excitation spectra emitted at 315 nm, 335 nm, 420 nm and 440 nm (bottom).

4.2.4 Florescence of silicon particles directly deposited on hexane

Another solvent investigated was hexane, the fluorescence spectra for which are shown in Figure 4-10. We expected to see different fluorescence bands as this solvent is oxygen-free and aprotic, and was a good test to assess the effect of oxidation, (though results were ultimately unsatisfactory in this regard, which may have been caused by contamination of the hexane sample with water). The Si-hexane sample shows its first fluorescence peak at 310 nm similar to all other samples. The second peak occurs at 400 nm, which is directly between the fluorescence wavelength of alcoholic and water samples. Our interpretation is that as the frozen sample defrosted in air, and was also exposed to air during our investigation, and clusters became oxidised, so we observed the band at 400 nm. Excitation spectra show peaks at 279 nm, and 343 nm; the peak at 343 nm has a shoulder at 315 nm. We produced only one hexane sample because its vapour is harmful.

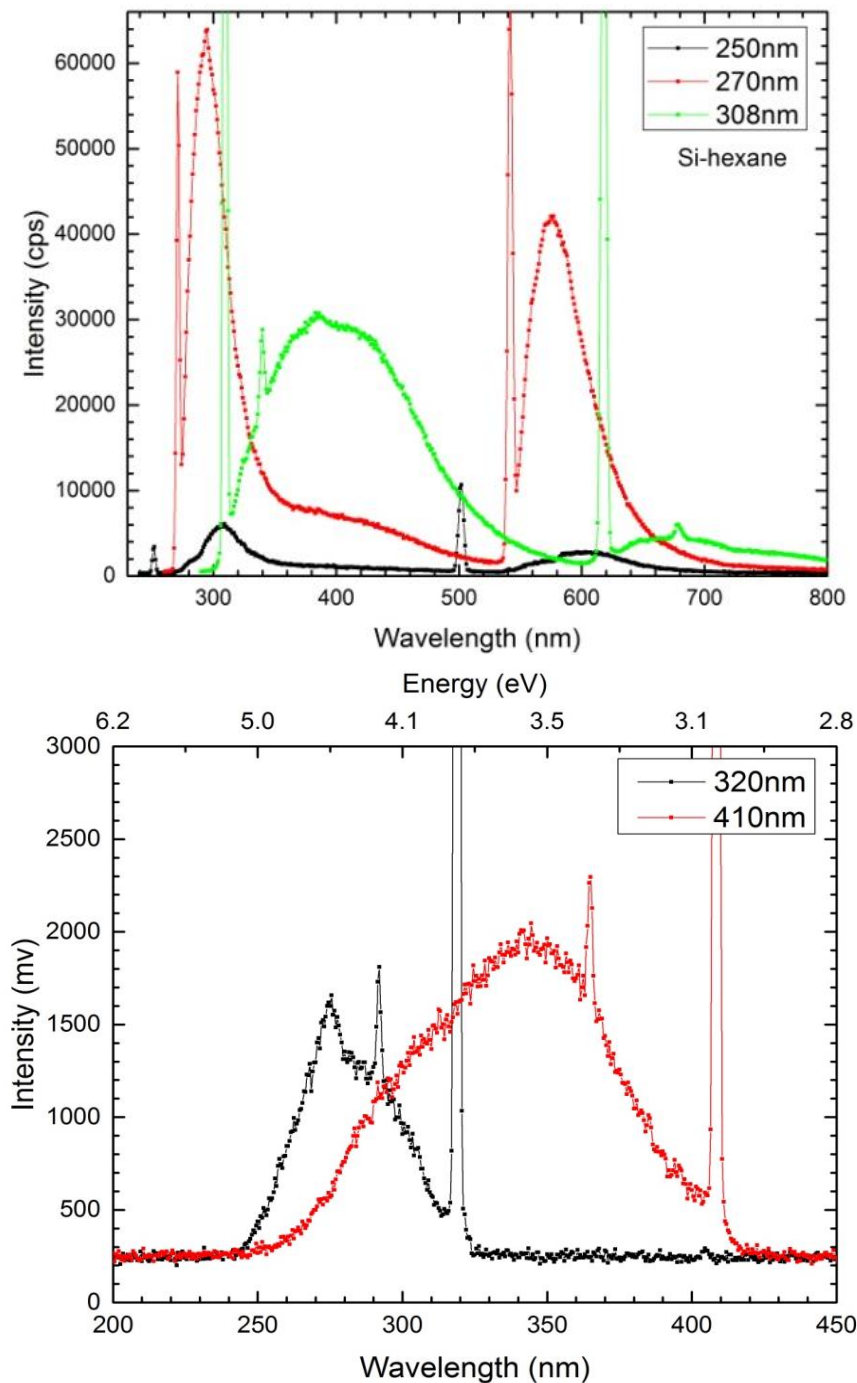


Figure 4-10. Figure showing fluorescence spectra of Si-hexane sample excited at 250 nm, 270 nm, and 308 nm (top) and excitation spectra emitted at 320 nm, and 410 nm (bottom).

4.2.5 Fluorescence of silicon particles directly deposited on formic acid

A sample was produced in formic acid to test a sample with different dipole moment and have another data point; its emission fluorescence spectra are shown in Figure 4-11. The emission spectra have peaks at 325 nm and 425 nm. As formic acid has two Raman

bands, it is difficult to recognize the peak at 325 nm, or if there is another peak at 310 nm.

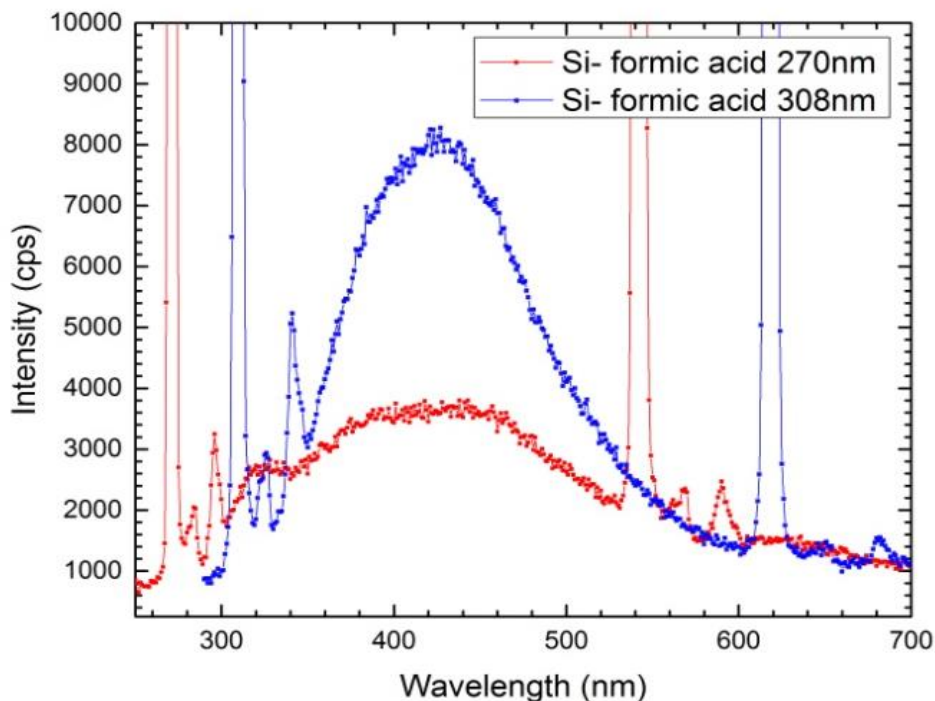


Figure 4-11. Figure showing fluorescence spectra of Si-formic acid sample excited at 270 nm, and 308 nm.

4.3 Characterisation of silicon nanoclusters using UV/Vis spectroscopy: absorbance spectra, and electronic structure of the samples

The fluorophores show different absorption spectra as they have different structures. The absorption spectrum defines the population distribution of the molecule in the ground state and thus the molecular structure in this level. Generally, excitation and absorption spectra are supposed to show their peaks at same wavelength if molecule does not undergo any other phenomena. The excitation spectrum is more accurate than the absorption spectrum because it defines the emitting fluorophore, while the absorption spectrum characterizes the sum of all absorbing molecules.

An absorption spectrum shows electronic, vibronic, and rovibronic transitions. The peak in the absorbance spectrum corresponds to the pure electronic transition, and the rest

of the spectrum is formed by several lines that correspond to rovibronic and vibronic transitions.

In the following sections the absorbance measurement results of all samples are shown.

4.3.1 Absorbance of silicon particles directly deposited on isopropanol

Absorbance spectra for all Si-IPA samples were recorded, the results of three samples which are more similar are shown in Figure 4-12; the absorbance spectra of all samples can be found in appendix 4. Although the emission spectra of Si-IPA are very similar, and they have fluorescence peaks at the same wavelength, their absorbance spectra are different, as only some of them have the same absorbance peak wavelength. As the absorbance spectrum shows the effect of all absorption processes, not just the ones lead to fluorescence, we can expect to see another bands in the absorbance spectrum; also, this spectrum will show *all* absorption by *all* molecules in the sample, even the solvent.

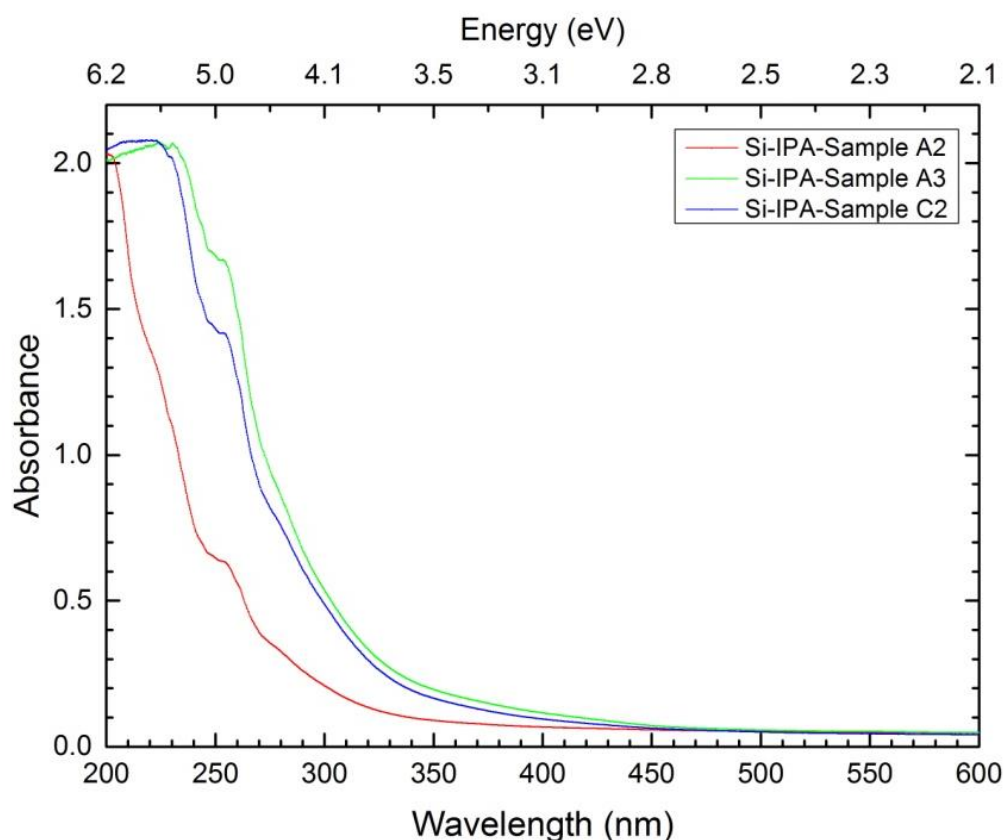


Figure 4-12. Absorbance spectra of Si-IPA samples.

4.3.2 Absorbance of silicon particles directly deposited on ethanol

Absorbance spectra of two Si-ethanol samples (A4 and A5) are shown in Figure 4-13 and for other samples are shown in appendix 4. Some of these spectra show absorbance peaks at the same wavelength at 280 nm, and very low intensity absorbance at 480 nm. As can be seen in Figure 4-5, excitation spectra of sample A4 shows a peak at 278 nm, which is the same transition as the absorbance spectrum of sample A4, which shows a band at 280 nm. The broad band at 480 nm may belong to other absorption processes than fluorescence decay.

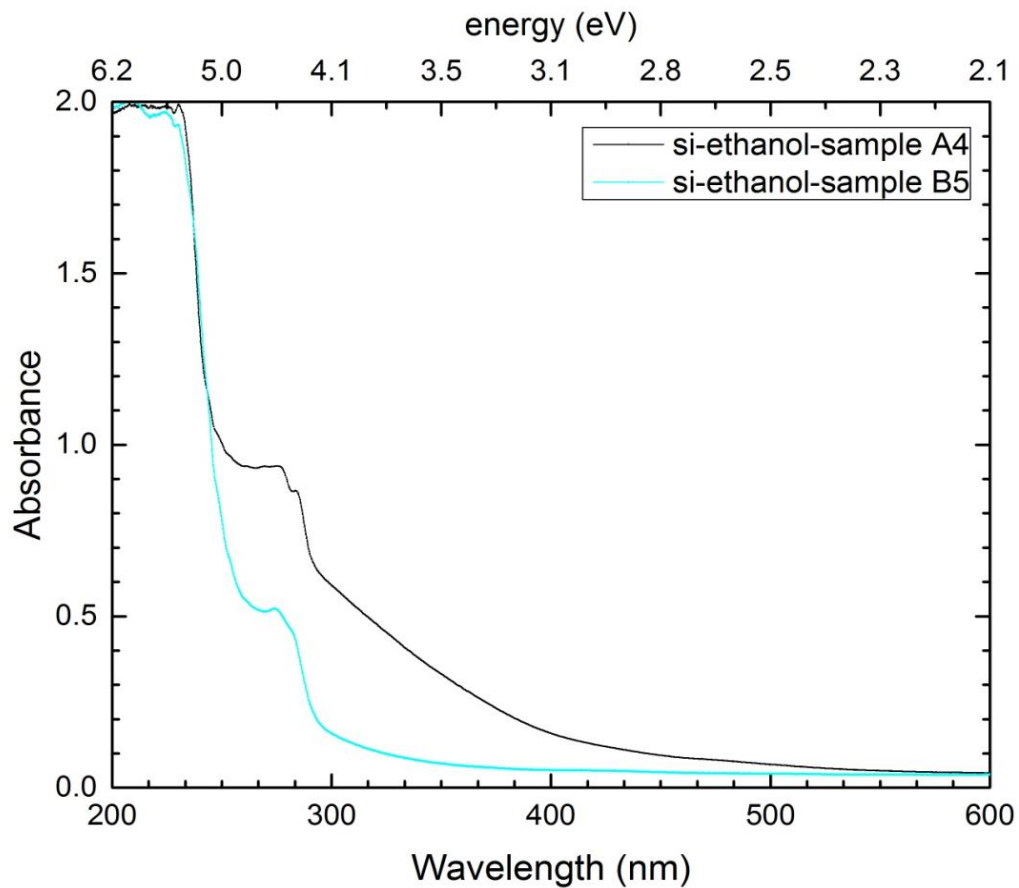


Figure 4-13. Absorbance spectra of Si-ethanol samples.

4.3.3 Absorbance of silicon particles directly deposited on water

Absorbance spectra of two Si-water samples (C9 and C2) are shown in Figure 4-14, and for other samples are shown in appendix 4. The absorbance of water samples is higher than for alcoholic samples. Similar to alcoholic samples, they do not absorb at the same

wavelength. The absorbance spectra of C9 and C2 are compared with excitation spectra in Figure 4-15. The absorbance spectrum of sample C9 shows a band around 260 - 270 nm, which is the same as the first fluorescence excitation band for sample C9, which is observed at 270 nm. Also, sample C9, (and some of other samples) show absorbance around 340 - 380 nm (broad absorbance band), which is the same band as the third fluorescence excitation peak for sample C9, which is observed at 380 nm.

The absorbance spectrum of sample C2 shows two shoulders, around 230 nm and 285 nm, which have the same wavelengths as the fluorescence excitation bands shown in Figure 4-15 for sample C2, observed at 230 nm and 284 nm. There is a peak around 320 nm in absorbance spectrum of sample C2 that shows a red shift with respect to the fluorescence excitation peak at 309 nm.

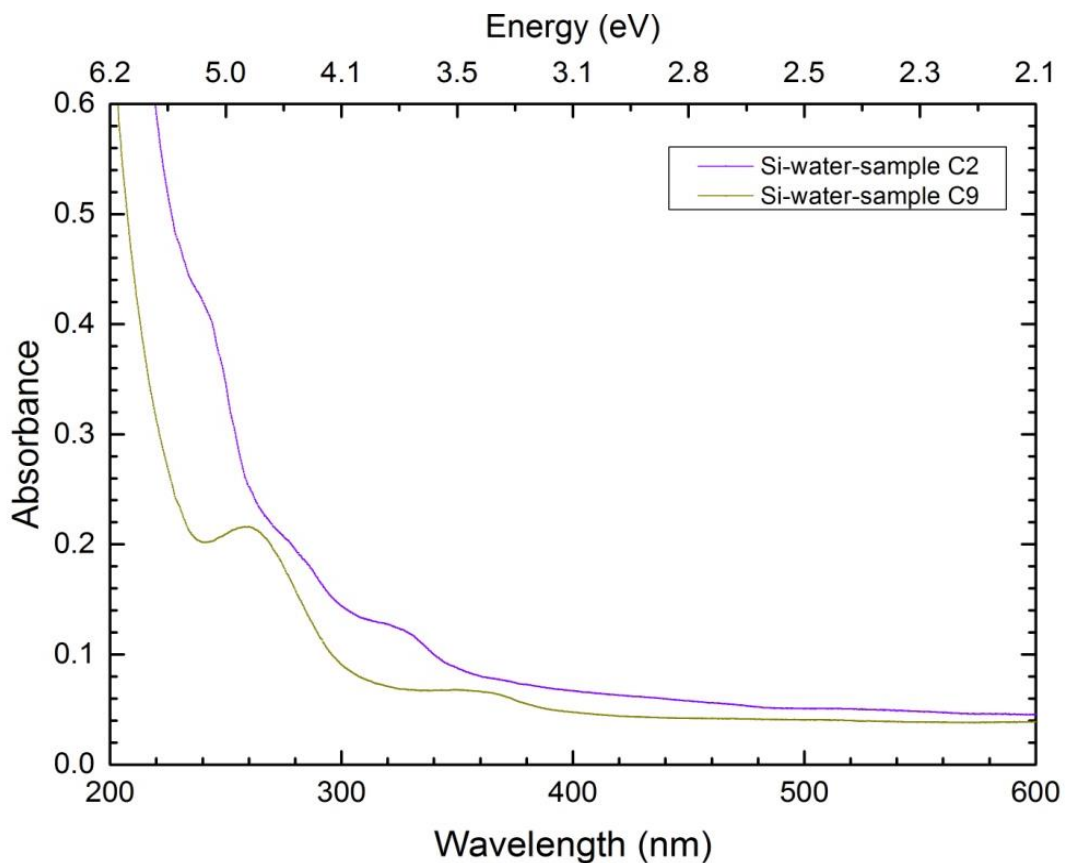


Figure 4-14. Absorbance spectra of Si-water samples.

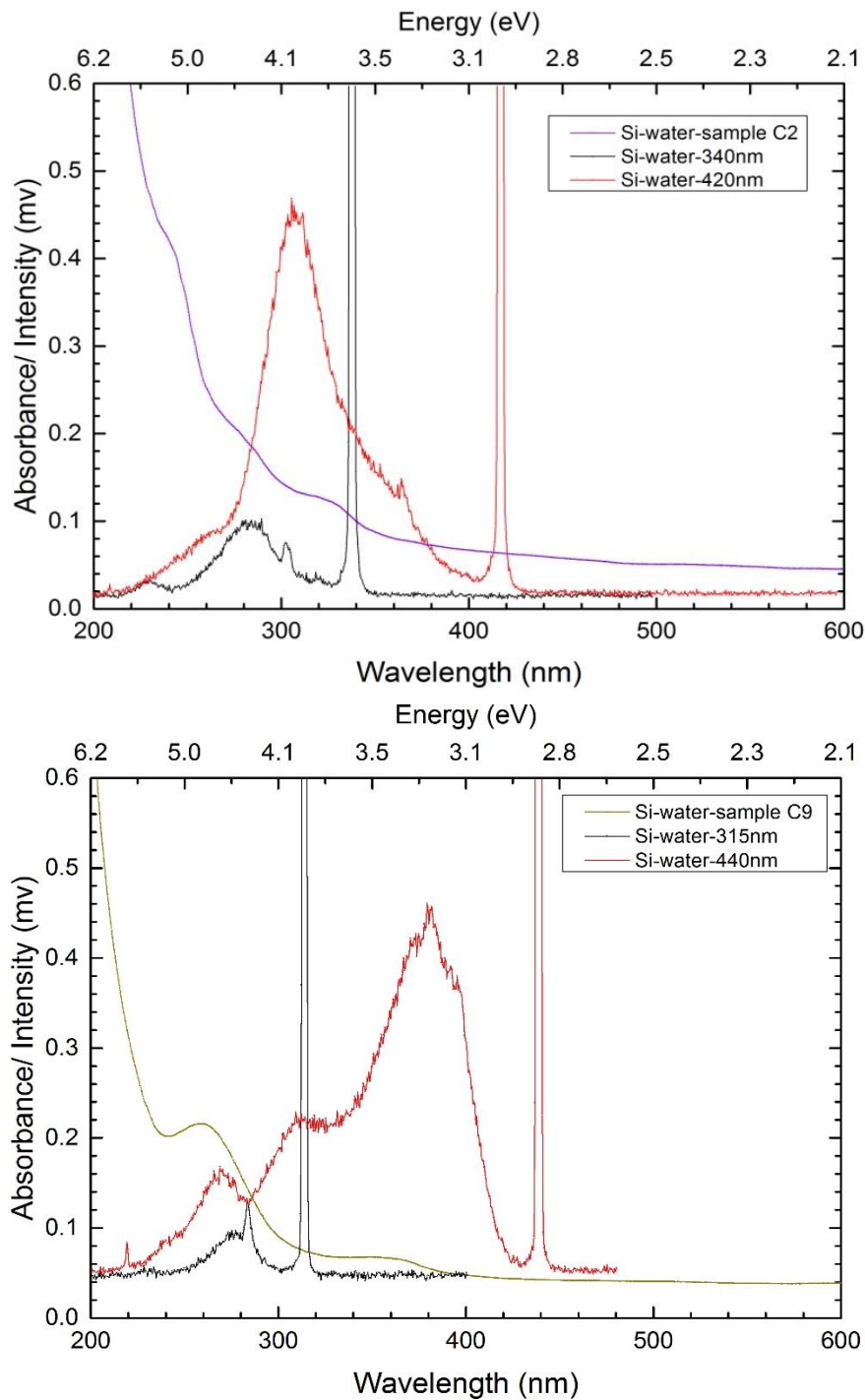


Figure 4-15. Comparison of absorbance and fluorescence excitation spectra of sample C2 and C9.

4.3.4 Absorbance of silicon particles directly deposited on hexane

The absorbance spectrum of Si-hexane is shown in Figure 4-16. The spectrum does not show any intense bands, only a very low intensity shoulder can be seen at 275 nm which is at the same wavelength as the first fluorescence excitation band shown in Figure 4-10.

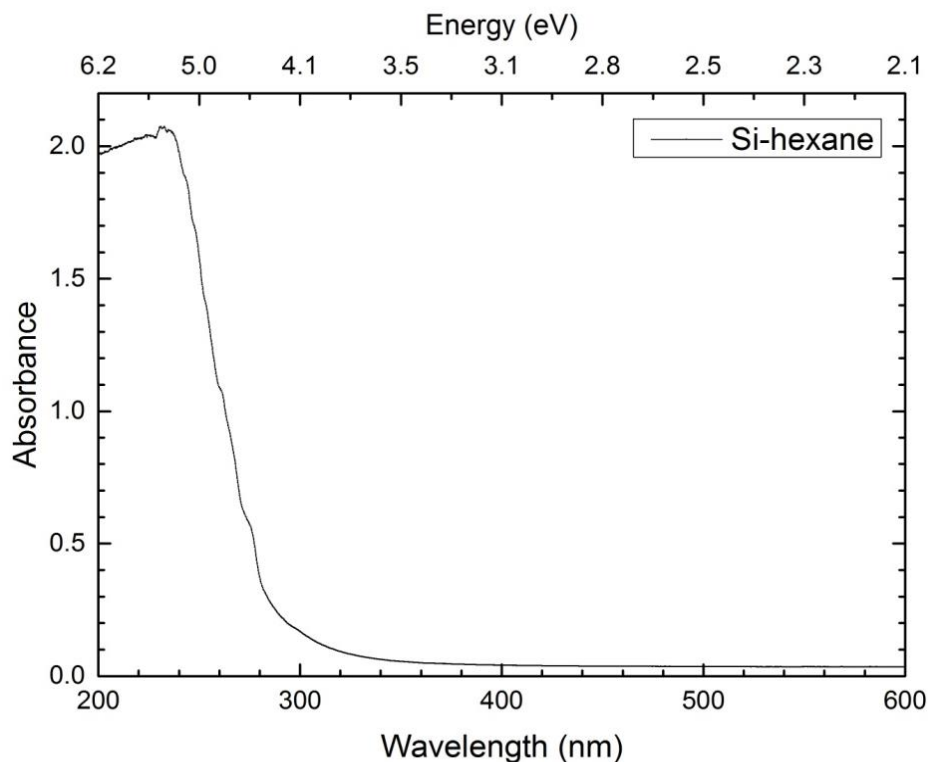


Figure 4-16. Figure showing the absorbance of Si-hexane.

4.4 Effect of solvent on absorbance and fluorescence wavelength and intensity

The nature of the environment and its interaction with the nanoparticles can affect all fluorescence parameters. Fluorescence spectra are unique to the [electronic] state distribution of the molecules and, particularly, the structure(s) of the excited state of the molecules that are populated in this distribution, so different molecules have different fluorescence spectra. Fluorescence depends not only on the structure of the molecules but also on their environment.

Emission and excitation fluorescence spectra of the samples produced in water, isopropanol and ethanol are compared in this section. All samples were produced in similar conditions. Figure 4-17 compares emission spectra at 250 nm; although the intensities of the peaks are lower at this excitation wavelength, all peaks are much more clearly resolved and the Raman peak is not too close to the first peak to prevent its deconvolution. Figure 4-19 shows excitation spectra for the first and the second fluorescence peaks.

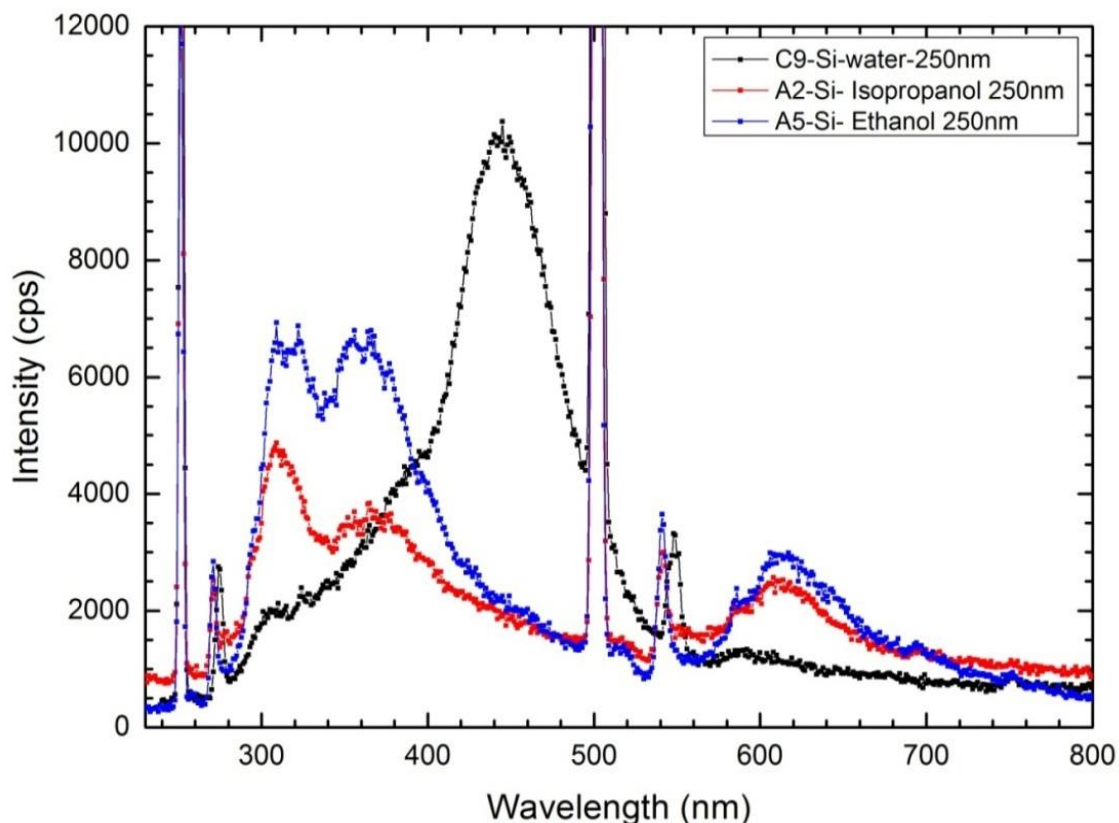


Figure 4-17. Figure showing fluorescence spectra of silicon clusters in isopropanol, ethanol and water. Their first fluorescence peaks are at 310 nm for all samples, with the second fluorescence peaks at 365 nm for Si-IPA, 370 nm for Si-ethanol, and ~440 nm for Si-water. Fluorescence shows sensitivity to solvents. The fluorescence wavelength depends on the solvent; alcohols show a blue shift in their fluorescence peaks relative to water.

The model we had developed for such systems attributed the first fluorescence peak to the bulk cluster, and is an intrinsic peak, so is always observed at the same wavelength (310 nm) regardless of solvent because bulk clusters cannot react, or interact, with the solvent itself; the fluorescence at same wavelength is due to a localised [bulk] transition, and is identical for all samples. However, after measuring the lifetime (section 4.12.1) we found samples produced in different solvents show different decay times for the first fluorescence peak, which means they could not have the same structure, and thus that they only coincidentally show the fluorescence feature at 310 nm.

The second fluorescence peak is attributed to cluster surface, so fluorescent states are localised at the cluster surface and can thus interact with the solvent; consequently, the fluorescence that characterises surface sites will vary with solvent; that is, the second peaks are solvent dependent. Fluorescence spectra show second fluorescence peaks at 365 nm for Si-IPA, 370 nm for Si-ethanol, and ~440 nm for Si-water samples. This

dependency shows particles interact with the solvent, and in a manner that is dependent on the solvent.

All produced nanoparticles show intense fluorescence whose peak wavelength depends on the specific solvent used for the liquid jet. This wavelength dependence was found to be related to the dipole moment of the solvent, the interaction between clusters and solvent, and steric effects of the solvent, which can vary the type and strength of the bonds affecting the energy levels of fluorescent sites on the surface. Depending on the bond strength with the solvent, the ground and excited states can show greater or lesser shifts with respect to each other, which may explain the observed solvent shift of the fluorescence wavelength. According to Equations 4.1 and 4.2, the second band may originate from silicon OH (SiOH) or SiO₂ 'defects' at the cluster surface. Chemical characterisation results in the next chapter attest to the blue luminescence of our samples coming from silicon-oxygen binding at the cluster surface.



To investigate dipole moment dependence as one possibility affecting fluorescence peak wavelength, the energy of the peaks were plotted versus the dipole moment of the solvent used; as can be seen in Figure 4-18, the peak position and dipole moment show a linear relationship for IPA, ethanol and water, though this relationship did not extend to hexane or formic acid, possibly due to water impurities. The linear relationship for alcoholic solvents and water suggests that the transition frequency shift is predominantly controlled by the dipole moment of the solvent. The sensitivity of the silicon nanoclusters to the dipole moment is defined by distinct solvent shifts of apparently localised electronic transitions. The solvent sensitivity and correlation of the fluorescence energy with solvent dipole moments also suggests that the transition is localised at polar sites on the surface of the clusters, and the interaction is controlled by dipole-dipole forces. When a molecule absorbs energy, its dipole has an orientation different to that in the ground state. Therefore, the molecule dipole-solvent dipole interaction in the ground state is different from that in the excited state, and furthermore is unstable. The molecule must redistribute energy to reorient the dipole and become stable. So, for a solvent with a higher polarity, fluorescence happens at lower energies and, therefore, longer wavelengths. Alcoholic

solvents have weaker dipole moments than water, so they show smaller red shifts in their fluorescence peaks. One possibility is the existence of [silanol] OH groups on the surface of the cluster allowing for different surface interactions, as it is well known that hydrofluoric acid etched crystalline silicon forms a hydroxyl group upon contact with deionised water [99], and we believe that a similar reaction may occur for our clusters. The hydroxyl group has a strong dipole moment which should align with the dipole moment of the solvent molecules, so inducing the spectral shift. The correlation of the transition wavelength with the dipole moments of the solvents observed for our samples indicates that the silicon OH group is hydrogen-bonded to the solvent molecules, and the interaction between the solvent molecules and nanoparticles occurs via electrostatic and hydrogen bonds. For a solvent with high dipole moment, the dipole-dipole interaction needs a high amount of energy, and thus the peak position will be located at high wavelength, which is exactly what happens for the Si-water sample. Although different dipole moments may cause the spectral shift, this is not the only reason for the fluorescence shift and, as mentioned earlier, the type of interaction between clusters and solvent and steric effects can also vary the wavelength of fluorescence peak; also, as will be explained in the next chapter, our samples show different levels of oxidation, so different peaks can originate from species of different oxidation states.

According to our observation in chapter 5, the red shift in the fluorescence wavelength may be related to oxidation state, so the Si-IPA fluorescence peak at 365 nm belongs to SiO, the Si-ethanol fluorescence peak at 370 nm belongs to SiO_x 1<x<2, and the 420- 440 nm peak belongs to SiO₂. Also chemical characterisation shows Si-water samples in addition to SiO₂ have SiO or SiO_x bands, which could explain the existence of three fluorescence peaks in fluorescence spectra of Si-water. Thus the peak around 380 nm, which exists in some Si-water samples, can be attributed to SiO_x. As we explain in the next chapter, Si-water samples show higher levels of oxidation than alcoholic samples, so we attribute the band at 440 nm to oxygen-rich samples. All Si-water samples show a band at 420 - 440 nm, which means Si-water samples are highly oxidised with respect to alcoholic samples; although they are oxidised as well and also may have OH groups at their surface, the silicon oxidation states in each are different (chapter 5).

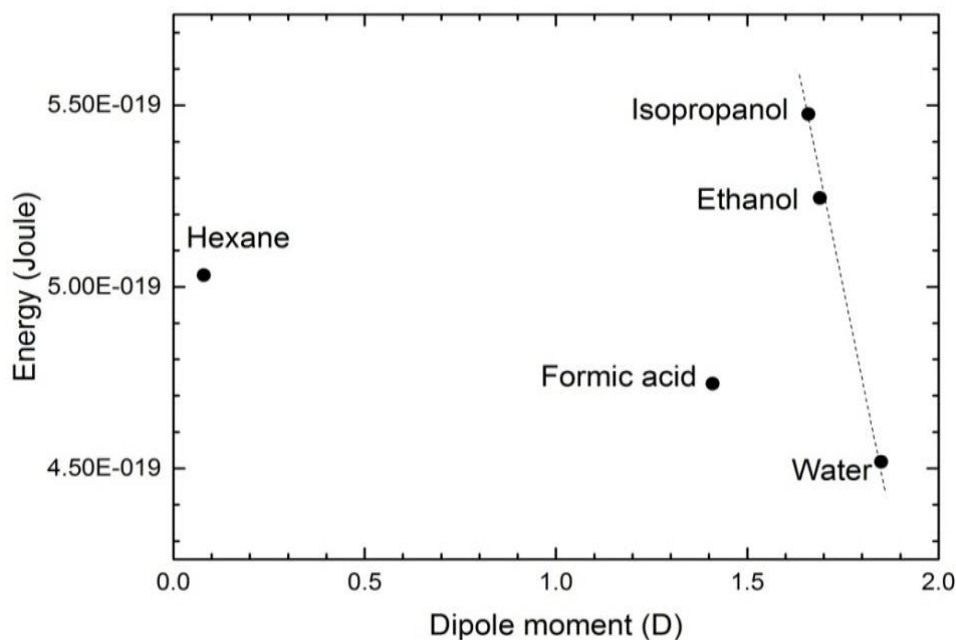


Figure 4-18. The relationship between dipole moment of the solvent and fluorescence shift. The figure shows the energy of the fluorescence bands and that, therefore, the fluorescence energy shift for alcoholic solvent and water depends on the dipole moments of the solvents; the larger the dipole moment, the greater the shift to longer wavelengths.

The Si-hexane sample shows its first fluorescence peak at 310 nm, similar to all other samples, which confirms our hypothesis regarding the existence of silicon bulk nanoclusters and the origin of a fluorescence peak at 310 nm. The Si-formic acid and Si-hexane did not satisfy our expectation for the second fluorescence band, which may have happened because of other parameters which affect fluorescence or because of water impurities in our formic acid and hexane samples.

The literature suggests that OH groups absorbed on a network of silica are responsible for the green/blue photoluminescence in oxidized porous silicon [80], which can be used to explain our sample fluorescence wavelength. Also, increases in OH group concentration will increase photoluminescence emissions [80], which is also in accord with our results. The increase in photoluminescence intensity may be explained as the result of surface passivation by the chemical oxidizing treatment [243]. As photoluminescence emission may be associated with Si-OH [80], or silicon oxygen bonds, in all cases we believe that OH groups or silicon-oxygen bonds are formed at the cluster surface, and not inside the cluster, because fluorescence peaks were dependent on the solvent used. Also, since the intensity, and thus quantum yield, are dependent on the number of emitted photons, they will be lower than emission that occurs in highly polar

environments, so silicon deposited in alcohols shows lower fluorescence intensity than in water.

In Figure 4-19 fluorescence excitation spectra of the first peak show the same wavelength as the analogous excitation fluorescence band, which means fluorescence may come from the same excited state (electronic transition) for silicon produced in all solvents, although it may just happen coincidentally. For the second fluorescence peaks, fluorescent states are solvent dependent and must therefore be localised at the cluster surface. Fluorescence excitation spectra show different wavelengths for fluorescence excitation bands, which means they come from different excited states. Si-water sample shows several transitions at the same excitation wavelength.

The Stokes shift is the difference between the energy of the excitation and emission fluorescence peaks. The Stokes shift is dependent on the structure of the molecules and their environment. By comparison of Figure 4-17 and Figure 4-19, it can be seen that clusters produced in different solvents show different Stokes shifts.

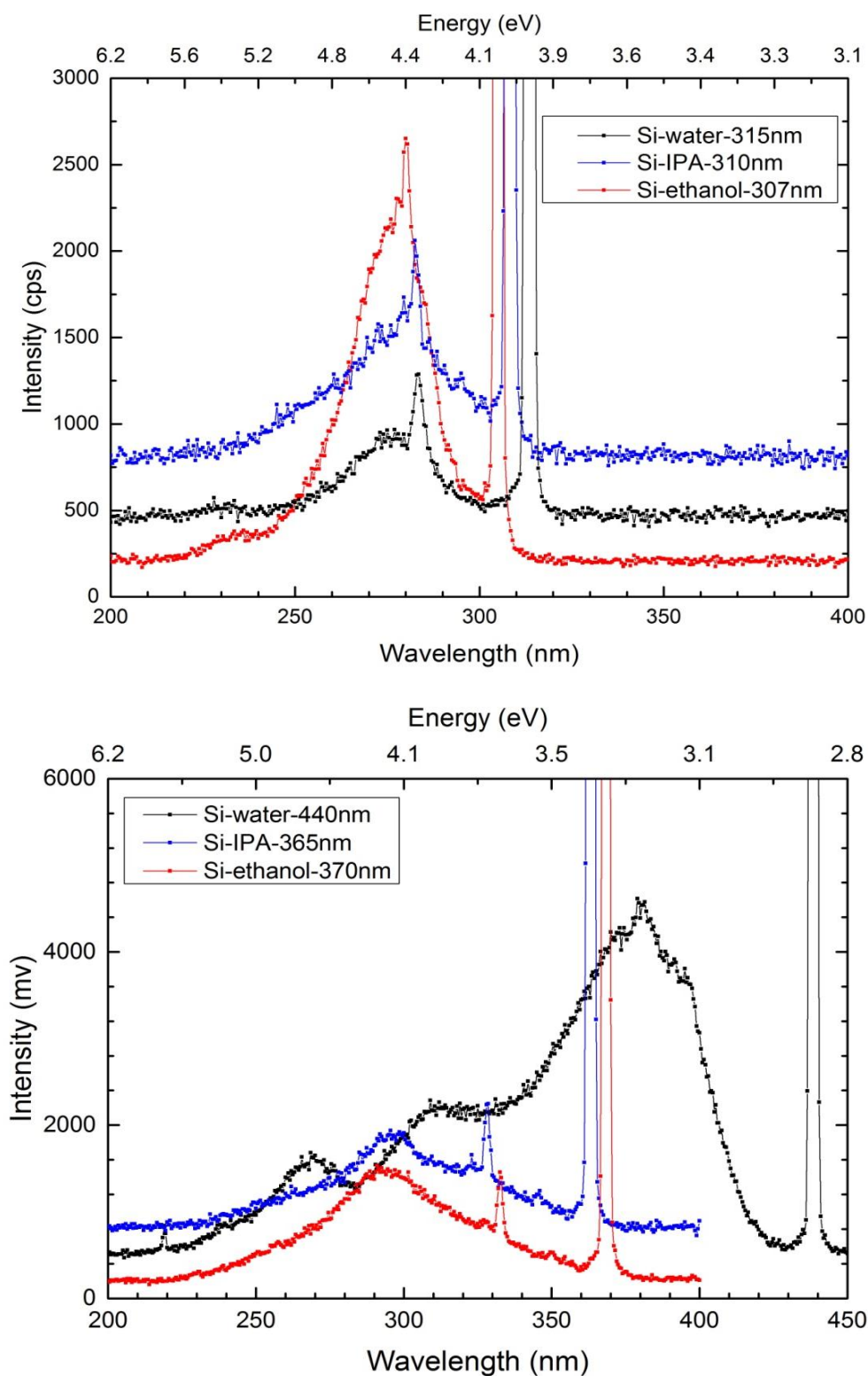


Figure 4-19. Excitation spectra for the first and second fluorescence peaks. Top: samples were investigated for the first fluorescence peaks; positions of the excitation spectra show that silicon particles in three different solvents have the same excited state. Bottom: excitation spectra of the second fluorescence peaks, which show sensitivity to the solvent used in each case.

Absorbance spectra of Si-IPA, Si-ethanol and Si-water are shown in Figure 4-20. All absorbance spectra show a peak around 260-270 nm, which belongs to the first fluorescence bands of the samples; blue shifts in the fluorescence excitation spectra for the first peak in each sample, which show bands around 278 nm, are due to the relatively low sensitivity of the UV/Vis spectrometer. Fluorescence spectra are more sensitive to environment than absorption spectra.

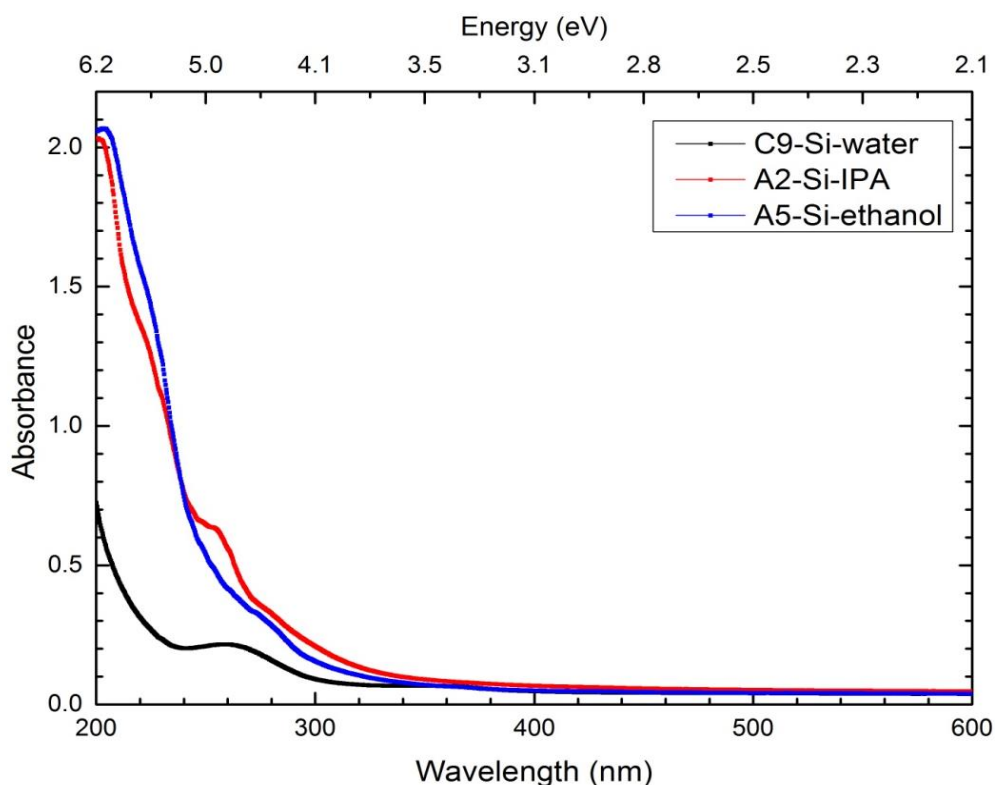


Figure 4-20. Absorbance of silicon clusters produced in three different solvents.

4.4.1 Jablonski diagram of silicon nanoparticles produced in different solvents

To gain a clear prospective of the processes that happen for excitation and emission, the schematics in Figure 4-21 and Figure 4-22 show Jablonski diagrams for the first and second fluorescence bands for silicon deposited in isopropanol, ethanol and water solvents. As can be seen, the excitation and emission energy for the first fluorescence peak is the same for all solvents, but there are different excitation and emission energy levels for the second peak which depend on the solvent used, and thus the interaction of silicon with the solvent.

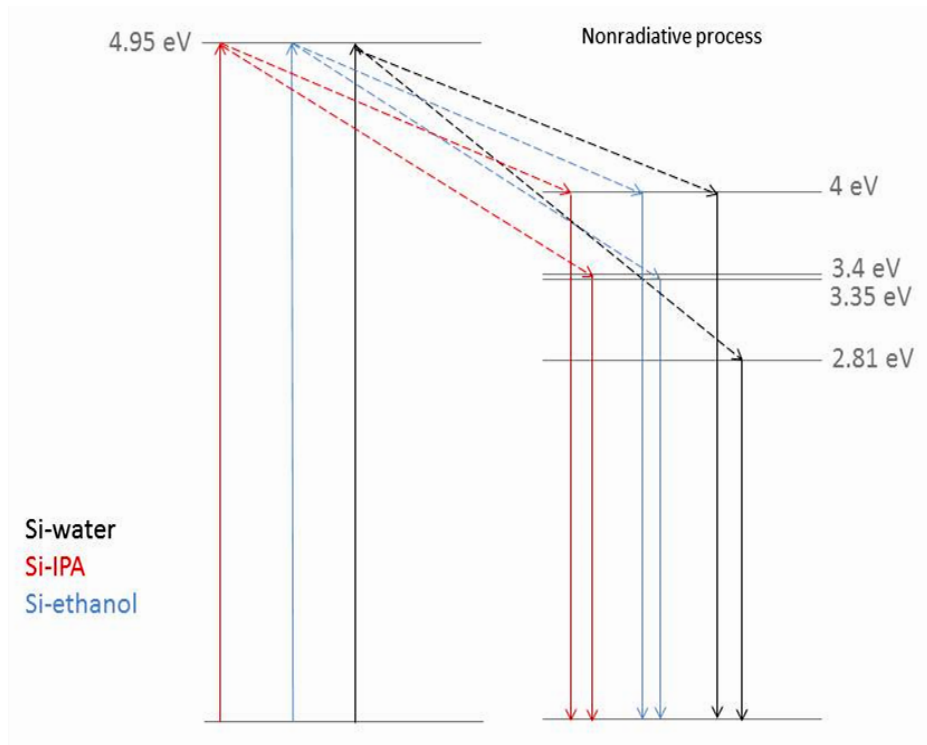


Figure 4-21. Jablonski diagram of the emission spectra. The diagram shows the transitions for the first and the second fluorescence peaks for Si-IPA, Si-ethanol and Si-water samples.

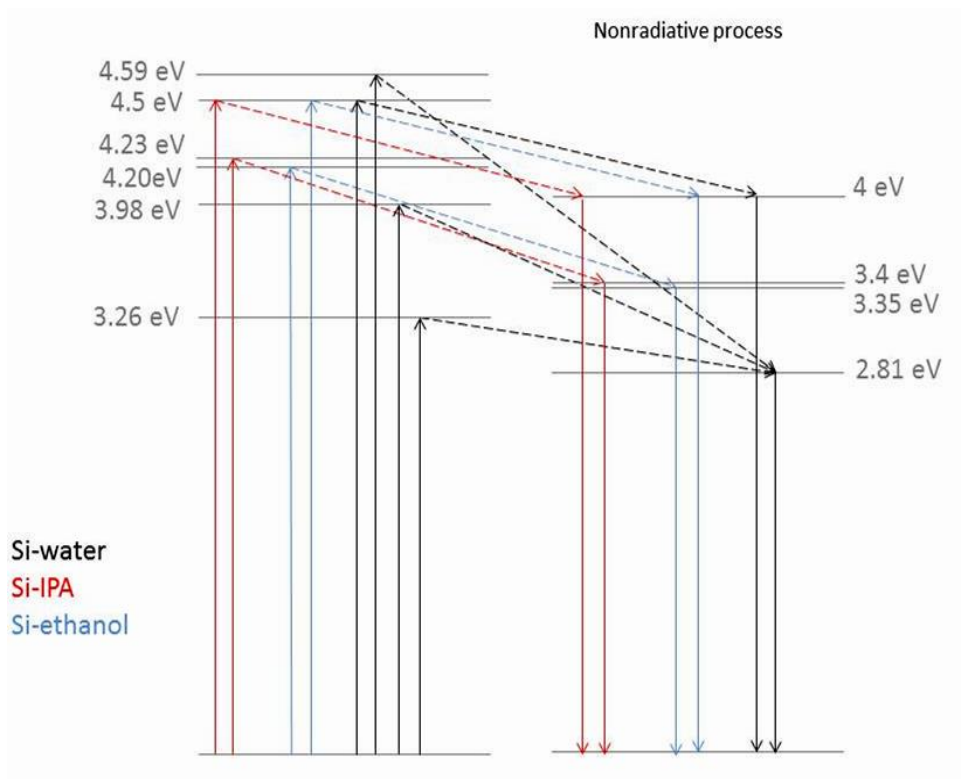


Figure 4-22. Jablonski diagram of the excitation spectra. The diagram shows the transitions for the first and the second fluorescence peaks for Si-IPA, Si-ethanol and Si-water samples.

4.4.2 Band gap measurements

To investigate the structure of the sample and the band gap of the species which exist in the sample we have plotted the Taus plot for silicon in IPA, ethanol and water (Figure 4-23). We use the direct band gap calculation to plot the Taus plot, as silicon in nano range is a semiconductor with a direct band gap. For each sample there are several absorbance bands which can be used to calculate the band gap. It can be shown that we have several species – with different structures – in our samples, some of which may not contribute to fluorescence processes, instead decaying non-radiatively. The plot suggests different structures with band gaps between 4.1 eV to 5.8 eV. Si-water has the larger band gap in three different samples. We cannot compare the band gap of our samples with SiO_2 directly due to the cut-off of the instrument at 6.2 eV.

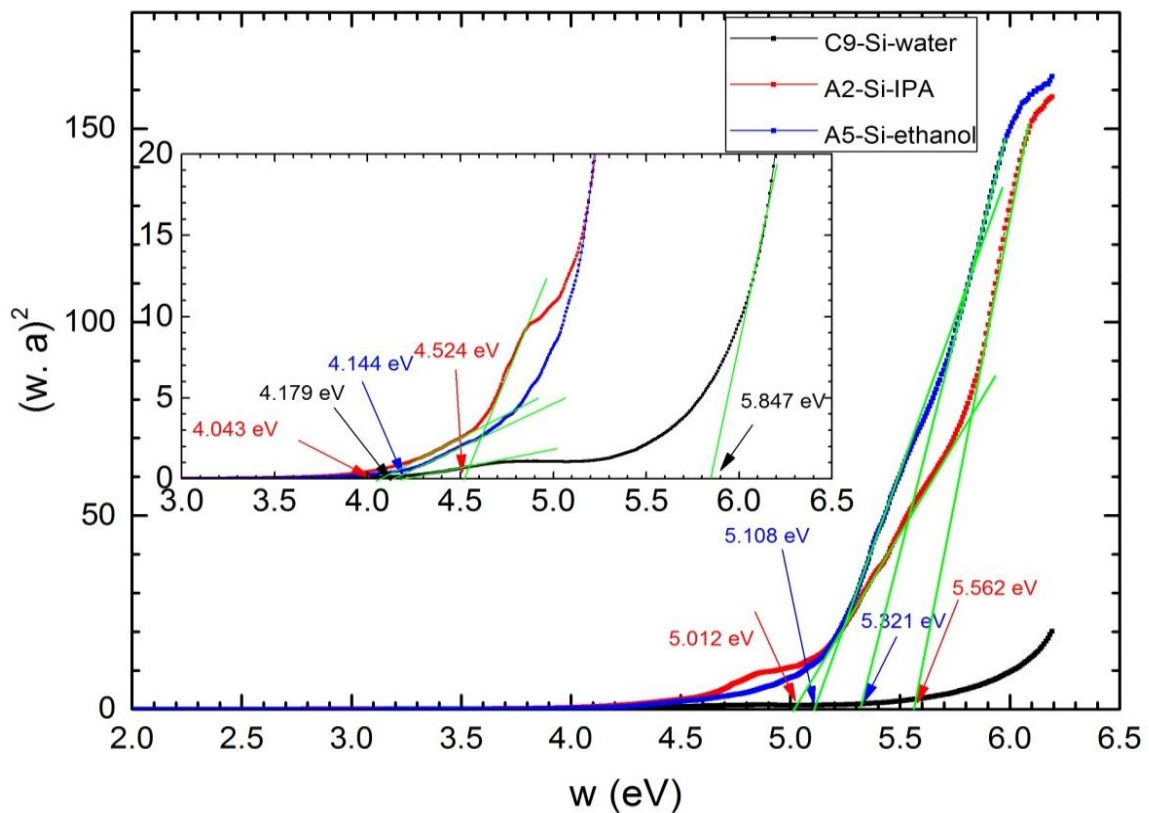


Figure 4-23. Taus plot of Si-IPA, Si-ethanol, and Si-water. The band gap can be calculated from this plot, as shown by the arrows.

4.5 Fluorescence stability

The fluorescence emission spectrum of a Si-water sample (C2) was measured immediately after production and, subsequently, a year later in order to investigate the stability of the fluorescence. The result of this study is shown in Figure 4-24.

The measurements show the fluorescence intensity barely changed over this time frame. So, the fluorescence of the sample is stable in the term period without requiring any kind of [chemical] stabilisation. Also, clusters formed a stable phase in water and did not agglomerate. The results of other groups who used other methods to produce silicon nanoclusters show the clusters are not stable, and their fluorescence spectra changed after a while even when using a stabilizer.

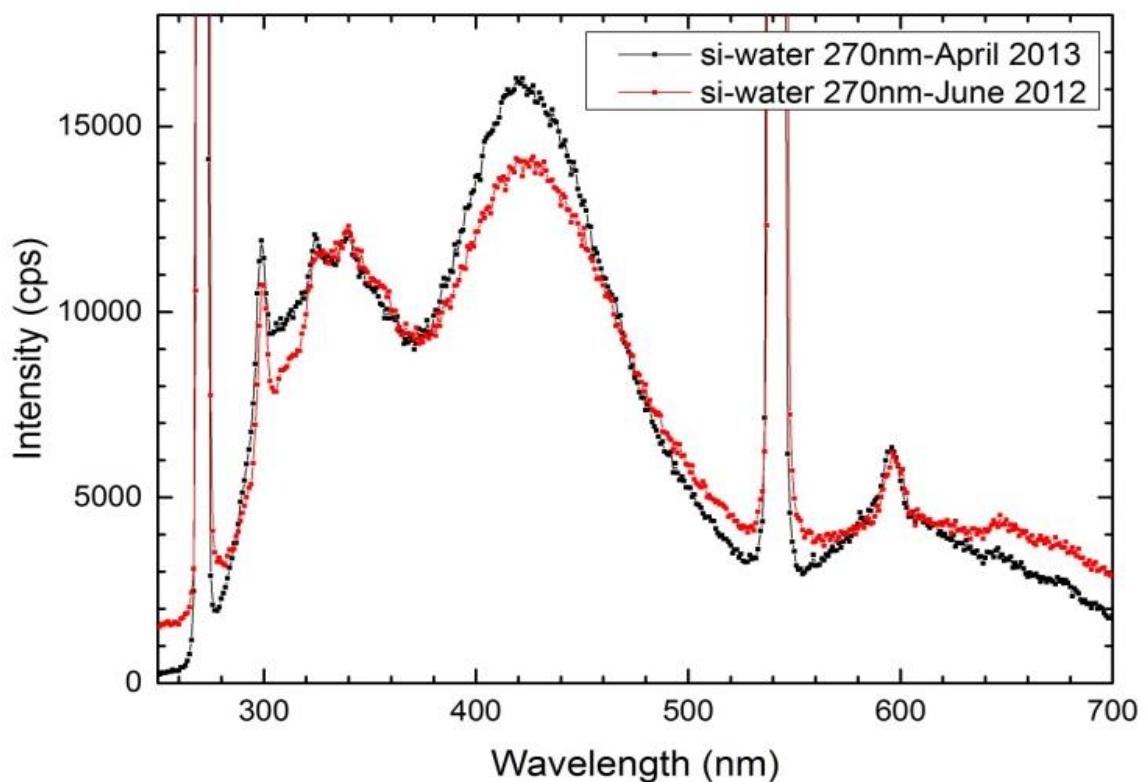


Figure 4-24. Figure showing emission spectra of a Si-water sample which was measured when produced (June 2012) and a approximately a year later (April 2013). The results show the samples are chemically stable.

4.6 Concentration of sample

A dilution experiment was performed for two samples, Si-ethanol (sample A5) and Si-water (sample C9). The fluorescence emission and excitation and absorbance of the samples were measured at each dilution step. The results of this experiment are shown in Figure 4-25 to Figure 4-28.

A Stern-Volmer plot of Si-ethanol sample is shown in Figure 4-26; the intensity was plotted versus concentration. As can be seen, the increasing intensity of the fluorescence peak with concentration is linear for the first six steps of dilution, but then deviates from a linear regime and becomes a plateau. This shows that at high concentration, fluorescence is quenched. This can happen for two reasons; in high concentration, fluorophores collide with each other and lose energy, so the intensity is less than the nominally expected value or, at high concentration, the concentration of non-fluorescent molecules is also high, so they collide or bind with fluorescent molecules, thereby lowering intensity. Although the fluorescence is quenched at high concentration, still the intensity of the fluorescence is higher than at low sample concentrations, purely because the number of fluorophores is higher (in the absolute sense). By increasing fluorescence intensity at higher concentration, the intensity of the Raman peaks and scattered light peaks are consequently decreased, because of the competition between these processes. So, at higher concentrations, the number of fluorophores in the solvent is higher and leads to higher fluorescence intensity. In low concentrations, the number of solvent molecules – which cause scattering – is very high, so the scattered light intensity is higher.

Absorbance spectra of diluted samples are compared and the relation between them is plotted in Figure 4-27. The results show that by increasing the concentration of the sample, the absorbance increases. As absorbance has a linear relationship with concentration (according Beer-Lambert law), it confirms fluorescence was quenched, because it shows fluorophores absorb light in high concentration but did not fluoresce, instead losing energy through collisions or the formation of non-fluorescent compounds. The linear relationship between absorbance and concentration shows the chemical stability of the sample.

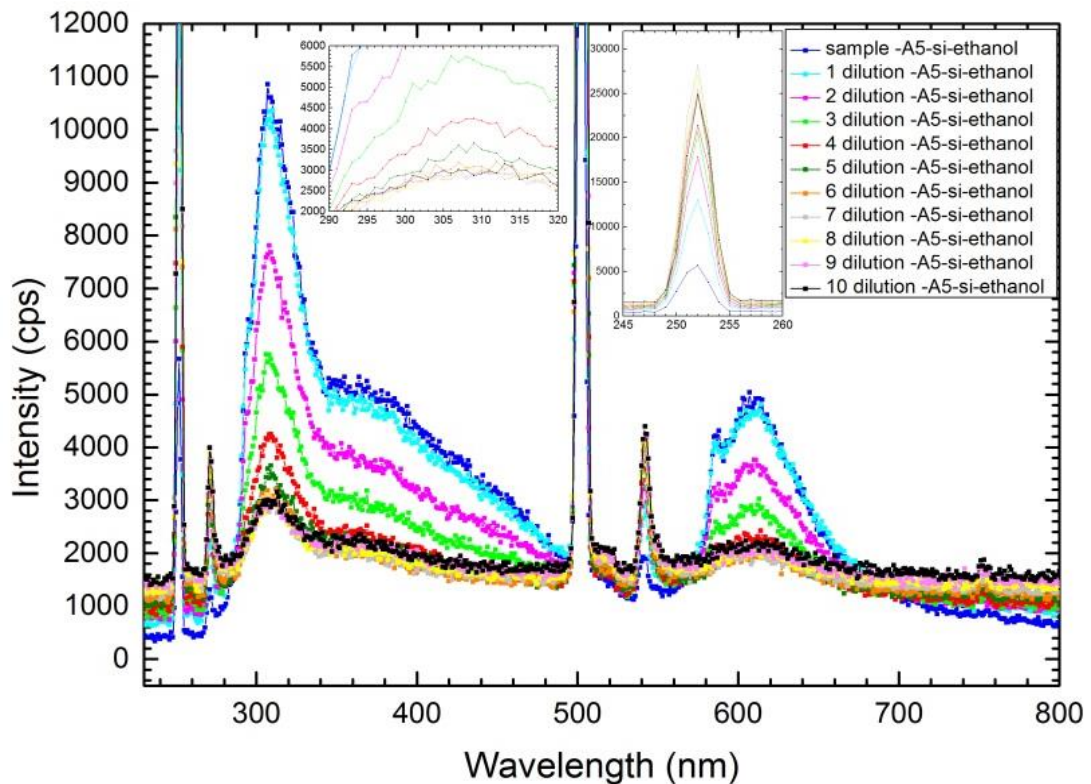


Figure 4-25. Si-ethanol sample, diluted in ten steps (by a factor of two at each stage). Fluorescence intensity is decreased by dilution. The insets show scattered light and the last seven steps of first fluorescence peak. The sample was excited at 270 nm.

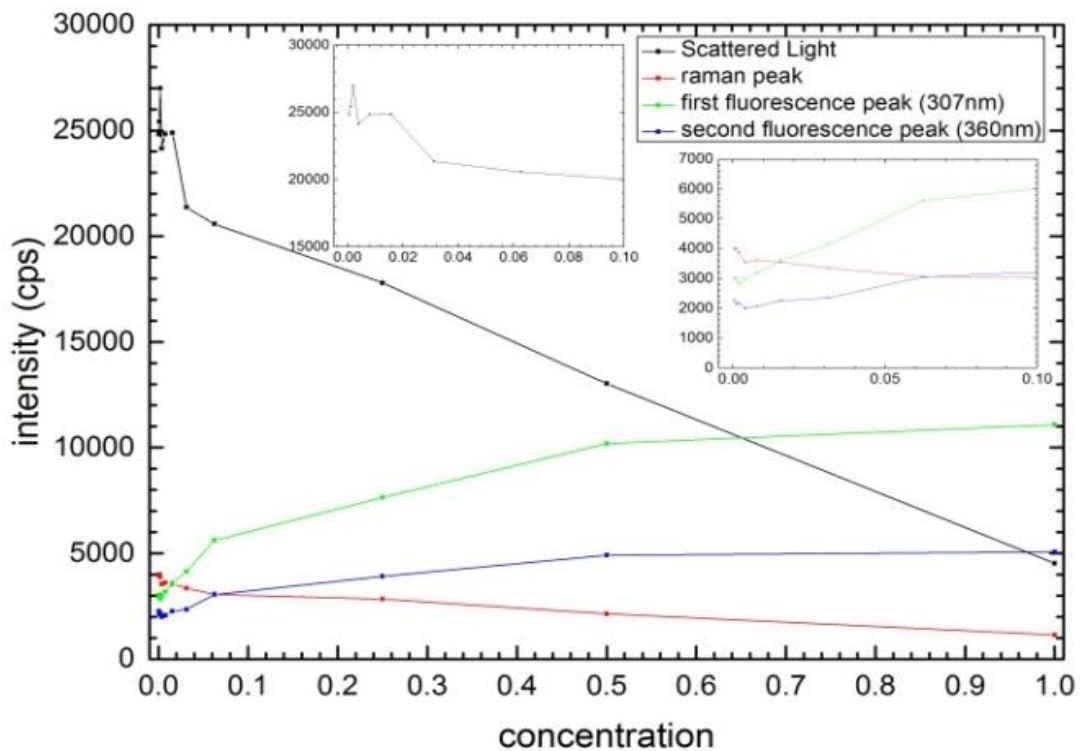


Figure 4-26. Figure showing the Stern-Volmer plot for Si-ethanol. As can be seen, the intensity of the Rayleigh peak and the Raman peak decrease with increasing the concentration whilst the intensities of the two fluorescence peaks increase.

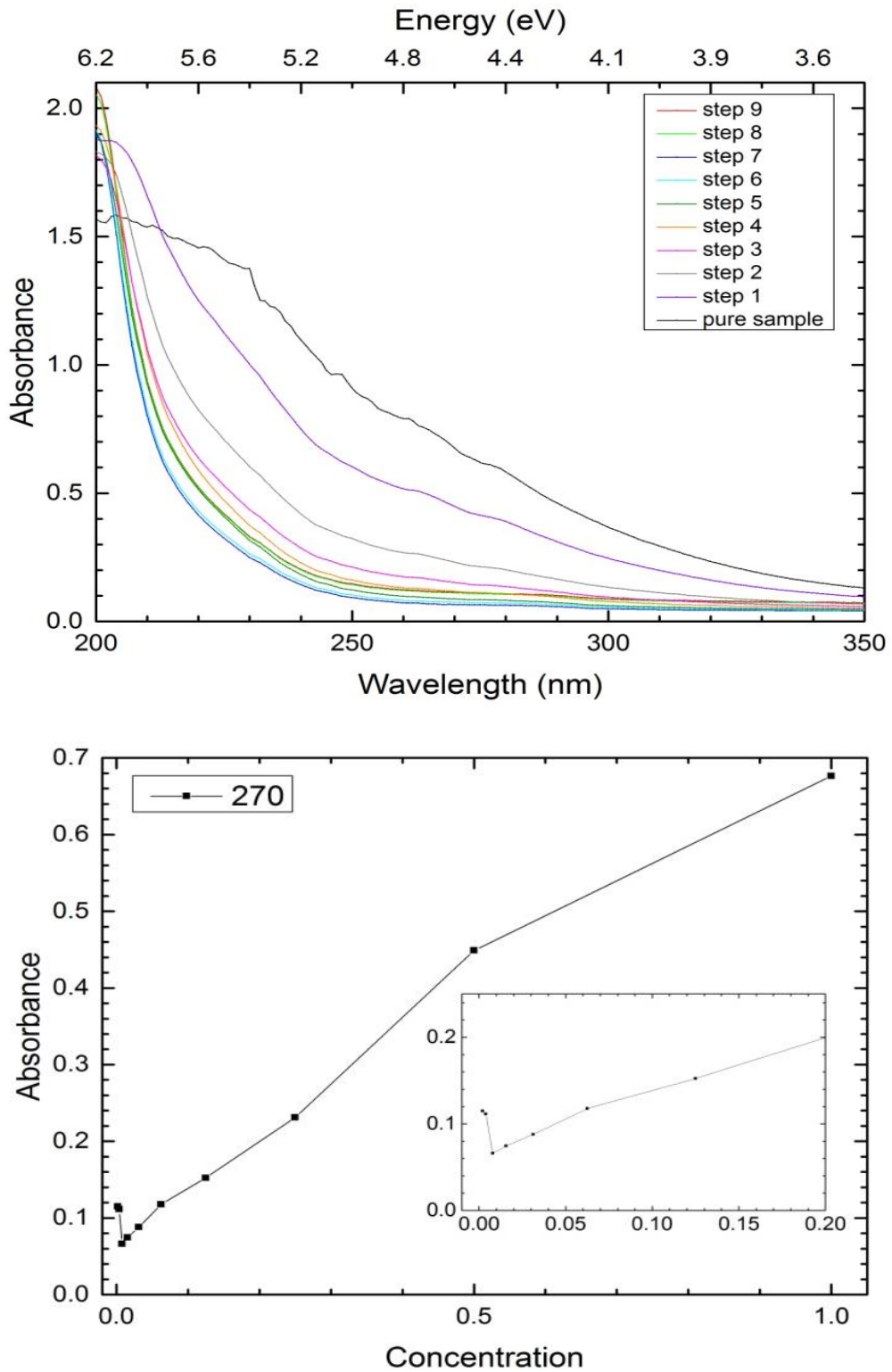


Figure 4-27. Figures show the changing absorbance of the sample with concentration. The absorbance was measured using a UV/Vis spectrometer. The relationship between absorbance and concentration is linear.

The same dilution experiment was performed for the Si-water sample; the results are shown in Figure 4-28.

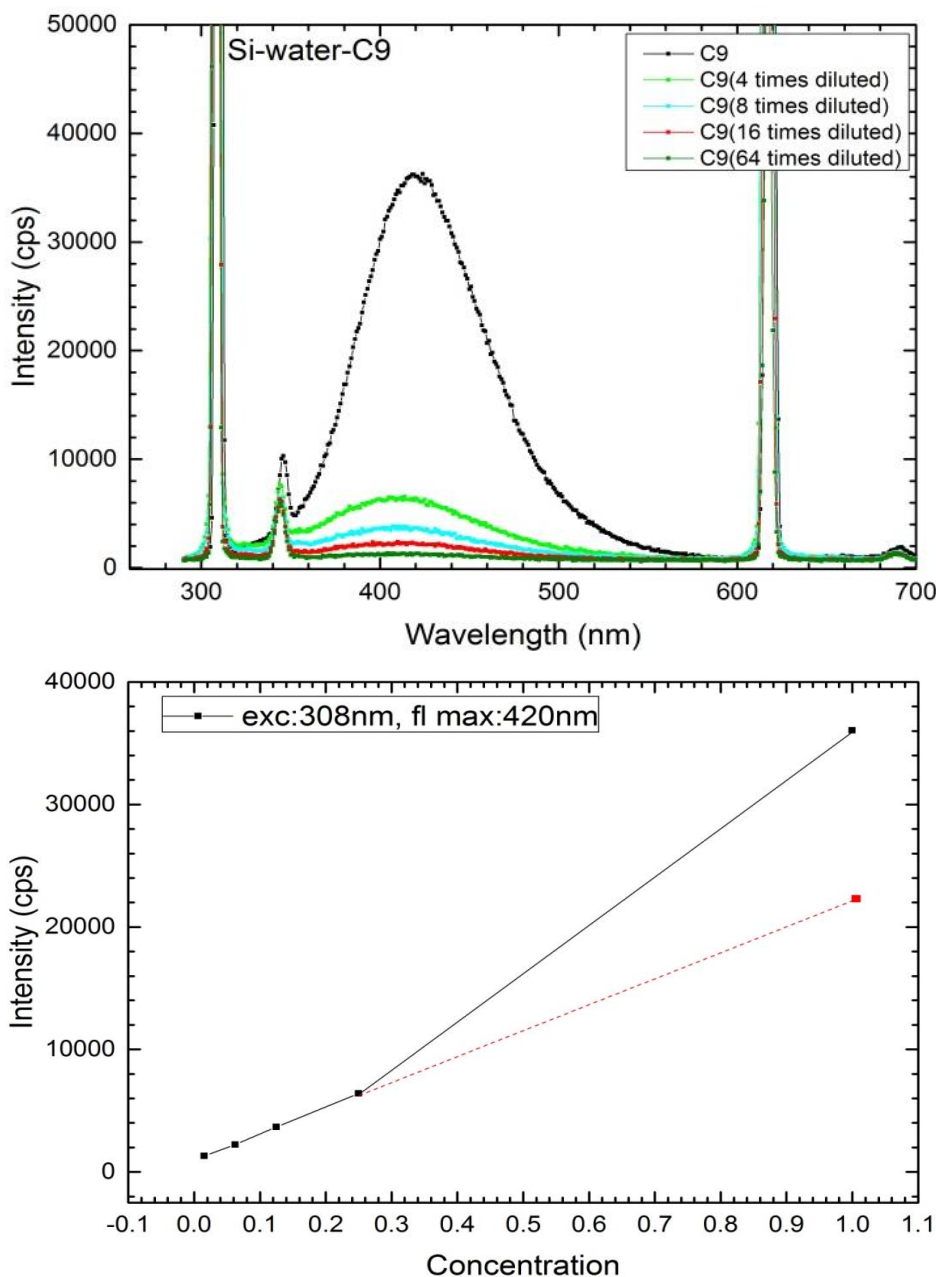


Figure 4-28. Dependence of fluorescence intensity on concentration. A Stern-Volmer plot shows fluorescence intensity decreases with decreasing concentration, and that this relationship is linear. There is a clear deviation from a linear relationship for the original sample, which is shown with red line.

The Stern-Volmer plot shows a linear relationship between intensity and concentration in the sample produced in water, which means quenching did not happen for the Si-water sample, however it shows deviation from linear relationship at high concentration. The data point at high concentration belongs to nondiluted sample. The deviation for this data point may arise from two different 'types' of water (they may be different in purity) to produce the sample and to dilute the sample. If an unknown

impurity in water (such as Na^+ , Cl^- and other ions that are difficult to remove below the ppm level) was responsible for the chemical activation or deactivation of fluorescence, then a change of the solvent could produce a change of fluorescence intensity. The present results can be interpreted in terms of an impurity rather than quench fluorescence. The linear relationship between fluorescence intensity and the concentration shows the dynamic stability of the Si-water sample.

4.7 Solvent exchange

To assess whether solvent dependence could be due to chemical reactions during nanoparticle growth on the surface of the liquid jet, and also to know the dependence of fluorescence to the solvent that the nanoparticles are kept in it, a solvent exchange experiment was performed where the samples were completely dried and then dissolved in another solvent. The sequence was repeated four times; fluorescence spectra were recorded each time at 250 nm, 270 nm and 308 nm excitation wavelengths (some of these wavelengths are shown here). Also, the solvent exchange cycle was repeated several times to investigate whether the solvent exchange was reversible or not. Figure 4-29 to Figure 4-33 show the results of investigating the difference between directly deposited samples and transferred samples.

Figure 4-29 shows the fluorescence spectra of silicon nanoclusters exchanged between ethanol and IPA in four steps. The fluorescence peaks alter between Si-ethanol and Si-IPA wavelength and intensity, by changing the solvent. In our previous model, the first peak is not solvent dependent, but is rather an intrinsic fluorescence peak indicating a possible location of the fluorescence site in the bulk of the nanocluster. The first peak does not shift when changing the solvent; in our hypothesis, this is presumably due to the non-polar character of the fluorescence site or a site location in the bulk volume of the nanoparticle. However, we already believe it happens at the same wavelength coincidentally. The second peak depends on the solvent, and must be associated with transitions at the cluster surface, and shifts with changing solvent due to clusters-solvent interaction. Also, the spectra show that the second peak is reversible when the solvents are repeatedly exchanged. In the third step of this process, when the nanoparticles are transferred back to ethanol, the IPA solvent did not evaporate completely, so some

digression can be seen in the third spectrum from that expected/ previously recorded for nanoparticles in pure ethanol. This indicates the solvent is trapped by the clusters and the bonds between solvent and cluster are not broken completely during the evaporation of the solvent.

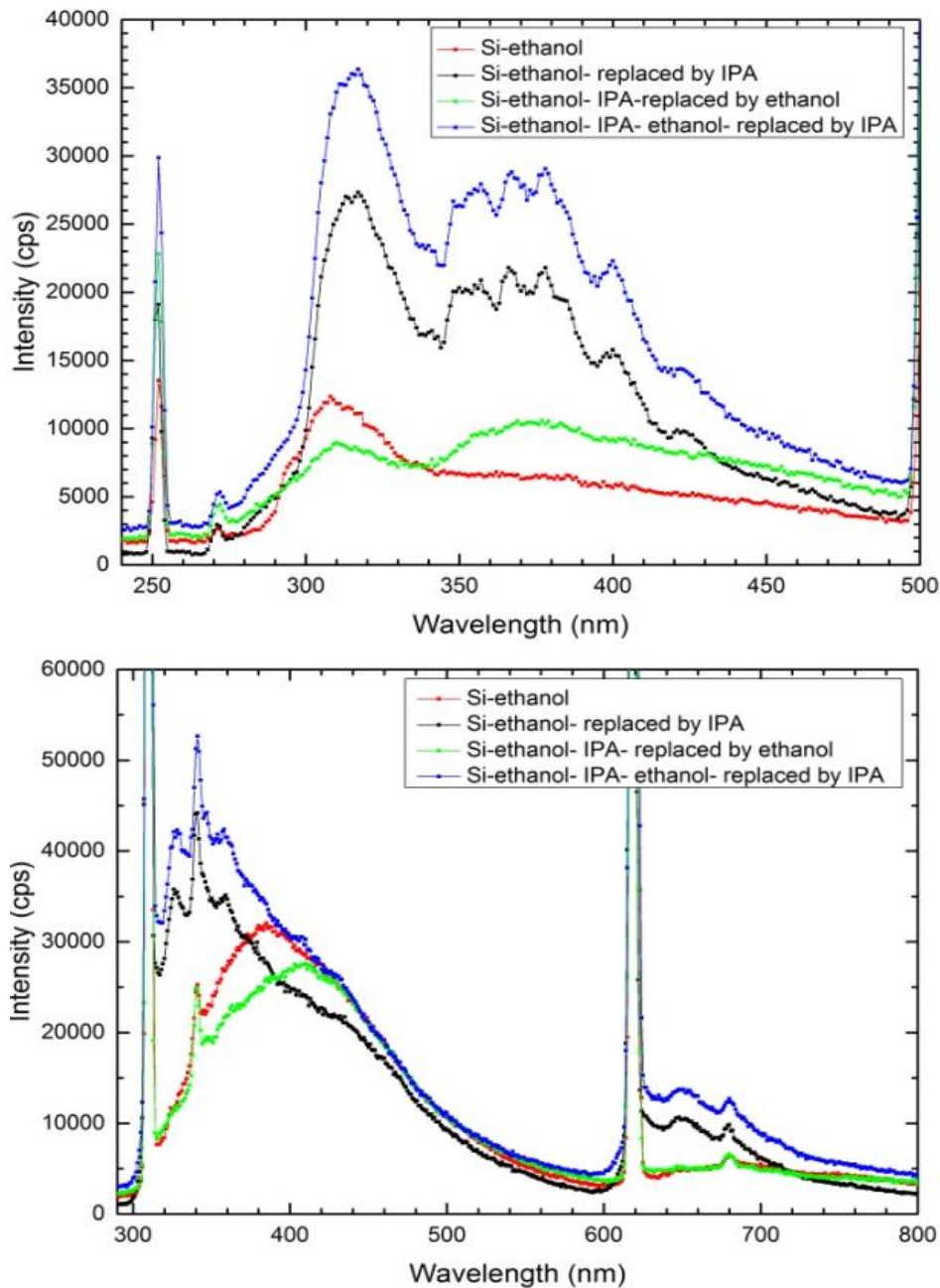


Figure 4-29. Figures showing the repeated transfer of the sample between ethanol and isopropanol over four steps. The original sample was produced in ethanol. In the top figure, samples were excited at 250 nm and show that the first peak did not change with solvent, but that second peak, which showed solvent dependence in the previous trials, did. In the bottom figure, samples were excited at 308 nm. Here, it is clear that the second peak changed with [each] solvent exchange.

Figure 4-30 shows the fluorescence spectra of four exchange steps of silicon particles between ethanol and water. A deviation for the second fluorescence band from the original spectrum can be seen in Figure 4-30 when the sample was transferred back to ethanol. This may have happened because of bonding between clusters and water molecules when sample transferred to the water, and when sample is left to evaporate, the solvent does not evaporate completely. To eliminate this deviation, we repeated this experiment with another sample such that the cluster was transferred between isopropanol and water; see Figure 4-31. Similar to other solvent exchange experiments, the first peak does not change when nanoparticles are transferred to another solvent, but the second peak changes in proportion to the dipole moment of the solvent, although the chemical interaction between cluster and solvent can also affect this shift. The peak at 420 - 440 nm (which belongs to Si-water samples) arises when clusters are topped up with water and disappears when clusters are returned to IPA. And, the peak at 360 - 380 nm (which is associated with Si-IPA samples) exists in the Si-IPA solution, but not in Si-water. The intensity of the first peak increases after first transferring. We don't know why this happens, but it is observed in several experiments when solvents are exchanged or solvents are mixed together.

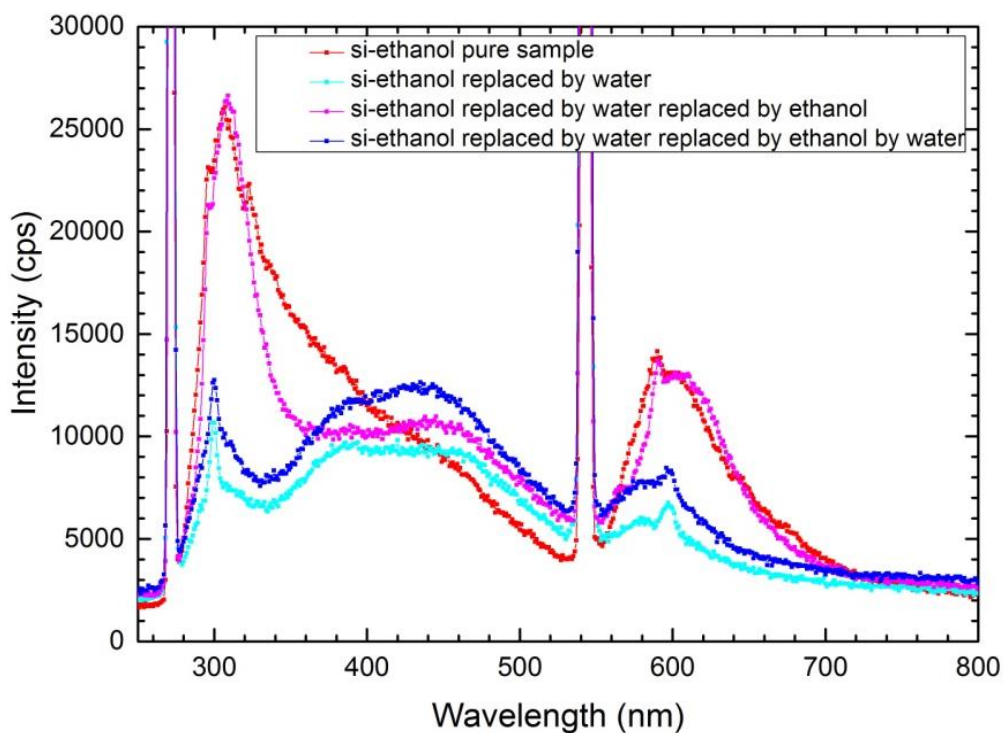


Figure 4-30. Figure showing the result of repeatedly transferring clusters between ethanol and water over four steps.

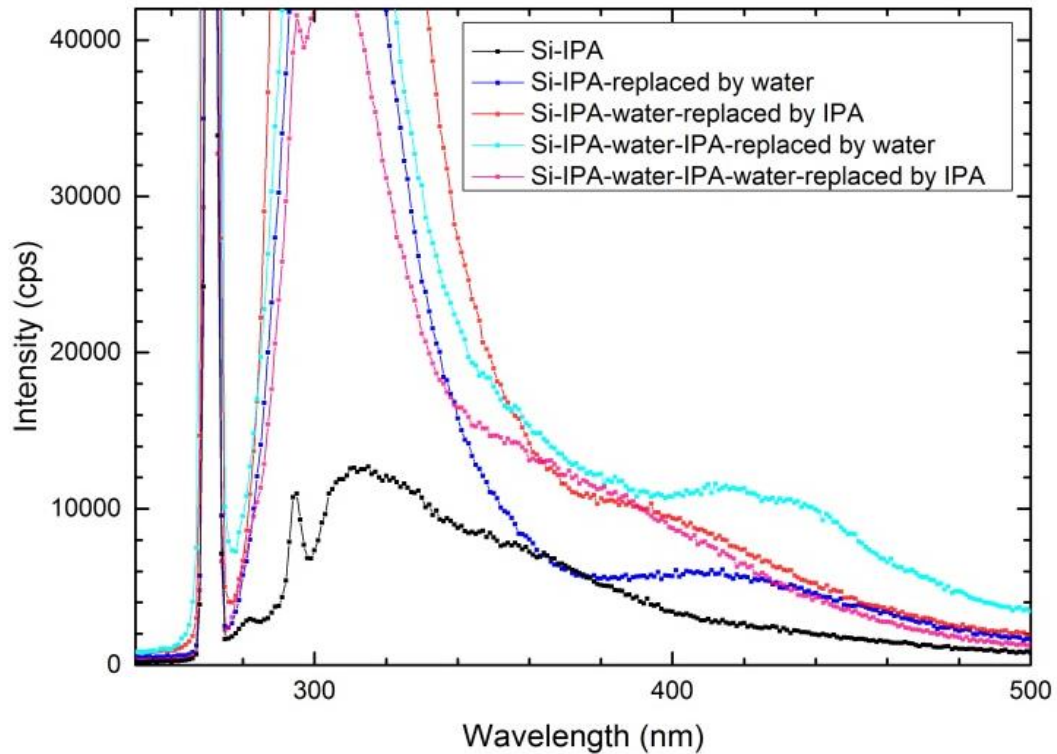


Figure 4-31. Figure showing replacement of IPA with water, and water with IPA, over four steps. Silicon clusters were produced in isopropanol. All spectra show a peak at 310 nm, which we attribute to intrinsic fluorescence of the bulk species in the nanoparticles. A second peak appears at ~370 nm and at ~420 nm, depending on the solvent. By swapping the solvents, the position of the second peak changes. Two spectra which belong to water have a peak at ~420 nm, and three spectra which belong to isopropanol have peak around 370 nm. The results also show that this process is reversible.

The excitation spectra and absorbance of directly deposited sample and transferred sample are compared in Figure 4-32 and Figure 4-33.

The wavelength (energy) of the excitation fluorescence peaks of transferred samples is exactly the same as directly deposited samples (see Figure 4-19).

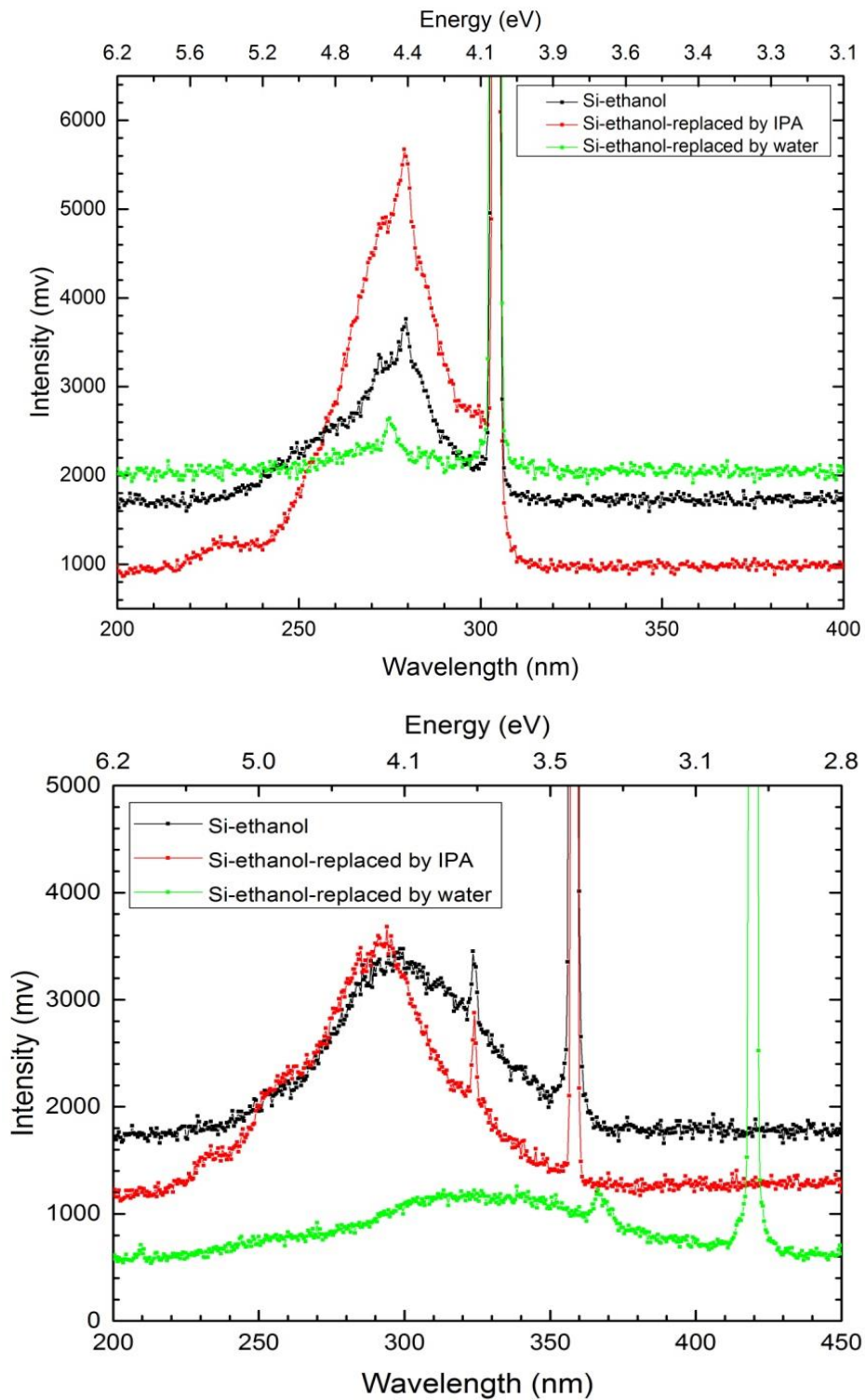


Figure 4-32. Figure showing fluorescence excitation spectra of directly deposited Si-ethanol and silicon particles transferred to IPA and water. The top figure shows fluorescence spectra which belong to the first fluorescence peak ($\lambda_{em} = 310$ nm). Similar to directly deposited samples, it shows the fluorescence of the first peak is not solvent dependent. The bottom figure shows excitation spectra for the second fluorescence peaks ($\lambda_{em(\text{alcohol})} = 360$ nm, $\lambda_{em(\text{water})} = 420$ nm) are solvent dependent, similar to the directly deposited sample.

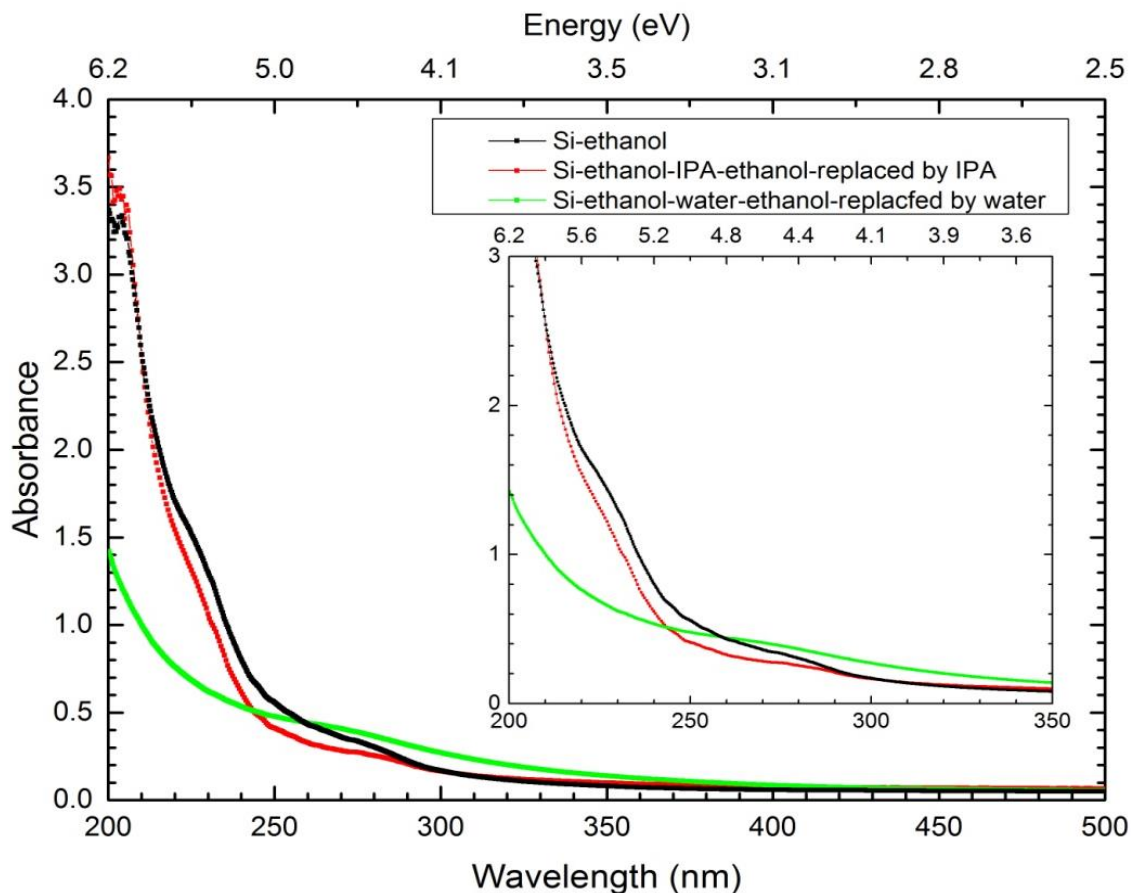


Figure 4-33. Figure showing absorbance of the original sample (Si-ethanol) and the absorbance when nanoparticles were transferred to IPA and water. The results are similar to those for direct deposition samples.

The results confirm that the transitions associated with the second peak are reversible in transfers between solvents and that the first peak is constant in all solvents. Comparison of fluorescence spectra of transferred samples with directly deposited samples for any specific solvent shows solvent transfer is equivalent to deposition onto different solvents, and transferring the sample to the new solvent is the same with the directly deposited sample. Clusters can be produced in any solvent, and depending on the application and required wavelength, they can be transferred without problem to an appropriate solvent.

As the results show, the reversibility of the solvent exchange wavelength shift appears to support a consistent change in silicon oxidation state of the surface of the cluster.

4.8 Quantum yield

The quantum yields of two Si-water samples (samples C9 and C2) were calculated by comparing the fluorescence and absorbance of each sample with stilbene 3 as a reference, using Equation (3.16). Stilbene 3 and both samples have fluorescence maxima at 422 nm. The absorbance peak for the reference and sample C9 is at 345 nm and for sample C2 is at 320 nm. As we excited samples at 308 nm for emission spectra (which is the stilbene 3 excited wavelength), the absorbance at 308 nm was measured to calculate the quantum yield. And, because the reference and sample C9 have the same absorbance wavelength, we recalculate the quantum yield for sample C9 by using the absorbance value at 345 nm for the reference and this sample.

The quantum yield measurement for Si-water sample C2 with fluorescence at 422 nm and absorbance at 308 nm:

$$\Phi_{sample} = \frac{Fl_{C2}/Fl_{ref}}{Abs_{C2}/Abs_{ref}} \left(\frac{n_{C2}}{n_{ref}} \right)^2 \Phi_{ref} = \frac{63088/289234}{0.133807/0.074412} \left(\frac{1.33}{1.36} \right)^2 (0.76) = 0.087 \quad (4.1)$$

The quantum yield measurement for Si-water sample C9 with fluorescence at 422 nm and absorbance at 308 nm:

$$\Phi_{sample} = \frac{Fl_{C9}/Fl_{ref}}{Abs_{C9}/Abs_{ref}} \left(\frac{n_{C9}}{n_{ref}} \right)^2 \Phi_{ref} = \frac{35858/289234}{0.079536/0.074412} \left(\frac{1.33}{1.36} \right)^2 (0.76) = 0.0837 \quad (4.2)$$

The quantum yield measurement for Si-water sample C9 with fluorescence at 422 nm and absorbance at 345 nm:

$$\Phi_{sample} = \frac{Fl_{C9}/Fl_{ref}}{Abs_{C9}/Abs_{ref}} \left(\frac{n_{C9}}{n_{ref}} \right)^2 \Phi_{ref} = \frac{35858/289234}{0.067307/0.078214} \left(\frac{1.33}{1.36} \right)^2 (0.76) = 0.104 \quad (4.3)$$

So the quantum yield for the water sample is between 8% and 10%. The fluorescence intensity is proportional to the quantum yield, i.e., a high quantum yield leads automatically to a high fluorescence intensity.

4.9 Oxidation investigation

As IR and XPS spectra (as discussed in the next chapter) suggest our particles are very reactive in water and can become highly oxidized in water, either in directly deposited samples or when particles are transferred to water. To investigate this hypothesis by fluorescence spectroscopy, we added one drop of pure water to a Si-IPA sample. The sample was measured before and after adding water. The result is shown in Figure 4-34.

The sample which was investigated was Si-IPA, which has two fluorescence bands at 310 nm and 365 nm. The intensity of the first peak is strongly increased by adding only one drop of pure water to the sample for reasons that are properly not understood. In addition, the peak at 440 nm appears which, according to all previous experiments with pure samples, is characteristic of Si-water samples. We will see later that samples that are brought in contact with water show features of oxidation in the IR and XPS spectra. We therefore can attribute this peak at 420 - 440 nm to change in oxidation state, the same as the sample produced in water. So, addition of one drop of water changes oxidation state of the clusters, and generates the new fluorescence states.

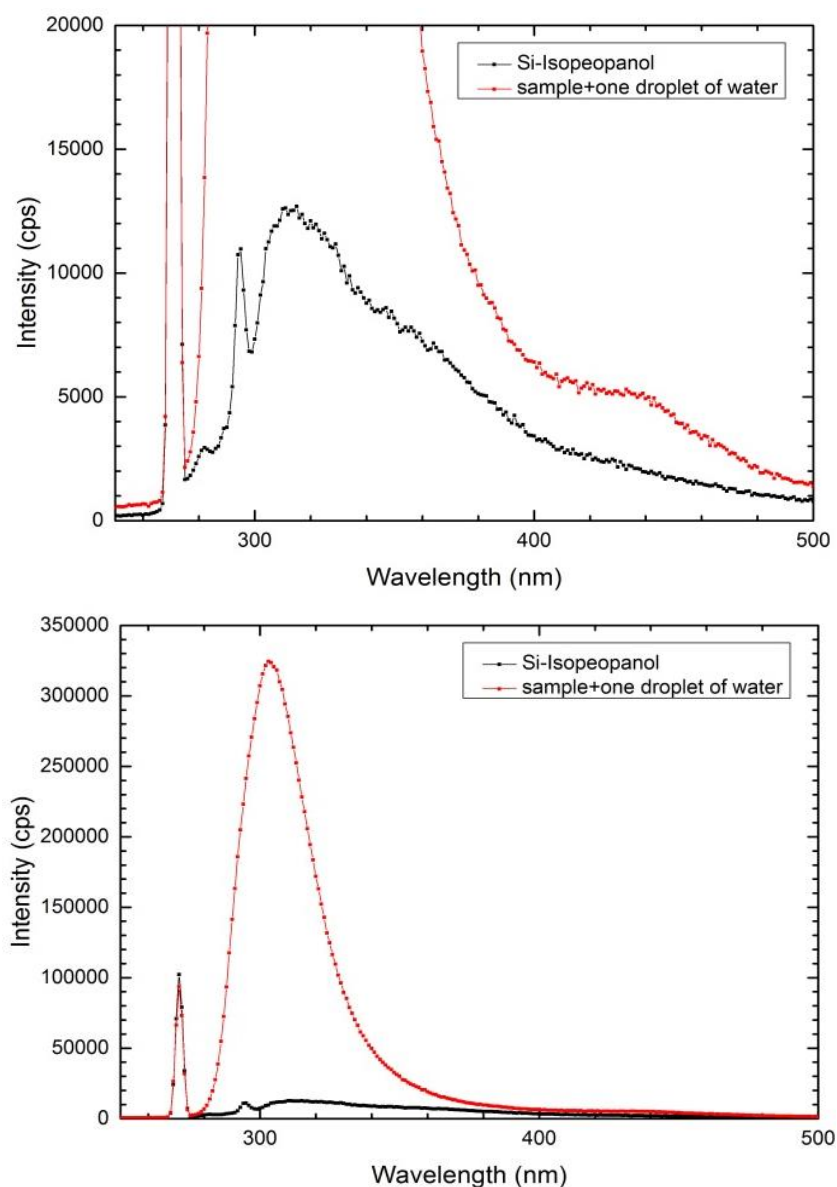


Figure 4-34. Figure showing the changing fluorescence profile of an Si-IPA sample when a drop of pure water was added. As can be seen, by adding only one drop of water, the peak at 440 nm appears and the peak at 360 nm almost vanishes. The sample is excited at 270 nm. The figure in the bottom shows the whole spectrum, while the figure on the top shows an expanded view of the spectrum.

4.10 Time-correlated fluorescence spectroscopy

The samples were measured at the Superlumi end station at beam I, HasyLab, DESY using the time-correlated single photon counting method. Time-correlated fluorescence excitation spectra, decay lifetime and spectrally dispersed fluorescence spectra of clusters in solutions and of cluster films on suprasil substrates were recorded under UHV conditions. The device in DESY had a bad spectral resolution in the fluorescence spectra

compared to the device we used earlier in Leicester. In this investigation we could detect the different components that attended to form the fluorescence and excitation spectra. The components were scattered light, the slow component of fluorescence, and the fast component of fluorescence, and also the device showed the integrated spectra of all these components, as the int component.

Experiments were performed for the film and liquid phases of the samples in three different solvents. Samples were investigated at different emission and excitation wavelengths. In this section, time-correlated fluorescence spectra were plotted for one emission and excitation wavelength for the int, fast and slow components of each sample; other spectra of other emission and excitation wavelengths can be found in appendix 4. The results presented here were detected by a photomultiplier; all samples were also measured by a CCD, the results from which are very similar.

In these experiments we used filters (WG225 and WG280) for each measurement to remove higher orders of the scattered excitation light. Each filter has its specific cut off wavelength. The filter WG280, has a cut off wavelength at 280 nm and removes all the scattered light below 280 nm; WG225 removes light below 225 nm.

We normalized all the excitation spectra, some of which are shown in appendix 4; here, the excitation spectra without normalization (raw spectra) are shown because the peak wavelength did not change after normalization, but distinguishing the peak is difficult when spectra were normalized as the baseline increased due to the detector's wavelength cut off.

4.10.1 Si-ethanol liquid sample

For emission measurements, filter WG280 was used. Experiments were done at room temperature. The sample used was the silicon directly deposited in ethanol (sample B5) in the liquid phase. An excitation measurement at 310 nm was performed at room temperature and by using filter WG280. The fluorescence emission and excitation spectra are shown in Figure 4-35.

The emission spectrum shows a peak at 304 nm, which is very close to the wavelength of the first fluorescence peak in the emission spectra [recorded in our lab]. The int component shows a shoulder around 350 – 360 nm, which coincides with the

second peak position. Excitation spectra also show two peaks: the first is a broad band centered at 210 nm, and a second at 275 nm. The excitation spectra are typical rather for molecular structures than band gap systems. The energy matches with the prediction in reference [18] and is presumably due to the vertical excitation of Si-OH, although this is just a hypothesis. The band at 275 nm was observed in our previous measurement as well, but due to the range of fluorometer we could not detect the band at 210 nm.

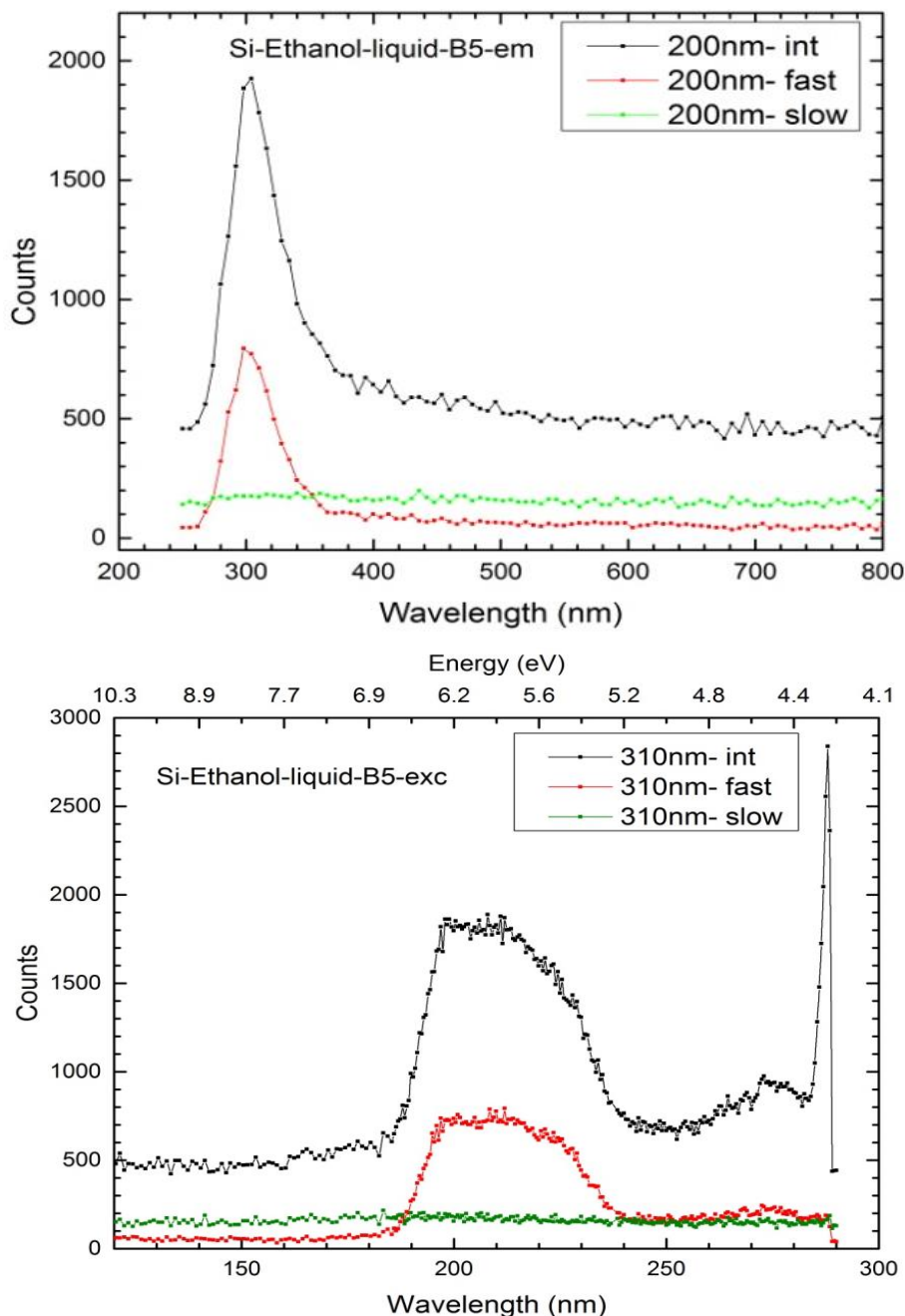


Figure 4-35. Figure showing emission (top) and excitation (bottom) spectra with int, fast and slow components for Si-ethanol in the liquid phase. The fluorescence peak is at 308 nm. The excitation spectra were cut off at 190 nm due to suprasil's cut-off wavelength.

4.10.2 Si-ethanol film sample

The same sample that was investigated in the liquid phase (sample B5) was used to form as a film for further investigation, the results of which are shown in Figure 4-36. Filter WG225 was used for excitation and emission measurements. The experiments were performed at room temperature.

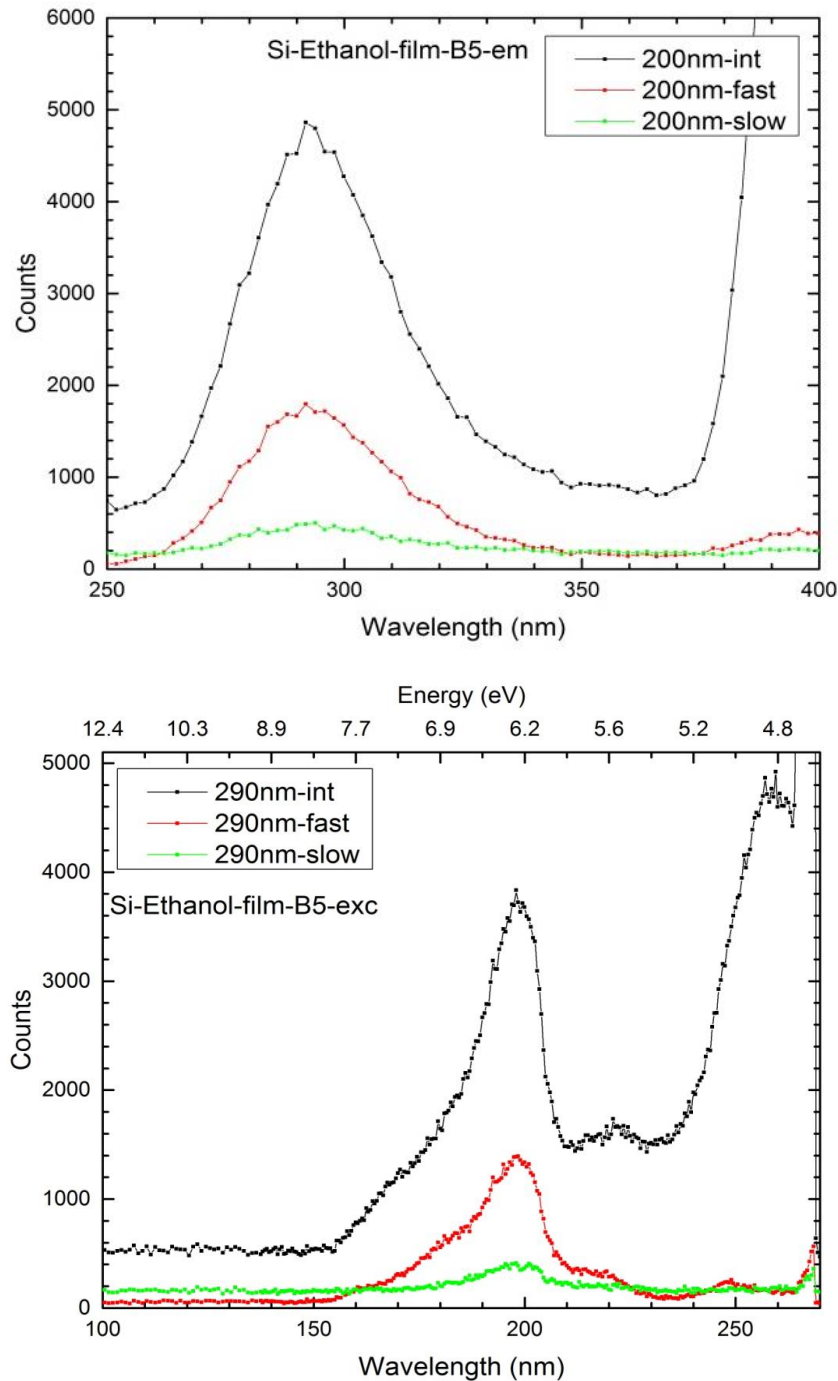


Figure 4-36. Figure showing emission (top) and excitation (bottom) spectra with int, fast and slow components for Si-ethanol in the liquid phase.

The sample shows a fluorescence peak at 294 nm. The second fluorescence peak cannot be detected in the emission spectra because the intensity of scattered light at 400 nm is too high, and was not removed properly by the filter. The film sample shows the first fluorescence peak at very close, but slightly shorter, wavelength than the liquid sample measured previously. An excitation peak was observed at 198 nm. It has a shoulder to shorter wavelength. There are two other excitation peaks at 220 nm and at around 250 - 260 nm.

We investigated another sample in the film phase at room temperature (sample B6), the results of which are shown in Figure 4-37. For emission spectra, filter WG225 was used. The excitation spectra of the sample were also measured, for which filter WG280 was used.

The emission spectrum has the same first peak as the liquid samples at 294 nm, but the second peak shifts to the longer wavelength in comparison to the liquid sample recorded previously. The fluorescence spectra of film samples show two components. The fast component has a peak at 415 nm, and is similar to the spectrum of clusters in water in that it shows a red shift with respect to the Si-ethanol liquid sample. The slow component, peaking at 450 nm, is comparatively weak (it can be seen if this region is expanded vertically by a factor of 10). The spectrum of the slow component of the fluorescence matches perfectly with the spin-forbidden $T_1 \rightarrow S_0$ fluorescence from oxygen deficient defects in amorphous silica [275]. The excitation spectrum shows its peak at 203 nm with a shoulder at 228 nm, which is the same as was found previously. It also shows a second excitation peak at 295 nm, which is the same band as for Si-ethanol liquid measured in Leicester (in our lab).

The first excitation peak for the liquid and film samples is almost identical, and occurs around 200 nm; this suggests the origin of first fluorescence peak of the film and liquid samples is the same and thus comes from the same excited state (electronic transition). The wavelength of the first fluorescence peak in both the liquid and film samples is the same, and observed in both at around 300 nm. As in our model this fluorescence peak is intrinsic, and is attributed to the bulk cluster, so evaporating the solvent should not affect this peak. The results confirm our hypothesis.

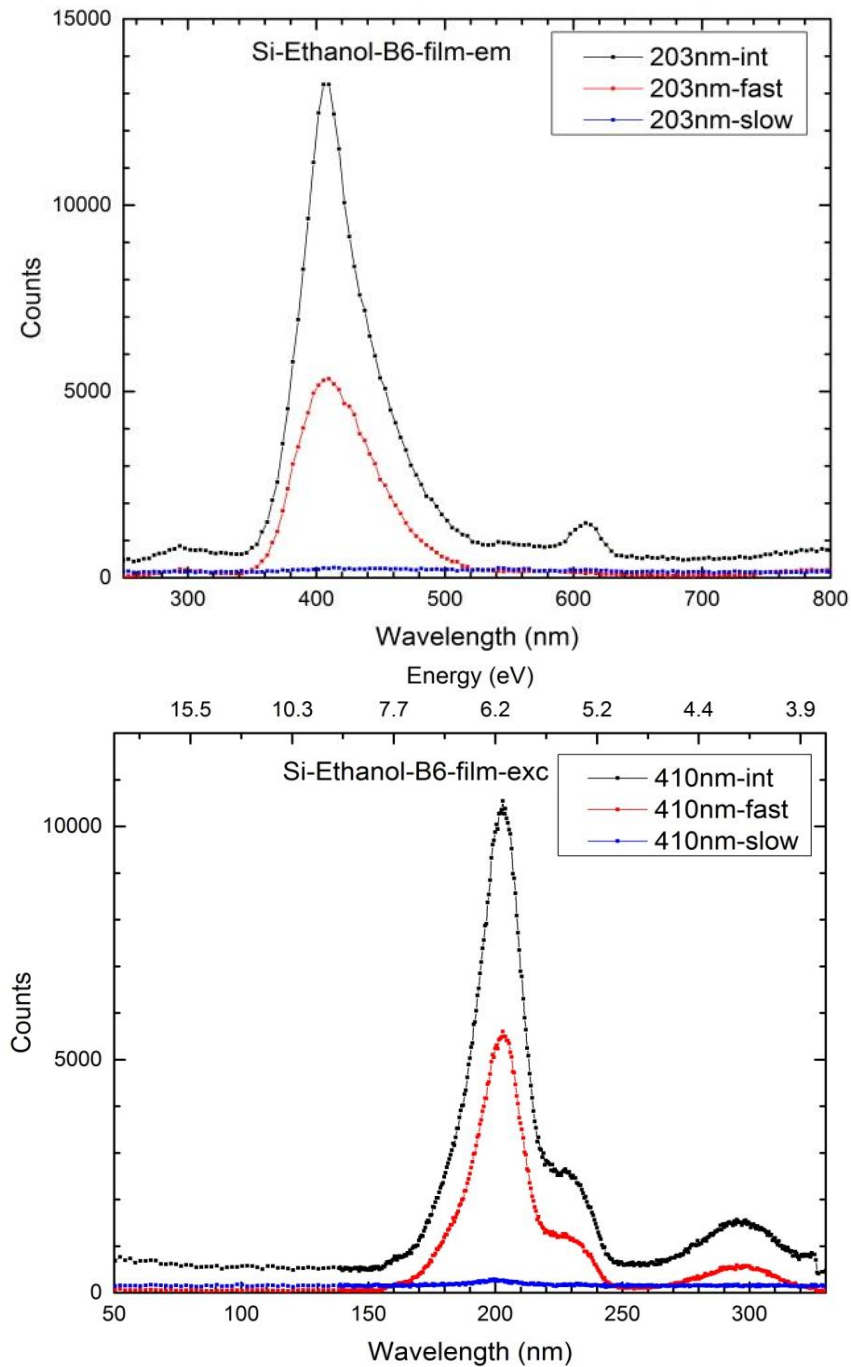


Figure 4-37. Figure showing emission (top) and excitation (bottom) spectra with int, fast and slow components for a Si-ethanol film sample. Fluorescence peaks are at 294 nm and 415 nm. The excitation spectrum shows peaks at 203 nm, 228 nm and 295 nm.

4.10.3 Si-IPA liquid sample

The emission and excitation fluorescence measurements of the Si-IPA liquid sample (sample A1) were performed at room temperature, and are shown in Figure 4-38. Filter WG225 was used for emission measurement and filter WG280 was used for excitation measurement.

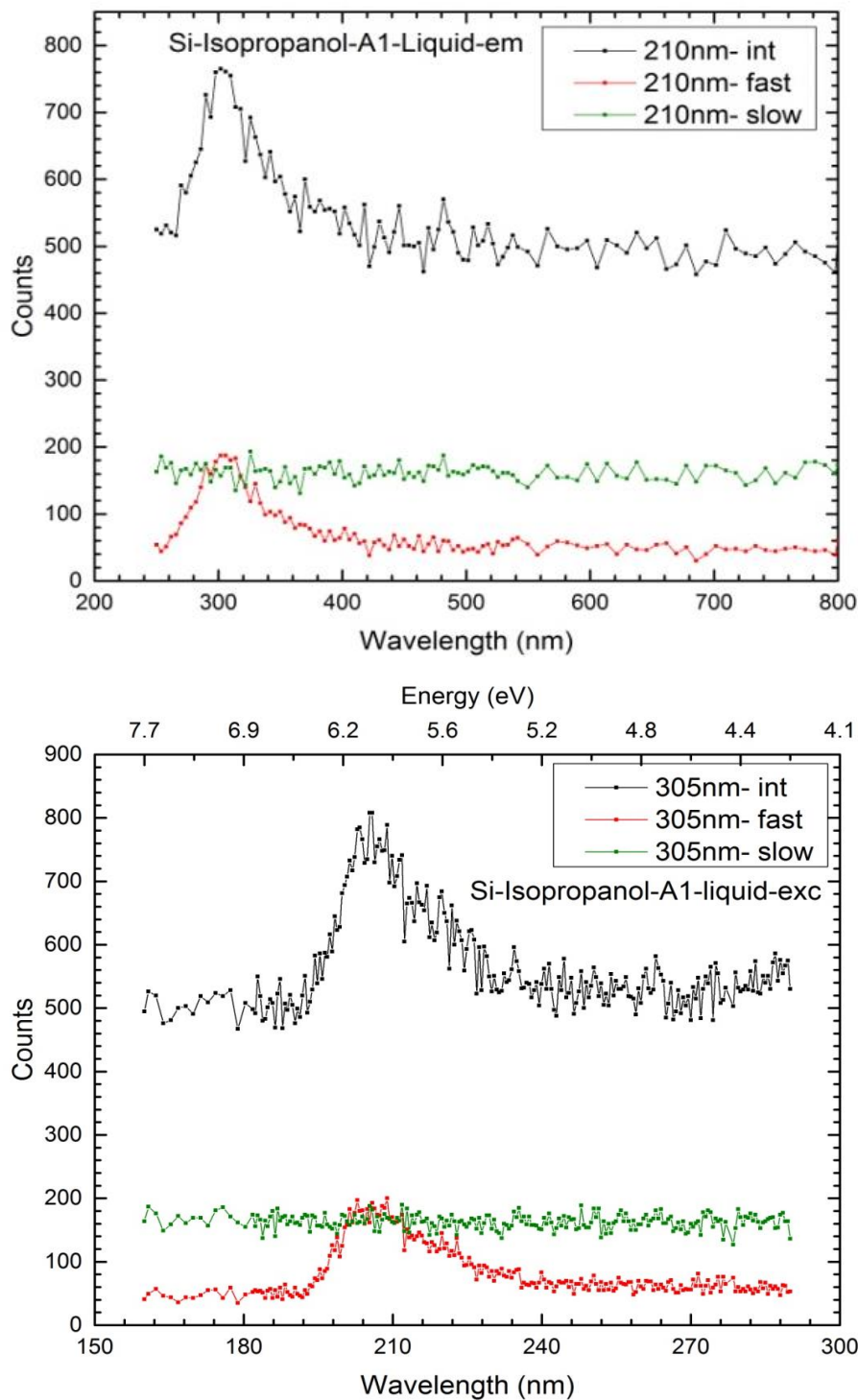


Figure 4-38. Figure showing emission (top) and excitation (bottom) spectra with int, fast and slow components for Si-IPA in the liquid phase. The fluorescence peak is at 306 nm. The excitation spectrum shows a peak at 206 nm.

Similar to all other samples, this sample's spectra show a fluorescence emission peak at 306 nm and a fluorescence excitation peak at 206 nm with a shoulder at 217 nm, but do not show any peaks at longer wavelength.

4.10.4 Si-IPA film sample

Experiments on Si-IPA film (sample C4) were performed at room temperature, and filter WG280 was used for emission and excitation measurements. The results are shown in Figure 4-39.

In emission spectra, the first fluorescence peak is the same as all other samples (at 300 nm) and the second peak's wavelength is almost the same wavelength as for the Si-ethanol film sample. The second peak at 412 nm shows a red shift with respect to the Si-IPA liquid sample [measured in our lab], which shows second peak at 365 nm. This may happen because of oxidation. Silicon clusters at the surface have bonds with solvent molecules; when the solvent evaporates, the bonds between clusters and solvent are broken, exposing the sample to atmosphere and thus causing oxidation (although a surface layer of solvent will not necessarily all evaporate, especially for water). Therefore, the peak wavelength observed here is the same as the peak wavelength observed for the Si-water samples, which has higher level of oxidation with respect to the alcoholic samples. There is another band at 585 nm which may be the second order of the first fluorescence peak.

Excitation spectra show five bands at 100 nm, 115 nm, 145 nm, 200 nm and 294 nm. The band at 200 nm was always observed. This may be the second harmonic of the band at 100 nm. As the intensity is very high for this sample, those peaks between 100 nm to 200 nm could be detected. We did not observe the peaks with wavelengths shorter than 200 nm for liquid samples due to suprasil's cut off wavelength. The peak at ~294 nm was observed in the Si-IPA liquid sample measured in our lab in Leicester.

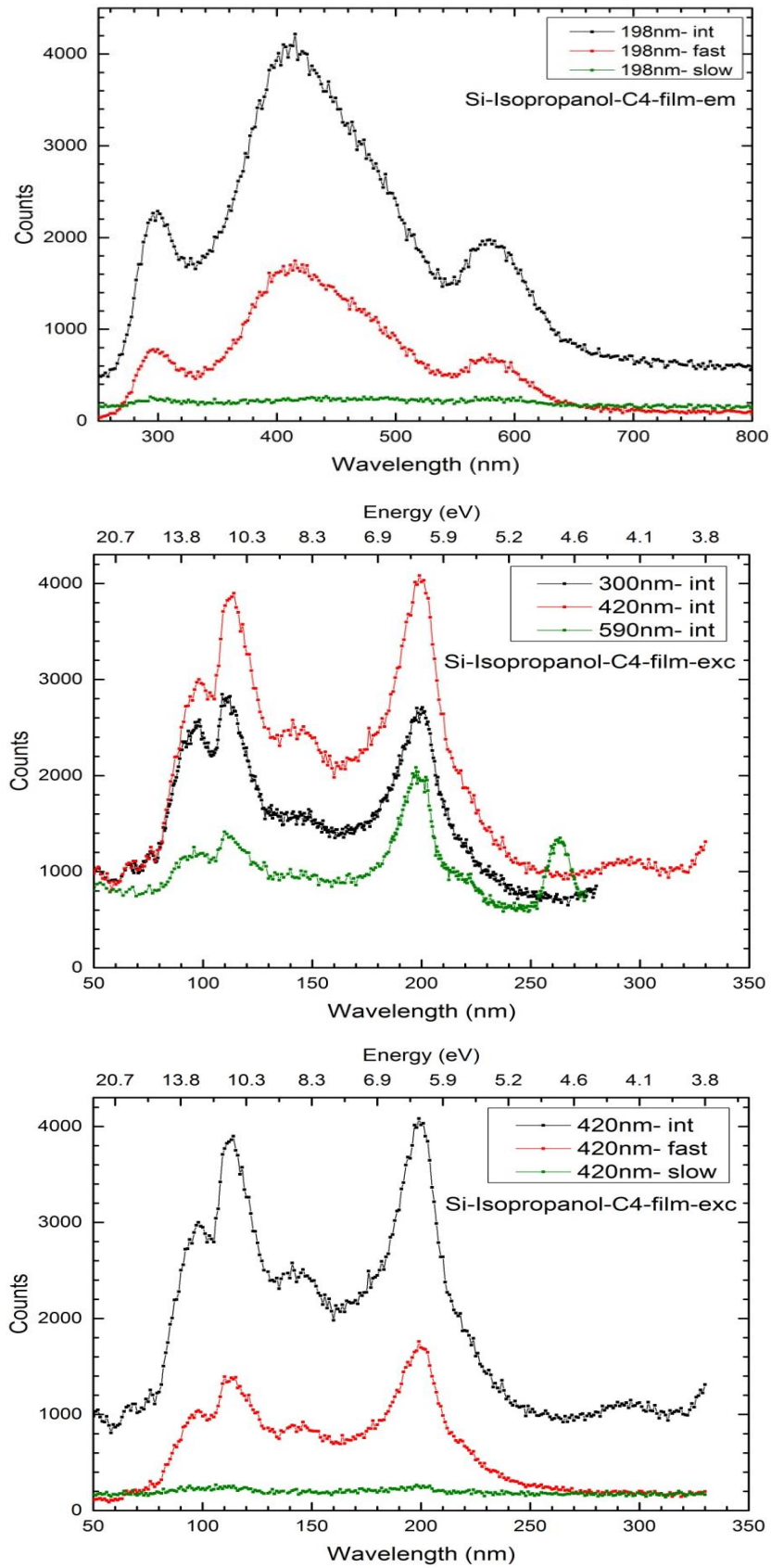


Figure 4-39. Figure showing emission (top) and excitation (bottom) spectra with int, fast and slow components for Si-IPA film. The fluorescence emission spectrum has three peaks at 300 nm, 412 nm and 585 nm. The excitation spectrum shows several peaks peak at 100 nm, 115 nm, 145 nm, 200 nm and 294 nm.

4.10.5 Si-water liquid sample

Silicon directly deposited in water (sample D8) was investigated in the liquid phase and at room temperature, using filter WG280 for both emission and excitation spectra. Fluorescence emission spectra show peaks at 320 nm and 422 nm, which is the same as the fluorescence peaks observed for the Si-water liquid sample previously. The first fluorescence peak at 320 nm is slightly red-shifted with respect to other samples first fluorescence peak, and also the Si-water sample first fluorescence peak, as measured in our lab. The fluorescence excitation spectra have peaks at 195 nm (similar to all bands observed using this method), 224 nm and 284 nm when emitted at 320 nm and have peaks at 207 nm (with a shoulder at 195 nm) and 303 nm when emitted at 422 nm.

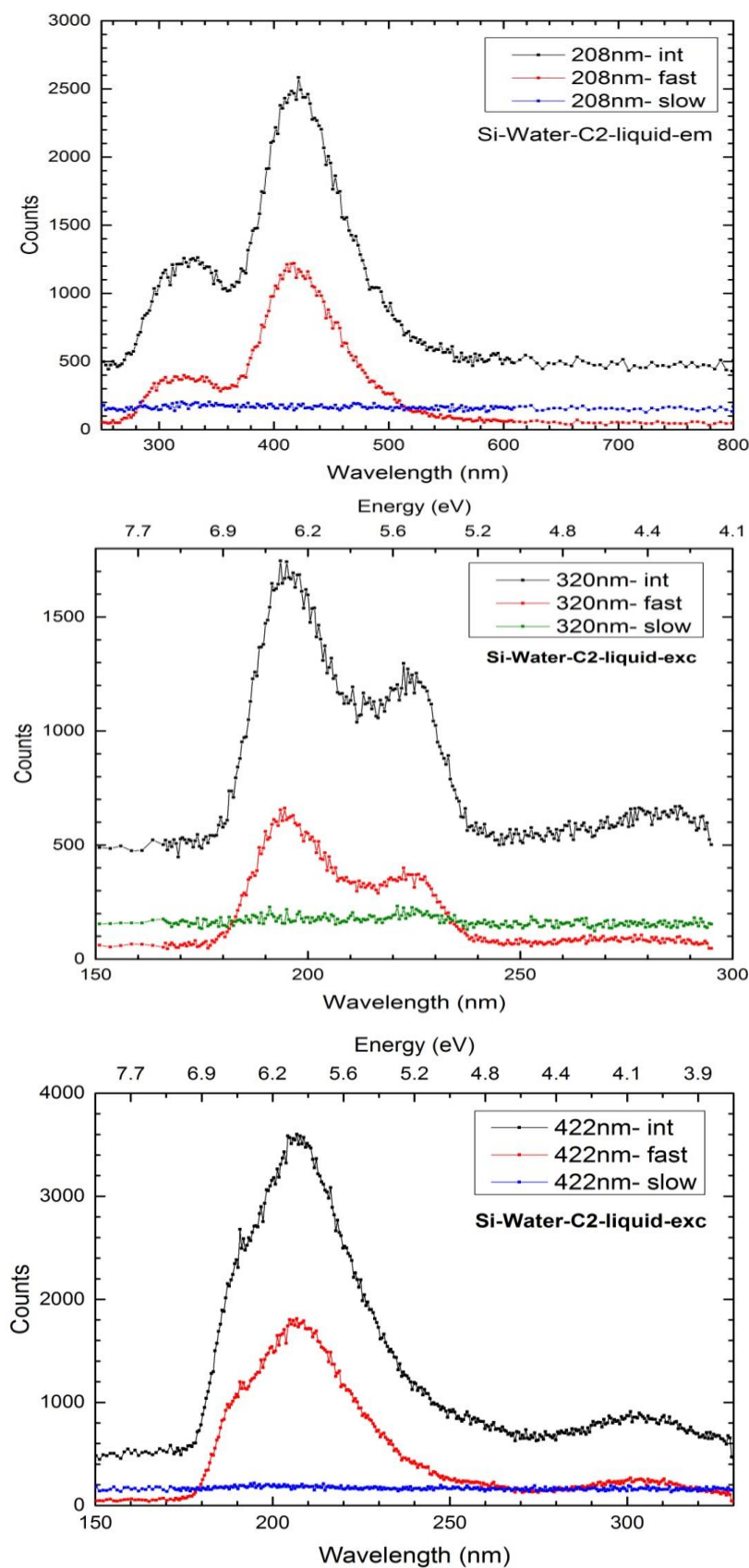


Figure 4-40. Figure showing emission (top) and excitation (bottom) spectra with int, fast and slow components for Si-water in liquid phase. Fluorescence emission peaks are observed at 320 nm and 422 nm. The excitation spectra shows peaks at 195 nm, 207 nm, 224 nm, 284 nm, and 303 nm.

4.10.6 Si-water film sample

A Si-water film (sample D8) was investigated at room temperature, with filters WG225 and WG280 used for recording emission and excitation spectra, respectively. The results are shown in Figure 4-41. Fluorescence emission spectra show peaks at 308 nm, 440 nm (the same band as the fluorescence peaks observed for the Si-water liquid sample using this method in our lab), and another band at 570 nm (the same band as was observed in Si-IPA film in Figure 4-39). The fluorescence excitation spectra have peaks at 190 nm, similar to all bands we observed using this method, and probably another band around 300 nm.

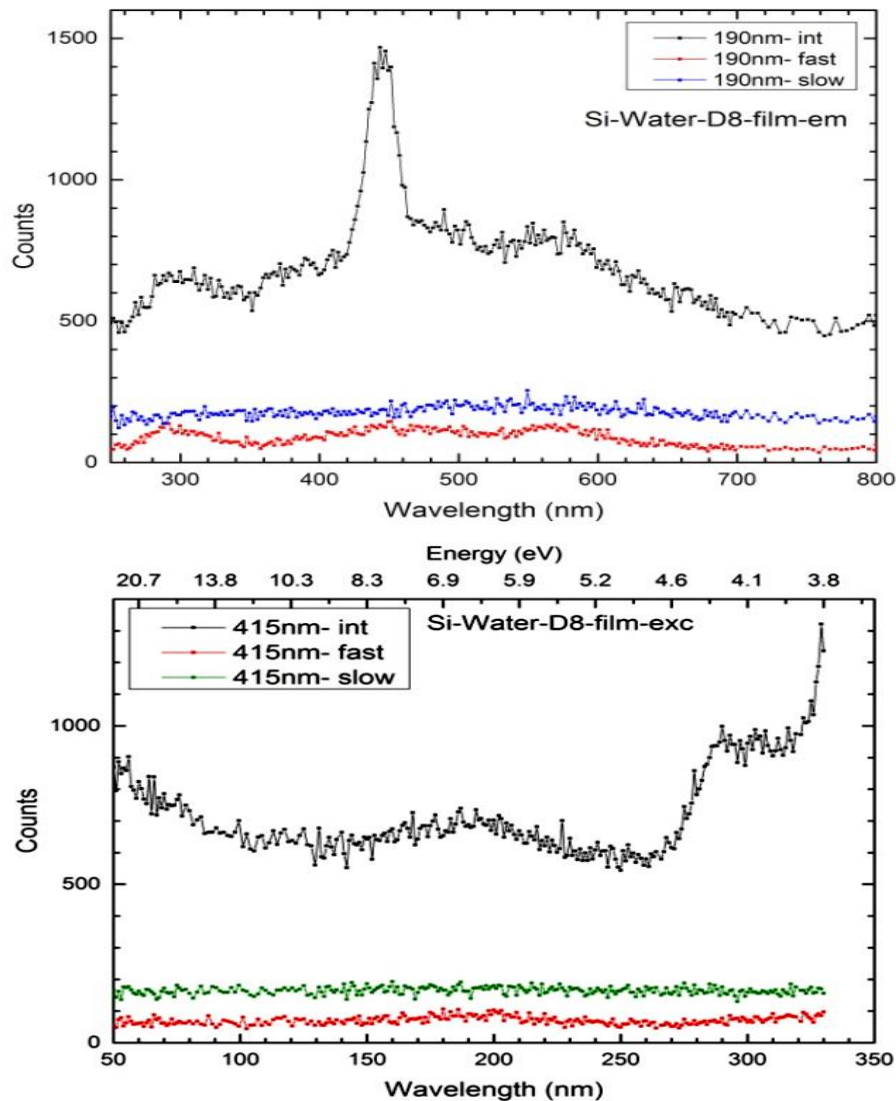


Figure 4-41. Figure showing emission (top) and excitation (bottom) spectra with int, fast and slow components for Si-water film sample. Fluorescence peaks are observed at 308 nm, 440 nm and 570 nm. The excitation spectrum shows peaks at 190 nm and around 300 nm.

The wavelength of emission and excitation of the first peak (~300 nm) is similar for all samples, either in film or liquid phase or in any solvent, suggesting that the electronic state involved and the underlying structure is identical. A possible explanation is that the fluorescent site is localised in the bulk region of the clusters, because it doesn't change during drying and it has no solvent dependence; however, as we explain later, they do show different lifetimes and the same fluorescence emission band might be purely coincidental. The second peaks observed in all film samples appear around 420 - 440 nm, and comes from the surface cluster; these cluster atoms interact with the solvent molecules, so when the solvent evaporates, all these samples (which are produced in different solvents) are identical; they then oxidise in air in a similar manner, so water and alcoholic solvents show the same fluorescence wavelength. This peak belongs to oxidised silicon at the surface of the nanoclusters, the same as was observed for the Si-water liquid sample.

The second fluorescence peak for Si-ethanol and Si-IPA in the liquid phase (measured in Desy) cannot be seen because of the broad first fluorescence peak, superposition with scattered light, or the intensity is just very low. In the case of weak intensity for the second bands in alcoholic samples, this can be seen as proof for oxidation of the alcoholic film samples. In alcoholic liquid samples, the intensity of the first peak (which is attributed to the bulk cluster) is higher than second peak (which is attributed to surface clusters), so when the solvent evaporates, the intensity of the second peak becomes higher than the first peak, similar to water samples (in film and liquid phases). This also confirms oxidation of alcoholic film samples. Si-IPA film and Si-water film samples show a third peak around 570 - 590 nm.

Fluorescence of the alcoholic films has higher intensity than observed for alcoholic liquid samples; since silicon oxide species are the reason for high fluorescence intensity in all samples, it confirms that a silicon-oxygen bond is formed when the sample is exposed to the air, as the Si-water liquid sample – which is a highly oxidised sample – has the highest fluorescence intensity amongst the liquid samples. However, we need to consider that measurements were out of focus for liquid measurements, so it might affect on the fluorescence intensity of liquid samples.

The short-lived fluorescence of the films is similar to the liquid water samples, which might be because of increased exposure to air; samples might be more highly oxidized, or this might be coincidental. We attribute these bands to silicon-oxygen bonds

or Si-OH groups at the surface of the nanoclusters which are hydrogen-bonded to residual water molecules, or to OH groups of neighbouring clusters.

For film samples, several peaks exist in shorter wavelengths, though it is not possible to see these in liquid samples because of suprasil's cut-off wavelength.

4.11 Dependence of fluorescence on temperature

To investigate the effect of temperature on fluorescence, we cooled the sample to 8 K. The sample used was a Si-ethanol film (sample B6) measured at 8 K, 28 K and 300 K. For all spectra, filter WG280 was used except for the spectrum which is measured at room temperature and excited at 203 nm, for which filter WG225 was used. The measurements were performed for several wavelengths and for different fluorescence components. In this section, the integrated components of fluorescence emission spectra excited at 203 nm at three different temperatures are illustrated in Figure 4-42; other spectra can be found in appendix 4. The temperature dependence of fluorescence intensity for this sample for the int, fast, and slow components are plotted in Figure 4-43.

Similar to the observation of reference [276], the intensity of photoluminescence depends on temperature; it decreases with increasing the temperature. As we expected, at low temperature the sample has higher intensity.

As Figure 4-43 shows, the intensity of the fluorescence peak decreases with increasing the temperature in an exponential way for all components. Increasing the temperature causes an increasing amplitude of vibration, and transfers energy to non-radiative decay in the sample. So, increasing the temperature induces a decrease in fluorescence intensity.

Changing the temperature can affect not only the fluorescence intensity but also the fluorescence bandwidth. However, this is dependent on the environment and the fluorophore itself. As can be seen in Figure 4-42, in our sample, the FWHM of spectral features does not change significantly as temperature is increased.

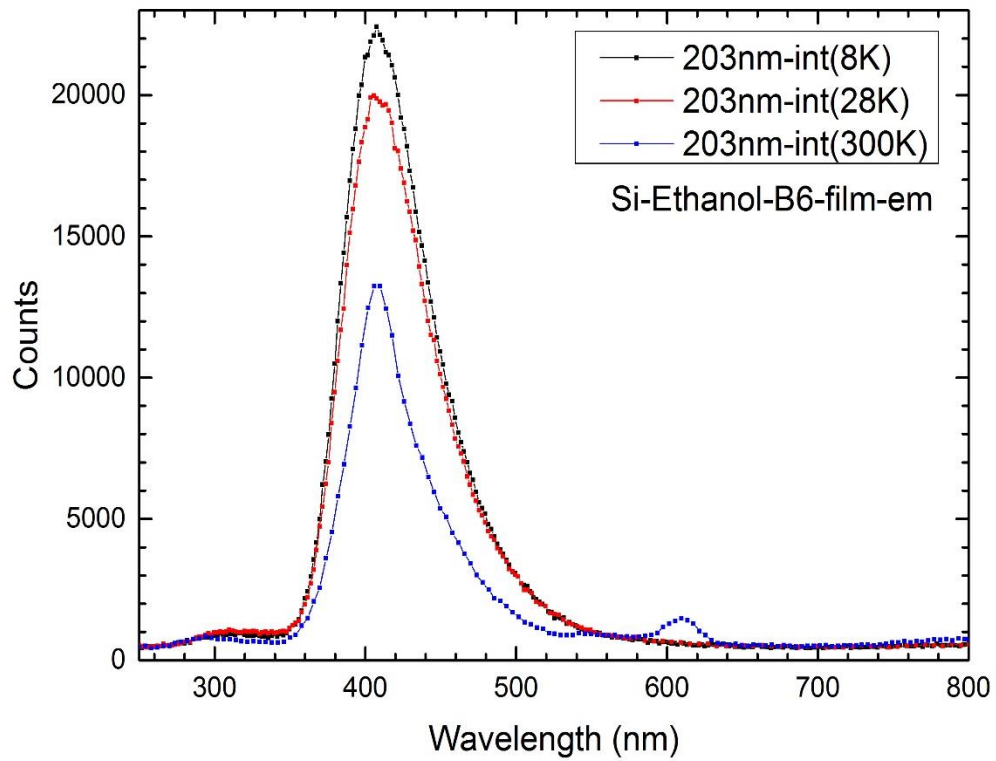


Figure 4-42. Figure showing the effect of changing temperature on fluorescence intensity. By cooling the sample, fluorescence intensity is increased.

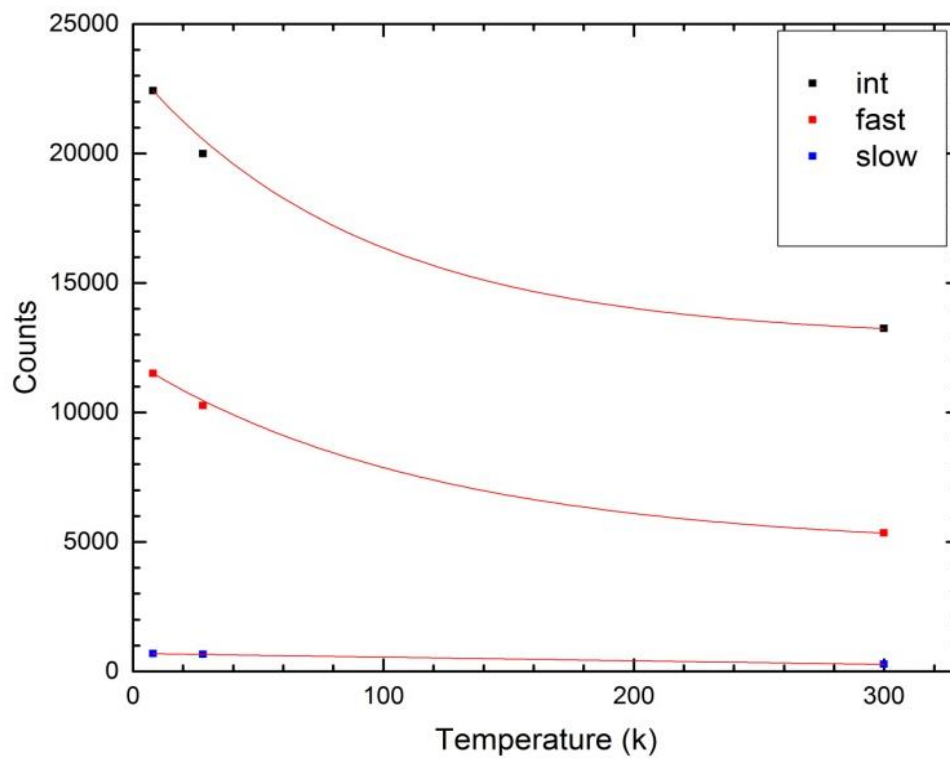


Figure 4-43. Figure showing the dependence of intensity on temperature for three different components of int, fast, and slow measurements.

4.12 Life time measurements

The fluorescence lifetime is the time spent by a molecule in its excited state, fluorescence occurs approximately, on the nanosecond timescale; while absorption occurs in around 10^{-15} s. Fluorescence lifetime measurement results are shown in Figure 4-44 to Figure 4-49.

4.12.1 Dependence of fluorescence lifetime on solvent

Fluorescence lifetime measurements for silicon clusters formed in three different solvents were performed to investigate the effect of environment on lifetime. Measurements were performed in the liquid phase and on film, the results of which are shown in Figure 4-44 (liquid samples) and Figure 4-46 (film samples). All lifetimes are in the range of a few nanoseconds and are formally allowed transitions.

As can be seen in Figure 4-44, for liquid samples the decay times correlate with the short wavelength peak (first fluorescence peak) in the fluorescence spectra, because it excited around 200 nm and emitted around 300 nm. Fluorescence lifetimes of liquid samples are in the range of a few nanoseconds. The Si-water sample shows a shorter lifetime compared with alcoholic samples. It suggests different structures for the fluorescent site of the first fluorescence band (at ~310 nm) for different solvents, so the first fluorescence band wavelength might be the same for all samples purely by coincidence, and clusters in the 'bulk' may have interactions with the solvent as their lifetimes show solvent dependency, or they may not even be in the 'bulk'. If these fluorescent sites have an interaction with solvent, the shorter lifetime of Si-water can be attributed to the stronger hydrogen bond of the water sample than alcoholic samples.

The lifetime of the second fluorescence band of the Si-water sample was recorded and the result was compared with the lifetime of first fluorescence band of this sample; spectra are shown in Figure 4-45. The lifetime of the second fluorescence peak of Si-water sample was measured as 3.95 ns, which is very close to the lifetime of the first fluorescence band of this sample. As the Si-ethanol and Si-IPA did not show the second fluorescence band in time-correlated fluorescence measurements, we could not measure the lifetime of the second band of these samples.

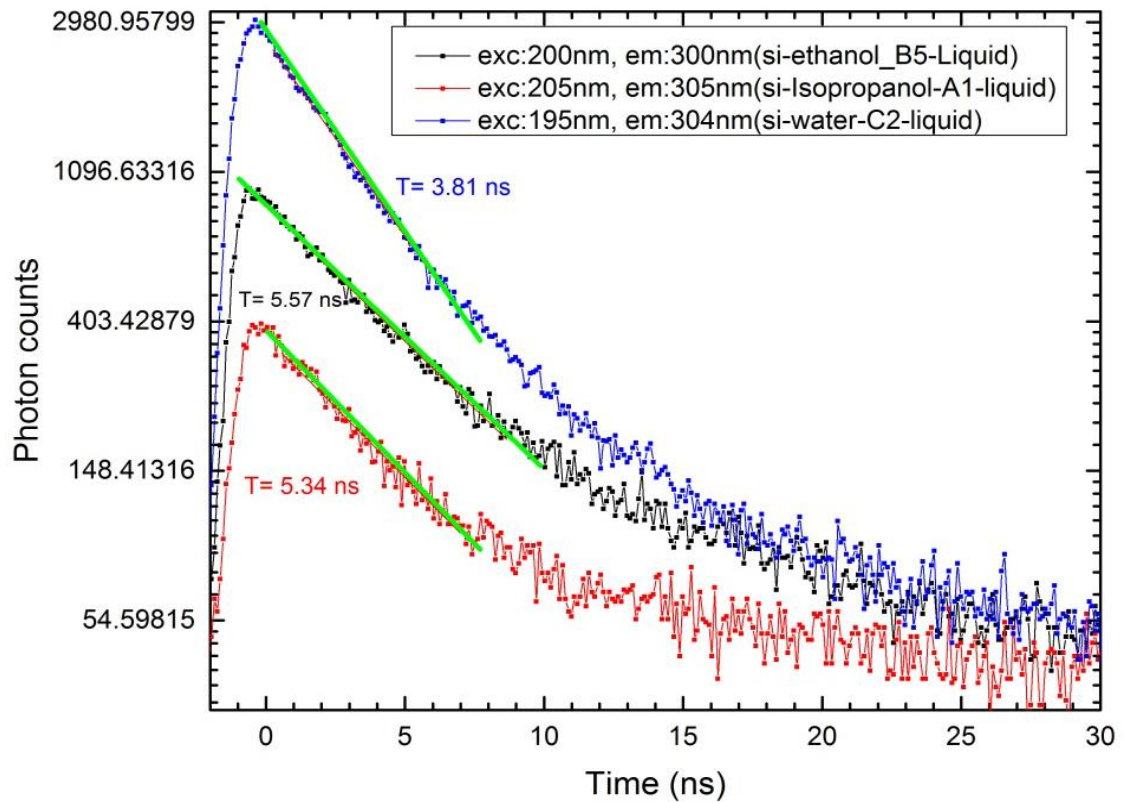


Figure 4-44. Figure showing the results of lifetime measurements for Si-water, Si-ethanol and Si-IPA. Measurements were done in the liquid phase. The figure has been plotted on a logarithmic scale.

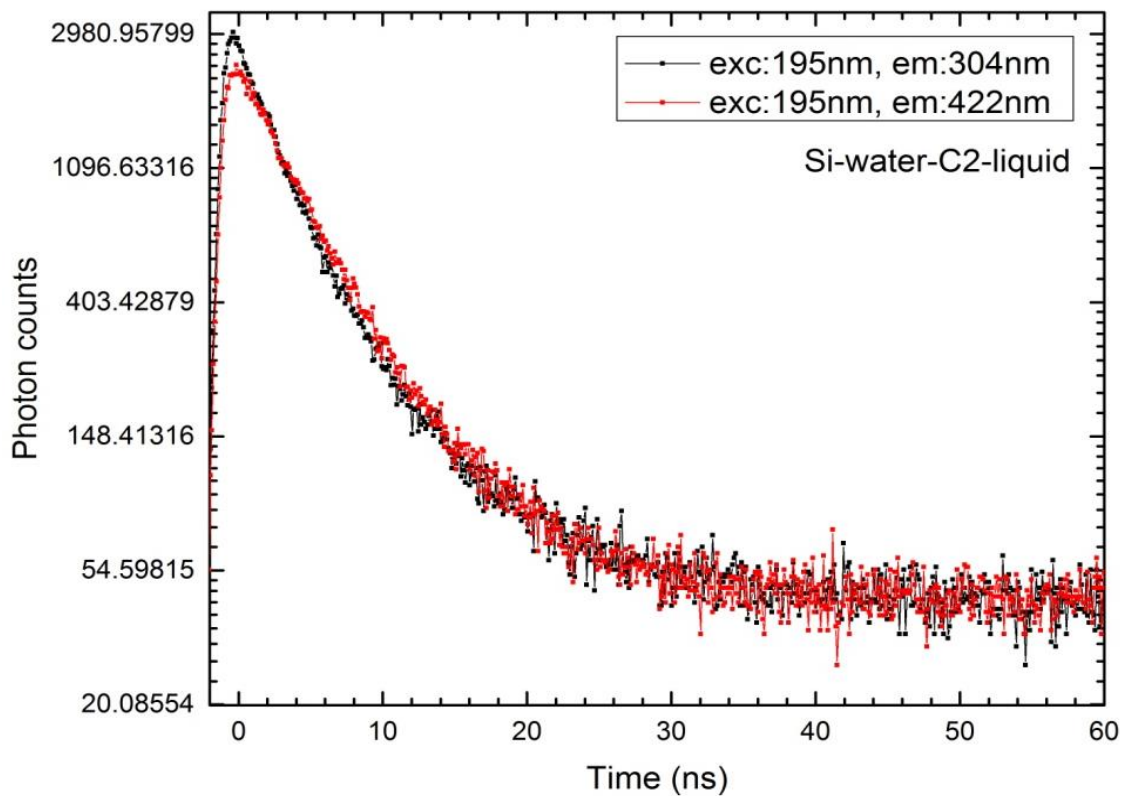


Figure 4-45. Comparison of first and second fluorescence peaks lifetime of Si-water.

Figure 4-46 shows the result of fluorescence lifetime measurements for film samples produced in different solvents for the first and second fluorescence bands.

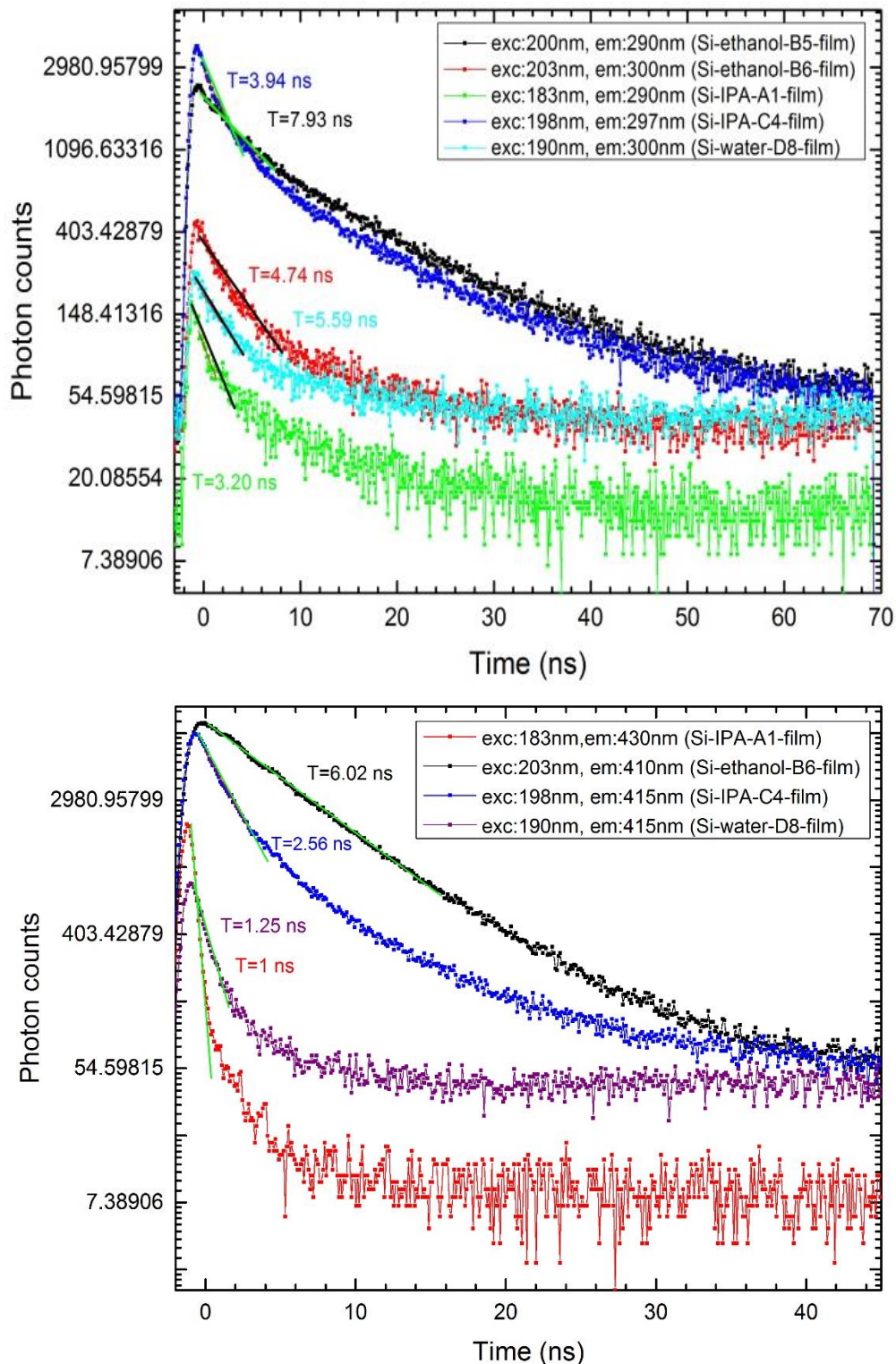


Figure 4-46. Figure showing the results of fluorescence lifetime measurements for the first (top) and second (bottom) fluorescence peaks for Si-water, Si-ethanol and Si-IPA film samples.

As the solvent was evaporated in film samples, solvent effects are not valid any longer, and the results show the decay time of film samples to be in the range of a few nanoseconds, and further that this decay time does not depend on the solvent that the clusters were produced in.

As can be seen in decay curves of the film samples, structure of clusters changed during the drying and making of the film sample, and film samples show multiexponential decay curves (more decay channel than liquid samples), whilst liquid samples show monoexponential curves, suggesting new fluorescent structures for film samples.

4.12.2 Dependence of fluorescence lifetime on emission and excitation wavelength

According to the quantum confinement model, lifetime decreases as emission wavelength is decreased, and is expected to decrease as the excitation energy is increased [277]. Figure 4-47 shows the dependence of lifetime on excitation wavelengths for the Si-ethanol film sample (B6); this experiment was also performed for other samples in different solvents, the results for which can be found in appendix 4. For measuring sample B6, filter WG225 was used for emission at 300 nm and filter WG280 was used for emission at 410 nm.

As can be seen in Figure 4-47, for a constant emission (300 nm or 410 nm), lifetime decreases as excitation wavelength is increased from 203 nm to 290 nm. Lifetime dependency to excitation wavelengths were measured for the first and second fluorescence peaks to confirm this trend.

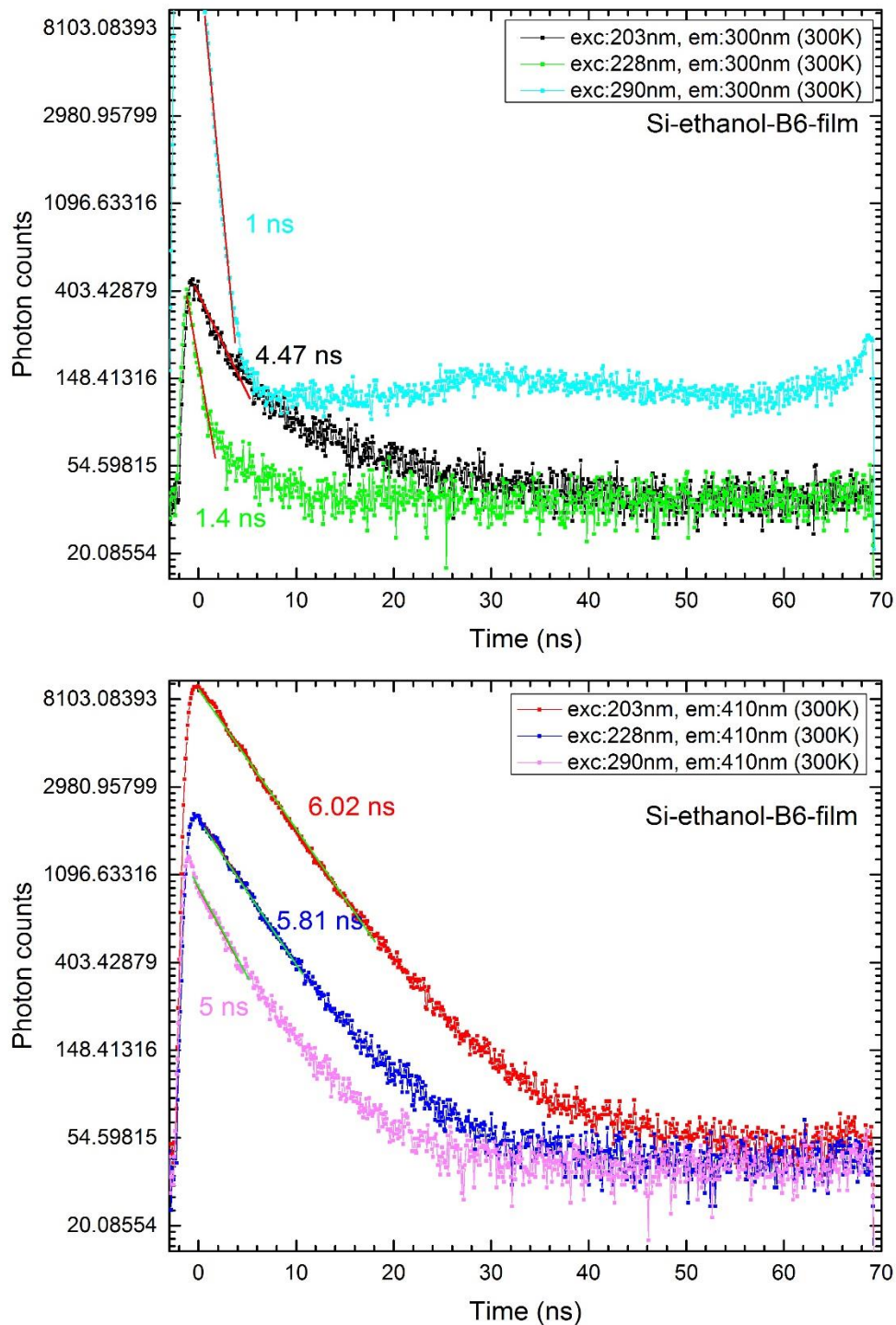


Figure 4-47. Figure showing lifetime dependence on excitation wavelengths. A Si-ethanol film sample was measured at three different excitation wavelengths (203 nm, 228 nm and 290 nm) for each fluorescence peak wavelength; lifetime measurements were performed for two emission wavelengths (300 nm and 410 nm).

4.12.3 Comparison of fluorescence lifetimes of liquid and film samples

In Figure 4-48, the result of a comparison of fluorescence lifetime of film and liquid silicon clusters produced in ethanol is shown.

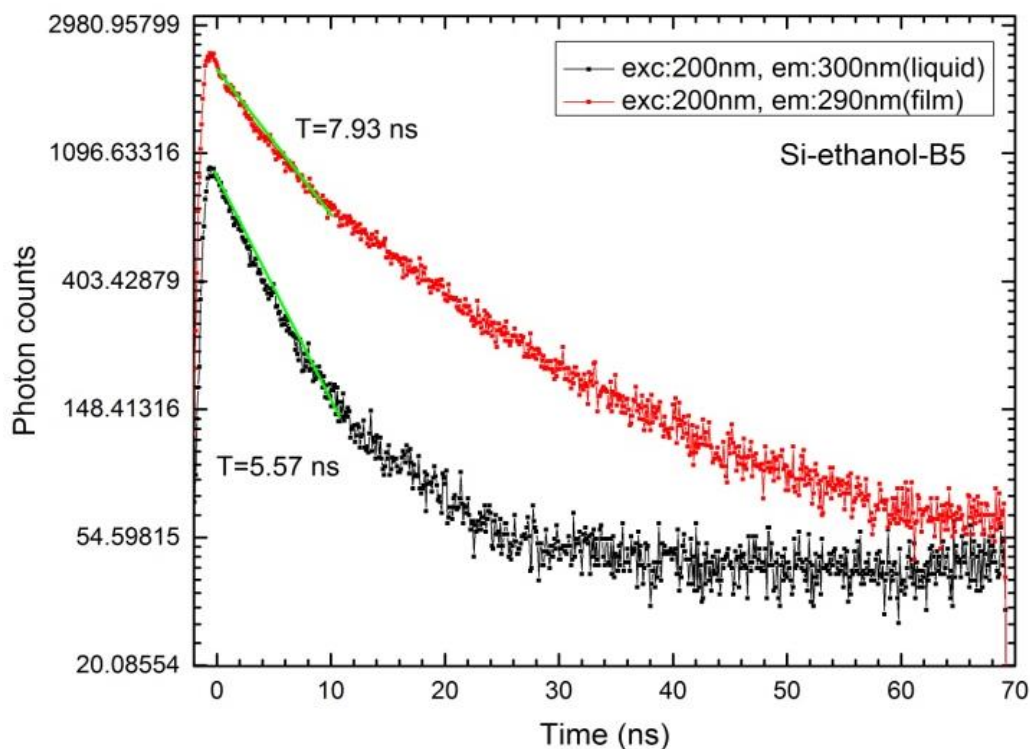


Figure 4-48. Comparison between fluorescence lifetime of Si-ethanol film and liquid samples.

The results show liquid samples have shorter decay lifetimes than film samples. As the Stern-Volmer plot in Figure 4-26 showed, the fluorescence of the Si-ethanol sample was quenched in the liquid phase, so by evaporating the solvent and hence eliminating solvent quenching, the intensity of fluorescence and the fluorescence lifetime are increased in film samples. Increasing the fluorescence intensity of film samples was shown in the previous section. Figure 4-48 shows the increased lifetime in the film sample.

4.12.4 Effect of temperature on fluorescence lifetime

To investigate the effect of temperature on fluorescence lifetime, decay time was measured at two different temperatures for three different excitation wavelengths. The results for the sample excited at 203 nm are shown in Figure 4-49. Other wavelengths are shown in appendix 4.

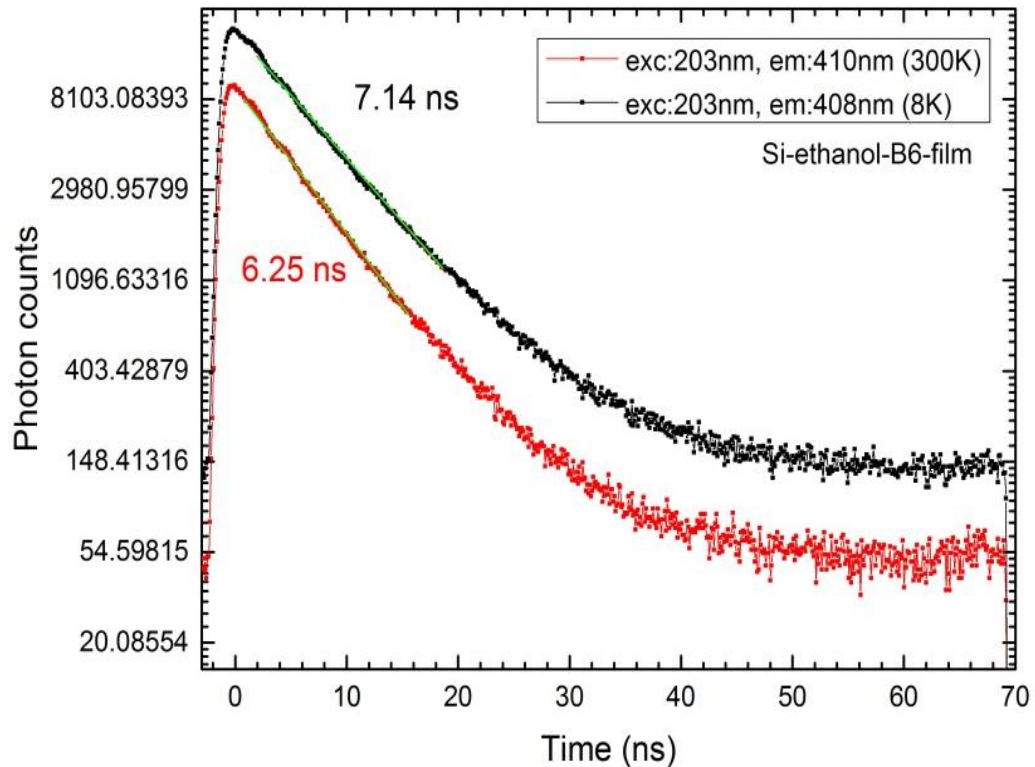


Figure 4-49. Figure showing lifetime dependence on temperature; lifetime decreases with increasing temperature [276].

As the results in Figure 4-49 show, lifetime depends on temperature; it decreases with increasing the temperature, similar to reported results in reference [276]. Fluorescence lifetime is not as sensitive as intensity to temperature, so decreases in fluorescence lifetime with temperature are not proportional to decreases in fluorescence intensity with temperature.

4.13 Effect of production parameters on the fluorescence spectrum

We investigated the effect of different parameters on the fluorescence spectrum such as stagnation pressure, magnetron power, deposition time, distance between capillary and cold target, and angle between liquid jet and cold target. The effect of different distances and angles are explained here, but the results of other effects are shown in appendix 4, as the results were not conclusive.

4.13.1 Effect of different distances and angles between cold trap and liquid jet

To investigate the importance of the distance and angle between the cold trap and the sputter head and liquid jet, four experiments were performed to produce Si-IPA samples at two directions and two distances. Other experimental conditions were exactly the same and experiments were performed immediately after each other (even the solvent in the liquid reservoir was not topped up). A schematic of the experiment is shown in Figure 2.5. The results of fluorescence emission experiments of these samples are shown in Figure 4-50, whilst absorbance effects are shown in Figure 4-51.

The liquid jet has a divergence angle, so the beam diverges at long distances. To study the effect of distance between the capillary and cold target, the cold target was located at two different distances with respect to both the capillary and also the magnetron.

In another experiment, the angle between the cold target and liquid jet was investigated. Firstly, the sample was produced when the cold target hole was aligned with the magnetron and liquid jet; the target was then tilted to reduce the amount of directly deposited atomic silicon vapour into the cold target, and have only co-deposition of silicon and liquid.

As can be seen in Figure 4-50 tilting did not change the appearance of the spectrum, either at short distances or long distances between the target and capillary, meaning silicon clusters form when they are trapped in the liquid jet, and not after co-deposition in the cold target or by entrance of atomic silicon vapour into the trap. Tilting did not affect the fluorescence intensity of the first fluorescence peak. For the second fluorescence peak, tilting did not change the intensity of fluorescence when cold target was located close to the capillary, but at long distance, tilting the cold target caused lower fluorescence intensity because less of the liquid jet enters the target.

The results show that different distances between the target and capillary affects the fluorescence spectrum. The peak at 400 nm arose when the cold target was located at a long distance from the capillary. As this peak is attributed to the cluster surface, it can be explained as these fluorescent sites need more time to form and bind to solvent molecules, and it may be due to increasing the concentration of the silicon trapped by liquid jet; as the liquid filament is longer, the concentration of silicon particles is higher. These

hypotheses also confirm the results of the tilting cold target experiment about forming fluorescent sites in liquid jet not after co-deposition. For the first peak, whilst the fluorescence intensity for different distances is almost the same, it is slightly higher for producing clusters at short distances; the intensity increases by decreasing the distance because the number of particles trapped by the target is greater at short distances.

UV/Vis spectroscopy shows absorbance spectra are different in intensity for long and short distances between the cold target and capillary. For long distances there are two intense peaks at 220 nm and 260 nm, whilst samples produced at short distances shows the first band at 220 nm with lower intensity, and the second band to be very weak. The higher absorption for long distance experiments may explain the higher concentration of silicon nanoparticles trapped by the liquid jet.

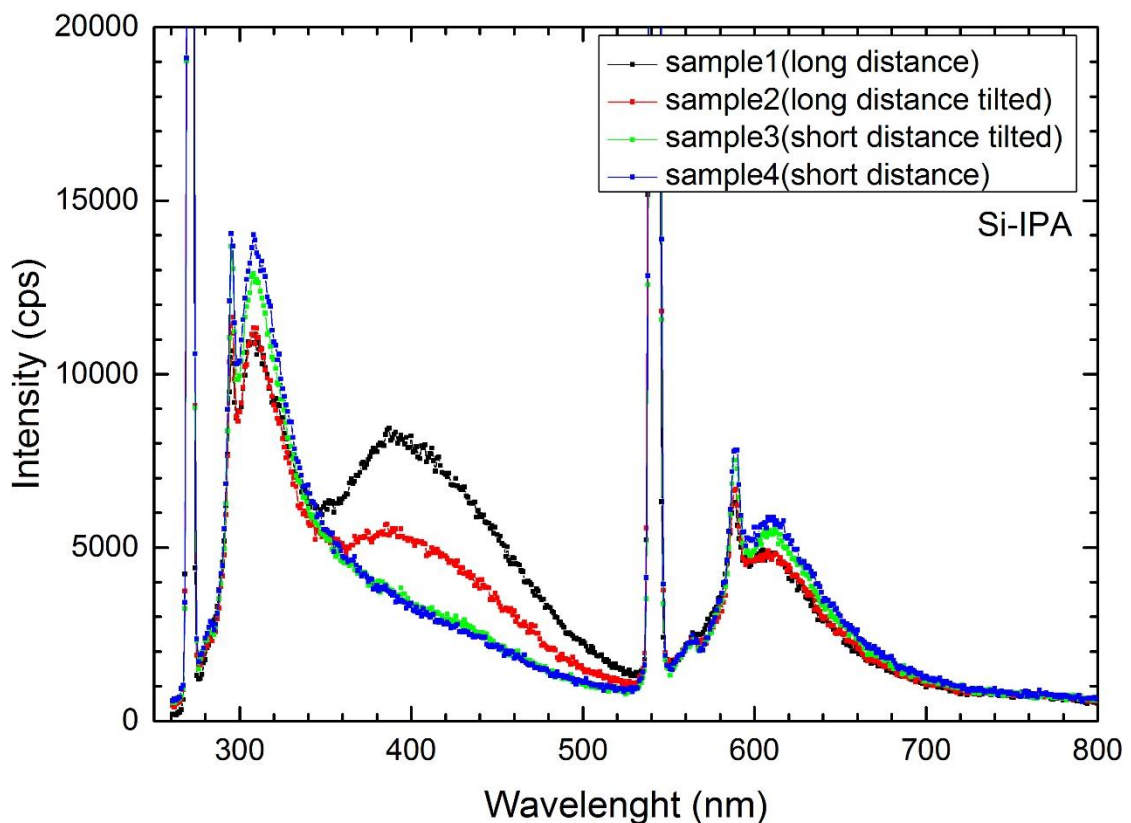


Figure 4-50. Figure showing spectra of Si-IPA samples which are produced at different distances and angles between the cold target and liquid jet.

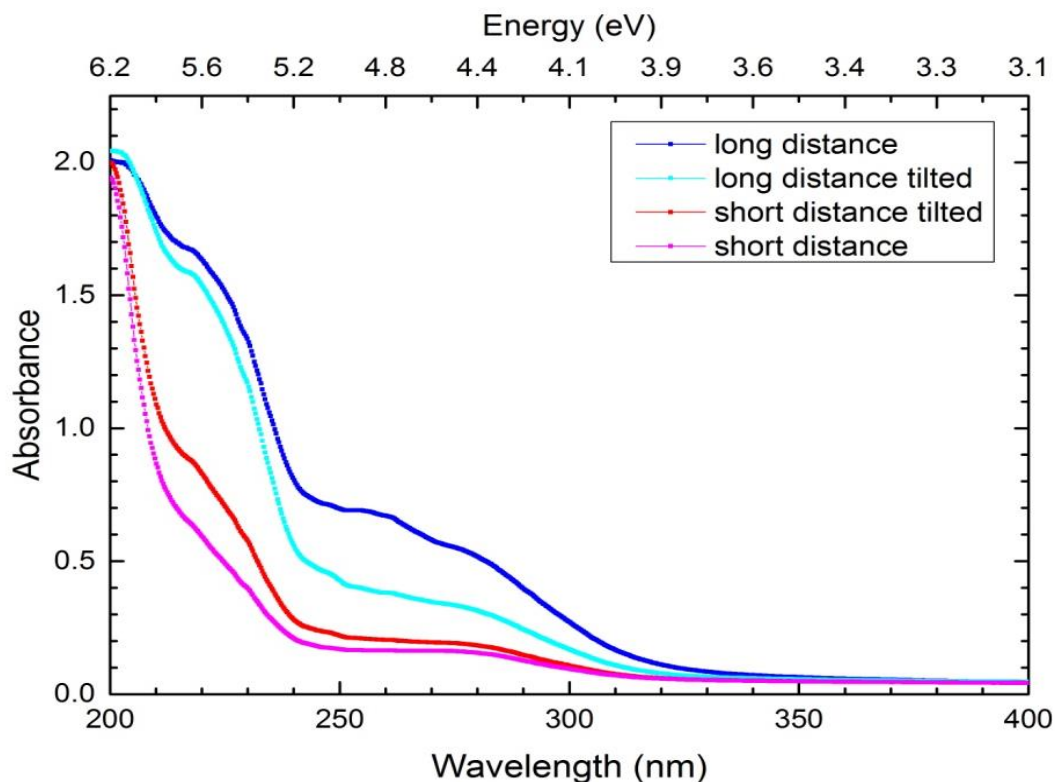


Figure 4-51. Figure showing spectra of Si-IPA samples which were produced at different distances and angles between the cold target and liquid jet.

4.14 Conclusion

Fluorescence spectra of more than 50 samples show the reproducibility and quality of the samples produced in different solvents with our novel method.

We introduced a model for observed fluorescence peaks, silicon particles produced with our novel method show two different fluorescence bands; the first band around 310 nm, which we attribute to the bulk clusters, is an intrinsic peak and does not depend on solvent with all samples in both liquid phase and film show this band; the second band appears at 365 nm to 440 nm, which is attributed to the fluorescent sites at the cluster surface is solvent dependent, and shows a fluorescence peak for Si-water sample at a longer wavelength than alcoholic samples. The lifetime measurements show different lifetimes for the first fluorescence band that suggests different structures for fluorescent sites of first fluorescence peak, so the fact that all samples show the same wavelength of fluorescence peak may be entirely coincidental. The results for the first and second fluorescence emission and excitation peak wavelength for three different solvents, and also their lifetimes, are summarised in Table 4-4.

Table 4-4. Fluorescence characteristics of silicon deposited in IPA, ethanol, and water.

Sample	Emission band wavelength (nm)	Excitation band wavelength (nm)	Lifetime (ns) (First band)	Lifetime (ns) (Second band)
Si-IPA (liquid)	310, 365	275 ($\lambda_{em}=310$ nm) 293 ($\lambda_{em}=365$ nm)	-	-
Si-IPA (liquid) (TCPC)	306	206 with a shoulder at 217 ($\lambda_{em}=305$ nm)	5.34	-
Si-IPA (film) (TCPC)	300, 412, 585	100, 115, 145, 200, 294 ($\lambda_{em}=420$ nm)	3.94	2.56
Si-ethanol (liquid)	310, 370	238, 278 ($\lambda_{em}=310$ nm) 278, 300 ($\lambda_{em}=370$ nm)	-	-
Si-ethanol (liquid) (TCPC)	304 with a shoulder at 350-360	210, 275 ($\lambda_{em}=310$ nm)	5.57	-
Si-ethanol (film- B5) (TCPC)	294	198, 220, 250-260 ($\lambda_{em}=290$ nm)	7.93	-
Si-ethanol (film- B6) (TCPC)	294, 415	203, 228, 295 ($\lambda_{em}=410$ nm)	4.74	6.02
Si-water (liquid)	310, 420- 440	275 ($\lambda_{em}=315$ nm) 270, 311, 380 ($\lambda_{em}=440$ nm)	-	-
Si-water (liquid) (TCPC)	320, 422	195, 224, 284 ($\lambda_{em}=320$ nm) 207, 303 ($\lambda_{em}=422$ nm)	3.81	3.95
Si-water (film) (TCPC)	308, 440, 570	190, 300 ($\lambda_{em}=415$ nm)	5.59	1.25

Our results confirm that oxidised silicon clusters emit blue luminescence; in solution, the long wavelength fluorescence band energy is directly related to the magnitude of the silicon-solvent interaction, indicating Si-OH hydrogen-bonding, or silicon bonding with the solvent molecules. The relationship of the second fluorescence wavelength on the solvent shows that the transition is (i) located at the surface of the clusters and (ii) that the fluorescent site has polar character. Interaction of water with silicon surfaces produces silicon-oxygen bonds, or perhaps OH defects [278], and we anticipate a similar reaction during cluster growth using water and alcohol jets. OH groups on surfaces are polar, and we anticipate in our case the formation of hydrogen bonds with the polar solvents. Amongst the three solvent we used, water has the greatest dipole moment of the solvents, and will draw electron density from the surface of the

silicon cluster, thereby producing an up-shift of the energy levels. Provided the changes in the excited state density are small, a gradual red shift related to the strength of the solvent dipole moment can be readily explained, although the dipole moment is not the only solvent property which can affect the solvent dependence on fluorescence wavelength. For the first fluorescence peak, the fluorescent site is not as exposed to the solvent as the surface cluster; in other words, the transition is characteristic of the bulk volume of the cluster.

The measurements of the fluorescence spectra of samples produced at different distances between cold target and capillary show for the samples produced at short distances that the second fluorescence peak is absent in fluorescence spectra. We speculate that this is because when using longer distances, the concentration of the particles in the jet is increased.

According to our observation in chapter 5, the red shift of the fluorescence wavelength may relate to oxidation state, so Si-IPA fluorescence peak at 365 nm belongs to SiO, Si-ethanol fluorescence peak at 370 nm belongs to SiO_x, 1 < x < 2, and 420 - 440 nm belongs to SiO₂. Also chemical characterisation shows Si-water samples in addition to SiO₂ have SiO or SiO_x bands, which could explain the existence of three fluorescence peaks in fluorescence spectra of Si-water. So the peak at 380 nm, which exists in some Si-water samples, can be attributed to SiO_x. So we can conclude the sample shows shifts in the fluorescence peak due to different levels of oxidation. Adding one drop of pure water to Si-IPA samples gives rise to a peak at 420- 440 nm, which is similar to Si-water samples and is attributed to oxidation of silicon clusters.

Solvent exchange experiments showed reversible solvent transfer effects, and showed the properties of nanoparticles depend on the solvent they are kept in. The results show the transferred sample is equivalent to a directly deposited sample, and depending on the required wavelength, particles can be transferred to an appropriate solvent.

All film samples of nanoparticles show a second fluorescence peak at 420- 440 nm and, hence, the presence of silicon-oxygen species defects. We believe that silica nanocrystallites with defects are formed by aggregation of the nanoclusters during the drying and oxidising process, so may not exist in liquid alcoholic samples.

All samples produced so far show that clusters are chemically stable and do not agglomerate during the years, and also clusters show stable fluorescence properties over

a storage time of just under a one year. Quantum yield measurements show Si-water samples have a quantum yield of 8% to 10%, which is high enough for many applications. A Stern-Volmer plot confirms fluorescence quenching at high sample concentrations in alcoholic solvents, and also showed that fluorescence in Si-water samples was not quenched and shows dynamic stability. A plot of absorbance versus sample concentration shows chemical stability of the samples.

Decay time measurements show samples have similar fluorescence lifetimes, in the range of a few nanoseconds, which is dependent on the solvent, phase of the sample and excitation wavelengths. For liquid samples, the fluorescence lifetime was recorded between 3 - 5 ns, depending on the solvent; water samples had the shorter lifetime. Lifetimes of the film samples do not depend on the solvent due to their evaporation, however film samples show lifetimes longer than liquid samples. As there is no quenching in film samples, intensities and lifetimes increase respect to liquid samples. The results show that lifetime is also dependant on the excitation wavelength; it decreases by increasing the excitation wavelength.

Changing the temperature affects fluorescence intensity and fluorescence lifetime. Fluorescence intensity and lifetime decreased as the temperature was increased from 8 K to 300 K.

Chapter 5

Chemical characterisation of silicon nanoparticles

Silicon nanoclusters produced using our novel method showed extraordinary physical and optical properties. Here we look to answer questions such as what the intramolecular chemical origins of these physical properties and/ or due to what intermolecular chemical interactions these properties arise; to address these issues, we used XPS and FTIR/ATR spectroscopy to investigate the samples. The method of characterisation was described in chapter 3; in this chapter, we present the results of XPS and ATR spectroscopy, which we then discuss.

5.1 XPS characterisation

In XPS, electrons are ejected from the sample due to a photoionization process, and these electrons are analysed to characterise a sample at the atomic level. The result is a plot of intensity versus residual kinetic energy of the electrons ejected from the sample, which can be straightforwardly used to determine their original – atomically unique – binding energies. XPS spectroscopy is a surface analysis method, which gives us information about elements or, indirectly, their originating molecular species allows for quantitative analysis of such and, again indirectly, gives information about chemical bonding and interactions with the environment.

The results of XPS measurements are shown in following sections. For the survey spectra see Appendix 5 (section 5.1). XPS spectra of a silicon wafer were recorded as a reference and are shown in Appendix 5 (section 5.2).

5.1.1 Effect of substrate

As a cluster may well interact with the XPS analysis substrate, which in turn might affect chemical bonding and cluster structure, we tried to find the best substrate with less interaction with particles, to know our particles properties with any changes due to interaction with substrate. Three different substrates were investigated for this experiment: copper plate, molybdenum plate, and HOPG. For all these three substrates, four peaks – which are considered to be the most important for our measurements – were recorded, which are those of silicon ($2p$), silicon ($2s$), carbon ($1s$) and oxygen ($1s$). The results are shown in Figure 5-1. According to our atomic binding energy library (integrated in the software), the binding energy of these peaks are: Si ($^2P_{1/2}$) at 99.8 eV, Si ($^2P_{3/2}$) at 99.2 eV, C ($1s$) at 284.70 eV, O ($1s$) at 531 eV, and Si ($2s$) at 150.5 eV.

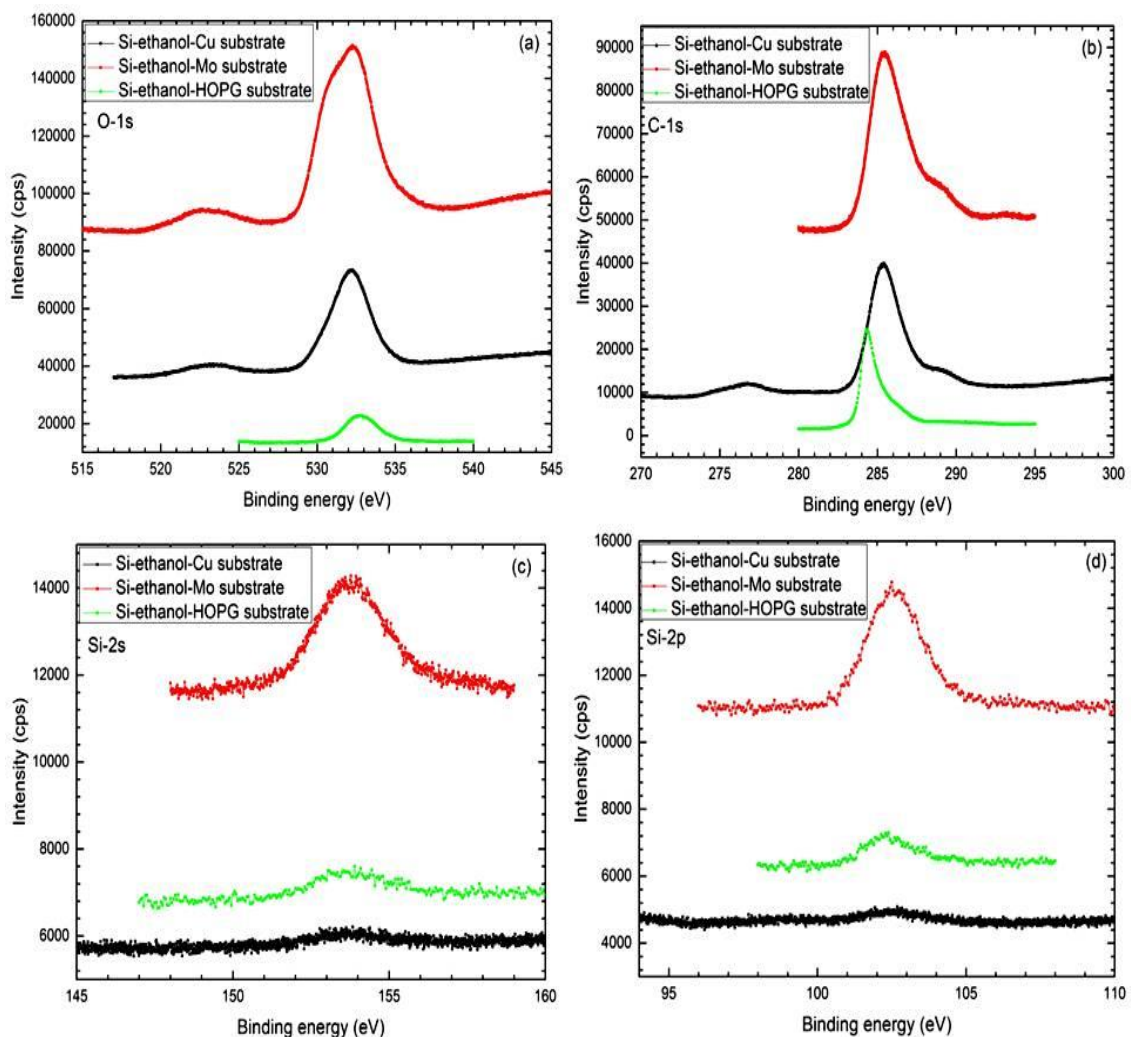


Figure 5-1. Figure comparing carbon ($1s$) (a), oxygen ($1s$) (b) and silicon peaks ($2s$, $2p$) (c, d) for one drop ($5\mu\text{l}$) of Si-ethanol sample on three different substrates (copper, molybdenum and HOPG).

All samples in any substrate show carbon peaks due to adventitious carbon contamination, due to exposure to the atmosphere [133, 279].

As it can be seen in Figure 5-1, the intensity of the peaks was very low on Cu plate for unknown reason, so this was immediately dismissed as a candidate substrate for analysis. Samples on HOPG and Mo plate showed acceptable intensities, indeed, this intensity was higher in the case of the Mo substrate. However, the peak belonging to Si-ethanol on Mo plate showed a sub-peak (shoulder) to lower binding energy of the oxygen peak which was not seen in cases of HOPG or Cu substrate. The carbon peak shows a strong dependence on the substrate, but the Si ($2p$) and Si ($2s$) do not. This could suggest that the carbon is binding to the surface, but the silicon is not. The Si ($2p$) peak had slightly higher binding energy when Mo was used as substrate with respect to HOPG, so the sample may have interacted with the molybdenum to some degree. To confirm this, the molybdenum peak of the Mo substrate was measured with and without sample, as was the carbon peak of HOPG.

To this end, the XPS spectrum of the Mo plate without sample was measured in the first step, to see the location of the bulk molybdenum peak and in a second step, the sample was added to the Mo plate and the Mo peak was again measured; the same was performed for HOPG. The result is shown in Figure 5-2. As it can be seen, we could conclude the sample interacted with the Mo substrate because the binding energy of the Mo peak was changed when sample was added to the substrate. The literature reported peaks for MoSiO_2 at 227.68 eV [205] and for Mo at 227.4 eV [280]. The same difference in binding energies between Mo and MoSiO_2 was observed in this study, from which we could conclude that the sample interacted with the Mo substrate. Therefore, molybdenum was also eliminated as a candidate substrate.

To confirm that HOPG was, in fact, itself suitable, this procedure was repeated using HOPG as substrate. The results show only a weak interaction with HOPG. For this reason, and for reason of the acceptable sample peak intensities seen previously, HOPG was chosen as our substrate for XPS experiments. For molybdenum, the intensity of the substrate peak dramatically reduced after adding the sample, because the electrons originated mainly from the sample rather than the substrate, but for HOPG, the intensity increased because the sample itself contains some carbon. All experiments described in this section were performed using one 5 μl drop of sample.

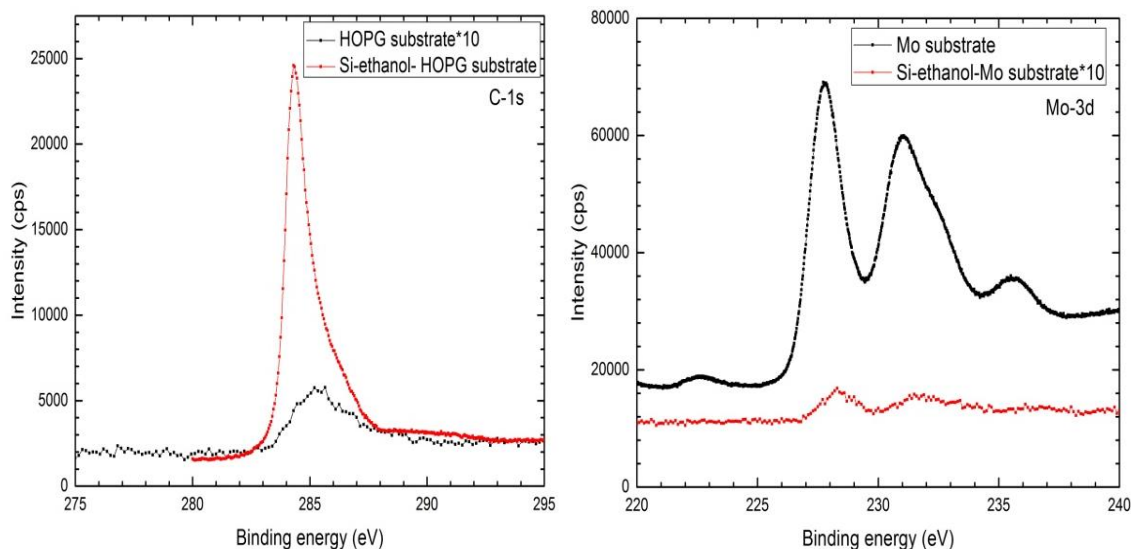


Figure 5-2. Figure showing the peaks belonging to the substrate before and after putting sample was applied.

5.1.2 Effect of sample thickness

As was explained in chapter 3, to investigate the effect of thickness on the XPS peak, we used one drop of Si-water on HOPG, ten drops of Si-water on HOPG and ten drops of Si-water at the centre of the HOPG. Also, a spectrum of five drops of pure water on HOPG was recorded as a reference. Each drop was about 10 μl . The effect of sample thickness on the XPS spectrum is shown in Figure 5-3.

Pure water shows silicon peaks because of its silicon containing impurities (0.1 ppm silica) [104], but this peak has different binding energy and shows a red shift with respect to the silicon species in the samples and, additionally, Si-water samples peaks are broader. The samples show a blue shift with respect to pure silicon for both Si ($2p$) and Si ($2s$), and also O ($1s$). In the following section, it is explained why the Si-water sample shows highly oxidised silicon.

The integrated area under the peak increases with the concentration of sample; as we used same sample for this experiment, and the particles had the same binding energy in the case of using one drop or ten drops, so the intensity is proportional to the number of particles. Therefore, as we expected, by increasing the thickness of the film (i.e., increased sample concentration) the peak intensity increased. This happened for all four peaks investigated in this experiment.

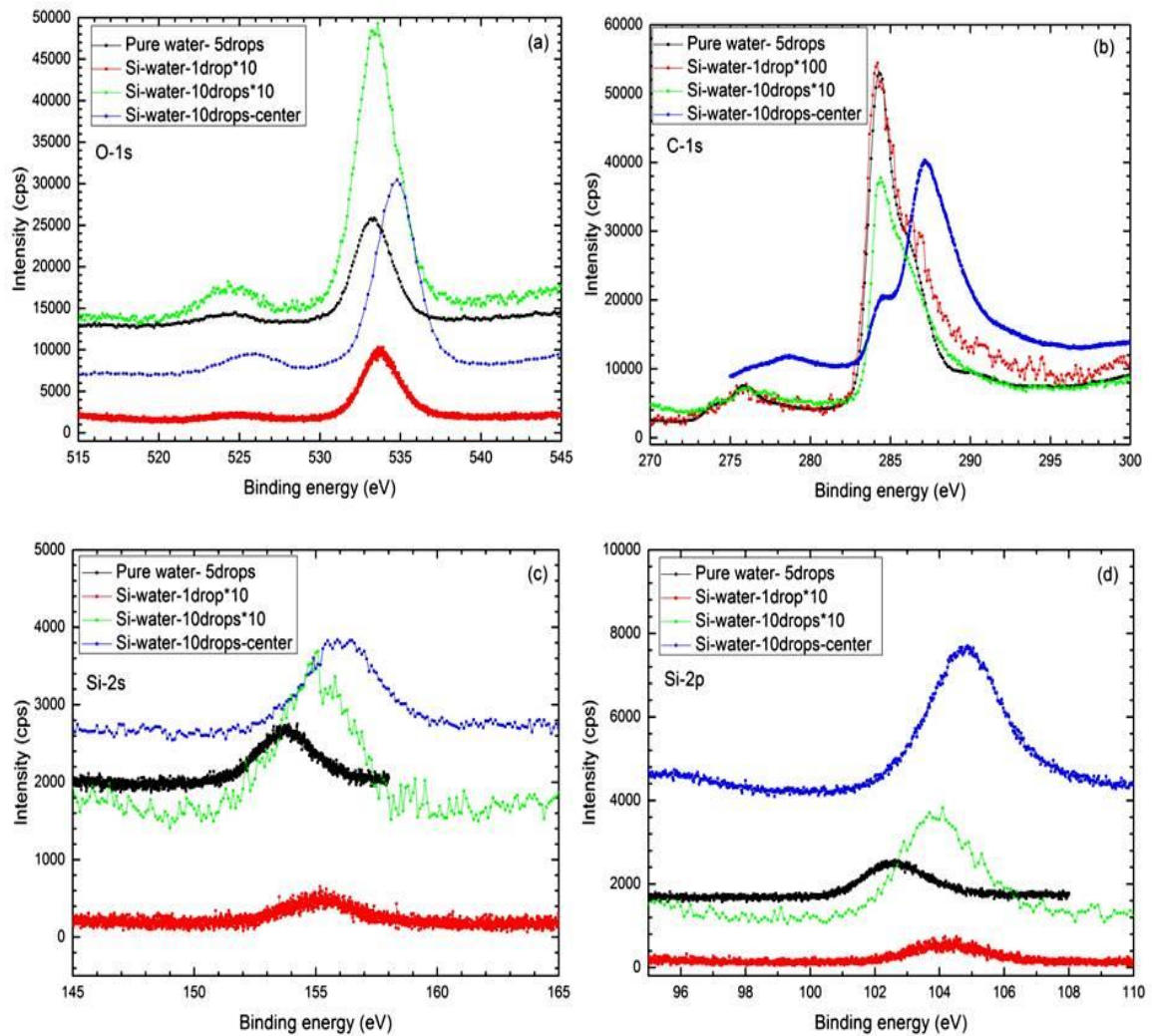


Figure 5-3. The effect of the sample thickness on the substrate. There are some silicon impurities in pure water, but this does not interfere with the peaks due to our samples, which show oxidised silicon.

By putting ten drops of sample in the centre of the HOPG, we expected two effects. First, we used the same amount of sample solution (ten drops), but placed only in the centre of HOPG in this case (in another, it was ensured that the sample covered the entire area of the HOPG substrate); so, the concentration should have been higher where the sample was restricted to the centre area of the HOPG substrate. As we expected, samples prepared in this manner showed higher intensity for all peaks (note the intensity of ten drops sample covered HOPG was multiplied by ten).

Second, we expected to see two different carbon peaks, one from the part of HOPG which was not covered with sample and another from where the sample did cover the substrate. As we expected, it showed two distinct peaks; the peak at 284.5 eV (first peak) belonged to pure carbon, and the peak at 287 eV (second peak) might arise due to species

like C-O-H or C-O-C. The two other samples and the pure water reference also show the first peak, but the intensity is very low for one drop and ten drop samples as we expected (note they are multiplied by ten for ten drops of sample and 100 for one drop of sample) but pure water shows higher intensity because it did not have any clusters; by evaporating the pure water, HOPG signals and HOPG species formed in air should have been seen, although our pure water had some impurities. Also, the two other samples and pure water have a shoulder to higher binding energy, which may belong to C-O-C or C-O-H.

5.1.3 Solvent effect

To investigate the structure of the silicon clusters in our samples, and also the effect of different solvents on structure, XPS measurements were performed for Si-water, Si-IPA, and Si-ethanol samples. We used the following parameters for short region scans: step 0.05eV; sweeps 15; dwell 1; and CAE 10. Our samples show blue shifts with respect to the bulk silicon, and it may be caused by interaction of silicon with other elements in solvents or substrate, but from the variation of the substrates outlined in section 5.1.1 (substrate effect experiment), we have learned that clusters do not interact with HOPG, so there were some interactions between silicon particles and their solvents.

Figure 5-4 shows these shifts from pure silicon and oxygen binding energies for our samples. Comparison between Si ($2s$), Si ($2p$), and O ($1s$) peaks of our samples and shifted peaks in the literature (which are mentioned in chapter 3 in Table 3.1-3.5) shows we may have silicon oxide in Si-IPA sample, SiO_x , $1 < x < 2$ in Si-ethanol, and silicon dioxide in water sample, so in going from IPA to water, there is an increase in the apparent oxidation state of the silicon, as evidenced by a blue shift in the associated XPS peaks. The C ($1s$) peak shows a superposition of two components which belong to C-C (284.4 eV) and C-O-C or C-O-H (~286.4 eV); also, the literature reported $\text{CH}_3\text{OH/Si}$ band at 286.8 eV [281] is another possibility for Si-ethanol sample and Si-water sample if we consider carbon impurities for water used for producing the sample. For these two samples, the carbon peak is a superposition of a pure carbon peak and carbon-oxygen (or silicon-carbon) binding peak(s), which can be distinguished due to the asymmetric shape of the peaks (also see section (5.1.5)). The intensity of the peak at 286.4 eV is very low for Si-ethanol, but in Si-water sample is very intense, and its intensity even higher than carbon peak (at 284.4 eV) in this sample. Tables 3.1-3.5 show the values for possible

species for our samples, so we can compare these values with our samples to find out our samples' structures.

In Figure 5-4 (c, d), different blue shifts of the silicon $2s$ and $2p$ binding energies, depending on the solvent used, are observed. The Si-water sample shows a greater shift than alcoholic samples. The peaks shifted with respect to bulk silicon, and comparison with the references shows the presence of SiO_2 in water samples, SiO_x in ethanol samples and SiO in IPA samples. So, the oxidation state of the compounds depends on the solvent and environmental effect. Therefore, the silicon $2s$ and $2p$ peaks indicate that silicon in water is in a higher oxidation state than in alcohol. In addition to this, XPS shifts can be observed due to size effects or charged clusters [282, 283]. In our case another possibility is that the level of oxidation is the same for all samples, but surface cluster-solvent interactions are different (depending on solvent), causing different XPS shifts. As the ATR results show later, we can attribute these shifts to different level of oxidation in different samples (depending on solvent) with more confidence. It is well known that isolated sample exposed to x-ray radiation become charged over time. This possibility can be excluded for both silicon in water and silicon in alcohol. The spectra in Figure 5-4 have been recorded within a series of at least three consecutive scans. Between these scans no shifts were observed.

In Figure 5-4 (b), in water samples, the area under the C-O-C (or C-O-H) peak is larger than the pure carbon peak, which means a large amount of carbon impurities in water are oxidised. If we attributed this peak to $\text{CH}_3\text{OH}/\text{Si}$ in water samples, the area under the $\text{CH}_3\text{OH}/\text{Si}$ peak is larger than the pure carbon peak, which means a large amount of carbon may have bound, or interacted with, silicon in water. In the ethanol samples, the intensity of the carbon peak is higher because it is less reactive than water and, in IPA samples, the intensity of $\text{CH}_3\text{OH}/\text{Si}$ is negligible.

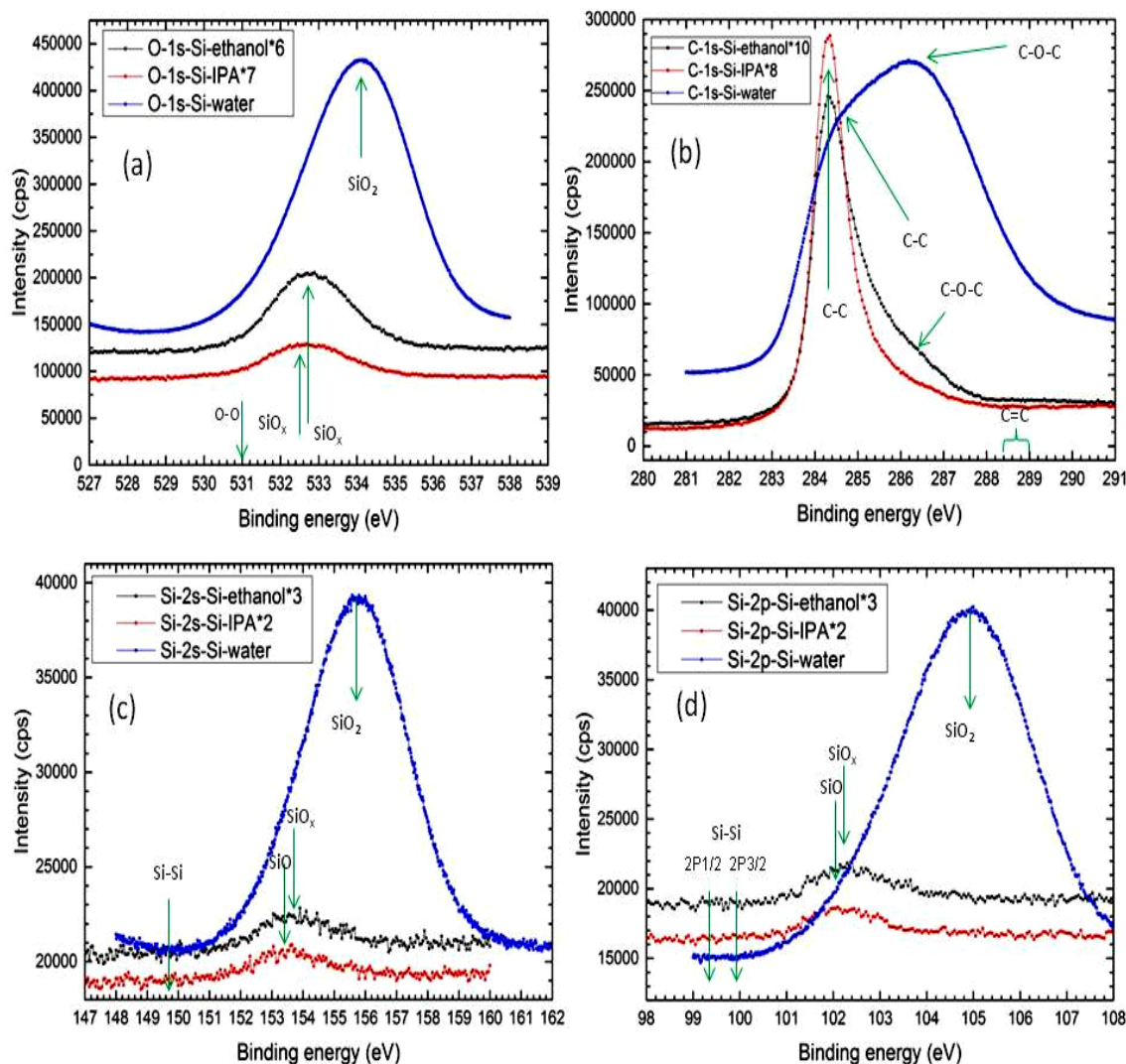


Figure 5-4. Figure showing XPS peaks of O ($1s$), C ($1s$), Si ($2s$), Si ($2p$) for silicon clusters in IPA, ethanol, and water on HOPG. High oxidation happens for the Si-water sample, and a lower level of oxidation for alcoholic samples.

The oxygen and silicon ($2p$) peaks of Si-water are broad and asymmetric bands, showing silicon binding with oxygen happens with different level of oxidation in the Si-water sample. The highest intensity peaks belong to SiO₂, though there are also the same components that alcoholic samples display, such as SiO, and SiO_x, $1 < x < 2$ (see section (5.1.5)).

The intensity (integrated) of the oxygen and silicon peaks for water samples is greater than for alcoholic samples. This could indicate that the number of silicon atoms bonded with oxygen in water was greater than in alcohol. It also may indicate that the silicon atoms dissolved better in water than alcohol, and large amount of silicon remained

undissolved in the alcohols. Another reason for large reaction between silicon and water may relate to oxygen dissolved in water.

To have a reference for our samples we recorded XPS spectra of a silicon wafer (see Appendix 5, section 5.2). Two different peaks for bulk silicon and silicon oxide are observed. Both silicon bulk peaks ($2p$ and $2s$) confirm the calibration of the instrument. The silicon oxide peaks match the literature values.

AFM results show all samples have silicon clusters of 1 nm, but the same amount of samples show different thickness layers. For alcoholic samples two to three layers of clusters can be seen in size distribution diagrams but water samples show six to seven layers, which could be the reason that water samples have higher intensities than alcoholic samples for the same amount of sample (see appendix 6).

5.1.4 Solvent exchange

As described in chapter 3, we recorded XPS spectra of a Si-ethanol sample, and then split it in two vials. The ethanol was allowed to evaporate in each, then one was topped up with water and the other with IPA. We then recorded XPS spectra for each of the samples in their new solvents. The results are shown in Figure 5-5.

Solvent exchange experiments show the same structures with directly deposited silicon in different solvents, although the intensity is different in some cases. The difference in the intensity changes with the concentration of the clusters and their bonding with the solvent, and was expected to change even for the same sample in different measurements. Since the structure and level of oxidation of the sample are almost the same as directly deposited samples, it confirms we can produce sample in any solvent and transfer it to any other solvent.

The intensity of the Si peak goes up by transferring to water, confirming that silicon particles in water form more bonds than in alcohol, and dissolved better than in alcohol.

A comparison between Si ($2s$, and $2p$) peaks shows the peak position and FWHM of the Si-ethanol and Si-IPA samples are the same for directly deposited samples and transferred samples, but they are slightly different, by around 1 eV, for Si-water samples. In directly deposited Si-water samples, the silicon $2s$ peak is at 155.78 eV, which is at 156.5 eV for transferred silicon particles to water; the band widths are 3.89 eV and 2.74

eV for directly deposited and transferred samples, respectively. For the silicon 2p peak, directly deposited Si-water has a peak at 104.96 eV, which is at 105.45 eV for silicon transferred to water; the band widths for the silicon 2p is 3.37 eV and 2 eV for directly deposited and transferred samples, respectively. Although the band width of the directly deposited Si-water sample is slightly different to the sample transferred to water, they show the same species. Directly deposited samples in the same solvent may show different band widths from sample to sample, but as the species for the specific solvent is always the same, the binding energy of the peaks remain constant.

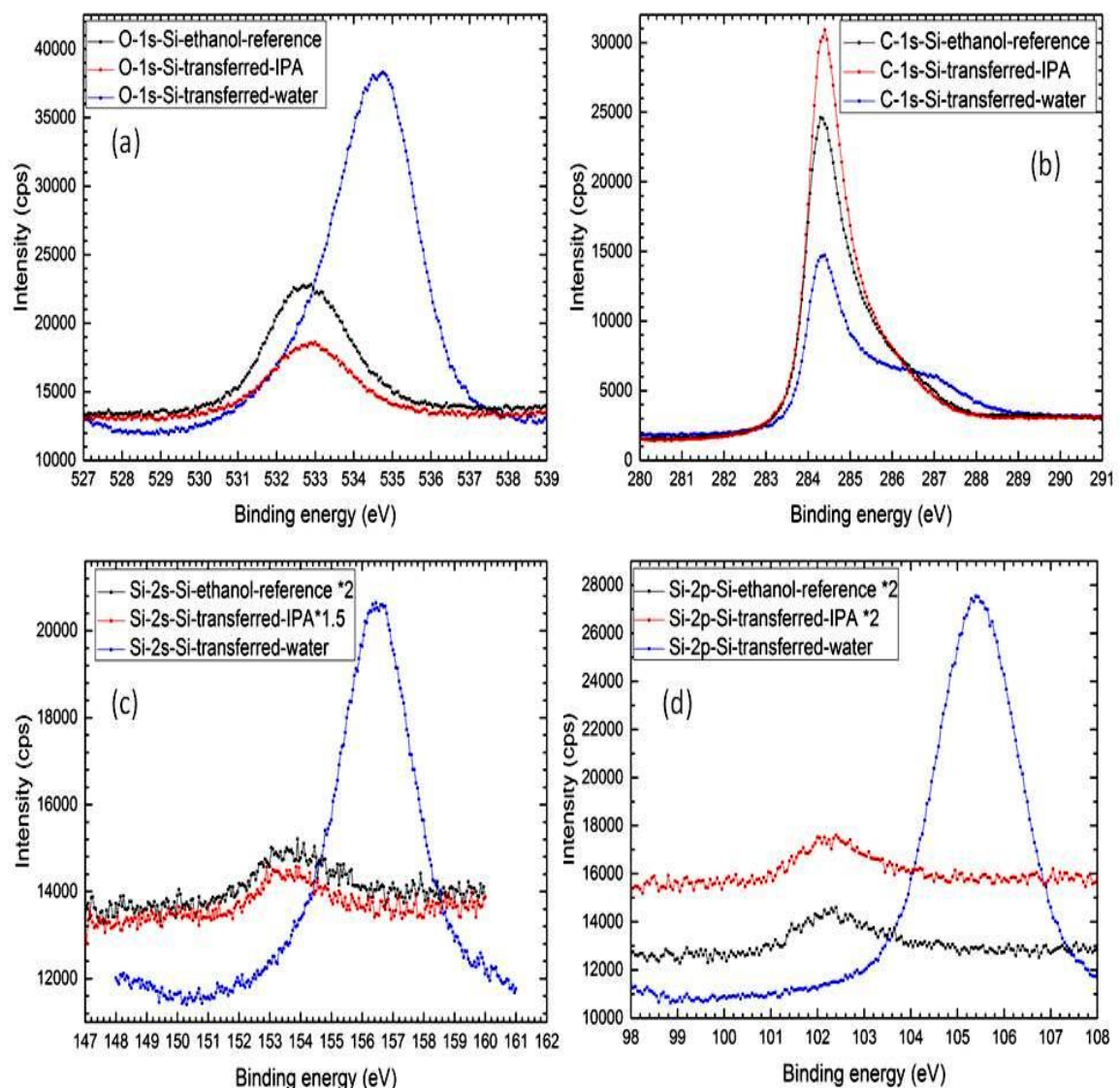


Figure 5-5. Figure comparing the XPS peaks of Si-ethanol sample on HOPG with the ones produced from subsequent solvent exchange with IPA and water on HOPG.

We transferred particles again from water to ethanol (by evaporating water and topping up with ethanol) and the results were the same as original sample with silicon directly deposited in ethanol.

5.1.5 Peak analysis with CASA XPS

CASA XPS software was used to characterise the XPS spectra. With this software, each peak can be deconvoluted into its components (if such exist), which then makes it easy to find the atomic structure of the sample. For example, C ($1s$), O ($1s$), Si ($2p$), and Si ($2s$) peaks of Si-water in Figure 5-4 were analysed with CASA XPS. The results are shown in Figure 5-6 and Figure 5-7. The blue parts show the region that we had chosen to fit a peak to. We used a 50% Gaussian- 50% Lorentzian lineshape for the components (we used different percentages and found by empirical observation this ratio worked well in fitting the peaks); note that CASA XPS allows the user to use a different ratio of Gaussian to Lorentzian. The shape of peak produced by superposition of fitted components should be (within reasonable error bounds) identical to the spectral peak.

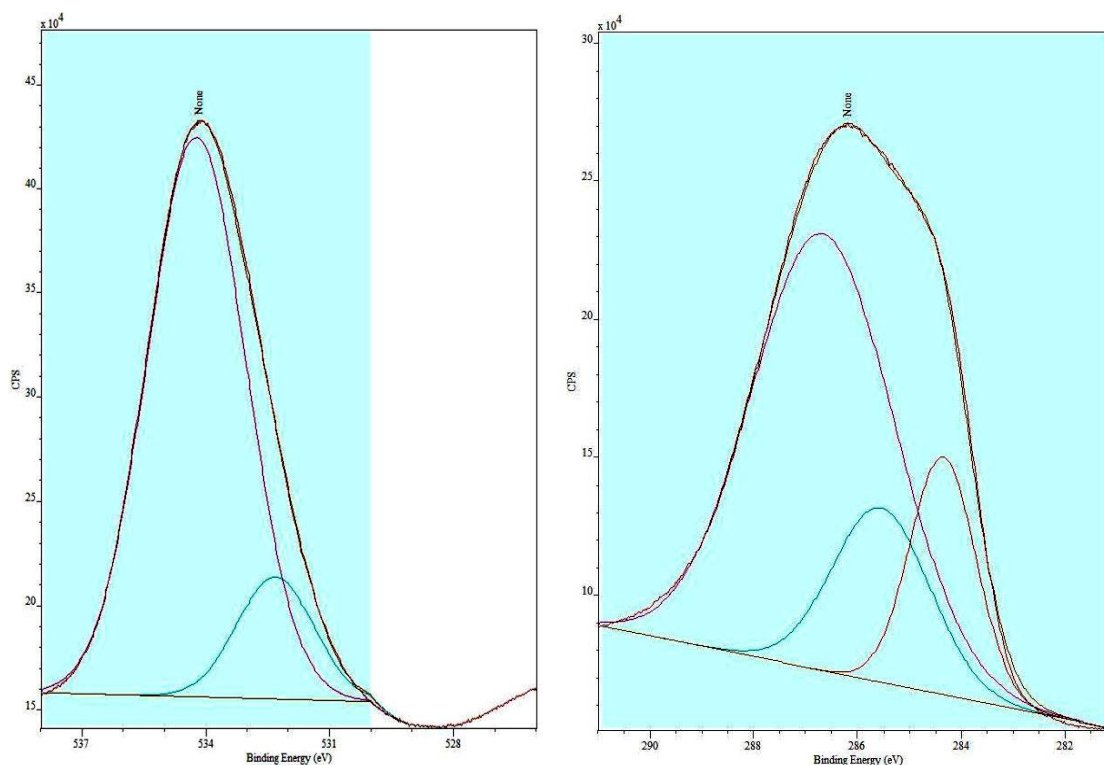


Figure 5-6. Oxygen peak (left) and carbon peak (right) of Si-water sample, as analysed with CASA XPS.

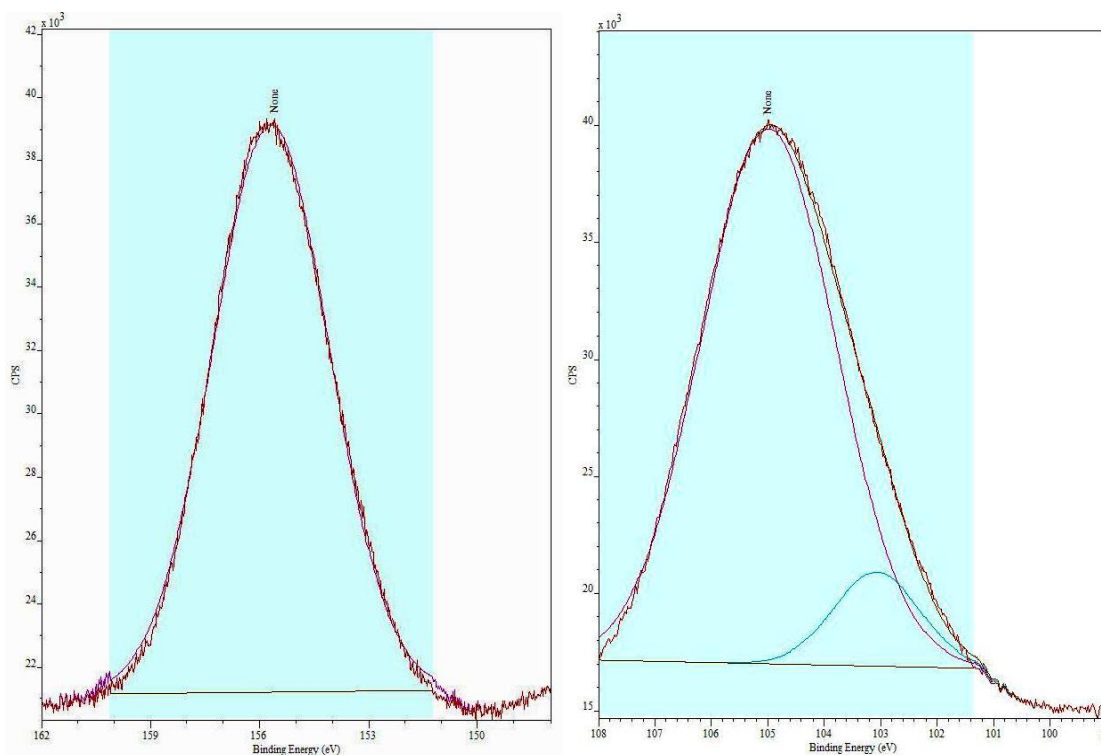


Figure 5-7. Figure showing the analysis the Si (2s) peak (left) and Si (2p) peak (right) of Si-water sample by using CASA XPS.

The results in Figure 5-6 show that the carbon peak is actually formed from three individual peaks, which suggest the existence of carbon, and carbon-oxygen species (C-O-C, C-O-H) or even carbon in $\text{CH}_3\text{OH}/\text{Si}$. The oxygen peak is, in fact, a superposition of oxygen and silicon dioxide peaks.

As can be seen in Figure 5-7, the silicon (2s) is just one peak which is silicon dioxide, and silicon (2p) is formed from two different silicon-oxygen species; SiO_2 , and, from the peak at 103 eV which can be attributed to a lower level of oxidation than SiO_2 , SiO_x ($1 < x < 2$) by comparing to the literature values summarized in the tables presented in chapter 3.

5.2 ATR/FTIR characterisation

ATR/FTIR spectroscopy measures absorption of the sample in the mid-infrared range when the sample is excited by infrared radiation. The result is a plot of absorbance or transmittance versus wavenumber. IR spectra are key to structural assignment. In ATR spectroscopy absorbance is usually measured, whilst transmittance is generally used in

FTIR. These methods are used to identify the molecular composition and bonding structure of the sample.

5.2.1 ATR characterisation

We used ATR spectroscopy to investigate film and liquid samples which were produced in IPA, ethanol and water. As experiments were recorded in atmosphere, we had difficulty due to atmospheric bands in our results, and the lab situation such as temperature, humidity, etc, also affected results. The wavenumber of the absorbance bands observed were compared to Table 3.6 to identify the bands and hence help determine the structure of the samples. All measurements were performed by using a drop(s) of 5 μl of sample (see sample preparation section (3.2.9)). The samples were recorded in the liquid phase and as films, a drop of 5 μl for liquid sample had a few microns height and the same amount of sample for film had a few nanometers height, as AFM shows 1 nm height for the clusters. The background recorded for samples were formed from 5 μl of the pure sample solvent to subtract the features of solvent, atmospheric gas and solvent impurities, although we could still see bands belonging to atmospheric gases and the solvent. To record a background spectrum we tried three different options as background; air, liquid solvent and making film of solvent. As the liquid absorbed a lot we could not use a liquid solvent as a background. The results for the air and film of solvent were the same, because pure solvent evaporated completely. In spite of this, we used pure solvent film as a background to subtract if there were any impurities in the pure solvent. The experiment was performed for all samples and repeated several times to ensure results. We expect to have Si-Si, Si-O, Si-H, and Si-C frequencies in our results. The results showed the existence of silicon oxygen species, but to assign specific bands we compared the fingerprint region with literature values and have made suggestions for each band assignment, though these assignments are not necessarily definitive.

5.2.1.1 Absorbance spectra of Si-IPA sample by using ATR spectroscopy

All Si-IPA samples were investigated by ATR spectroscopy; some of the spectra recorded had low absorbance intensity or had negative signal due to subtracting the background. We chose two spectra which showed clear bands, as shown in Figure 5-8

and Figure 5-10. To have a reference for silicon deposited on isopropanol samples, pure isopropanol film was investigated, and compared with the Si-IPA sample. Also we prepared films of increasing thickness and tested whether a proportionality of absorbance with film thickness could be established. Figure 5-8 shows a film which made of ten layers. For each layer, one 5 μ l drop of sample was used. Figure 5-9 shows the effect of increasing thickness of sample on absorbance, from one layer to ten layers.

Peak assignments were made as follows: the Si-C stretching band at 798 cm^{-1} , though this peak can be attributed to the Si-O bending vibration as well because its frequency is almost the same, the Si-OH stretch is at 960 cm^{-1} , the Si-O stretch at 1077 cm^{-1} , the SiO₂ stretch at 1145 cm^{-1} , the Si-CH₃ symmetric bend at 1261 cm^{-1} , the CH bend at 1376 cm^{-1} , the Si-CH₃ asymmetric bend at 1407 cm^{-1} , the CH bend at 1455 cm^{-1} , the OH bend at 1587 cm^{-1} , the C=O stretch at 1710 cm^{-1} , the SiH stretch at 2169 cm^{-1} (it is negative because of subtracting the background artefact), the CO₂ doublet asymmetric stretch bands are at 2328-2375 cm^{-1} , the CH stretch at 2872 cm^{-1} , the CH₂ stretch at 2932 cm^{-1} , the CH₃ stretch at 2974 cm^{-1} , and the OH stretch is a broad band ranging from 3200 to 3500, with maximum at 3360 cm^{-1} , are features apparent in this spectrum. Some features belong to isopropanol (which are also observed in IPA film spectra). As the measurement was performed in air, features characteristic of atmospheric water vapour and atmospheric CO₂ can also be seen in the spectrum. The great variety of references makes it difficult to assign a peak with confidence, for example for the Si-O stretch, the literature reports values from 930 cm^{-1} to 1200 cm^{-1} . So we could not assign a band to a specific species, and the assignment in the figures is the most possible bond for our sample.

Silicon-oxygen bands in the fingerprint region shows silicon interacted with the solvent and may have oxidised in IPA. In the Si-IPA sample, silicon also apparently bonded with carbon and hydrogen, but the intensities of these peaks are very low.

Although the peak positions in our sample are in agreement with reference values in Table 3.6, some features which belong to pure isopropanol are very close in vibrational frequency to silicon compounds, so the bands in our sample could be due to the superposition of silicon features with those of pure IPA. We expected that, by evaporating the solvent, solvent bands would not appear in the spectrum; however, the pure IPA film spectrum in Figure 5 11 still shows some IPA bands were detected after evaporation, and also there are some bands which are not in the pure IPA film (because of evaporation) but

are in the Si-IPA sample. These are the same as the liquid Si-IPA sample or liquid IPA, which shows the solvent did not evaporate completely due to bonding to silicon and trapping by the clusters, so solvent bands still can be detected in Si-IPA film samples.

As can be seen in Table 3.6, those alcohol vibrational frequencies which might be coincident with our sample bands can be listed as: have the following vibrational C-C-C bend at 1100 cm^{-1} , C-O stretch at 1102 cm^{-1} , and 1210 to 1320 cm^{-1} , C-O-H bend at 1395 to 1440 cm^{-1} , OH bend at 1620 cm^{-1} , C=O stretch between 1630 and 1820 cm^{-1} , and various C-H stretch modes at 2850-3000 cm^{-1} (CH₂ symmetric stretch at 2860 cm^{-1} , CH₂ asymmetric stretch at 2921 cm^{-1} , and CH₃ asymmetric stretch at 2960 cm^{-1}).

In Figure 5.9, the effect of sequentially increasing the number of layers from one to ten is shown; although the baseline height increased, increasing peak intensity for some peaks is clear by thickness of the film, whilst for some intensity is independent of the thickness. This dependence for peaks at 798 cm^{-1} , 1077 cm^{-1} and 3360 cm^{-1} is shown in Figure 5.9. We used the data point at 2500 cm^{-1} to calculate the height of the peaks.

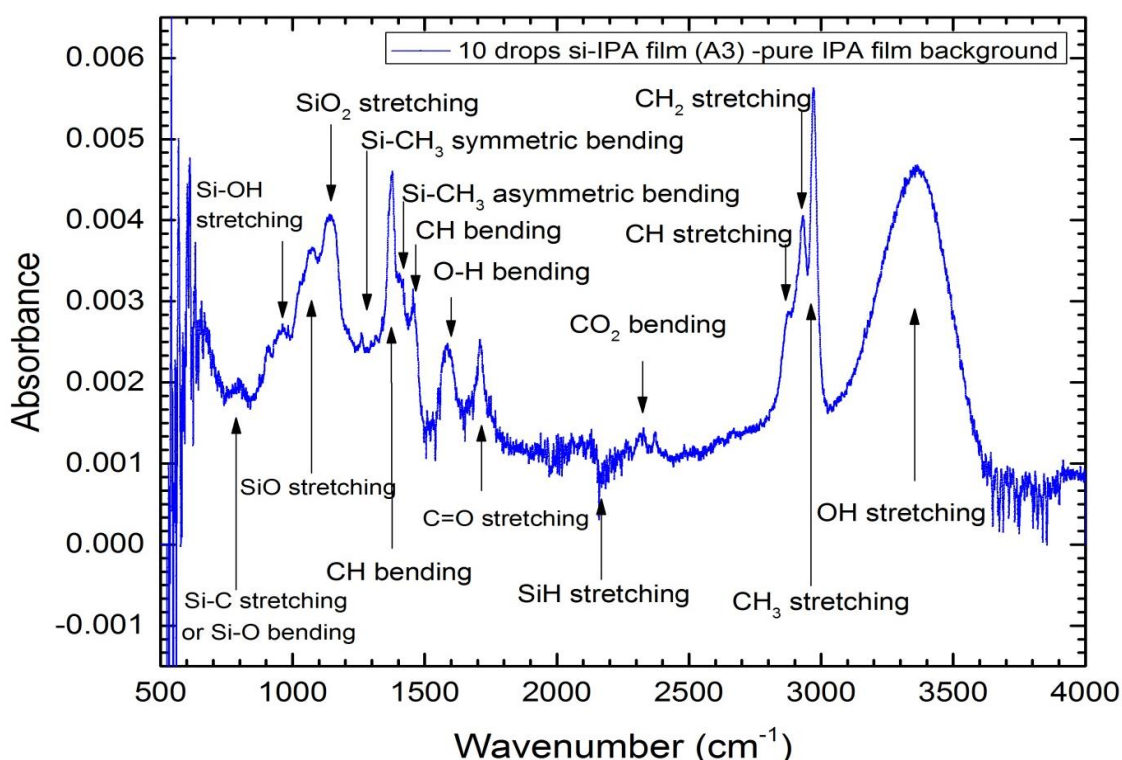


Figure 5-8. Absorbance spectrum of Si-IPA film. The sample shows silicon-oxygen, silicon-hydrogen and silicon-carbon bands in this spectrum.

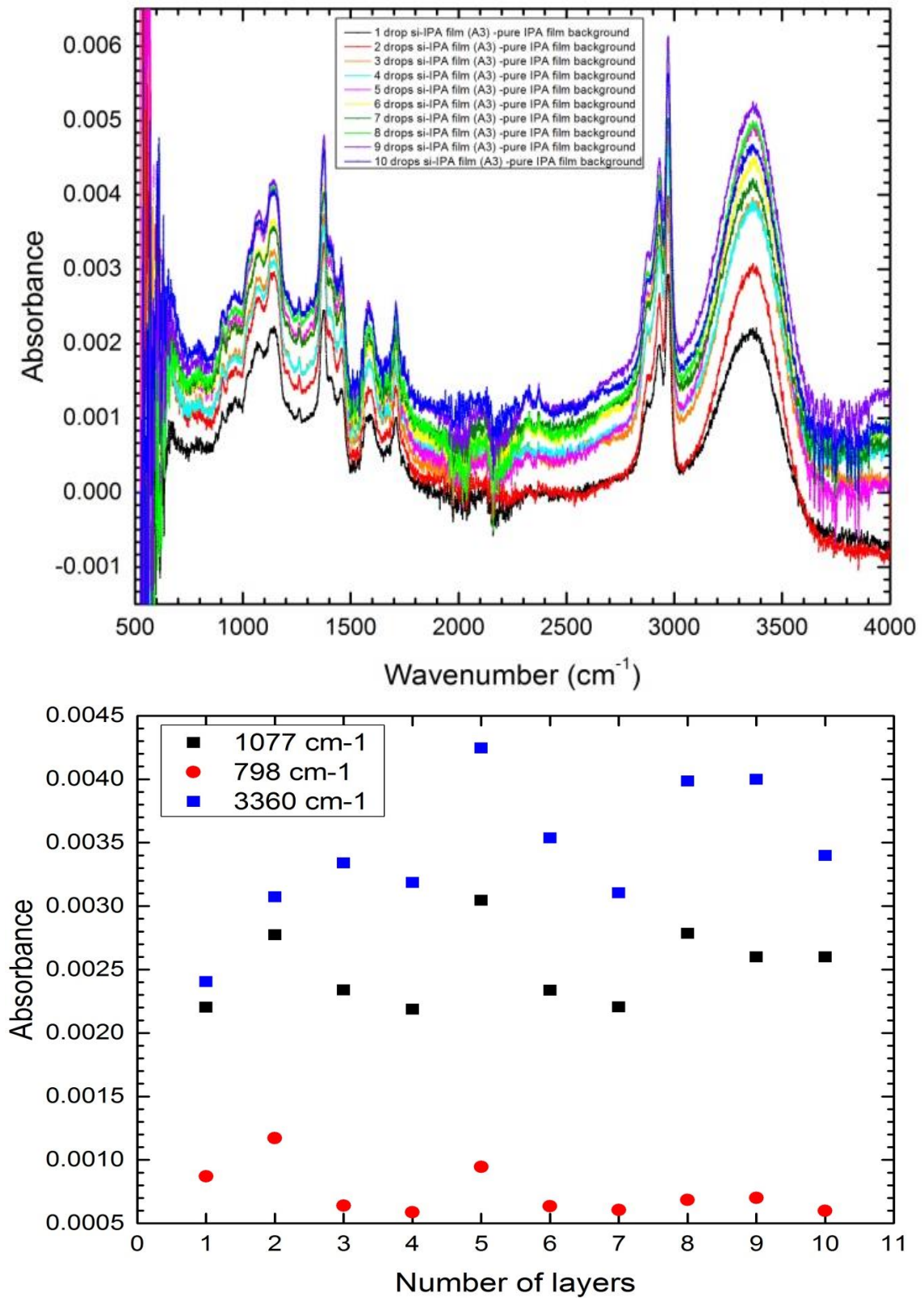


Figure 5-9. Increasing the film thickness of Si-IPA sample A3.

The same measurements have been performed for all samples of silicon in IPA to investigate reproducibility, quality and similarity of the samples. In these experiments the background spectrum was recorded from pure IPA film. Because of this, some bands which belong to IPA molecules vibration may appear negative due to subtracting by background.

Another good sample is shown Figure 5-10 (sample A1) which has the same bands, these bands are sharper, but their intensities are weaker, with respect to Figure 5-8 (sample A3), because only one layer of sample was used.

In spectrum of sample A1, the Si-CH₃ bending vibration is a sharp and intense peak which was very weak in sample A3 (it may have been swamped by other spectral features). The SiH stretching band is clear in this spectrum. Figure 5.10 shows some noise around 1400 - 1500 cm⁻¹, so those peak at 1407 cm⁻¹, 1455 cm⁻¹ are not distinguished here.

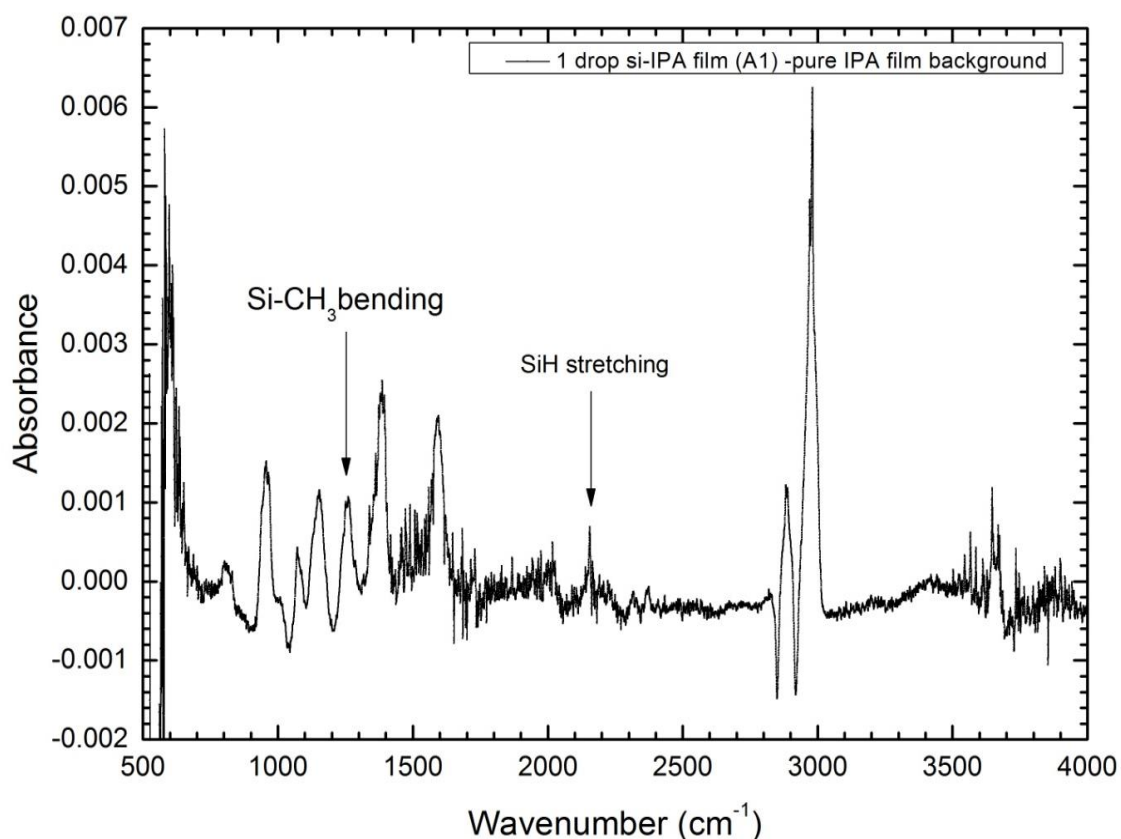


Figure 5-10. ATR spectrum of Si-IPA film, sample A1. This sample has all the peaks which were seen in sample A3, and in addition it has a peak characteristic of the Si-CH₃ bending vibration at 1260 cm⁻¹.

To compare these samples for similarities and also to distinguish between samples and pure solvent bands, sample A3, pure isopropanol film, and sample A1 are plotted in the same scale in Figure 5-11, a film of one 5 μl drop for each was used in this experiment. As spectra are plotted on same scale, we can conclude the features belong to silicon species and not IPA; on the other hand, we might not be able to detect IPA features in pure IPA film, as pure IPA might evaporate completely, so samples compared with liquid samples (which are the same as liquid pure IPA) in the following.

In appendix 5, all silicon samples which are produced in isopropanol have been plotted together to give a perspective on the similarity of the samples in the same solvent. All the samples show the silicon species peak, although the intensities are different. Some samples show negative bands for atmospheric gas. A difficulty of ATR measurements of our sample is the low concentration of the sample in the film samples. In addition to the film, samples were measured in the liquid phase, but absorption was very high so distinguishing between the samples and pure IPA was not possible, with samples showing essentially the same behaviour as the pure IPA.

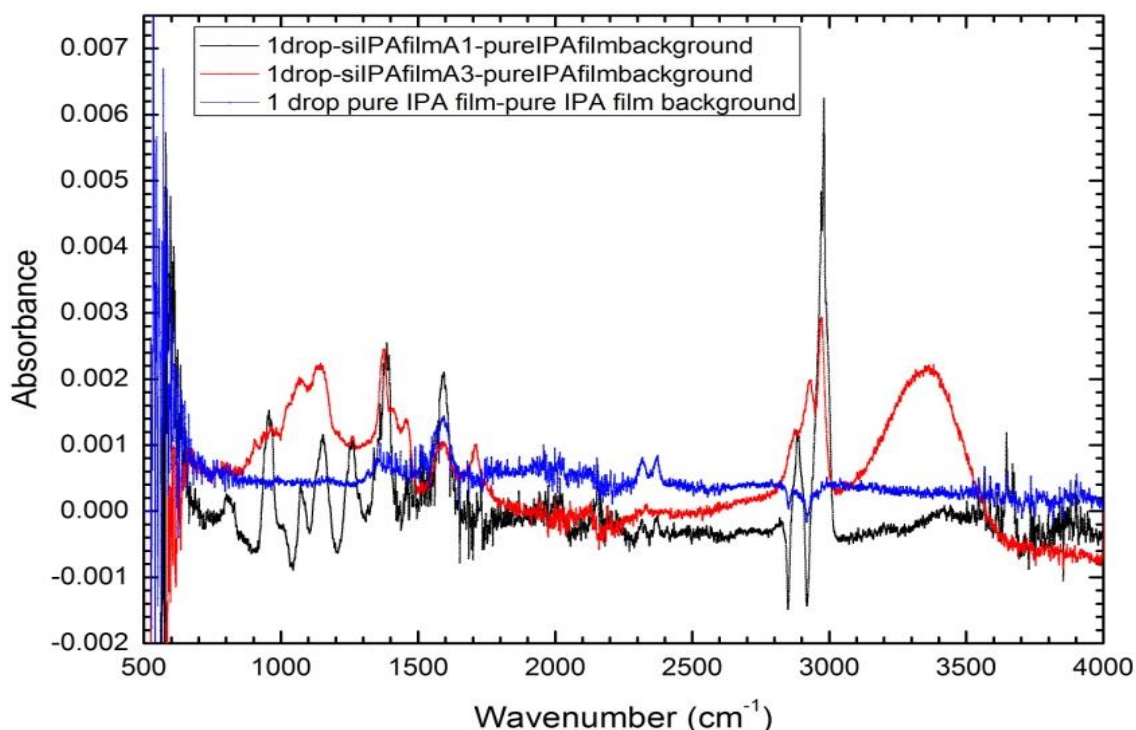


Figure 5-11. The ATR spectra of sample A1, sample A3, and pure IPA are compared. The peaks related to silicon species are clear when these data are plotted on same scale with pure isopropanol.

Liquid and film spectra of samples A1 and A3 in IPA are compared in Figure 5-12. Sample A3 shows almost similar features in both liquid and film spectra but with different intensities and with the exception of the vibrational bands at 1580 cm^{-1} , 1710 cm^{-1} , 1261 cm^{-1} , 1077 cm^{-1} , attributed to the OH bending, C=O stretch, Si-CH₃ bending and SiO stretch vibrations, respectively. As experiments were performed in atmosphere, OH bending features can be seen in the film spectra, although the liquid samples were measured in the same situation, the thickness of liquid samples was higher than $2\text{ }\mu\text{m}$, so the signal due to atmosphere is weak, although we should see OH bending features of IPA. The peak at 960 cm^{-1} (Si-OH) in film samples show slightly shifted and broader than liquid samples, this peak is a different band from pure IPA and attributed to silicon-oxygen species (as we did) or it may be due to an IPA feature which is shifted due to interaction with silicon particles. The two peaks at 798 cm^{-1} and 1407 cm^{-1} have very low intensities when compared with the equivalent liquid sample in same scale so these peaks are not clear, although they can be seen in the spectrum in Figure 5-8. The peak at 798 cm^{-1} is broad and could be the superposition of an Si-C (or Si-O) band and an IPA band (at 810 cm^{-1}). In sample A1, the same was observed for the OH bending vibrations, and the Si-CH₃ bending vibration at 1261 cm^{-1} could be seen in the film sample when it was not observed in the liquid phase. The band at 1077 cm^{-1} which attributed to SiO, which is slightly shifted with respect to the IPA band at 1100 cm^{-1} , so again it could be an SiO band or an IPA band which is shifted due to interaction with silicon particles. The bands which are belong to silicon compounds show silicon interacted with the solvent but, after evaporation, not all the solvent has been driven off as they can still be detected in ATR, albeit to some lesser degree.

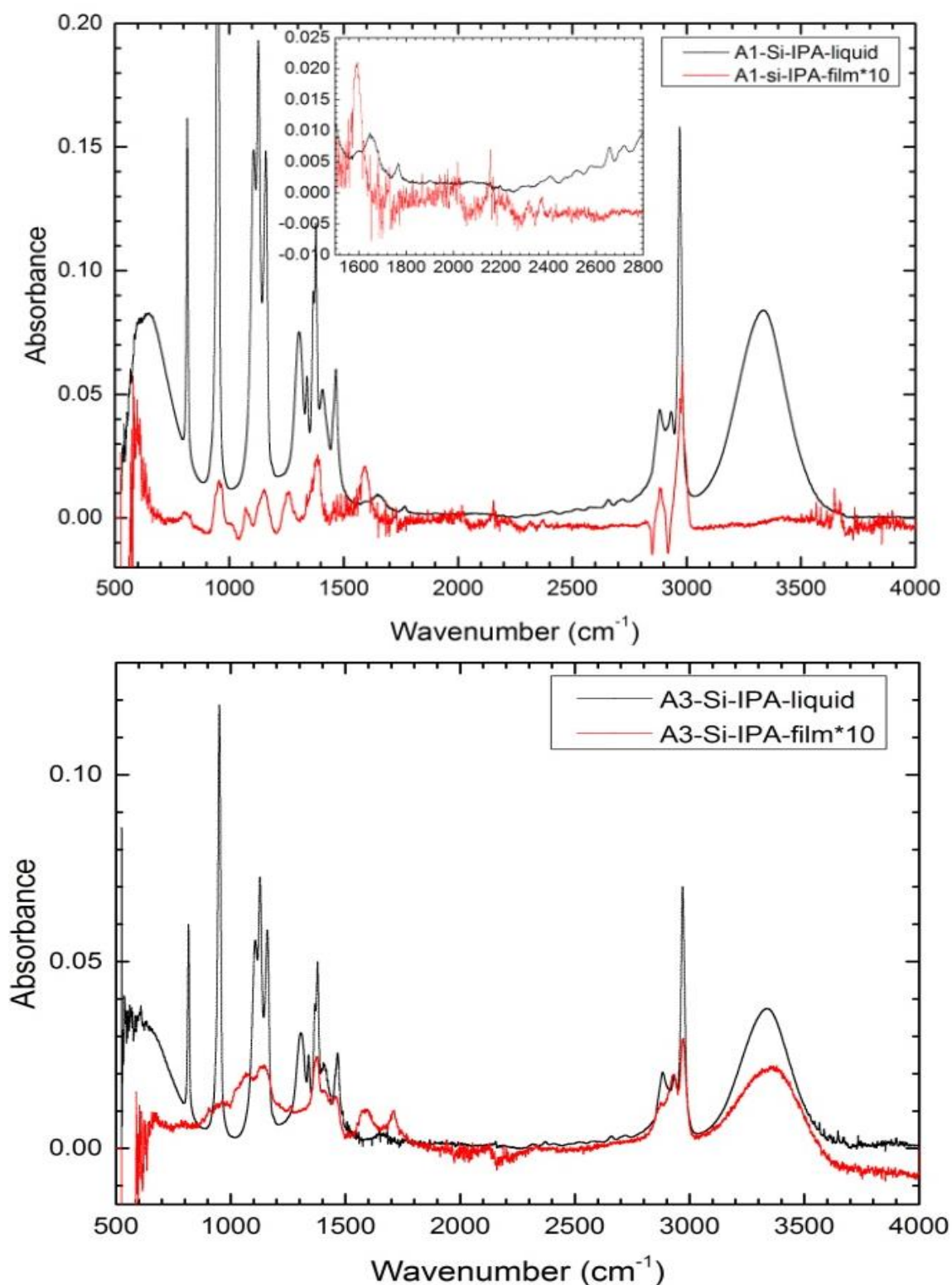


Figure 5-12. In this figure, film and liquid phase samples are compared; shown are sample A3 (bottom) and sample A1 (top).

The solvent in film sample could not be dried completely due to solvent bonding with silicon and trapping on the cluster.

5.2.1.2 Absorbance spectra of Si-ethanol samples using ATR spectroscopy

The same experiments as above were performed for pure ethanol and silicon deposited in ethanol samples.

To investigate silicon directly deposited in ethanol samples, spectra of all Si-ethanol samples were recorded and two samples were chosen for our discussion herein. Sample A6 is an exceptional sample, showing much higher absorbance than the other samples (see Figure 5-13). This sample was a yellow sample with a precipitant produced with a high power setting for the magnetron sputtering (100 W); for the other samples, the power was set between 40 W and 75 W, as described in chapter 2; the samples produced using lower powers are clear. Yellow samples had very low fluorescence intensities, lower than 1500 cps, whilst clear samples showed intense fluorescence above 15000 cps. As a normal sample, the spectrum of a Si-ethanol film formed from sample D5 is shown in Figure 5-15. To compare these two samples, and also with pure ethanol, all three spectra were plotted on the same scale (Figure 5-16). As sample A6 had some precipitate, it was shaken before the experiment.

Figure 5-14 shows increasing the peak intensity with increasing film thickness. When the thickness was increased, the bands became sharper and more distinguishable; for example, the absorbance of the band at 900 cm^{-1} was very low for the few first layers, but became very sharp and clear for the film with ten layers. The intensity of peaks increases with increasing the thickness of the samples, and the relationship between increasing intensity and thickness is linear. The data at 2500 cm^{-1} were used as baseline.

ATR spectra of Si-ethanol samples shows the following features: Si-OH bend at 900 cm^{-1} , CO stretch at 1054 cm^{-1} , SiO stretch at 1095 cm^{-1} , CH bend at 1379 cm^{-1} , C-O-H bend at 1436 cm^{-1} , OH bend at 1549 cm^{-1} , SiH stretch at 2196 cm^{-1} (this peak may belong to O-Si-H as references show both bands at the same vibrational frequency), CO_2 stretch at 2349 cm^{-1} , CH stretch at 2870 cm^{-1} , CH_2 stretch at 2945 cm^{-1} , CH_3 stretch at 2970 cm^{-1} , and OH stretch at 3356 cm^{-1} . Like the Si-IPA samples, the spectra show vibrational features belonging to silicon interacting with ethanol. As mentioned above, sample A6 was a yellow sample with high absorbance, but most of samples produced in ethanol were clear with high fluorescence and low IR absorbance.

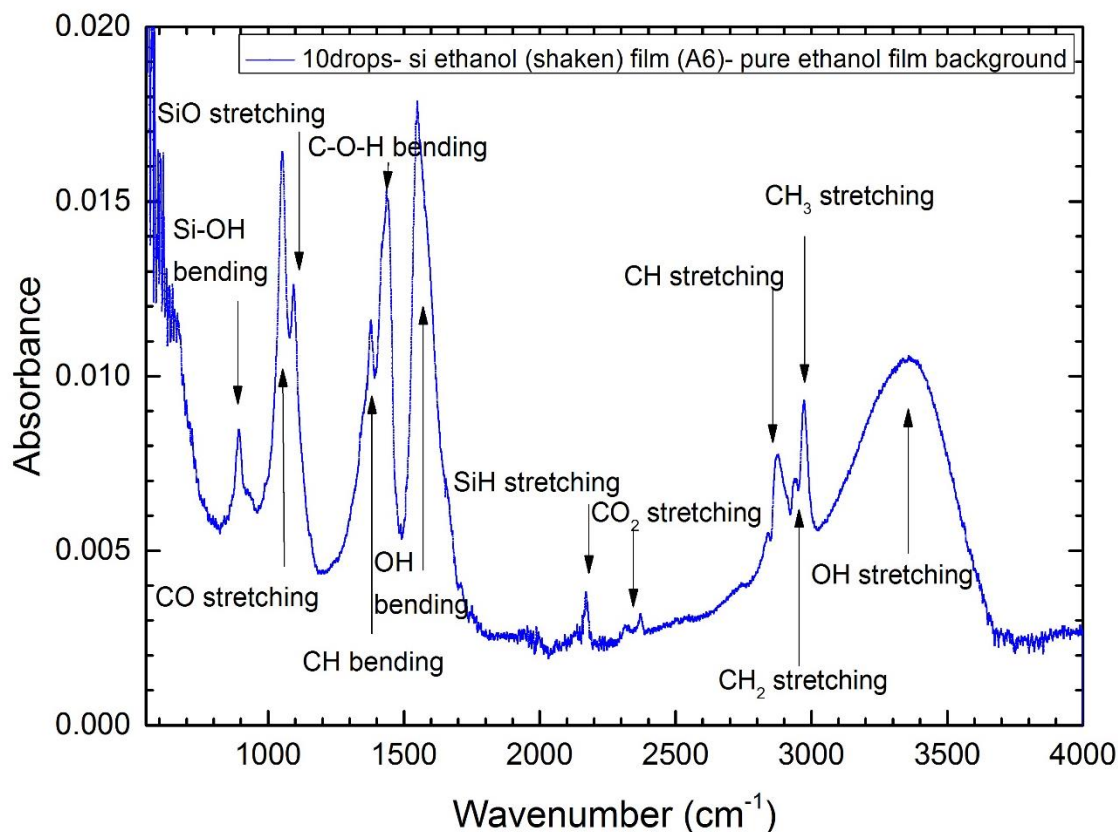


Figure 5-13. ATR spectrum of Si-ethanol film sample. The spectrum shows SiO, SiOH, and SiH bands which are due to silicon bonding with ethanol molecules (cluster-solvent interaction).

Most of the bands in Figure 5-15 are the same as sample A6 in Figure 5-13, but the intensity has been reduced to one tenth. In this sample, the Si-OH band at 900 cm^{-1} is very weak. The bands from 1330 cm^{-1} to 1430 cm^{-1} are in a very noisy region of the spectrum and furthermore cannot be individually distinguished, the broad band observed in this region may be a superposition of CH, C-O-H and Si-CH₃ vibrational features. Increasing the thickness for this sample show some deviation due to very low intensity, the CO₂ doublet band is sharper for some spectra but is not clear in several other spectra. In spite of this variation, the results show the absorbance is increased with increasing thickness, but it is not as linear as sample A6 showed (it is similar to Si-IPA sample A3). C-H bands at $2850\text{-}2980\text{ cm}^{-1}$ are negative due to background subtracting.

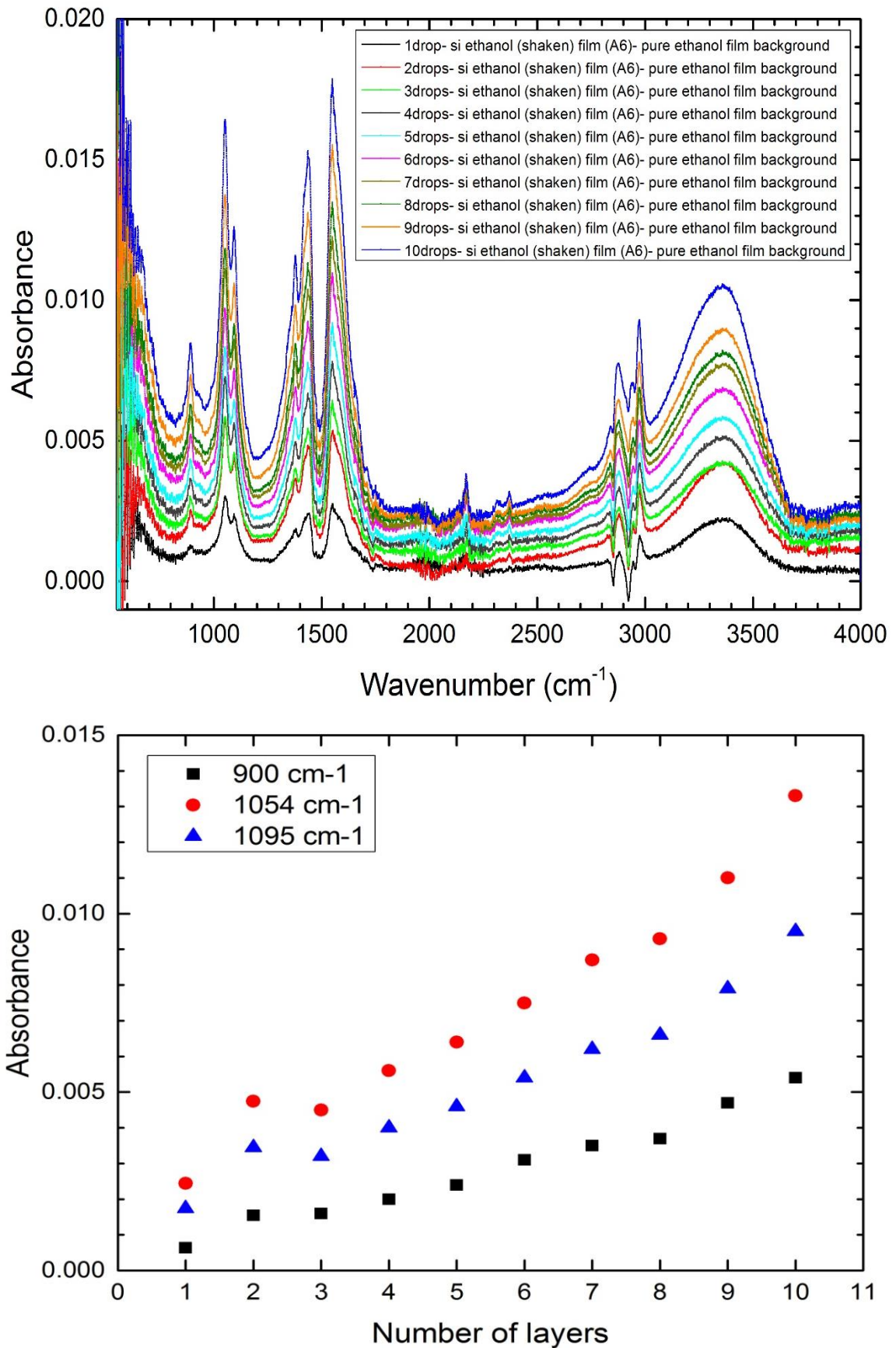


Figure 5-14. Affect on absorbance of increasing the film thickness of Si-ethanol sample A6.

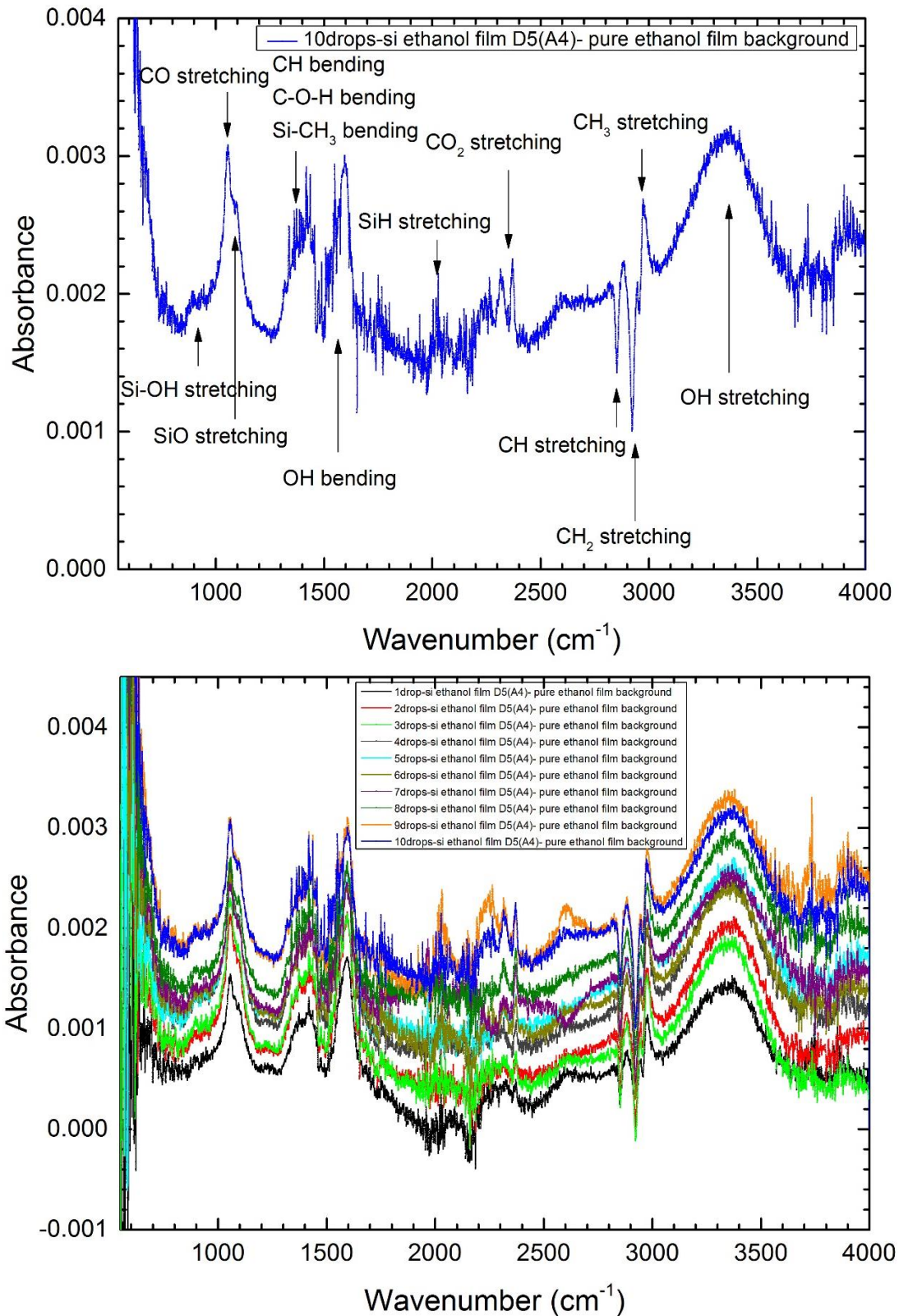


Figure 5-15. Absorbance of Si-ethanol with ten layers film, sample D5, (top) and increasing the thickness of the film from one layer to ten layers (bottom).

The samples A6 and D5 and film made from pure ethanol are compared in Figure 5-16.

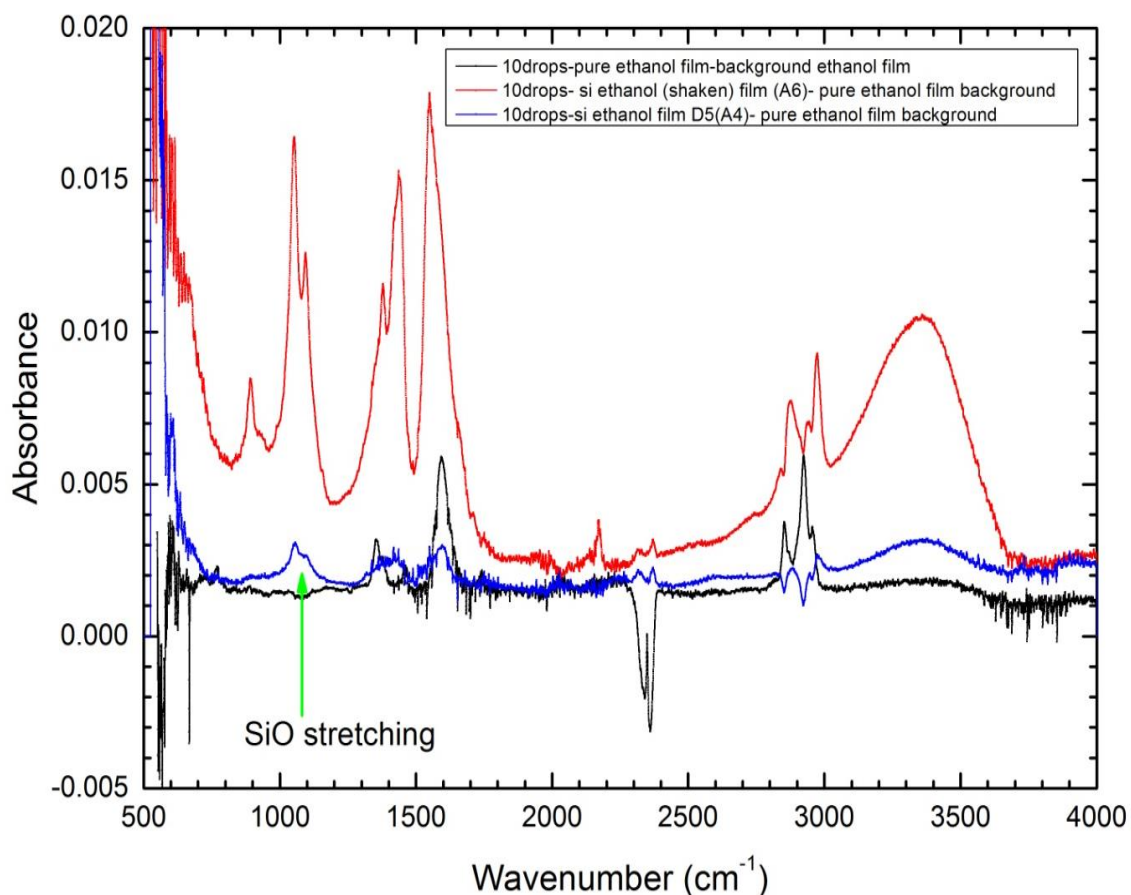


Figure 5-16. Comparison between Si-ethanol films samples A6 and D5, and pure ethanol film. As can be seen, the intensity of the sample A6 ATR spectrum is much higher than D5, but the SiO band, as indicated by the green arrow, is clear in the ATR spectrum of sample D5.

ATR spectra of samples of silicon deposited on ethanol confirm silicon bonding with the solvent molecule, the associated spectra showing features belonging to these bonds which are not observed in pure ethanol film spectrum. The peak at 1054 cm⁻¹, which could be attributed to the C-O stretching vibration, does not exist in pure ethanol film, so it may as well belong to the Si-O stretching mode, as the two are very close in vibrational frequency. Another possibility is that, on evaporating the solvent, the bond between some ethanol molecules and silicon clusters was not broken, a few solvent molecules being trapped on the cluster surfaces, so the feature associated with ethanol molecules can be observed in our spectra, whilst in the case of pure ethanol, the solvent evaporated completely, so this band is absent in the associated [film] absorbance spectra.

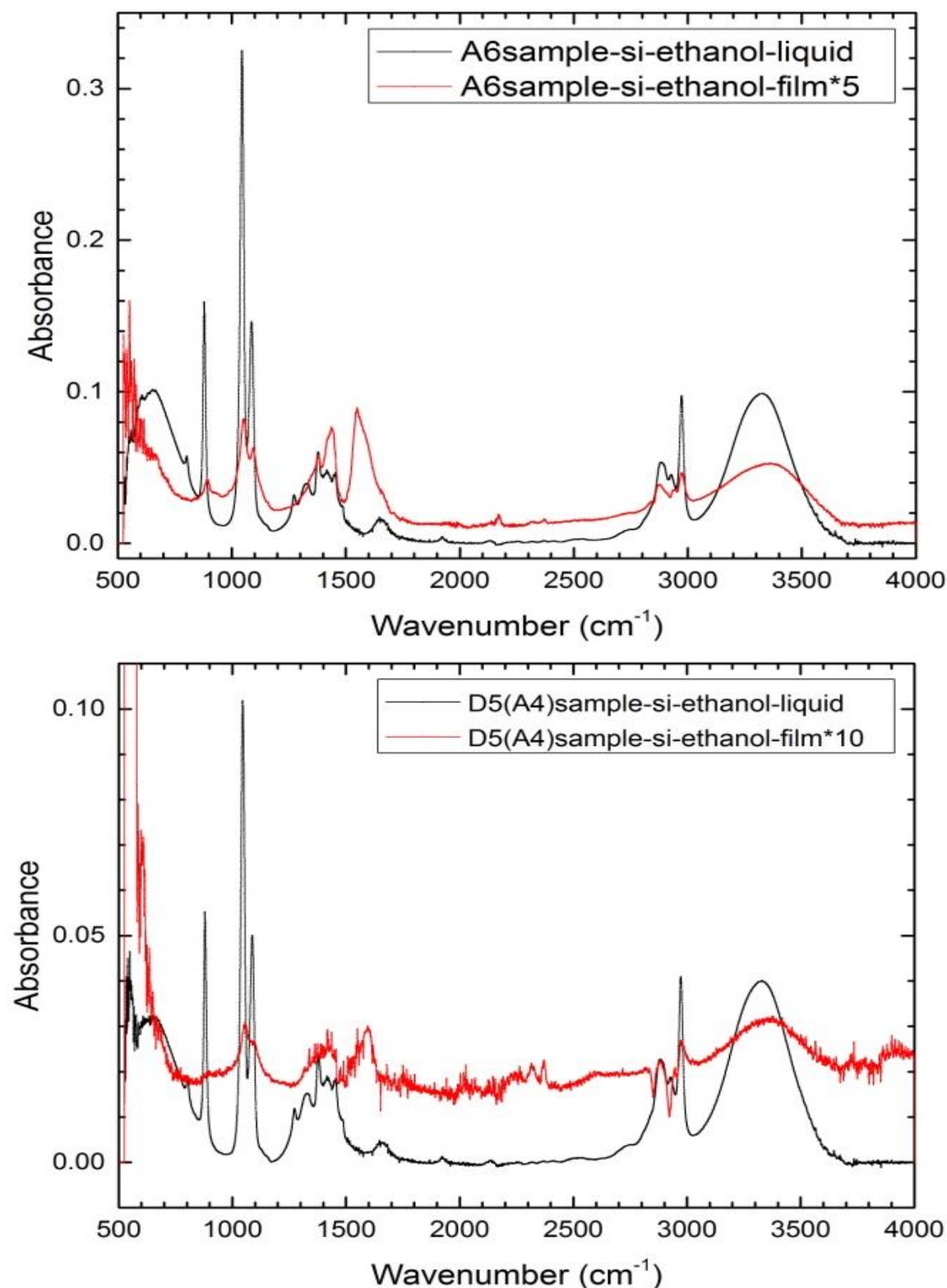


Figure 5-17. Film and liquid Si-ethanol samples A6 (top) and D5 (bottom) are compared.

An overview of all film samples is shown in appendix 5. Measurements for pure liquid ethanol and all samples were performed. As the absorbance was very high in the liquid phase, one could not distinguish between pure solvent and the sample.

Comparison between sample A6 in the liquid phase and film, and also between sample D5 in the liquid phase and film, is shown in Figure 5-17. As absorbance in liquid samples is very high, the spectra are similar to that of pure ethanol; but, whilst the silicon bands are not clear for liquid samples, in film they are easily distinguishable. Although the vibrational frequencies of ethanol molecule bands are very close to those of silicon species, we can recognize those of silicon because they are broader (as silicon particles are solid), whilst ethanol features are sharp. The SiO bands at 1095 cm^{-1} for both film samples are broader and slightly shifted to higher vibrational frequency; the same is observed for the Si-OH band at 900 cm^{-1} for sample A6. Also, the SiH band at 2196 cm^{-1} , which exists in sample A6 (although it is very weak), is absent in pure ethanol.

5.2.1.3 Absorbance spectra of Si-water sample using ATR spectroscopy

The same experiments as above have been performed for pure water and silicon deposited on water. The experiment was performed for all water samples and pure water; the results of the two samples are shown here: sample D2, which shows the highest absorbance amongst Si-water samples, and sample C9, which had the highest fluorescence intensity (see section 4.2.3).

Si-water samples were very sensitive to laboratory conditions. As experiments were done in air, any change in humidity or air temperature, or even the air flow, could affect the region from $1400\text{-}1600\text{ cm}^{-1}$, because this region shows CH and OH bands. Existence of too much noise in this region prevents us from being able to distinguish other bands at these vibrational frequencies. Therefore, the measurement for sample D2 was repeated on three different days, particularly because there was a lot of noise evident in the $1400\text{-}1600\text{ cm}^{-1}$ region on the first day. Figure 5-18, Figure 5-19, and Figure 5-20 show ATR results for Si-water film sample D2. As can be seen in Figure 5-19, the noise is lower, though the silicon features were clearer and sharper in the previous measurement.

As can be seen in Figure 5-18, the intensity of the features in the Si-water sample is much higher than for alcoholic samples. There are several vibrations belonging to silicon bonds with water molecules, and also silicon bonding with carbon shows as carbon in the air interacts with the sample. Also, the triplet bands of CH, CH₂ and CH₃ exist in the spectrum, which may be due to impurities in the water, or exposure of the sample to the air. It also may be due to the roughing pump oil in the air as our pumps in lab are not

vented to the outside. The peak that can be seen in the Figure 5-18 are: SiC stretch at 800 cm^{-1} (though this peak can also be attributed to the SiO_2 bend because its vibrational frequency is almost the same), Si_2O_3 stretch at 880 cm^{-1} , Si-O-Si stretch at 1018 cm^{-1} , SiO stretch at 1096 cm^{-1} , Si- CH_3 symmetric bend at 1262 cm^{-1} , CH bend at 1378 cm^{-1} , OH bend around 1600 cm^{-1} , SiH stretch (composed of several closely-spaced peaks, but which all arise due to SiH) around 2156 cm^{-1} , CO_2 doublet bands at $2317\text{-}2366\text{ cm}^{-1}$, CH, CH_2 , CH_3 bands (which are not distinct in this sample) with their origin at 2950 cm^{-1} , and the OH stretch with a maximum at 3356 cm^{-1} . By increasing the thickness of the film, two bands at 1018 cm^{-1} and 1096 cm^{-1} became broader, and a shoulder appeared at 1177 cm^{-1} , which belongs to SiO_2 or higher oxidation state of silicon (SiO_{2+x}) [81]. Also the band at 1378 cm^{-1} attributed to CH bending more prominent in thick film sample.

Figure 5-19 shows the repeated experiment for this sample. Although the noise around the CH and OH bands is lower than the previous measurements, absorbance is lower for this measurement (we consider signal to noise ratio as the intensity of the peaks).

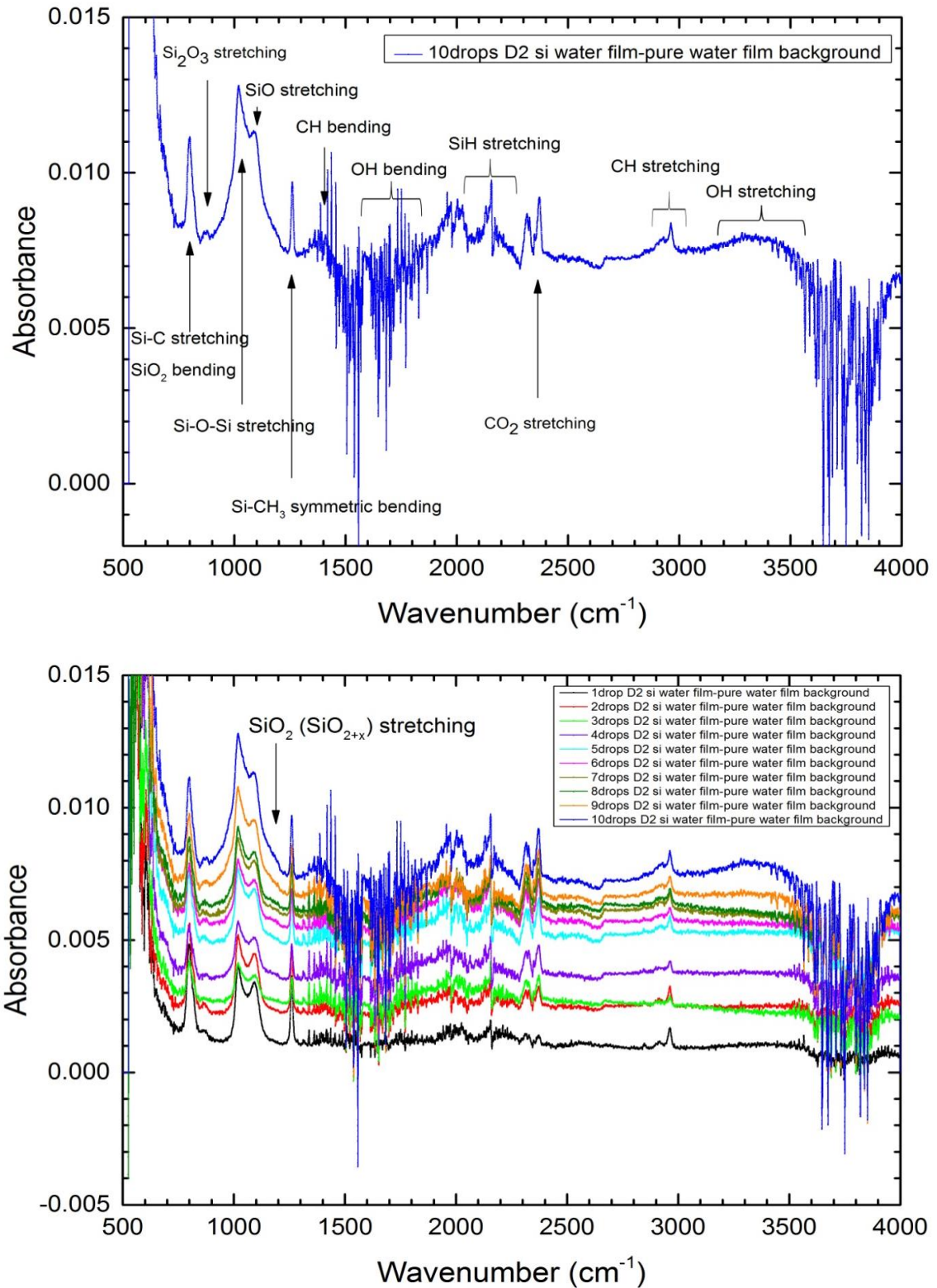


Figure 5-18. Si-water film ATR spectrum of sample D2 (first measurement). Increasing the thickness shows not only the absorbance increased by increasing the thickness, but also the peak around 1100 cm^{-1} became broader and a shoulder at 1177 cm^{-1} arose, which belongs to an SiO_2 (or SiO_{2+x}) vibration.

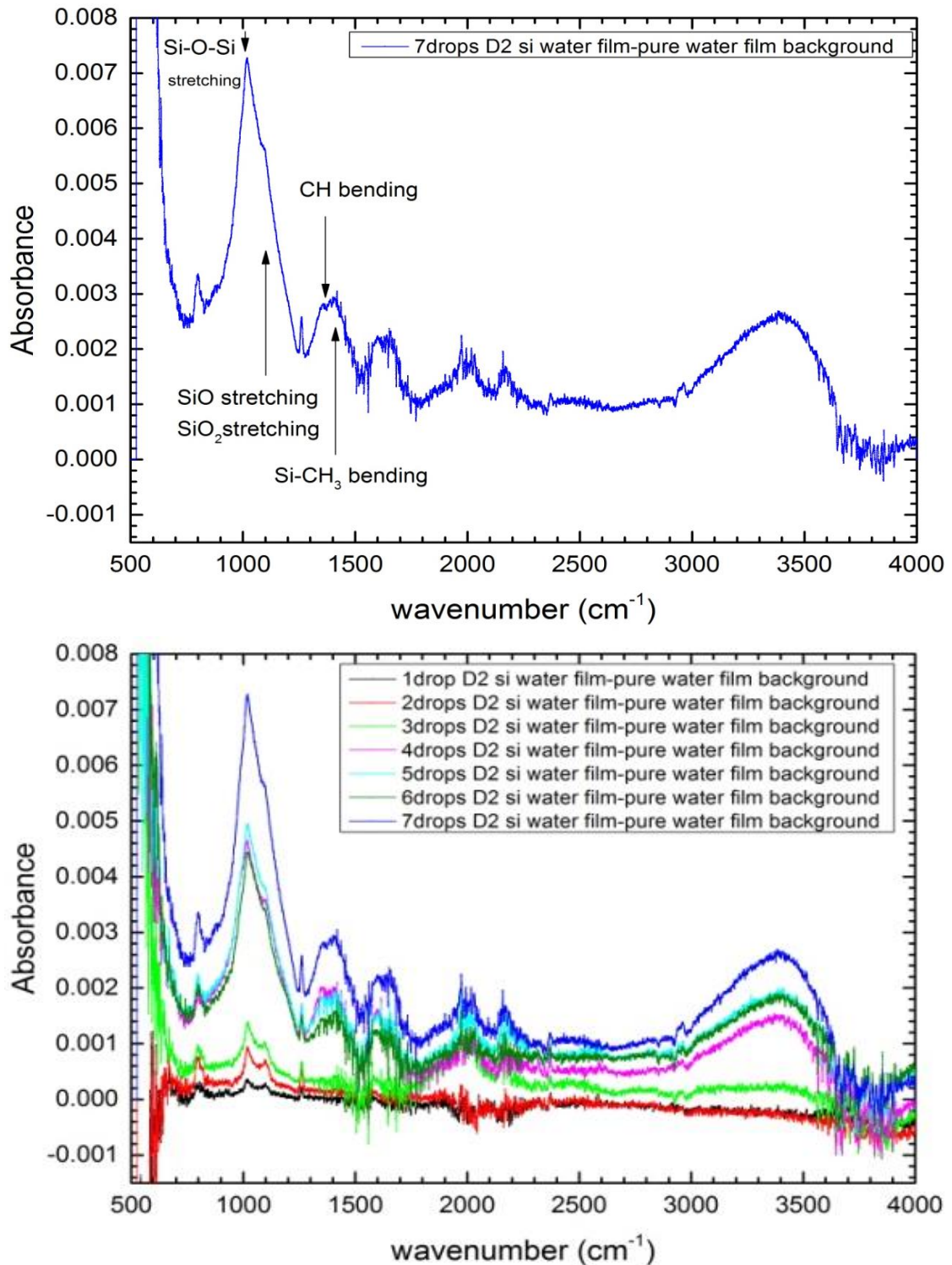


Figure 5-19. ATR spectrum of Si-water film from sample D2 with less noise (top). Effect of the thickness of the film on the ATR spectrum is depicted in this figure (bottom).

There is a broad band in the fingerprint region composed of several bands whose vibrational frequencies match with Si-O-Si, SiO and SiO₂ stretching vibrations. In the water sample, a very low intensity, broad band can be seen around 1900 - 2000 cm^{-1} . This

band may consist of another group of SiH stretching bands followed by SiH stretching bands around 2160 cm^{-1} ; however, this wavenumber may be related to the C=C stretch, so in this case our water sample may just have carbon impurities. The other bands are the same as for the previous measurement.

Although the intensity increased by adding layers, the peaks in the fingerprint region became broader in both experiments and overlapped, making it difficult to distinguish even two separate bands at 1018 cm^{-1} and 1096 cm^{-1} , peaks which were completely separate when the film had a thickness of one to three layers. Although they were clearer in the spectrum recorded with three layers of sample, their intensity was very low. The signal to noise ratio increases with increasing thickness. The OH stretching vibration at 3400 cm^{-1} arose by adding layers. The features of SiH bands around 2150 cm^{-1} were not observed for the first three layers; by increasing the thickness the intensity of these peaks increased.

The experiment for this sample was repeated for a third time. In the third measurement, the intensity was higher and the bands were very broad, as shown in Figure 5-20. Although increasing the thickness increased peak intensity, noise also increased for this sample (Figure 5-21). As the thickness was increased the peak at 1130 cm^{-1} (which is related to SiO_2) could be observed, but at same time some peaks (like the sharp peak at 1660 cm^{-1} attributed to the C=C stretch vibration) disappeared because the baseline increased as well; furthermore, peaks were always broader with more Si-water layers, preventing us from distinguishing small bands. To see peaks present in thin sample layers and then not clear in thick sample layers, the ATR spectrum for a sample with two layers was recorded as well, in shown in Figure 5-20; this shows the SiO peak at 1059 cm^{-1} , a new peak at 1660 cm^{-1} (this could be a C=C stretch vibration), and some small and sharp peaks around $2700 - 2800\text{ cm}^{-1}$, which are related to CH stretches.

The features observed in this sample are: Si-Si vibration at 606 cm^{-1} , OH out-of-plane bend at 766 cm^{-1} , SiH_2 wag at 830 cm^{-1} , Si-O-Si stretch at 1014 cm^{-1} , SiO stretch at 1059 cm^{-1} , SiO_2 stretch at 1130 cm^{-1} , CH bend at 1353 cm^{-1} , OH bend at 1600 cm^{-1} , the CO_2 doublet bands at 2363 cm^{-1} , CH stretch around $2700 - 2900\text{ cm}^{-1}$, and the OH stretch at 3390 cm^{-1} .

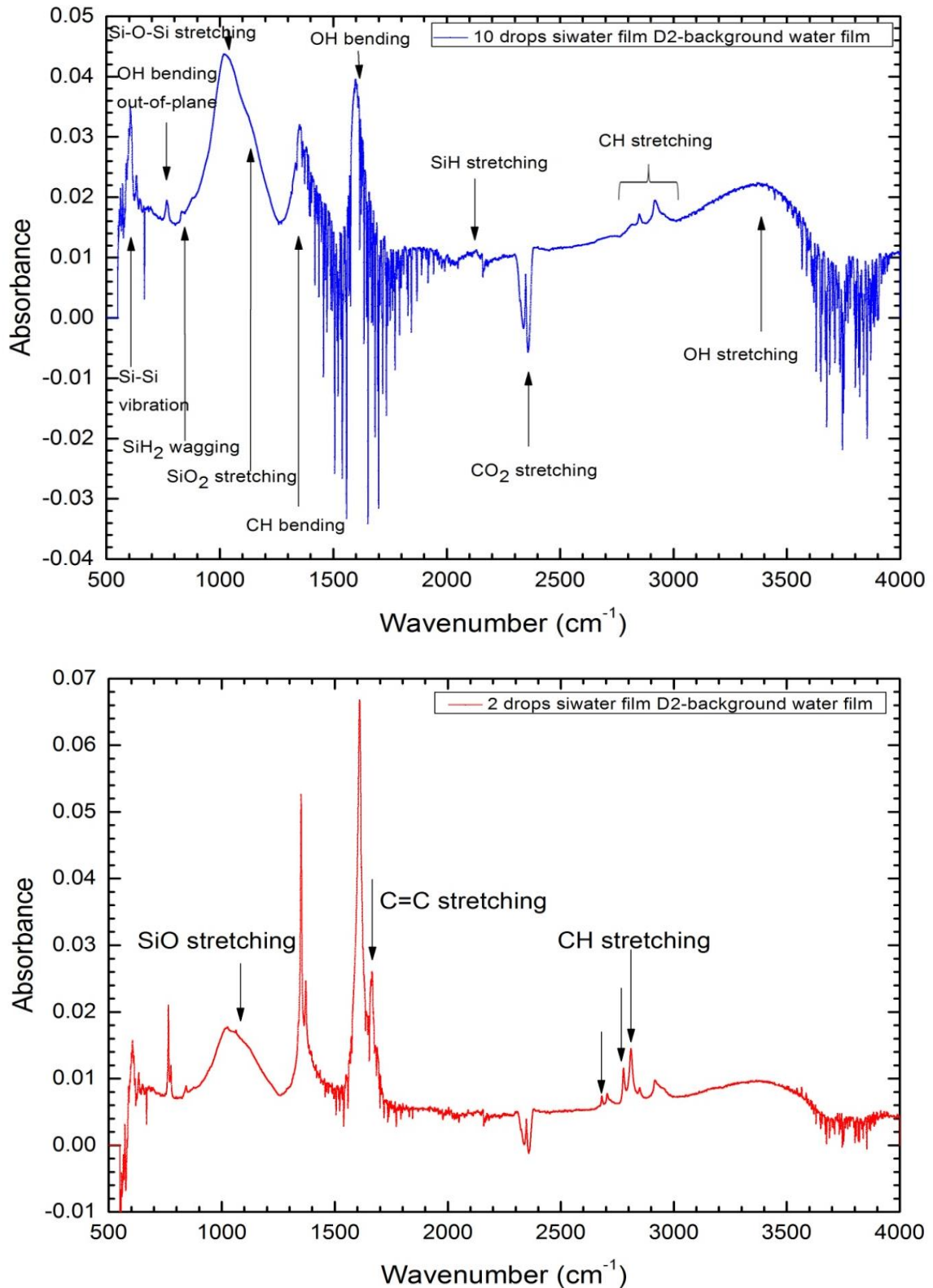


Figure 5-20. Third measurement for sample D2. The intensity is very high and the position of the peaks identical to those in previous measurements; however, peaks are broader in this measurement, and the peaks at 1014 cm^{-1} - 1130 cm^{-1} have overlapped. Some features detected for thin sample layers could not be observed for thicker sample layers.

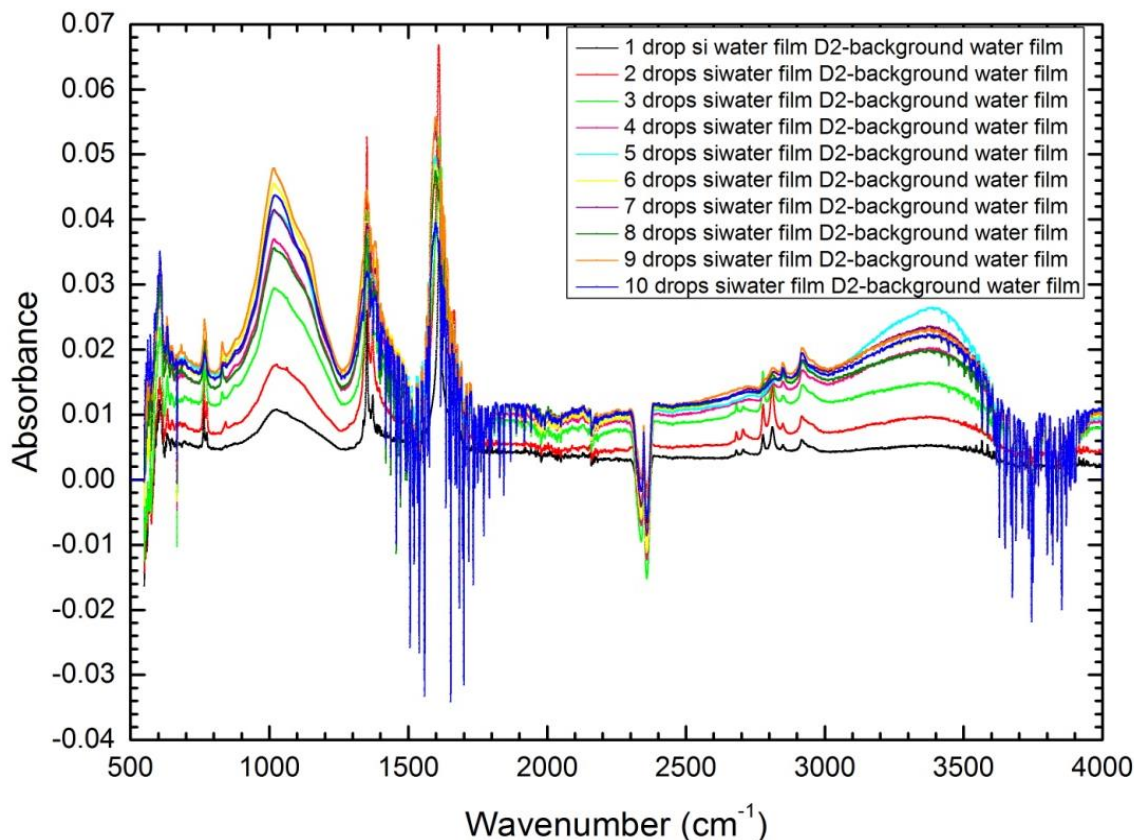


Figure 5-21. Effect of thickness for Si-water film for sample D2 (in third measurement) is shown. By increasing the thickness, the intensity of the bands is increased, which shows an emerging band at 1130 cm^{-1} ; however, broadening the bands leads to deconvolution difficulties and the actual disappearance of some smaller features.

As this sample had high intensity, we could detect a new peak at 606 cm^{-1} which was attributed to an Si-Si vibration in the bulk, helping to confirm our hypothesis regarding bulk and surface clusters. This peak should exist in all samples but other sample had very low absorbance so this peak was not clear. Although, we cannot be confident about this region assignment due to the limitations of detector and crystal cut off in this region.

The intensity of two bands at 1014 cm^{-1} and 1130 cm^{-1} is high but also very broad, making them difficult to distinguish, so another sample (C9, Si-water) was investigated, the spectrum of which is shown in Figure 5-22 in order to show these two bands more clearly, which in this sample are separated. In addition to these bands, this sample has another peak which may be attributed to higher oxidation states of silicon (SiO_{2+x}) or the SiO_2 stretch at 1176 cm^{-1} . Also, there is another peak at 1290 cm^{-1} detected only in thickness film up to five layers, and then swamped in the thick film. This band may

attribute to SiO_3 [81]. These two peaks at 1176 cm^{-1} and 1290 cm^{-1} are the new peaks. Sample C9 is the sample with the highest fluorescence, which might be proof that the fluorescence at 420 - 440 nm comes from such highly oxidized samples. When the sample was not too thick, four separated bands can be seen in the fingerprint region by increasing the thickness of the film; as usual, intensity increased and peaks became broader, so these four peaks convolve to two. Sample C9 does not show the two peaks at 800 cm^{-1} and 830 cm^{-1} , but it has an additional peak at 918 cm^{-1} , attributed to the SiH_2 scissor vibration. Sample C9's ATR spectra are shown in Figure 5-22 and Figure 5-23.

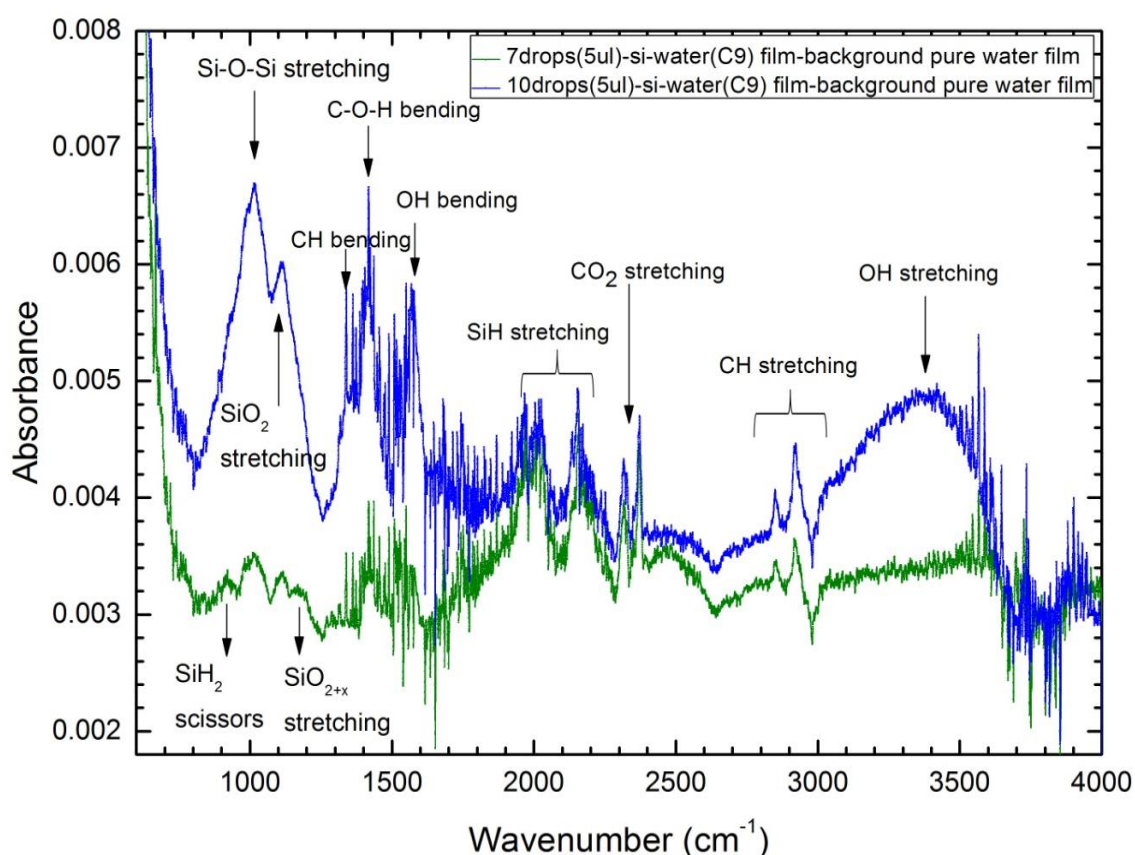


Figure 5-22. ATR spectrum of Si-water film, sample C9. The blue spectrum shows sample measurement after putting on the tenth layer. The intensity of the peak is high enough for silicon compounds bands, but for Si-water samples, even though the intensity is high for such a thick sample, broadening prevents us distinguishing the peaks. For this reason, the sample with seven layers of thickness is shown (green spectrum); although the intensity is lower in this spectrum, it is obvious that there are four silicon-water related peaks, which are SiH_2 scissors at 918 cm^{-1} , Si-O-Si stretch at 1015 cm^{-1} , SiO_2 stretch at 1117 cm^{-1} , and the SiO_{2+x} (or SiO_2) stretch at 1176 cm^{-1} .

The peaks which exist in the ATR spectrum of Si-water film sample C9 are: SiH₂ scissors at 918 cm⁻¹, Si-O-Si stretch at 1015 cm⁻¹, SiO₂ stretch at 1117 cm⁻¹, SiO_{2+x} (or SiO₂) stretch at 1176 cm⁻¹, SiO₃ stretch at 1290 cm⁻¹ (can be seen in first five layers), CH bend at 1348 cm⁻¹, C-O-H bend at 1424 cm⁻¹, OH bend at 1570 cm⁻¹, SiH stretch around 1970 - 2180 cm⁻¹ (the bands around 1970 - 2000 cm⁻¹ may consist of C=C stretching bands as well due to impurities), CO₂ doublet stretch at 2327 - 2371 cm⁻¹, CH stretch at 2850-2970 cm⁻¹ (the third band belonging to CH₃ is negative here), and the OH stretch at 3380 cm⁻¹. This sample shows silicon species bonding in a different oxidation state through clear and distinct spectral features. The peak at 1176 cm⁻¹, with a higher oxidation state (SiO_{2+x}) is a new peak, which is only observed in this Si-water sample. The silicon oxide bond (Si-O-Si) is the same bond shown in references [240, 243], and also the SiO₂ bond is the same as that mentioned in references [84, 239].

This sample was investigated in different thickness similar to other samples, from one layer to ten layers; see Figure 5-23. The relationship between the intensity of the peaks and increasing the thickness is plotted for the bands at 918 cm⁻¹, 1015 cm⁻¹, 1176 cm⁻¹, the baseline was the data points at 2500 cm⁻¹.

It can be seen in the fingerprint region that four (five for the first five layers) bands convolute to two due to peak broadening, so we may have the band belong to SiO_{2+x} in Si-water, sample D2, as well, as we have seen in the spectrum of the first measurement of sample D2, there was a shoulder at this frequency in the thick film. However, its intensity was very low in thin samples, so it would not be detected and in thick film as would be swamped. The SiO₃ band at 1290 cm⁻¹ did not exist in sample D2 (or any other sample).

These two Si-water samples were compared with pure water in Figure 5-24, to show the peaks belonging to silicon species in the samples.

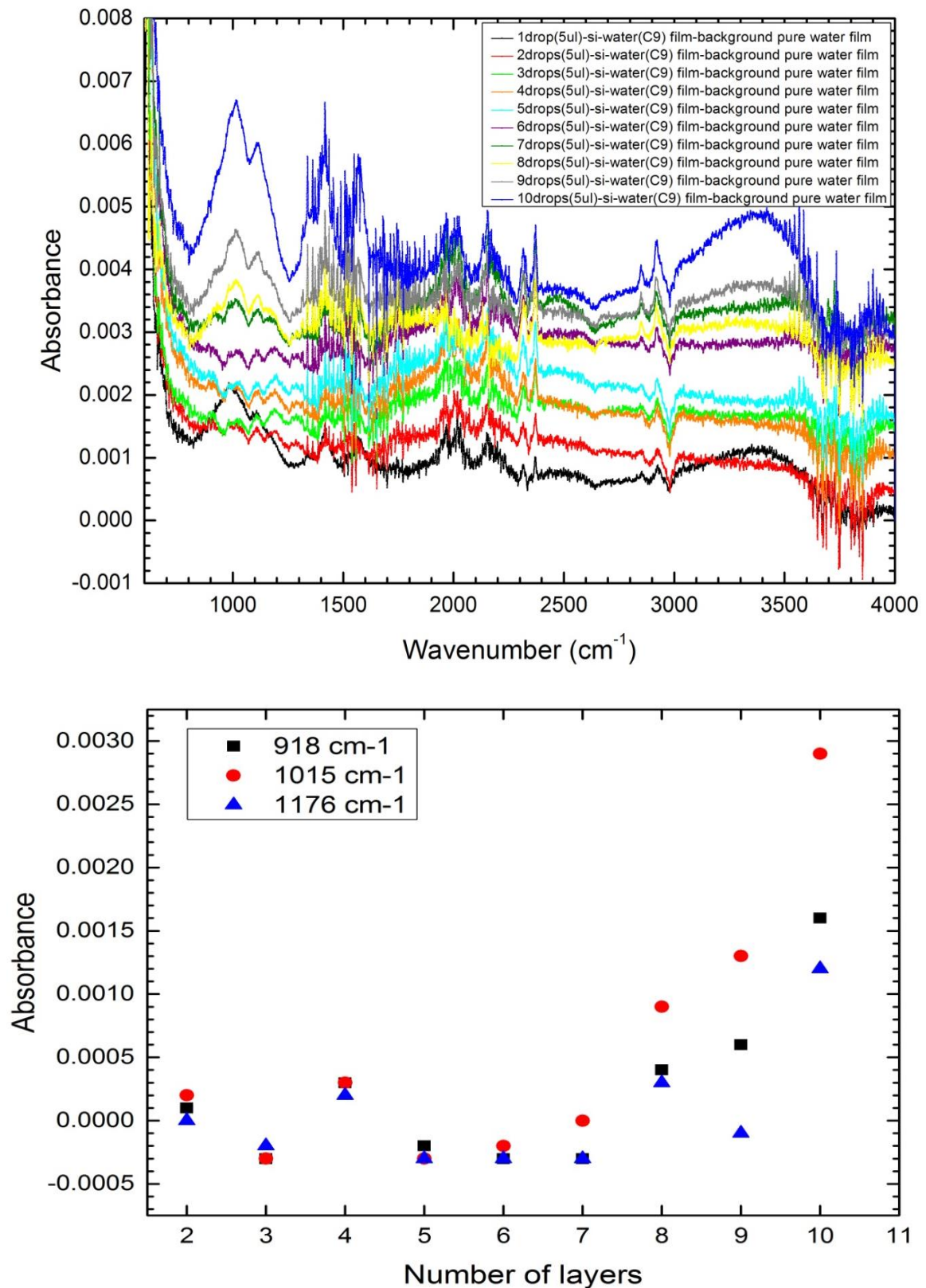


Figure 5-23. Different thicknesses of Si-water, sample C9. By increasing the thickness, the OH stretching band could be observed. Note the conversion of four bands to two bands in fingerprint region.

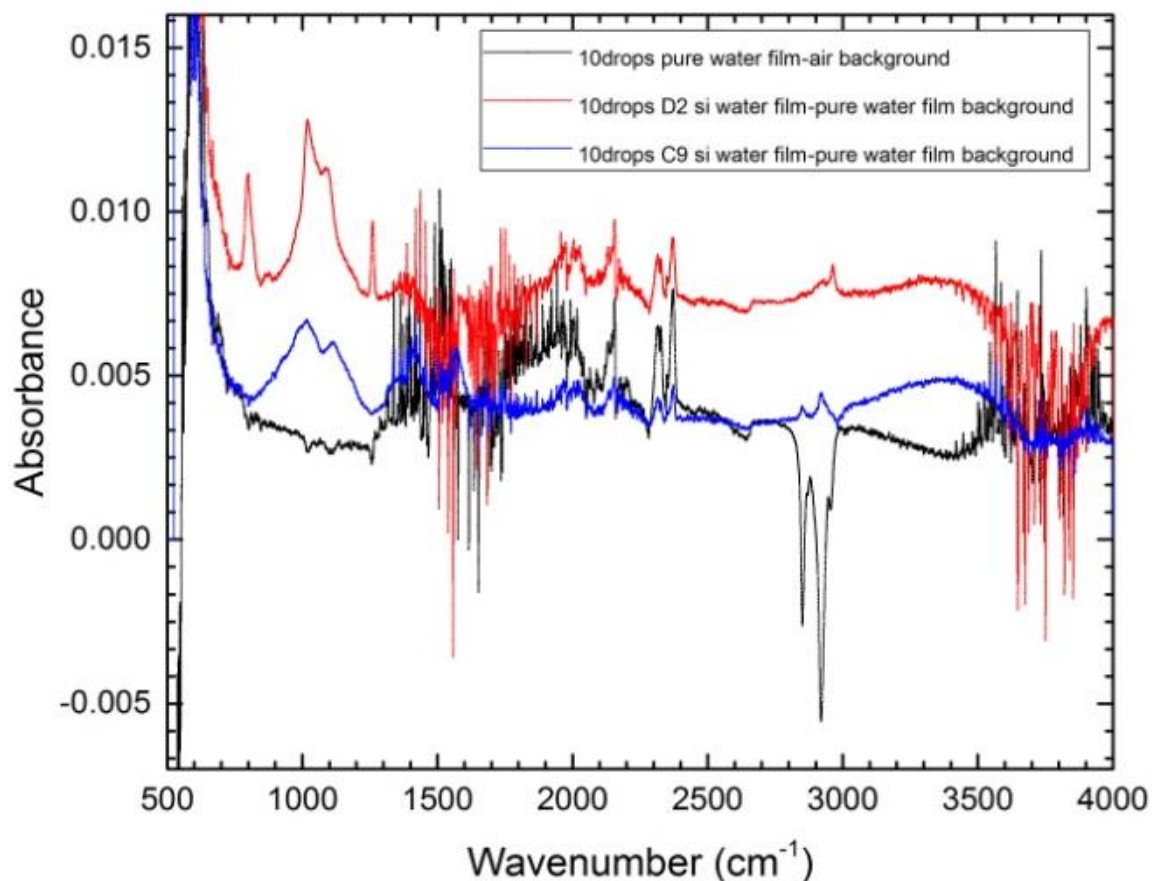


Figure 5-24. Comparison between the ATR spectra of pure water film and those of silicon deposited in water samples. The peaks related to silicon-water species are clear and intense. Pure water has negative signal for the triplet bands around 2900 cm⁻¹ because this band may exist in the background (air), thus subtracting makes it negative in the pure water film.

All Si-water samples show some carbon peaks that show the samples might have some carbon impurities, or might otherwise happen because the experiments were performed in atmosphere. The comparison with pure water confirms the existence of silicon species in our Si-water samples. The background of pure water was air; as water has a high absorbance, we could not subtract a pure water film background, as the sample signal was already swamped.

A comparison between sample C9 and sample C2 Si-water film and liquid phases is shown in Figure 5-25.

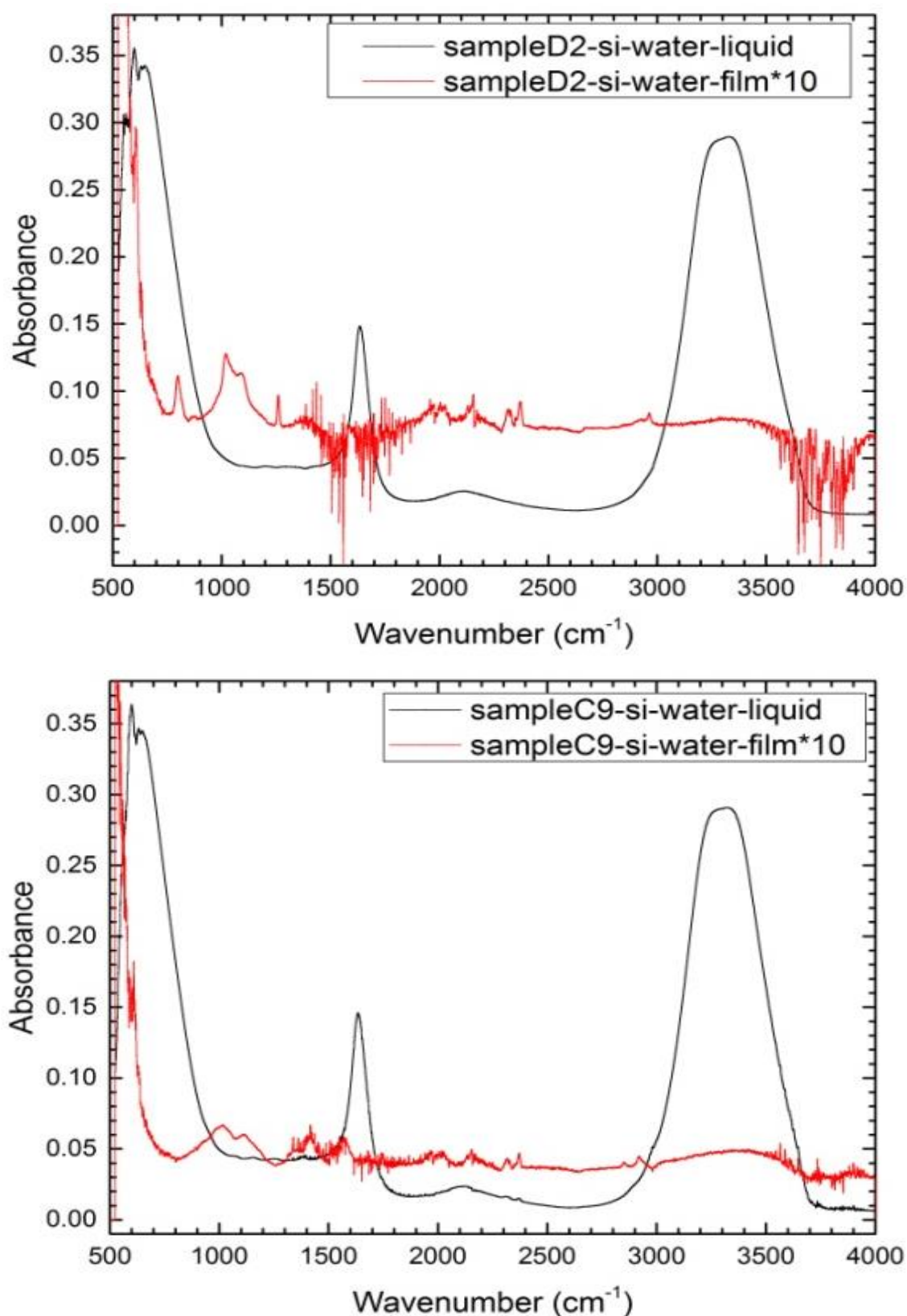


Figure 5-25. Figure showing the comparison of spectra of samples C9 and C2 in film and liquid phases. Bands belong to silicon bonding with water molecules are very clear in the film samples.

Even though the absorbance of liquid samples was very high, making it difficult to distinguish the silicon compound bands, some small silicon-oxygen species peaks can be seen in the fingerprint region.

The variation in volume of each droplet, humidity and also subtracting the background spectrum slightly change the shape, but the position of the peaks which show silicon-oxygen species in the sample are all almost constant, although in different conditions they become broader or sharper, or the intensity differs, but the structure they show is the same. An overview of all Si-water film samples can be found in appendix 5.

5.2.2 Solvent effect on ATR spectrum

To compare ATR measurements of silicon deposited in three different solvents (water, ethanol, and IPA), spectra were plotted in the same scale and are shown in Figure 5-26.

All samples show silicon-oxygen bands, although these bands are different in intensity and oxidation state depending on the samples and solvent used. Si-water has the highest absorbance amongst the samples, suggesting that the amount of silicon which had bonded with oxygen was larger in water than in the alcoholic samples. Also, the ATR spectrum of Si-water sample shows this sample was highly oxidized due to existence of SiO_2 , SiO_{2+x} , and SiO_3 bands. SiH bands which exist in all samples shows silicon particles also interacted with hydrogen. In this case H-passivated/ H-terminated silicon clusters replace surface Si-Si dangling bonds with Si-H bonds; if this happens, it reduces the formation of a surface oxide layer [284].

The results of ATR measurements for silicon deposited in the different solvents are in agreement with the XPS results, as they show the number of bonds between silicon and oxygen is larger in the Si-water sample – due to an intense silicon-oxygen band in XPS, and silicon-oxygen bands in ATR spectra – with respect to alcoholic samples, and also the oxidation state in Si-water sample is higher than that in alcoholic samples, showing that Si-water samples are highly oxidized and confirms the reason behind the greater blue shift in the XPS spectrum of Si-water samples. Also the highly oxidised silicon species in Si-water samples may be the origin of the fluorescence band at 420- 440 nm in emission spectra of Si-water. So, the oxidation state of the silicon species has some considerable dependence on the solvent.

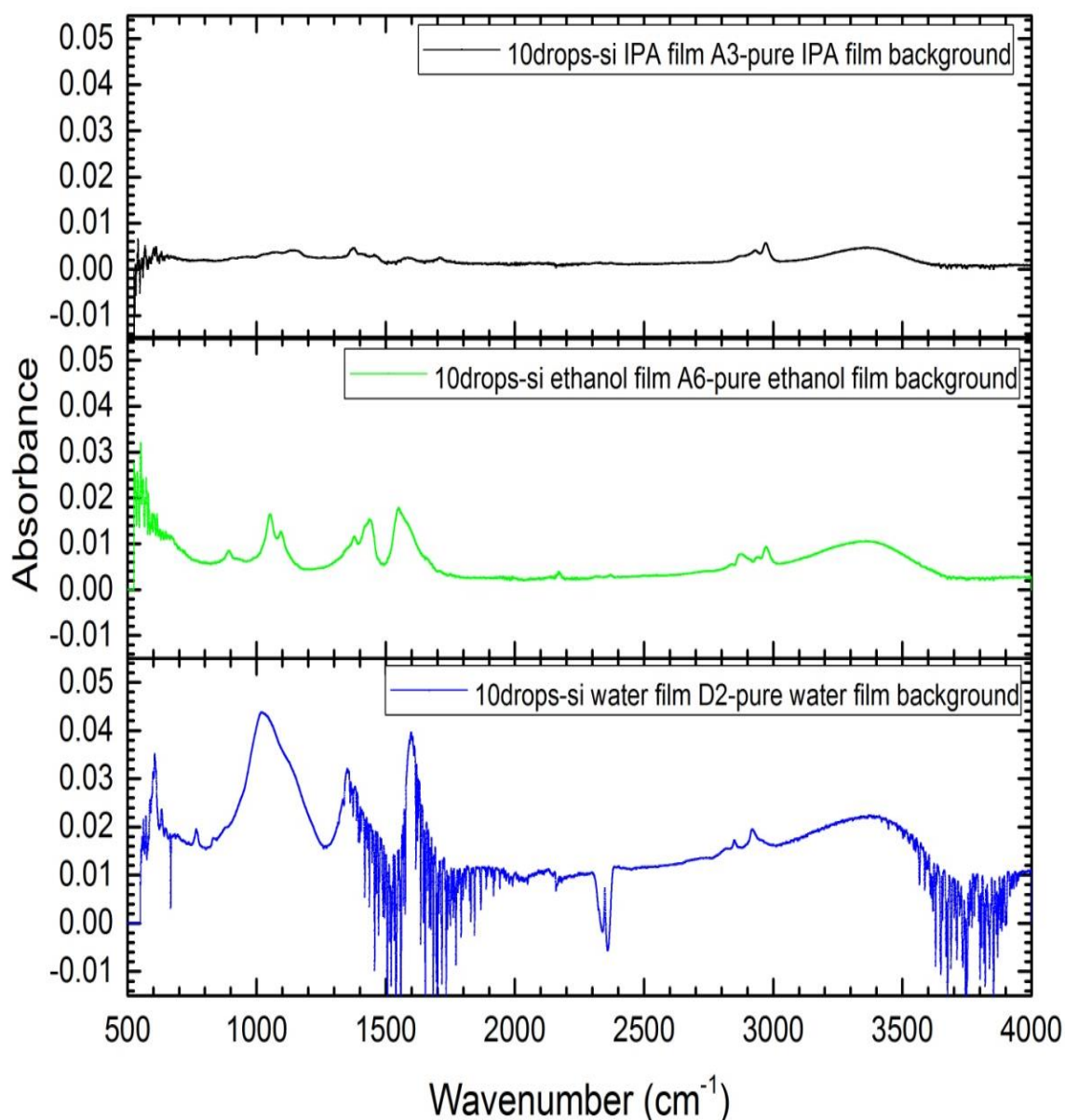


Figure 5-26. ATR spectra of silicon deposited in three different solvents are compared in this figure. The Si-IPA sample has the lowest absorbance and Si-water sample has the highest. As ATR spectra shows the bands and therefore the silicon oxygen species exist in samples as well as their intensity depend on the solvent.

To compare the bands which exist in different solvents, silicon deposited in three different solvents were plotted together without scaling in Figure 5-27. As the intensity is not important in this plot, we show the spectra of thin samples to see the distinct peaks. They show similar frequencies for silicon-oxygen species and SiH bands, but alcoholic samples show a Si-C band which is absent in Si-water samples, and Si-water samples have bands attributed to highly oxidised silicon that do not exist in alcoholic samples.

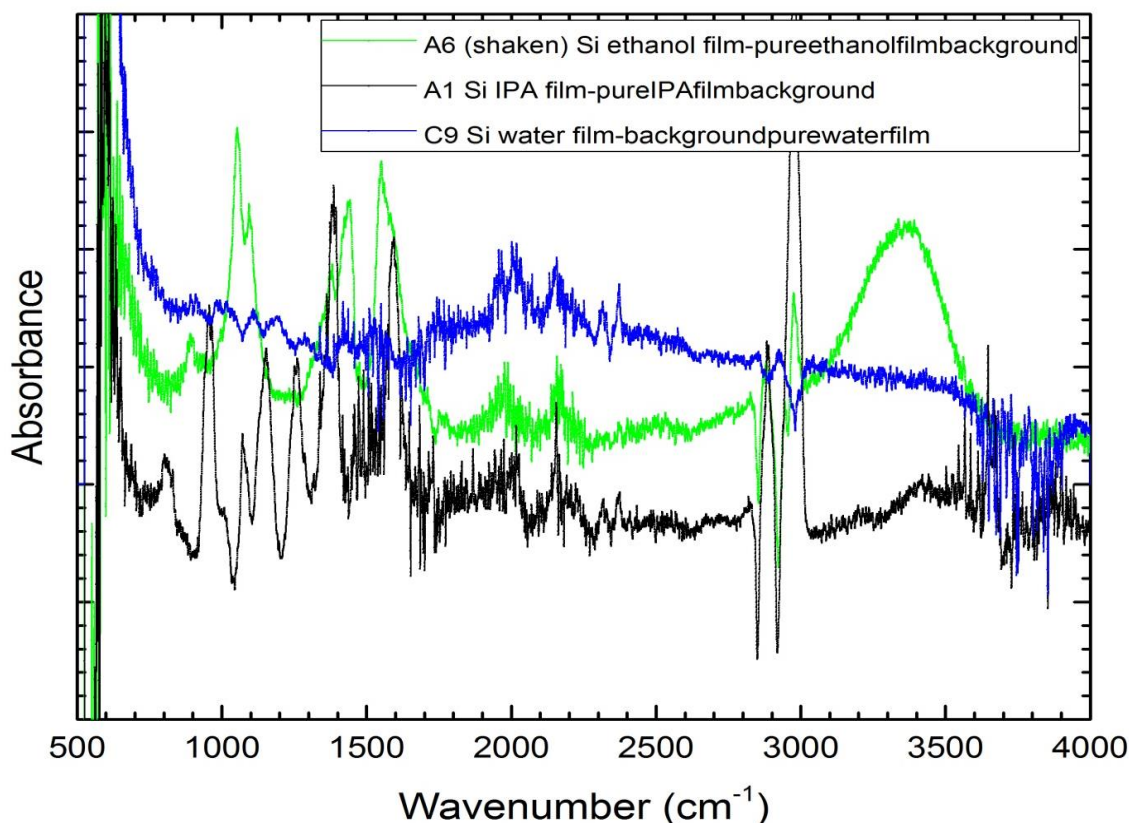


Figure 5-27. Comparison of ATR spectra of silicon deposited in IPA, ethanol and water.

5.2.3 Solvent exchange

As was described earlier, the solvent of Si-ethanol sample A5 was evaporated and the residue nanoparticles transferred to the other solvents. Figure 5-28 shows the process and results for the solvent exchange experiment.

As inset of Figure 5-28 shows, the ATR spectrum of the reference sample was measured and then solvent alternated three times between ethanol and water (by evaporating the solvent and adding the other solvent to the residue). In step four, the ATR of silicon particles in water was measured to compare with silicon directly deposited to water. The sample of silicon nanoparticles transferred to water was split into two vials. The vial with water was left open to allow the water to evaporate, and was then topped up with ethanol to transfer back the particles to the original solvent. An ATR measurement was performed to be compared with the first spectrum (third spectrum). Another vial was topped up with IPA to compare with silicon directly deposited on IPA during fabrication.

As it can be seen, the interaction of silicon nanoparticles with water is much higher than with alcohol. When nanoparticles were transferred to water absorbance increased, and subsequently decreased when the sample was transferred back to ethanol; the same was observed when nanoparticles were transferred from water to IPA. Also, we can see in Figure 5-28 that when particles were transferred to water, they became highly oxidized, when they transferred from water to IPA they became deoxidized. In addition to the oxidation/deoxidation process, the cluster-solvent interaction is different for different solvents. This was the case even when transferred back from water to ethanol, although the intensity of the peaks was higher than the reference sample. The difference between the reference Si-ethanol sample and the 'transferred' Si-ethanol sample may have been due to incomplete water evaporation during the drying process, with water molecules left trapped [on the cluster surfaces] by the silicon clusters, similar to the Si-water (or Silicon transferred to water) sample itself (because of high reactivity between silicon and water). Also, the sharp peaks in this spectrum can be attributed to ethanol, possibly showing that the ethanol did not evaporate completely. A sharp peak at 670 cm^{-1} appears – which belong to a SiH bending mode – which was not in the Si-ethanol samples. ATR results show the interaction of silicon particles with IPA are very low, either during the production or when transferred to the IPA solvent.

The spectra of transferred nanoparticles show the same bands as the spectra of silicon clusters directly deposited in ethanol, IPA or water.

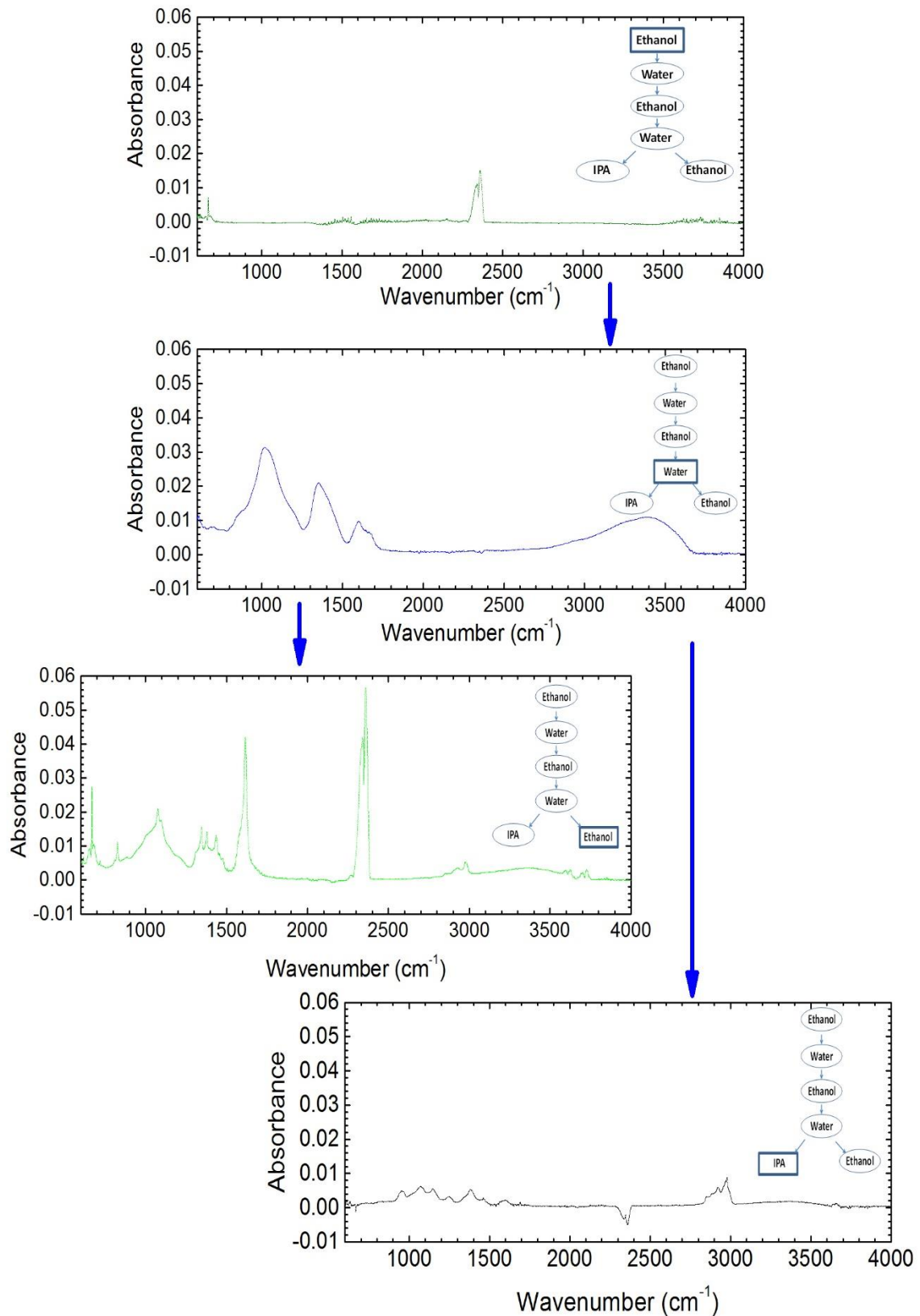


Figure 5-28. Figure showing the ATR spectra of recorded during the solvent exchange experiment. The reference sample was silicon deposited in ethanol (sample A5, as a film). In the inset, the highlighted square shows which sample step was actually being recorded.

As has been mentioned, the ATR crystal is very small, and when a small drop of alcoholic sample is put on it, the drop typically spreads beyond the crystal. This can be straightforwardly controlled for water samples, but for alcoholic samples this is far more difficult, especially for IPA due to its low viscosity. We thought that this may wash the nanoparticles beyond of the crystal boundaries as the solvent spread over the crystal, and thus the intensities observed for alcoholic samples is very low or occasionally non-existent. So, we decided to perform an experiment by using HOPG crystal as a substrate; in this case, intensity was higher, however the same bands were detected (see appendix 5).

5.2.4 FTIR characterisation

For transmission measurements, as previously mentioned, a liquid cell was used. Different spacers were used to alter absorption and transmission characteristics. By using thicker spacers, all source beam was absorbed by water in Si-water samples, and was also very high for alcoholic samples. Hence, the smallest spacer, which is 20 microns, was used, although the absorbance was still very high.

Since absorption was very high for these solvents we could not use pure solvent measurements to take a background, so background spectra were taken from empty cell. Because of high absorbance of the sample, we could not distinguish features due to silicon species, so we decided to measure the samples as film.

All water samples transmittance spectra and the associated pure water spectrum are shown in appendix 5. The transmittance spectra of Si-water are very similar to the absorbance spectra measured by ATR spectroscopy and show the same bands, although transmittance spectra had slightly higher intensities. Pure water did not show any transmittance band, so all features can be attributed to silicon species. The same experiments were performed for sample A1 in Si-IPA and sample A5 in Si-ethanol; the peaks were very weak for alcoholic samples (see appendix 5). As the intensity was very low for Si-ethanol and Si-IPA samples, the pure solvent was not measured.

5.2.4.1 Solvent dependence transmittance

Transmittance spectra of silicon deposited in three different solvents are compared in Figure 5-29. In all these spectra, the sample was a film on a ZnSe window, with the film formed by a 10 μl drop of sample, with a background recorded using the same amount of pure solvent as was used to produce the sample.

The transmittance bands are very similar to the absorbance measurement and show solvent dependence. We believe silicon particles in alcoholic samples tends to bond with the alcohol less than they do with water and, in water, they interact with solvent molecules more and also have a higher oxidation state. As the experiment was performed in atmosphere, an intense CO_2 band can be seen for the alcoholic samples, though given the change in appearance of the atmospheric water bands, this appears to be purely coincidental.

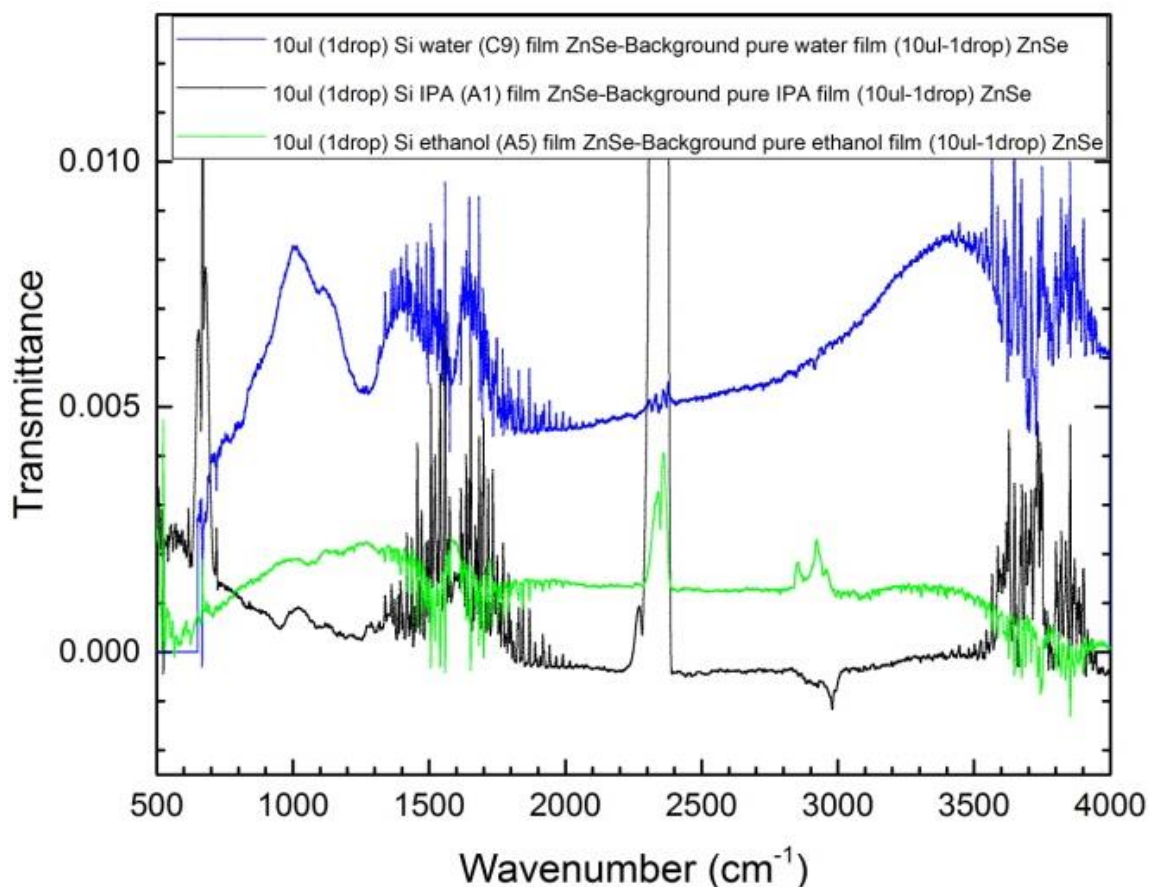


Figure 5-29. A comparison between transmittance spectra of silicon deposited in different solvents. It shows that transmittance of silicon clusters depend on the solvent used.

As the intensity was very low for the alcoholic samples, the experiment was repeated with a mask for Si-IPA. In this experiment, the ZnSe substrate was covered by a mask, so the IR source light only passed the area which was covered by sample (in previous experiments, the source light passed beyond the sample on the ZnSe plate. however, the intensity of transmittance spectra did not change.

5.2.5 Comparison of ATR and FTIR spectroscopy

To see the difference between ATR spectroscopy and FTIR spectroscopy, the absorbance and transmittance spectra of sample C9, as a Si-water film, are compared in Figure 5-30.

In a first experiment, the same amount of sample (10 μ l) was used for the absorbance and transmittance measurements. The intensity in the transmittance spectrum is much higher than in the absorbance spectrum. Although one can see several distinct bands in the absorbance spectrum, the intensity is very low with respect to the transmittance spectrum.

In a second experiment, five times the amount of sample was used for absorbance spectra than transmission spectra; despite this, the absorbance spectra intensities was still lower. The position and shape of the peaks was exactly the same in both methods.

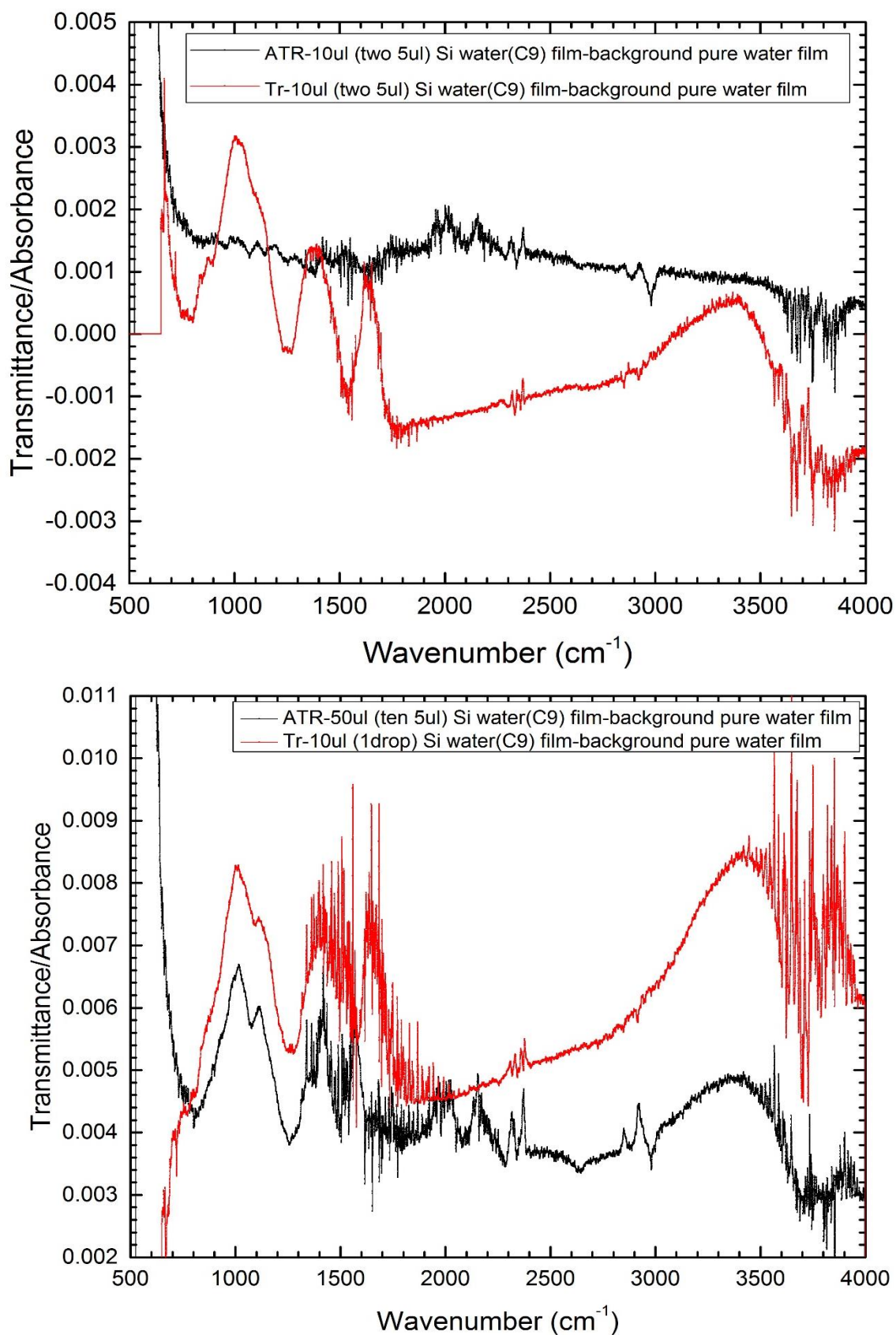


Figure 5-30. Figure showing absorbance and transmission spectra for Si-water sample C9. The top figure shows the use of the same amount of sample for all measurements (10 µl). In the bottom figure, the amount of sample used for the absorbance experiment was five times higher.

5.3 Conclusions

Experiments with the different substrates showed the appropriate substrate for our samples is HOPG, and the results showed the samples did not interact with the HOPG.

XPS peaks were blue shifted respect to those of bulk silicon, which shows silicon was oxidized or interacts with the solvent in our method, and these bonds still exist even when the solvent evaporates. ATR spectroscopy confirms this, and shows the bands which belong to silicon species due to interaction of the silicon with the solvent, and that by evaporating the solvent, some of these bonds remain and can be detected by ATR.

The ATR and XPS results show that silicon particles were oxidized in all solvents, but oxidation states and the intensities of associated peaks depend on the solvent. XPS spectra showed different binding energies for silicon deposited in IPA, ethanol and water due to different levels of oxidation. According to both ATR and XPS results, water samples had the highest level of oxidation and IPA samples had the lowest. ATR spectra showed SiO_{2+x} , and SiO_3 bands were only observed in water samples. We attributed the fluorescence band of Si-water at 420- 440 nm in emission spectra to highly oxidised silicon in Si-water samples, and the fluorescence bands of Si-IPA at 365 nm and Si-ethanol at 370 nm attributed to silicon-oxygen species with lower levels of oxidation.

The intensity of the peaks in XPS and ATR spectra indicated that the number of silicon particles that bonded with solvent was greater in water than in alcohols. Amongst the three solvents, the tendency for interaction with nanoparticles was lowest for IPA. Silicon particles in IPA did not interact greatly with the IPA, when it was used either during production or during solvent exchange experiments.

The ATR and XPS results show spectra of transferred particles are the same as the spectra of silicon clusters directly deposited, so transferred samples are identical and equivalent to directly deposited samples. The ATR results also showed that solvent exchange is a reversible process.

Chapter 6

Conclusions, discussion, and further work

In this chapter, our work, a general discussion and conclusions regarding this project are summarised. Also a few suggestions for further work are also presented.

6.1 Discussion and Conclusions

In this project we synthesised fluorescent silicon nanoclusters using a novel liquid jet method by deposition of the silicon particles directly onto the liquid phase. In this method, the user can vary the interaction between solvent and silicon particles. Different parameters can affect cluster properties: the solvent which is used as liquid jet, stagnation pressure of the liquid jet, the power of magnetron (sputter head), capillary diameter, distance and angle between cold target and capillary, and duration of deposition. Samples can be produced in different solvents such as water, ethanol and isopropanol, depending on the required application. Of these solvents, water is especially important as the production material as a mechanism for application *in vivo*, i.e., in modern medicine. In this method several millilitres of sample solution can be produced in less than 20 minutes. The AFM measurements show clusters have a 1 nm height.

All nanoparticles produced so far show intense fluorescence, with two fluorescence peaks. In our model, the first peak originated from fluorescent silicon clusters localised in the bulk volume, which shows an intrinsic band with a fluorescence wavelength of ~310 nm in any solvent, although our decay measurements showed it might be coincidental as they showed different lifetimes. The second peak, attributed to fluorescence at a cluster surface site (fluorescent states are localised at the cluster surface), has a peak fluorescence wavelength that is dependent on the specific solvent used for the liquid jet. The second peaks for IPA, ethanol and water were observed at 365 nm, 370 nm, and 420 - 440 nm, respectively. The second peak wavelength shows sensitivity to the surface silicon cluster-solvent interaction, dipole moment of solvent

molecules, and steric effects. The sensitivity is manifested by distinct solvent shifts of a supposedly localised electronic transition, and suggests that the transition is localised at the surface of the nanoparticles. A tentative assignment relates the fluorescence to defects at the cluster surface, caused by a chemical reaction of pure silicon clusters with molecules of the solvent. Here, we presented results that support this assignment: silicon clusters in alcoholic solvents show fluorescence bands that are blue-shifted with respect to the fluorescence in aqueous solvent. We interpret this finding as due to a similar chemical interaction of silicon in alcohol and water: in both cases, we believe that silicon-oxygen and SiOH groups are formed at the cluster surface. However, the fluorescence wavelengths differ, which we believe is caused by the different interaction of clusters with solvent, and different dipole moments (the larger the dipole moment, the greater the fluorescence shifts towards longer wavelength for IPA, ethanol and water samples), and also we need to consider steric effects.

The excitation energy dependence of the fluorescence for each sample shows unshifted bands, which gives evidence that the fluorescent transitions originate from localised defects. Excitation spectra of the first fluorescence band confirm that fluorescence at ~310 nm comes from the same excited state for silicon clusters produced in different solvents (it might be coincidental), whilst the second fluorescence bands originate from different excited states, depending on the solvent.

Fluorescence investigation of the film samples also show the first band at ~310 nm, and the second band around 410 - 440 nm for any solvent. We assume that by evaporating the solvent, particles no longer bond with solvent molecules and, by exposing to the air, clusters become oxidised and show the same band as the Si-water sample in the liquid phase, which leads us to conclude particles are oxidised in water more than in alcohol. Measurements of film and liquid samples in the same condition (measured in Desy) show film samples have higher intensity than liquid samples, because there is no quenching in film sample.

First peak around 310 nm is present in all film and liquid sample in produced in any solvent.

Our observations and our specific production method, without the need for further treatment to stabilize our solutions, also suggests that an intrinsically stable form of silicon nanoclusters in solution exists, and shows stable fluorescence over long period.

Our aging experiment proves that these fluorescent particles have not agglomerated and remained chemically stable in solution after several years, and that the fluorescence intensity did not change on the timescale of approximately a year. Si-water samples showed quantum yields of 8% to 10% three years after their original production, which is a high quantum yield for applications such as medical and biological imaging and diagnostic labelling. The Stern- Volmer plot of diluting the samples shows fluorescence of silicon clusters produced in alcohol were quenched at high concentrations by particle-particle interaction, while Stern-Volmer plots do not show any quenching for Si-water which shows dynamic stability of the sample. A linear relationship between absorbance and concentration of the sample shows chemical stability of our samples. Fluorescence intensities of the samples were measured at different temperatures from 8 K to 300 K, by subsequent cooling, the sample fluorescence intensity increases.

Solvent exchange experiments show that the position of fluorescent peaks of the nanoclusters not only depends on chemical reactions between silicon particles and the liquid jet during growth, but also on the solvents that nanoclusters have been kept in. The first peak did not change during solvent exchange. However, the second peak, which belongs to surface clusters, shifted every time the solvent was changed. The results of solvent exchange showed the transferred particle to a specific solvent is equivalent to silicon directly deposited in that solvent. Observation showed solvent transfer is fully reversible. Distinct correlation with the solvent and the reversibility of the process supports our initial assignment for nanoparticles regarding the existence of a fluorescent site on the surface of the cluster for the second peak, and the fluorescence wavelength dependency of the second peak on the solvent. As we can change the fluorescence wavelength by transferring the particles to another solvent, samples can be produced in any solvent and, depending on application and required wavelength, can be transferred to appropriate solvent at a later time.

Decay time measurements show fluorescence lifetimes of our samples are in the range of a few nanoseconds, which varies from 3.7 ns for Si-water samples to 5.6 ns for alcoholic samples. Several parameters can affect fluorescence lifetime, such as: excitation wavelength, the lifetime can be decreased as excitation wavelength is increased, phase of the sample (liquid or film, as the solvent evaporated for film samples, they did not show dependency to samples' solvent), film samples show lifetime longer than liquid sample as there is no quenching for film sample so lifetime (and also intensity) increases by

making film sample, temperature, lifetime decreases with increasing temperature from 8 K to 300 K, and the solvent (in liquid samples), Si-water samples have shorter lifetimes with respect to alcoholic samples. Although these parameters can affect the fluorescence lifetime, its range is still in the order of a few nanoseconds.

X-ray photoelectron spectroscopy (XPS) and attenuated total reflection (ATR) was used to analyse the chemical composition of the materials. Chemical analysis of nanoparticle films revealed that silicon within the nanoparticles interacted with the solvent and was oxidized. Silicon peaks in XPS spectra are blue-shifted with respect to those of bulk silicon, and binding energies recorded for silicon peaks show silicon is oxidized in our production method, which is confirmed by ATR results. The silicon nanoclusters have different chemical properties and different oxidation states of the species depend on the solvent. Silicon ($2s$, $2p$) peaks and oxygen ($1s$) peaks show silicon in water oxidises much more than in alcohol (pure silicon and oxygen peaks were not detected in XPS spectra for any sample). The Si-IPA sample had a peak at the binding energy of SiO, ethanol showed its peak at the binding energy of SiO_x ($1 < x < 2$) and Si-water showed SiO₂ binding energy peak. The Si-water peak was a broad band which showed it had other components of silicon oxide like SiO and SiO_x. Si-water samples have the highest level of oxidation and Si-IPA samples have the lowest.

Integrating the area under the XPS peaks, and thereby determining peak intensity, shows that the number of silicon nanoparticles that interacted and bonded with the solvent was greater in water than in alcohols.

ATR spectra show silicon particles interact with oxygen, hydrogen, and carbon. Infrared absorption bands were attributed to Si-Si, SiC, SiH, SiH₂, SiCH₃, SiOH, Si₂O, SiO, SiO₂, Si₂O₃, SiO_{2+x} (only in water sample) and SiO₃ (only in sample C9 which is high fluoresct sample) species, although all these bands were not present in every sample, and different samples showed different intensities for the same band. ATR shows the presence of bonds related to oxidation states linked to Si₂O, SiO, SiO_{2+x}, and SiO₂. ATR results, similar to XPS results, show all samples were oxidized but, depending on the solvent, samples were at different oxidation states, and also that the intensity of the peaks (absorbance) were different, an effect which is related to sample solvent.

The intensities of the peaks (absorbance) in ATR spectra is proportional to the number of nanoparticles interacting, and forming bonds, with solvent molecules. The

intensities observed in ATR spectra confirm XPS results, and higher absorption intensities of silicon species in Si-water samples show the interaction of the silicon particles with water molecules is higher than alcoholic samples, and that nanoparticles form more bonds with water molecules than alcohol molecules, so the number of oxidised silicon clusters in water is greater than in alcohol. ATR peak frequencies also show higher oxidation states in Si-water samples than in alcoholic samples, which is also in agreement with XPS results.

The intensity and existence of silicon-oxygen bands in XPS and ATR shows that, amongst the three solvents, IPA has the lowest reaction rate and the lowest tendency to oxidation, and highest for water. Observation shows that even one drop of pure water added to alcoholic samples can oxidize the sample and cause a fluorescence shift from 370 nm to 420 nm. As XPS and ATR analysis confirms that the silicon in water is present in a high oxidation state, and additionally that the clusters are extremely oxygen rich, this leads us to conclude that the deep-blue fluorescence at 420 - 440 nm emerges from oxygen rich states, and that the bands at 365 nm and 370 nm for alcoholic samples come from lower oxidation states.

The solvent exchange results of XPS and ATR experiments show spectra of transferred particles are identical to, and show the same bands and almost same intensity as, the spectra of silicon clusters directly formed in the same solvent. Therefore, a sample transferred to another solvent, and its structure and chemical characteristics in that solvent, are equivalent to those seen for the sample prepared directly on that solvent. So, clusters can be produced in any solvent and transferred to appropriate solvent at some later stage, as appropriate to circumstance.

Oxidation of silicon particles in IPA is very low, either during production or when the sample is transferred to IPA. The results show that when the sample is transferred to alcohol, its oxidation state is lowered; when the nanoparticles are transferred to water, the oxidation state is increased. Hence, the solvent exchange experiments suggest that several stable forms of silicon nanoclusters, in different oxidation states, exist. These can be interchanged by reversible reduction and oxidation. Similar to directly deposited samples, the intensity of the XPS and ATR peaks indicates that the number of oxidised silicon clusters in water is greater than in alcohol.

The results show with our novel method we can produce several millilitres of oxidised stable fluorescent silicon nanocluster (of 1 nm height) solution by deposition of silicon in a liquid jet, which can be any solvent, in less than 20 minutes. Optical and chemical characterisation for more than 50 samples show reproducibility of the sample with this novel method.

6.2 Further work

In our synthesis method, it is interesting to study the effect of the production parameters, which can affect cluster properties to a significant degree. It is also very important to know exactly how the user can control these parameters, for example: how much silicon vapour is deposited on the liquid jet, how much does the liquid jet interact with particles and what volume of liquid is required for production.

We suggest, as further work, the synthesis of clusters with mixed solvents, for example water and alcohol, to investigate the effects on the fluorescence band and chemical composition. There are two possibilities, the results show both fluorescence and XPS peaks which belong to silicon in alcohol and water, or all particles may be oxidised in water, as particles interact more with water molecules. Although our experiments show by adding one drop of water to an alcoholic sample that clusters were oxidised, so we predict particles will be oxidised in mixed solvents as liquid jet.

Dilution experiments and Stern-Volmer analysis showed the fluorescence of silicon deposited in alcohol was quenched, so calculation of particle-particle interactions to investigate the quenching effect on fluorescence could help to characterise the sample.

A study of the concentration of particles in solution, and the effect of production method on sample concentration, would be useful in sample characterisation.

Appendix 1

Equipment operation to produce silicon nanoclusters

To start the experiment, the user should place the bell jar and make sure it is stuck to the plate, and then on the monitor screen (which is touch screen), press start. The rotary pump starts, and on the screen a “backing pump” message appears. After a few minutes the pressure will reach to 10^{-2} mbar. At this stage the turbopump automatically starts working and the valve between chamber and pump opens, at which point the screen shows a “high vacuum” message. If there is no leak in any of the chamber seals, it takes less than 20 minutes for the pressure to reach 10^{-6} mbar. We sometimes also added liquid nitrogen through a pipe into a cold trap to accelerate the speed of evacuation by removal of excess water vapour. A base pressure around 2×10^{-6} - 6×10^{-6} mbar is ideal to start the experiment.

At this stage one should press the “cycle” button on screen, which closes the valve between the chamber and turbopump, at which point the monitor shows a “Roughing Pump” message. After a few seconds, the pressure stabilises, and the user can open the argon valve and let argon gas into the chamber, which is necessary for sputtering. The user should control the amount of the argon gas which enters the chamber because if it is allowed to get too high, and the pressure reaches to 8×10^{-1} mbar, the device will automatically stop working. A good pressure for the experiment is $\sim 2-3 \times 10^{-2}$ mbar. Sputtering requires argon at a pressure of 10^{-2} mbar to be introduced into the vacuum system. During sputtering and liquid jet operation, one should monitor the pressure and keep it in the above range by varying the amount of argon gas. When the sample has been produced and the sputtering and liquid jet stopped, the device is ready for venting. By pressing the “vent” button on the screen and opening the argon valve, the turbopump stops working and the chamber is vented by argon gas; the pressure reaches atmosphere pressure in less than two minutes.

The ability to achieve good vacuum quickly allows us to change experimental parameters and fix problems in a very short time, allowing for maximum uptime of the experiment.

Appendix 2

XPS operation

When the sample is ready (as explained in chapter 3) it can be inserted into the load lock chamber. In this stage, the load lock chamber is under vacuum and need to be vented. There are two pumps for load lock chamber: a turbopump and a backing pump. First, the turbopump should be allowed to spin down, at which point the backing pump can be switched off. Argon gas is used to vent the load lock chamber; when the pressure is 760 mbar, this chamber can be opened and the sample located in the holder, which is mounted on the end of a magnetic transfer arm. By closing the chamber window and stopping the flow of argon gas, one can turn the backing pump on. Then turbopump is switched to fan until the pressure reaches to 1-2 mbar and can be switched on fully, after which it takes ~1 - 2 hours to evacuate the load lock to a suitable pressure. The sample is then ready to be transferred to preparation chamber.

Before transfer, the ion gauge in the preparation chamber should be turned off and a current setting of 0.1 mA should be set on its controller box. The user should do the following steps in sequence: open the valve between load lock and preparation chambers, transfer the sample to the sample head, withdraw the transfer arm and close the valve, set autocurrent on the ion gauge controller for the ion gauge in the preparation chamber, and then leave the system for about two hours until the pressure of preparation chamber again reaches its nominal base pressure of 10^{-10} mbar. At this point, the sample should be ready to transfer to the analysis chamber, although the sample may be kept in the preparation chamber for longer if it needs further degassing/ cleaning.

To transfer the sample to the analysis chamber, the gate valve between preparation and analysis chambers should be opened and the sample transferred to the *xyzr*-manipulator in the analysis chamber; the magnetic transfer arm used to achieve this should then be withdrawn from the analysis chamber and the gate valve closed.

At least 10 minutes before turning on the X-ray source, the cooling water circulator should be turned on. Set the sample in the optimum position for analysis via the *xyzr*-manipulator – the sample can be seen through the [lead glass] window at the end of the analysis chamber –, and move the X-ray source, via the *z*-manipulator it is mounted on, as close as possible to the sample.

There are two interlocks that control the safety (in terms of overpressure, overheating, current/voltage spark, etc.) of the X-ray head, both interlock buttons on the controller box should be set to “on”. Afterward, turn on the X-ray power, EAC2000-125 [Omicron energy analyser controller] and multiplier power supply at the controller and, also, the EA125 [Omicron hemispherical energy analyser] controller should be turned on.

Figure A.2-1 shows picture schematic of the XPS spectrometer and its controller box. To operate the spectrometer, the user should use the Omicron X-ray 554 control software. In the software the following parameters should be set: switch to the emission mode, select the magnesium (Mg) anode, set the anode voltage to 15 kV, set emission to 15 mA, and switch the X-ray gun on. The user should then wait until the voltage and emission current from the X-ray source matched their set points in the software inputs (and the appropriate indicators in the software change to green), as shown in Figure A.2-2.



Figure A.2-1. Left: Top view of the XPS spectrometer. Right: Ion gauge controllers showing the pressures of the different chambers.

At this point, the experiment can be started. To this end, one must open the EIS software and select the XPS experiment. The EIS software interface is shown in Figure A.2-3. At the bottom of the window, the parameters for the experiment can be set, as were

described for our experiment in chapter 3. A survey scan can then be recorded. Figure A.2-3 shows a survey recorded for our sample, and an example of the software library used to identify the observed peaks.

To optimize the experiment, the user should open the EA125 software control interface shown in Figure A.2-4, check the multiplier box, and start to change the angle (ϕ) and position parameters (x , y , z , r) of the $xyzr$ -manipulator to maximise counts and optimise the signal/noise ratio.

The procedure to turn the X-ray gun off is as follows: close the EIS software, in the Omicron X-ray 554 control software turn the current to zero and wait until the current is in the region of 3 mA or less before turning the voltage to zero, wait until voltage is zero (along with emission and leak currents) and turn the controller software off and, finally, close the software. The user should then turn off the X-ray power, EAC2000-125, multiplier supplies, and waiting for X-ray unit to cool (leaving the chiller circulating for at least half an hour after turning off the power). Finally, the X-ray source should be withdrawn from the sample region via its z -manipulator and the chiller should be turned off.

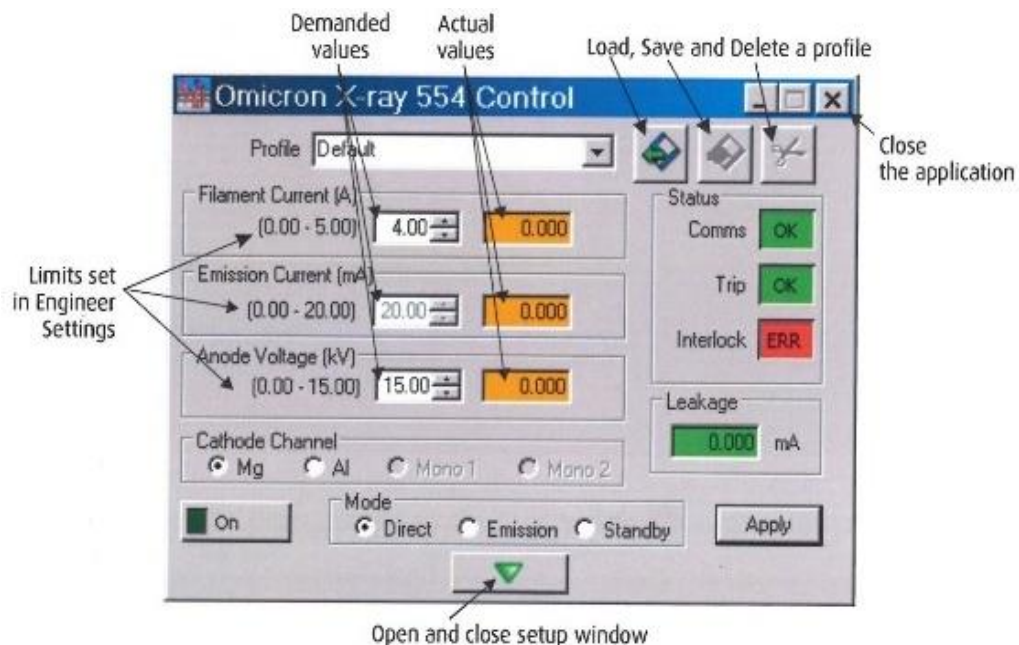


Figure A.2-2. X-ray controller software. In this interface we can choose the anode, and also define filament current, emission current and anode voltage.

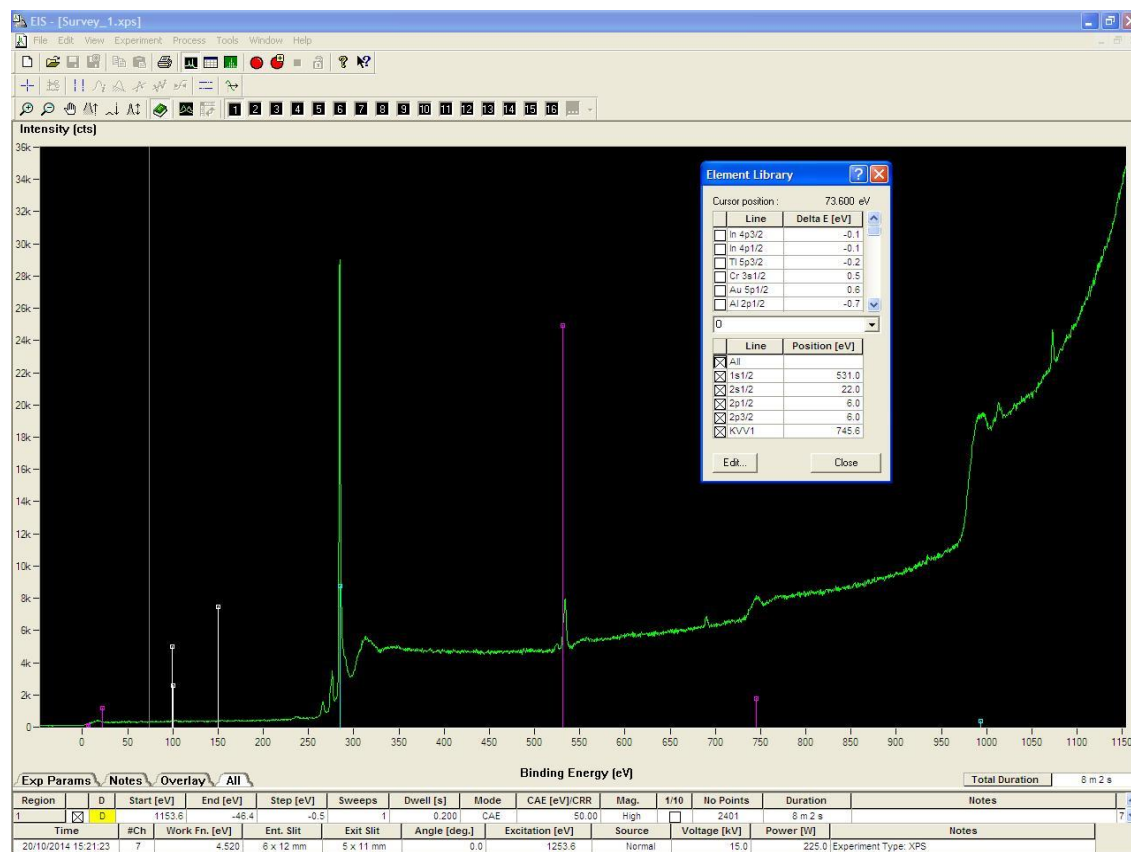


Figure A.2-3. An example survey spectrum. The parameters which were chosen for experiment can be seen in the table at the bottom of the software interface (these are generally just used as file metadata when the experimental data is saved, and mostly do not actually affect the experiment itself). By choosing appropriate elements in the software library, the probable identity of each atomic peak is defined.

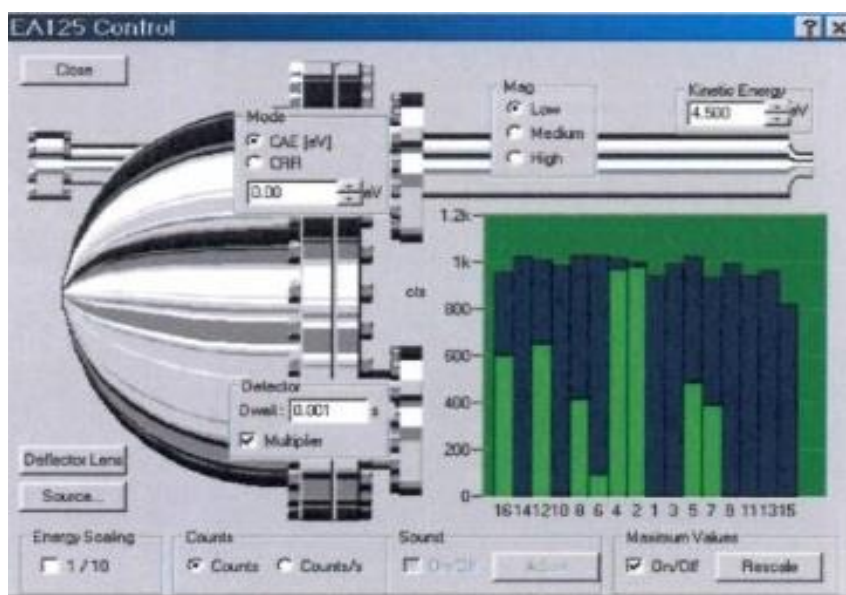


Figure A.2-4. EA125 software control interface. By changing the position of the sample, the intensity will change and one can optimize the peak intensity and signal/noise ratio of the experiment.

Appendix 3

Complementary information about ATR and FTIR experiments

3.1 Quality of the beam and PV test

When an accessory is installed in the IR spectrometer, the Omnic control software automatically asks user to approve the type of accessory and crystal type, otherwise one should select them manually in the software. The software automatically optimizes the quality of the beam, but the user needs to check the quality and quantity of the source via an interferogram. The interferogram should be in the range of maximum and minimum intensity (0.2 - 9.8) that is described in the software, and the shape of interferogram should be symmetric in the horizontal and vertical axes.

Once a month, or whenever the energy throughput decreases, the user needs to align the spectrometer. To do an alignment, one needs to run a Performance Verification (PV) test. The PV test checks the system, performs an alignment, and checks the laser calibration. The alignment maximizes the energy throughput. The user can align the spectrometer without doing a PV test, but running the PV test will do this automatically.

3.2 ATR and FTIR accessories

As was described in chapter 3, the iD5 accessory was used for ATR measurements. It has a pressure tower, called an anvil, which is used for powdered and solid samples to press them against the ATR crystal. The anvil is not suitable for liquid samples or, as it turned out, our drop-cast film samples. Figure A.3-1 shows the iD5 ATR device installed in a Nicolet iS5 spectrometer. For transmission measurements, the iD1 accessory is

installed in the spectrometer. It can be used for gas, liquid and film samples. Figure A.3-2 shows the spectrometer working in transmission mode, and a liquid cell (described in chapter 3) is used to record IR spectra of liquid samples. There were several slots in the iD5 accessory that the sample can be placed in, but a slot at or near the focal point of the beam was the best position. The focus position is indicated by arrows within the device bay.

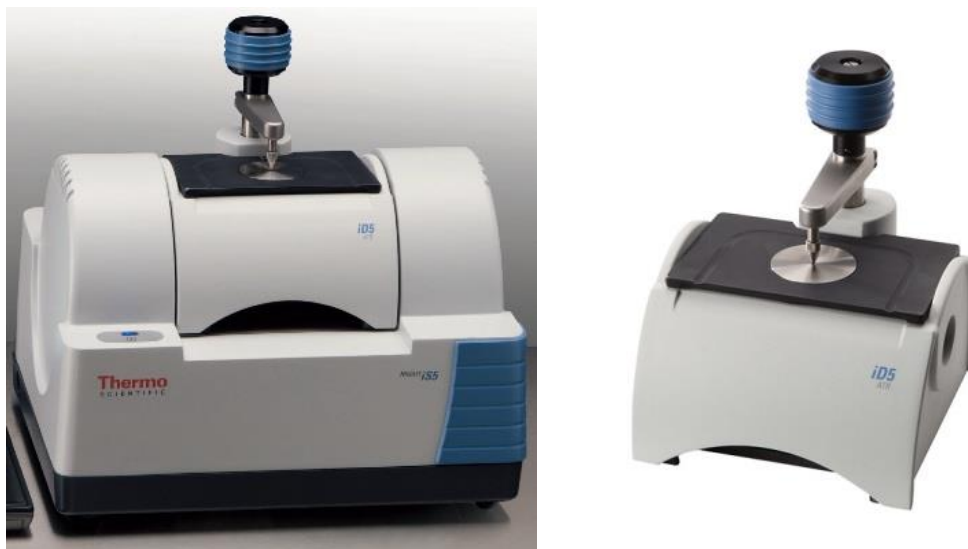


Figure A.3-1. The iD5 accessory for ATR measurements. Picture on the right shows iD5 device, and it has been installed in iS5 spectrometer in picture on the left.



Figure A.3-2. The iD1 transmission accessory. Left, the device has been installed in an iS5 spectrometer, to measure transmission spectra. The position of the liquid cell in the transmission accessory is shown in the picture on the right.

3.3 ATR spectra correction

One can interconvert between absorbance and transmittance spectra in the data acquisition and analysis software. To convert spectra, the spectrum should be selected and, in the process menu tab - depending on the required spectrum - absorbance or transmittance should be chosen.

Generally, the spectra measured by ATR (absorption) and spectra measured by FTIR (transmission) should have the same frequency for a specific band, but sometimes ATR spectra are slightly shifted in vibrational frequency. To correct for this shift, one can use the Advanced ATR Correction Result tab in the software, and the software will correct the spectrum according to the common shift that often happens in ATR measurements, automatically. These common shifts can be seen in ATR spectra because the refractive index of a sample causes changes the region of its absorption peaks, known as 'anomalous dispersion'. Anomalous dispersion shifts the peak slightly from its location in the equivalent transmission spectrum. Advanced ATR correction corrects this shift through application of mathematics and/or empirically shifting peaks by comparison to the analogous transmission spectrum. It may be helpful but not always, when the correction is applied, the positions of the peaks are matched more closely to those of the transmission data (sometimes, however, the software cannot do the correction properly because it matches a recorded peak with a known peak, which may be different band with measured band). To be able to apply this correction (in the Advanced ATR Correction Result tab) one has to select the crystal which was used for experiment, the angle of incidence (which was always 45° because in ATR experiments the IR beam enters the crystal at this angle), the number of bounces within the ATR crystal, and also sample refractive index (note that if an unknown sample was used, one could use an average of 1.5 which would be reasonable). Data corrected with the software in this manner is, nevertheless, still an approximation to the data that would have been collected in the transmission mode of the spectrometer.

Appendix 4

Complementary spectra to chapter 4

4.1 Absorbance spectra

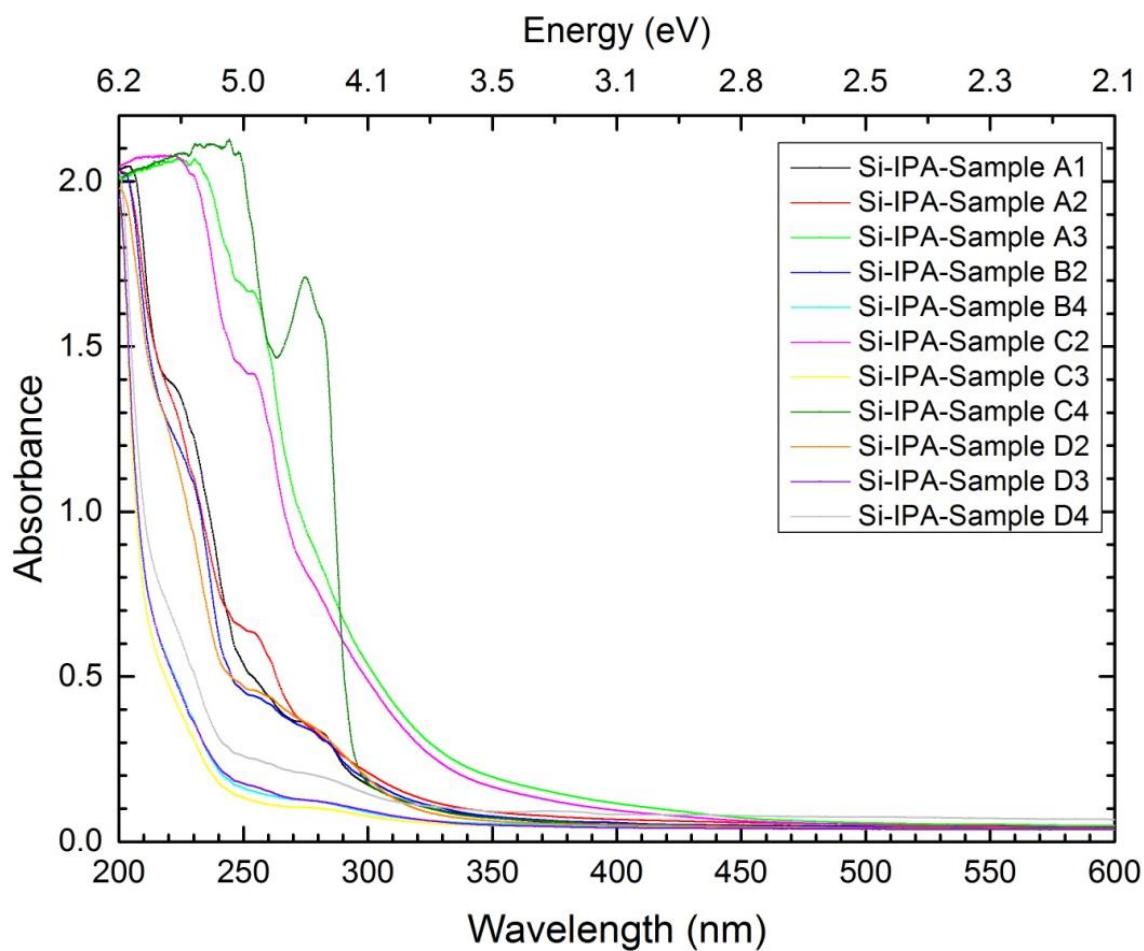


Figure A.4-1. Absorbance spectra of Si-IPA samples. The absorption peak wavelength is different for different spectra.

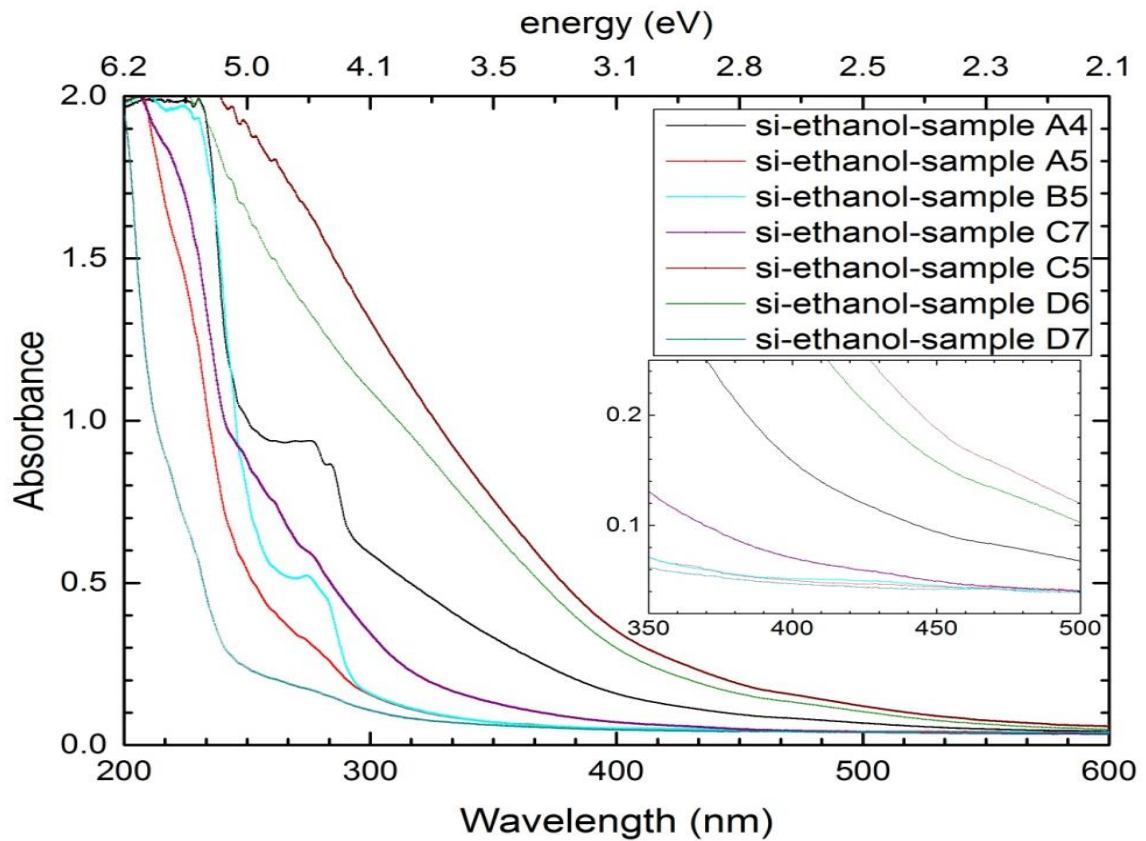


Figure A.4-2. Absorbance spectra of Si-ethanol samples.

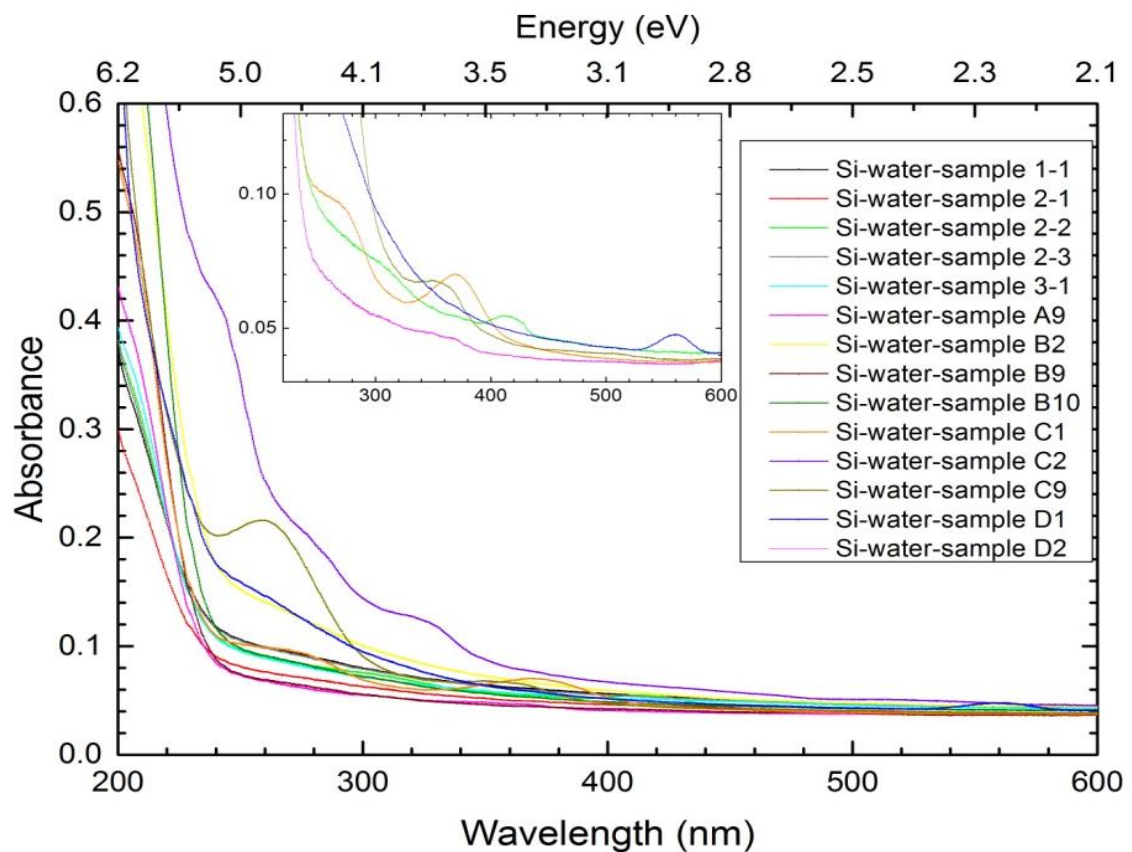


Figure A.4-3. Absorbance spectra of Si-water samples.

4.2 Effect of filter on fluorescence

Although the AFM measurement shows the size of the clusters is ~ 1 nm, some larger particles may still exist in the sample. It is, *a priori*, not clear if all clusters in the samples fluoresce or if the fluorescence is only due to a subset of clusters within a specific size distribution. To investigate whether the fluorescence comes from all clusters or a specific subset, and to study the relationship between the size of clusters and fluorescence intensity, we performed a filtering experiment and investigated the cluster size dependence for Si-IPA and Si-ethanol samples. 200 nm Acrodisc Eppendorf filter was used for this experiment. The results for a Si-IPA sample before and after filtration for three different wavelengths are shown in Figure A.4-4.

As can be seen, fluorescence intensity increased after filtration. This suggests that fluorescence predominantly comes from only small clusters, and larger particles do not fluoresce and, possibly, may even scatter fluorescent light from those particles that do emit. We attribute the increasing fluorescence intensity to fluorescence quenching due to collisions with bigger particles in the unfiltered solution. Both fluorescence peaks increased when the sample was passed through the filter. The Rayleigh peak should be more abundant in larger clusters; hence, the intensity is reduced after filtration. Big clusters are strong scatterers, and cause more scattering of light.

The results for Si-ethanol are shown in Figure A.4-5.

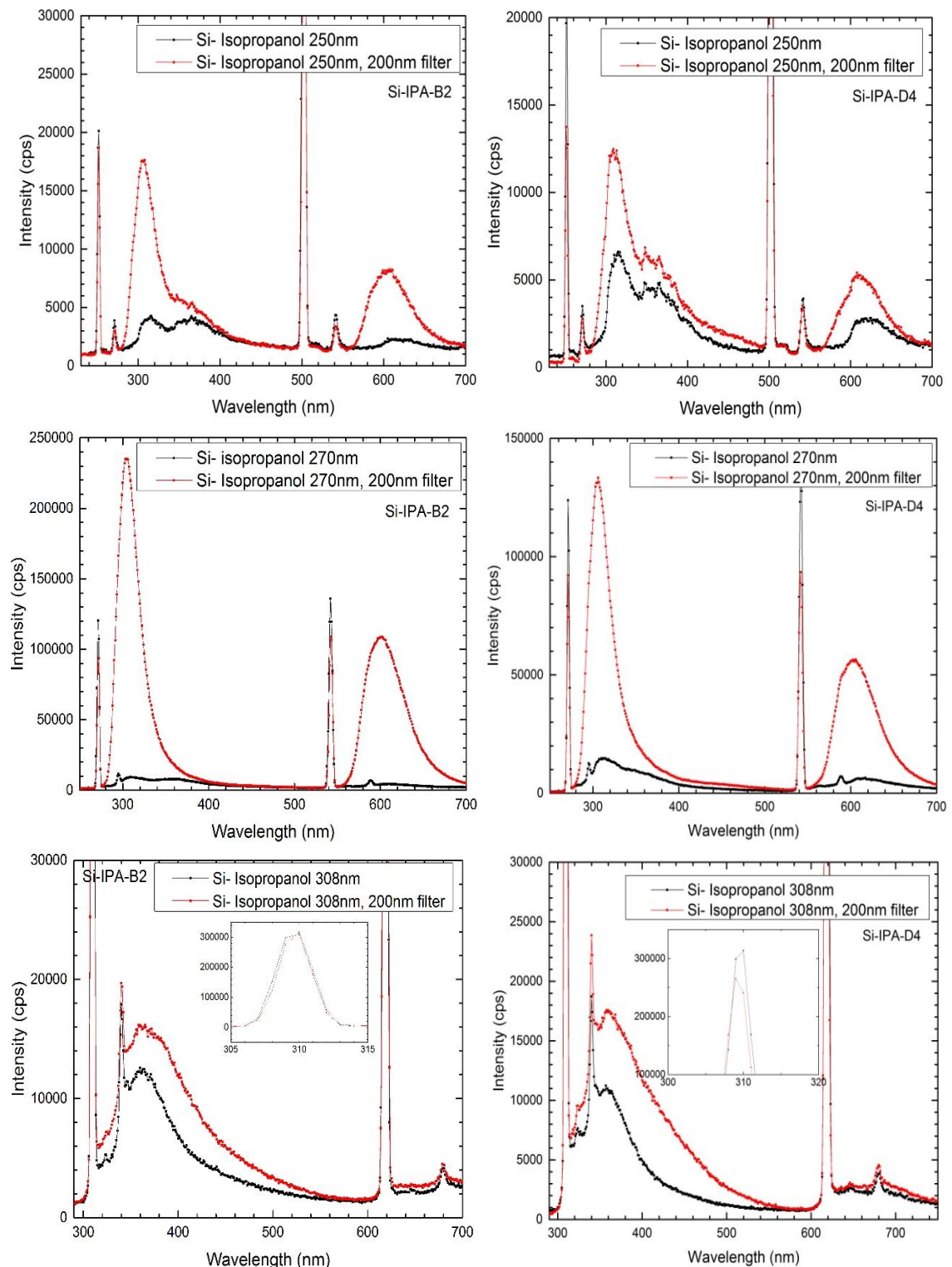


Figure A.4-4. Figure comparing emission spectra of samples before and after filtration. The samples were excited at 250 nm, 270 nm, and 308 nm. The plots on the right belong to Si-IPA sample D4, and the left to Si-IPA sample B2.

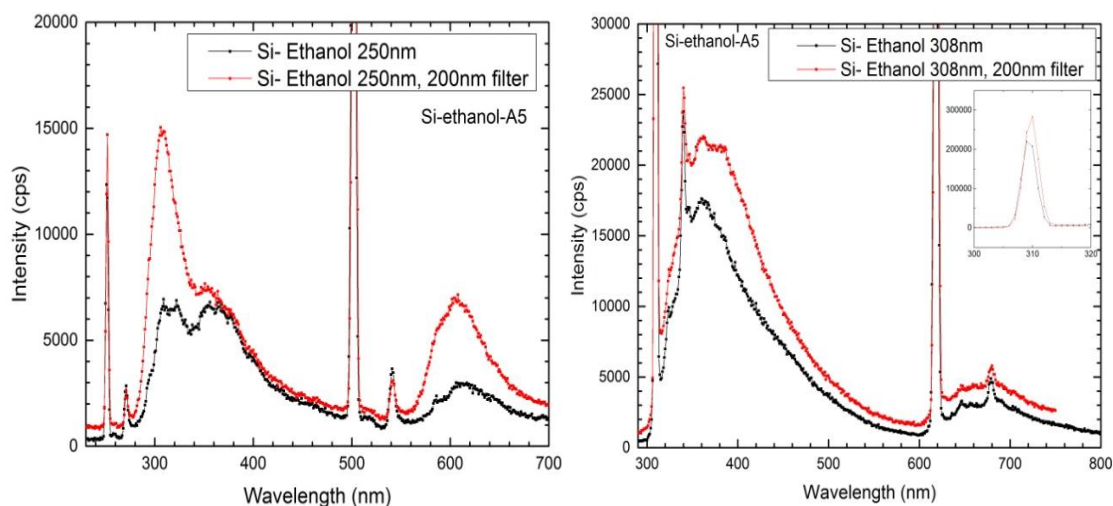


Figure A.4-5. Difference between fluorescence intensity before and after filtration of Si-ethanol sample.

4.3 Time-correlated fluorescence spectroscopy

In chapter 4, the spectra of three different components (int, fast, slow) of each sample at one excitation and one emission wavelength were shown; here, spectra for other excitation and emission wavelengths for each component are shown.

4.3.1 Silicon-ethanol liquid

Sample B5 is Si-ethanol in the liquid phase. Experiments were performed at room temperature. For all emission spectra, filter WG280 was used. The emission spectra are shown in Figure A.4-6. For excitation spectra emitted at 300 nm and 330 nm, filter WG225 was used, whilst for 310 nm, filter WG280 was used. The excitation spectra are shown in Figure A.4-7.

All the spectra were normalised; A normalized excitation spectrum (int) emitted at 300 nm is shown in Figure A.4-6 as a comparison with the same spectrum before normalization.

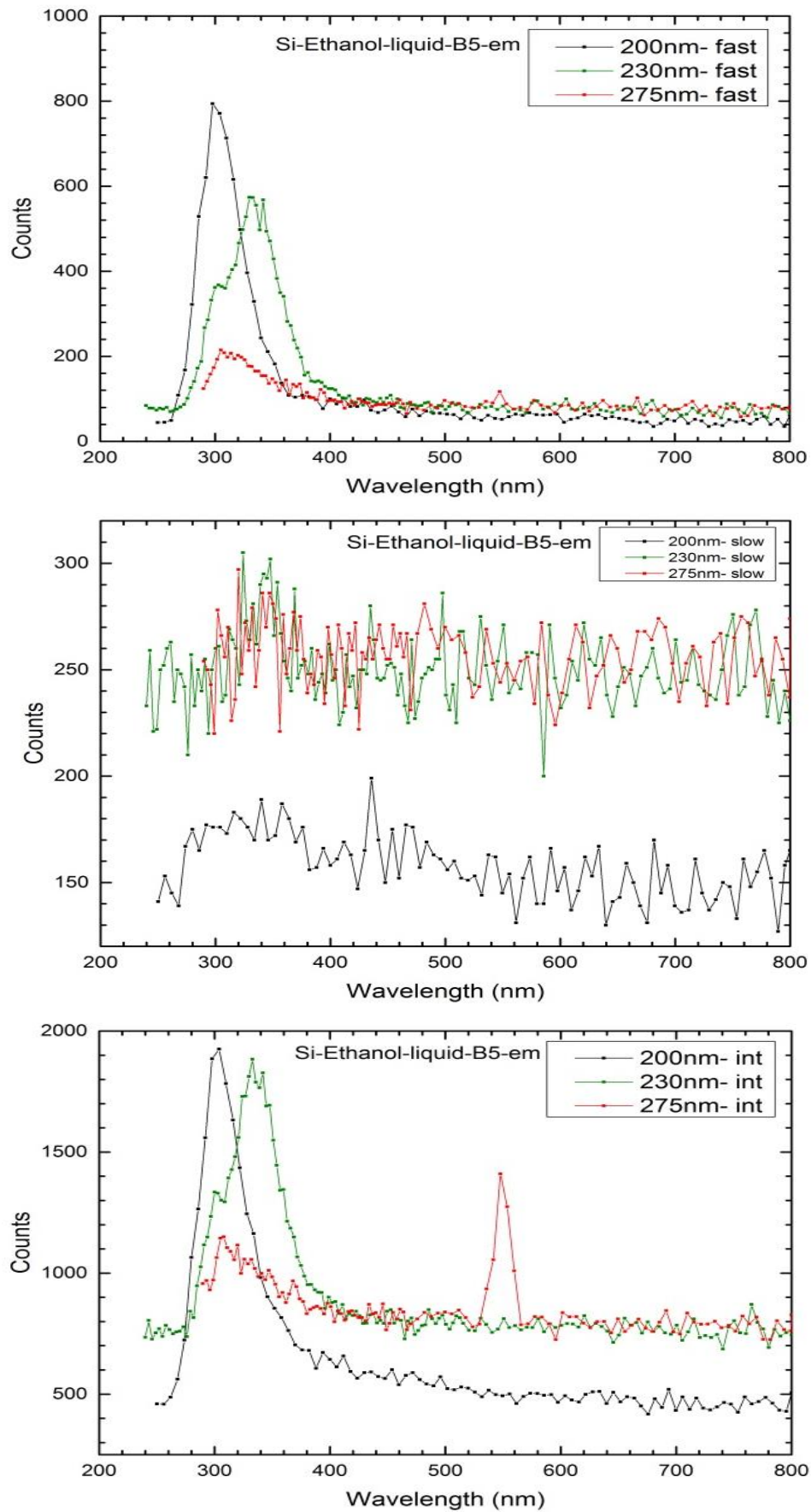


Figure A.4-6. Emission spectra of different components of Si-ethanol liquid sample.

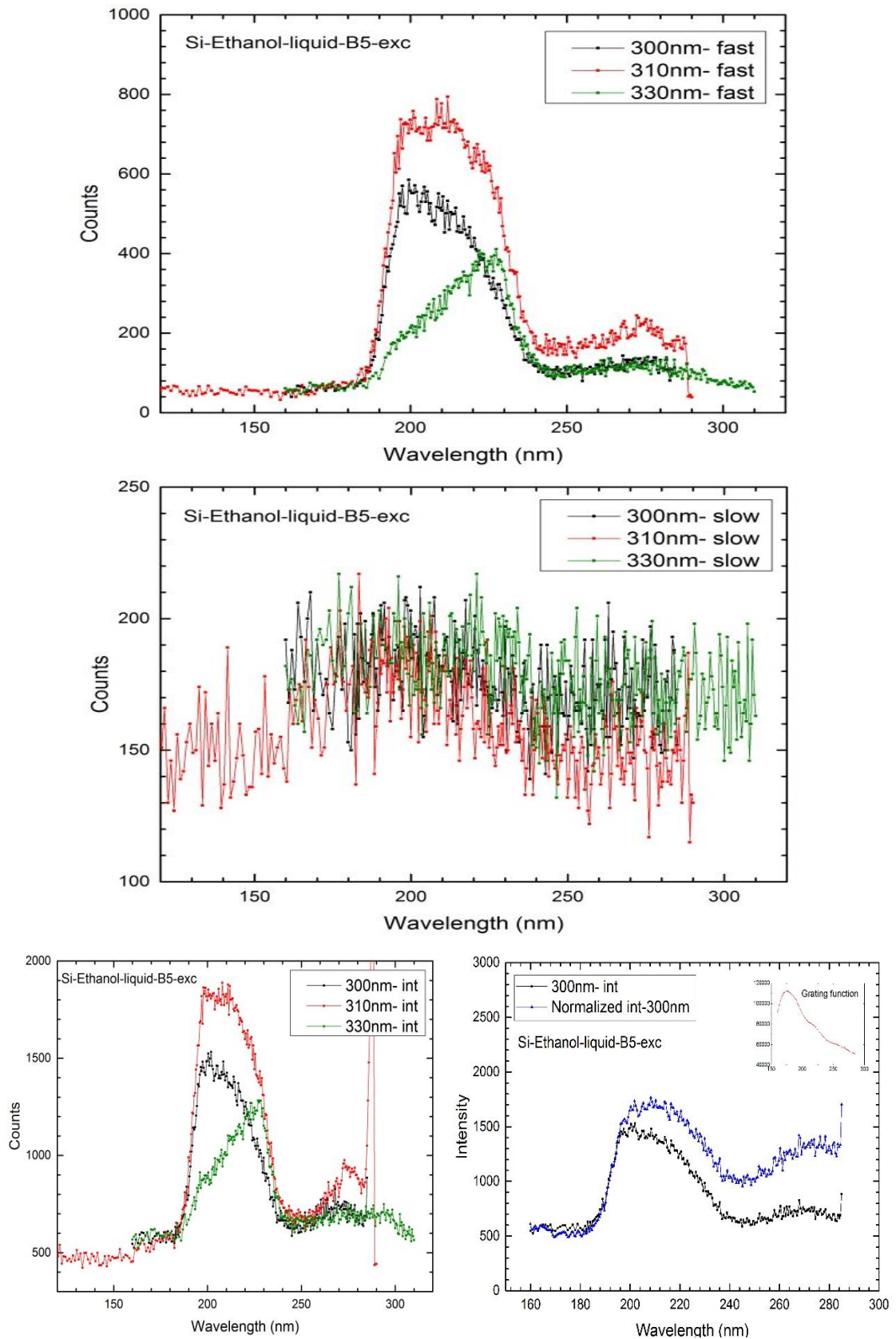


Figure A.4-7. Excitation spectra of different components of Si-ethanol liquid sample. The normalised int component at 300 nm is shown as a comparison with the same spectrum before normalization.

4.3.2 Silicon-ethanol-film

Emission spectra of sample B5, as a Si-ethanol film, are shown in Figure A.4-8. For recording emission spectra, filter WG225 was used. The experiment was performed at room temperature.

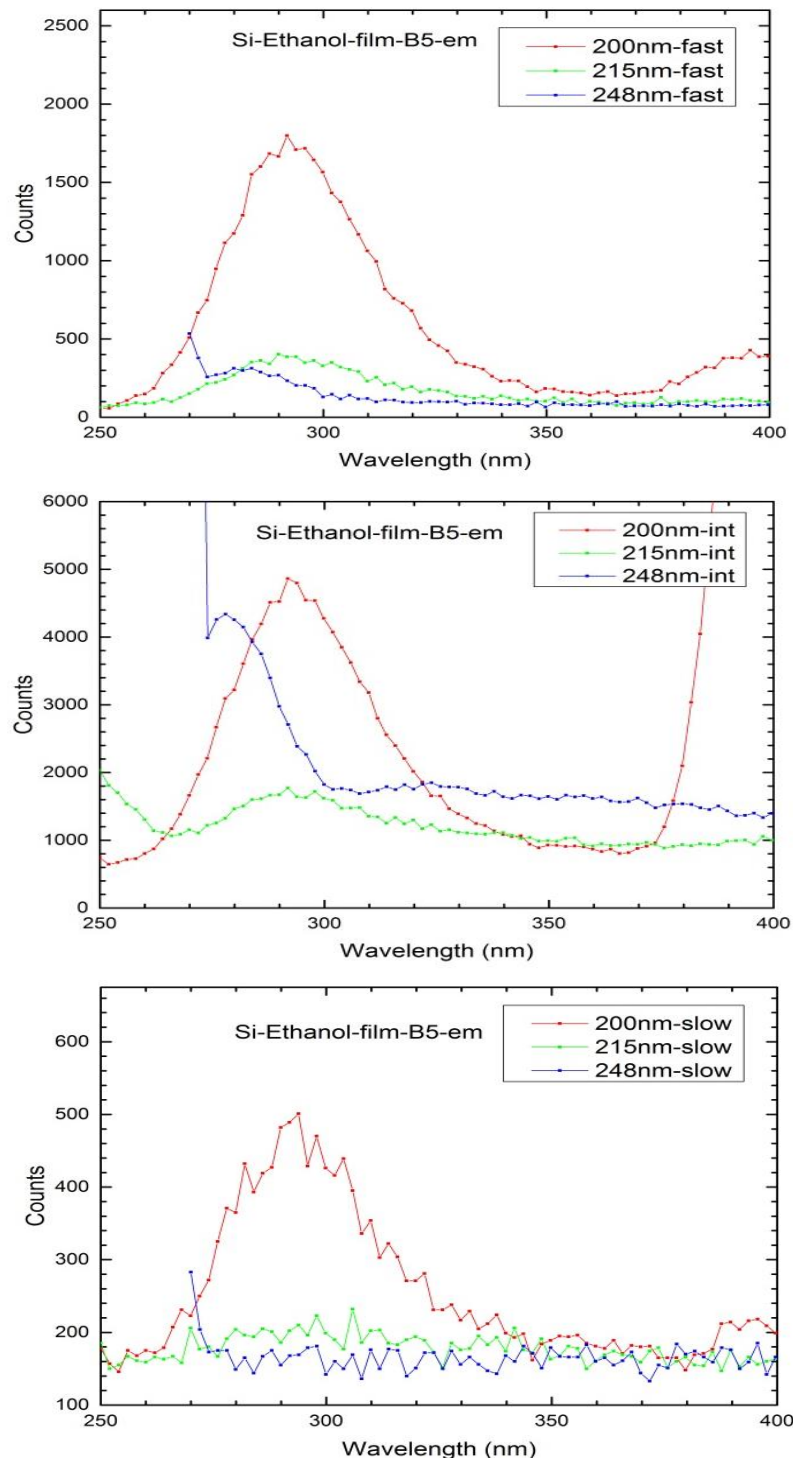


Figure A.4-8. Emission spectra of different components of Si-ethanol B5 film sample.

Excitation spectra of Si-ethanol film for sample B5 is shown in Figure A.4-9. The filter used for 410 nm and 300 nm emission wavelengths was WG280, and for 290 nm was filter WG225.

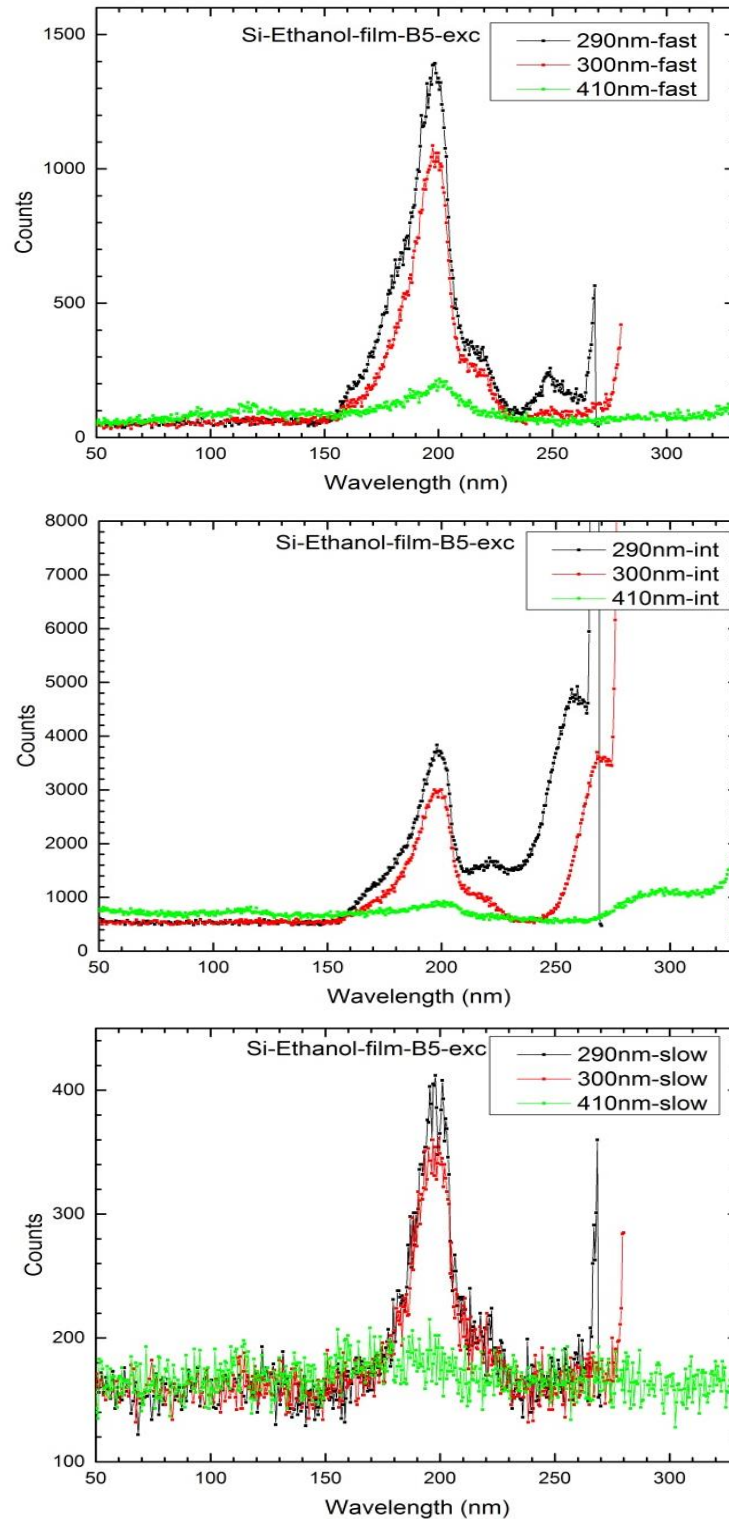


Figure A.4-9. Excitation spectra of different components of sample B5 Si-ethanol B5 film.

Another Si-ethanol film sample was investigated, sample B6. For excitation at 203 nm filter WG225 was used, and for excitation at 228 nm and 290 nm, filter WG280 were used. Measurements were performed at room temperature. Emission spectra are shown in Figure A.4-10.

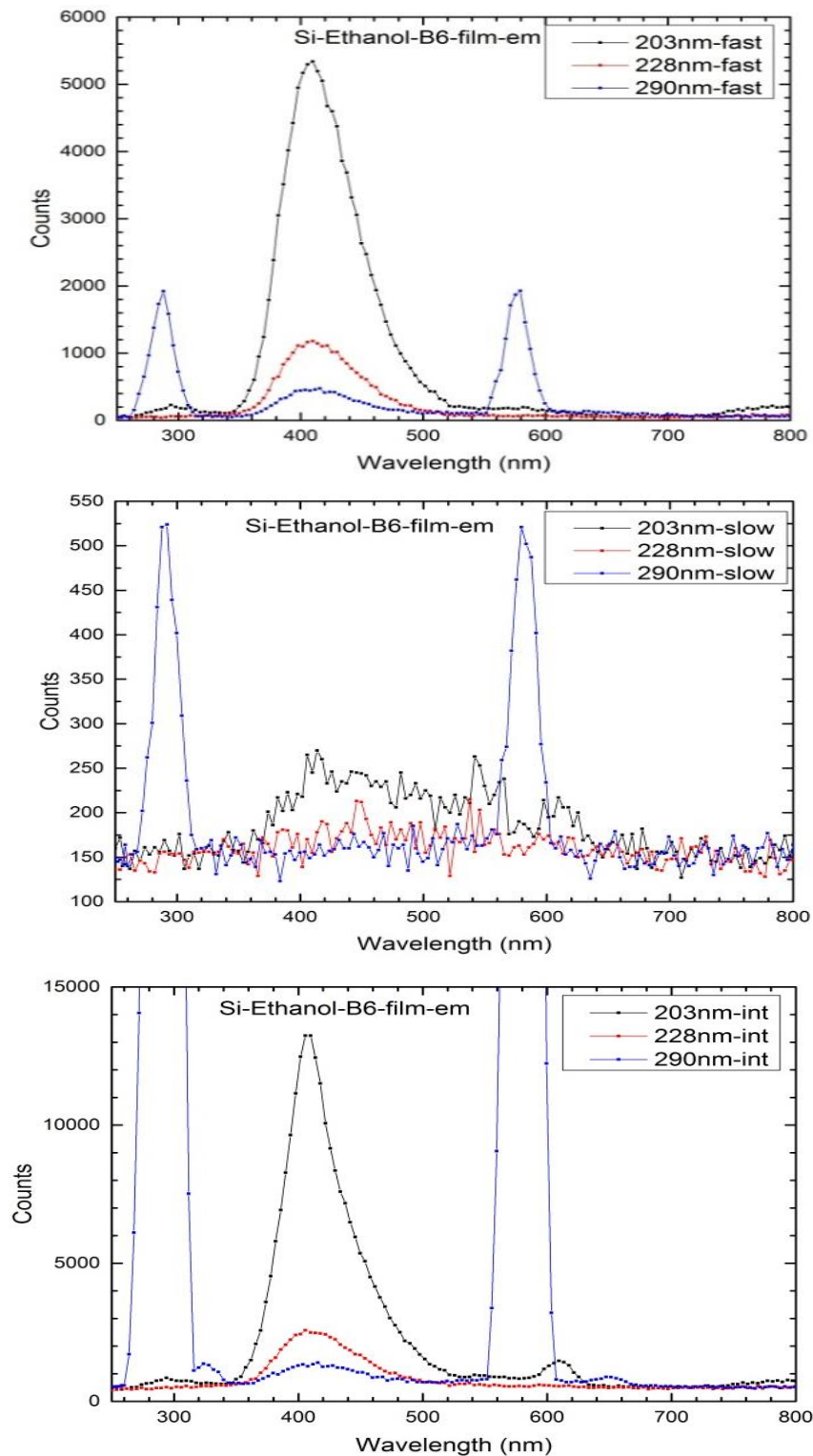


Figure A.4-10. Emission spectra of different components of Si-ethanol film, sample B6.

The excitation spectra of this sample were measured and are shown in Figure A.4-11. They were recorded at room temperature using filter WG280.

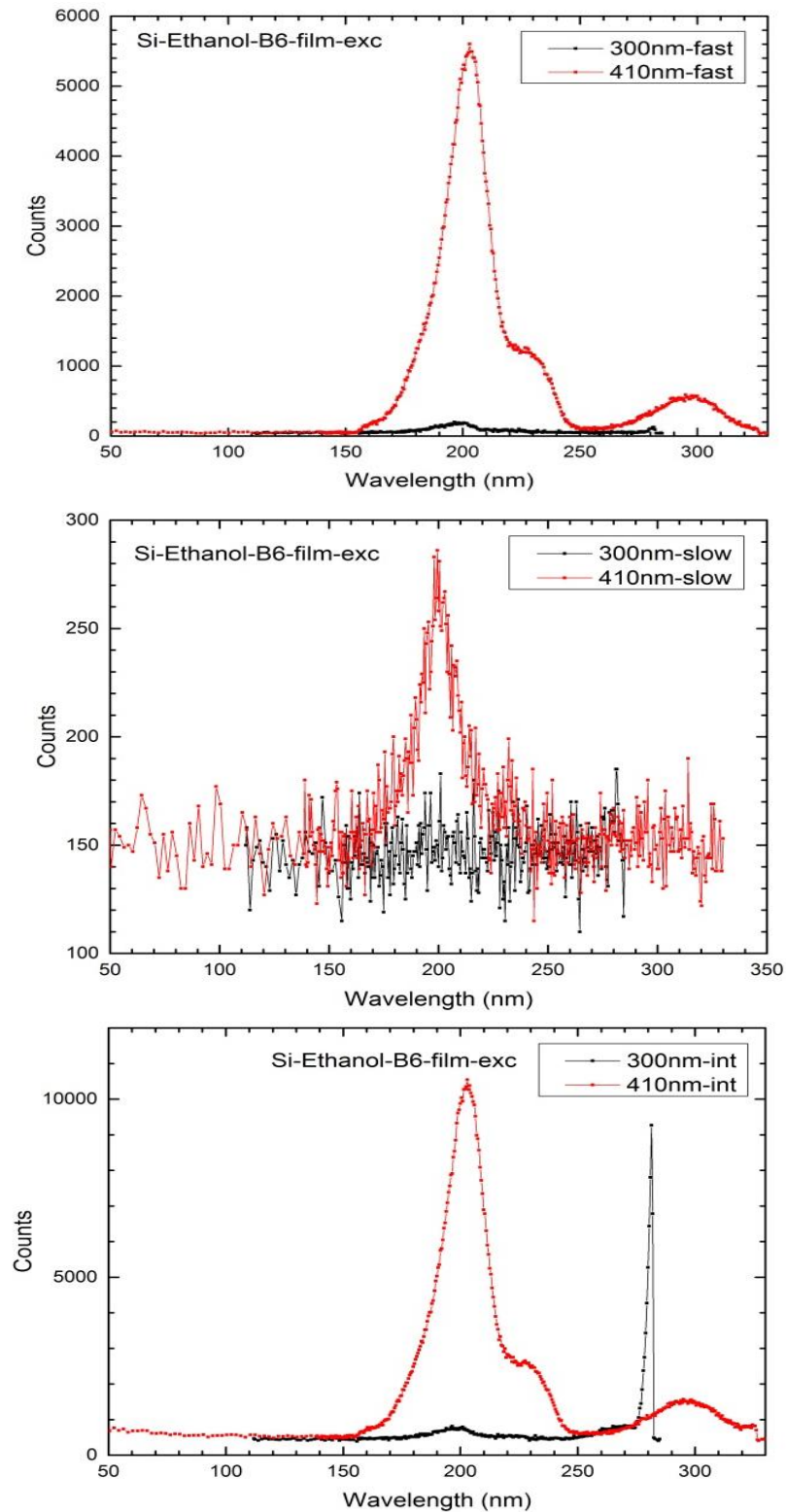


Figure A.4-11. Excitation spectra of different components of Si-ethanol film, sample B6.

4.3.3 Si-IPA-film

Emission spectra of Si-IPA film, sample C4, are shown in Figure A.4-12. Experiments were performed in room temperature and filter WG280 was used.

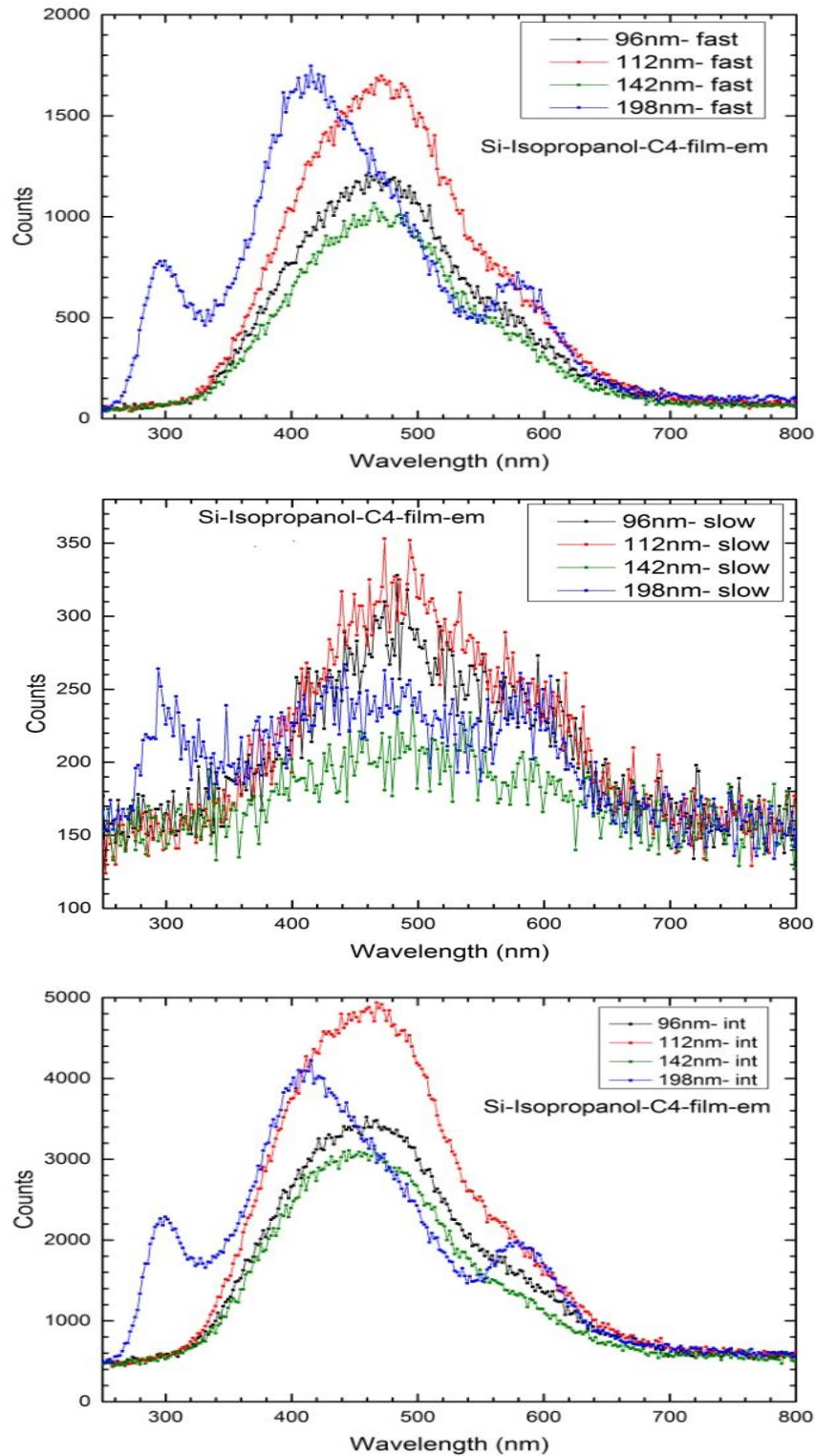


Figure A.4-12. Emission spectra of different components of Si-IPA C4 film sample.

The excitation spectra recorded at room temperature using filter WG280 are shown in Figure A.4-13. A normalized excitation spectrum (int) emitted at 420 nm is shown also.

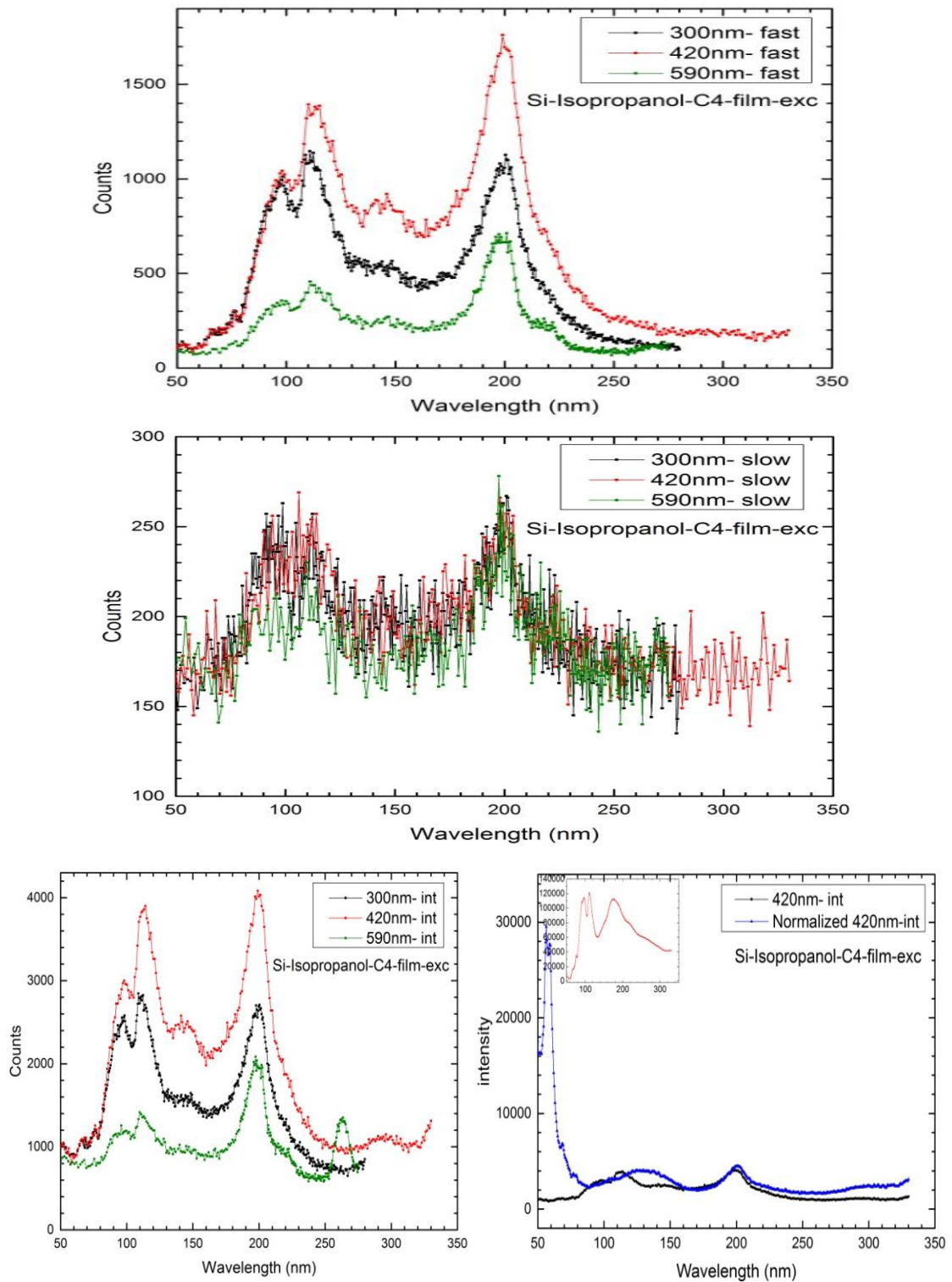


Figure A.4-13. Excitation spectra of different components of Si-IPA C4 film sample.

4.3.4 Si-water-film

Si-water film, sample D8, was investigated in room temperature. Filter WG225 was used for all measurements except measurement at 259 nm, where filter WG280 was used. Emission spectra recorded for this sample are shown in Figure A.4-14.

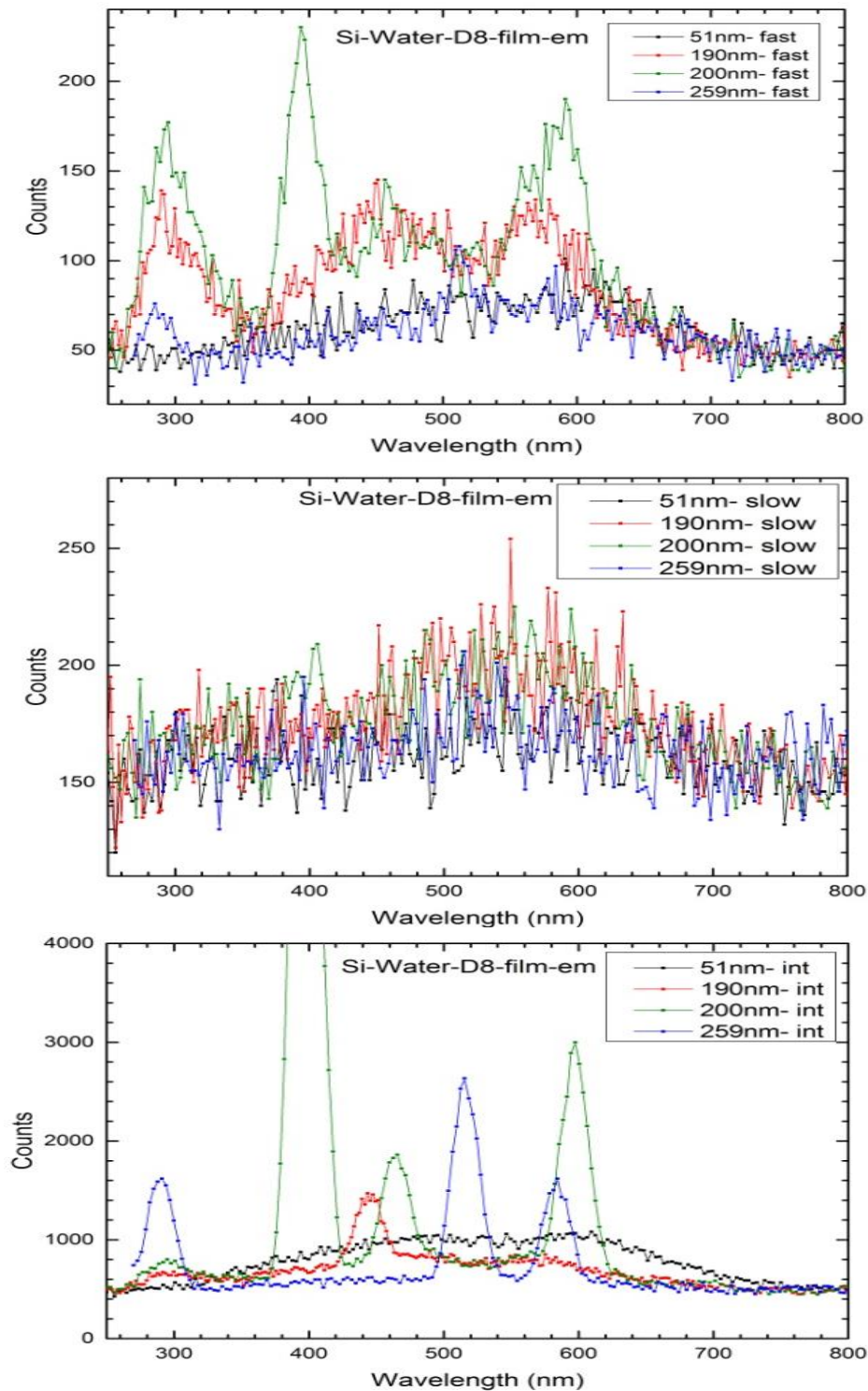


Figure A.4-14. Emission spectra of different components of Si-water D8 film sample.

The excitation spectra of Si-water film, sample D8, were recorded at room temperature and filter WG280 was used for all measurements except the measurement at 563 nm, where filter WG225 was used.

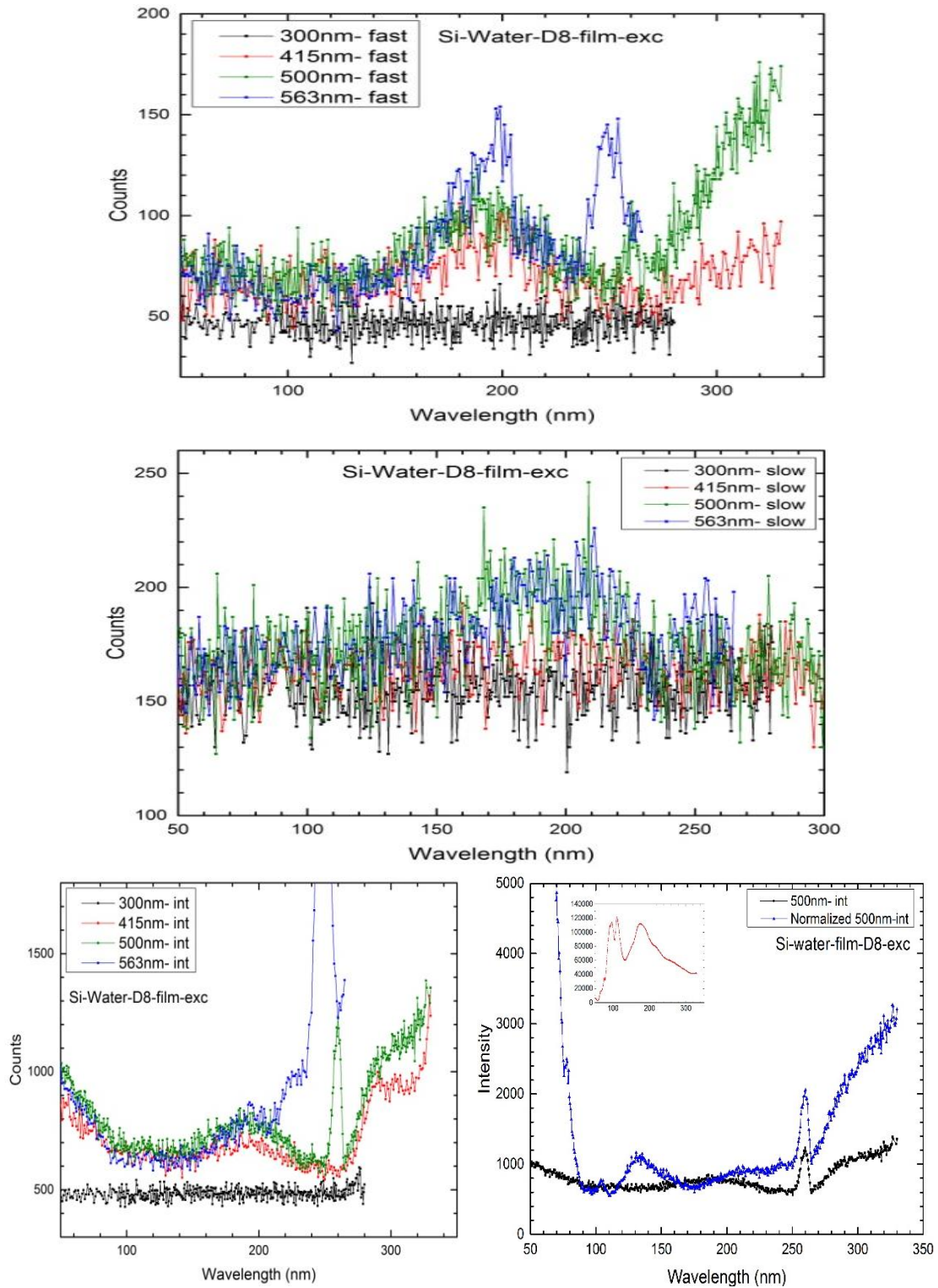


Figure A.4-15. Excitation spectra of different components of Si-water D8 film sample.

4.3.5 Si-water-liquid

Emission and excitation spectra of Si-water liquid sample C2 were recorded at room temperature, using filter WG280. The results are shown in Figure A.4-16 and Figure A.4-17.

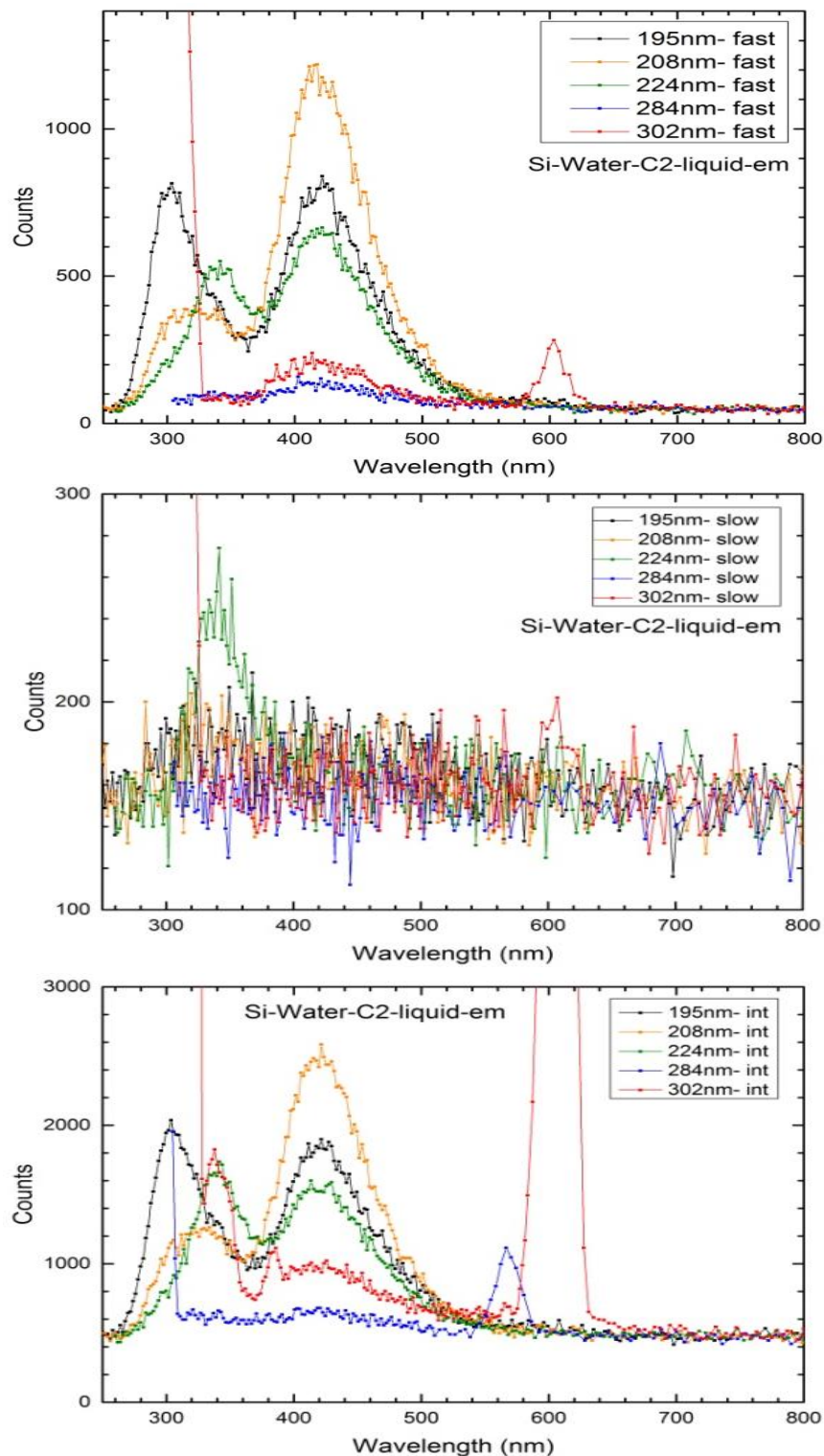


Figure A.4-16. Emission spectra of different components of Si-water liquid sample C2.

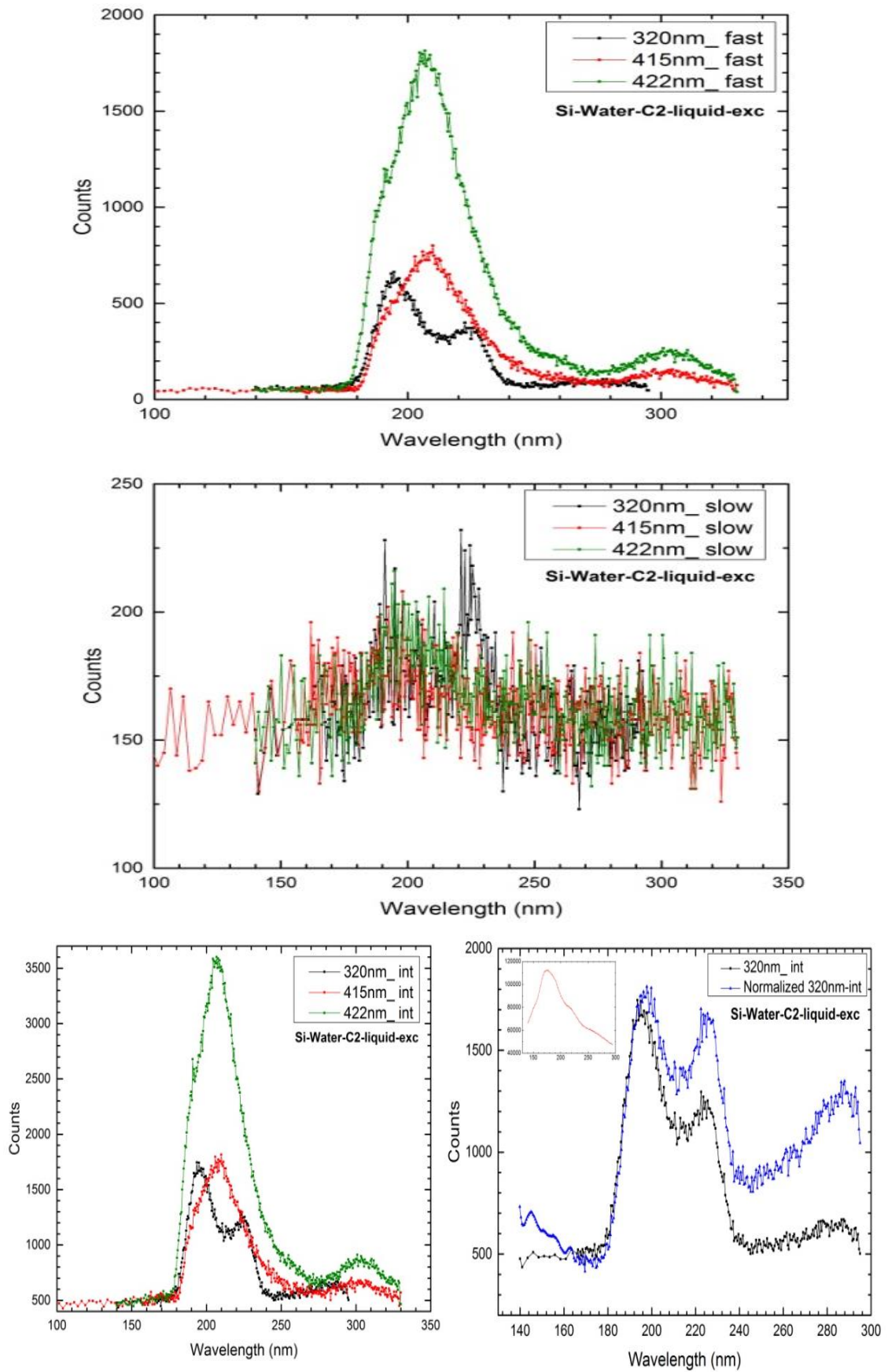


Figure A.4-17. Excitation spectra of different components of Si-water liquid sample C2.

4.4 Dependence of fluorescence on temperature

The dependence of fluorescence spectra on temperature was discussed in chapter 4, and results for int components excited at 203 nm at three different temperatures were shown. Here, the results for all components (fast, slow, and int) and different wavelengths (203 nm, 228 nm, and 290 nm) at 8 K, 28 K, and 300 K are shown. All spectra were recorded by using filter WG280, except the spectrum at room temperature excited at 203 nm, where filter WG225 was used. Figure A.4-18, Figure A.4-19, and Figure A.4-20 show spectra at 203 nm, 228 nm, and 290 nm, respectively.

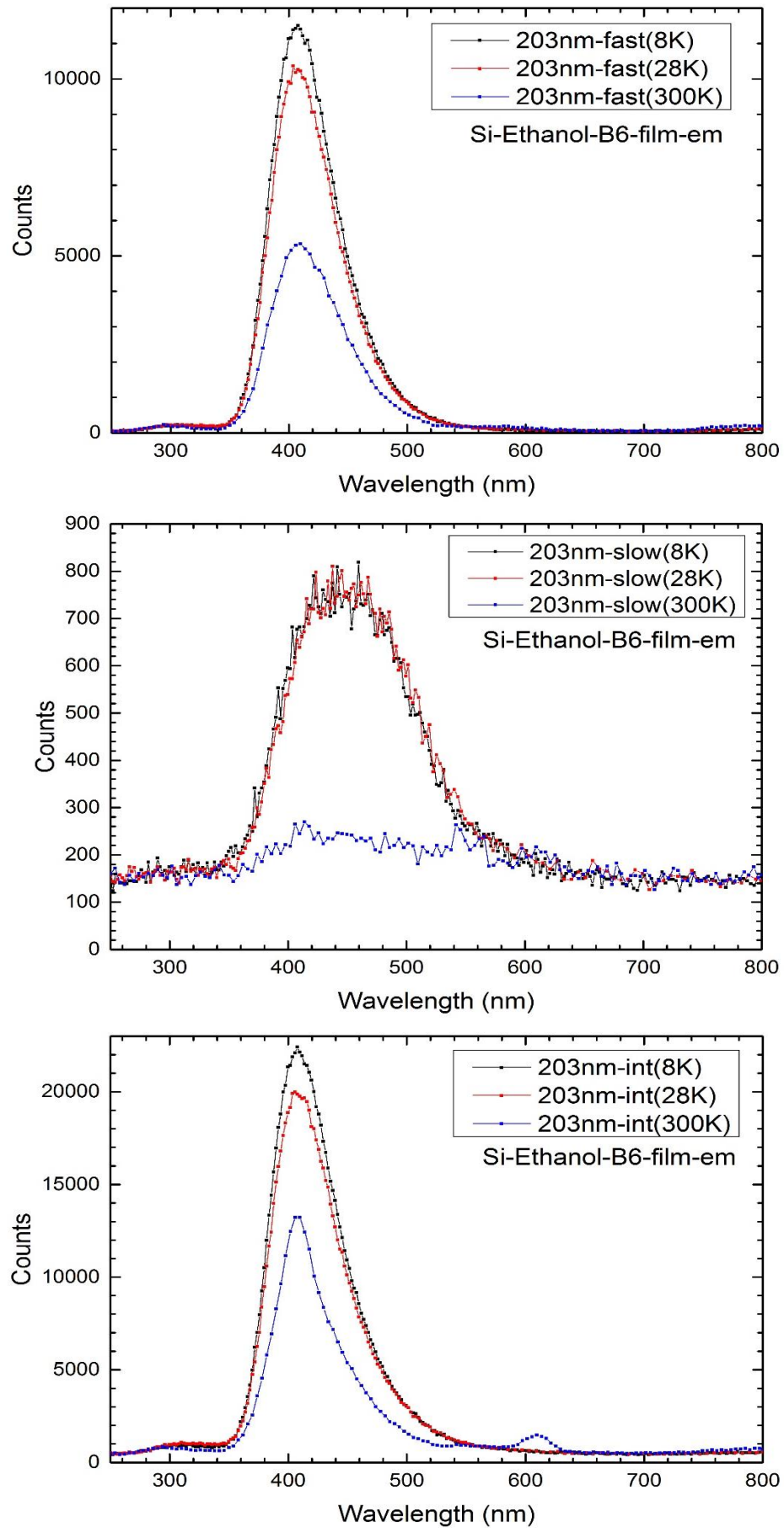


Figure A.4-18. Temperature dependence study of emission spectra excited at 203 nm.

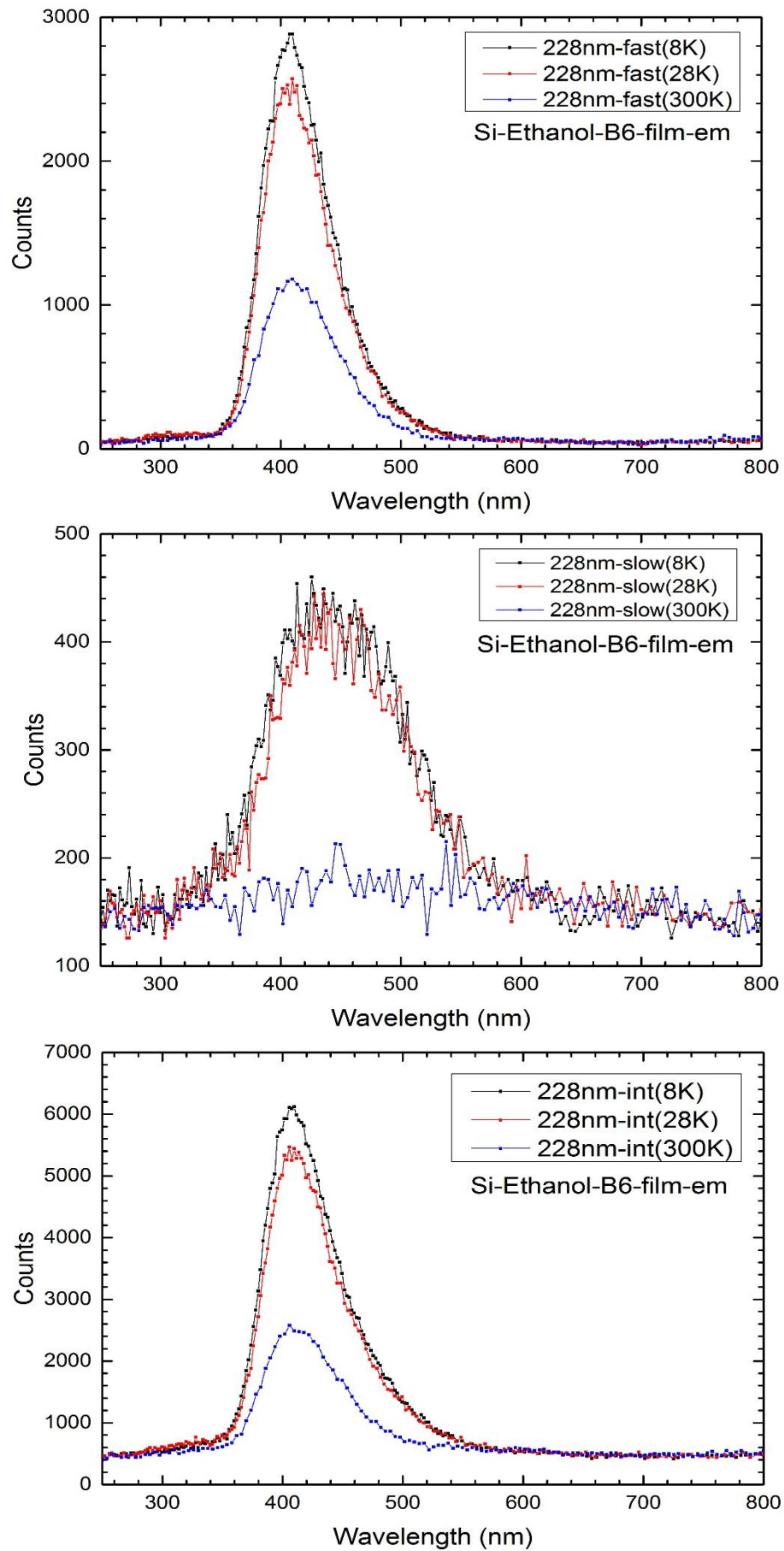


Figure A.4-19. Temperature dependence study of emission spectra excited at 228 nm.

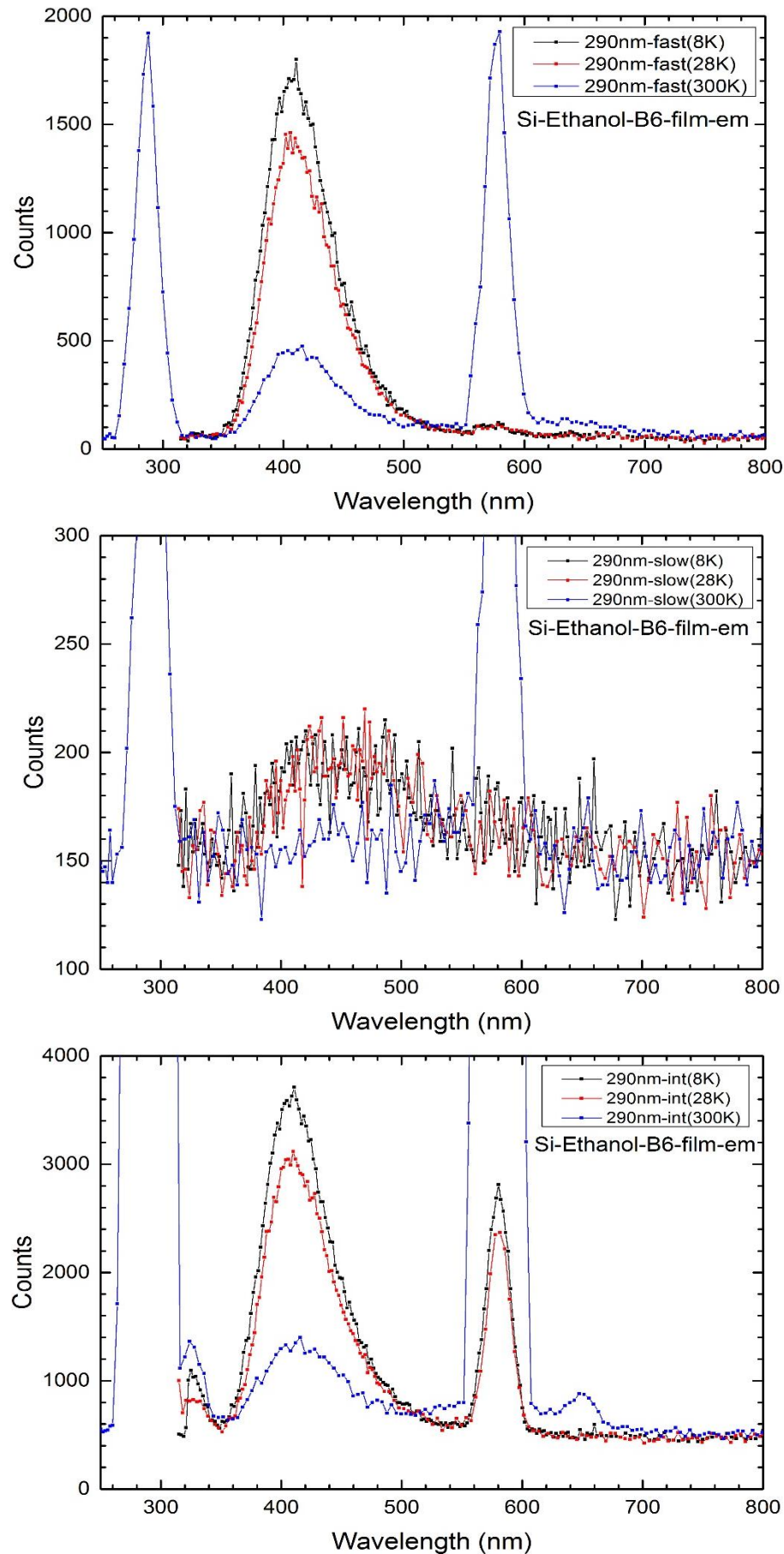


Figure A.4-20. Temperature dependence study of emission spectra excited at 290 nm.

4.5 Lifetime measurements

4.5.1 Dependence of fluorescence lifetime on emission and excitation wavelength

In chapter 4, the results of fluorescence lifetime dependence on excitation wavelength for Si-ethanol film sample B6 were shown; here, additional decay time measurements for other samples are given. Figure A.4-21 shows fluorescence lifetime measurements for Si-ethanol film sample B5, which were performed at room temperature using filter WG225. Figure A.4-22 shows the results for Si-IPA film sample C4 at room temperature and using filter WG280. Si-water liquid sample C2 was measured at room temperature and using filter WG280, and is shown in Figure A.4-23.

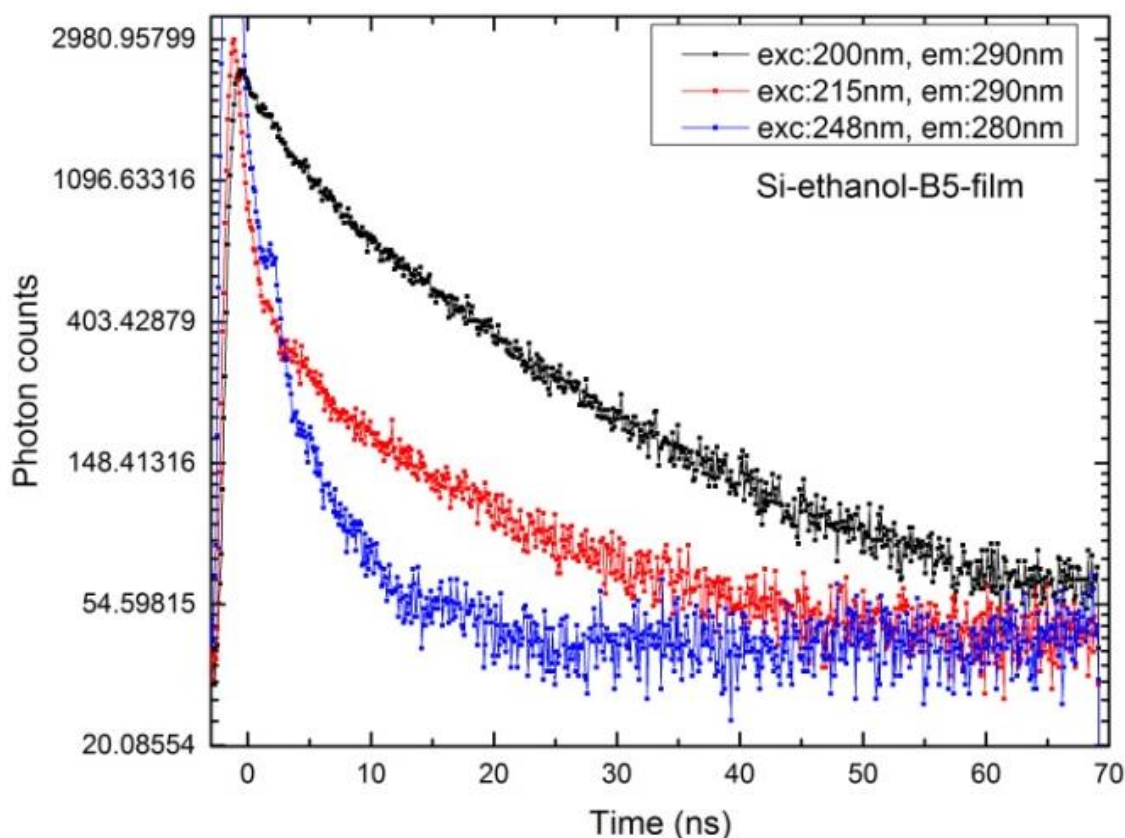


Figure A.4-21. Fluorescence lifetime dependence excitation wavelength for Si-ethanol film sample B5.

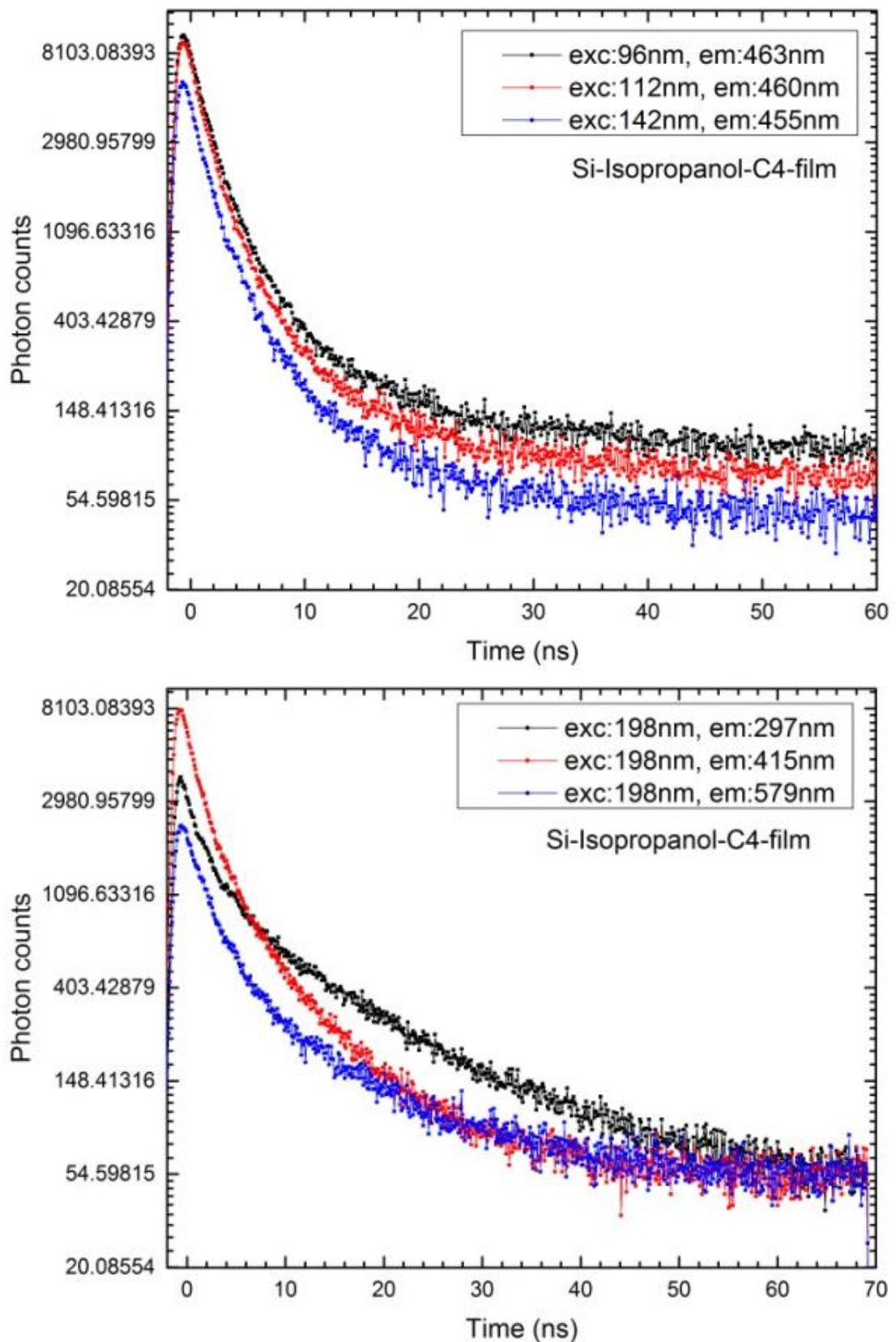


Figure A.4-22. Fluorescence lifetime dependence on emission and excitation wavelength for Si-IPA film sample C4.

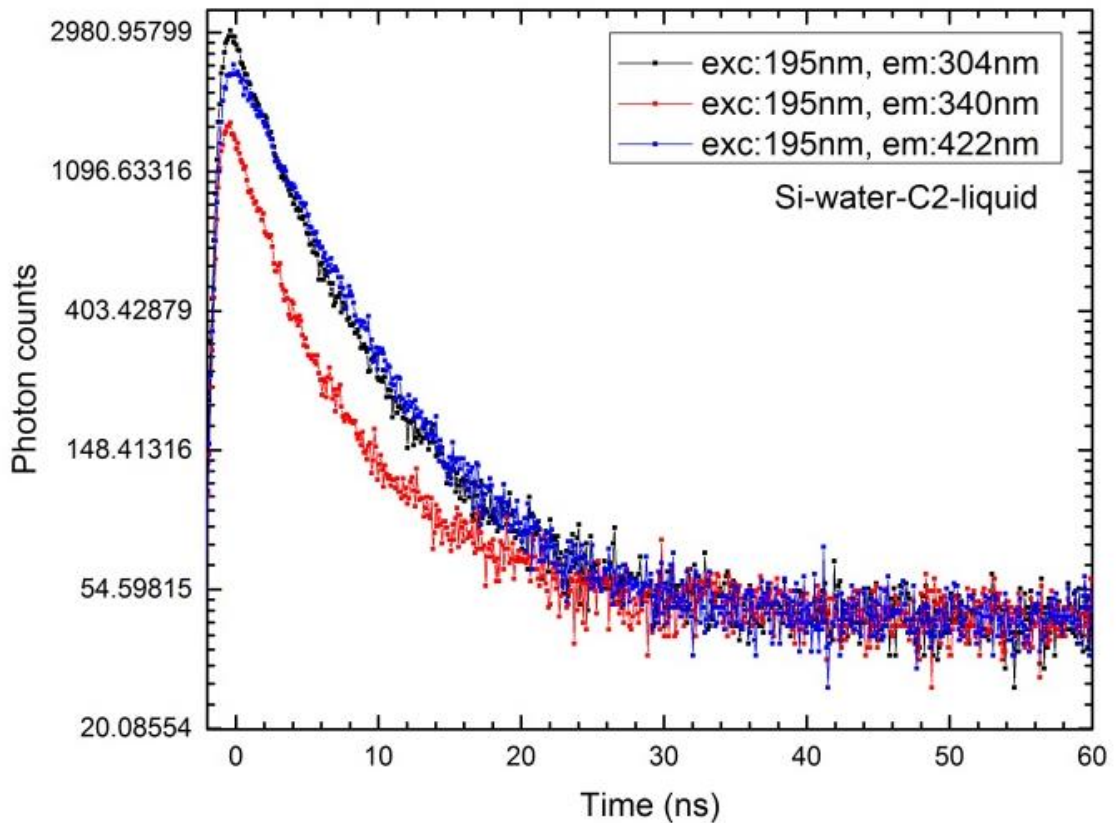


Figure A.4-23. Fluorescence lifetime dependence on emission wavelength for Si-water liquid sample C2.

4.5.2 Fluorescence lifetime measurement at low temperature

Fluorescence lifetime measurements were performed at low temperature and compared with the lifetime measurements conducted at room temperature in chapter 4. Here, lifetime results of Si-ethanol film sample B6 at 8 K is shown in Figure A.4-24, and results for Si-ethanol film sample A6 at 10 K is shown in Figure A.4-25. Experiments were performed at different excitation and emission wavelengths. For all measurements, filter WG280 was used.

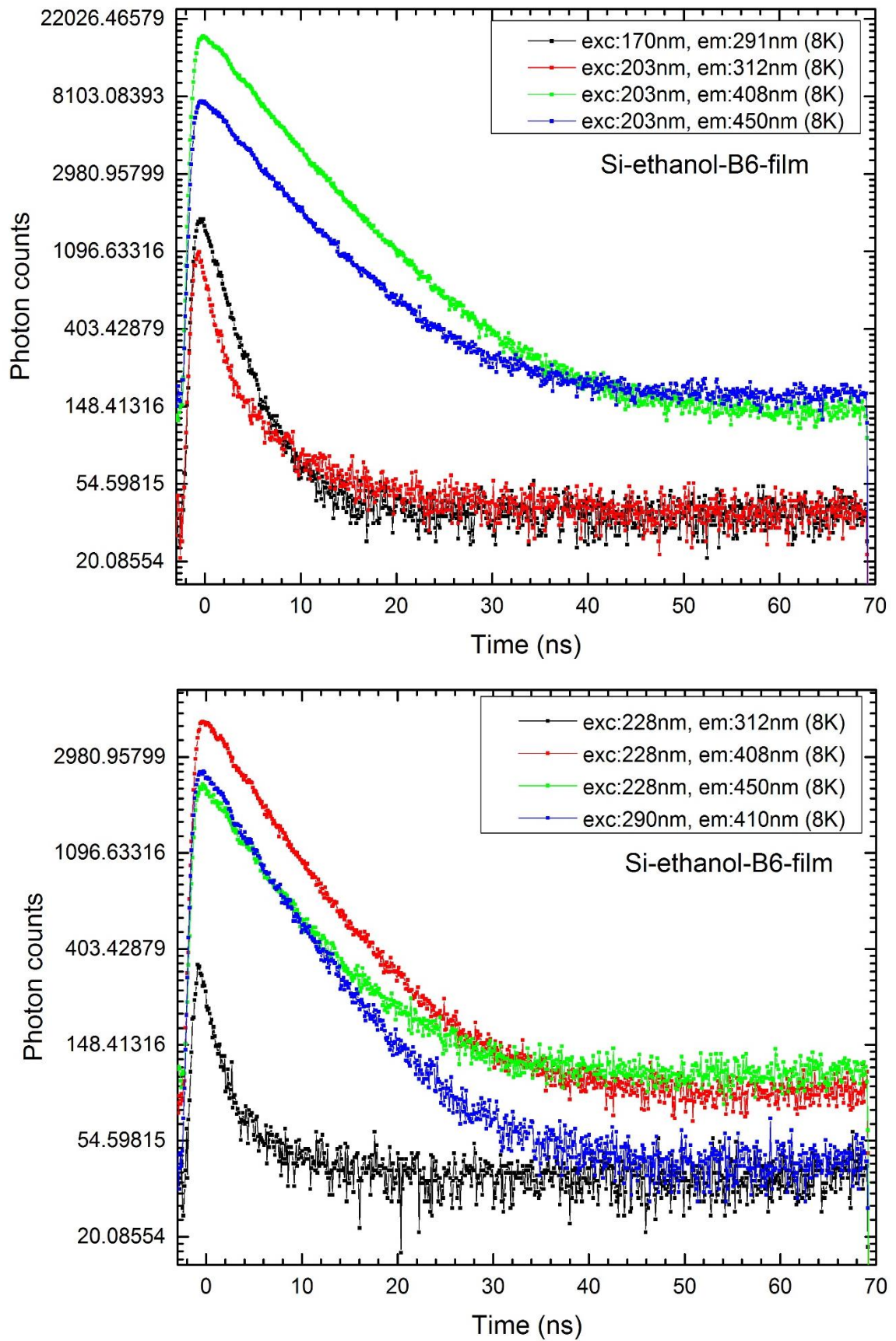


Figure A.4-24. Decay time measurements of Si-ethanol film sample B6 at 8 K.

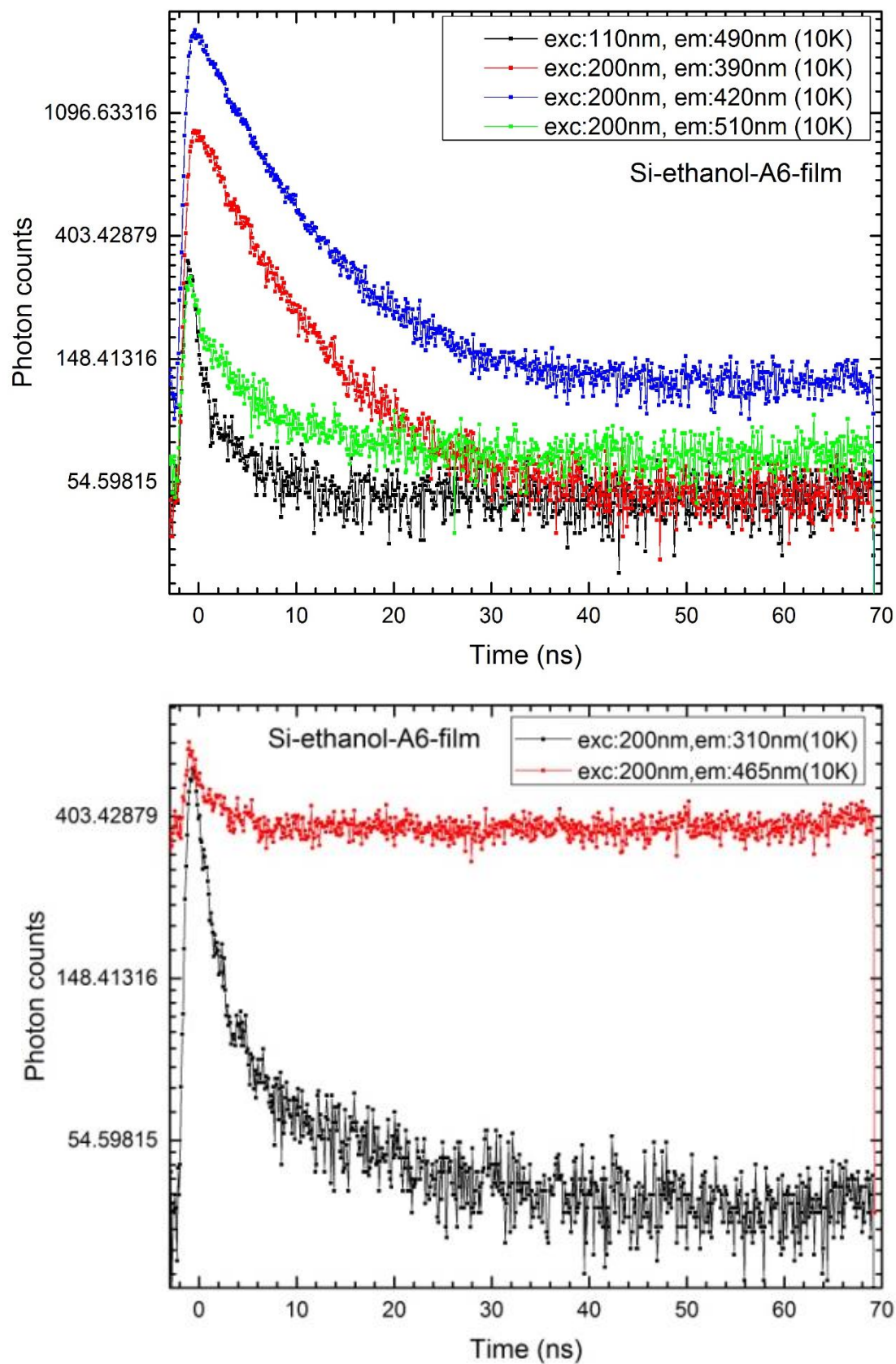


Figure A.4-25. Decay time measurements of Si-ethanol film sample A6 at 10 K.

4.5.3 Effect of temperature on fluorescence lifetime

The effect of temperature on fluorescence lifetime was discussed in chapter 4, and spectra for Si-ethanol film sample B6 excited at 203 nm at two different temperatures (8 K and 300 K) were shown in chapter 4. Here, the results of measurements for the sample at 290 nm and 228 nm excitation wavelengths are shown in Figure A.4-26.

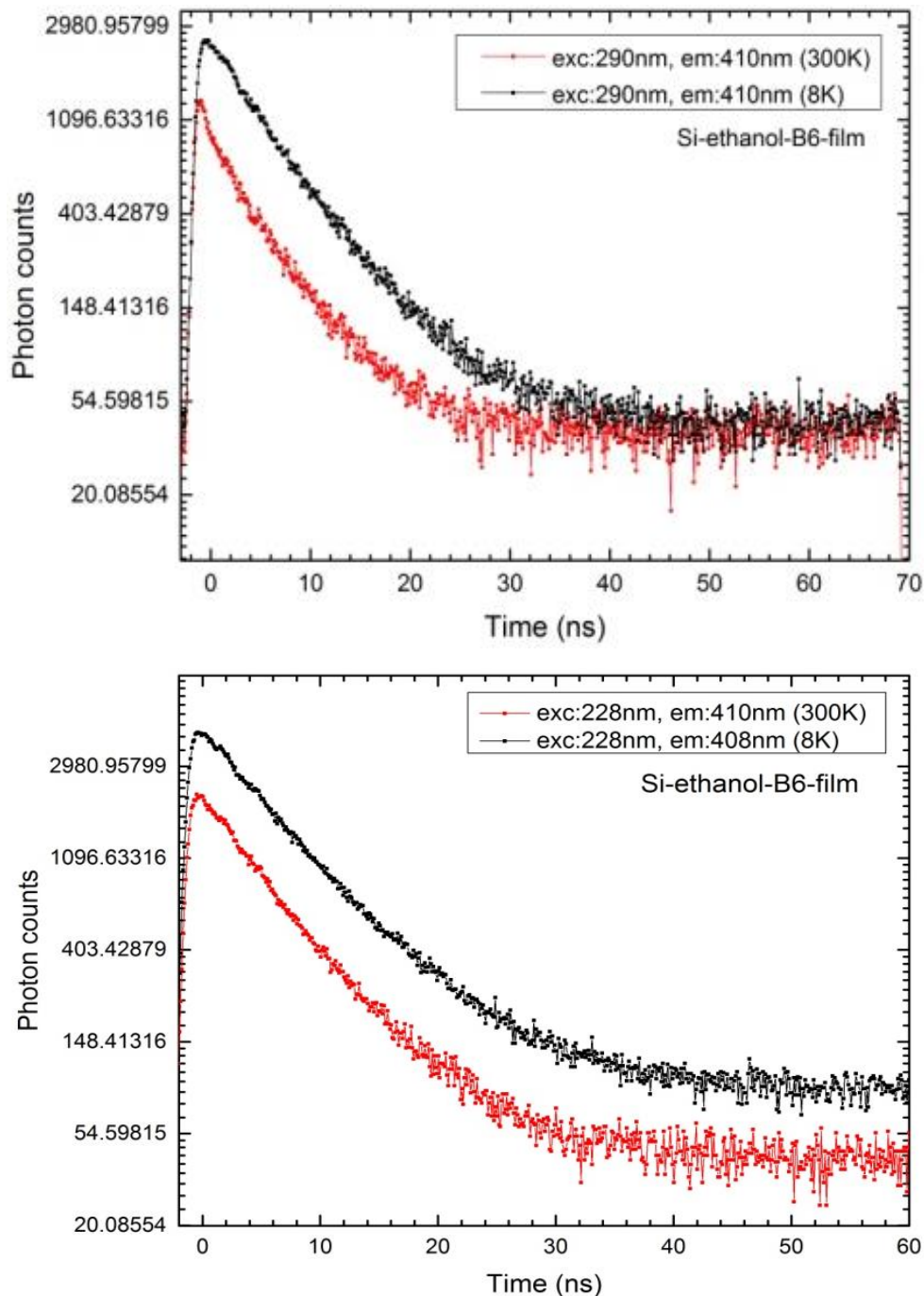


Figure A.4-26. Figure showing lifetime dependence on temperature; lifetime decreases with increasing temperature.

4.6 Effect of argon pressure, sputter head power and Deposition time

In this section, the parameters which are important during sample production, such as stagnation pressure, magnetron power, and deposition time, were investigated. In each experiment, two of these parameters were kept constant and the third one was adjusted. The results of this study are shown in Figure A.4-27 to Figure A.4-29. All the results in this section are belong to liquid samples and excited at 270 nm.

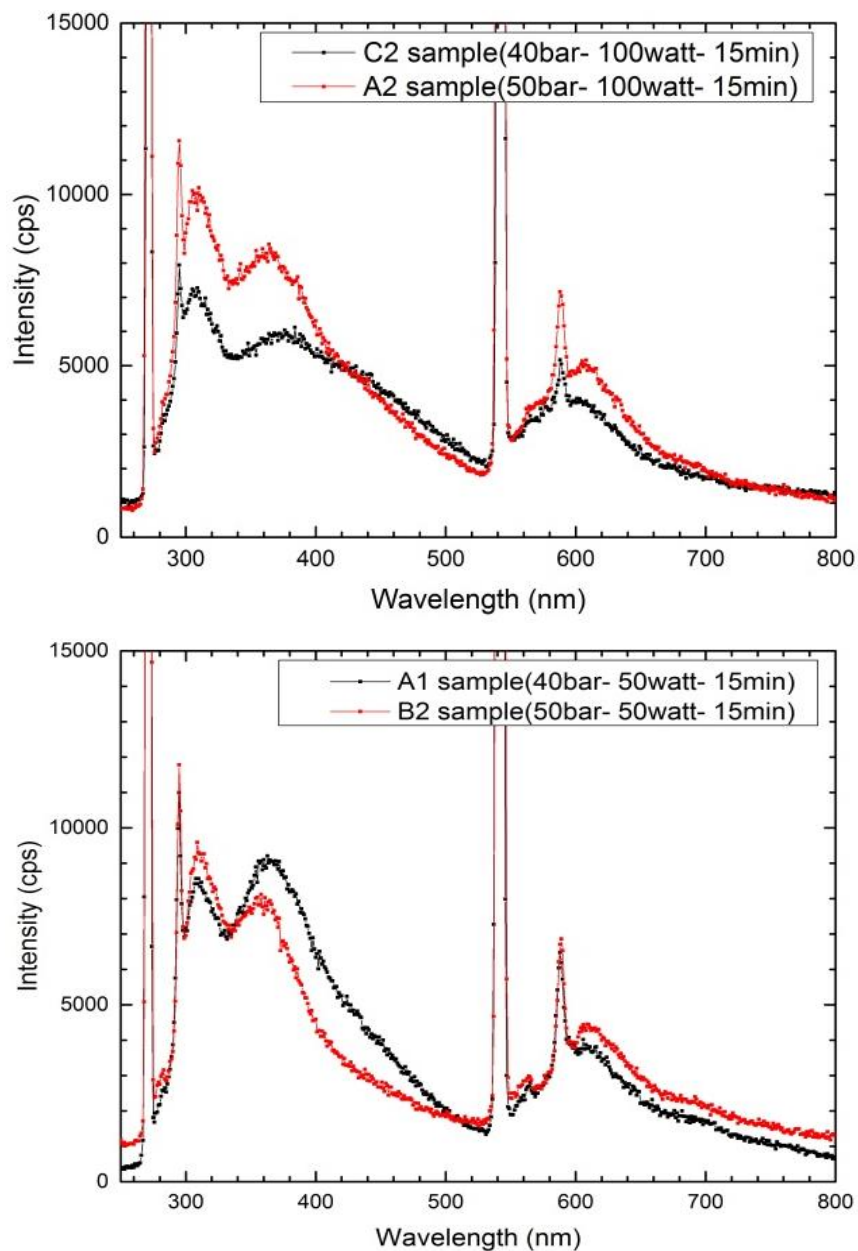


Figure A.4-27. Figure showing the effect of changing the stagnation pressure on fluorescence spectrum.

The experiments for different stagnation pressure were performed twice. The results do not show any conclusive effect on fluorescence intensity.

The power of the sputter head was set twice as high as normal to see the effect of power on fluorescence. Although the volume of atomic vapour produced doubles, it does not show any conclusive change in associated fluorescence spectra; only the sample produced at 100 W shows a shoulder to the longer wavelength side of the second fluorescence peak.

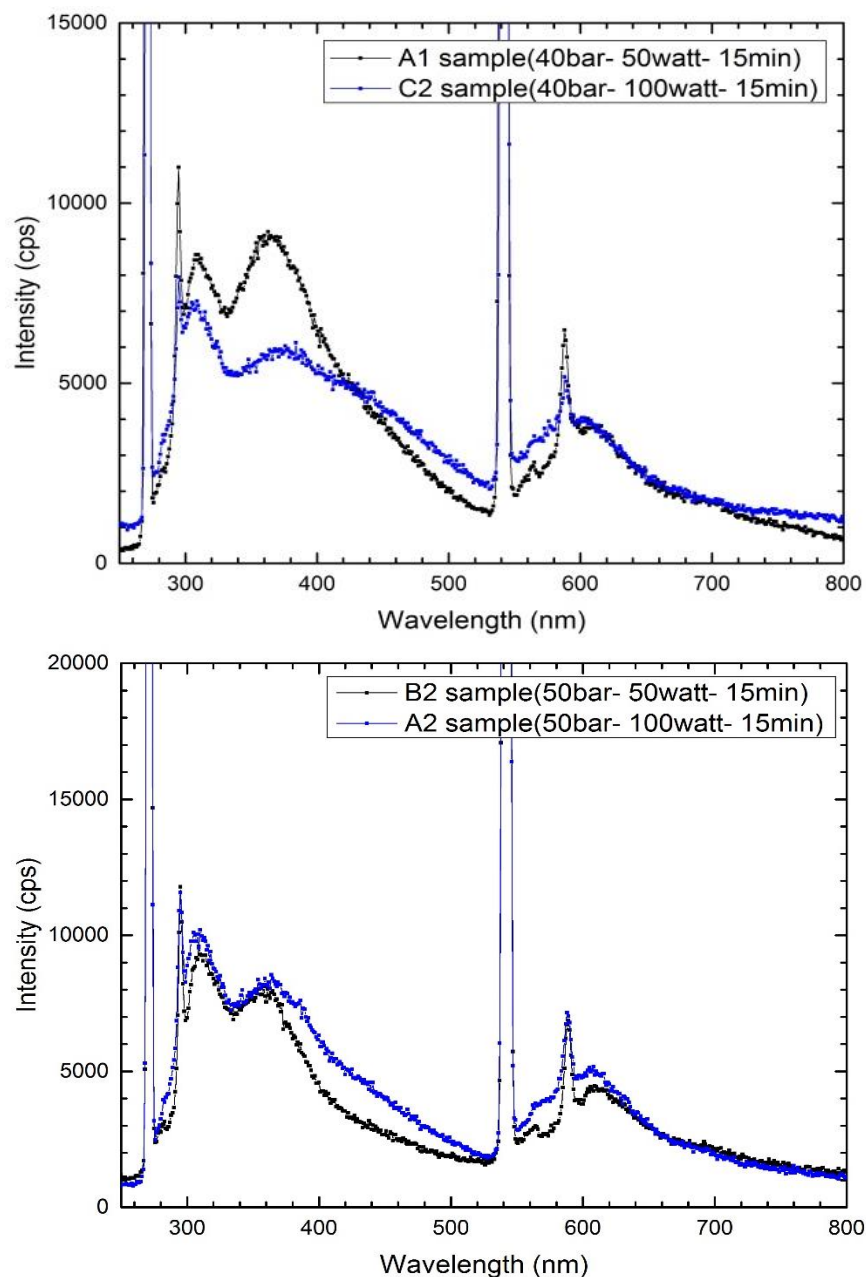


Figure A.4-28. Figure showing the effect of changing the magnetron power on fluorescence spectrum.

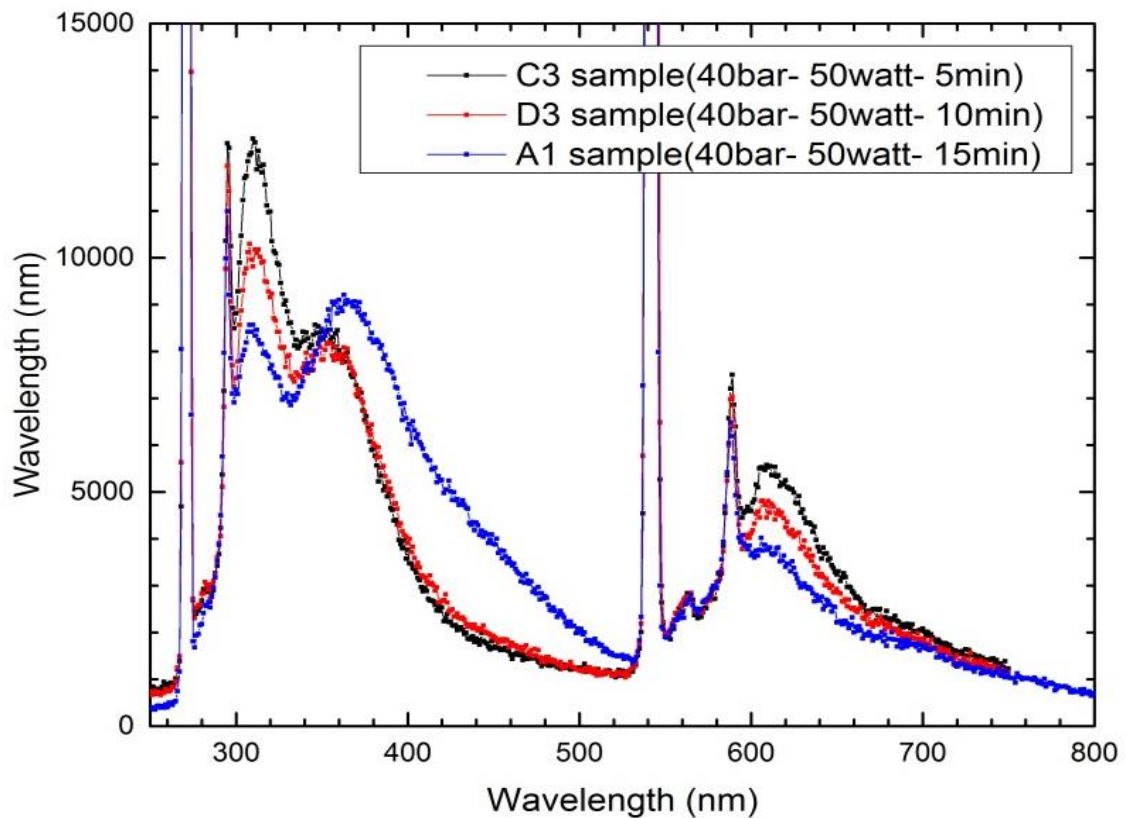


Figure A.4-29. Figure showing the effect of deposition time on the fluorescence spectrum.

As Figure A.4-29 shows, by increasing the deposition time, the intensity of the first peak decreases, but it does not show any conclusive effect on the second fluorescence peak's intensity.

Appendix 5

Complementary spectra to chapter 5

5.1 XPS survey spectra

Before taking XPS spectra of specific peaks with high resolution, a survey spectrum for each sample was recorded. The following figures show survey spectra for all samples discussed in section 5.1.

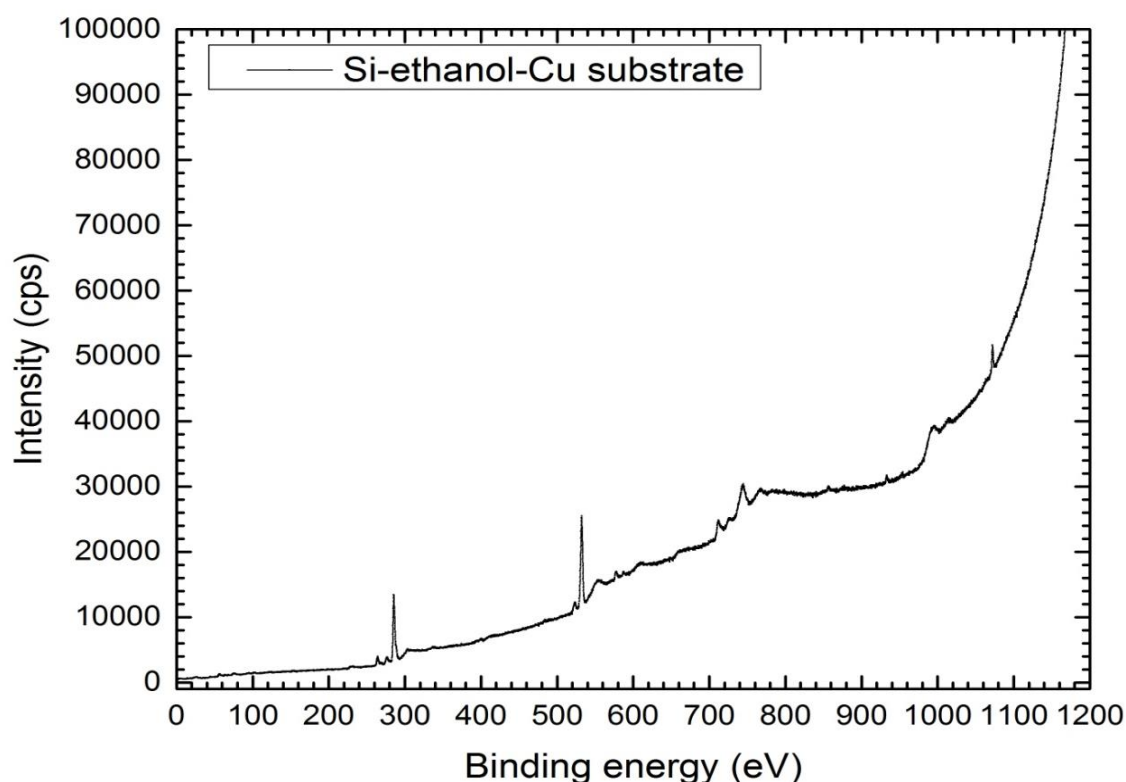


Figure A.5-1. XPS survey spectrum of nanoparticle film produced by deposition of silicon onto an ethanol liquid jet. The colloidal nanoparticles were drop cast in air onto an unspecified copper substrate.

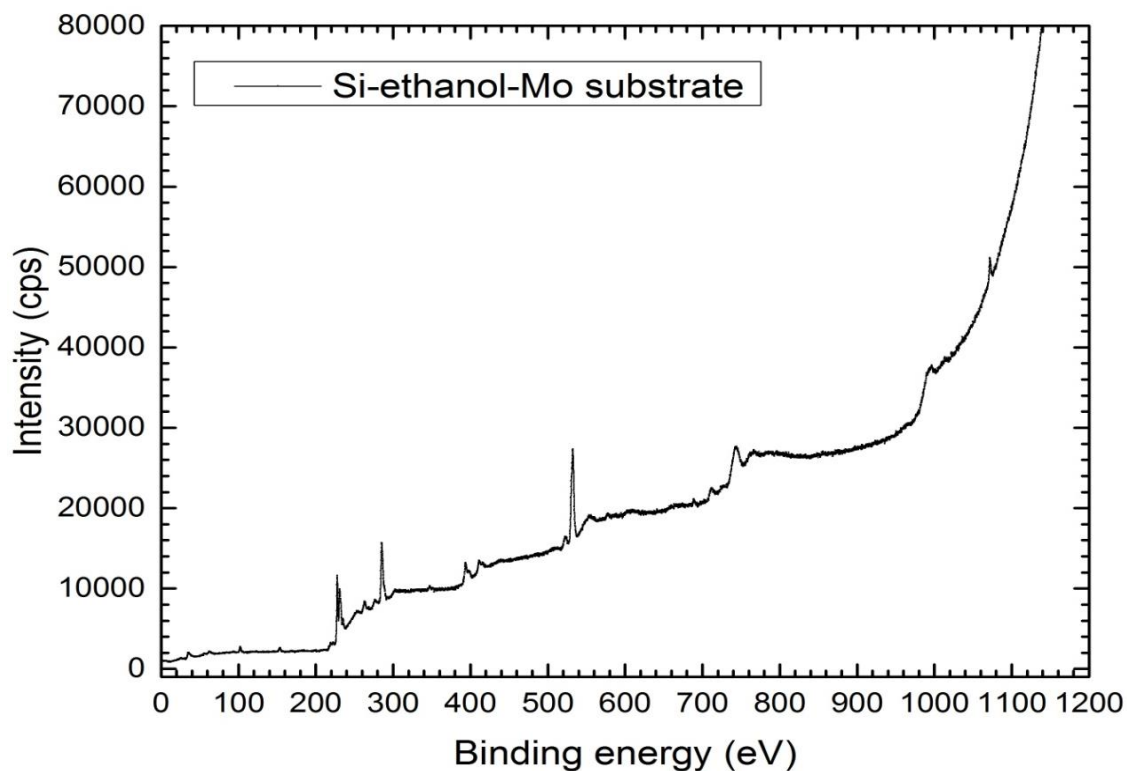


Figure A.5-2. XPS survey spectrum of Si-ethanol sample on Molybdenum substrate.

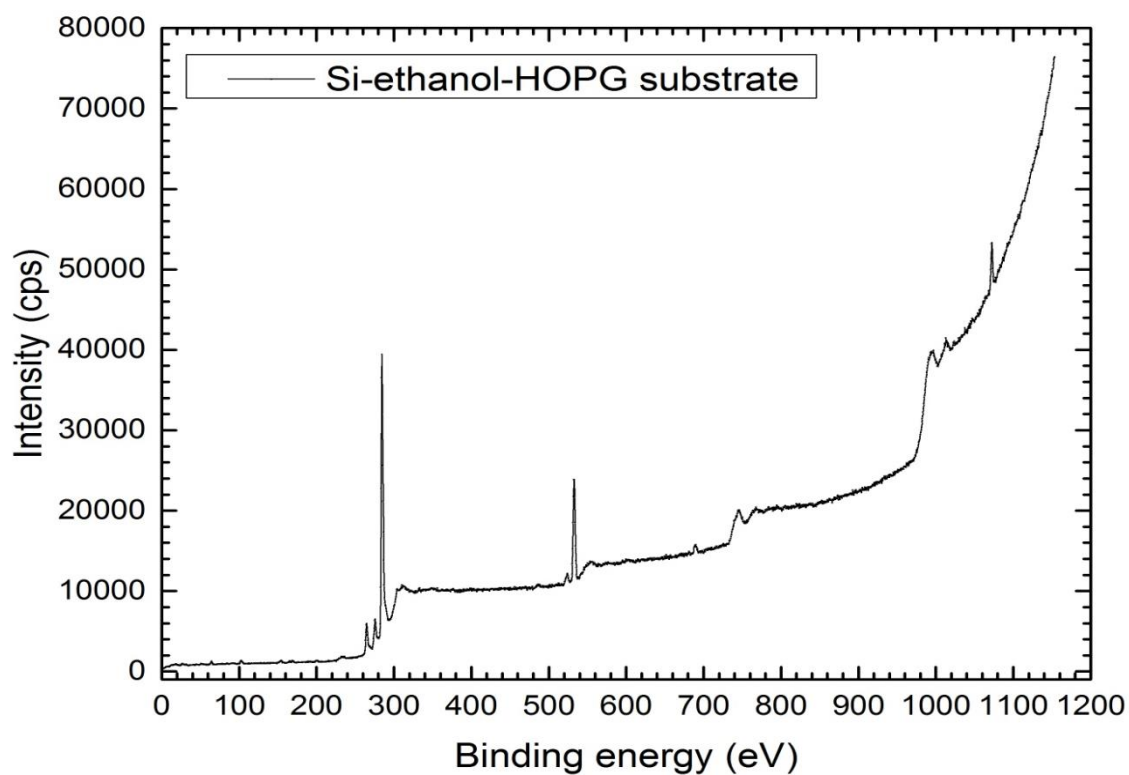


Figure A.5-3. XPS survey spectrum of Si-ethanol sample on HOPG substrate.

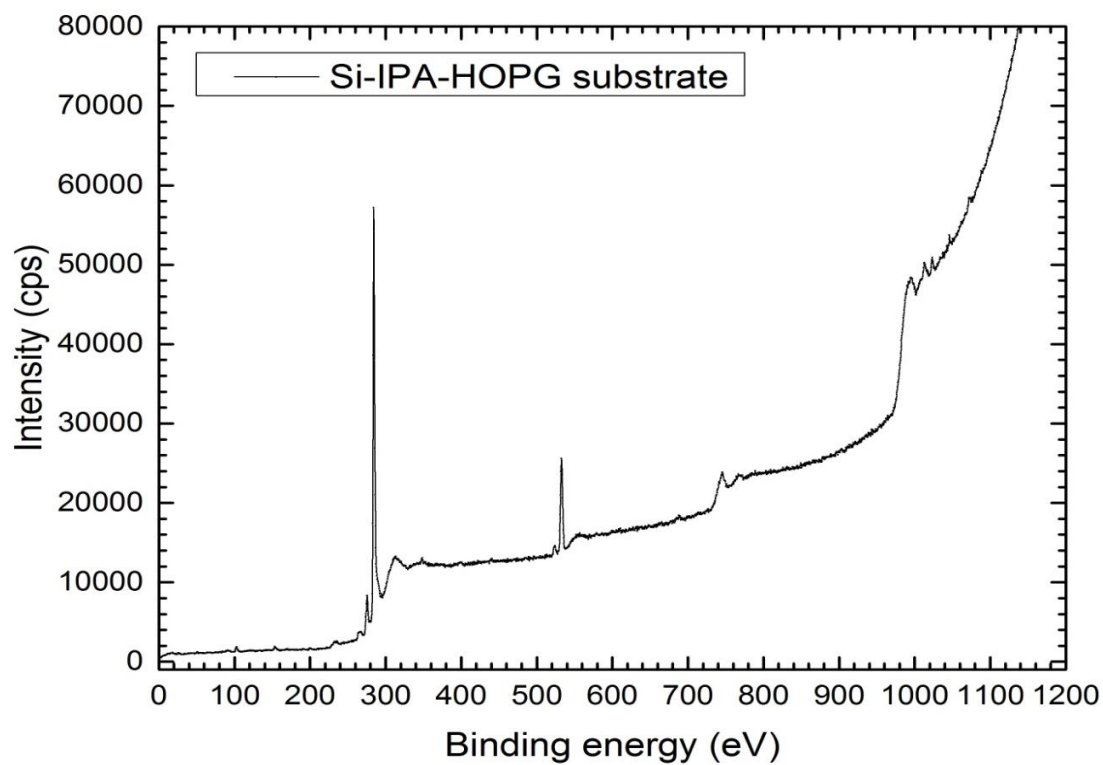


Figure A.5-4. XPS survey spectrum of Si-IPA sample on HOPG substrate.

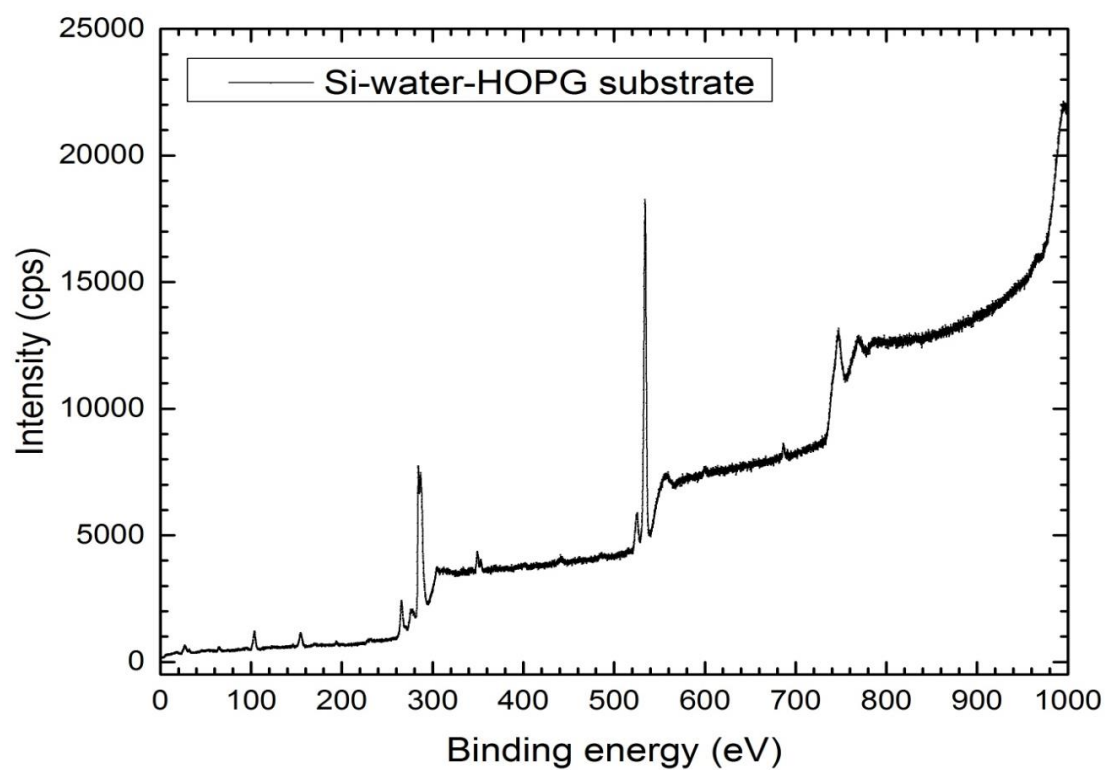


Figure A.5-5. XPS survey spectrum of Si-water sample on HOPG substrate.

5.2 Silicon wafer XPS spectra

We recorded silicon wafer spectra to have reference for our sample. The silicon 2s and 2p peaks show silicon bulk and silicon oxide peaks.

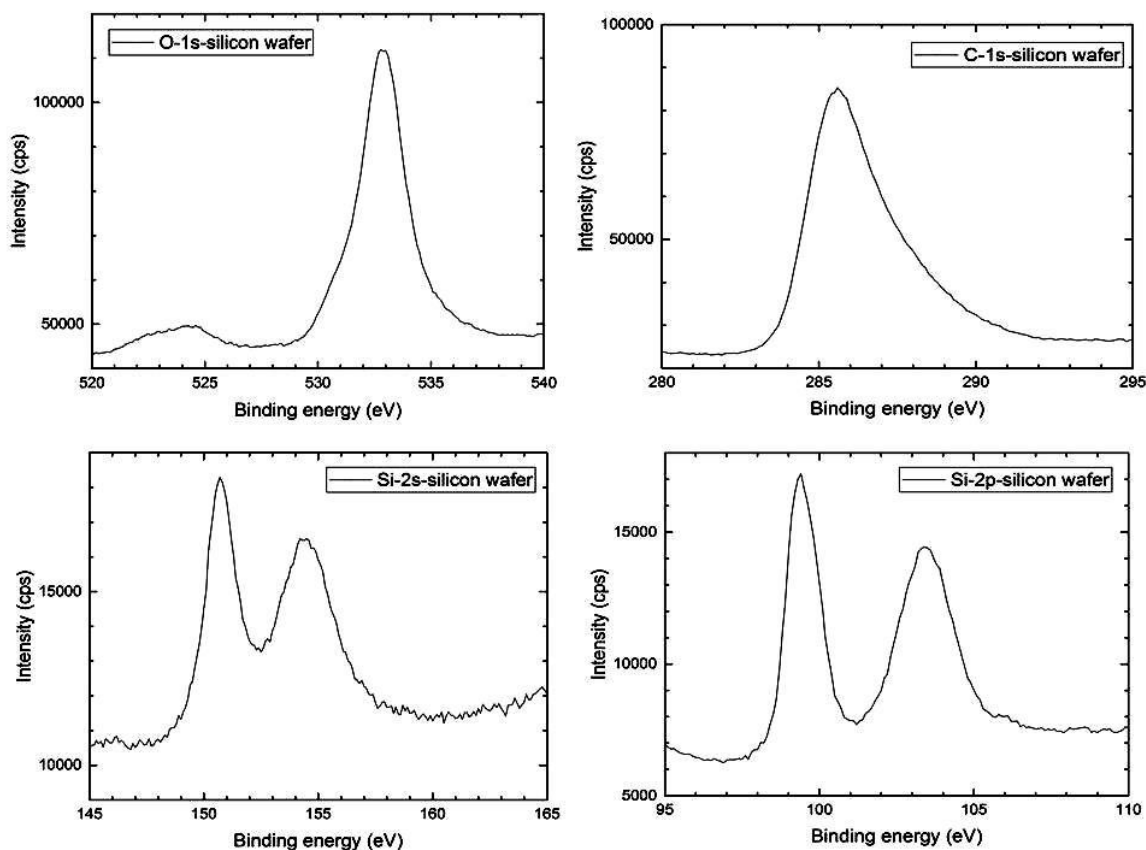


Figure A.5-6. XPS spectra of silicon wafer are recorded as a reference.

5.3 ATR spectra of film samples

All silicon samples which were produced in IPA are plotted in Figure A.5-7 to give a perspective on the similarity of samples produced in the same solvent. The pure IPA spectrum also is recorded as a reference (shown by yellow line); as can be seen, the signal to noise is very weak for pure IPA and it shows only the bands belonging to atmospheric species (i.e., CO₂ and water vapour) or the residue of incompletely evaporated IPA. The absorbance spectra of samples are similar, but most of them show a negative OH band at 3200 - 3500 cm⁻¹ due to background subtraction. The same is true for the negative bands

of the molecules that exist in the atmosphere. Some samples show negative Si-O peak in the fingerprint region because this band is very close to the frequency of the C-O band and, if silicon band intensities are very low, they become negative by subtracting the background. (Conversely, of course, and if they are intense, they can overcome the subtraction process).

The same experiments were performed for all Si-ethanol and Si-water samples. If humidity is high, water bands around $1400 - 1600 \text{ cm}^{-1}$ are very noisy, preventing identification of other bands in this region. An overview of all Si-ethanol film samples is shown in Figure A.5-8. Some Si-water samples show high absorbance intensities with respect to other Si-water samples. However, the bands are very broad in these samples. In samples with lower absorbances, four sharp, distinct bands can be seen in the fingerprint region, whilst these bands convert to two broad bands in samples with higher absorbances. An overview of all Si-water film samples with lower intensities is shown in Figure A.5-9, and with higher intensities in Figure A.5-10.

The background spectra for all measurements were recorded for the same solvent as the sample solvent.

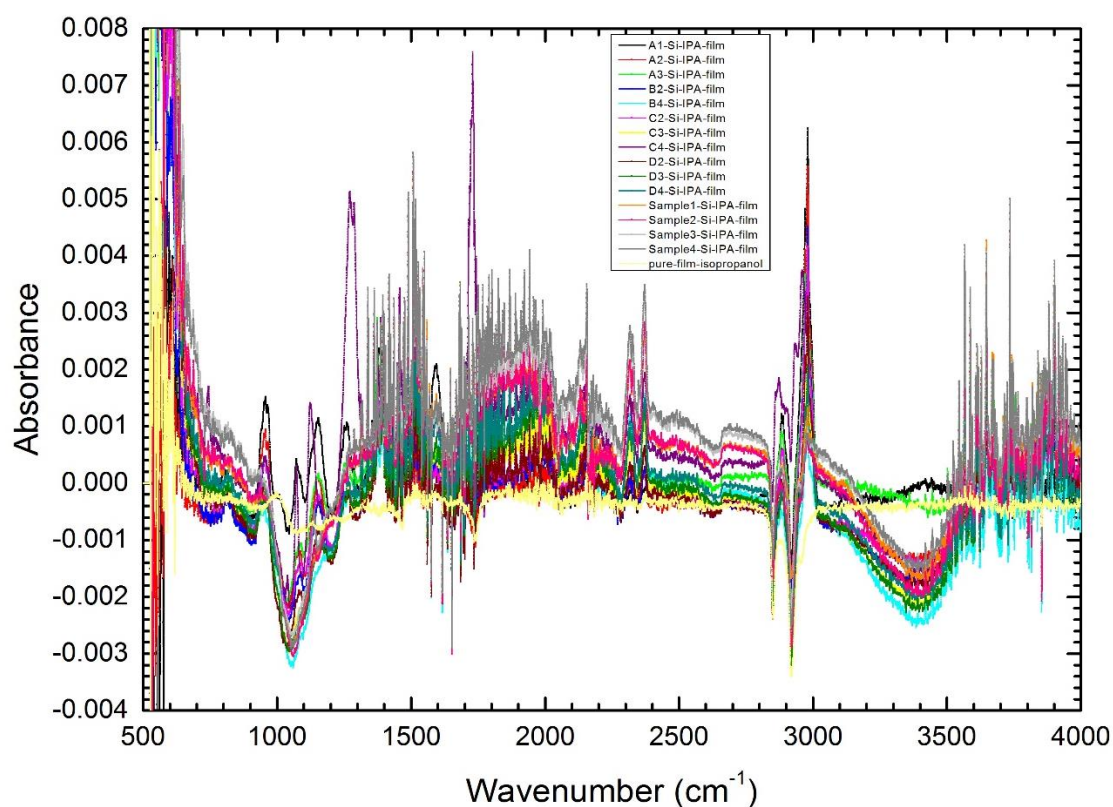


Figure A.5-7. Si-IPA sample absorbance spectra.

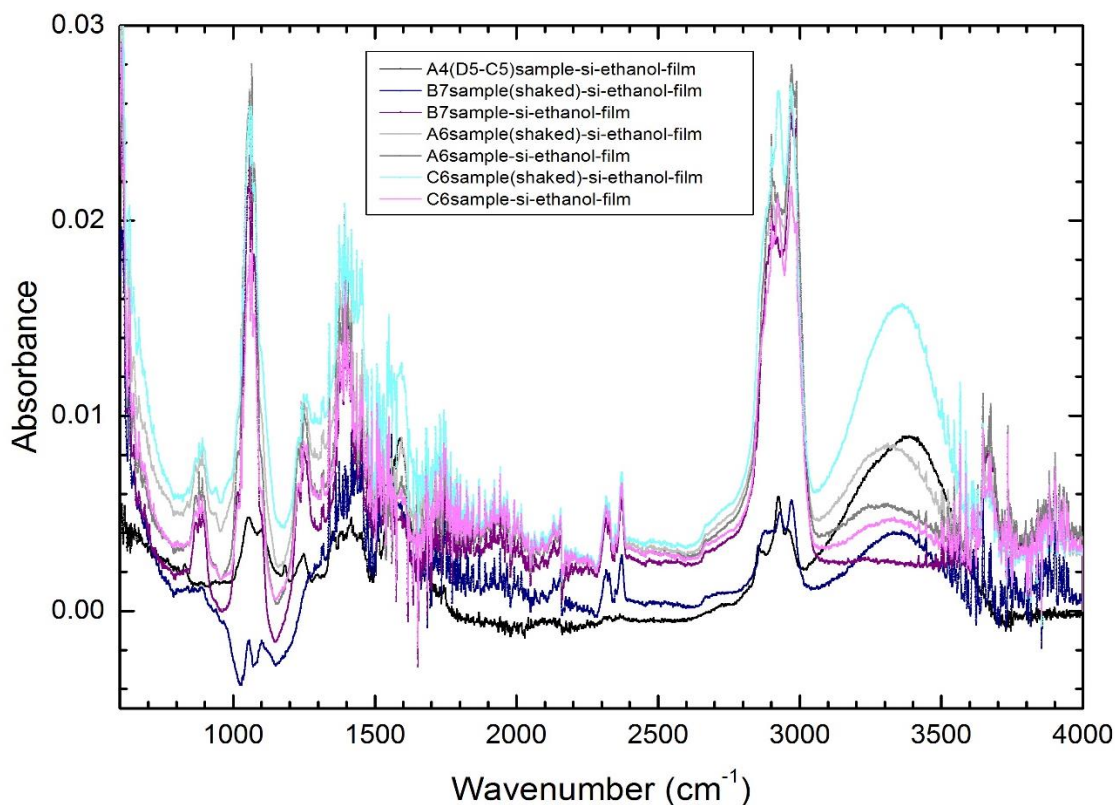


Figure A.5-8. Si-ethanol sample absorbance spectra.

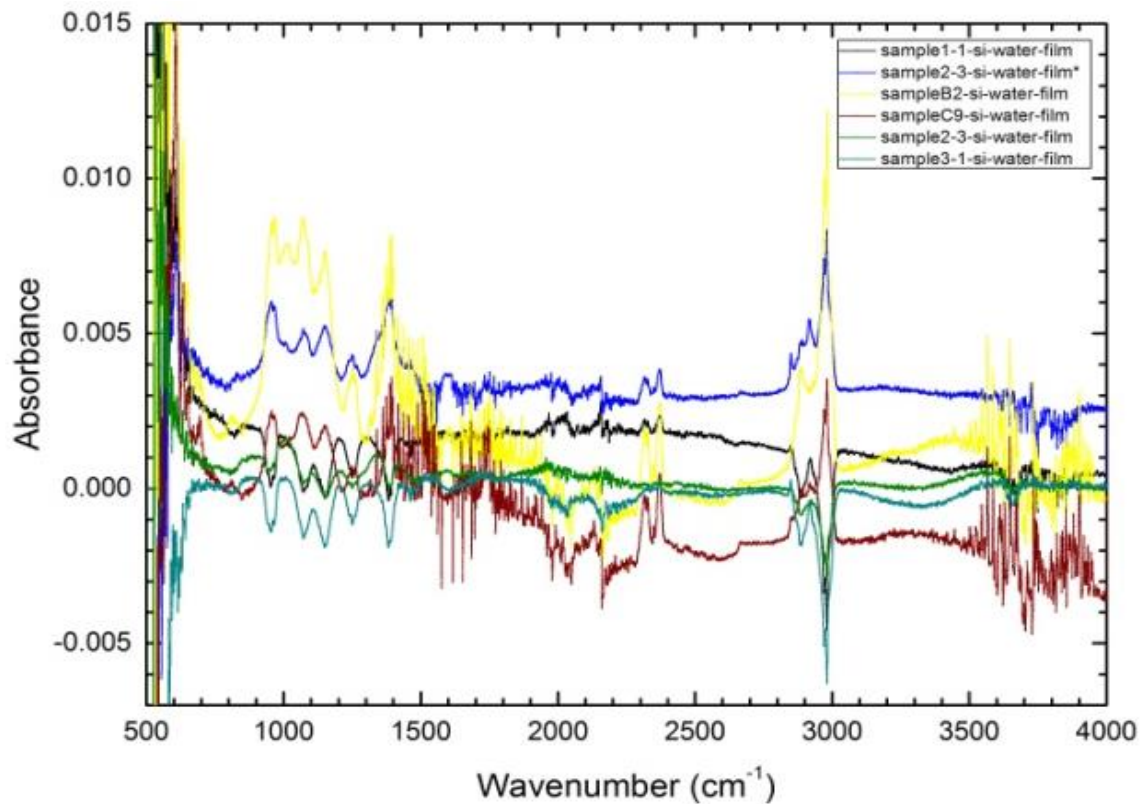


Figure A.5-9. Si-water sample absorbance spectra. These samples show four bands around $950\text{--}1300\text{ cm}^{-1}$.

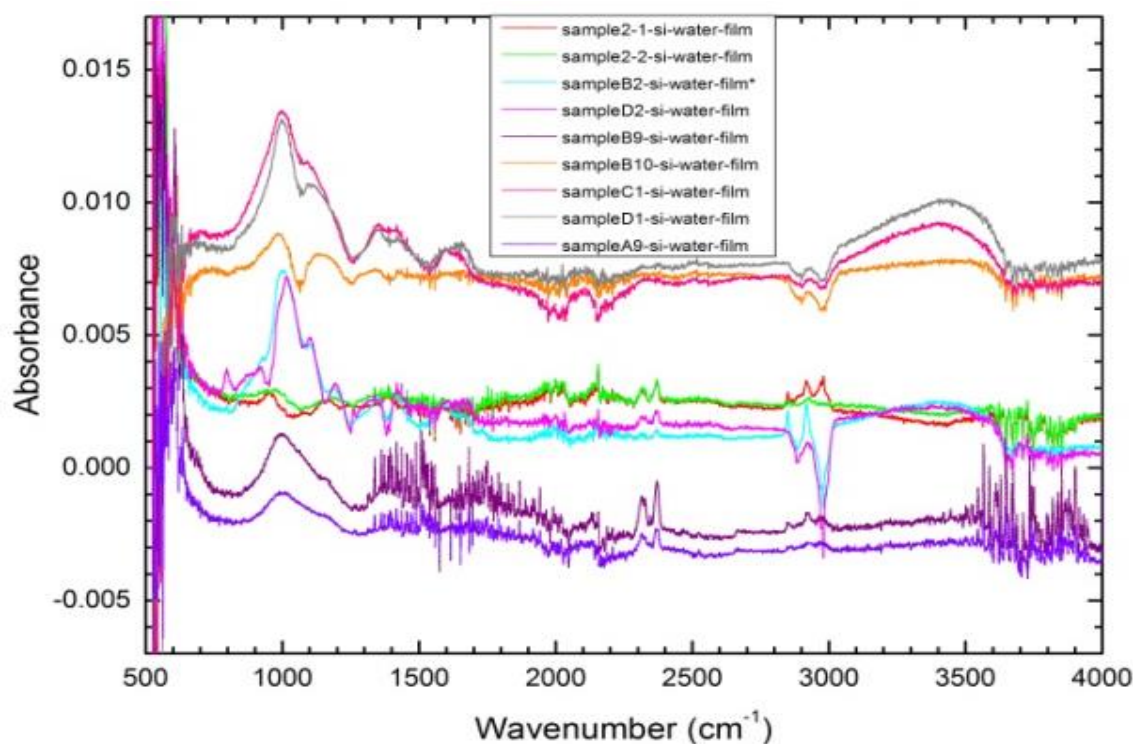


Figure A.5-10. Si-water sample absorbance spectra. The two broad bands in the fingerprint region are a superposition of four narrow peaks in lower absorbance samples.

5.3.1 ATR spectra of film samples using HOPG substrate

In this method, HOPG was used as a substrate. It was cleaved, and 1 μl of solvent was put on the clean HOPG surface. The HOPG/sample was located upside down on a diamond ATR crystal (so as to be exposed to the source beam) and a background was recorded. Then, a 1 μl drop of sample was put on HOPG in the same place as previous drop (used as background) and the sample spectrum was measured. When a solid sample is used for ATR measurement, one should use the anvil to hold and press the sample on the crystal. The experiments were performed for Si-IPA sample A2 and Si-water sample C9 are shown in Figure A.5-11 and Figure A.5-12. For sample C9, 10 μl of sample was applied in two steps, using 5 μl in each step. For sample A2, measurement continued to four steps, with a 1 μl drop of sample in the first step, and ten 1 μl drops of in each subsequent step. HOPG affected the baseline, as it can be seen in these figures.

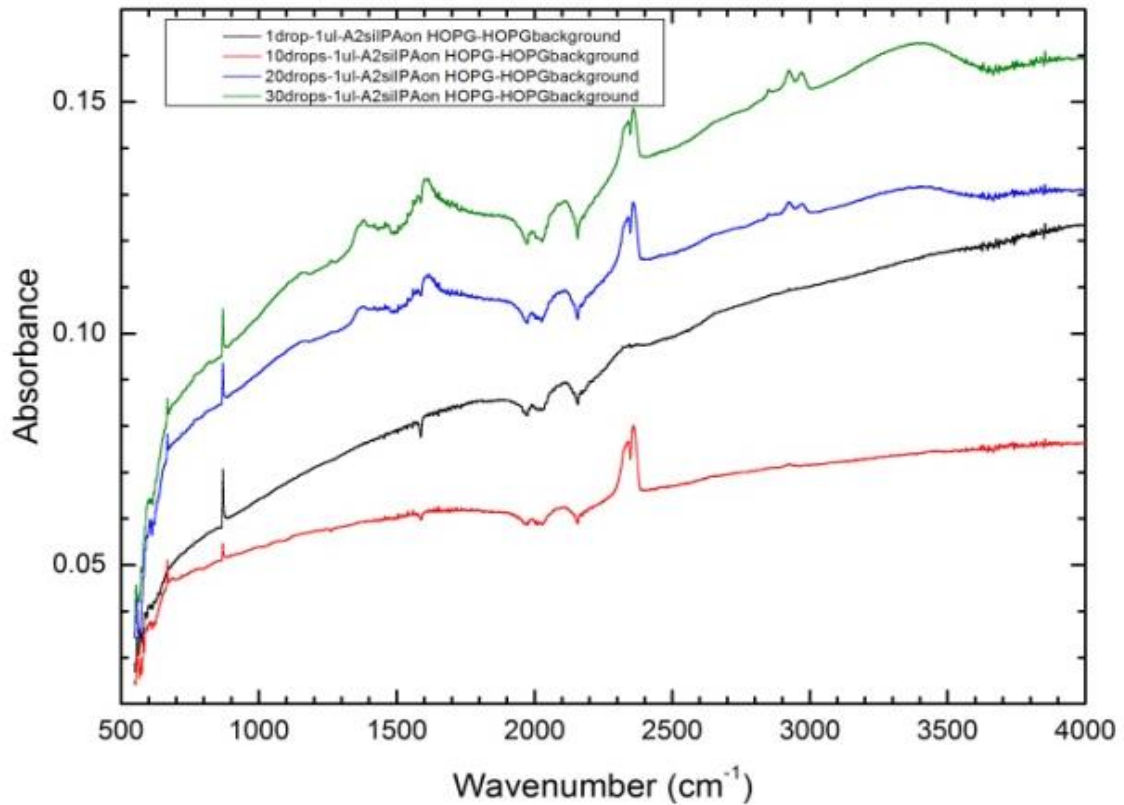


Figure A.5-11. ATR spectra of Si-IPA sample A2 using HOPG substrate applied in four steps.

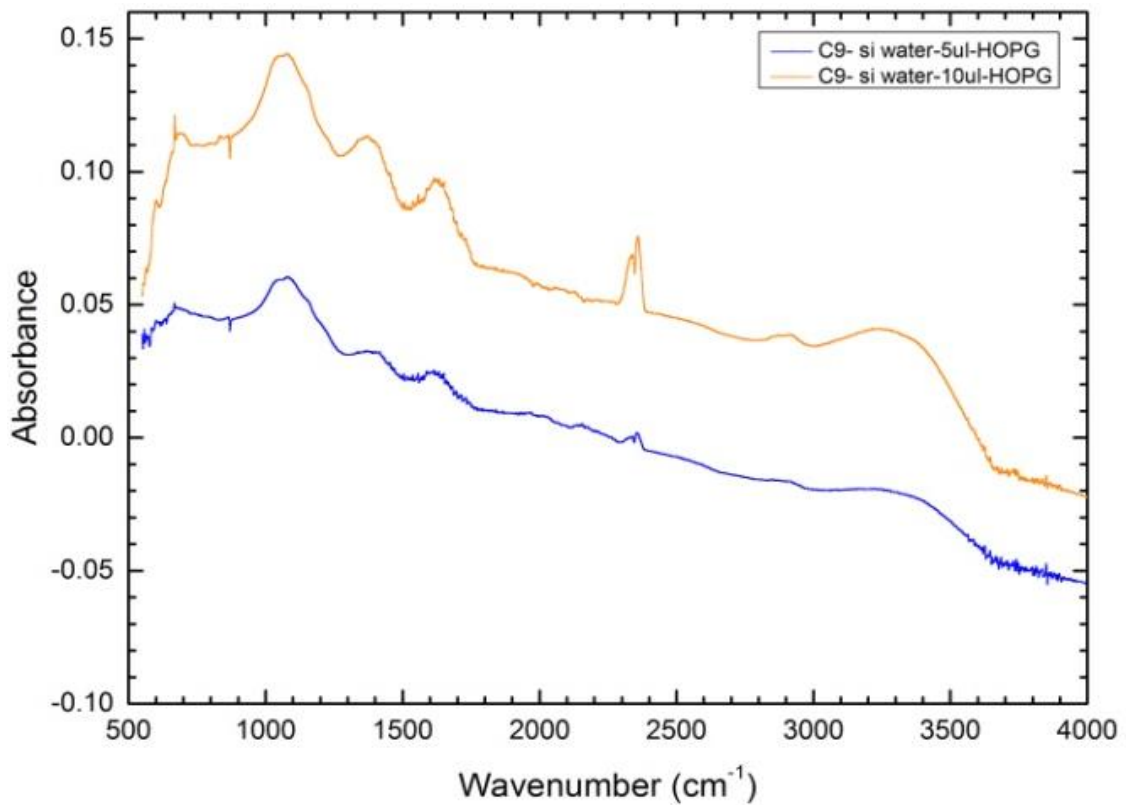


Figure A.5-12. ATR spectra of Si-water sample C9 using HOPG substrate applied in two steps.

The spectra recorded for Si-IPA sample A2 do not show any vibrational features using this method. For the Si-water sample, the intensity of the peaks is much higher than when the film was formed directly on the ATR crystal, although HOPG affected the baseline, and the vibrational features observed were not sharp and distinct. By this method the sample was confined to a small area so the intensity increased with respect to direct measurements. The vibrational frequencies of the bands are the same as those observed in other sample preparation methods.

The results of Si-water sample C9 on the ATR crystal with and without HOPG are compared in Figure A.5-13.

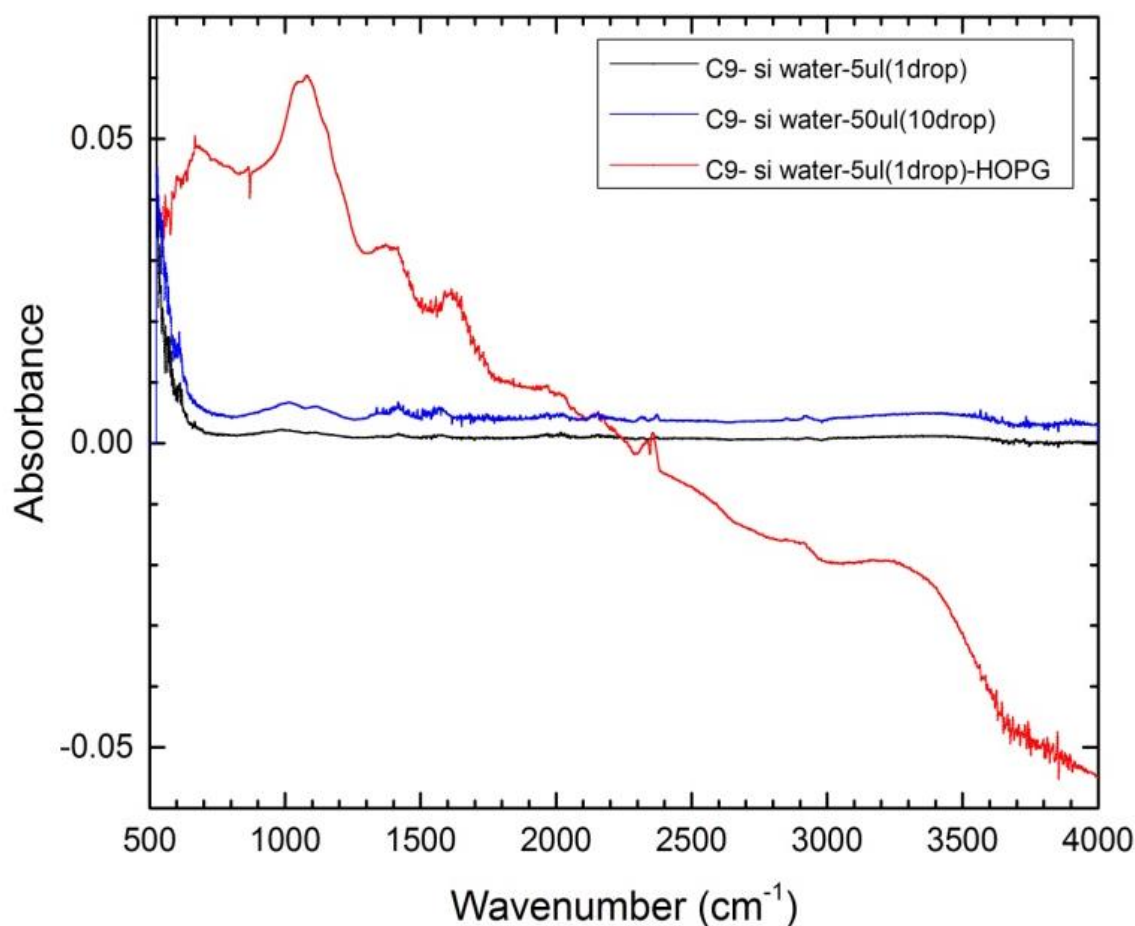


Figure A.5-13. A comparison between ATR measurements with and without HOPG are illustrated. Although for the blue line (without HOPG) the amount of sample is ten times more than for red line (with HOPG), the absorbance of the sample on HOPG is five times higher.

5.3.2 ATR spectra of film samples using one layer HOPG substrate

As the anvil was used on its highest pressure (as it should be in maximum pressure), the top layer of the HOPG could become cracked, so the detector detected the layers beneath the top layers and adversely affected the spectra. Therefore, we decide to clean the HOPG by cleaving, and then cleaved another layer of HOPG using sellotape, which left a fresh and clean layer on the sellotape on which to drop cast the sample. This face was then placed, upside down, on the ATR crystal. Although for this experiment the anvil was also used, as it was just one layer of HOPG, we did not have to contend with a substrate with the fragility of the HOPG crystal itself.

The results of Si-water (sample C9), Si-ethanol (sample A5), and Si-IPA (sample A1) are shown and compared in Figure A.5-14. For all samples, a 1 μ l drop of sample was used. Using a layer of HOPG has effectively negated the effect of the HOPG on the baseline. The peaks are sharper, and much more similar to those seen from direct measurement on the ATR crystal, but with considerably higher intensities. Also the noise around the OH bands is almost gone with the help of this method. As can be seen, similar to previous measurements, for the vibrational features of the various silicon species observed the intensities in the Si-water sample are higher than in alcoholic samples. This suggests a highly oxidized sample, which is in agreement with direct ATR measurements.

ATR spectra of Si-water sample C9 on an HOPG crystal and on a layer of HOPG on sellotape are compared in Figure A.5-15. This shows that, although the amount of sample which is used to measure absorbance using the HOPG substrate is five times greater, the intensities seen in subsequent ATR spectroscopy is low and vibrational features are not distinct. This shows that a layer of HOPG on sellotape had less effect on recorded spectra, and also that the spectrum intensity is very high even for small amount of sample (on this substrate).

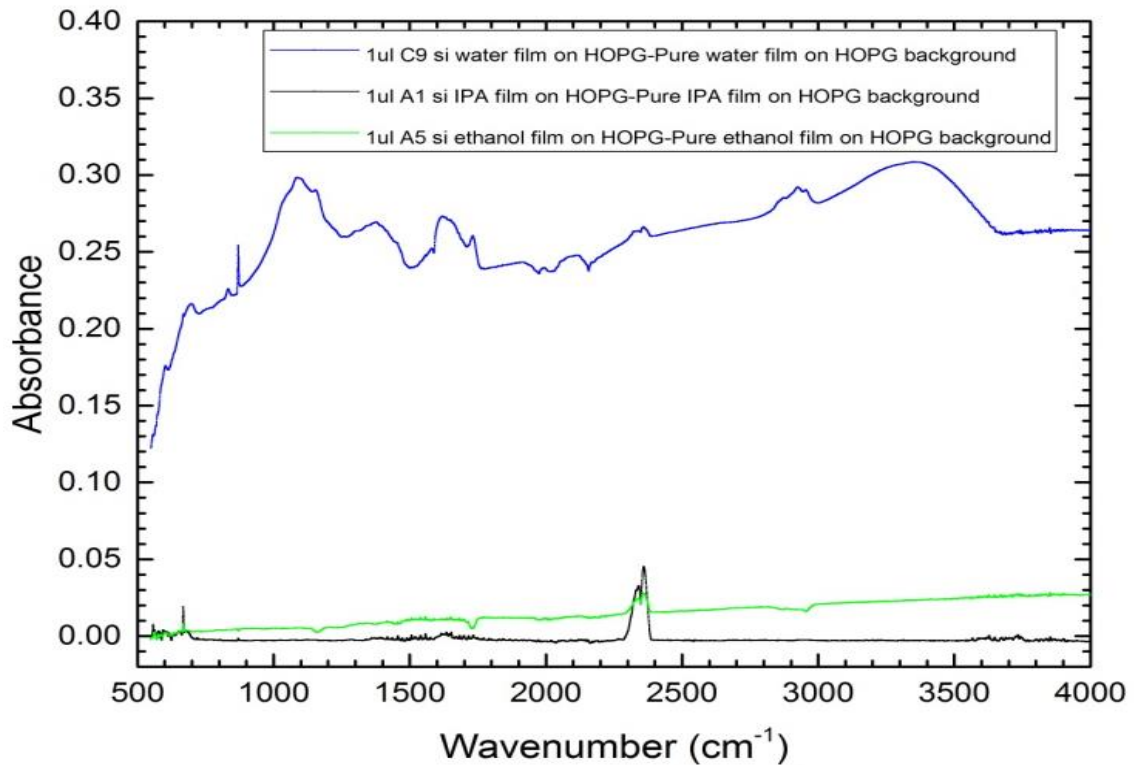


Figure A.5-14. Figure showing ATR spectra of silicon deposited on three different solvents by using a layer of HOPG as substrate.

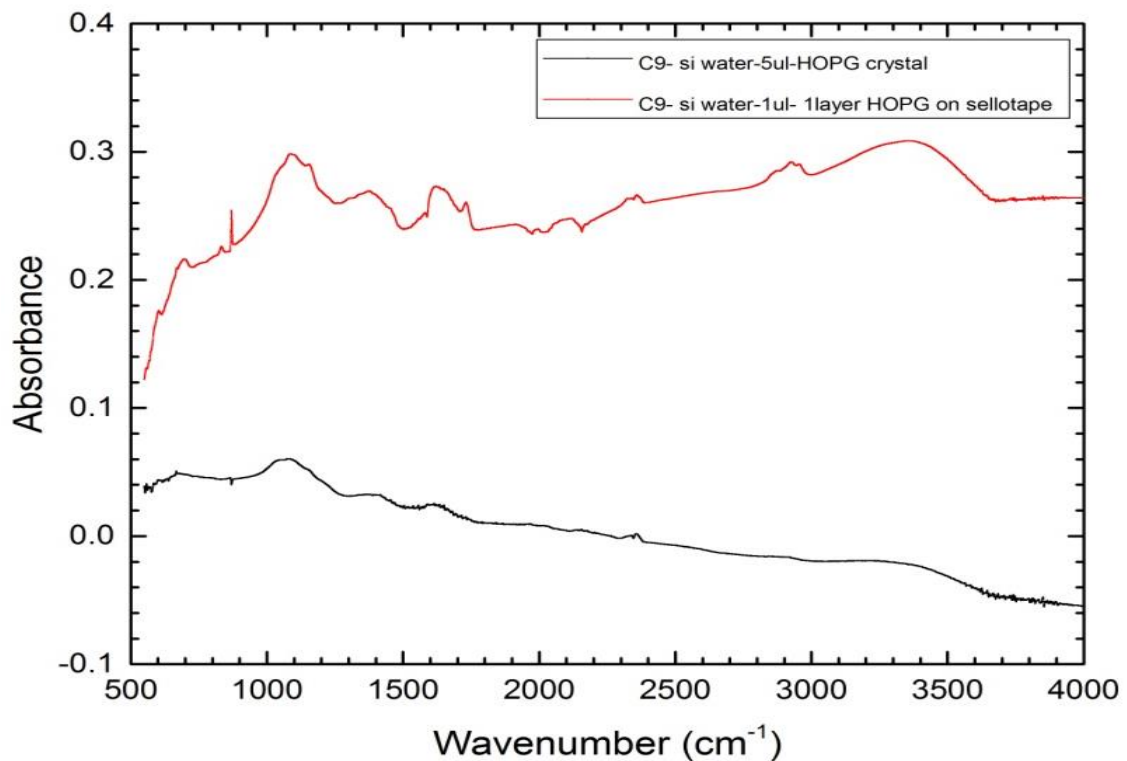


Figure A.5-15. A comparison of ATR spectra of Si-water sample on HOPG substrate and a layer of HOPG on sellotape. Using a layer of HOPG on sellotape gives peaks with higher intensities that are also sharper and distinguishable

5.3.3 FTIR spectra of film samples

Transmission spectra of Si-water samples are shown in Figure A.5-16, where silicon oxide bands can be clearly seen. The spectra are very similar to ATR spectra, and the peak positions are the same. The intensity is slightly higher in transmittance spectra than ATR spectra.

Although the intensity of Si-water sample C9 spectra is less than other samples here, it shows several peaks between 850 cm^{-1} to 1200 cm^{-1} and two distinct silicon compounds bands which are not clear in other samples, because similar to ATR spectra they have a broad peak formed from the superposition of several low intensity peaks. To have a reference for Si-water samples, pure water film was investigated and is shown in the same graph. As can be seen, pure water does not show any features, which suggests that all peaks observed for Si-water samples arise due to silicon species.

The transmittance spectra of Si-IPA and Si-ethanol samples are shown in Figure A.5-17. As can be seen, some silicon oxide peaks exist in these samples, but their intensities are very low.

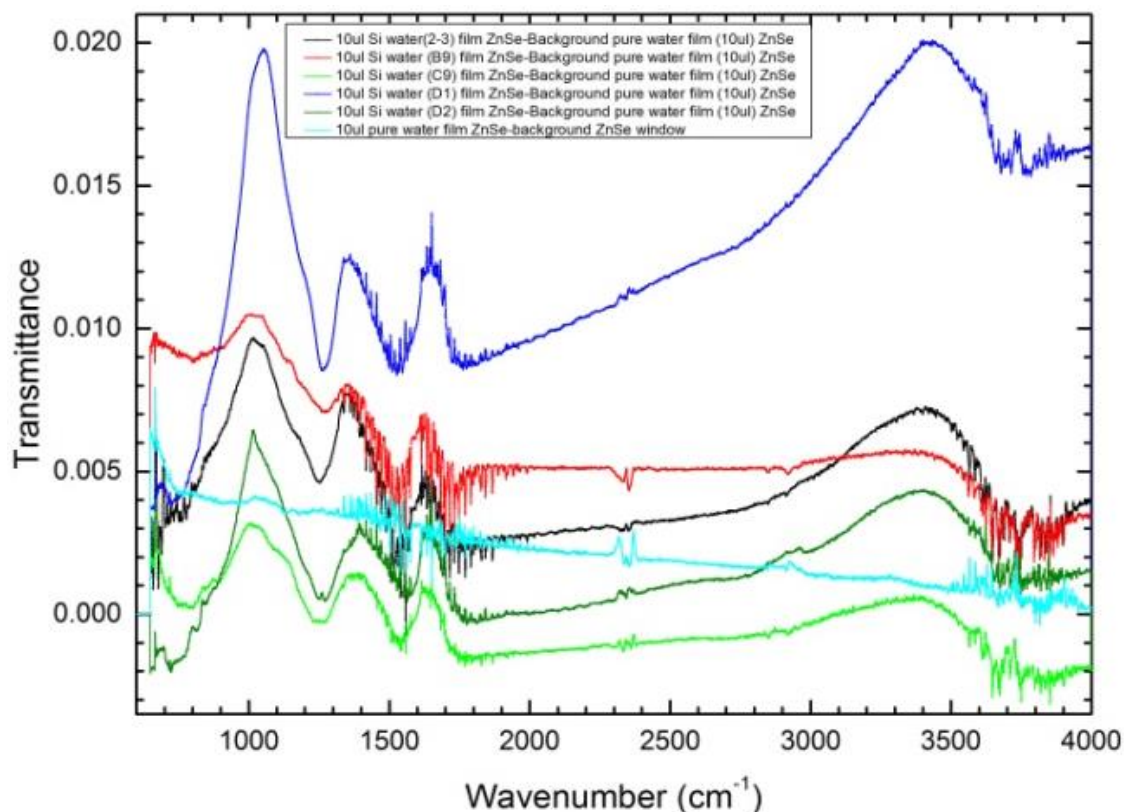


Figure A.5-16. All water solvent sample transmittance spectra and a pure water spectrum as a reference are shown in this figure.

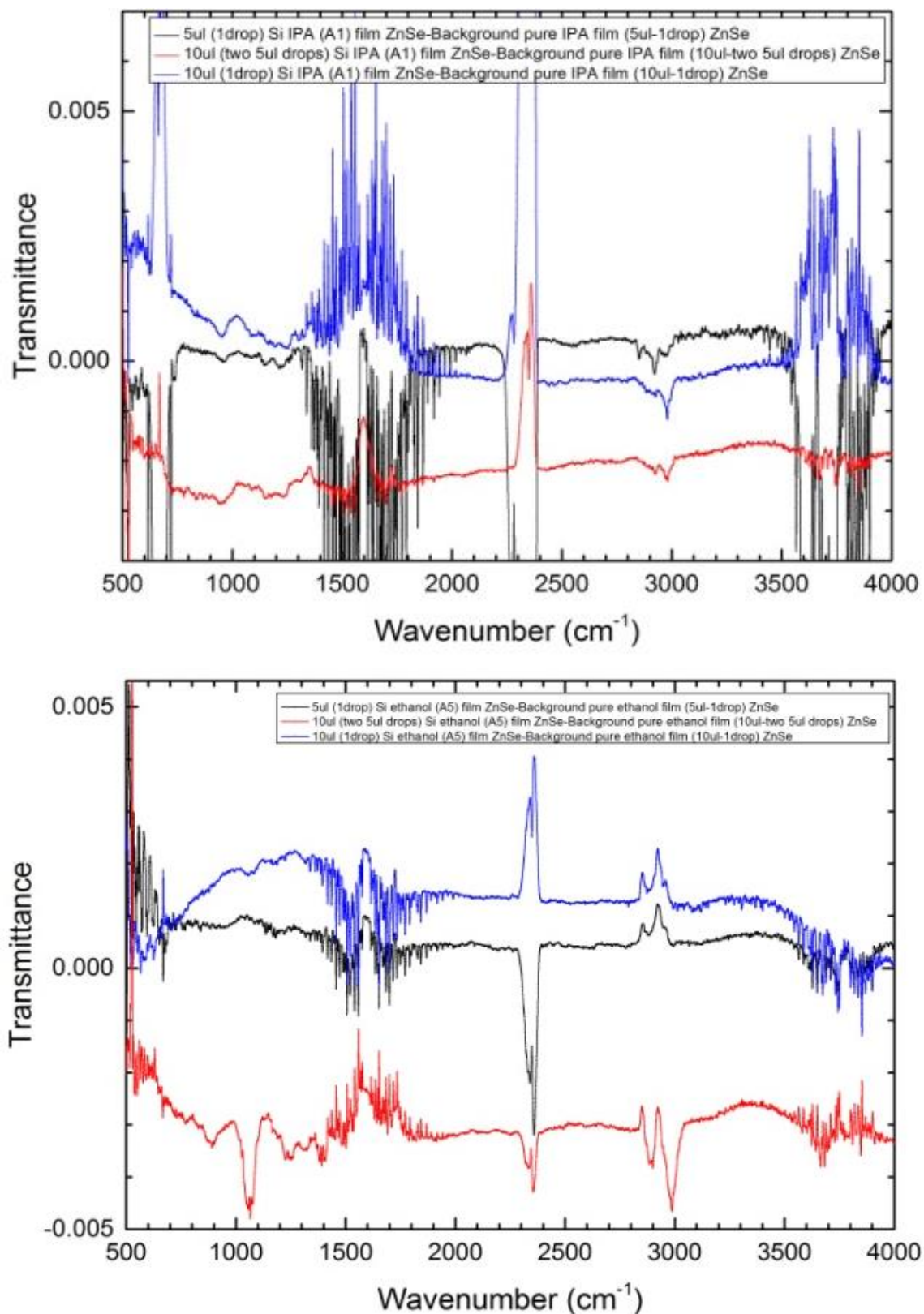


Figure A.5-17. Transmittance spectra of Si-IPA (top) and Si-ethanol (bottom). As it can be seen, some silicon oxide peaks exist in these spectra but, similar to ATR measurements, the intensities of vibrational frequencies due to silicon species deposited in alcohol is very low.

Appendix 6

Atomic Force Microscopy (AFM)

6.1 AFM image and size distribution

AFM images and size distributions of Si-IPA, Si-ethanol and Si-water samples are shown in Figure A.6-1, Figure A.6-2, and Figure A.6-3, respectively. Images and size distributions show several layers of clusters in the samples, for example in the Si-water sample, five layers of clusters can be seen in the AFM image in different colours; the black area shows the HOPG, dark brown, brown, light brown, and yellow areas show other top layers and the bright white spots is the topmost layer. These layers can be seen in size distribution as well. AFM measurements for all samples show the clusters have ~1 nm height. AFM measurements for our samples were performed by Mümin Koç [285].

AFM measurements were performed for silicon particles which were deposited in ethanol and transferred to IPA and water. The results are shown in Figure A.6-4 and Figure A.6-5. The size distribution of the transferred clusters to IPA and water are the same as the size distributions of clusters deposited in IPA and water.

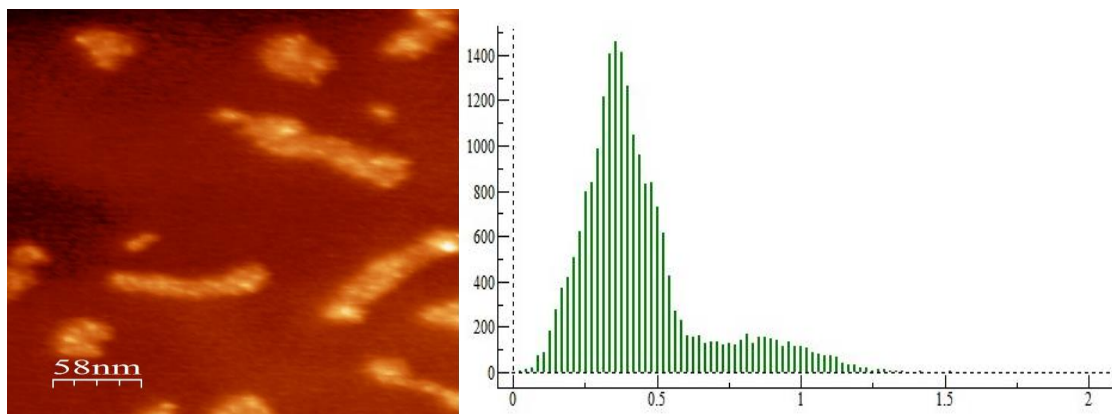


Figure A.6-1. AFM image and size distribution of Si-IPA sample. Distance between two peaks show the height of layer.

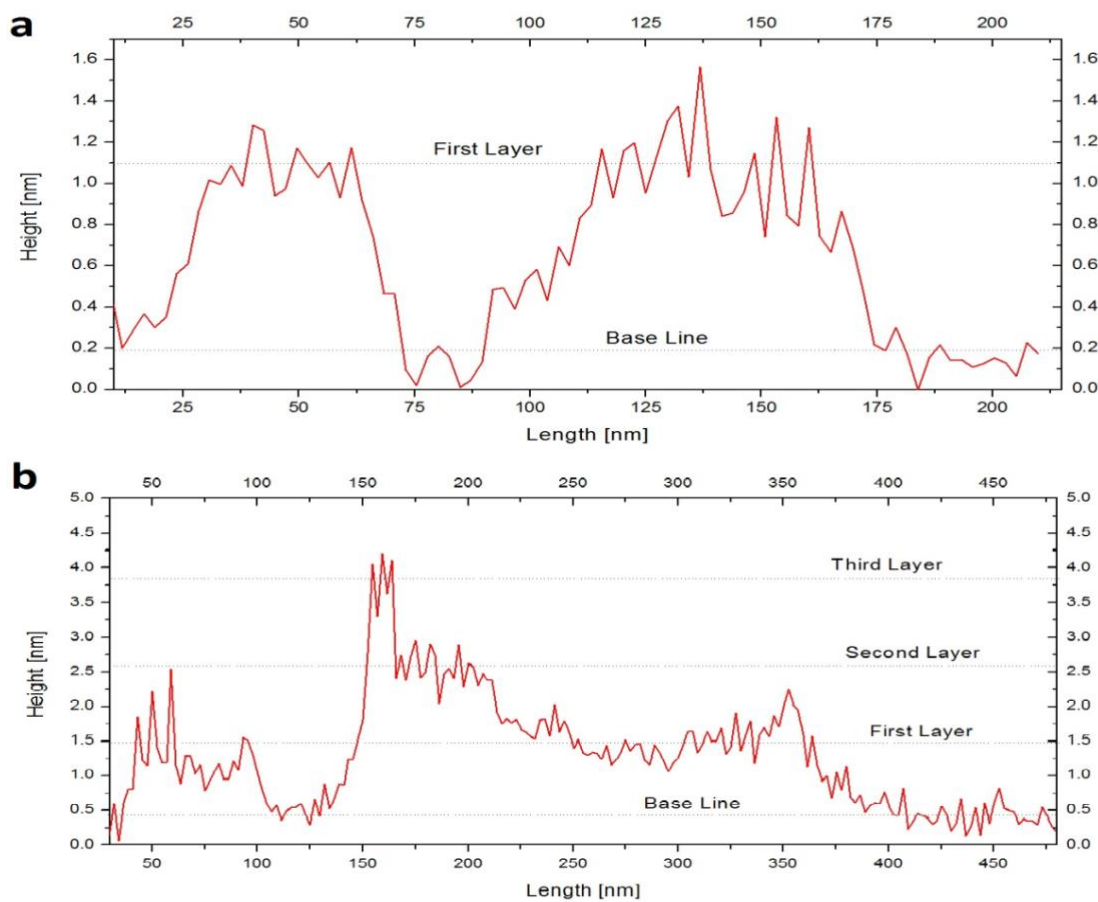
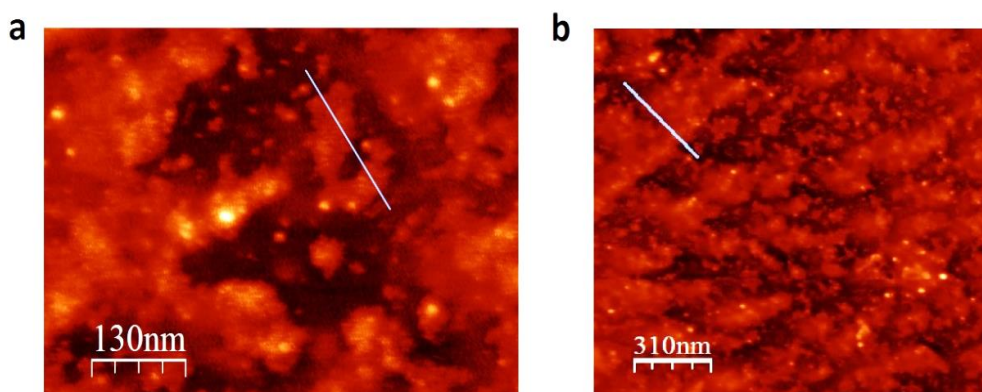
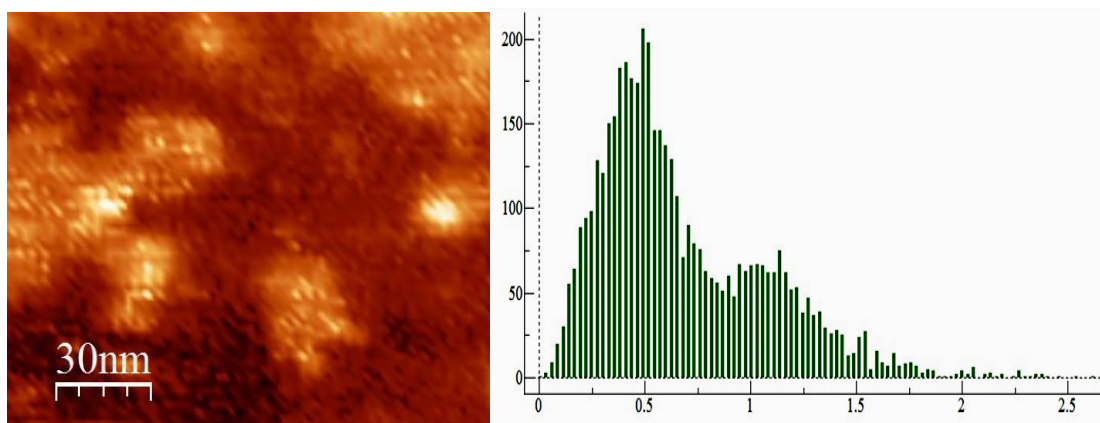


Figure A.6-2. AFM imagea, size distribution and height profiles of Si-ethanol sample.

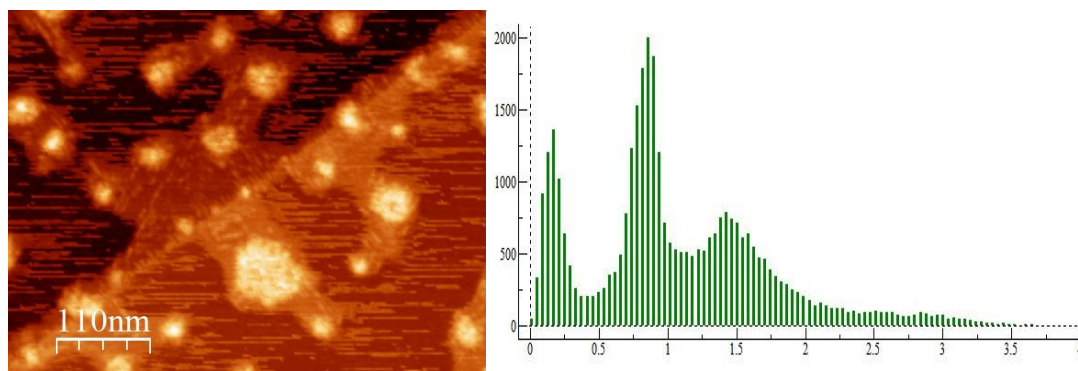


Figure A.6-3. AFM image and size distribution of Si-water sample.

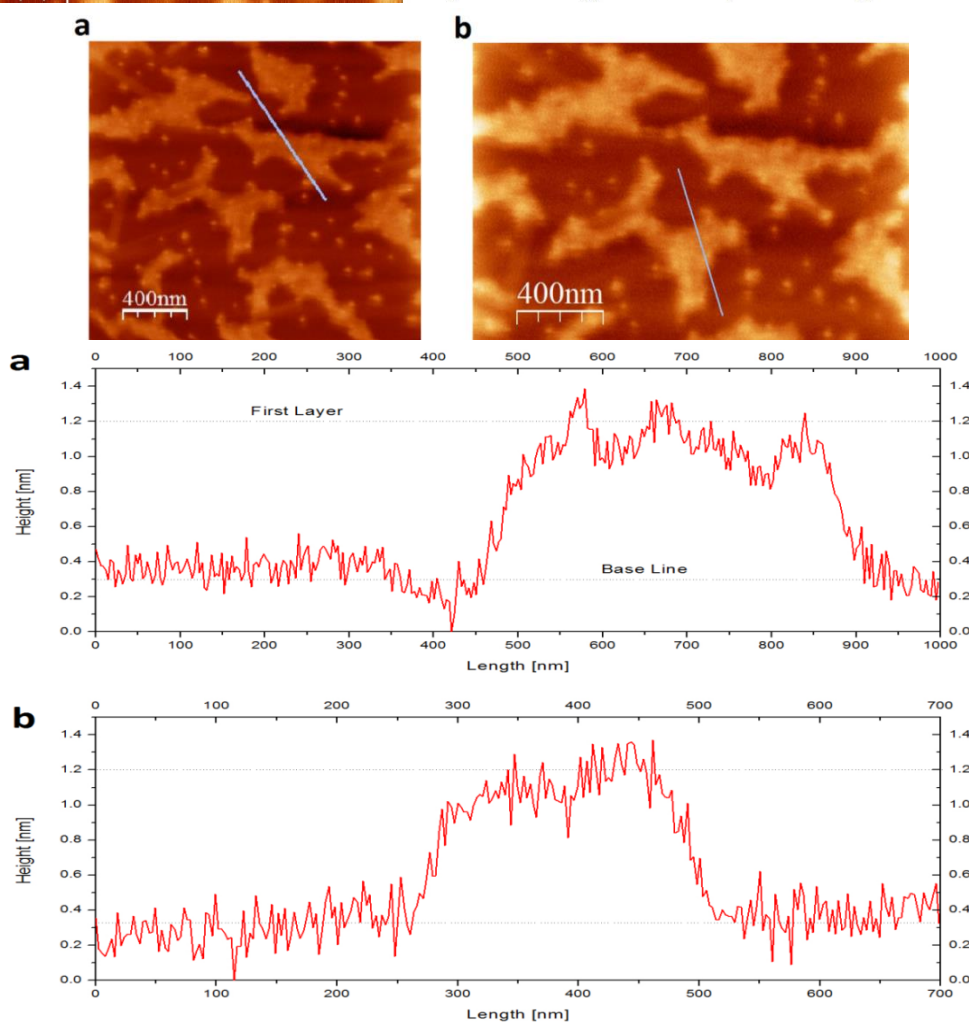
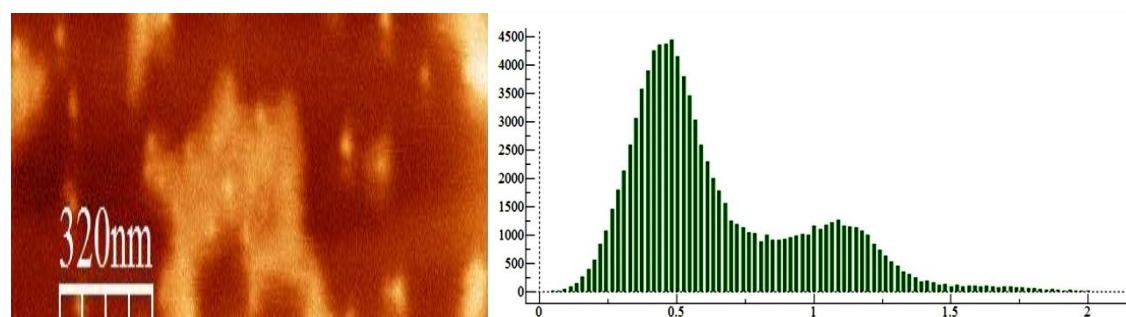


Figure A.6-4. AFM image and size distribution of silicon clusters transferred to IPA.

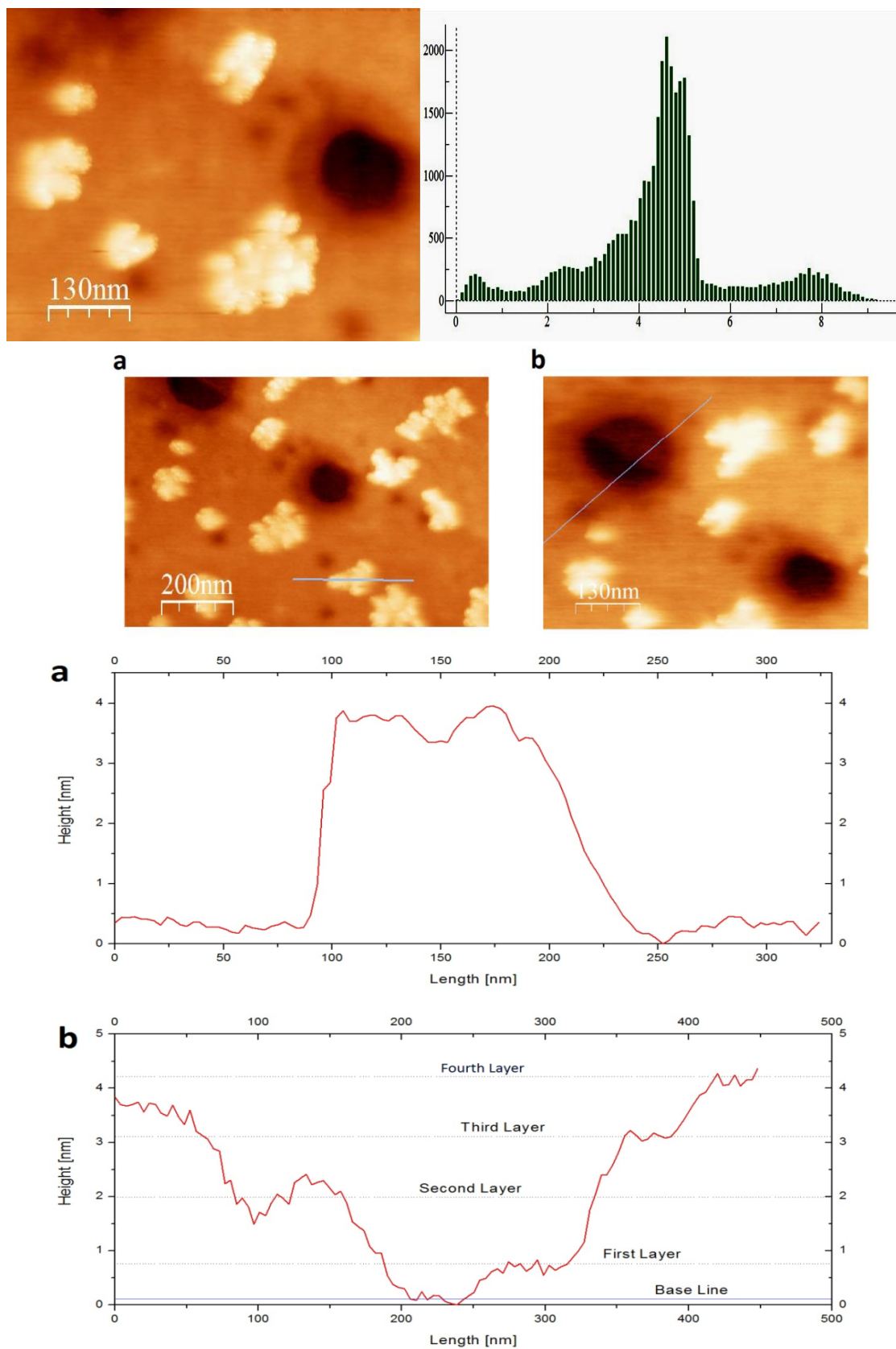


Figure A.6-5. AFM image and size distribution of silicon clusters transferred to water.

List of publications and presentations

PUBLICATIONS:

Galiniš G, **Yazdanfar H**, Bayliss M, Watkins M, von Haeften K. Towards biosensing via fluorescent surface sites of nanoparticles, *J. Nanopart. Res.* **14**, 1019 (2012).

Yazdanfar H, McNally MJ, Watkins M, Koç MM, von Haeften K. Surface oxide luminescence silicon nanoclusters. (Preparing for submission to *The Journal of Physical Chemistry C*)

Yazdanfar H, Watkins M, von Haeften K, Quantum yield measurement of stable fluorescence of silicon nanoclusters in water. (Preparing for submission to *The Journal of Physical Chemistry C*)

CONFERENCE PRESENTATIONS:

Yazdanfar H, McNally MJ, Galiniš G, Watkins M, von Haeften K. Fluorescent oxidized Si nanoclusters and reversible interactions with solvent, International Symposium on Small Particles and Inorganic Clusters ISSPIC 17, Fukuoka, Japan, 2014.

Yazdanfar H, Galiniš G, McNally MJ, Koç MM, Youle O, Torricelli G, Watkins M, von Haeften K. Surface oxide luminescence of silicon nanoclusters, International Symposium on Small Particles and Inorganic Clusters ISSPIC 17, Fukuoka, Japan, 2014.

Yazdanfar H, McNally MJ, Galiniš G, Watkins M, von Haeften K. X-ray photoelectron spectroscopy of novel oxidised silicon nano-clusters, CCP9/CECAM Workshop, Electronic excitations and photoelectron spectroscopy: bridging theory and experiment, Oxford, UK, 2013.

Yazdanfar H, McNally M, von Haeften K. X-ray photoelectron spectroscopy of novel oxidised silicon nano-clusters, RSC Postgraduate Symposium on Nanotechnology, Birmingham, UK, 2013.

Yazdanfar H, McNally M, Torricelli G, Koç MM, Galiniš G, Mendoza Luna LG, Watkins M, von Haeften K, Kotlov A, Coles B, Botchway S. Chemical analysis and photoluminescence studies of novel oxidised silicon nanoparticles, RSC Postgraduate Symposium on Nanotechnology, Birmingham, UK, 2013.

Yazdanfar H, von Haeften K. Fluorescent hydrogen-bonded surface sites of oxidised silicon nano-clusters, RSC Postgraduate Symposium on Nanotechnology, Birmingham, UK, 2012.

Yazdanfar H, Galinis G, Torricelli G, Watkins M, von Haeften K. Investigation of solvent and size effects of fluorescent silicon nano-clusters, International Symposium on Small Particles and Inorganic Clusters ISSPIC 16, Luven, Belgium, 2012.

Yazdanfar H, Galinis G, Torricelli G, Watkins M, von Haeften K. Photo-fluorescence spectroscopy of a novel form of ultra-stable silicon nanoparticles, RSC Postgraduate Symposium on Nanotechnology, Birmingham, UK, 2011.

Bibliography

1. Noone KM, Ginger DS. Doping for speed: colloidal nanoparticles for thin-film optoelectronics. *ACS Nano*. 2009;3(2):261-265.
2. Canham L. Gaining light from silicon. *Nature*. 2000;408(6811):411-412..
3. Pavesi L, Will silicon be the photonic material of the third millenium? *Journal of Physics: Condensed Matter*. 2003;15(26):R1169.
4. Zhao X, Hilliard LR, Mechery SJ, Wang Y, Bagwe RP, Jin S, Tan W. A rapid bioassay for single bacterial cell quantitation using bioconjugated nanoparticles. In: *Proceedings of the National Academy of Sciences of the United States of America*. 2004. 101(42): p. 15027-15032.
5. Nel AE, Mädler L, Velegol D, Xia T, Hoek EM, Somasundaran P, Klaessig F, Castranova V, Thompson M. Understanding biophysicochemical interactions at the nano–bio interface. *Nature Materials*. 2009;8(7):543-557.
6. He Y, Su Y, Yang X, Kang Z, Xu T, Zhang R, Fan C, Lee ST. Photo and pH stable, highly-luminescent silicon nanospheres and their bioconjugates for immunofluorescent cell imaging. *Journal of the American Chemical Society*. 2009;131(12):4434-4438.
7. Rejman J, Oberle V, Zuhorn I, Hoekstra D. Size-dependent internalization of particles via the pathways of clathrin-and caveolae-mediated endocytosis. *Biochem. J*. 2004;377:159-169.
8. Fuller JE, Zugates GT, Ferreira LS, Ow HS, Nguyen NN, Wiesner UB, Langer RS. Intracellular delivery of core–shell fluorescent silica nanoparticles. *Biomaterials*. 2008; 29(10):1526-1532.
9. Sakai N, Matsui Y, Nakayama A, Tsuda A, Yoneda M. Functional-dependent and size-dependent uptake of nanoparticles in pc12. In: *Journal of Physics: Conference Series*. IOP Publishing; 2011. 304(1): p. 012049.
10. Wang G, Yau ST, Mantey K, Nayfeh MH. Fluorescent Si nanoparticle-based electrode for sensing biomedical substances. *Optics Communications*. 2008;281(7):1765-1770.
11. Park JH, Gu L, von Maltzahn G, Ruoslahti E, Bhatia SN, Sailor MJ. Biodegradable luminescent porous silicon nanoparticles for *in vivo* applications. *Nature Materials*. 2009;8(4):331-336.

12. Erogbogbo F, Yong KT, Roy I, Xu G, Prasad PN, Swihart MT. Biocompatible luminescent silicon quantum dots for imaging of cancer cells. *ACS Nano*. 2008;2(5):873-878.
13. Kimura K. Blue luminescence from silicon nanoparticles suspended in organic liquids. *Journal of Cluster Science*. 1999;10(2):359-380.
14. Qiu T, Wu X, Kong F, Ma H, Chu PK. Solvent effect on light-emitting property of Si nanocrystals. *Physics Letters A*. 2005;334(5):447-452.
15. Zhang Q, Cao YQ, Tsien RW. Quantum dots provide an optical signal specific to full collapse fusion of synaptic vesicles. In: Almers W, editor. *Proceedings of the National Academy of Sciences*. 2007. 104(45): p. 17843-17848.
16. von Haefen K, Binns C, Brewer A, Crisan O, Howes PB, Lowe MP, Sibley-Allen C, Thornton SC. A novel approach towards the production of luminescent silicon nanoparticles: sputtering, gas aggregation and co-deposition with H₂O. *The European Physical Journal D*. 2009;52(1-3):11-14.
17. Brewer A, von Haefen K. *In situ* passivation and blue luminescence of silicon clusters using a cluster beam/H₂O codeposition production method. *Applied Physics Letters*. 2009;94(26):261102.
18. Galinis G, Yazdanfar H, Bayliss M, Watkins M, von Haefen K. Towards biosensing via fluorescent surface sites of nanoparticles. *Journal of Nanoparticle Research*. 2012;14(8):1-5.
19. Torricelli G, Akraiam A, von Haefen K. Size-selecting effect of water on fluorescent silicon clusters. *Nanotechnology*. 2011;22(31):315711.
20. Svrcek V, Mariotti D, Kondo M. Ambient-stable blue luminescent silicon nanocrystals prepared by nanosecond-pulsed laser ablation in water. *Optics Express*. 2009;17(2):520-527.
21. Hirschman K, Tsybeskov L, Duttagupta S, Fauchet P. Silicon-based visible light-emitting devices integrated into microelectronic circuits. *Nature*. 1996;384(6607):338-41.
22. Rong H, Liu A, Jones R, Cohen O, Hak D, Nicolaescu R, Fang A, Paniccia M. An all-silicon Raman laser. *Nature*. 2005;433(7023):292-294.
23. Yu D, Hang QL, Ding Y, Zhang H, Bai Z, Wang J, Zou Y, Qian W, Xiong G, Feng S. Amorphous silica nanowires: Intensive blue light emitters. *Applied Physics Letters*. 1998;73(21):3076-3078.
24. Holmes JD, Johnston KP, Doty RC, Korgel BA. Orientation of solution-grown silicon nanowires. *Science*. 2000;287:1471.
25. Peng X, Wang X, Zhang J, Wang Y, Sun S, Meng G, Zhang L. Blue-light emission from amorphous SiO_x nanoropes. *Applied Physics A*. 2002;74(6):831-833.
26. Dai L, Chen X, Jian J, Wang W, Zhou T, Hu B. Strong blue photoluminescence from aligned silica nanofibers. *Applied Physics A*. 2003;76(4):625-627.

27. Chen Z, Wang Y, He H, Zou Y, Wang J, Li Y. Mechanism of intense blue photoluminescence in silica wires. *Solid State Communications*. 2005;135(4):247-250.
28. Shang N, Vetter U, Gerhards I, Hofsäss H, Ronning C, Seibt M. Luminescence centres in silica nanowires. *Nanotechnology*. 2006;17(13):3215.
29. Salhi B, Gelloz B, Koshida N, Patriarche G, Boukherroub R. Synthesis and photoluminescence properties of silicon nanowires treated by high-pressure water vapor annealing. *physica Status Solidi (a)*. 2007;204(5):1302-1306.
30. Kanemitsu Y, Ogawa T, Shiraishi K, Takeda K. Visible photoluminescence from oxidized Si nanometer-sized spheres: Exciton confinement on a spherical shell. *Physical Review B*. 1993;48(7):4883.
31. Belomoin G, J Therrien, Nayfeh M. Oxide and hydrogen capped ultrasmall blue luminescent Si nanoparticles. *Applied Physics Letters*. 2000;77(6):779-781.
32. Li X, Tang Y, Lin L, Li J. Blue light emission in mesoporous SiO_x nano-structure. *Microporous and Mesoporous Materials*. 2008;111(1):591-595.
33. Ehbrecht M, Kohn B, Huisken F, Laguna M, Paillard V. Photoluminescence and resonant Raman spectra of silicon films produced by size-selected cluster beam deposition. *Physical Review B*. 1997;56(11):6958.
34. Huisken F, Kohn B, Alexandrescu R, Cojocaru S, Crunteanu A, Ledoux G, Reynaud C. Silicon carbide nanoparticles produced by CO₂ laser pyrolysis of SiH₄/C₂H₂ gas mixtures in a flow reactor. *Journal of Nanoparticle Research*. 1999;1(2):293-303.
35. Shimizu-Iwayama T, Nakao S, Saitoh K, Itoh N. Photoluminescence from nanoparticles of silicon embedded in an amorphous silicon dioxide matrix. *Journal of Physics: Condensed Matter*. 1994;6(39):L601.
36. Rebohle L, von Borany J, Fröb H, Skorupa W. Blue photo-and electroluminescence of silicon dioxide layers ion-implanted with group IV elements. *Applied Physics B*. 2000;71(2):131-151.
37. Rehm J, McLendon G, Tsybeskov L, Fauchet P. How methanol affects the surface of blue and red emitting porous silicon. *Applied Physics Letters*. 1995;66(26):3669-3671.
38. Canham L. Silicon quantum wire array fabrication by electrochemical and chemical dissolution of wafers. *Applied Physics Letters*. 1990;57(10):1046-1048.
39. Hillenbrand R, Taubner T, Keilmann F. Phonon-enhanced light-matter interaction at the nanometre scale. *Nature*. 2002;418(6894):159-162.
40. Cullis A, Canham L. Visible light emission due to quantum size effects in highly porous crystalline silicon. *Nature*. 1991;353:335-338.
41. Cullis A, Canham L, Calcott P. The structural and luminescence properties of porous silicon. *Journal of Applied Physics*. 1997;82(3):909-965.

42. Zhang D, Kolbas R, Milewski P, Lichtenwalner D, Kingon A, Zavada J. Light emission from thermally oxidized silicon nanoparticles. *Applied Physics Letters*. 1994;65(21):2684-2686.
43. Pavesi L, Dal Negro L, Mazzoleni C, Franzo G, Priolo F. Optical gain in silicon nanocrystals. *Nature*. 2000;408(6811):440-444.
44. Kenyon A. Erbium in silicon. *Semiconductor Science and Technology*. 2005;20(12):R65.
45. Brus L, Szajowski P, Wilson W, Harris T, Schuppler S, Citrin P. Electronic spectroscopy and photophysics of Si nanocrystals: relationship to bulk c-Si and porous Si. *Journal of the American Chemical Society*. 1995;117(10):2915-2922.
46. Lockwood, DJ. Light emission in silicon nanostructures. *Journal of Materials Science: Materials in Electronics*. 2009;20(1):235-244.
47. Echt O, Sattler K, Recknagel E. Magic numbers for sphere packings: experimental verification in free xenon clusters. *Physical Review Letters*. 1981;47(16):1121.
48. Knight WD, Clemenger K, de Heer WA, Saunders WA, Chou M, Cohen ML. Electronic shell structure and abundances of sodium clusters. *Physical Review Letters*. 1984;52(24):2141.
49. Billas IM, Chatelain A, de Heer WA. Magnetism from the atom to the bulk in iron, cobalt, and nickel clusters. *Science*. 1994;265(5179):1682-1684.
50. Schmidt M, Kusche R, Hippler T, Donges J, Kronmüller W, von Issendorff B, Haberland H. Negative heat capacity for a cluster of 147 sodium atoms. *Physical Review Letters*. 2001;86(7):1191.
51. Baletto F, Ferrando R. Structural properties of nanoclusters: Energetic, thermodynamic, and kinetic effects. *Reviews of Modern Physics*. 2005;77(1):371.
52. Moussavizadeh L, von Haeften K, Museur L, Kanaev A, Castex M, R von Pietrowski, Möller T. Photochemistry with fast sample renewal using cluster beams: formation of rare-gas halides in charge-transfer reactions in NF₃-doped rare-gas clusters. *Chemical Physics Letters*. 1999;305(5):327-333.
53. Heiz U, Vanolli F, Sanchez A, Schneider WD. Size-dependent molecular dissociation on mass-selected, supported metal clusters. *Journal of the American Chemical Society*. 1998;120(37):9668-9671.
54. Lengen M, Joppien M, Müller R, Wörmer J, Möller T. Site-specific excitation and decay processes in XeAr N clusters. *Physical Review Letters*. 1992;68(15):2362.
55. von Pietrowski R, von Haeften K, Laarmann T, Möller T, Museur L, Kanaev A. Electronic and geometric structure of doped rare-gas clusters: surface, site and size effects studied with luminescence spectroscopy. *The European Physical Journal D-Atomic, Molecular, Optical and Plasma Physics*. 2006;38(2):323-336.
56. Lindblad A, Bergersen H, Rander T, Lundwall M, Öhrwall G, Tchapyguine M, Svensson S, Björneholm O. The far from equilibrium structure of argon clusters doped with krypton or xenon. *Physical Chemistry Chemical Physics*. 2006;8(16):1899-1905.

57. von Haeften K, Laarmann T, Wabnitz H, Möller T, Fink K. Size and isotope effects of helium clusters and droplets: Identification of surface and bulk-volume excitations. *The Journal of Physical Chemistry A*. 2011;115(25):7316-7326.
58. Moriarty P. Nanostructured materials. *Reports on Progress in Physics*. 2001;64(3):297.
59. Yates Jr J. Surface chemistry of silicon-the behaviour of dangling bonds. *Journal of Physics: Condensed Matter*. 1991;3(S):S143.
60. Lemke B, Haneman D. Dangling bonds on silicon. *Physical Review B*. 1978;17(4):1893.
61. Fauchet PM. Light emission from Si quantum dots. *Materials Today*. 2005;8(1):26-33.
62. El-Shall M, Li S, Turkki T, Graiver D, Pernisz U, Baraton M. Synthesis and photoluminescence of weblike agglomeration of silica nanoparticles. *The Journal of Physical Chemistry*. 1995;99(51):17805-17809.
63. Yamani Z, Ashhab S, Nayfeh A, Thompson WH, Nayfeh M. Red to green rainbow photoluminescence from unoxidized silicon nanocrystallites. *Journal of Applied Physics*. 1998;83(7):3929-3931.
64. Ledoux G, Guillois O, Porterat D, Reynaud C, Huisken F, Kohn B, Paillard V. Photoluminescence properties of silicon nanocrystals as a function of their size. *Physical Review B*. 2000;62(23):15942.
65. Han M, Zhou J, Song F, Yin C, Liu M, Wan J, Wang G. Silicon-riched-oxide cluster assembled nanostructures formed by low energy cluster beam deposition. *The European Physical Journal D-Atomic, Molecular, Optical and Plasma Physics*. 2003;24(1):269-272.
66. Pratontep S, Carroll S, Xirouchaki C, Streun M, Palmer R. Size-selected cluster beam source based on radio frequency magnetron plasma sputtering and gas condensation. *Review of Scientific Instruments*. 2005;76(4):045103.
67. Wegner K, Piseri P, Tafreshi HV, Milani P. Cluster beam deposition: a tool for nanoscale science and technology. *Journal of Physics D: Applied Physics*. 2006;39(22):R439.
68. Ehbrecht M, Huisken F. Gas-phase characterization of silicon nanoclusters produced by laser pyrolysis of silane. *Physical Review B*. 1999;59(4):2975.
69. Hoffmann MA, Wrigge G, Issendorff Bv, Müller J, Ganteför G, Haberland H. Ultraviolet photoelectron spectroscopy of Si 4-to Si 1000. *The European Physical Journal D-Atomic, Molecular, Optical and Plasma Physics*. 2001;16(1):9-11.
70. Laarmann T, Wabnitz H, von Haeften K, Möller T. Photochemical processes in doped argon-neon core-shell clusters: The effect of cage size on the dissociation of molecular oxygen. *The Journal of Chemical Physics*. 2008;128(1):014502.
71. Montano P, Shenoy G, Alp E, Schulze W, Urban J. Structure of copper microclusters isolated in solid argon. *Physical Review Letters*. 1986;56(19):2076.

72. Riedler M, De Castro A, Kolmakov A, Löfken J, Nowak C, Soldatov A, Wark A, Yalovega G, Möller T. Na 1s photoabsorption of free and deposited NaCl clusters: Development of bond length with cluster size. *Physical Review B*. 2001;64(24):245419.
73. Jarrold MF, Constant VA. Silicon cluster ions: evidence for a structural transition. *Physical Review Letters*. 1991;67(21):2994.
74. Ho KM, Shvartsburg AA, Pan B, Lu ZY, Wang CZ, Wacker JG, Fye JL, Jarrold MF. Structures of medium-sized silicon clusters. *Nature*. 1998;392(6676):582-585.
75. Maus M, Ganteför G, Eberhardt W. The electronic structure and the band gap of nano-sized Si particles: competition between quantum confinement and surface reconstruction. *Applied Physics A*. 2000;70(5):535-539.
76. Zhou Z, Friesner RA, Brus L. Electronic structure of 1 to 2 nm diameter silicon core/shell nanocrystals: surface chemistry, optical spectra, charge transfer, and doping. *Journal of the American Chemical Society*. 2003;125(50):15599-15607.
77. Binns C. Nanoclusters deposited on surfaces. *Surface Science Reports*. 2001;44(1):1-49.
78. de Heer, WA. The physics of simple metal clusters: experimental aspects and simple models. *Reviews of Modern Physics*. 1993;65(3):611.
79. Zhong Y, Peng F, Bao F, Wang S, Ji X, Yang L, Su Y, Lee ST, He Y. Large-scale aqueous synthesis of fluorescent and biocompatible silicon nanoparticles and their use as highly photostable biological probes. *Journal of the American Chemical Society*. 2013;135(22):8350-8356.
80. Yao B, Shi H, Zhang X, Zhang L. Ultraviolet photoluminescence from nonbridging oxygen hole centers in porous silica. *Applied Physics Letters*. 2001;78(2):174-176.
81. Yang X, Wu X, Li S, Li H, Qiu T, Yang Y, Chu P, Siu G. Origin of the 370-nm luminescence in Si oxide nanostructures. *Applied Physics Letters*. 2005;86(20):201906-201906-3.
82. Kontkiewicz AJ, Kontkiewicz AM, Siejka J, Sen S, Nowak G, Hoff A, Sakthivel P, Ahmed K, Mukherjee P, Witanachchi S. Evidence that blue luminescence of oxidized porous silicon originates from SiO₂. *Applied Physics Letters*. 1994;65(11):1436-1438.
83. Ondič L, Kůsová K, Ziegler M, Fekete L, Gärtnerová V, Cháb V, Holý V, Cibulka O, Herynková K, Gallart M. A complex study of the fast blue luminescence of oxidized silicon nanocrystals: the role of the core. *Nanoscale*. 2014;6(7):3837-3845.
84. Gelloz B, Mentek R, Koshida N. Ultraviolet and long-lived blue luminescence of oxidized nano-porous silicon and pure nano-porous glass. *ECS Journal of Solid State Science and Technology*. 2014;3(5):R83-R88.
85. Liu P, Liang Y, Li H, Xiao J, He T, Yang G. Violet-blue photoluminescence from Si nanoparticles with zinc-blende structure synthesized by laser ablation in liquids. *AIP Advances*. 2013;3(2):022127.

86. Xu Y, Han Y. Effects of natural oxidation on the photoluminescence properties of Si nanocrystals prepared by pulsed laser ablation. *Applied Physics A*. 2014;117(3):1557-1562.
87. Yang S, Li W, Cao B, Zeng H, Cai W. Origin of blue emission from silicon nanoparticles: direct transition and interface recombination. *The Journal of Physical Chemistry C*. 2011;115(43):21056-21062.
88. Ray M, Jana K, Bandyopadhyay N, Hossain S, Navarro-Urrios D, Chattopadhyay P, Green MA. Blue–violet photoluminescence from colloidal suspension of nanocrystalline silicon in silicon oxide matrix. *Solid State Communications*. 2009;149(9):352-356.
89. Sattler K, Mühlbach J, Recknagel E. Generation of metal clusters containing from 2 to 500 atoms. *Physical Review Letters*. 1980;45(10):821.
90. Haberland H, Karrais M, Mall M. A new type of cluster and cluster ion source. *Zeitschrift für Physik D Atoms, Molecules and Clusters*. 1991;20(1):413-415.
91. von Haeften K, Binns C, Brewer A, Crisan O, Howes P, Lowe M, Sibley-Allen C, Thornton S. A novel approach towards the production of luminescent silicon nanoparticles: sputtering, gas aggregation and co-deposition with H₂O. *The European Physical Journal D-Atomic, Molecular, Optical and Plasma Physics*. 2009;52(1):11-14.
92. von Haeften K, Lowe M, Brewer A. Fluorescence of Silicon Nanoparticles Suspended in Water. In: *SASP Erwin Schrödinger Gold Medal 2010: Proceeding of the 17th Symposium on Atomic, Cluster and Surface Physics 2010 (SASP 2010)*, 24 - 29 January 2010, Universitätszentrum Obergurgl, Austria. 2010. p. 54.
93. von Haeften K, Akraiam A, Torricelli G, Brewer A. Fluorescence of silicon nanoparticles suspended in water: reactive co-deposition for the control of surface properties of clusters. In: Borsella E, editor. *Proceedings of the BONSAI Project Symposium: Breakthroughs in Nanoparticles for Bio-Imaging*, 8–9 April 2010, Frascati, Italy. American Institute of Physics (AIP); 2010. 1275: p. 40.
94. Faubel M, Schlemmer S, Toennies J. A molecular beam study of the evaporation of water from a liquid jet. *Zeitschrift für Physik D Atoms, Molecules and Clusters*. 1988;10(2-3):269-277.
95. Alsharif NH, Berger CE, Varanasi SS, Chao Y, Horrocks BR, Datta HK. Alkyl-capped silicon nanocrystals lack cytotoxicity and have enhanced intracellular accumulation in malignant cells via cholesterol-dependent endocytosis. *Small*. 2009;5(2):221-228.
96. Pellegrino T, Kudera S, Liedl T, Muñoz Javier A, Manna L, Parak WJ. On the development of colloidal nanoparticles towards multifunctional structures and their possible use for biological applications. *Small*. 2005;1(1):48-63.
97. Parak WJ, Pellegrino T, Plank C. Labelling of cells with quantum dots. *Nanotechnology*. 2005;16(2):R9.
98. Zhang YH, Li XJ, Zheng L, Chen QW. Nondegrading photoluminescence in porous silicon. *Physical Review Letters*. 1998;81(8):1710.

99. Cullis AG, Canham LT, Calcott PDJ. The structural and luminescence properties of porous silicon. *Journal of Applied Physics*. 1997;82(3):909-965.
100. Sattler K, Mühlbach J, Recknagel E. Generation of metal clusters containing from 2 to 500 atoms. *Physical Review Letters*. 1980;45(10):821-824.
101. Auto 306 vacuum coating systems [Internet]. BOC Edwards; 2005. Available from: <http://www.rubion.rub.de/files/pdf/edwards-auto-306.pdf>.
102. Northrop RB. *Introduction to instrumentation and measurements*. 3rd. Boca Raton: CRC Press; 2014. p. 799.
103. Krasnokutski S, Rouillé G, Jäger C, Huisken F, Zhukovska S, Henning T. Formation of silicon oxide grains at low temperature. *The Astrophysical Journal*. 2014;782(1):15.
104. Certificate of analysis [Internet]. VWR, BDH Prolabo; 2015. Available from: https://uk.vwr.com/store/asset?assetURI=https://uk.vwr.com/stibo/hi_res/std.lang.all/44/67/14854467.pdf.
105. Ethyl alcohol, pure [Internet]. Sigma-Aldrich Co.; Available from: <http://www.sigmaaldrich.com/catalog/product/sial/459828?lang=en®ion=GB>.
106. 2-Propanole [Internet]. Sigma-Aldrich Co.; Available from: <http://www.sigmaaldrich.com/catalog/product/sial/34863?lang=en®ion=GB>.
107. Albani JR. *Principles and applications of fluorescence spectroscopy*. Blackwell; Publishing; 2007.
108. Jabłoński A. Über den mechanismus der photolumineszenz von farbstoffphosphoren. *Zeitschrift für Physik*. 1935;94(1-2):38-46.
109. Guilbault GG, editor. *Practical fluorescence*. Vol. 3. 2nd ed. New York: CRC Press; 1990.
110. Gauglitz G, Vo-Dinh T, editors. *Handbook of spectroscopy*. Weinheim: Wiley-VCH; 2003.
111. FluoroMax series [Internet]. Horiba Scientific Ltd.; Available from: <http://www.horiba.com/scientific/products/fluorescence-spectroscopy/steady-state/fluoromax/fluoromax-series-524/>.
112. Operation manual, DataMax version 2.20 [Internet]. Horiba Scientific Ltd.; 2001. Available from: <http://www.rose-hulman.edu/~brandt/DATAMAX.PDF>.
113. Operation manual, Fluoromax-4 & Fluoromax-4P version 1.1 [Internet]. Jobin Yvon Inc.; 2006. Available from: <http://www.chimica.unipd.it/danilo.pedron/privata/documentazione/insegnamenti/STRUMENTI/FluoroMax-P.pdf>.
114. Operation manual, Fluoromax-3 & Fluoromax-P, Fluoromax-3 version 2.0, Jobin Yvon Inc.; 2001.
115. Zimmerer G. Status report on luminescence investigations with synchrotron radiation at HASYLAB. *Nuclear Instruments and Methods in Physics Research Section A*:

- Accelerators, Spectrometers, Detectors and Associated Equipment. 1991;308(1):178-186.
116. Zimmerer G. SUPERLUMI: A unique setup for luminescence spectroscopy with synchrotron radiation. *Radiation Measurements*. 2007;42(4):859-864.
117. Skoog DA, Holler FJ, Crouch SR. *Principles of Instrumental Analysis*. 6th ed. Belmont: Thompson Brooks/Cole; 2007.
118. Robinson JW. *Atomic spectroscopy*. 2nd ed. New York: CRC Press; 1996.
119. User manual, UV-Visible and fluorescence spectroscopy, Evolution 200 series, Glossary of terms. Thermo Fisher Scientific Inc.; 2007-2012.
120. Evolution™ 201/220 UV-Visible spectrophotometers [Internet]. Thermo Fisher Scientific Inc; 2015. Available from: <https://www.thermofisher.com/order/catalog/product/840-210600>.
121. Thermo Scientific Evolution 201 and 220 UV-Visible spectrometers [Internet]. Thermo Fisher Scientific Inc; 2011. Available from: <https://static.fishersci.com/cmsassets/downloads/segment/Scientific/pdf/ThermoScientific/UVvis/TS-Evolution201-220.pdf>.
122. Gauglitz G, Lorch A, Oelkrug D. Fluorescence quantum yields of laser dyes determined by on-line computer evaluation. *Zeitschrift Naturforschung Teil A*. 1982;37:219.
123. Parker, C., *Photoluminescence of solutions*. New York: American Elsevier Publishing Company, Inc; 1968.
124. Barik A, Priyadarsini KI, Mohan H. Photophysical studies on binding of curcumin to bovine serum albumin. *Photochemistry and Photobiology*. 2003;77(6):597-603.
125. Albani J. New insights in the interpretation of tryptophan fluorescence. *Journal of Fluorescence*. 2007;17(4):406-417.
126. Sauer M, Hofkens J, Enderlein J. Basic principles of fluorescence spectroscopy. *Handbook of Fluorescence Spectroscopy and Imaging: From Single Molecules to Ensembles*. Weinheim: Wiley-VCH; 2011. p. 1-30.
127. Watts JF, Wolstenholme J. *An introduction to surface analysis by XPS and AES*. Wiley-VCH; 2003.
128. NIST X-ray Photoelectron Spectroscopy Database, NIST Standard Reference Database 20, Version 4.1 [Internet]. National Institute of Standards and Technology; 2012. Available from: <http://srdata.nist.gov/xps/Default.aspx>.
129. Omicron Nanotechnology, editor. *Multiprobe surface science systems user's guide*, Germany: Omicron; 2010.
130. Omicron Nanotechnology, editor. *DAR 400 X-ray source*, Germany: Omicron; 2009.
131. *Electron spectroscopy (XPS, AES, UPS)* [Internet]. Tampere University of Technology; 2012. Available from: <http://www.tut.fi/en/about-tut/departments/optoelectronics-research-centre/research/surface-science/electron-spectroscopy/index.htm>.

132. Omicron Nanotechnology, editor. EA 125 Energy analyser, Germany: Omicron; 2006.
133. Evans S. Correction for the effects of adventitious carbon overlayers in quantitative XPS analysis. *Surface and Interface Analysis*. 1997;25(12):924-930.
134. Peden C, Rogers Jr J, Shinn N, Kidd K, Tsang K. Thermally grown Si₃N₄ thin films on Si (100): Surface and interfacial composition. *Physical Review B*. 1993;47(23):15622.
135. Magnusson K, Wiklund S, Dudde R, Reihl B. Adsorption of Cs on Si (111) 7×7: Studies of photoemission from surface states and core levels. *Physical Review B*. 1991;44(11):5657.
136. Blair D, Rogers Jr J, Peden C. Potassium-assisted, facile oxidation of Si₃N₄ thin films. *Journal of Applied Physics*. 1990;67(4):2066-2073.
137. Ley L, Wang Y, Van VN, Fisson S, Souche D, Vuye G, Rivory J. Initial stages in the formation of PtSi on Si (111) as followed by photoemission and spectroscopic ellipsometry. *Thin Solid Films*. 1995;270(1):561-566.
138. Atzrodt V, Wirth T, Lange H. Investigation of NiSi and Pd₃Si thin films by AES and XPS. *Physica Status Solidi (a)*. 1980;62(2):531-537.
139. Reichl R, Gaukler K. XPS study of the Y/SiO_x interface at room temperature. *Surface and Interface Analysis*. 1990;15(3):211-214.
140. Sirotti F, De Santis M, Rossi G. Synchrotron-radiation photoemission and X-ray absorption of Fe silicides. *Physical Review B*. 1993;48(11):8299.
141. Alfonsetti R, Lozzi L, Passacantando M, Picozzi P, Santucci S. XPS studies on SiO_x thin films. *Applied Surface Science*. 1993;70:222-225.
142. Baptist R, Pellissier A, Chauvet G. Chemical bonding in layered Y Si_{≈ 1.7}. *Solid State Communications*. 1988;68(6):555-559.
143. Ingo G, Zacchetti N, Della Sala D, Coluzza C. X-ray photoelectron spectroscopy investigation on the chemical structure of amorphous silicon nitride (a-SiN_x). *Journal of Vacuum Science & Technology A*. 1989;7(5):3048-3055.
144. Jeske M, Jung K, Schultze J, Thönissen M, Munder H. XPS investigations of electrochemically modified porous silicon layers. *Surface and Interface Analysis*. 1994;22(1-12):363-366.
145. Chang W, Bello I, Lau W. X-ray photoelectron spectroscopy study of low energy CF₊ ion interactions with silicon. *Journal of Vacuum Science & Technology A*. 1993;11(4):1221-1225.
146. Iwakuro H, Tokonami M, Kuroda T, Tamaki S, Kitatsuji Y. Interfacial layers of high-barrier Schottky diode of Al/n-type (100) Si exposed to H₂ plasma. *Japanese Journal of Applied Physics*. 1993;32(12R):5487.
147. Montero I, Galan L, De La Cal E, Albella J, Pivin J. Incorporation of OH radicals in anodic silicon oxide films studied by secondary-ion mass spectroscopy, X-ray photoelectron spectroscopy and ir analysis. *Thin Solid Films*. 1990;193:325-332.

148. Bell F, Ley L. Photoemission study of SiO_x ($0 \leq x \leq 2$) alloys. *Physical Review B*. 1988;37(14):8383.
149. Anwar M, Hogarth C, Bulpett R. An XPS study of amorphous MoO_3/SiO films deposited by co-evaporation. *Journal of Materials Science*. 1990;25(3):1784-1788.
150. Finster J. SiO_2 in 6: 3 (stishovite) and 4: 2 Co-ordination—Characterization by core level spectroscopy (XPS/XAES). *Surface and Interface Analysis*. 1988;12(5):309-314.
151. Finster J, Klinkenberg ED, Heeg J, Braun W. ESCA and SEXAFS investigations of insulating materials for ULSI microelectronics. *Vacuum*. 1990;41(7):1586-1589.
152. Hagio T, Takase A, Umebayashi S. X-ray photoelectron spectroscopic studies of β -sialons. *Journal of Materials Science Letters*. 1992;11(12):878-880.
153. Dang TA, Chau CN. Electron spectroscopy for chemical analysis of cool white phosphors coated with SiO_2 thin film. *Journal of The Electrochemical Society*. 1996;143(1):302-305.
154. Alexander MR, Short RD, Jones FR, Stollenwerk M, Zabold J, Michaeli W. An X-ray photoelectron spectroscopic investigation into the chemical structure of deposits formed from hexamethyldisiloxane/oxygen plasmas. *Journal of Materials Science*. 1996;31(7):1879-1885.
155. Laczka M, Beier W, Stoch L. Synthesis, structure and certain properties of melted and sol-gel glasses in the SiO_2 and $\text{Al}_2\text{O}_3\text{-SiO}_2$ systems. *Glastechnische Berichte*. 1989;62(9):320-327.
156. Rueda F, Mendialdua J, Rodriguez A, Casanova R, Barbaux Y, Gengembre L, Jalowiecki L. Characterization of Venezuelan laterites by X-ray photoelectron spectroscopy. *Journal of Electron Spectroscopy and Related Phenomena*. 1996;82(3):135-143.
157. Chao S, Takagi Y, Lucovsky G, Pai P, Custer R, Tyler J, Keem J. Chemical states study of Si in SiO_x films grown by PECVD. *Applied Surface Science*. 1986;26(4):575-583.
158. Jin YS, Yan QJ, Yin ZR, Chen Y. Secondary ion mass spectrometry and X-ray photoelectron spectroscopy of $\text{Na}_2\text{MoO}_4/\text{SiO}_2$ catalysts for methane oxidative coupling. *Journal of the Chemical Society. Faraday Transactions*. 1995;91(2):381-384.
159. Tanizawa Y, Suzuki T. Effects of silicate ions on the formation and transformation of calcium phosphates in neutral aqueous solutions. *J. Chem. Soc., Faraday Trans*. 1995;91(19):3499-3503.
160. Paparazzo E. X-ray photo-emission and Auger spectra of damage induced by Ar^+ -ion etching at SiO_2 surfaces. *Journal of Physics D: Applied Physics*. 1987;20(8):1091.
161. Venezia A, Bertoncetto R, Deganello G. X-ray photoelectron spectroscopy investigation of pumice-supported nickel catalysts. *Surface and Interface Analysis*. 1995;23(4):239-247.
162. Galuska A, Uht J, Marquez N. Reactive and nonreactive ion mixing of Ti films on carbon substrates. *Journal of Vacuum Science & Technology A*. 1988;6(1):110-122.

163. Kibel MH, Leech PW. X-ray photoelectron spectroscopy study of optical waveguide glasses. *Surface and Interface Analysis*. 1996;24(9):605-610.
164. Edgell M, Baer D, Castle J. Biased referencing experiments for the XPS analysis of non-conducting materials. *Applied Surface Science*. 1986;26(2):129-149.
165. Paparazzo E, Fanfoni M, Severini E. Studies on the structure of the SiO_x/SiO₂ interface. *Applied Surface Science*. 1992;56:866-872.
166. Aoyama T, Sugii T, Ito T. Determination of band line-up in β -SiC/Si heterojunction for Si-HBT's. *Applied Surface Science*. 1990;41:584-586.
167. Parrill T, Chung Y. Surface analysis of cubic silicon carbide (001). *Surface science*. 1991;243(1):96-112.
168. Didziulis SV, Fleischauer PD. Effects of chemical treatments on silicon carbide surface composition and subsequent molybdenum disulfide film growth. *Langmuir*. 1990;6(3):621-627.
169. Tabata A, Fujii S, Suzuoki Y, Mizutani T, Ieda M. X-ray photoelectron spectroscopy (XPS) of hydrogenated amorphous silicon carbide (a-Si_xC_{1-x}:H) prepared by the plasma CVD method. *Journal of Physics D: Applied Physics*. 1990;23(3):316.
170. Mizokawa Y, Geib K, Wilmsen C. Characterization of β -SiC surfaces and the Au/SiC interface. *Journal of Vacuum Science & Technology A*. 1986;4(3):1696-1700.
171. Delplancke MP, Powers J, Vandentop G, Salmeron M, Somorjai G. Preparation and characterization of amorphous SiC: H thin films. *Journal of Vacuum Science & Technology A*. 1991;9(3):450-455.
172. Bozack MJ. Single Crystal 6H-SiC (0001) by XPS. *Surface Science Spectra*. 1994;3(1):82-85.
173. Contarini S, Howlett S, Rizzo C, De Angelis B. XPS study on the dispersion of carbon additives in silicon carbide powders. *Applied Surface Science*. 1991;51(3):177-183.
174. Gat E., El Khakani M, Chaker M, Jean A, Boily S, Pepin H, Kieffer J, Durand J, Cros B, Rousseaux F. A study of the effect of composition on the microstructural evolution of a-Si_xC_{1-x}: H PECVD films: IR absorption and XPS characterizations. *Journal of Materials Research*. 1992;7(09):2478-2487.
175. Yamamoto H, Baba Y, Sasaki TA. Electronic structures of N₂⁺ and O₂⁺ ion-implanted Si (100). *Surface and Interface Analysis*. 1995;23(6):381-385.
176. Alfonsetti R, De Simone G, Lozzi L, Passacantando M, Picozzi P, Santucci S. SiO_x surface stoichiometry by XPS: a comparison of various methods. *Surface and Interface Analysis*. 1994;22(1-12):89-92.
177. Das S, Webb J, de Castro S, Sundaram V. Photoelectron spectra of amorphous Si_xH_y alloy films: The effect of microstructure on the Si-2p level shift. *Journal of Applied Physics*. 1986;60(7):2530-2535.

178. Pitts J, Thomas T, Czanderna A, Passler M. XPS and ISS of submonolayer coverage of Ag on SiO₂. *Applied Surface Science*. 1986;26(1):107-120.
179. Witek G, Noeske M, Mestl G, Shaikhutdinov S, Behm R. Interaction of platinum colloids with single crystalline oxide and graphite substrates: a combined AFM, STM and XPS study. *Catalysis Letters*. 1996;37(1-2):35-39.
180. Johansson G, Hedman J, Berndtsson A, Klasson M, Nilsson R. Calibration of electron spectra. *Journal of Electron Spectroscopy and Related Phenomena*. 1973;2(3):295-317.
181. Xie Y, Sherwood PM. Ultrahigh purity graphite electrode by core level and valence band XPS. *Surface Science Spectra*. 1992;1(4):367-372.
182. Hrbek J. Carbonaceous overlayers on Ru (001). *Journal of Vacuum Science & Technology A*. 1986;4(1):86-89.
183. Morar J, Himpfel F, Hollinger G, Jordan J, Hughes G, McFeely F. C 1s excitation studies of diamond (111). I. Surface core levels. *Physical Review B*. 1986;33(2):1340.
184. Vasquez RP. A Polycrystalline Diamond Film by XPS. *Surface Science Spectra*. 1992;1(2):188-191.
185. Schmiege SJ, Belton DN. Polycrystalline diamond film on Si (100) by XPS. *Surface Science Spectra*. 1992;1(4):329-332.
186. Waldrop J, Grant R, Wang Y, Davis R. Metal Schottky barrier contacts to alpha 6H-SiC. *Journal of Applied Physics*. 1992;72(10):4757-4760.
187. Kennou S. An X-ray photoelectron spectroscopy and work-function study of the Er/ α -SiC (0001) interface. *Journal of Applied Physics*. 1995;78(1):587-589.
188. Waldrop J, Grant R. Formation and Schottky barrier height of metal contacts to β -SiC. *Applied Physics Letters*. 1990;56(6):557-559.
189. Smith K, Black K. Characterization of the treated surfaces of silicon alloyed pyrolytic carbon and SiC. *Journal of Vacuum Science & Technology A*. 1984;2(2):744-747.
190. Johansson L, Owman F, Mårtensson P. High-resolution core-level study of 6H-SiC (0001). *Physical Review B*. 1996;53(20):13793.
191. Muehlhoff L, Choyke W, Bozack M, Yates Jr JT. Comparative electron spectroscopic studies of surface segregation on SiC (0001) and SiC (0001). *Journal of Applied Physics*. 1986;60(8):2842-2853.
192. Nalwa HS, editor. *Silicon-based material and devices, two-volume set: materials and processing, properties and devices*. Vol. 1. San Diego: Academic Press; 2001.
193. Vickerman JC, Gilmore IS, editors. *Surface analysis: the principal techniques*. 2nd ed. Chichester: Wiley; 2009.
194. Gelius U, Heden P, Hedman J, Lindberg B, Manne R, Nordberg R, Nordling C, Siegbahn K. Molecular spectroscopy by means of ESCA III. Carbon compounds. *Physica Scripta*. 1970;2(1-2):70.

195. Taylor JA, Lancaster GM, Ignatiev A, Rabalais JW. Interactions of ion beams with surfaces. Reactions of nitrogen with silicon and its oxides. *The Journal of Chemical Physics*. 1978;68(4):1776-1784.
196. Sprenger D, Bach H, Meisel W, Gütlich P. XPS study of leached glass surfaces. *Journal of Non-Crystalline Solids*. 1990;126(1):111-129.
197. Miller ML, Linton RW. X-ray photoelectron spectroscopy of thermally treated silica (SiO₂) surfaces. *Analytical Chemistry*. 1985;57(12):2314-2319.
198. Shalvoy R, Reucroft P, Davis B. Characterization of coprecipitated nickel on silica methanation catalysts by X-ray photoelectron spectroscopy. *Journal of Catalysis*. 1979;56(3):336-348.
199. Carnera A, Mazzoldi P, Boscolo-Boscoletto A, Caccavale F, Bertonecello R, Granozzi G, Spagnol I, Battaglin G. On the formation of silicon oxynitride by ion implantation in fused silica. *Journal of Non-Crystalline Solids*. 1990;125(3):293-301.
200. Seyama H, Soma M. Bonding-state characterization of the constituent elements of silicate minerals by X-ray photoelectron spectroscopy. *Journal of the Chemical Society, Faraday Transactions 1: Physical Chemistry in Condensed Phases*. 1985;81(2):485-495.
201. Netterfield RP, Martin P, Pacey C, Sainty W, McKenzie D, Auchterlonie G. Ion-assisted deposition of mixed TiO₂-SiO₂ films. *Journal of Applied Physics*. 1989;66(4):1805-1809.
202. Taylor JA. Further examination of the Si KLL Auger line in silicon nitride thin films. *Applications of Surface Science*. 1981;7(1):168-184.
203. Paparazzo E. XPS and Auger spectroscopy studies on mixtures of the oxides SiO₂, Al₂O₃, Fe₂O₃ and Cr₂O₃. *Journal of Electron Spectroscopy and Related Phenomena*. 1987;43(2):97-112.
204. Paparazzo E. XPS analysis of oxides. *Surface and Interface Analysis*. 1988;12(2):115-118.
205. Wagner C, Passoja D, Hillery H, Kinisky T, Six H, Jansen W, Taylor J. Auger and photoelectron line energy relationships in aluminum-oxygen and silicon-oxygen compounds. *Journal of Vacuum Science and Technology*. 1982;21(4):933-944.
206. Takagi-Kawai M, Soma M, Onishi T, Tamaru K. The adsorption and the reaction of NH₃ and NO_x on supported V₂O₅ catalysts: effect of supporting materials. *Canadian Journal of Chemistry*. 1980;58(20):2132-2137.
207. Nefedov V, Gati D, Dzhurinskii B, Sergushin N, Salyn YV. X-ray electron study of oxides of elements. *Zhurnal Neorganicheskoi Khimii*. 1975;20(9):2307-2314.
208. Cimino A, Gazzoli D, Inversi M, Valigi M. X-ray photoelectron spectroscopic and thermogravimetric studies of rhenium oxides supported on silica. *Surface and Interface Analysis*. 1987;10(4):194-201.
209. Barr TL. An XPS study of Si as it occurs in adsorbents, catalysts, and thin films. *Applications of Surface Science*. 1983;15(1):1-35.

210. Taylor JA, Lancaster GM, Rabalais JW. Chemical reactions of N²⁺ ion beams with group IV elements and their oxides. *Journal of Electron Spectroscopy and Related Phenomena*. 1978;13(3):435-444.
211. Görlich E, Haber J, Stoch A, Stoch J. XPS study of α -quartz surface. *Journal of Solid State Chemistry*. 1980;33(1):121-124.
212. Clarke T, Rizkalla E. X-ray photoelectron spectroscopy of some silicates. *Chemical Physics Letters*. 1976;37(3):523-526.
213. Puppini E, Lindau I, Abbati I. Photoemission core level shifts in Gd silicides. *Solid State Communications*. 1991;77(12):983-986.
214. Mesarwi A, Ignatiev A. X-ray photoemission study of Y-promoted oxidation of the Si (100) surface. *Surface Science*. 1991;244(1):15-21.
215. Ogama T. A new method to detect energy-band bending using x-ray photoemission spectroscopy. *Journal of Applied Physics*. 1988;64(2):753-757.
216. Bekkay T, Sacher E, Yelon A. Surface reaction during the argon ion sputter cleaning of surface oxidized crystalline silicon (111). *Surface Science*. 1989;217(1):L377-L381.
217. Behner H, Wecker J, Matthée T, Samwer K. XPS study of the interface reactions between buffer layers for HTSC thin films and silicon. *Surface and Interface Analysis*. 1992;18(9):685-690.
218. Anpo M, Nakaya H, Kodama S, Kubokawa Y, Domen K, Onishi T. Photocatalysis over binary metal oxides. Enhancement of the photocatalytic activity of titanium dioxide in titanium-silicon oxides. *The Journal of Physical Chemistry*. 1986;90(8):1633-1636.
219. Gross T, Ramm M, Sonntag H, Unger W, Weijers H, Adem E. An XPS analysis of different SiO₂ modifications employing a C 1s as well as an Au 4f_{7/2} static charge reference. *Surface and Interface Analysis*. 1992;18(1):59-64.
220. Iimura Ki, Suzuki N, Kato T. Studies on Spread Monolayers and LB Films of Long-Chain Alkylchlorosilanes by Brewster Angle Microscopy and X-Ray Photoelectron Spectroscopy. *Bulletin of the Chemical Society of Japan*. 1996;69(5):1201-1211.
221. CasaXPS: Processing software for XPS, AES, SIMS and more [Internet]. Casa Software Ltd.; 2015. Available from: <http://www.casaxps.com/>.
222. Nawrocka A, Lamorska J. Determination of food quality by using spectroscopic methods. In: Grundas S, Stepniewski A, editors. *Advances in Agrophysical research*. InTech; 2013.
223. Manual- Nicolet iS5 spectrometer fast facts. Thermo Fisher Scientific Inc.: 2010.
224. Nicolet™ iS™ 5 FT-IR spectrometer [Internet]. Thermo Fisher Scientific Inc.; 2015. Available from: <https://www.thermofisher.com/order/catalog/product/IQLAADGAAGFAHDMZA>.
225. Thermo Scientific Nicolet iS5 FT_IR spectrometer [Internet]. Thermo Fisher Scientific Inc.; 2010-2014. Available from:

- <https://tools.thermofisher.com/content/sfs/brochures/PS51984-E-0214M-iS5-H-web.pdf>.
226. iD5 ATR accessory for the Nicolet™ iS5 spectrometer [Internet]. Thermo Fisher Scientific Inc.; 2015. <https://www.thermofisher.com/order/catalog/product/IQLAADGAAGFAJAMAYY>.
227. Thermo Scientific Nicolet iS5 FT-IR spectrometer iD accessories [Internet]. Thermo Fisher Scientific Inc.; 2011. Available from: <https://static.fishersci.com/cmsassets/downloads/segment/Scientific/pdf/ThermoScientific/UVvis/TS-Nicoletis5-ftir-Accessories.pdf>.
228. IR sampling accessories & press solutions [Internet]. Specac Ltd.; 2015. Available from: <http://www.specac.com/products/liquid-transmission-cell/ft-ir-liquidtransmission-cell/530>.
229. Specac brilliant spectroscopy, data sheet [Internet]. Specac Ltd.; Available from: <http://www.specac.com/userfiles/file/N35OmniCellSystem.pdf>.
230. OMNIC™ series software [Internet]. Thermo Fisher Scientific Inc.; 2015. Available from: <http://www.thermoscientific.com/en/product/omnic-series-software.html>.
231. Luna-López J, Carrillo-López J, Aceves-Mijares M, Morales-Sánchez A, Falcony C. FTIR and photoluminescence of annealed silicon rich oxide films. *Superficies y Vacío*. 2009;22(1):11-14.
232. Pai P, Chao S, Takagi Y, Lucovsky G. Infrared spectroscopic study of SiO_x films produced by plasma enhanced chemical vapor deposition. *Journal of Vacuum Science & Technology A*. 1986;4(3):689-694.
233. Ay F, Aydinli A. Comparative investigation of hydrogen bonding in silicon based PECVD grown dielectrics for optical waveguides. *Optical Materials*. 2004;26(1):33-46.
234. Brandt M, Fuchs H, Stutzmann M, Weber J, Cardona M. The origin of visible luminescence from “porous silicon”: A new interpretation. *Solid State Communications*. 1992;81(4):307-312.
235. Fuchs H, Stutzmann M, Brandt M, Rosenbauer M, Weber J, Breitschwerdt A, Deak P, Cardona M. Porous silicon and siloxene: Vibrational and structural properties. *Physical Review B*. 1993;48(11):8172.
236. Fendler JH, editor. *Nanoparticles and nanostructured films: Preparation, characterization, and applications*. Wiley-VCH; 2008.
237. Hench LL, West JK. The sol-gel process. *Chemical Reviews*. 1990;90(1):33-72.
238. Infrared spectroscopy [Internet]. 2013. Available from: <http://www2.chemistry.msu.edu/faculty/reusch/VirtTxtJmL/Spectrpy/InfraRed/infrared.htm>.
239. Tischler M, Collins R. On the relationship of porous silicon and siloxene. *Solid State Communications*. 1992;84(8):819-822.

240. Young T, Chen C, Liou J, Yang Y, Chang T. Study on the Si–Si vibrational states of the near surface region of porous silicon. *Journal of Porous Materials*. 2000;7(1-3):339-343.
241. Collins R, Fan H. Infrared lattice absorption bands in germanium, silicon, and diamond. *Physical Review*. 1954;93(4):674.
242. Hart T, Aggarwal R, Lax B. Temperature dependence of Raman scattering in silicon. *Physical Review B*. 1970;1(2):638.
243. Vasquez-A M, Rodriguez GA, García-Salgado G, Romero-Paredes G, Pena-Sierra R. FTIR and photoluminescence studies of porous silicon layers oxidized in controlled water vapor conditions. *Revista Mexicana de Física*. 2007;53(6):431.
244. Mihalcescu I, Ligeon M, Muller F, Romestain R, Vial J. Surface passivation: a critical parameter for the visible luminescence of electrooxidised porous silicon. *Journal of Luminescence*. 1993;57(1):111-115.
245. Lucovsky G, Yang J, Chao S, Tyler J, Czubytyj W. Oxygen-bonding environments in glow-discharge-deposited amorphous silicon-hydrogen alloy films. *Physical Review B*. 1983;28(6):3225.
246. Glinka YD, Lin SH, Chen YT. The photoluminescence from hydrogen-related species in composites of SiO₂ nanoparticles. *Applied Physics Letters*. 1999;75(6):778-780.
247. Inokuma T, Kurata Y, Hasegawa S. Cathodoluminescence properties of silicon nanocrystallites embedded in silicon oxide thin films. *Journal of Luminescence*. 1998;80(1):247-251.
248. Bairle R J, Caldas MJ, Molinari E, Ossicini S. Optical emission from small Si particles. *Solid State Communications*. 1997;102(7):545-9.
249. Ratner BD, Castner DG, editors. *Surface modification of polymeric biomaterials*. Springer: 1997.
250. Rangel-Vázquez NA, Leal-García T. Spectroscopy analysis of chemical modification of cellulose fibers. *J. Mex. Chem. Soc*. 2010;54:192-197.
251. Morioka T, Kimura S, Tsuda N, Kaito C, Saito Y, Koike C. Study of the structure of silica film by infrared spectroscopy and electron diffraction analyses. *Monthly Notices of the Royal Astronomical Society*. 1998;299(1):78-82.
252. Nakamura M, Mochizuki Y, Usami K, Itoh Y, Nozaki T. Infrared absorption spectra and compositions of evaporated silicon oxides (SiO_x). *Solid State Communications*. 1984;50(12):1079-1081.
253. Tiwari A, Soucek MD, editors. *Concise encyclopedia of high performance silicones*. John Wiley & Sons: 2014.
254. Cheah K, Chan T, Lee W, Teng D, Zheng W, Wang Q. Multiple peak photoluminescence of porous silicon. *Applied Physics Letters*. 1993;63(25):3464-3466.
255. Deng Y, White GN, Dixon JB. Effect of structural stress on the intercalation rate of kaolinite. *Journal of Colloid and Interface Science*. 2002;250(2):379-393.

256. [Internet]. Chemistry and Biochemistry, University of Colorado Boulder; Available from: <http://orgchem.colorado.edu/Spectroscopy/irtutor/carbacidsir.html>.
257. Xu C, Uddin KMA, Shen X, Jayawardena HSN, Yan M, Ye L. Photoconjugation of molecularly imprinted polymer with magnetic nanoparticles. *ACS Applied Materials & Interfaces*. 2013;5(11):5208-5213.
258. López TM, Avnir D, Aegerter MA, editors. *Emerging fields in sol-gel science and technology*. Springer; 2013.
259. Swihart M, Barreca D, Adomaitis R, Wörhoff K, editors. *EuroCVD 17/CVD 17: ECS Transactions*. Vol. 25. Pennington: The Electrochemical Society; 2009.
260. Meunier A, editor. In: *Clays and hydrosilicate gels in nuclear fields: Proceedings of the European Materials Research Society Symposia, E-MRS Conference*, Vol. 26, 4-7 November 1991, Strasbourg, France. Amsterdam: Elsevier; 1992.
261. Dantas NO, Ayta WE, Silva AC, Cano NF, Silva SW, Morais PC. Effect of Fe₂O₃ concentration on the structure of the SiO₂-Na₂O-Al₂O₃-B₂O₃ glass system. *Spectrochimica Acta Part A: Molecular and Biomolecular Spectroscopy*. 2011;81(1):140-143.
262. [Internet]. Chemistry and Biochemistry, University of Colorado Boulder; <http://orgchem.colorado.edu/Spectroscopy/irtutor/alcoholsir.html>.
263. Parker FS. *Applications of infrared, Raman, and resonance Raman spectroscopy in biochemistry*. Springer; 1983.
264. Kaiser W, Keck PH, Lange C. Infrared absorption and oxygen content in silicon and germanium. *Physical Review*. 1956;101(4):1264.
265. Koropecski R, Arce R. Infrared study of the kinetics of oxidation in porous amorphous silicon. *Journal of Applied Physics*. 1986;60(5):1802-1807.
266. Pong K, Chen S, Cheah K. Photoluminescence of laser ablated silicon. *Solid State Communications*. 1996;99(12):887-890.
267. Grainger D, Knutson K, Kim S, Feijen J. Poly (dimethylsiloxane)-poly (ethylene oxide)-heparin block copolymers II: Surface characterization and in vitro assessments. *Journal of Biomedical Materials Research*. 1990;24(4):403-431.
268. Oh T. Optical properties of photoluminescence of carbon doped silicon oxide films annealed by rapid temperature for passivation. In: Lee G, Howard D, Ślęzak D, editors. *Convergence and Hybrid Information Technology: Proceedings of the 5th International Conference, ICHIT 2011, Communications in Computer and Information Science 206*, September 22-24, 2011, Daejeon, Korea. Springer Berlin Heidelberg; 2011. p. 423-428.
269. Noh JS. Highly conductive and stretchable poly (dimethylsiloxane): poly (3, 4-ethylenedioxythiophene): poly (styrene sulfonic acid) blends for organic interconnects. *RSC Advances*. 2014;4(4):1857-1863.

270. Tsai C, Li KH, Sarathy J, Shih S, Campbell J, Hance B, White J. Thermal treatment studies of the photoluminescence intensity of porous silicon. *Applied Physics Letters*. 1991;59(22):2814-2816.
271. Ruiz F, Vázquez-López C, González-Hernández J, Allred DD, Romero-Paredes G, Peña-Sierra R, Torres-Delgado G. Mesostructure of photoluminescent porous silicon. *Journal of Vacuum Science & Technology A*. 1994;12(4):2565-2571.
272. Ubara H, Imura T, Hiraki A. Formation of SiH bonds on the surface of microcrystalline silicon covered with SiO_x by HF treatment. *Solid State Communications*. 1984;50(7):673-675.
273. Tolstoy VP, Chernyshova IV, Skryshevsky VA. *Handbook of infrared spectroscopy of ultrathin films*. Wiley; 2003.
274. Yorikawa H, Muramatsu S. Photoluminescence and particle size distribution in porous silicon. *Journal of Luminescence*. 2000;87:423-425.
275. Skuja L, Streletsky A, Pakovich A. A new intrinsic defect in amorphous SiO₂: twofold coordinated silicon. *Solid State Communications*. 1984;50(12):1069-1072.
276. Wilson WL, Szajowski P, Brus L. Quantum confinement in size-selected, surface-oxidized silicon nanocrystals. *Science-New York Then Washington-*. 1993;262:1242-1242.
277. Moyer PJ, Pridmore A, Martin T, Schmidt J, Hasche T, Eng L, Gole JL. Dependence of radiative lifetimes of porous silicon on excitation wavelength and intensity. *Applied Physics Letters*. 2000;76(19):2683-2685.
278. Weldon MK, Stefanov BB, Raghavachari K, Chabal Y. Initial H₂O-induced oxidation of Si (100)-(2× 1). *Physical Review Letters*. 1997;79(15):2851.
279. Carbon, Thermo Scientific XPS [Internet]. Thermo Fisher Scientific Inc.; 2013-2016. Available from: <http://xpssimplified.com/elements/carbon.php>.
280. Poole R, Kemeny P, Liesegang J, Jenkin J, Leckey R. High resolution photoelectron studies of the d bands of some metals. *Journal of Physics F: Metal Physics*. 1973;3(3):L46.
281. Tanaka K, Matsuzaki S, Toyoshima I. Photodecomposition of adsorbed methoxy species by UV light and formaldehyde adsorption on silicon (111) studied by XPS and UPS. *The Journal of Physical Chemistry*. 1993;97(21):5673-5677.
282. Vogel M, Kasigkeit C, Hirsch K, Langenberg A, Rittmann J, Zamudio-Bayer V, Kulesza A, Mitrić R, Möller T, Issendorff BV, Lau JT. 2 p core-level binding energies of size-selected free silicon clusters: Chemical shifts and cluster structure. *Physical Review B*. 2012;85(19):195454.
283. Kasigkeit C, Hirsch K, Langenberg A, Möller T, Probst Jr, Rittmann J, Vogel M, Wittich Jr, Zamudio-Bayer V, von Issendorff B, Lau JT. Higher ionization energies from sequential vacuum-ultraviolet multiphoton ionization of size-selected silicon cluster cations. *The Journal of Physical Chemistry C*. 2015;119(20):11148-52.

284. Silicon, Thermo Scientific XPS [Internet]. Thermo Fisher Scientific Inc.; 2013-2016. Available from:<http://xpssimplified.com/elements/silicon.php>.
285. Koç MM. Non contact atomic force microscopy investigation of silicon nanoparticles deposited on HOPG [PhD Thesis]. Department of Physics and Astronomy, University of Leicester.